[CONTROL OF THERMAL EXPANSION, BEHAVIOR ON COMPRESSION, AND GUEST LOADING IN FRAMEWORK MATERIALS]

A Dissertation
Presented to
The Academic Faculty

by

Samuel J. Baxter

In Partial Fulfillment
of the Requirements for the Degree
Doctor of Philosophy in the
School of Chemistry and Biochemistry

Georgia Institute of Technology
[AUGUST 2020]

CONTROL OF THERMAL EXPANSION, BEHAVIOR ON COMPRESSION, AND GUEST LOADING IN FRAMEWORK MATERIALS

Approved by:

Dr. Angus P. Wilkinson, Advisor
School of Chemistry and Biochemistry
School of Materials Science and Engineering
Georgia Institute of Technology

Dr. Younan Xia
School of Chemistry and Biochemistry
School of Biomedical Engineering
Georgia Institute of Technology

Dr. Henry La Pierre
School of Chemistry and Biochemistry
Georgia Institute of Technology

Dr. Christopher Jones
School of Chemical and Biomolecular Engineering
Georgia Institute of Technology

Dr. Z. John Zhang
School of Chemistry and Biochemistry
Georgia Institute of Technology

Date Approved: [04/30/2020]

ACKNOWLEDGEMENTS

Although this section appears first, it is often the final section written for a graduate thesis. The amount of encouragement, guidance, and support from both my fellow students and the faculty at Georgia Tech was enough to give me pause when trying to decide where to begin. My hopes for this section were to be succinct, but that is difficult when considering the amount of time others have put into my general wellbeing and the potential success of this thesis. Like many, maybe most, my time at Georgia Tech was not just fulfilling, but challenging and difficult. There were plenty of times where I wanted to give up early on, convinced that I could not handle this lifestyle. In truth, it is easy to forget that everyone is being challenged here, and almost nobody gets through without a few scrapes. Some of my closest friends helped me to remember this important fact. While writing this section I tried to be as inclusive as possible whilst still remaining succinct, my hopes were to not have forgotten anyone but I apologize if anyone was left out.

First and foremost I am thankful for my family and all of the support they have given me over the years. Lesie Baxter, Andrew Baxter, William (Bobo) Mcnay, Mary Mcnay, James Mcnay, Heather, Billy, Jack, and Lila were there for me through the years where I could barely move my arms without pain and the two major surgeries that followed. Every Sunday during our family coffee sessions this group of beloved individuals were consistently there for eachother and I am so thankful to be a part of this family. Most specifically I would like to thank the above and beyond effort of my mother, Leslie, and grandfather “Bobo” for talking me through my most difficult times. I would also like to thank the extended family that have made sure to keep in touch and encourage me over the

years including John & Jamie Waiveris and Rosie & Charlie Waiveris. Last but not least, I would like to thank my late father, Bruce Baxter, who unfortunately passed long before the writing of this thesis. The devotion he showed to his family's future while struggling with a fatal heart disease is a standard I can only hope to one day live up to.

I also owe my gratitude to the friends that have been there for me through thick and thin over the years. This endeavor would have been much more difficult without support from this ragtag group of misfits. Dylan Shands, Cem Digermenci, David Hamilton, Joe & Jacob Cauthen, Patrick Eaves, Giovanni DeLuca, Nathan Sims, Tim Gleeson, Andrew Chronic, and Geralt of Rivia. I would also like to give an extra special thanks to my girlfriend Joelle Zapotosky, who has shown me love and unwaivering patience through one of the most difficult periods of graduate school. She also makes the best pies (despite being allergic to gluton), which are necessary for peak performance during Fall semester.

Because my work at Sandia National Labs was such a large part of my thesis work, I am thrilled to acknowledge the support of my California family including Nicholas Burtch, Andreas Schneemann, Pavithra Wijeratne, Ruben Van de Viver, Matthias Jorgenson, and Sally Fromm.

Early on at Georgia Tech, I moved in with my good friend Jiyao Yu. Jiyao helped expand my perspective and was one of the first to share in the suffering that comes with the first year of graduate school. This first semester I made some of my closest friends that I hope to keep in touch with the rest of my life. Chris Kuehner has always been available to help with my struggles as a potentially misplaced organic TA or to encourage me to leave campus at just the right time to get indian food instead of spending another hour in

lab. Luis Manuel Aguirre Quintana could always be counted on through thick and thin and always took the time to ask how things were going. I am also pretty sure that I still owe him money from all the times he jumped at the opportunity to buy food for me or a group at lunch. Brandon Yik was another friend who had a significant impact on my outlook. Brandon truly cares about those he interacts with and is not shy when giving advice, an important quality these days. I would additionally like to acknowledge Marie-helen Tremblay, Claudia Montllor Albalate, Cole Stapleton, Dr. Henry La Pierre, Dr. Amanda Stephens, Dr. Kimberly Schurmeier, and Dr. Leighanne Gallington for their encouragement, friendship, and support throughout my work at Georgia Tech.

I considered the Molecular, Science, and Engineering building at Georgia Tech to be a second home over the past 4 years. This second home came with a second family, known as the Wilkinson group. I wish to express my deepest gratitude for the years of assistance and guidance provided by Dr. Angus Wilkinson. As a leader, he has helped me through some of the most complicated problems I have ever faced and made me far more confident than I deserve to be through his guidance and encouragement. I would also like to acknowledge Brett Hester, who not only provided advice and expertise for almost three years but also provided some very useful figures for this thesis introduction. I would also like to thank Anthony Lloyd II, Breauna Wright, and Shangya Ma for being part of such a significant part of my life at Georgia Tech.

As a final note I would like to thank my committee members for the opportunity to defend this thesis and for the help and guidance they gave throughout my years at Georgia Tech.

Table of Contents

LIST OF TABLES

LIST OF FIGURES

LIST OF SYMBOLS AND ABBREVIATIONS

(NTE) NEGATIVE THERMAL EXPANSION

(PTE) POSITIVE THERMAL EXPANSION

(ZTE) ZERO THERMAL EXPANSION

(MOF) METAL ORGANIC FRAMEWORK

(QHO) QUANTUM HARMONIC OSCILLATOR

(CTE) COEFFICIENT OF THERMAL EXPANSION

(RUM) RIGID UNIT MODE

(PDF) PAIR-DISTRIBUTION FUNCTION

(DAC) DIAMOND ANVIL CELL

(ADP) ATOMIC DISPLACEMENT PARAMETER

(EOS) EQUATION OF STATE

SUMMARY

Each chapter in this thesis focuses on open framework systems found to display anomalous properties relating to their unique structures. The systems investigated were chosen for their open framework form, flexibility, and modifiability. These three key factors can allow for the structural control necessary for tunable thermal expansion and phase stability to be achieved in materials that inherently display large negative thermal expansion (NTE). Concepts necessary for the understanding of thermal expansion research will be covered in sufficient detail as well as examples from the different materials classes being investigated in this thesis. Definitions, mechanisms, applications, and real examples of thermal expansion, behavior upon compression, and composite research are reviewed in chapter 1.

Chapters 2, 3 and 4 examine the control of thermal expansion in ReO_3-type metal fluoride systems. ReO_3-type materials exhibit the simplest crystalline structure found to exhibit strong NTE. Because of its inherent simplicity, modification and analysis of these structures is relatively straightforward. This being the case, the coefficients of thermal expansion (CTEs) of ReO_3-type materials have been found to range from strongly positive to strongly negative. This fact reveals deeper complications involving the ionicity, bond strength, and general flexibility of these structures that lead to diverse thermodynamic behavior. In these chapters certain metal fluorides were chosen that have previously been found to exhibit both structural tunability and large NTE. The structural tunability allows for certain flexible structural components to be replaced by more rigid counterparts (systematically) to control the properties related directly to flexibility, such as thermal

behavior. Specifically, $Mg_{1-x}Zr_{1+x}F_{6+2x}$ and $Sc_{1-x}Zr_xF_{3+x}$ solid solutions were found to display tunable thermal expansion and phase stability upon the introduction of edge-sharing polyhedra within their structures. The introduction of this specific defect is mediated by the metal ratio within these systems. The use of defects to control thermodynamic behavior is a common theme in this thesis, but the work in chapter 4 shows that the techniques involved in behavioral control must be modified specifically for each system they are being applied to. In chapter 4, $Ca[Zr^{(IV)}_{1-x}Nb^{(V)}_x]F_{6+x}$ solid solutions are investigated using the same general technique applied successfully to the materials of chapters 1 and 2. Interestingly, it is shown that this specific variation of the technique does not appear to introduce the same defect that was found in the previous two systems. This new defect introduced leads to changes in the structural behavior that are non-ideal for application but demonstrates the importance of developing a diverse toolkit when approaching thermodynamic behavioral modification.

Chapters 5 and 6 investigate an even broader range of thermal behavior control techniques, which span from structural scaffold modification to guest inclusion. A comparison of how effective these techniques are for a diverse set of metal organic frameworks (MOFs) is drawn and previously unexplored routes of structural control are introduced for these systems. While some techniques facilitated direct tunability of thermal expansion from positive to negative within a measured temperature range, others simply showed non-systematic changes in the thermal expansion or just the controlled inhibition of pronounced NTE. Insights into the origin of these differences in thermal behavior are obtained through an in-depth analysis of synchrotron-radiation total scattering and diffraction experiments, as well as complementary molecular simulations performed by

collaborators. The implications of these works on the prospects for MOFs as an emergent material class for NTE-related applications are also discussed.

While several metal–organic frameworks are known to display negative thermal expansion, there have been no reports where the thermal expansion of a MOF has been tuned continuously from negative to positive through the formation of single-phase solid solutions. In the system Zn-DMOF-TMx, Zn2[(bdc)2–2x(TM-bdc)2x][dabco], the introduction of increasing amounts of TM-bdc, with four methyl groups decorating the benzene dicarboxylate linker, leads to a smooth transition from negative to positive thermal expansion in the a–b plane of this tetragonal material. The temperature at which zero thermal expansion occurs evolves from ∼186 K for the Zn-DMOF parent structure (x = 0) to ∼325 K for Zn-DMOF-TM (x = 1.0). The formation of mixed linker solid solutions is likely a general strategy for the control of thermal expansion in MOFs and its prospects are also discussed.

Finally, Chapter 7 expands upon the recent discovery of a new class of hybrid ReO_3-type fluoride perovskites that contain a neutral molecule (He) in the perovskite A-site. These experiments involve taking a prototypical NTE metal fluoride, ScF_3, and exposing it to high pressure helium at high temperature. The pore aperture and activation barriers for diffusion are compared to that of the first known hybrid fluoride perovskite with the formula [He]$CaZrF_6$. Evidence for the inclusion of He in ScF_3 is reviewed and future directions for the project are discussed.

INTRODUCTION

1.1 Thermal Expansion

1.1.1 Significance and Applications

Advanced development of industrial technology has led to increasingly strong demands for control of thermal expansion. This is because a material's response to heating or cooling can have drastic effects on its dimensional stability in the face of large temperature variations. Understanding the foundational physics that underpin this response is necessary to develop control of a material's response to its changing thermal environment. Generally, most materials experience modest Positive Thermal Expansion (PTE) due to increasing anharmonic vibrational amplitudes of the constituent atoms, ions, or molecules (discussed further in section 1.1.3). On a macroscopic level, this effect manifests as an overall increase in the dimensions or volume of a material. The converse, or contraction upon heating, is known as Negative Thermal Expansion (NTE). Zero Thermal Expansion (ZTE) and NTE are considered anomalous and have been extensively studied due to their potential use in applications that are sensitive to the inherent drawbacks of PTE. Such applications include but are certainly not limited to, heat shields, high temperature electronics (fuel cells, thermoelectrics, etc.), precision components, and optics.

All ZTE and NTE materials will eventually become PTE materials at high enough temperatures due to the increasing influence of anharmonic vibrations. Progressing the understanding of these phenomena is of interest because of fundamental curiosities and

more practical application-based reasons, and a substantial number of reviews on these topics have been published. [1-7]

In addition to the appreciation of ZTE and NTE materials, understanding the various degrees and influence of PTE in more typical functional materials is also necessary. PTE materials are commonly found in close contact with one another, which can be an issue if they have significantly different magnitudes of thermal expansion (thermal expansion mismatch). Their inherent expansion against one another as temperature is varied can create interfacial stresses that accumulate and can lead to structural degradation, cracking, and eventually material failure. The various impacts of hydrostatic stress on materials and their thermal expansion will be discussed in more detail in section 1.4.2. One way of addressing this issue is through the formation of thermal expansion composites that incorporate an NTE material in an attempt to neutralize the overall PTE of a functional material. By manipulating the structure and amount of the NTE component, its ability to bind with the PTE matrix, and control over the thermal expansion of the composite material can be achieved while maintaining or potentially improving upon the strength, structural integrity, and other original properties of the functional material. Controlled thermal expansion composites will be discussed further in section 1.2.1. Materials systems in which the structure of a parent NTE material can be systematically modified/tuned to yield ZTE at various temperatures within a temperature window allow for another method of thermal expansion control. One way of achieving this is by introducing systematic deviations from the original NTE structure and in turn deviating from the thermal behavior of that parent structure. This can take the form of introducing a new structural component or modifying

an existing component to methodically inhibit the mechanics that lead to NTE (section 1.2.2).

In this thesis, along with other related investigations, advances specific to the design specifications, synthesis, characterization, and application of high magnitude NTE materials and materials that exhibit tunable thermal expansion will be covered. This work focuses on ReO_3-type metal fluorides and Metal Organic Frameworks (MOFs). Specifics of materials classes will be discussed later in more detail (section 1.2.3).

1.1.2 Thermal Expansion in Solid Materials

As mentioned, the ubiquitous form of thermal expansion is PTE. This is due to a variety of different structural mechanisms that are all occurring at once in a material. As will be discussed later, each individual contribution to a material's thermal expansion must be summed in order to achieve a representation of the overall thermal expansion. On the most fundamental level, PTE can be attributed primarily to the presence of anharmonic vibrations in between atoms and along bond axes. This major contribution to all known molecules and materials is known as bond anharmonicity.

1.1.2.1 Lattice Dynamics and Bond Anharmonicity

Over the past century, several different models have attempted to describe the vibrational motion atoms experience when bonded to one another. One of the earlier models was that of a quantum harmonic oscillator (QHO). The QHO was an approximation representing the quantum mechanical analog of the classical harmonic oscillator. Using this model, a harmonic potential can be found within the vicinity of a stable equilibrium point, such as

the center of a purely covalent bond in a diatomic molecule. This assumption leads to a potential energy curve with a parabolic shape, where the interatomic distance representing the lowest energy point is found to be the average bond distance. In this case, the two atoms have a restoring force equivalent to their displacement, and there is no increase in the average bond length with temperature. This curve representing the QHO model is shown below in figure 1.1 in red.

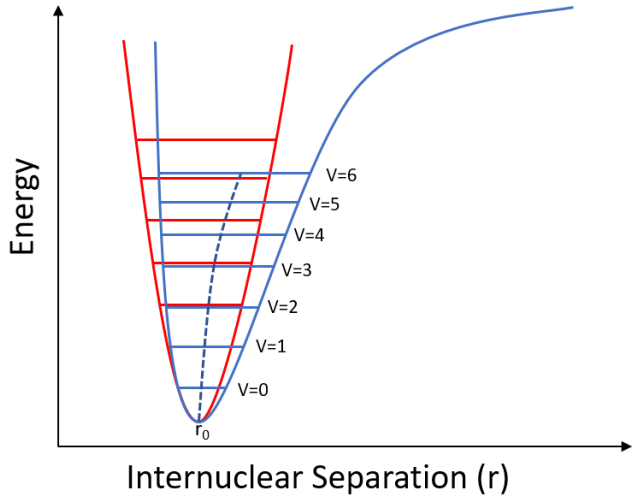

Figure 1.1: Morse potential (blue) vs. QHO potential (red) for a diatomic molecule in vacuum.

An improvement upon the QHO model is that of the Morse potential, shown in blue in figure 1.1. The Morse potential accounts for anharmonic perturbations of the QHO model and includes a dissociation term to represent eventual bond breaking. In this case, the restoring force of the two objects is no longer proportional to the displacement. The anharmonicity of this vibrational mode is due to the energetic barrier the two atoms will experience as they approach one another due to interactions of their electron clouds and Pauli's exclusion principle. As higher energy vibrational modes become occupied the

average length (r_o) of the bond will increase, in contrast with the QHO model. The increase in energy of this system can be supplied as thermal energy from the molecule's environment. So, as the temperature of this system is increased the average bond length will increase. In more complex systems, the thermal expansion of all bonds become interdependent on one another. This is considered along with changes in bond angles and the population of the entire phonon density of states when analysing a solid's thermal expansion.

Very strong bonds might begin to approach ZTE as the potential energy well narrows but they will never contract upon heating unless they are coupled with some larger scale structural changes. Therefore, for a solid to exhibit NTE, superstructural mechanisms beyond changes in bond length must contribute to the overall changes in dimensionality.

1.1.2.2 Phonon Modes, Grüneisen Theory, and Quantifying Thermal Expansion

Just like the beforementioned diatomic molecule, crystalline solids experience vibrations at finite temperatures. Vibrations take the form of collective excitations that move through the elastic crystal system. Phonons can be classified as different types or 'modes' of vibration and individual phonon modes are not independent from each other within a crystal system. At any given point, there are many different phonon modes activated at once within a crystal system. Some of these modes resemble the longitudinal vibrations that result from bond anharmonicity, while others involve larger groups of atoms that displace atoms in directions nonparallel with interatomic bonds. In order to deduce the overall thermal expansion of a complex solid with multiple phonon modes existing at once, their contributions must be combined to give an overall coefficient of thermal expansion

(CTE) for a solid. This type of analysis has roots in Grüneisen's work on thermal expansion, dating back to the early 1920's.[8-10] Grüneisen showed that the volume dependence of a phonon mode's frequency corresponds to a dimensionless term, aptly named the thermodynamic Grüneisen parameter (γ_T). This parameter represents the contribution of various phonon modes to the overall volumetric coefficient of thermal expansion (α_v).

$$\alpha_V = \gamma_T \frac{C_V}{K_T V} \tag{1.1}$$

The thermal and mechanical properties that join with γ to calculate α_v are the solids specific heat at constant volume (C_v), isothermal bulk modulus (see section 1.4.2), and volume (V). Because the specific heat capacity of a material is strongly dependent on temperature and volumetric thermal expansion is proportional to specific heat capacity, equation 1.1 implies that thermal expansion will change with temperature, as it is seen to. Additionally, because V, C_V, and K_T are all necessarily positive values, γ is what dictates the sign (+/-) of thermal expansion. For the thermodynamic Grüneisen parameter to represent the combination of all phonons present at a specific temperature, it must have a characteristic contribution from each individual phonon in a given system. These individual contributions are known as the mode Grüneisen parameters, denoted γ_i. γ_T represents the average of all mode Grüneisen parameters (Equation 1.2) and c_i is the weighted contribution of each vibrational mode to the specific heat.

$$\gamma_T = \frac{\boldsymbol{\Sigma}\gamma_i c_i}{\boldsymbol{\Sigma} c_i} \quad \textbf{(1.2)}$$

Going one step further, the Grüneisen parameter can also be described in terms of each vibrational modes change in frequency (v) with respect to a change in volume (V) of the material (Equation 1.3).

$$\gamma_i = \frac{-\boldsymbol{d}(\boldsymbol{ln}\,\nu)}{\boldsymbol{d}(\boldsymbol{ln}\,\boldsymbol{V})} \quad \textbf{(1.3)}$$

Essentially, if there is an increase in volume with a decrease in frequency, it will be positive whereas if there is a decrease in volume associated with a decrease in frequency the Grüneisen parameter will be negative. The physical meaning of the parameter can be coupled with a microphysics model for the vibrating atoms within a crystal system. If an atom is displaced from its equilibrium position and the restoring force acting on that atom is linear in the atom's displacement, the frequencies of the individual phonons will not depend on the volume of the crystal or on the presence of other phonons. If the restoring force is non-linear in the displacement, then the phonon frequencies change with volume. The phonon modes that give rise to negative Grüneisen parameters can be preferentially excited if they are of lower energy than the interatomic longitudinal vibrations that lie along bond axes. This can lead to strong negative contributions to the CTE. Thus, it is seen theoretically that for a material to show pronounced NTE, in the absence of a phase

transition, a material should have discrete low energy vibrational modes that soften upon decrease in volume.[27]

Thermal expansion can be quantified using the previously mentioned CTE. This coefficient can represent a linear change in unit cell dimensions or a true/averaged volumetric change. The linear CTE (equation 1) can correspond to a specific change in length of a unit cell edge, or an averaged change in length for all three-unit cell edges. The linear CTE will most often be different for each unit cell edge in non-cubic materials. In equation 1.4a, L represents the final lattice constant length, L_0 represents the initial lattice constant length, T represents the final temperature, and T_0 represents the initial temperature. The volumetric CTE can be expressed as the average cubed unit cell edge length or in terms of the volumetric heat capacity of a material (equation 1.4b).

$$a)\ \alpha_L = \frac{d(\ln L)}{dT} = \frac{1}{L}\frac{dL}{dT}\ ,\ b)\ \alpha_V = \frac{d(\ln V)}{dT} = \frac{1}{V}\frac{dV}{dT} \qquad \textbf{(1.4)}$$

Because the elasticity and heat capacity of different solid materials varies widely, so does the CTE. The volumetric CTE of solids can vary from strongly negative (>-100 ppm/K) in the Metal Organic Framework (MOF) known as UiO-66(Hf)[11] to strongly positive (230 ppm/K at300 K) in isotropic polyethylene.[12] Because the CTE strongly depends on temperature, comparing the thermal expansion of vastly different materials over wide temperature ranges becomes complicated because of the temperature limits of each material's phase stability. However, materials are often classified based on their linear CTE near room temperature.[6]

High Expansion Group, $\alpha > 8$ ppm/K

Intermediate Positive Group, $2 < \alpha < 8$ ppm/K

Very Low Expansion Group, $0 < \alpha < 2$ ppm/K

Intermediate Negative Group, $-2 > \alpha > -8$ ppm/K

High Negative Group, $\alpha < -8$ ppm/K

1.1.3 Diffraction Analysis

Thermal expansion can be analysed using a variety of different techniques depending on the phase, crystallinity, and amount of material under investigation. The scope of this introduction is limited to the study of solid crystalline materials. These materials can take the form of single crystals or powders, both of which are suitable for diffraction analysis. Most materials in this thesis are crystalline powders. Therefore, the primary methods of studying the thermal expansion of these materials will be powder diffraction. Other related methods such as dilatometry and microscopic analysis were not performed for the included materials and thus will not be discussed.

Diffraction is a phenomenon associated with the spreading of waves around particles. This takes place with sound waves, electromagnetic radiation (x-rays, gamma rays, etc), and small moving particles (electrons, neutrons, etc). When two waves interact or overlap with one another, they have the capability of reinforcing or inhibiting each other. This is can take the form of either constructive or destructive interference where the waves will fortify or diminish one another, respectively. In a typical powder diffraction experiment,

scattering from atoms that end up in constructive interference form the peaks of a diffraction pattern. Each peak can be related back to the specific lattice planes associated with the diffraction maxima using Miller indices. Using this phenomenon, along with Bragg's law of diffraction (equation 1.6), reliable lattice parameters, atomic positions, and CTEs can be obtained. In this equation, λ represents the wavelength of radiation, "d" represents the spacing in between lattice planes, and Θ represents half the angle between the incident radiation beam and the elastically scattered beams.

$$n\lambda = 2dsin\theta \quad \textbf{(1.5)}$$

Using a typical diffraction setup, the intensity (y-axis) of each peak will be compared to a 2Θ value (x-axis) representing the angle between the incident and scattered beams on a typical flat plate powder diffraction setup.

This thesis will involve primarily x-ray and neutron diffraction. Both can contribute to the investigation of more complex materials because of their different sensitivities. X-rays scatter off electron clouds, making them more sensitive to less absorbing, heavier elements. Neutron diffraction scatters off nuclei and will be more sensitive to the lighter elements. When used together, they can elucidate both the lighter and heavier components of a crystal structure. Each method will also have specific examples where they do not contribute much to the analysis of specific atoms or specific structure types. For example, X-ray cannot detect hydrogen atoms very well because of their small single electron clouds.

X-ray scattering can also come from synchrotron radiation sources, which was an invaluable technique for the work in this thesis. Synchrotron x-rays are produced as electrons are accelerated around a 'synchrotron loop'. Within this loop, the electrons move within a vacuum, and powerful magnets are used to change their course within this vacuum. As the electrons change direction, energy is released in the form of radiation that can be collected and processed in different ways specific to the desired experimental setup.

1.2 Negative Thermal Expansion

1.2.1 Applications

As mentioned previously, NTE materials have the potential for significant and broad application in industry. In principle, they can be used in composites where they can compensate for the positive thermal expansion of typical materials, or can have their thermal expansion tuned to 'near zero' over specific temperature regions where no expansion is desired for specific applications.[10,13,14] When picking a NTE material to be blended into a composite, certain specifications must be met in order for the final 2-component material to be functional. Specifically, the two materials often require some affinity at their interfaces, the size and shape of the imbedded NTE particles must also be uniformly distributed within the PTE matrix, and the difference in CTEs of the components must be considered because thermal expansion mismatch can lead to increased stress at the material interfaces. These stresses can accumulate and contribute to both sustained or deleterious phase transitions, similar to what materials may experience within a high-pressure environment (discussed further in section 1.4).[15-18] These problems can be avoided when the CTE of a single material can be tuned to zero at different temperatures. Because

of this, a significant thrust has been made to find NTE materials in which the structure can be modified to systemically modify the phonons that lead to contraction upon heating and thus, control thermal expansion. This will be discussed further in section 1.3.1.

1.2.2 Mechanisms

NTE has been known for almost 100 years, and for almost as long the theory behind the mechanisms leading to this phenomenon have been investigated. At this point, there are several related but distinct groups of NTE materials separated by their primary mechanism of expansion.[19] Typically, this can be broken into two groups. Conventional NTE arises from flexible framework materials or anisotropic thermal expansion where large PTE in one direction inevitably leads to the contraction of another direction. The other family of NTE materials relies on phase transitions, and the mechanisms found in this group are quite diverse. The phase transition mechanisms include ferroelectric transitions[26,32], magnetic transitions[20-23], and charge transfer transitions.[19] The materials to be discussed in this thesis experience their NTE due to the presence of low frequency phonon modes.

1.2.2.1 Low Energy Phonon Modes

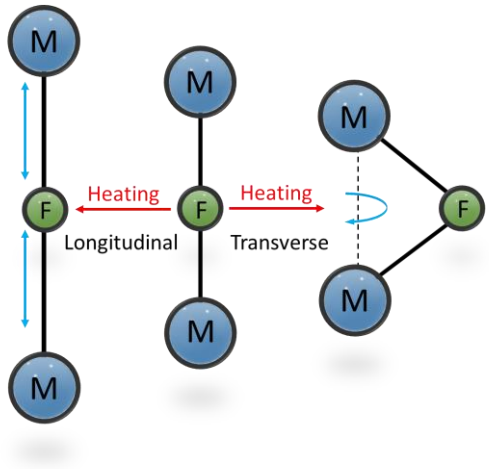

Figure 1.2: Comparison between longitudinal and transverse thermal vibrations that occur on heating.

Section 1.1 introduced that idea that bond lengths typically expand upon heating due to the activation of 'longitudinal' vibrational modes (illustrated in figure 1.2). This phenomenon is true for all known materials and molecules. Therefore, for a material to contract upon heating, other superstructural mechanisms must be present. The primary mechanism for framework materials involves transverse thermal vibrations that take the form of low energy phonons in the structure. These vibrations will displace atoms from their primary bond axis, in some cases leading to a contraction between two points within a unit cell. This can be seen for M-F-M bonds in ReO_3-type metal fluorides (discussed in more detail in section 1.2.3.5). These transverse vibrations typically become activated at lower energies which in some cases allows them to dominate the Grüneisen parameter, leading to low PTE and sometimes NTE. This is also why some materials, like ReO_3, only exhibit significant NTE at very low temperatures.

These transverse vibrations are most common in flexible, insulating, open framework structures, like ScF_3.[24,25] In materials that are found to exhibit open framework structures containing 'near-rigid' polyhedra these vibrational modes are found to lead to coupled rocking of the polyhedra (figure 1.3). This is known as a Rigid Unit Mode (RUM).

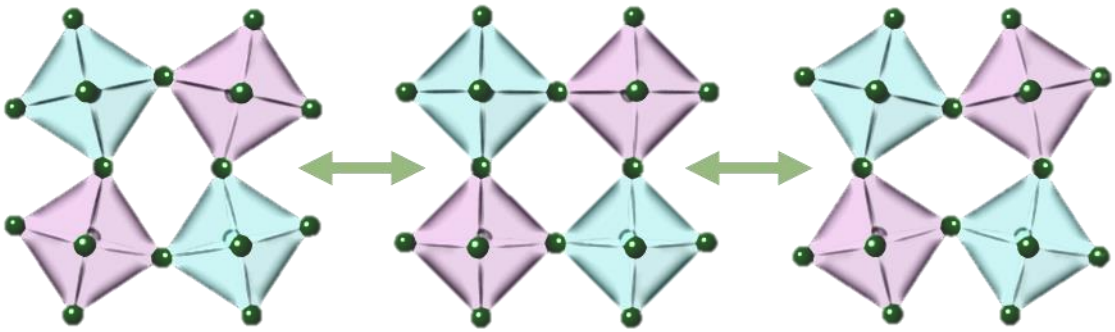

Figure 1.3: Example of transverse thermal vibrations leading to the formation of RUMs in a ReO_3-type structure.

Within this model, the energetic barrier to tilting the polyhedra is less than that of distorting the polyhedra. This contributes to a contraction of the unit cell which outweighs that of the expanding bonds within the polyhedra. The simplicity of this model has been challenged to expand beyond purely rigid polyhedra and now involves more complex models using scissor-type vibrational modes that involve distortions of the polyhedra.[3] Materials found to exhibit low energy phonon mode mediated NTE include oxides[26,27], fluorides[25,28-32], cyanides[33-37], phosphates[38], and MOFs[39,40].

1.2.2.2 Ferroelectric Transitions

Ferroelectrics are crystalline solids that undergo spontaneous electrical polarizations, mediated by the application of an external electric field. $PbTiO_3$[41] and and tungsten bronzes[42] are some ferroelectrics that exhibit NTE because of this phenomenon. In these

materials the anharmonic phonons that contribute to PTE are competing with ferroelectric ordering, which contributes to NTE. In these, and other related ferroelectrics, the primary cations are displaced during polarization. Displacement from the center of a polyhedra generates a dipole moment and distorts the polyhedra leading to an increase in size. Because the polarization happens below a critical temperature, this enlarging effect happens upon cooling (NTE). Because this polarization is often associated with a phase transition, the temperature range over which contraction occurs is typically narrow, but some modifications to the structure can impede the rate of transition and effectively increase the temperature window over which it occurs.

1.2.2.3 Charge Transfer

This mechanism involves charge transfer between atoms within a bonded network. In the most basic sense, electron-accepting species will enlarge and electron-donating species will shrink. The amount of expansion/contraction of an atom will depend on it's identity (electronic configuration) and pre/post charge states. For there to be an overall contraction in the unit cell of a material due to this effect, the contraction of the donating species must be larger in magnitude than that of the accepting species while still compensating for the increase in volume from anharmonic vibrations. One example of charge-transfer mediated NTE is that of the double-perovskite $LaCu_3Fe_4O_{12}$.[43,44] The formal valence state of the components of this material are $La^{3+}Cu_3^{3+}Fe_4^{3+}O12$ under ambient conditions. Upon heating above 393 K, charge transfer occurs between Cu^{3+} and Fe^{3+} which results in the formation of the 'high temperature' phase $La^{3+}Cu_3^{2+}Fe_4^{3.75+}O_{12}$. This leads to an overall contraction of about 1% of the unit cell volume from a drastic shortening of Fe-O bonds upon charge transfer. Because this transition is first order and discontinuous, it would be

difficult to apply this material within a typical NTE application because the change in volume is very large with an immediate onset. However, replacing Sr^{2+} with La^{3+} afforded a new material that exhibited a linear CTE of -22.6 ppm/K between 200 and 230 K. Other related solid solutions such as $LaCu_3Fe_{4-x}Mn_xO_{12}$ involved systematic modifications to the structure, which allowed for tuning of the properties to fit a desired thermal expansion behavior between two parent structures. This type of systematic structural modification will be discussed further in section 1.3.

1.2.2.4 Magnetic Transitions

Transitions from paramagnetic to ferromagnetic (and vice versa) phases can in some cases lead to contraction of the unit cell with an increase in temperature. This is known as a magnetovolume effect. It occurs due to the onset and movement of magnetic moments as the temperature changes. Theoretically, an increase in volume should suppress the overlap of electronic orbitals and reduce the overall width of electronic bands in a solid. This narrowing of the bandwidth can increase the density of states at the Fermi energy, which fortifies magnetism.[13] Anti-perovskite manganese compounds with formula Mn_3XN (X=Ga, Al, Zn, Cu, or Sn) have attracted a significant amount of attention for their interesting physical properties over the past two decades. Little of this attention was because of their thermal expansion behavior, initially. Upon further investigation, it was found that when Mn_3ZnN was doped with different elements, solid solutions could be formed that exhibited varying amounts of the magnetovolume effect. Specifically, large volumetric NTE (-81 ppm/K) was found in $Mn_3Zn_{0.5}Ag_{0.5}N$ over a ΔT of 18 K and $Mn_3Zn_{0.5}Sn_{0.5}N$ exhibited -19 ppm/K over a ΔT of 60 K.[45]

1.2.3 Examples

The primary NTE material classes will be reviewed in the following section. Understanding the different but related mechanisms, magnitudes, and temperature ranges of these different materials contributes to the development of new materials, but also helps to interpret the progressive research in the less studied groups of materials (in terms of thermal expansion), such as ReO_3-type fluorides and MOFs.

1.2.3.1 Zeolites and Other Metal Oxides

Out of all the classes of NTE materials, metal oxides have been the most rigorously investigated. Many common metal oxides display open framework structures and involve corner linked octahedra and tetrahedra that are susceptible to transverse thermal vibrations. Zeolites, which are composed of silica and alumina tetrahedra have shown NTE that is believed to result from cooperative tilts of these polyhedra through the activation of low energy phonon modes. Early aluminosilicates (and related materials) like β-eucryptite ($LiAlSiO_4$)[46], cordierite ($Mg_2Al_4Si_5O_8$)[47-49], Chabazite[50], siliceous faujasite[51], and $AlPO_4$-17[52] were found to exhibit NTE by various groups over the last 50 years. Some of these materials, such as cordierite found use in early catalytic converters, interior walls of high-temperature furnaces, and in industrial heat exchangers.[53] One of the less attractive qualities of some of these earlier discoveries were that the majority of them displayed either low magnitude or anisotropic NTE. Anisotropic thermal expansion can lead to many of the thermal stress issues discussed earlier.

Of all metal oxides found to contract upon heating, ZrW_2O_8 has become the most discussed and investigated for its thermal expansion. This material was introduced in the late 1950's

by Graham et al[54] and initially studied for its thermal expansion capabilities in the late 1960's. This work was done without knowing its crystal structure, however. In 1995 and 1996, the crystal structure of ZrW_2O_8 was determined and the correlation between this structure and its large isotropic NTE was elucidated by Auray and Sleight, respectively.[55,56] The structure of ZrW_2O_8 contains both octahedra (ZrO_6) and tetrahedra (WO_4) that are bound at their corners, except for one terminal oxygen on each tetrahedra. Phonon density of states measurements and calculations show negative contributions to the materials thermal expansion from low energy phonon modes with negative Grüneisen parameters.[7] The linear thermal expansion was found to be -9.1 ppm/K in the α phase (below 350 K), and -5 ppm/K in the β phase that appears at 450 K. This transition is described as an order-disorder phase transition between two cubic phases involving a disordering of oxygen at higher temperatures.

As the research progressed, it was found that substitutions to both metal sites in the ZrW_2O_8 family could be made. Through this, related materials such as HfW_2O_8, $ZrMo_2O_8$, $HfMo_2O_8$, and $ZrMoWO_8$ were synthesized and studied.[57,58] These substitutions led to minimal changes in the thermal expansion coefficients, however, the Mo species maintained a single cubic phase Pa-3 from 200 to 600 K, which is about a 150 K increase from the Zr analog's phase transition. Later, increasing interest led to the investigation of more AM_2O_8, AM_2O_7, $A_2M_3O_{12}$, AMO_5, and M_2O species. Solid solutions related to this family of materials will be discussed later in section 1.3.2.

Of the NTE metal oxides, ReO_3 is possible the most related to the NTE metal fluorides discussed throughout this work. Pristine ReO_3 contains only corner-sharing octahedra in a primitive cubic unit cell. The simplicity of this structure has made it useful for describing

the RUMs that are believed to occur in a wide array of open framework NTE materials composed purely of polyhedral units. ReO_3, however, displays quite complex thermal expansion. In the typical powder synthesis, it only exhibits modest NTE at very low temperatures, below 200 K, and again in the range of 600-700 K.[59] The changes in thermal expansion behavior as temperature increases have been attributed to large anisotropic thermal parameters of the oxygen atoms. Different average magnitudes of thermal expansion and different thermal expansion crossover temperatures have been reached using different synthetic techniques.[27] The differences in thermal behavior are attributed to structural defects involving the static disorder of oxygen. Several isostructural oxyfluorides and fluorides display low and negative thermal expansion, the differences in thermal expansion between these materials and the original ReO_3 have been investigated.[24,60]

1.2.3.2 Prussian Blue Analogs and Other Metal Cyanides

The first metal cyanide found to display NTE was $Zn(CN)_2$ in 1997.[61] Much like the silicates, this material is bound together through corner sharing tetrahedra but utilizes the diatomic cyanide linker as the bridging component instead of oxygen. The greater flexibility and range of motion afforded using a diatomic linker yielded higher magnitudes of NTE than most oxides (α_v = -59 ppm/K below 180 K). This large magnitude NTE is attributed to the transverse motion of the CN atoms, like the transverse motion of oxygen in the metal oxides or fluoride in the metal fluorides.[33,62] Substitutions to this structure involving transition metals such as $Cd(CN)_2$ have also shown large magnitude volumetric NTE (-61.2 ppm/K). This system is normally doubly interpenetrated, but clathrate models show the possibility for substituting one of the interpenetrated frameworks with molecular guests that can be subsequently removed to form the non-interpenetrated structure. This

model was applied to $Cd(CN)_2 \cdot CCl_4$, which showed even higher magnitude volumetric NTE (-100 ppm/K, 170-375 K) upon desorption of CCl_4. These high magnitudes of NTE made the metal cyanides the NTE record holders at the time they were discovered. Other related metal cyanides known as Prussian Blue Analogs (PBAs) take on the formula $M_y[M'(CN)_6]$ where M and M' are transition metals. These materials exhibit a rock-salt ordered ReO_3-type structure (discussed further in section 1.2.3.5) constructed from cyanide (CN^-) ligands connecting together octahedrally coordinated M and M' nodes by their corners. Several different transition metal combinations have been explored.[63] $Zn_3[Fe(CN)_6]_2$, $Fe_3[Co(CN)_6]_2$, and $Co_3[Co(CN)_6]_2$ were found to display very high magnitudes of NTE (α_l = -44 ppm/K) with $Mn_3[Co(CN)_6]_2$ being the highest (α_l = -48 ppm/K).[64,65]

1.2.3.3 Metal Trifluorides (MF_3)

A significant amount of work has been done on a class of fluorides known as ReO_3-type fluorides. This family of materials are cubic and made up of corner sharing octahedra, and a fair number have been found to display NTE due to the inherent flexibility of this structure type. Of these materials, the first discovered to display interesting thermal behaviour was ScF_3.[25] ScF_3 displayed strong NTE (α_l = -14 ppm/K from 60-110 K) which persisted (while slowly increasing) all the way out to ~1100 K (figure 1.4. This magnitude and range of NTE made it one of the most significant vibrationally driven NTE materials of its time. NTE in this material was originally attributed to the coupled rotations of near-rigid octahedra, but more recent studies argue that the vibrational modes of this family of fluorides might rely more on scissor-type vibrations or even what is described as a "guitar-string" effect.[24,66-68]

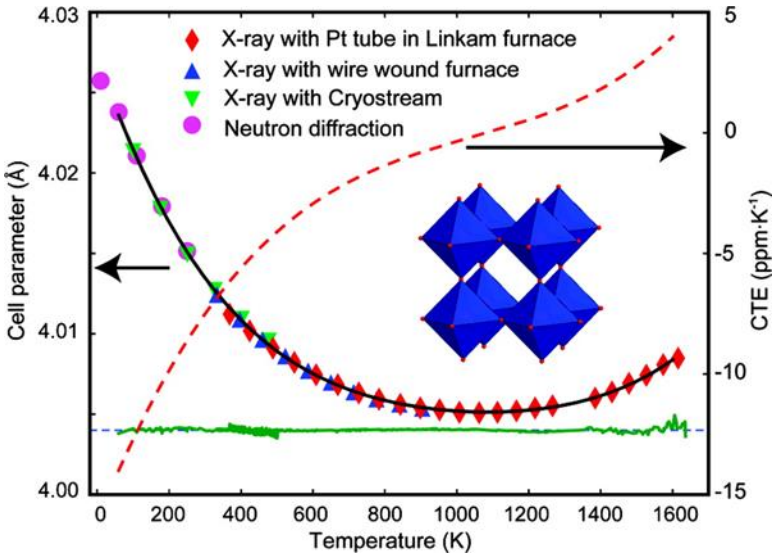

Figure 1.4: Unit cell constant and CTE for Pm-3m ScF_3 from 10-1700 K. [25] (Reprinted with permission from B. K. Greeve et al. *J. Am. Chem. Soc.*, 2010, *132(44)*, 15496-15498. Copyright 2010 American Chemical Society)

The crystal structures and thermal behaviour of many other metal trifluorides have been studied and found to exhibit the cubic ReO_3-type phase under ambient conditions and elevated temperatures.[32,69-74] Upon cooling however, a phase transition from the cubic phase to a "VF_3" rhombohedral phase is typically seen in this family.[75,76] This rhombohedral phase is expected to display drastically different properties than that of the cubic ReO_3-type phases. It is expected to display PTE as well as unique behaviour upon compression making it undesirable for both NTE and tuneable thermal expansion-based applications. The thermal expansion of other metal trifluorides has also been investigated, though none displayed a higher magnitude NTE than ScF_3.[32,77]

1.2.3.4 Mixed Metal Fluorides ($M^{II}M^{IV}F_6$)

Another related family of ReO_3-type fluorides are known as mixed-metal fluorides of the composition $M^{II}M^{IV}F_6$. These typically exhibit a double-ReO_3 Fm-3m structure, and like

the metal trifluorides, are susceptible to relatively low pressure phase transitions to a rhombohedral phase (R-3).[78-80] Originally, most of the work on this family of fluorides investigated syntheses, varied structure types, and magnetic properties.[81-84] More recently, $CaZrF_6$ and $CaNbF_6$ were found to exhibit strong NTE over a wide temperature range and exhibit their cubic structures down to low temperatures (< 10 K). [78-80,85] $MgZrF_6$ undergoes a structural phase transition to its rhombohedral phase at ~100 K and shows weaker magnitude NTE than its $CaM^{IV}F_6$ analogues. Another Mg analogue, $MgNbF_6$, transitioned to the rhombohedral phase at a much higher temperature (~280 K) and did not display NTE over the measured temperature range of 100 - 950 K. The larger difference in thermal behaviour from substituting Mg for Ca (as opposed to Zr for Nb) is attributed to the increased polarizability of Ca relative to Mg.[80] A large number of other ReO_3-type mixed metal fluorides are under investigation due to these prominent early findings. The respective phases of several mixed metal fluorides of the $M^{II}M^{IV}F_6$ variety are diagrammatically shown below in figure 1.5.

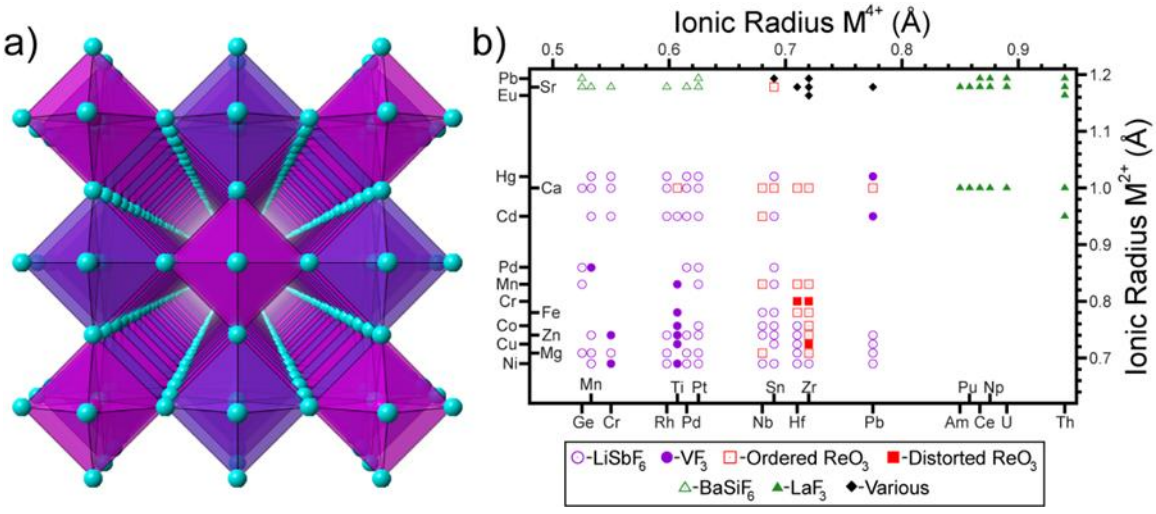

Figure 1.5: 1) Depiction of a cation ordered ReO_3-type mixed metal fluoride $M^{II}M^{IV}F_6$, and b) structure variations of mixed metal fluorides and their respective

known phases.[86](reproduced with permissions from Brett Hester *Doctoral Thesis: Negative Thermal Expansion, Behavior on Compression, and Other Anomalous Behaviors in ReO_3-Type Mixed Metal Fluorides, Georgia Tech, 2019, Atlanta, GA.)*

1.2.3.5 Fluoride-Excess ReO_3-type Materials ($M^{III}M^{IV}F_7$)

Similar to the ReO_3-type fluorides, materials could be made by substituting the M^{II} or the M^{IV} metal in mixed metal fluorides with a higher valent species, such as Yb^{III} in $YbZrF_7$. In some cases, depending on composition and synthetic conditions, cation ordered cubic phases can be formed for this material, which are analogous to the $M^{II}M^{IV}F_6$ cubic phases but with extra anions to compensate for the substitution of M^{II} with a higher valent metal. Theoretically, this type of material could also exist with a cation site deficiency, but early characterization by the Poulain group determined that charge balance was kept by introducing interstitial anions.[87] It was proposed that the excess fluoride leads to the formation of higher coordinate polyhedra that share edges. Ticknor *et al*.[88] further investigated the local structure using pair distribution functions, which validated the edge-sharing polyhedral model initially presented for this material. Thermal expansion analysis of $YbZrF_7$ showed ZTE at room temperature and low NTE below room temperature. The difference in thermal expansion of this material and the higher magnitude NTE $M^{II}M^{IV}F_6$ materials have been attributed to the presence of the edge sharing polyhedra, leading to research involving the formation of solid solutions between these two structure types in the hopes of achieving controllable thermal expansion within a single system.

1.2.3.6 MOFs

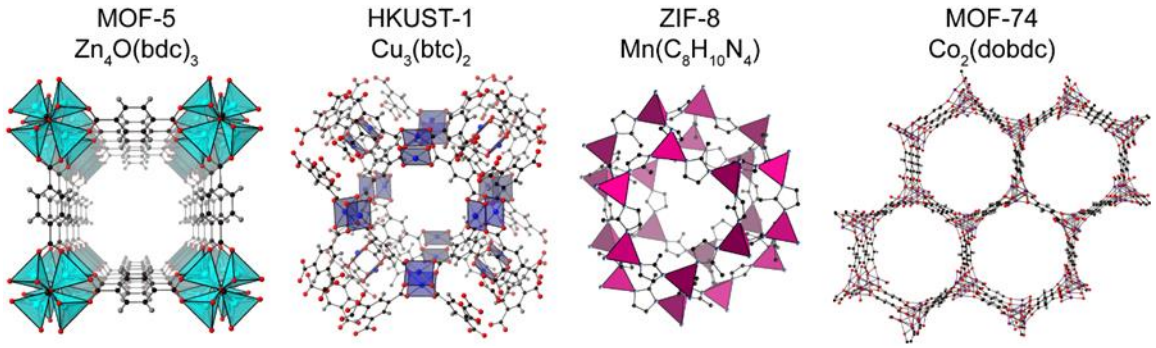

Figure 1.6: Examples of prototypical MOF topologies displaying unique pore shapes and sizes.[86](reproduced with permissions from Brett Hester Doctoral Thesis: Negative Thermal Expansion, Behavior on Compression, and Other Anomalous Behaviors in ReO3-Type Mixed Metal Fluorides, Georgia Tech, 2019, Atlanta, GA.)

MOFs have emerged as a unique and extensive class of porous crystalline materials that typically exhibit ultrahigh porosity and enormous internal surface areas that in some cases extend beyond 7000 m^2/g.[89] These properties, as well as the design flexibility attributed to the modular build-up of this class of materials, have led to a considerable amount of research in a number of different fields including clean energy, membranes, thin film devices, catalysis, thermoelectrics, and more recently in thermal expansion composites. By combining different aspects of organic and inorganic chemistry, MOFs can in some cases be 'tuned' to meet specific needs by modifying/functionalizing the two primary components of a MOF, namely, the metal node and the organic linker. The metal node can consist of a single ion or cluster of ions that take on a variety of different coordination environments similar to transition metal-based inorganic molecules. The organic linkers are multitopic, sometimes linking upwards of 4 metal nodes together at once, and bind strongly to the metal nodes typically through M-O, M-N, or M-S bonds. The sum of the contributions from both components and the possible synergistic interaction between them can potentially provide unmatched potential. Because of the vast amount of possible

coordination spheres and the availability of a wide array of potential organic linking components, an enormous number of unique topologies have been developed (figure 1.6). Early work by Yaghi[90] showed that MOFs could be modified while maintaining the same basic topology by using different organic linkers that bind in a similar fashion. These groups of topologically similar MOFs came to be known as isoreticular series and is one of the first examples of controlling the properties of MOFs by modifying a single component at a time.

In terms of thermal expansion, MOFs have been predicted to exhibit widespread NTE due to the inherent flexibility of their linking units and high porosity.[91] Initial molecular dynamics studies of some of the more prototypical MOFs in the IRMOF series such as IRMOF-1, IRMOF-10, and IRMOF-16 have shown that this family of MOFs all exhibit exceptionally large NTE. It was shown that longer, more flexible linkers, lead to larger unit cell volumes and higher magnitude NTE over the measured temperature range. IRMOF-1 was found to exhibit a volumetric CTE of -40 ppm/K from 80-500 K and IRMOF-16 displayed a volumetric CTE of -65 ppm/K over this same temperature range.[92] It was also determined that the variety of vibrational modes displayed in MOFs expected to significantly contribute to thermal expansion were more complex than those of other related framework materials such as zeolites or metal cyanides. Later, new topologies were found to exhibit strong NTE as well, such as HKUST-1 [$Cu_3(btc)_2$] and UiO-66(Zr) showing relatively high magnitude NTE (α_v = -12 ppm/K and α_v = -18 ppm/K, respectively) and UiO-66(Hf) showing colossal NTE (α_v = -100 ppm/K).[93,94] In some cases, the negative thermal expansion in MOFs can be accompanied by phase transitions, leading to strong discontinuities in the displayed thermal expansion behavior.[95] This is more common in

MOFs that display “breathing” modes that accompany pronounced topological flexibility. Although MOFs have been studied extensively for their ability to adsorb or filter guest species, deeper understanding and control of their thermal expansion remains comparatively unexplored.

1.3 Tunable Thermal Expansion

As previously mentioned, ZTE is emphasized in thermal expansion investigations due to its importance in practical applications. It is the only form of thermal expansion that does not experience the issues associated with changing volume, but it is rarely exhibited over a wide temperature range. Of the systems that claim to have control over thermal expansion, ZTE is often displayed as an average over a temperature range (which can be misleading) or at one specific temperature. There are a number of systems have been developed using charge-transfer, magnetovolume, and ferroelectric transitions that show tunability of this phenomenon, but the current works only pertain to investigations in which control of thermal expansion is achieved through inhibition/modification of a systems low energy phonon modes.

1.3.1 Applications

In any application of a functional material which undergoes large temperature variations, the thermal expansion of said material must be as low as possible to avoid the related stresses (thermal shock, interfacial stresses, etc). Ideally, ZTE is desirable, but often difficult to achieve without significant structure modification to an NTE material. An often-used example of near-ZTE materials is in catalytic converters. The performance of a catalyst carrier is reliant on its ability to remain pristine while being subjected to hot

corrosive exhaust fumes and while maintaining good thermal shock resistance. This is one of the principle advantages of ceramic catalyst supports that have low (< 2 ppm/K) thermal expansion and average thermal conductivity. Near-ZTE materials also find use in high precision instruments or high precision components of instruments that are subject to large temperature variations. Because each type of application that requires ZTE will have its own unique temperature region over which this trait is desired, systems that allow tuning of near-ZTE behavior over broad temperature ranges show more potential than those that only exhibit ZTE at one specific temperature. Of the material systems that have been found capable of this tuneability, few have found direct application. This calls for broader investigations into new material families to further the understanding of this phenomenon and to discover new systems that show potential for direct application of their tuneable thermal expansion.

1.3.2 Solid Solutions and Guest Inclusion

One primary method for the development of control of thermal expansion is through the synthesis of solid solutions. Solid solutions have been developed in numerous occasions for the purpose of achieving tuneable properties in solids, and it turns out some of these systems were inadvertently also tuning properties that they were not directly measuring, such as thermal expansion and behaviour upon compression. One mechanism of control in solid solutions involves the controlled introduction of structural defects as the composition of the solid solution is varied. As the ratio of charged components is varied, defects such as cation/anion vacancies/interstitials will form in order to maintain charge balance within the system. Whether or not a material exhibits one specific type of defect or a combination of types depends on what its lattice can accommodate both sterically and electronically.

Properties that are dependent on a defect free structure have been shown to deteriorate with the introduction of vacancies/interstitials. If the property can be varied systematically with defect amount while not exhibiting any major phase transitions that disrupt continuous behaviour, the property is considered tuneable.

Another method of controlling thermal expansion involves the infiltration of a porous system with guest molecules. This typically involves a steric inhibition of low energy vibrational modes that rely on the open pore space around linking unit by placing a large enough guest species within the pore. This can take the form of purposeful inclusion of the guest species in varying amounts to try and systematically tune properties, or can be a consequence of residual species in air or a reaction solvent becoming trapped in porous framework materials that haven't been properly activated.

1.3.2.1 Metal Oxides

A fair amount of work has previously been done on tuneable thermal expansion in oxide materials. $ZrV_{2-x}P_xO_7$ and $HfV_{2-x}P_xO_7$ solid solution systems developed by Sleight et al. were shown to supress an order-disorder phase transition.[96] Near the middle range (x ~ 0.3-0.5). Above 300 K, the phase transitions were entirely supressed. It has also been shown that doping ZrW_2O_8 with Mo can effectively lower the temperature of its order-disorder phase transition.[97] Tuneable thermal expansion has been achieved in $PbTi_{1-x}Fe_xO_3$[98], $Zr_{1-x}Sn_xMo_2O_8$[99], $(1-x-y)PbTiO_3$-xBi$(Ni_{1/2}Ti_{1/2})O_3$-yBiFeO$_3$[100], and $Pb_{1-x}Sr_xTiO_3$.[101] In cordierite $Mg_{2-x}Ca_xAl_4Si_5O_{18}$ solid solutions, increasing the ratio of Ca to Mg resulted in reductions of thermal expansion anisotropy by reducing the magnitude of thermal expansion in along both primary axes. In the $Zr_{1-x}Sn_xMo_2O_8$ system, the thermal expansion

was systematically varied from negative, to zero, to positive within a single-phase system from 12-500 K. Specifically the parent structures, $ZrMo_2O_8$ (x = 0) and $SnMo_2O_8$ (x = 1), were known to exhibit NTE and PTE respectively. The x = 1 material showed pure PTE across this temperature range, attributed to increased stiffness of the material via the formation of smaller SnO_6 octahedra (and decreased unit cell volume relative to $ZrMo_2O_8$) whose positive contribution to the overall thermal expansion overwhelmed that of the low energy phonon modes present. This method of tuning between two known structures that display vastly different thermal expansion behavior was an essential component in devising the experiments for chapters 2-6.

1.3.2.2 Metal Cyanides

The control of thermal expansion has also been investigated in metal cyanides. In a $YFe(CN)_6$ - based Prussian blue analog, the effects of guest incorporation on thermal expansion were probed. Notably, the presence of guest species (K^+ and H_2O) can substantially alter the volumetric thermal expansion within this system from -33 ppm/K to 42 ppm/K over the measured temperature range. Variable temperature diffraction analysis, x-ray absorption fine structure analysis, and DFT calculations indicate the inhibition of transverse thermal vibrations within this system – leading to the dampening of NTE vibrational modes. Even more interesting, is that near-systematic control could be achieved by slowly varying the guest content of this framework system.[102]

1.3.2.3 ReO_3-type Fluorides

As previously mentioned, substituting the metal site in ReO_3-type fluorides while maintaining stoichiometry did not afford strictly ‘tunable’ thermal expansion. Other

methods, such as the formation of solid solutions have been explored to see if structures in between ReO_3-type and fluoride excess-type fluorides will have intermittent properties.[103] Similar experiments on $Sc_{1-x}Zr_{1+x}F_{3+\delta}$ solid solutions where ScF_3 was being doped with varying amounts of Zr showed more advanced control of thermal expansion from α_l = -4 ppm/K to α_l = 16 ppm/K over the temperature range of 298 - 648 K.[104] This control of thermal expansion has been attributed to local structure distortions that were not investigated at length, but similar reports on related $Ti^{2+}_xTi^{3+}_{1-x}ZrF_{7-x}$ (x = 0, 0.5, and 1) solid solutions that also show tunable thermal expansion attribute these local structure distortions to the formation of interstitial fluoride which takes the form of edge-sharing polyhedral units similar to what has been found in other fluoride-excess materials.[105] Varying the amount of edge-sharing polyhedra in these fluoride-excess materials is believed to allow control of thermal expansion from NTE to PTE. This method of thermal expansion control is further explored in chapters 2-4.

1.3.2.4 MOFs

A few MOFs have been found to exhibit tunable thermal expansion along specific axes through solid solution formation or guest inclusion strategies. The highly porous MOF $[Zn(L)_2(OH)_2]_n \cdot nCH_3OH$ displays unusually large anisotropic thermal expansion coefficients. Its structure consists of eclipsed 4,4-nets that are interconnected by polymeric Zn-OH-Zn chains. The structure contains 1D square shaped channels that have a diameter of about 6Å. By incorporating different amounts of alcohols (MeOH, EtOH, n-PrOH, and iPrOH) into this 1D channel space the CTE along a specific axis could be tuned from negative, to near zero, to positive over a temperature range of 100 - 375 K.[106] Later, molecular dynamics calculations performed on MOF-5 indicated the same type of tunable

thermal behavior through different loading of guest species including benzene, isopropanol, and propane.[107] According to the calculations and simulations, the strongest adsorption sites in MOF-5 are on the organic linkers. At low-loading, the host-guest interactions along the organic linkers causes them to buckle which leads to a contraction of the unit cell. This inhibits vibrational modes along the linker. As the guest loading is increased towards 100% potential capacity, all three MOF-5 simulations approach PTE over the calculated temperature range.

A ZIF-8 analog, $Zn_{1-x}Cd_x(mIm)_2$ (HmIm = 2-methylimidazole), was found to display tunable behavior by modifying the ratio of Zn:Cd while maintaining the same structural topology. This tunability was limited to the PTE range, however. A threefold decrease in the magnitude of PTE took place going from x values of 0 to 1. The Cd species was found to be more structurally flexible and this is expected to increase the density of NTE vibrational modes.

It has been shown that controlled amounts of defects can be introduced into some of the more canonical MOFs.[108] This suggested the possibility of developing defect-property relationships in MOFs, similar to what has been developed in the more thoroughly studied open framework materials. There have been cases where defect introduction and non-stoichiometry have been exploited in MOFs to develop systems with otherwise unobtainable physical properties. Early studies focused on understanding and controlling the nature of defects to enhance catalytic activity and guest sorption.[109-111] Within this realm of investigation, UiO-66(Zr) was found to exhibit increased catalytic activity through a simple structure modulation approach. Open cavity defect sites were introduced through post synthetic thermal activation. These open reactive sites made the material a highly

active catalyst for several Lewis acid catalyzed reactions. In a similar system, defective UiO-66(Hf) was found to display thermal behavior with a defect concentration dependence. As open site defect concentrations are increased the thermal expansion is shown to increase from α_v = -97 ppm/K to α_v = -70 ppm/K.

It is apparent that full control of thermal expansion has not been achieved in MOFs, but every successful systematic change in thermal expansion moves the theory closer to actuality. Chapters 5 and 6 focus more on this concept and elucidate new methods for control of thermal expansion in MOFs.

1.4 Behavior Upon Compression in NTE materials

As previously mentioned, the NTE materials described throughout the primary chapters of this thesis involve open framework-type structures. Flexibility is one of the more ubiquitous properties of this type of structure and is often an attribute to the high magnitude NTE found in this subset of materials. This being the case, susceptibility to structural changes with temperature and pressure is also attributed to high flexibility in open framework materials. In some cases, this can help fundamentally advance the understanding of a material's specific vibrational modes, while also potentially limiting their applicability. Further development of the theory linking together structure types and phonons, and their relation to thermal expansion and behavior upon compression is necessary for the prediction of future advanced materials that display the most ideal aspects of thermodynamic behavior.

1.4.1 Applications

The applicability of NTE materials has been correlated with their phase stability upon compression. Of the two primary classes of materials in this thesis (ReO_3-type fluorides and MOFs) neither are very resistant to phase transitions in their unaltered forms. For all NTE materials that are embedded within a PTE matrix within a ZTE composite, interfacial stresses that occur at the boundaries of the NTE and PTE materials can lead to changes in thermal expansion behavior as well as pressure-induced phase transitions. Previous studies have shown this effect in the prototypical NTE material, ZrW_2O_8. When embedded in a Cu composite, the post-processing material exhibited remnants of a high-pressure phase known as γ-ZrW_2O_8, while the composite was held under ambient conditions.[112] This high-pressure phase is known to exhibit PTE, and thermal cycling of the composite material showed remnants of partial phase transitions leading to thermal behavior inconsistent with that of the pristine materials combination. Phase transitions to the PTE rhombohedral phase of the canonical NTE fluoride, ScF_3, were also seen when mixed with the PTE material known as GE-7031 varnish (used as a thermal conductivity supplement).[113] As the material mixture was cooled, the shrinking varnish compressed ScF_3 which resulted in the apparent phase transition as characterized by x-ray diffraction.

Some ReO_3-type fluorides have been found to be IR transparent due to a lack of absorbing species and d-electrons.[114] If ReO_3-type fluorides were to be used as near-ZTE materials in optics-related applications, they would likely have to undergo some amount of processing. Processing conditions can vary tremendously for different materials classes. For typical ceramics, it involves high heat and high pressure. In an ideal scenario, these fluorides would be compressed to >95% theoretical density to mitigate the ability of water or other atmospheric molecules to adsorb in microporous regions of the bulk material. This

can be accomplished through compressed sintering, and further description of these processes can be found in the related literature.[115] In all of these methods, the resulting material could have microstructural regions under static compression. If the amount of compression reaches the phase-stability limitations (which are relatively low for ReO_3-type fluorides) there will be inconsistent thermal expansion behavior throughout the final product which could lead to undesirable thermal behavior and further degradation of the material upon thermal cycling. There is also no guarantee that the new higher-pressure phase will have the same optical properties as the original phase. Chapters 2, 3 and 4 discuss modifications made to ReO_3-type fluorides that, in some cases, result in drastically increased phase stability upon compression.

In MOFs, the amount of porosity has been linked to extremely unstable behavior upon compression. Of the known materials classes, they are the most flexible, and because of this they are more prone to phase transitions at lower pressures. In quite a few cases, to be discussed, they will also transition to amorphous phases that do not recover upon decompression at miniscule pressures such as those experienced in typical pestle and mortar grinding. Interestingly, MOFs are found to be more resistant to phase instability while their pores are filled with solvent. Because of this, MOF crystals are often ground or processed while solvent loaded before being activated for further analysis. This phenomenon of increased stability upon guest loading will be discussed further in section 1.5 as well as chapters 7 and 8 for both MOFs and ReO_3-type fluorides.

Because of the obvious importance of flexibility in these types of studies, the elastic behavior, bulk modulus, and pressure derivatives must be understood.

1.4.2 Elastic Behavior, Bulk Modulus, and Pressure Derivatives

Elasticity is the ability to resist a permanent change in the face of an applied stress. This can result in macrostrain, where a crystalline material changes it's lattice constant uniformly with stress, or microstrain, where lattice constant becomes unevenly distributed across a crystalline sample. Under ambient conditions, the atoms or molecules in most crystals are held in equilibrium. If an external force is applied that disrupts this equilibrium, the atoms/molecules will distort to reach a new physical state that accommodates the input of stress. This can be take the form of plastic deformation, where a material does not recover the it's equilibrium state, or elastic deformation where the original crystalline state fully recovers upon decompression. The resistance to volumetric compression is known as a material's bulk modulus.

The isothermal bulk modulus (abbreviated as K_T) quantifies a material's resistance to uniform (or isotropic) compression. Or in other words, it is the inverse of compressibility and can be defined as in equation 1.6.

$$\boldsymbol{K = V\left(\frac{\partial P}{\partial V}\right)_T} \qquad \textbf{(1.6)}$$

In equation 1.6, the bulk modulus is proportional to the volume of a material and changes proportionally with (∂P/∂V) at constant temperature. Unless otherwise stated, the constant temperature at which bulk moduli are normally compared is 298 K. The bulk modulus is an easy way to compare the stiffness or 'flexibility' of one material to another. Because flexibility is so important to thermal expansion, quantifying it and using it to compare the

thermal behavior of different materials within a family becomes relatively straightforward. Bulk moduli typically range from around 443 GPa (diamond) in very stiff materials to less than 5 GPa for the most flexible MOFs. NaCl has an intermediate bulk modulus for a salt at around 24 GPa at room temperature. Just like thermal expansion, the bulk modulus is found to vary significant with temperature and pressure. One way to quantify the magnitude of change is through pressure derivatives.

The pressure derivative shows how the bulk modulus of a material changes with pressure. This is typically obtained through equation of state (EoS) fits to volume vs. pressure data. Typically, materials stiffen on compression. In other words, the bulk modulus increases with increasing pressure. The converse, or softening upon compression, is most commonly seen in relatively flexible open framework materials and is considered rare. Some studies have linked pressure induced softening to phonon induced NTE, which isn't surprising considering the fact that both properties have the same structural limitations.[3,116]

1.4.3 Effects of Pressure on CTE

Different phases will inherently exhibit their own unique thermal behavior, so it is no surprise that phase transitions will have an impact on the thermal expansion of a material to some degree. Another crucial component to a material's thermal behavior is that of pressure. Higher pressures can lead to higher concentrations of guest species, which in some cases can infiltrate the pores of frame materials, this effect will be discussed more in section 1.5. Aside from the behavior of atmospheric atoms/molecules, pressure can also have profound effects on a material's phonon density of states. The relationship between

pressure, temperature, and phonon behavior has been investigated rather thoroughly by Fang, Dove, and other research groups for a diverse set of framework materials including basic ceramics likes metal oxides and fluorides but also large pore framework materials like MOFs.[3,117] A thermodynamic quantity representing the change in thermal expansion with varying pressure is identified in Equation 1.7.[118]

$$\left(\frac{\partial \alpha}{\partial P}\right)_T = \left(\frac{1}{{K_T}^2}\right)\left(\frac{\partial K_T}{\partial T}\right)_P \quad \textbf{(1.7)}$$

This thermodynamic relation has been used in molecular dynamics simulations with other simple models to investigate open framework materials such as metal fluorides, cyanides, oxides, and MOFs. Typically, highly flexible open framework materials show unique pressure-temperature behavior related to the more anomalous phonon density of states displayed in these types of materials. In equation 1.7, α is the volumetric CTE, K_T is the temperature dependent bulk modulus, T is temperature, and P is pressure. K_T can be calculated using the zero kelvin bulk modulus (K_{0K}) and other constants using equation 1.8.

$$K_T = K_{0K} - bTe^{-T_0/T} \quad \textbf{(1.8)}$$

Taking the derivative of equation 1.8 with respect to temperature will yield an equation for the temperature derivative of the bulk modulus that can be used to calculate the bulk modulus with varying temperature (equation 1.9).

$$\left(\frac{\partial K_T}{\partial T}\right)_P = -be^{-T_0/T}\left(1 + \frac{T_0}{T}\right) \quad \textbf{(1.9)}$$

The T_0/T term cannot be negative, and b is positive for almost every known material. This means that equation 1.9 will be negative for the vast majority of materials, meaning most materials will have a decrease in bulk modulus with an increase in temperature. Additionally, K_T is a necessarily positive and $\left(\frac{\partial K_T}{\partial T}\right)_P$ will generally be negative. Plugging these signs into equation 1.6 will yield a negative pressure dependence on the CTE. In other words, the CTE is expected to decrease as the pressure is increased. For a PTE material, this leads to a decrease in magnitude of the CTE until it eventually becomes negative. For an NTE material, the CTE will become increasingly negative with increasing pressure. This can be interpreted differently depending on the material being investigated. One reason for the negative relationship between CTE and pressure is the suppression of longitudinal vibrational modes along bond axes that is not equally applied to transverse vibrational modes in some materials. Some studies have shown that transverse modes associated with RUMs in metal fluorides are reinforced at higher pressures by increasing the angular displacement in vibrational modes specific to the rotation of the 'rigid' octahedra. This increasingly negative contribution from RUMs can couple with the decreased magnitude

of the longitudinal modes to give the negative pressure-CTE relationship.[119] Studies showing pressure enhancement of NTE behavior in cyanides have also been performed.[120] In zinc cyanide, NTE is attributed to the thermal population of vibrational modes involving transverse vibrations of the cyanide linking unit. The enhanced flexibility of the CN linker vs. single atom linkers allows for generally higher magnitudes of NTE and is also expected to lead to more anomalous behavior upon compression. Using a variable temperature/pressure apparatus, it was determined that the linear CTE changed from ~-17ppm/K to -19 ppm/K when moving from ambient pressure to .4 GPa.[120] Fits to the diffraction data also showed that the atomic displacement parameters of all atoms in the cell increased proportionally with one another, indicating that superstructural distortions were accompanying the increased pressure. Indeed, increased bending distortions associated with increasing pressure are considered the driving force behind the pressure-temperature relationship of the CTE.

1.4.4 Pressure Induced Amorphization

Historically, investigations regarding pressure induced amorphization (PIA) have had significant impacts on the understanding of glassy minerals. Meteorite craters containing feldspar and quartz were found to exhibit glass-like compounds that resulted from shockwave compression following meteorite impact.[121] At high enough pressures, the crystalline materials lost their long-range ordering as the structures distorted leaving behind a disordered or ‘amorphous’ material with the same composition as the crystalline material but without long-range ordering. As interesting and useful as this effect can be in very specific applications, it is often considered a detrimental effect to be avoided in typical applied materials. Depending on the phase stability, bulk modulus, and basic atomic

structure, PIA can happen over a wide range of pressures for materials within the same class or family. In some cases, such as $CaZrF_6$, PIA occurs at relatively low pressures (0.4 GPa), while in others, like the MOF IRMOF-1, it can occur below even 0.1 GPa.[85,122,123] In materials that exhibit NTE due to low energy phonon modes, any structural changes that inhibit the transverse thermal vibrations will have drastic consequences on the CTE. In a fully amorphized material, the CTE will be positive due to the cancellation of superstructural effects that contributed to NTE. Therefore, structural modifications of framework materials that increase their resistance to phase transitions and PIA are crucial to the broader application of this class of materials. This will be discussed further in chapter 2, 3, 4, 7 and 8.

1.5 Guest Loading of Porous Materials Under Pressure

All the materials discussed in chapters 2-7 are porous open framework materials. A porous material can be defined as any material with aperture-accessible pores/cavities/voids/interstices/channels which are permeable to liquids/gases. Because of the large pore sizes, high pressure experiments involving pressure transmitting mediums must utilize molecules/atoms that do not fit into the pore space, as this would disrupt hydrostatic compression as a pressure cell is squeezed. Disregarding the detriments of this phenomenon to certain applications, the filling of pores in open framework materials has been widely investigated for purposes relating to gas separation/storage, catalysis, thermal expansion, induced conductivity, and more fundamental studies involving the creation of new stable structures post-loading. Currently, a wide range of materials have been found to exhibit large porosity and gas/liquid permeability including coals, clays, carbons, zeolitic metal oxides, metal cyanides, phosphide framework materials, metal fluorides, and

MOFs. A distinction has been made between the crystalline materials and their non-ordered counterparts. The amorphous materials such as coals, clays, and carbons have non-uniform pores, which makes control of their adsorption behavior difficult. It also leads to the inhibition of strategic pore design, which is the primary proponent of the crystalline alternatives. Understanding the applicability of porous solids as well as the current fundamental understanding of the related mechanisms is crucial to the work in this thesis as well as the progression of all related fields of study.

1.5.1 Applications

The most obvious and highly investigated uses of porous materials is in gas storage and separation. For molecules like H_2, storage can involve high pressure cylinders, cryogenic liquid storage, chemical storage (metal hydrides, etc), or within porous materials. The two latter options greatly reduce the danger associated with the hazards of high-pressure flammable gases, such as explosion. It is even predicted that, due to strong molecule-framework interactions, that gas storage in porous materials will exceed the capacities of high pressure and liquid storage entirely. Outside of industrial use, gas storage is also closely associated with the alleviation of greenhouse effects caused by atmospheric pollutants.[124]

All materials display some finite interaction between atoms, molecules, and ions with their external surface area. Unique to porous materials, interactions involving the inner surface area can also occur. The previously mentioned applications are all dependent on the bulk materials ability to take up gases/liquids. The primary attributes that lead to favourable bonding, adsorption, or capture are pore aperture, internal surface area, surface-particle

interactions, and general topology. Reviews on porous materials and their related applications can be found and are generally organized with a specific application in mind.[124-131] Some examples will be given to further illustrate the importance of this research and some specific advances that strongly relate to this thesis.

1.5.2 Examples

1.5.2.1 Zeolites

Gas storage and separation in crystalline porous materials had early roots in the use of open framework metal oxide materials. Specifically, zeolites found increased use as their porosity was found to be accessible by several industrially important gasses such as methane, carbon dioxide, and hydrogen. Due to the high surface area and structural tunability, zeolites have been extensively studied for their ability to store and separate gases. They found their first use as adsorbents in the 1950's when the Union Carbide Corporation began preparing them for gas capture and hydrocarbon-conversion catalysis. Since then, they have been prepared in large industrial quantities for a variety of other applications relating to their accessible structures and are still used to this day as the primary catalysts in hydrocarbon conversion processes performed by the oil and gas industry.

Because of the quadrupole moments of CO_2, it has a stronger interaction with zeolites than molecules with non-polar character such as CH_4. Because of this, extensive research has been performed to develop zeolites that can adsorb CH_4 on the same levels that have been previously seen for CO_2 capture. It is also pertinent to have CH_4/CO_2 selectivity because natural sources of these gases are almost always mixed. These rigorous demands, in some

ways, have been addressed by investigating zeolites that display strong binding sites that enhance the zeolite-CH_4 interaction and CH_4-CH_4 interactions at higher loading pressures. Early work showed that silicalite was able to adsorb organic species from aqueous solution, and later advances put zeolites A, X, and Y at the forefront of zeolitic gas storage and capture.[132,133] Breck and coworkers were a major proponent to the use of zeolites in gas storage and separation and made a number of breakthroughs on zeolite A, eventually discovering that the ability to capture gas could be modified by external stimuli such as pressure, heat, and light. The unit cell volume and symmetry were found to be temperature dependent in a manner that could directly change the pore apertures to allow gas permeation over specific temperature ranges.[134] This method of guest-uptake control is going to be revisited in chapter 7.

For hydrogen storage, a basic temperature-controlled capture and release mechanism has been explored for zeolites. The thermodynamic energy of hydrogen, coupled with the temperature-dependent flexibility of framework materials, can allow for guest inclusion at elevated temperatures. Upon cooling hydrogen (and other gases) can be captured in the porous framework, and released again upon heating.[135] It has been found that the storage capacity is highly dependant on the structure and composition of the zeolite framework. Specifically, hydrogen was found to be entrapped in the smaller zeolitic pores known as sodalite cages, as opposed to the larger α-cages. The storage capacity of zeolites, although high, is still currently lower than that of metal hydrides and other larger pore framework species such as MOFs.

1.5.2.2 MOFs

The most rigorously investigated use for MOFs, to date, is as a sorbent for gas capture and separation-based applications. For sorbent-based separations, one notable MOF is Mg-MOF-74, which is notable for its high capacities of CO_2 uptake under dry conditions (5.28 mmol/g at 40 °C). Having this uptake at 40 °C is important because this is within the temperature range of flue gas exhaust. Its high uptake capacity has been attributed to the large availability of open metal sites, which have a strong interaction with CO_2 in atmospheres where it does not have to compete with the stronger interaction of H_2O. Because flue gasses typically contain some amount of water, developing MOFs that are both resistant to hydrolysis and have higher CO_2/H_2O selectivity has been a recent area of focus for sorbent-based MOF applications.

Hydrogen capture by MOFs has also been substantially investigated because of its potential as an excellent alternative to fossil fuel energies. Unlike some of the other gases, the larger pore MOFs are not attractive for storage of H_2. This is because the attractive forces between hydrogen and the inner surface area of large pore MOFs is not experienced in the pore void space. The primary interaction between H_2 and the inner pore surface area of MOFs is from Van der Waals forces between the organic linker and non-polar H_2. It has been found in other porous materials with a large carbon presence, that pore diameters of around 9Å are optimal for pore surface interaction with hydrogen due to the overlap of potential fields from multiple pore walls at once.[136] MOFs that display pore diameters in this range have so far been the most successful in uptake. With uptake capacities of up to 10 wt% at 100 bar and 77 K in some of the earliest studied prototypical MOFs such as MOF-5, the field has developed a lot of attention over the past 10 years. Other MOFs such as SNU-6 and PCN-10 can obtain comparable hydrogen storage capacity at 77 K under milder pressure

conditions (10 wt% at 70 bar and 6.84 wt% at 3.5 bar, respectively). Because H_2 has no dipole moment, the interactions between the surfaces of cages composed primarily of organic linkers at room temperature is weak. Because of this, strong H_2 adsorption sites (as opposed to weak field interactions) must be developed further to obtain suitable storage close to room temperature.

Aside from H_2, methane has also been investigated for its potential to replace current hydrocarbon-based fuel because of its high H:C ratio and natural abundance.[137] Similar to hydrogen, the energy density of methane under ambient conditions is very low (0.04 MJ/mol), making this aspect of CH_4 storage research of great importance. Also, like H_2 storage, the current industrial methods for increasing the energy density of CH_4 come with high energy costs and explosion hazards. By contrast, sorbent storage allows for ambient condition storage with relatively mild loading pressures. For CH_4, Van der Waals forces with the organic linkers and electrostatic interactions at open metal sites allows for high capacity adsorption. Therefore, MOFs that have high densities of open metal sites such as the previously mentioned MOF-74 species have been thoroughly probed for CH_4 uptake. The strength of interaction depends on the polarizing ability of the open metal site. Thus, for the M-MOF-74 series (Ni, Co, Mg, Zn, Mn), Ni^{2+} showed the highest adsorption capability, corroborated by the highest isosteric heat of absorption for open metal sites in Ni-MOF-74.[138] Aside from uptake, working capacity is also of importance. Working capacity can be defined as a ratio of gas release to gas uptake, and materials with high isosteric heats of absorption have the potential to not release CH_4 upon return to ambient conditions. The MOFs with the highest current working capacities for CH_4 at room

temperature and 65 bar are Co(bdp) and Fe(bdp) (197 and 190 cm^3/cm^3), HKUST-1 (190 cm^3/cm^3), UTSA-76a (197 cm^3/cm^3), and MAF-38 (187 cm^3/cm^3).

1.5.2.3 Metal Fluorides

Very recently, a ReO_3-type metal fluorides has been found to trap He gas at 70 K after recovery from elevated pressure. The insertion of He into the ReO_3-type structure results in the formation of a perovskite ABX_3-type structure containing He in the previously empty A-site. Because some of the A-sites are vacant, this is considered a defect perovskite, and has the formula $(He_{2-x}\square_x)(CaZr)F_6$. Before this, there were no prior examples of perovskites containing noble gases. Other examples of perovskites containing neutral species are extremely rare. The synthesis of this defect perovskite involved compression the parent material ($CaZrF_6$) at room temperature, where the porous framework structure is permeable to He gas. When brought down to 70 K, He can no longer enter/exit the pore apertures and becomes trapped within the void space of the metal fluoride, forming the perovskite A-site. Upon He insertion it was found that the material elastically stiffens, consistent with the observed loss of NTE magnitude. Similarly, phase stability is also reliant on the available open space within the fluoride framework. Because the transverse motion of the fluoride ions is dependent on their ability to enter the pore space, creating an unfavorable interaction between fluoride and a guest species will inhibit all related properties. Measuring the gas uptake and release at room temperature along with Rietveld analysis of diffraction data shows that exposure to He at around 500 MPa leads to a stoichiometry close to $(He_1\square_1)(CaZr)F_6$, where half of the pore are occupied by He. Intriguingly, the H_2 analog of this perovskite with all its pores filled would exceed H_2

storage capacity of current DOE targets. Since this discovery, other defect perovskites of similar build are expected. This area of research is addressed further in chapter 7 with the investigations of He insertion into the related ReO_3-type fluoride, ScF_3.

1.6 Summary and Thesis Goals

The thermal expansion of solids has been rigorously studied in the past and has been found to be the product of a variety of correlated mechanisms. On a fundamental level, PTE has to do with the increase of bond lengths with temperature due to bond anharmonicity (section 1.1.2). Although most materials expand upon heating, NTE materials have been found to expand upon cooling (section 1.2). At this point, the unique properties and applicability of framework NTE materials has been thoroughly demonstrated. The various fields that interact with these types of materials are already vast and still growing. Because of this, a deeper understanding of the properties inherent in this structure-type are necessary to continue to progress and find new useful materials at the current pace. Thermal expansion is related to bond anharmonicity, lattice dynamics, phase stability, and general framework flexibility. The nature of all these contributions to thermal expansion are correlated, and through further investigation of these mechanisms, more idealistic thermal behavior can be obtained. Specifically, near-ZTE is the most useful form of thermal expansion because it avoids the negative side effects associated with large changes in volume such as thermal shock and interfacial stress.

Of the phonon mediated NTE materials, those that were shown to exhibit the most open internal space and highest flexibility exhibited the largest magnitude NTE. Having large magnitude NTE is useful for compensating for the PTE exhibited in typical functional

materials. The primary method of applying NTE in this sense is through the formation of near-ZTE composites where they compensate for the PTE of a matrix material while ideally maintaining functionality. Although controlled thermal expansion composites have been shown to reach ZTE over controlled temperature ranges, interfacial stresses associated with the NTE and PTE material interactions are still present and can lead to degradation upon cycling in some systems.

As important as large NTE is to the application of NTE materials in thermal expansion composites, the ability to reach near-ZTE over a desired temperature range makes NTE materials with tunable structures just as viable for application. Although thermal expansion has been found to change drastically in phase transitions, smoother thermal expansion transitions over broader temperature ranges are necessary to avoid stresses associated with large volume change. The materials in which the structures could be systematically modified through the incorporation of guests or the formation of solid solutions have in some cases shown direct thermal behavior tunability. In some cases, the ZTE temperature could be moved over hundreds of Kelvin while maintaining the same basic structural topology. It has also been shown that the modification of thermal expansion also modifies the other related properties, in some cases this can be beneficial while in others, detrimental. In ReO_3-type fluorides, exchanging the metal identity afforded very little thermal expansion tunability, but did show drastic changes in the thermal expansion behavior. However, forming solid solutions by varying the ratio of metal identities in $M^{II}M^{IV}F_6$ fluorides has been shown to be much more useful in creating near-ZTE behavior. This aspect of ReO_3-type fluoride research will be explored more in chapters 2 - 4.

Due to the flexibility of open framework materials, phase transitions upon compression are relatively common and add an interesting but often unattractive component to the application of this class of materials. Flexibility can be directly quantified using elastic constants for solids. The bulk modulus and pressure derivatives (section 1.3.2) represent a material's response to uniform compression and are used throughout this thesis to compare the flexibility of different materials. In this thesis, strategic design of open framework materials is employed to mitigate the unwanted effects of phase transitions. The same strategies that are used to modify the thermal expansion can in some cases lead to direct increases in phase stability for ReO_3-type fluorides. This will be discussed further in chapters 2 - 4.

It has also been shown that compression is also directly tied to thermal behavior. In the obvious case of a phase transition, abrupt changes in thermal behavior occur upon compression. In the absence of a phase transition, some materials have been shown to have increases in NTE magnitude with increasing pressure. This has been attributed to the suppression of longitudinal vibrations along bond axes as well as an increased range of motion for transverse thermal vibrations (section 1.4.3). Methods for evaluating and controlling this effect are explored in chapter 7. Additionally, the pressure-induced amorphization of framework materials upon compression (and the inhibition of this deleterious effect) is explored in chapters 2-4, and 7.

Finally, the guest loading of porous materials upon compression is explored for unique framework systems. The ReO_3-type metal fluoride, $CaZrF_6$, has been shown to be permeable to helium under elevated pressure at room temperature, and to capture helium when cooled to 70 K under the same pressure conditions (section 1.5.2.3). Applying this

same method of gas storage to other ReO_3-type fluorides in which storage can be achieved under ambient conditions is both of fundamental interest and potentially important for the gas storage industry. ScF_3 is investigated for this rare property in chapter 7 of this thesis.

CONTROLLING THE NEGATIVE THERMAL EXPANSION AND RESPONSE TO PRESSURE IN REO_3-TYPE FLUORIDES BY THE DELIBERATE INTRODUCTION OF EXCESS FLUORIDE: $Mg_{1-X}Zr_{1+X}F_{6+2X}$, (X = 0.15, 0.30, 0.40, AND 0.50)

This chapter is directly adapted from an article of the same name, "Controlling The Negative Thermal Expansion and Response to Pressure in ReO_3-type Fluorides by the Deliberate Introduction of Excess Fluoride: $Mg_{1-X}Zr_{1+X}F_{6+2X}$, (X = 0.15, 0.30, 0.40, and 0.50)" Chem. Mat. Volume 31, issue 9 ***2019*** *with permissions from Samuel J. Baxter (thesis author) et al and Chem. Mat.*[29]

1.7 Introduction

Thermal expansion is a key consideration when designing components that have to display excellent dimensional stability in the face of temperature variations, or in any application where there are rapid or large temperature changes. Zero thermal expansion (ZTE) provides for both excellent dimensional stability in precision optical and other devices, and good thermal shock resistance. Negative thermal expansion (NTE) can be used to compensate for the positive thermal expansion (PTE) of other materials using either composites made from both NTE and PTE materials or by incorporating NTE components into a device. Since Sleight's report on NTE in ZrW_2O_8 over a very wide temperature range,[56] there has been a resurgence of interest in the discovery and development of NTE and ZTE materials.[7,39,139-143] This body of work has included the examination of magnetic

materials where magneto-volume effects are exploited, including intermetallics[20-22] and anti-perovskite nitrides,[23] ferroelectrics that display NTE coupled to the paraelectric-ferroelectric transition,[139,144] NTE associated with charge transfer in, for example, $BaNiO_3$[145] and $SrCu_3Fe_4O_{12}$,[146] and a diverse group of relatively low density framework solids including oxides, fluorides, cyanides and MOFs.[39,40] For the latter group, low frequency vibrational modes that soften on volume reduction are responsible for the NTE.[147,148] Unfortunately, framework materials displaying NTE also typically display structural phase transitions at low pressure.[149] This is a significant weakness from an applications perspective, as they can experience stresses while being processed or due to thermal expansion mismatch when used in composites.

Amongst framework NTE materials, metal fluorides with ReO_3-type structures have received attention[30,66,78,79,85,103,113,150-157] as they provide many opportunities for chemical substitution and, with the correct choice of cations, they can provide optical transparency from the UV down into the mid-IR.[85] After the initial discovery of NTE over a very wide temperature range in ScF_3,[153] cation substitution in this material,[30,103,151,157,158] and in cubic cation ordered ReO_3-type solids related to $CaZrF_6$,[78,79,85,150,154-156] has been explored as a means of tailoring properties. While this approach provides some control, cation substitutions that reduce the magnitude of the NTE often destabilize the cubic NTE phase and lead to undesirable transitions to a lower symmetry PTE phase on cooling or very modest compression.[103,151,152] The large low temperature NTE in materials that remain cubic on cooling, such as ScF_3 and $CaZrF_6$, has been associated with a quantum structural phase transition or incipient instability.[159-161] Nano sizing[162,163] and redox insertion[164] in ReO_3-type solids have also received some attention as methods for the rational tuning of

properties. Methods for tuning the NTE of ReO_3-type fluorides while stabilizing the cubic phase against unwanted phase transitions on cooling and compression are needed. The incorporation of "excess fluoride" into ReO_3-type compositions, where the extra fluoride is in interstitial sites, is one possible route to this goal.

Many different cubic ReO_3 related phases containing "excess fluoride", meaning more than three fluorides per metal ion, are known, for example, cubic $LnZrF_7$ (Ln – Tm, Yb, Lu),[87,165] $Ti_{1-x}Zr_xF_{3+x}$,[166] and $[M^{II}_{1-x}Zr_x]ZrF_{6+2x}$ (M^{II} – Mg, Ca, Mn, Fe, Co, Ni, Zn).[165,167] Some, such as, $Sc_{1-x}Zr_xF_{6+\square}$,[168] $YbZrF_7$,[88,169] $TiZrF_{7-x}$[170] and $Ti_{1-x}Zr_xF_{3+x}$,[171] have received very recent attention from the perspective of controlled thermal expansion. In materials such as $YbZrF_7$,[88] $TiZrF_{7-x}$[170] and $Ti_{1-x}Zr_xF_{3+x}$,[171] the excess fluoride is believed to be incorporated into the structure by replacing a single fluoride, acting as a shared corner between two octahedra, with a pair of fluorides, serving as a shared edge between two coordination polyhedra.[87,88,170,171] A substitution of this type changes the flexibility of the framework and, hence, the phonons responsible for the material's thermal expansion characteristics. It is also likely to impede the correlated tilting of octahedra associated with the structural phase transitions that are often seen on cooling and compressing ReO_3-type fluorides. In the current work, the incorporation of excess fluoride into the structure of $MgZrF_6$, as magnesium is replaced by zirconium, is examined along with its effect on thermal expansion and the material's response to compression.

1.8 Experimental

1.8.1 Synthesis

All syntheses were carried out in a dry, nitrogen- filled glovebox. ZrF_4 (99.9%) and MgF_2 (99.5%) were purchased from STREM Chemicals and Alpha Aesar respectively. $Mg_{1-x}Zr_{1+x}F_{4+2x}$ (x = 0.15, 0.30, 0.40 and 0.50) were prepared via the solid state reaction of ZrF_2 and MgF_2. The reactants were mixed according to the target stoichiometry, ground, pelletized, and placed into nickel tubes, which were then sealed via arc-welding under an argon atmosphere. The unjacketed nickel tubes were heated to 850 °C (heating rate: 4.13 °C/min), held at 850 °C for 18 h, and then slowly cooled to room temperature. The final samples were white powders. The syntheses were performed on a ~ 5 g scale for use in both the X-ray and neutron experiments.

1.8.2 X-ray Powder Diffraction and Total Scattering.

Powder diffraction data were collected at the 17-BM beamline of the Advanced Photon Source, Argonne National Laboratory using a precisely determined wavelength of 0.45240 Å and a Perkin Elmer amorphous silicon 2D detector. The samples were sealed, using epoxy, in Kapton capillary tubes under a dry nitrogn atmosphere. Temperature was controlled using an Oxford Cryosystems Cryostream (100 − 500 K). Most of the data sets were recorded with a sample to detector distance of 450 mm leading to Q_{max} ~ 5.8 $Å^{-1}$. However, for each sample a data set was collected at nominally 100 K using a sample to detector distance of 250 mm, giving Q_{max} ~ 8 $Å^{-1}$. As the set point temperature of the Cryostream does not indicate the true sample temperature, actual sample temperatures were estimated by a separate run with a thermocouple in place of the powdered samples.

Room temperature data suitable for the calculation of pair distribution functions were recorded for all the samples at beamline 11- IDB of the Advanced Photon Source. A wavelength of 0.1378 Å was used for these measurements.

1.8.3 Neutron Powder Diffraction

Neutron diffraction measurements were made using the PAC (POWGEN AutoChanger) sample environment on the POWGEN beamline at the Spallation Neutron Source, Oak Ridge National Laboratory. ~2 g $Mg_{1-x}Zr_{1+x}F_{6+2x}$ samples were loaded into vanadium cans under helium. They were cooled to 10 K and heated in steps to 300 K with 3 min equilibration times at each temperature prior to recording a diffraction pattern. Data were acquired using a 1 Å wide wavelength band, centered at ~0.7 Å, with ~15 min of data acquisition per sample. Additionally, for each sample higher quality data (~4 hour data acquisition) suitable for the calculation of a Pair Distribution Function (PDF) were collected at 10 K (usable Q_{max} ~ 35 $Å^{-1}$).

1.8.4 High Pressure X-ray Diffraction Measurements

High-pressure X-ray powder diffraction data (298 K, P_{max} ~6 GPa) were recorded for the $Mg_{2-x}Zr_xF_{4+2x}$ samples at beamline 17-BM of the Advanced Photon Source using an EasyLab "Diacell Bragg-(G)" diaphragm diamond anvil cell (DAC) while the pressure was continuously increased with the aid of a programmable syringe pump. The samples were loaded into the DAC under a dry nitrogen atmosphere. CaF_2 was used as an internal pressure calibrant and silicone oil obtained from Alfa Aesar (mol wt 237 g mol^{-1}) served as the pressure-transmitting fluid. The pressure was determined using the unit cell volume for CaF_2 along with its known equation of state.[172]

1.8.5 Rietveld Analysis

Rietveld/Le Bail refinements were used to determine structural parameters and lattice constants. All the fits were done using the General Structure Analysis System (GSAS)[173] along with the EXPGUI[174] interface. Fourier difference maps calculated in GSAS from both the X-ray and neutron data were used to develop a structural model for the excess fluoride containing materials.

1.8.6 Density Measurements

Powder samples were lightly pressed into pellets, weighed and then loaded into a Micromeritics AccuPyc-2 1340 helium pycnometer. The weight of each pellet was used along with its volume to determine the sample densities. All sample handling was performed in a glove box filled with dry nitrogen.

1.9 Results and Discussion

1.9.1 Sample Purity and the Mechanism of Excess Fluoride Incorporation.

Powder X-ray diffraction data collected both in house (Figure A.1) and using synchrotron radiation (Figure 2.1) indicate that all four samples ($Mg_{1-x}Zr_{1+X}F_{6+2x}$, x = 0.15, 0.30, 0.40 and 0.50) are cubic (Fm-3m) ReO_3-type materials at room temperature. Over the composition range examined, their lattice constants decrease with increasing zirconium content in an approximately linear fashion (inset Figure 2.1).

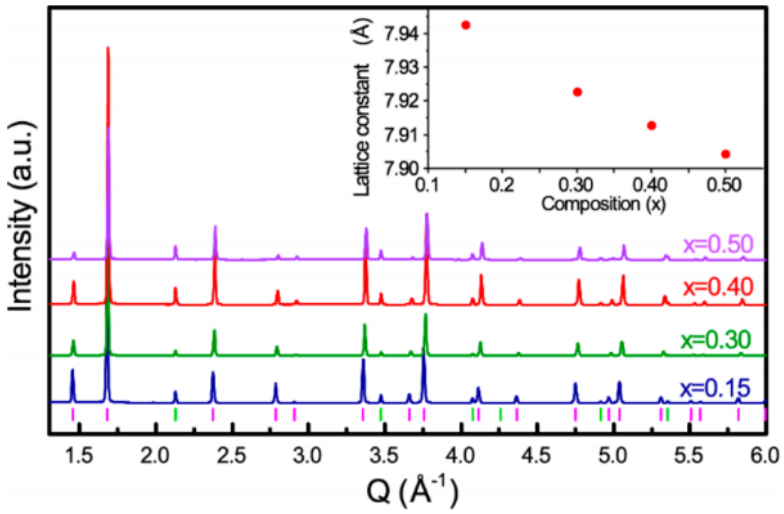

Figure 2.1: Room temperature synchrotron XRD patterns for $Mg_{1-x}Zr_{1+x}F_{6+2x}$. Ticks at the bottom indicate peaks from cubic $Mg_{1-x}Zr_{1+x}F_{6+2x}$ (pink) and silicon (neon green), which was added as an internal standard. The inset shows the lattice constant as the zirconium content is increased.

In principle, the incorporation of excess fluoride while maintaining a single ReO_3-type phase can occur by either the generation of cation vacancies or anion interstitials. These two scenarios are readily distinguishable by density measurements and prior work on ReO_3-type materials containing excess fluoride indicates that the generation of anion interstitials is the norm.[165,167] Density measurements (Figure 2.2) clearly indicate that as the zirconium content of $Mg_{1-x}Zr_{1+x}F_{6+2x}$ increases beyond x = 1, which corresponds to stoichiometric $MgZrF_6$, the excess fluoride is incorporated in interstitial sites.

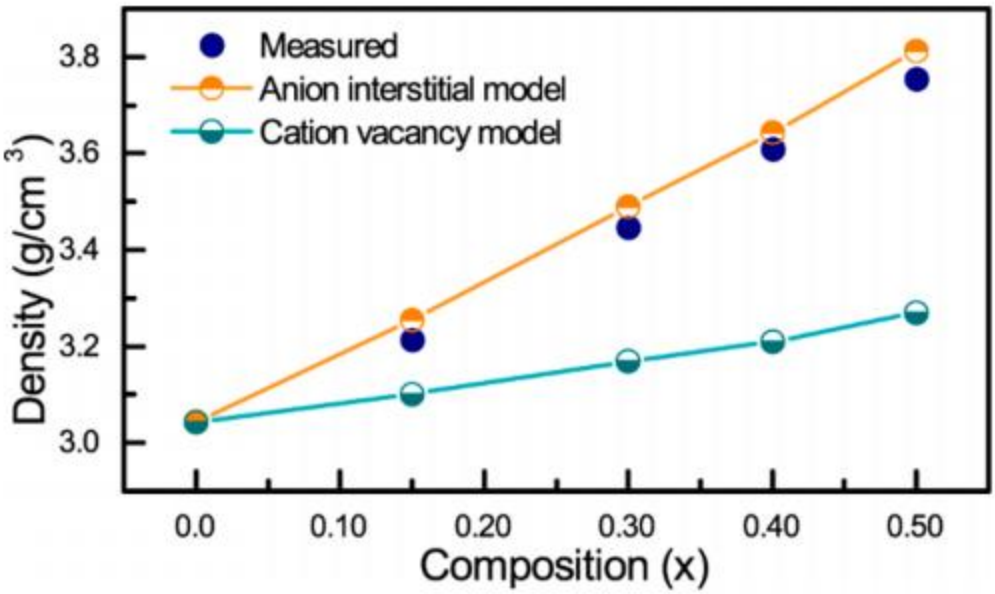

Figure 2.2: Measured densities for the $Mg_{1-x}Zr_{1+x}F_{6+2x}$ samples (dark blue) compared to those calculated for anion interstitial (orange) and cation vacancy (teal) defect mechanisms. All the density calculations used experimentally determined unit cell volumes.

1.9.2 Local Structure of $Mg_{1-x}Zr_{1+x}F_{6+2x}$ as seen by X-ray and Neutron Total Scattering.

The X-ray and neutron derived pair distribution functions (Figure 2.3) show systematic changes with increasing zirconium content indicative of major changes in local structure.

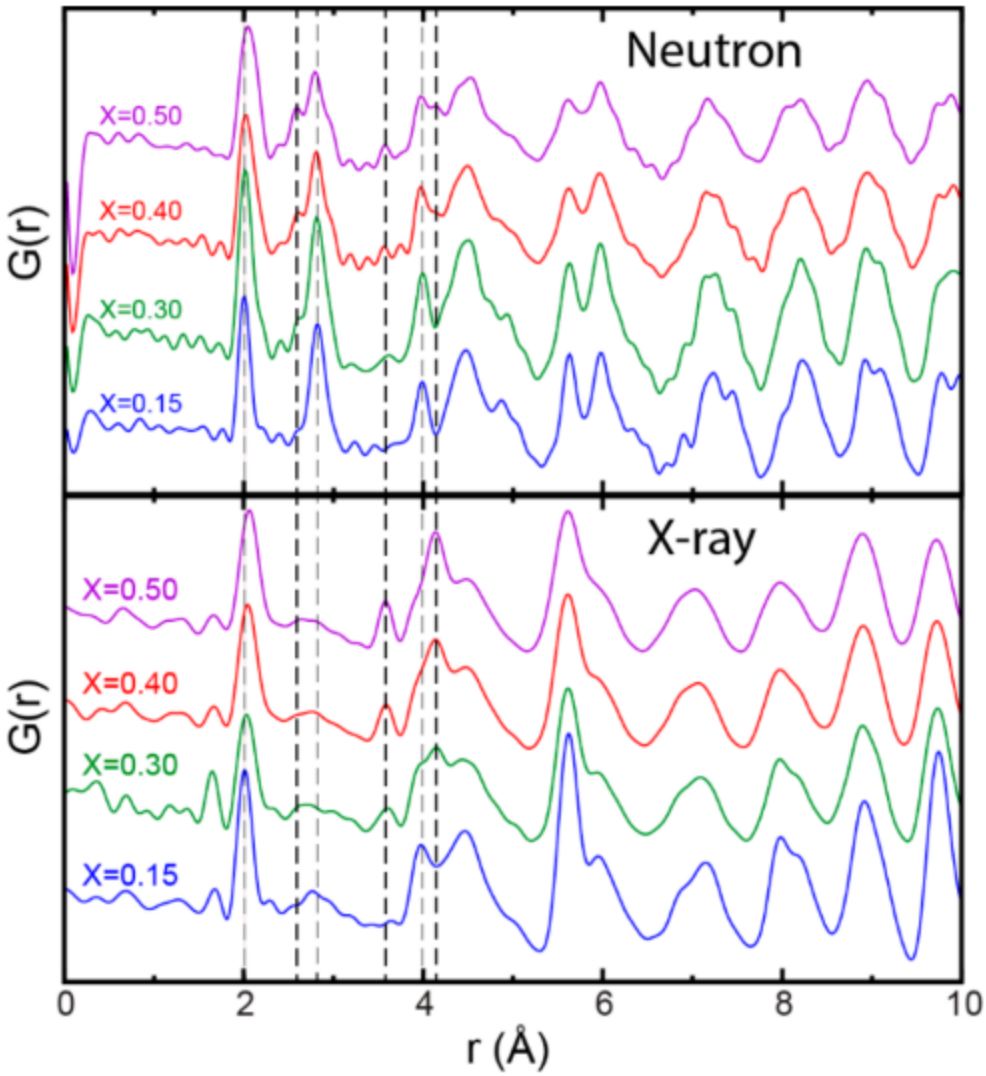

Figure 2.3: Pair distribution functions (PDFs) from room temperature X-ray and low temperature (10 K) neutron total scattering data. Dashed vertical lines have been added as guides to the eye in some regions where peak position and areas change significantly with composition.

In both the neutron and X-ray derived PDFs, the nearest neighbor M – F peak at ~ 2 Å broadens and moves to longer average distance as the zirconium content increases from x = 0.15 to 0.50 (Figure 2.3 and Figure A.8). In stoichiometric $MgZrF_6$, two distinct but very similar metal fluoride distances (Mg - F and Zr - F) associated with linear Mg – F - Zr links are expected. As the density measurements clearly support the incorporation of excess

fluoride by an anion interstitial mechanism, the introduction of extra zirconium must lead to the replacement of some magnesium by zirconium so that the excess fluoride materials will contain both Mg – F - Zr and Zr – F - Zr links. The presence of multiple types of link presumably leads the observed broadening of the nearest neighbor M - F peak. The observed decrease in lattice constant with increasing zirconium constant (see Figure 2.1) is not consistent with the increase in average M - F distance, seen in the PDFs, if all of the fluoride lies on a line between the cations. However, if the incorporation of interstitial fluoride is associated with a change from all corner sharing polyhedra to a mixture of corner and edge sharing units (see Figure 2.4), as previously proposed by Poulain for $YbZrF_7$[87] and supported by other recently published work,[88,168] the average M - F distance can increase while the average nearest neighbor M - M distance, and the lattice constant, decreases. An increase in average M - F distance is to be expected as the coordination number of the metal ions increases due to the introduction of interstitial fluoride.

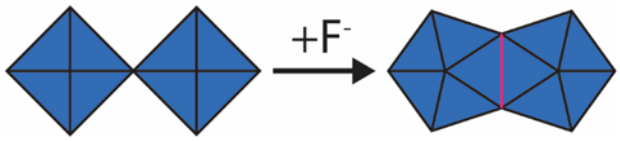

Figure 2.4: The incorporation of excess fluoride transforms pairs of corner sharing octahedra to edge sharing polyhedra.

The nearest neighbor F - F correlation peak in the neutron PDF (~ 2.7 Å) is quite sharp for the x = 0.15 sample, but develops shoulders at both higher and lower distances as extra zirconium and fluoride are introduced into the samples. This is consistent with a move away from corner sharing octahedra, where a single nearest neighbor F - F distance within each octahedron is expected, to more irregular geometry higher coordination number polyhedra, which are partially edge sharing. F - F pairs that lie on a shared edge are likely

to be closer together, see for example β-$BaZr_2F_{10}$[175] and α-$SrHfF_6$[176] where distances of 2.38 and 2.35 Å respectively were reported for F – F pairs associated with the shared edges of two ZrF_7, or HfF_7, polyhedra. It is also notable that the Zr – Zr and Hf – Hf separations across this shared edge were 3.61 Å[175] and 3.63 Å[176] respectively.

In the X-ray PDFs, a peak grows in at ~ 3.6 Å as extra zirconium is introduced. A similar feature in the X-ray PDF for $YbZrF_7$ [88] was attributed to the development of a short M - M distance as the introduction of extra fluoride leads to the conversion of corner sharing octahedra to edge sharing polyhedra (see Figure 4). This distance is consistent with the observed Zr - Zr separation for edge sharing polyhedra in β-$BaZr_2F_{10}$,[175] α-$SrHfF_6$[176] and ZrF_4.[177,178] However, in studies of $TiZrF_{7-x}$[170] and $Ti_{1-x}Zr_xF_{3+x}$[171] a similar peak in the PDF was attributed to the development of a new M - F distance associated with a change in metal coordination number. As the correlation peak at ~ 3.6 Å is much more obvious in the X-ray derived PDFs than in the neutron derived PDFs for the same samples, the assignment of this peak to the distance between pairs of metals lying on opposite sides of a shared polyhedra edge appears to be appropriate for the current samples.

In both the X-ray and neutron derived PDFs there are systematic changes in the region 4 – 5 Å. For the end member composition $MgZrF_6$, with pure octahedral coordination for both cations, nearest neighbor M - M and next nearest neighbor F - F distances are expected to be 4 Å. The proposed transformation of corner sharing octahedra to edge sharing polyhedra with higher coordination number is expected to both broaden the distribution of next nearest neighbor F - F distances and introduce both short and long M-M nearest neighbor distances, where the short M-M distance are associated with metal pairs on opposite sides of a shared edge, and the longer distances are associated with pairs of metals in higher

coordination number polyhedra sharing a common corner. The observed changes in the PDFs are consistent with these expectations.

1.9.3 Crystal Structure of $Mg_{1-x}Zr_{1+x}F_{6+2x}$ as seen by X-ray and Neutron Powder Diffraction.

A crystallographic (average structure) model was developed for $Mg_{0.5}Zr_{1.5}F_7$ using a combination of the X-ray data collected nominally at 100 K, using a short sample-to-detector distance, and the neutron diffraction data collected at 10 K. Initially, the X-ray data were fit using a model based on the ideal $MgZrF_6$ structure, but with a mixture of zirconium and magnesium on the magnesium site to give a stoichiometry of "$Mg_{0.5}Zr_{1.5}F_6$", using GSAS.[173] A Fourier difference calculation was then used to look for any metal displacements from the ideal positions. The model was updated and the occupancies and positions were refined with constraints on both the isotropic atomic displacement parameters (ADPs) and the fractional occupancies for the metal sites in order to maintain the correct stoichiometry. This model was then used to fit the low temperature neutron diffraction data. Another Fourier difference calculation was performed, which revealed new positions around the original fluoride site and indicated that the occupancy of the original fluoride site was too high. The model was updated to include the new fluoride sites and the coordinates, occupancies, and atomic displacement parameters were refined. All the metal sites were constrained to have the same isotropic ADPs and ADPs for the three fluoride sites were allowed to vary independently of one another. Constraints on the fractional occupancies maintained the stoichiometry while allowing for population of the interstitial sites. The resulting model (Table 2.1) was then used in Rietveld fits of the both the X-ray and neutron diffraction data (Figure 2.5). While the Bragg peaks were fit very

well, a strong diffuse background associated with local deviations from the average structure is apparent in both data sets.

Table 2.1: Coordinates, fractional occupancies and atomic displacement parameters for $Mg_{0.5}Zr_{1.5}F_7$ derived from the 10 K neutron diffraction data.

	x	y	z	Occ.	U_{iso} ($Å^2$)
Mg	0	0	0	.5000	.0129(3)
Zr	0	0	0	.25(3)	.0129(3)
Zr	.5	.5	.5	1.000	.0129(3)
Zr	0	.044(2)	0	.041(4)	.0129(3)
F	.2493(4)	0	0	.872 (6)	*
F	.249(5)	.135 (2)	0	.034(2)	.047(4)
F	.251(4)	.0986(6)	.0986 (6)	.039(1)	.032(3)
* U_{11} and U_{22} are 0.0105(3) and 0.0413(3) $Å^2$ respectively					

The final anion interstitial model includes a Zr position, (0, .044, 0), slightly displaced from the original magnesium location, (0, 0, 0), in stoichiometric $MgZrF_6$. This is consistent with the proposal of short cation-cation distances due to the presence of edge sharing polyhedra. Additionally, there are two new fluoride positions corresponding to the locations of interstitial anions. These fluoride positions could form the shared edge of two polyhedra within the framework. However, the distances calculated for the shortest F - F pairs (2.20 and 2.14 Å) that might correspond to these edges are short when compared to those seen in β-$BaZr_2F_{10}$[175] and α-$SrHfF_6$[176] (~2.35 Å) and the main shoulder on the nearest neighbor F-F correlation in the neutron derived PDF for the x = 0.5 sample is seen at ~ 2.55 Å (Figure 2.3).

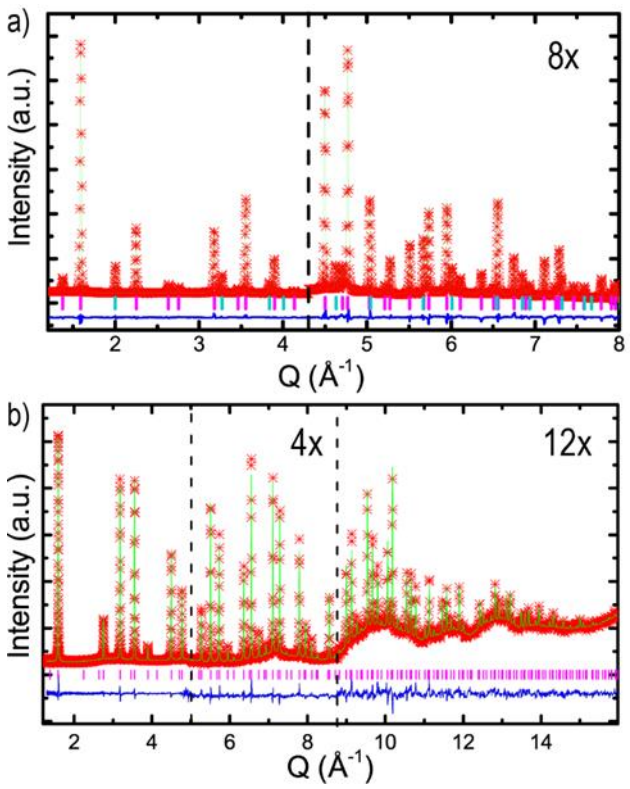

Figure 2.5: Rietveld fits to the a) nominally 100 K X-ray data and b) the 10 K neutron diffraction data using the model for $Mg_{0.5}Zr_{1.5}F_7$ shown in Table 2.1. The sample used for the X-ray experiment included a silicon internal standard, whose peak positions are marked in teal.

1.9.4 Temperature Dependent Phase Behavior and Thermal Expansion.

In previous work, stoichiometric $MgZrF_6$ was found to display a phase transition from Fm-3m to R-3 on cooling to less than ~100 K.[150] Below the transition temperature, the material showed strong positive volume thermal expansion. Above 120 - 130 K, negative thermal expansion was observed on heating up until ~ 500 K. In contrast, the neutron diffraction data for the fluoride excess materials show no evidence of any structural phase transition above 10 K, which was the lowest temperature studied. The phase transition seen in stoichiometric $MgZrF_6$ is associated with a cooperative titling of the MgF_6 and ZrF_6 corner sharing octahedra. The introduction of interstitial fluoride, and the conversion of an

all corner sharing ReO_3-type framework to one containing edge-shared polyhedra, apparently prevents this cooperative titling from occurring even for relatively low levels of excess fluoride. For the proposed local structure model, in the lowest fluoride content sample, with x = 0.15, ~ 5% of the links between neighboring polyhedra would involve shared edges rather than corners.

Le Bail fits were performed on both the variable temperature X-ray and neutron diffraction data to obtain lattice constants. Individual plots, derived from the X-ray experiments, showing lattice constant vs. temperature and expansion coefficient vs temperature are shown in Figures A.3 and A.4. The results from the X-ray and neutron diffraction data are consistent with one another and show a clear trend with composition (Figure 2.6a). For all the compositions, the unit cell volume goes through a minimum (zero thermal expansion) on heating, and the temperature at which zero thermal expansion occurs (Figure 2.6b) decreases smoothly with increasing zirconium content. This clearly indicates that the deliberate introduction of excess fluoride can be used as a strategy to tune the thermal expansion of ReO_3-type materials and that samples with $x \sim 0.22$ would likely show exactly zero thermal expansion at close to room temperature.

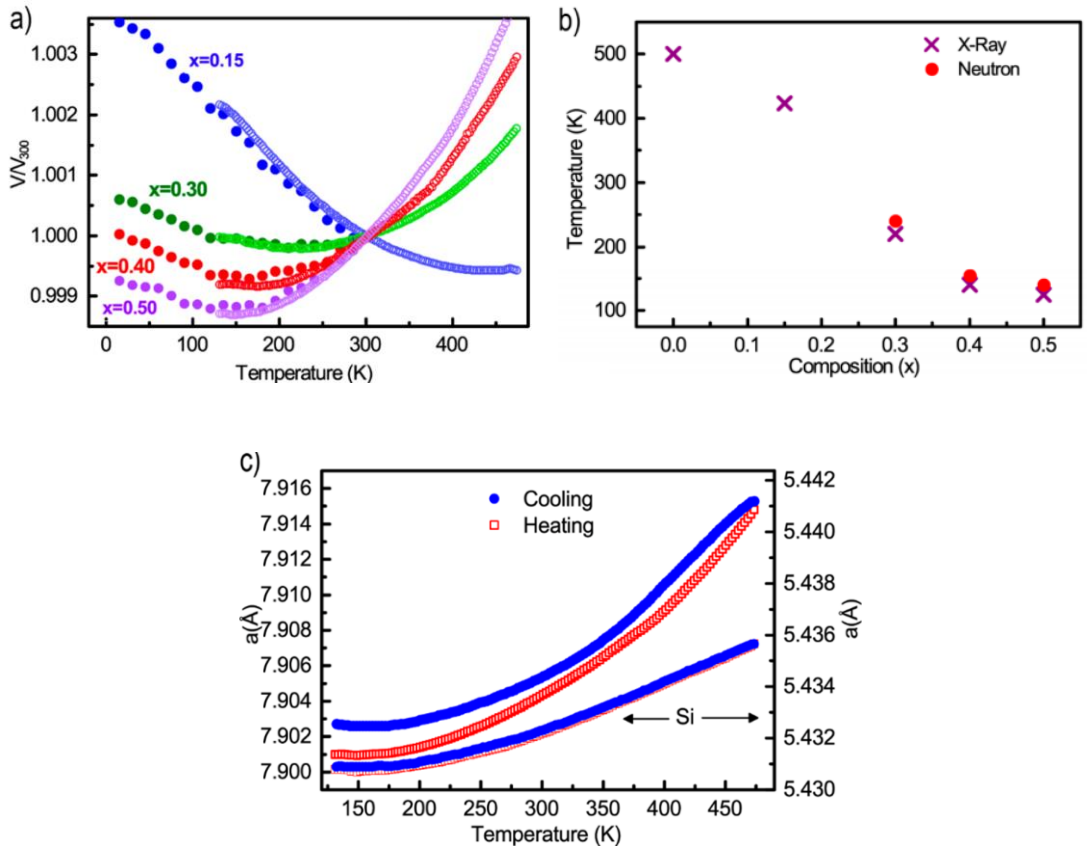

Figure 2.6: a) Normalized unit cell volumes determined by Le Bail analysis of the neutron and X-ray diffraction data (on heating). b) The temperature at which zero thermal expansion occurs as a function of composition for $Mg_{1-x}Zr_{1+x}F_{6+2x}$ ($0.0 < x < 0.50$). The data for x = 0.0 are from Hester *et al.*[150] c) Lattice constant versus temperature for the x = 0.50 sample on heating and cooling, along with the lattice constant for the silicon internal standard. The ranges for the two y-axes were selected to span the same Δa/a.

For modest amounts of excess fluoride (x = 0.15) the volume coefficient of thermal expansion (CTE) reaches a minimum value of ~ - 16 $ppmK^{-1}$ at ~ 175 K (see Figure A.4). On heating the volume CTE increase to + 3 $ppmK^{-1}$ at 475 K. These values are slightly different from those observed for $MgZrF_6$ ($\alpha_{V(175K)}$ ~ -12 $ppmK^{-1}$ and $\alpha_{V(475K)}$ ~ -2 $ppmK^{-1}$). Most notably the NTE at 175 K for the fluoride excess material (x = 0.15) is greater in magnitude than that for the stoichiometric material, presumably because the incorporation excess fluoride completely suppresses the occurrence of the cubic to rhombohedral phase

transition that is seen on cooling the stoichiometric material to ~ 100 K. On increasing the amount of excess fluoride in the samples, both the observed minimum and maximum volume CTEs move to greater values. For the x = 0.50 sample on heating, α_{V125K} ~ -5 $ppmK^{-1}$ and α_{V475K} ~ +37 $ppmK^{-1}$. As has previously been observed for the fluoride excess material $YbZrF_7$, the unit cell volumes and thermal expansion coefficients for the fluoride excess $Mg_{1-x}Zr_{1+x}F_{6+2x}$ are not fully independent of thermal history (see Figure 2.6c). The synchrotron diffraction measurements for the x = 0.50 sample, along with a silicon internal standard, show a significant thermal history dependence for the lattice constant of the sample, but none for the internal standard. This implies that the structural features associated with the incorporation of the excess fluoride relax on heating during the experiment.

1.9.5 Phase Behavior and Compressibility as a Function of Pressure.

Open framework NTE materials, including ReO_3-structured solids, are susceptible to phase transitions at relatively low pressures.[149] This is a significant weakness when it comes to their potential application in composites, where they can experience stresses due to differential thermal expansion of the filler and matrix. Consequently, it is important to understand, and ideally tailor, the response of NTE solids to stress or, less generally, pressure**.**

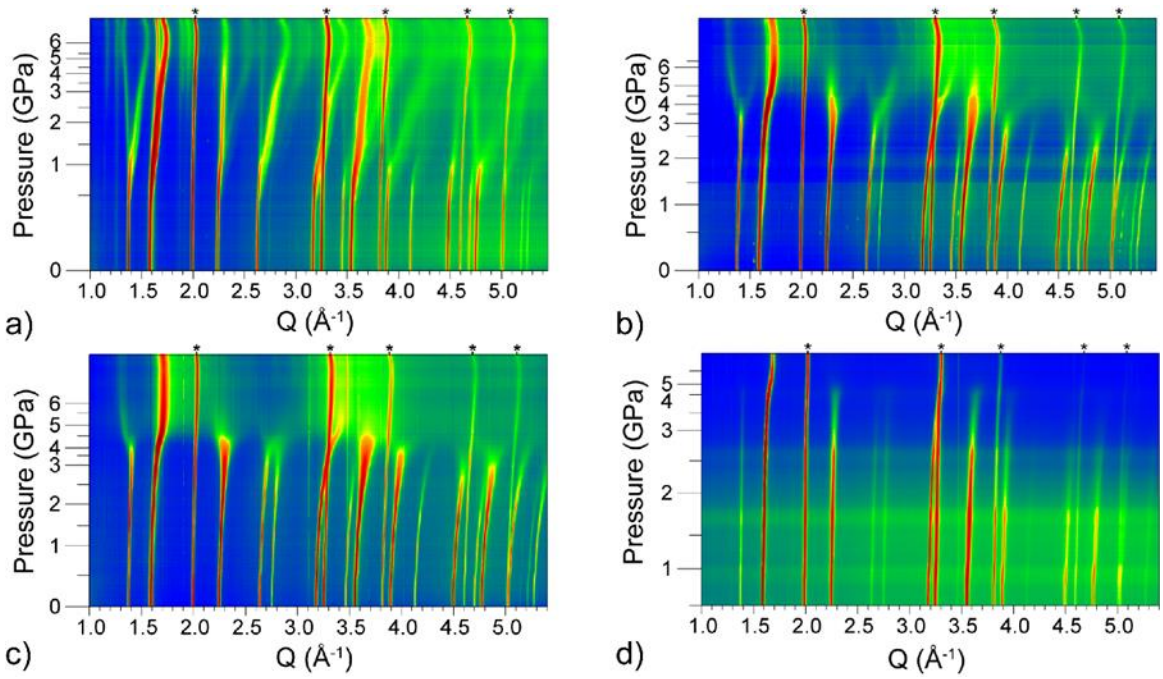

Figure 2.7: Powder diffraction data for $Mg_{1-x}Zr_{1+x}F_{6+2x}$ on compression in a diamond anvil: a) x =0.15, b) x =0.30, c) x = 0.40 and d) x = 0.50. *indicate peaks from the pressure standard CaF_2.

The synchrotron powder diffraction data shown in Figure 2.7 indicate that as the zirconium content of the $Mg_{1-x}Zr_{1+x}F_{6+2x}$ samples increases, the initial cubic (Fm-3m) ReO_3-type phase becomes stable to higher pressures. The first phase transition from cubic to rhombohedral (R-3) for the stoichiometric sample (x = 0.0) was reported to occur at ~0.37 GPa.[150] However, for x= 0.15 the cubic phase remains until ~ 0.65 GPa and for greater fluoride excesses the cubic phase survives until > 3 GPa. The suppression of this initial phase transition, which is associated with the cooperative tilting of octahedra,[150] is consistent with the conversion of corner sharing octahedra to edge sharing polyhedra as excess fluorides is incorporated into the structure. The edge sharing units do not provide the flexibility to readily rotate in a cooperative fashion.

In stoichiometric $MgZrF_6$, a second crystalline to crystalline phase transition was seen on compression to ~1 GPa. For the x = 0.15 sample, a similar transition seems to occur at ~ 3 GPa, but there are no signs of a related transition for the other samples. On decompression to ambient the x = 1.15 sample largely recovered (Figure 2.8). Similar behavior was not seen for the x = 0.30 and 0.40 samples (see Figure A.6), although in the case of the x = 1.40 sample the pressure on decompression never went below 1.9 GPa. Surprisingly, decompression of the x = 1.50 sample led to essentially complete recovery of the starting cubic phase (Figure A.6). The reason for the different behaviors on decompression is unclear, but it may be related to the amount of sample packed in each DAC and the associated presence of non-hydrostatic stresses for some samples but not others.

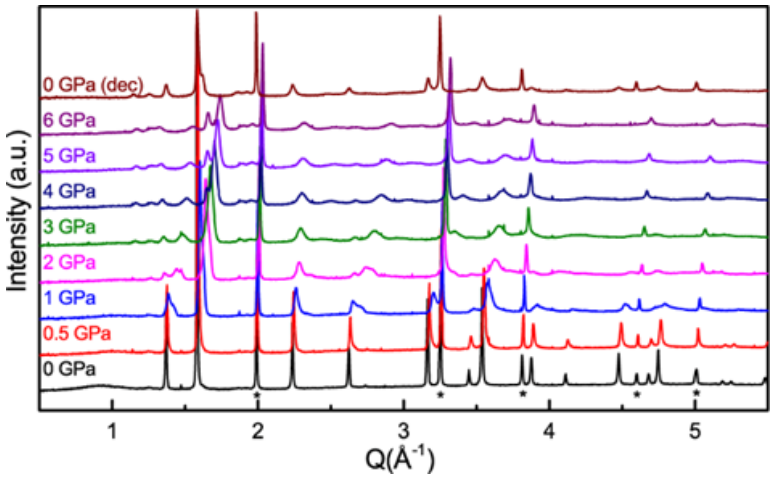

Figure 2.8: Selected diffraction patterns for the $Mg_{1-x}Zr_{1+x}F_{6+2x}$, x = 0.15, sample on compression and decompression. *indicate peaks from the pressure standard CaF_2.

A Birch-Murnaghan equation of state (EoS) was fit to unit cell volume versus pressure for the cubic phase of each sample using the program EoSfit7.[179] These data, along with a best fit to either a 3rd or 4th order EoS, are shown in Figure 9. Separate plots of the fits for each sample are shown in Figure A.5.

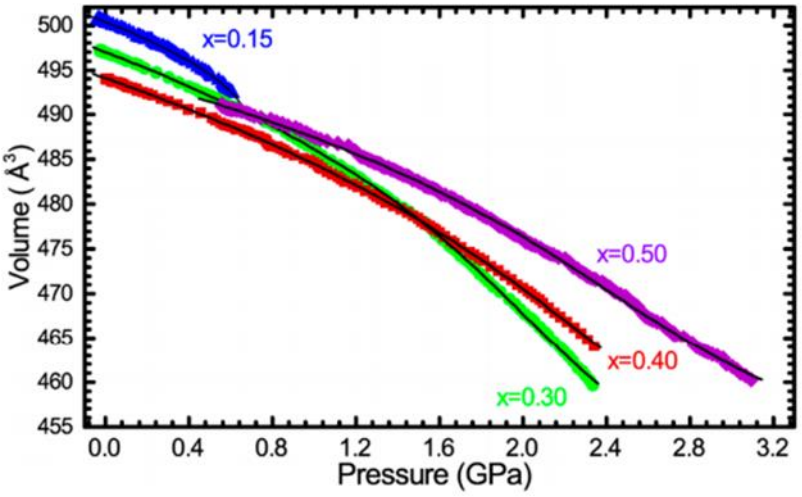

Figure 2.9: Unit cell volume vs. pressure for $Mg_{1-x}Zr_{1+x}F_{6+2x}$ with x = 0.15, 0.30, 0.40 and 0.50, along with fits to 3rd or 4th order Birch-Murnaghan equations of state.

The parameters from the EoS fits are given in Table 2.2 along with the values previously reported for $MgZrF_6$.[150] The maximum pressure used in each fit was chosen so that it was either just below the phase transition pressure, or so that all the data in the fit range could be reliably described by the EoS. For x = 0.15, the maximum pressure at which a reliable fit could be obtained was ~ 0.64 GPa. Beyond this pressure shoulders begin to appear on the most prominent peaks indicating that the peak-splitting that leads to the R-3 phase had already begun (Figure 2.8).

Table 2.2: Parameters from fitting an equation of state to unit cell volume vs. pressure for cubic $Mg_{1-x}Zr_{1+x}F_{6+2x}$.

x	V_o (Å^3)	K_o (GPa)	K'_o	K''_o (GPa^{-1})
0.0*	500.77(1)	48.2(5)	-53.2(2)	
0.15	500.4(1)	54(4)	-36(9)	
0.30	496.9(1)	55(2)	-18(2)	-2.5(4)
0.40	495.0(3)	61(5)	-16(5)	-1.6(5)
0.50	494.8(1)	77(2)	-21(1)	-2.1(2)

*from Hester et al.[150]

The parameters from fitting the Birch-Murnaghan EoS (Table 2.2) indicate that as excess fluoride is introduced into the structure, by replacing magnesium with zirconium, the bulk modulus (K_0) of the sample increases. This stiffening is consistent with the conversion of corner sharing octahedra to edge sharing polyhedra as interstitial fluoride is introduced, which should reduce the flexibility of the structure. All of the samples show softening upon compression (negative K'_0), which has been predicted to be common amongst materials with a vibrational mechanism for their NTE[118,148,180] and seen in other ReO_3-type NTE materials.[79,85,150] As the amount of excess fluoride increases, the extent of the pressure induced softening, as indicated by K_0' generally decreases in magnitude, which is consistent with both the conversion of corner to edge sharing polyhedra and the stability of the cubic phase to increasingly high pressures.

1.10 Conclusions

The introduction of excess fluoride into cation ordered $MgZrF_6$, by replacing some Mg^{2+} with Zr^{4+}, involves the population of interstitial fluoride sites and the conversion of the initially all corner sharing framework to one where some polyhedra share common edges. The presence of excess fluoride suppresses the symmetry lowering phase transition seen on cooling $MgZrF_6$ and it also stabilizes the cubic ReO_3-type phase on compression. Both of these effects presumably arise because the conversion of corner shared to edge shared polyhedra inhibits the correlated rotation of coordination polyhedra, which is typically associated with phase transitions in ReO_3-type structures. The deliberate introduction of excess fluoride provides a powerful means of tuning thermal expansion, with the temperature at which zero thermal expansion occurs varying from ~ 500 K at x = 0.0 to ~

150 K for x = 0.50, while simultaneously avoiding unwanted structural phase transitions that plague many other open framework NTE materials.

CONTROLLING THE PHASE BEHAVIOR OF LOW AND NEGATIVE THERMAL EXPANSION REO_3-TYPE FLUORIDES USING INTERSTITIAL ANIONS: $Sc_{1-x}Zr_xF_{3+x}$

This chapter is directly adapted from the article "Controlling the Phase Behaviour of Low and Negative Thermal Expansion ReO_3-type Fluorides Using Interstitial Anions: $Sc_{1-x}Zr_xF_{3+x}$" with permissions from Samuel J. Baxter (thesis author) et al.[181]

1.11 INTRODUCTION

Since the first report of negative thermal expansion (NTE) over a wide temperature range in ScF_3,[153] ReO_3-type fluorides have attracted considerable interest both for their potential application as controlled thermal expansion materials and because their simple crystal structures make them relatively easy to study. Several different strategies have been explored to tune their thermal expansion. These include: a) forming solid solutions by isovalent cation substitution to make $Sc_{1-x}Y_xF_3$,[152] $Sc_{1-x}Al_xF_3$,[151] $Sc_{1-x}Ti_xF_3$,[103] $Sc_{1-x}Fe_xF_3$,[30,157] $Sc_{1-x}(Ga/Fe)_xF_3$,[182] $Sc_{1-x}(Al/Fe)_xF_3$,[183] b) preparing cation-ordered double ReO_3-type materials such as $CaZrF_6$,[85] other $M^{II}ZrF_6$,[150,156] $CaTiF_6$,[79] $M^{II}Nb^{IV}F_6$ [78,150] and solid solutions based on these materials,[154,184] c) the inclusion of guests in the open A-sites of the ReO_3-structure by redox insertion[164] or high pressure gas treatment,[185] and d) the deliberate introduction of excess fluoride by aliovalent cation substitution to make materials such as $Sc_{1-x}Zr_xF_{3+\delta}$,[168] $YbZrF_7$,[88] $Ti_{1-x}Zr_xF_{3+x}$[186] and $[Mg_{1-x}Zr_x]ZrF_{6+2x}$.[187] Isovalent cation substitution, and the creation of stoichiometric double ReO_3-type

materials, often leads to compositions that undergo an undesirable structural phase transition from the cubic phase, which has interesting thermal expansion characteristics, to a lower symmetry or disordered material on cooling or modest compression. However, our recent work on $[Mg_{1-x}Zr_x]ZrF_{6+2x}$[187] demonstrated that the introduction of excess fluoride by aliovalent cation substitution not only provides control of thermal expansion, it suppresses the undesirable cubic to rhombohedral phase transition that is seen on cooling or compressing the parent composition $MgZrF_6$.[150] This was attributed to changes in the local structure of the material, which inhibit the cooperative octahedral tilting associated with the cubic to rhombohedral transition. In this paper, we explore generality of this observation by examining the local structure and behavior on compression of $Sc_{1-x}Zr_xF_{3+x}$.

1.12 EXPERIMENTAL SECTION

1.12.1 2.1. Syntheses.

Syntheses were performed in a dry, nitrogen filled glovebox. ScF_3 (99.9%) and ZrF_4 (99.9%) were purchased from STREM Chemicals. $Sc_{1-x}Zr_xF_{3+x}$ (x = 0.1, 0.2, 0.3, 0.4, and 0.5) samples were prepared via solid state reaction of ZrF_4 and ScF_3. Stoichiometric amounts of the reactants were ground, pelletized, and loaded into nickel tubes. Each tube was sealed by arc-welding in an argon atmosphere. The tubes were heated to 850 °C (heating rate: 6.88 °C/min), held at 850 °C for 6 h, and then quenched to room temperature using an ice bath. The final samples were white powders. The syntheses were carried out on a ~ 1 g scale.

1.12.2 High-Pressure X-ray Diffraction.

High-pressure X-ray powder diffraction data (~298 K, P_{max} ~7 GPa) were recorded for the $Sc_{1-x}Zr_xF_{3+x}$ (x = 0.0, 0.1, 0.2, 0.3, 0.4, and 0.5) samples at beamline 17-BM of the Advanced Photon Source, Argonne National Laboratory using a wavelength of 0.45395 Å. The x = 0 (ScF_3) sample was used as received from STREM. Each sample was loaded into an EasyLab Diacell Bragg-(G) DAC, which was equipped with 500 μm cullet diamonds, under a dry argon atmosphere in a glovebag. CaF_2 was used as an internal pressure calibrant and silicone oil obtained from Alfa Aesar (mol. wt. 237 $g.mol^{-1}$) served as the pressure-transmitting fluid. Data were collected while the pressure was continuously increased by pumping methanol into a diaphragm attached to the DAC. Data was also collected as the methanol pressure in the diaphragm was reduced and after complete decompression.

1.12.3 X-ray Total Scattering.

Room temperature data were recorded at beamline 11- IDB of the Advanced Photon Source, Argonne National Laboratory, for all samples using wavelengths of 0.1430 and 0.2113 Å. GSAS-II[188] was used to calculate pair distribution functions from the data collected at the shorter wavelength. A Q_{max} of ~23.1 $Å^{-1}$ was used for these calculations along with a Lortch damping function.

1.12.4 Diffraction Data Analysis.

Rietveld or Le Bail fits, within the software package GSAS-II, [188] were used to determine lattice constants. Example fits for cubic and rhombohedral phases are shown in Figure S1.

The average pressure for each diffraction data set was determined using the unit cell volume for the CaF_2 internal standard along with its known equation of state.[172] The

experimentally determined unit cell volume after complete decompression was used as V_0 for CaF_2 during this pressure determination. Equations of state (EoS) were fit to volume versus pressure for cubic $Sc_{1-x}Zr_xF_{3+x}$ (x = 0.0, 0.1, 0.2, 0.3, 0.4 and 0.5) and rhombohedral ScF_3 using the program package EoSFit7.[189] A Birch-Murnaghan equation of state was employed for the fits to the cubic phases. V_0 was fixed at the values obtained from analyses of the ambient temperature and pressure diffraction data recorded on 11-IDB at a wavelength of 0.2113 Å.

1.12.5 Density Measurements.

Ground samples of loose powder were weighed and then loaded into a Micromeritics AccuPyc-2 1340 helium pycnometer for volume determination. The weight of each sample was used along with its volume to calculate the sample densities. All sample handling was performed in a glove box filled with dry nitrogen.

1.13 Results and Discussion

1.13.1 Sample Purity and Mechanism for Excess Fluoride Incorporation

Powder diffraction data recorded at beam line 11-IDB (Figure 1) show that all the $Sc_{1-x}Zr_xF_{3+x}$ samples (x = 0.0, 0.1, 0.2, 0.3, 0.4, 0.5) were single phase cubic (Pm-3m) at room temperature, in agreement with a prior study of this system.[168] Over this composition range the observed lattice constant decreases with increasing zirconium content (inset Figure 3.1), although to a lesser extent than previously reported.[168] It may be significant that the samples for the present study were prepared in a somewhat different fashion from those of Wang et al.[168] as it is known that the thermal history of fluoride excess ReO_3-type materials

can change their lattice constants.[88,187] The reduction in lattice constant with increasing zirconium content will have a contribution from the different cation radii of Zr^{4+} (six coordinate, 0.72 Å) when compared to Sc^{3+} (six coordinate, 0.745 Å),[190] but also a contribution from changes in the coordination environment of these ions associated with the introduction of excess fluoride (see later).

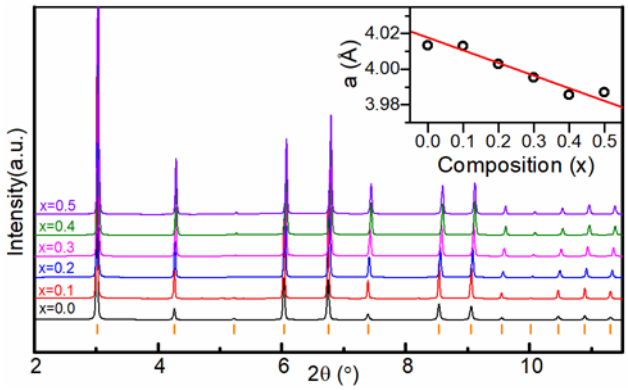

Figure 3.1: Room temperature powder diffraction patterns for $Sc_{1-x}Zr_xF_{3+x}$. The orange tic marks at the bottom indicate the expected peak positions for a cubic ReO_3-type structure (Pm-3m). The inset shows the variation of lattice constant with composition. The redline is a guide to the eye.

The incorporation of excess fluoride by aliovalent cation substitution, while maintaining a +4 oxidation state for zirconium and a cubic ReO_3-type crystal structure, can be accomplished by the creation of cation vacancies, anion interstitials, or some combination of the two. These possibilities can be distinguished via density measurements. The experimental densities of the current samples are compared with those expected for cation vacancy and anion interstitial models in Figure 3.2. With the exception of the x = 0.5 sample, the data are reasonably consistent with an anion interstitial model. The intermediate value for the density of the x = 0.5 sample may indicate a change in defect mechanism at high zirconium content and/or some evaporative loss of ZrF_4 during

synthesis. The occurrence of an anion interstitial mechanism is consistent with recent work on $[Mg_{1-x}Zr_x]ZrF_{6+2x}$,[187] and earlier work on other fluoride excess ReO_3-type materials.[167]

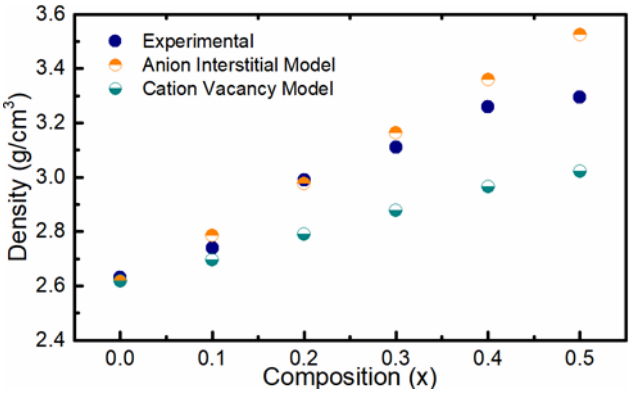

Figure 3.2: Experimental and calculated densities for $Sc_{1-x}Zr_xF_{3+x}$. The expected densities for anion interstitial (half-filled orange) and cation vacancy (half-filled cyan) models are directly compared to the measured densities (dark blue). All the density calculations used experimentally determined unit cell volumes.

1.13.2 Local Structure of $Sc_{1-x}Zr_xF_{3+x}$ as Seen by X-ray Total Scattering

Pair distribution functions for the $Sc_{1-x}Zr_xF_{3+x}$ samples are shown in Figure 3.3. Systematic changes in G(r) can be seen with increasing zirconium content, similar to what was recently reported for $[Mg_{1-x}Zr_x]ZrF_{6+2x}$.[187] In $[Mg_{1-x}Zr_x]ZrF_{6+2x}$, the incorporation of excess fluoride was associated with a move away from all corner sharing octahedral coordination to a mixture of corner and edge sharing polyhedra.

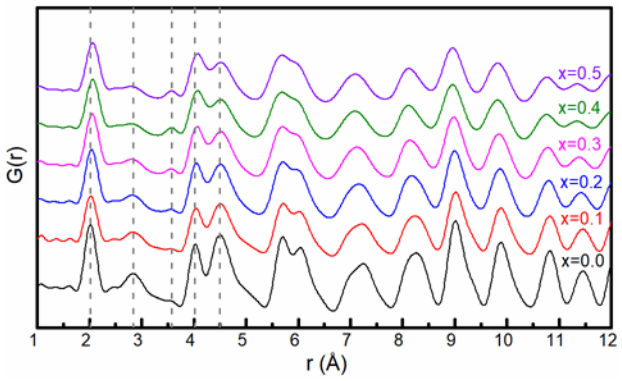

Figure 3.3: X-ray pair distribution functions for the $Sc_{1-x}Zr_xF_{3+x}$ samples. Dashed vertical lines have been added to draw attention to regions where changes occur

The first peak in G(r) at ~2 Å arises from nearest neighbor M - F distances. In the end member ScF_3 (x = 0), a single well defined M - F distance of ~ 2.005 Å is expected. On incorporation of ZrF_4, the nearest neighbor M- F peak broadens and moves to larger r. As six coordinate Zr^{4+} is smaller than six coordinate Sc^{3+}, the observed increase in the average M – F distance indicates that the solid solution samples must contain cations with a coordination number greater than six. This is in agreement with the anion interstitial defect mechanism proposed based on the density measurements. The observed decrease in lattice constant with increasing zirconium content (Figure 3.1) can only be consistent with the observed increase in the average nearest neighbor M – F distance if the incorporation of zirconium leads to the creation of some nonlinear M – F – M links between neighboring metals. The nearest neighbor F – F correlation peak, seen at ~2.84 Å for ScF_3, broadens considerably upon the incorporation of ZrF_4 into the samples, consistent with a move away from well-defined octahedral coordination in ScF_3 to a mixture of cation coordination environments in the solid solution samples.

Further evidence of changes in local structure can be seen in the 3.5 - 4.5 Å region of the pair distribution function. In ScF_3, the peak at 4.0 Å has contributions from both nearest neighbor Sc – Sc and next nearest neighbor F – F correlations. As zirconium is incorporated into the solid solution, a new peak grows in at ~3.6 Å and the peak at ~4.0 Å seems to shift to longer distances. Given the ill-defined nature of the nearest neighbor F – F correlation peak for the high zirconium content samples, it is likely that the peak at 3.6 Å is associated with a new M – M distance in the solid solutions. A similar correlation peak was also observed for $YbZrF_7$[88] and the $[Mg_{1-x}Zr_x]ZrF_{6+2x}$ system,[187] and attributed to metal pairs on opposite sides of a shared polyhedral edge. It is notable that in β-$BaZr_2F_{10}$[175] and α-$SrHf_6$,[176] which are well ordered and contain edge sharing ZrF_7 and HfF_7 polyhedra, the Zr - Zr and Hf - Hf separations across a shared edge are 3.61 Å and 3.63 Å respectively. The apparent shift in the correlation peak at ~ 4 Å to longer distances on the incorporation of zirconium can be attributed to an increase in the average nearest neighbor M – M distance for metals that share a single fluoride (corner sharing polyhedra) rather than a pair of fluorides (edge sharing polyhedra). Both the density measurements and total scattering data are consistent with the conversion of corner shared to edge shared polyhedra as the excess fluoride is incorporated into interstitial sites with increasing zirconium content.

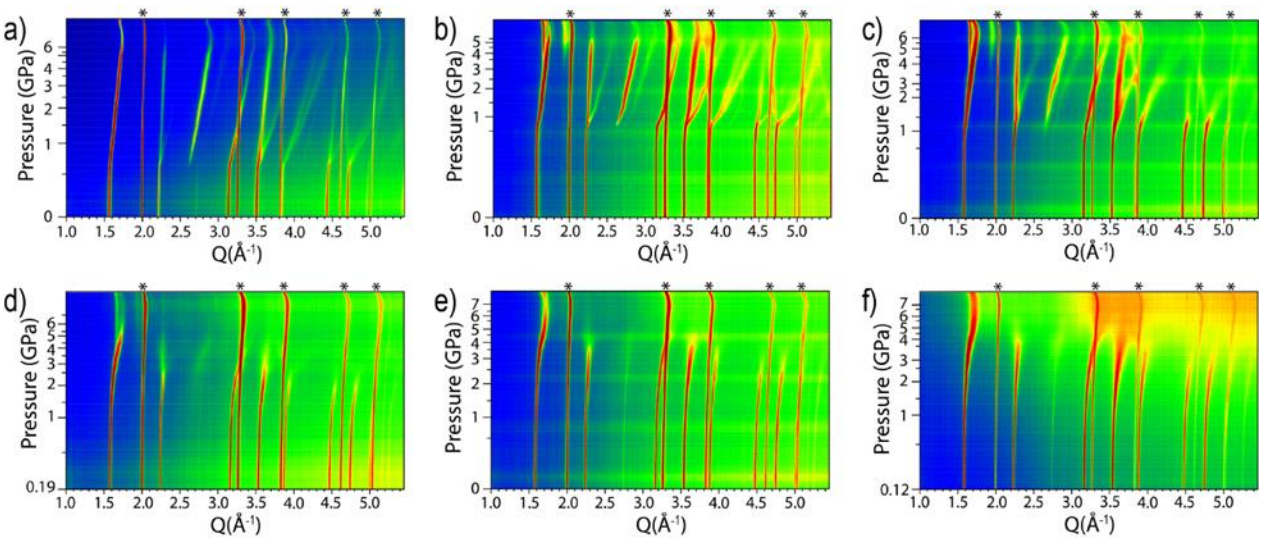

Figure 3.4: Powder diffraction data as a function of pressure for $Sc_{1-x}Zr_xF_{3+x}$; a) x = 0, b) x= 0.1, c) x = 0.2, d) x =0.3, e) x = 0.4 and f) x =0.5. Each sample contained CaF_2 as a pressure marker. CaF_2 peaks are indicated by *

1.13.3 Behavior on Compression

Diffraction data recorded while compressing the $Sc_{1-x}Zr_xF_{3+x}$ samples are shown in Figure 3.4 and Figure B.2. Two independent measurements were made for ScF_3 and they are subsequently denoted as x = 0.0a and x = 0.0b. As the behavior observed in these two runs is essentially identical, only the results from one run are presented in detail. However, data from both are shown in Figure B.2.

A second order cubic (Pm-3m) to rhombohedral (R-3c) phase transition is observed on compression of ScF_3 to ~0.7 GPa (see Figures 3.4a and 3.5), which is consistent with prior high pressure studies of this material.[153,191-194] A temperature or pressure induced transition of this type is typical of ReO_3-connectivity MF_3,[32,103,195] and involves the cooperative tilting ($a^-a^-a^-$)[196] of octahedra. Some of the prior *in-situ* high pressure studies of ScF_3 indicate a further phase transition, to an unidentified phase, at pressures of 3.0 GPa[193] or

3.2 GPa.[194] Ex-situ studies indicate that an orthorhombic form of ScF_3, with a structure analogous to that of β-YF_3, can be formed at high pressures and temperatures and that this may be stable at ~ 5 GPa and ambient temperature.[197,198] However, no further phase transition was observed on compression up to 6 GPa (see Figure B.2). On decompression the cubic phase was recovered.

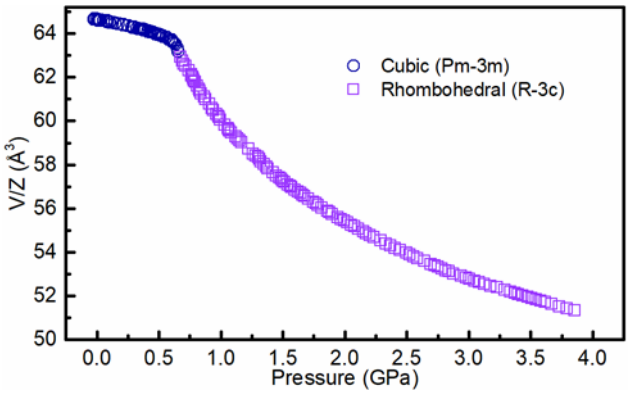

Figure 3.5: Unit cell volume per formula unit as a function of pressure for ScF_3

The incorporation of zirconium leads to different behavior on compression. For the x = 0.1 and 0.2 samples, the diffraction data (Figure 3.4) indicate that a cubic to rhombohedral transition still occurs, but at higher pressures (~0.75 and ~1.0 GPa respectively) than for the x = 0.0 sample. Additionally, a further phase transition is observed at greater than ~ 4 GPa for these two samples. The behavior of the x = 0.3, 0.4 and 0.5 samples is qualitatively different, as there is no obvious signature of a cubic to rhombohedral transition and the materials appear to largely disorder on compression. This evolution in behavior on compression is consistent with the proposed defect mechanism, as the conversion of corner to edge sharing polyhedra, by the incorporation of excess fluoride as interstitials, should reduce the flexibility of the framework and inhibit the cooperative tilting of octahedra, which is associated with the cubic to rhombohedral transition. The disordering seen on

compressing the x = 0.4 and x = 0.5 samples is similar to that previously observed for $YbZrF_7$ at ~ 0.95 GPa.[88] $YbZrF_7$, if formulated in the same way as the $Sc_{1-x}Zr_xF_{3+x}$ samples, would have x = 0.5. On decompression most of the samples show a crystalline phase recovery except for the x = 0.3 sample, which shows only partial recovery. The difference in decompression behavior is potentially related to experimental error, such as going non-hydrostatic at higher.

A Birch-Murnaghan equation of state (3^{rd} order for x = 0.0, 0.1 and 0.2 and 4^{th} order for x = 0.4 and 0.5) was fit to volume versus pressure for the cubic phases in order to examine the effect of zirconium and excess fluoride incorporation on bulk moduli. The maximum pressure used in these fits was either the point where the cubic phase no longer existed, or peak broadening led to an unsatisfactory determination of the unit cell volume. The results from these fits are summarized in Table 3.1 and the fits compared with one another in Figure 3.6. Separate fits are shown in Figure B.3.

Table 3.1: Parameters derived from fitting Birch-Murnaghan equations of state to pressure vs. volume for cubic $Sc_{1-x}Zr_xF_{3+x}$.

x	V_o (Å^3)	K_o (GPa)	K'_o	K''_o (GPa^{-1})
0.0a	64.640	61(3)	-44(5)	-
0.0b	64.640	60(2)	-39(3)	-
0.1	64.629	67(3)	-44(6)	-
0.2	64.138	67(3)	-32(4)	-
0.3	63.769	70(2)	-34(5)	-3.1(1)
0.4	63.312	73(2)	-23(3)	-2.7(3)
0.5	64.375	74.9(8)	-21.7(6)	-3.0(1)

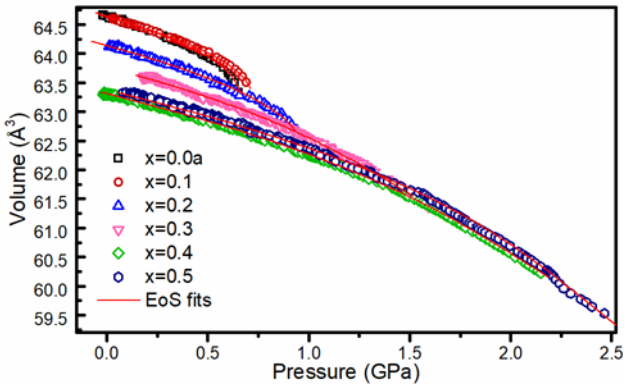

Figure 3.6: Unit cell volume vs. pressure for $Sc_{1-x}Zr_xF_{3+x}$. 3rd or 4th order Birch-Murnaghan equation of states were fit. Data were not available for all the samples at close to zero pressure, due to the generation of some pressure on initial closure of the cell.

The estimated zero pressure bulk moduli, K_0, from both ScF_3 experiments (Table 3.1) are in excellent agreement with a prior measurement (60 GPa)[152] using a cell that allowed for very precise control of pressure.[199] The incorporation of zirconium and excess fluoride leads to an increase in the estimated K_0 for the cubic phase, which likely arises from the loss of framework flexibility as corner sharing polyhedra are converted to edge sharing by the incorporation of interstitial fluoride. Similar behavior was also observed as the zirconium content increased in $[Mg_{1-x}Zr_x]ZrF_{6+2x}$.[187] For all the samples, the estimates for K_0' were strongly negative, indicating marked pressure induced softening, which is quite obvious in Figure 6. Pressure induced softening of this type has been observed in many ReO_3-type cubic fluorides[79,85,88,150,187] and is predicted to be common in materials displaying NTE by virtue of a phonon mechanism.[116,118,148,180]

An attempt to fit a Birch-Murnaghan equation of state to volume versus pressure for rhombohedral (R-3c) ScF_3 (x = 0.0a) over the pressure range 0.7 – 3.9 GPa was unsuccessful, presumably because the material is extremely soft at pressures just above the

cubic to rhombohedral phase transition. The behavior in this region could be captured using a Vinet equation of state (Figure B.4a), but this led to a very low estimate for K_0 and a physically unreasonable value for V_0. In order to get a clearer sense of how the bulk modulus for the rhombohedral phase evolves with pressure, a 4^{th} order polynomial was fit to volume versus pressure, and then differentiated, to estimate the bulk modulus as a function of pressure (Figure B.4b). Just above the phase transition pressure the rhombohedral phase is very soft (bulk modulus ~ 5 GPa), as volume reduction can be readily accomplished by increasing the magnitude of the octahedral tilts. The material stiffens considerably on volume reduction presumably due to increasing anion-anion repulsion. Behavior of this type is typical of ReO_3-type rhombohedral fluorides.[78]

1.14 Conclusions

The incorporation of excess fluoride, by the aliovalent substitution of Zr(IV) for Sc(III), in ScF_3 occurs via a similar mechanism to that reported for the system $[Mg_{1-x}Zr_x]ZrF_{6+2x}$.[187] The introduction of interstitial anions leads to the conversion of the all corner sharing framework of ScF_3 to one with some edge sharing coordination polyhedra. This reduces the flexibility of the framework, so that the excess fluoride not only provides for control of thermal expansion in $Sc_{1-x}Zr_xF_{3+x,}$ as reported by Wang et al.,[168] it also suppresses the generally undesirable cubic to rhombohedral phase transition, which is seen on compression of ScF_3 to 0.7 GPa.

THE EFFECT OF EXCESS FLUORIDE ON THERMAL EXPANSION, RESPONSE TO COMPRESSION, AND HISTORY DEPENDENCE IN CATION ORDERED REO_3-TYPE FLUORIDES: $CA[ZR(IV)_{1-X}NB(V)_X]F_{6+X}$

This chapter is largely adapted and modified from the thesis of Brett R. Hester titled "Negative Thermal Expansion, Behaviour on Compression, and Other Anomalous Behaviours in ReO3-Type Mixed Metal Fluorides".[200] *and Samuel J. Baxter (thesis author) et al. Original Syntheses were performed by Brett Hester while additional syntheses were performed by Samuel Baxter (thesis author). Thermal expansion and behaviour upon compression experiments and analyses were performed by Brett Hester while subsequent structure analysis including density measurements, PDF analysis, and history-dependent behavioural studies were performed by Samuel Baxter (thesis author).*

1.15 Introduction

As discussed in section 1.2, NTE is a rare property that has been observed in a number of different material classes.[2,5,7,19,139,141] Although rare, the property has been investigated for a wide variety of different applications including thermal expansion composites and near-ZTE stand-alone materials.[14,142,201-208] Dimensional control and resistance to thermal shock are the main industrial drivers for thermal expansion research. This being the case, some of the applications, including ZTE composites, will still put the application components under some amount of stress due to thermal mismatch with neighboring components.[17,203,205,209,210] Because of this, it is crucial to not only understand the relative

CTEs of the various composite components but also to understand the behavior upon compression.

As mentioned in section 1.2.2, there are multiple unique mechanisms that can lead to NTE.[19,139,142] In open framework materials the primary contributor to NTE is often low energy phonon modes that involve transverse thermal vibrations of a polyhedral bridging component.[211,212]

A variety of fluorides are known to adopt ReO_3-type cubic structures as discussed in section 1.2.3.5. As previously mentioned, this structure type is known to display specific low energy phonon modes that can contribute a negative component to the overall thermal expansion of a material. The search for NTE in metal fluorides is partly motivated by their potential for mid-IR to UV optical transparency, which could be utilized in multispectral optical applications. The first ReO_3-type fluoride found the display NTE was ScF_3. Interestingly, this material remains cubic with relatively high magnitude NTE over a broad temperature range (< 10 - 1100 K).[153] Many mixed metal fluorides, including $CaZrF_6$ and $CaNbF_6$, have subsequently been studied with several showing strong isotropic NTE down to low temperatures.[79,150,156,213,214]

A variety of different methods for controlling thermal expansion in ReO_3-type fluorides have been investigated.[32,103,151,163,168,170,182,195,215-217] Some of which involve the deliberate introduction defects.[29] Cation ordering in mixed metal ReO_3-type fluorides can lead to materials with the formula $M^{2+}M^{4+}F_6$. These can accommodate the substitution of either metal by one in a higher oxidation state.[87,218-220] Charge balance is preserved by the introduction of defects accompanying the varying metal content. This can take the form of

interstitial fluoride or cation vacancy sites. Interstitial anion species have been found to create higher coordinate polyhedra within framework materials which are bound to effect the thermal expansion behavior. This is especially true for the formation of edge-sharing polyhedra in place of corner sharing polyhedra.[87,170,215,216,219,221] Defects involving the formation of edge-sharing polyhedra are expected to drastically decrease the flexibility of the framework. This loss in flexibility can interfere with the low-frequency transverse vibrations that are the primary contributors to NTE.

Changes in composition involving metal substitution have been shown to drive the transition from partial edge-sharing polyhedra to corner sharing polyhedra. This was shown to tune thermal expansion from positive to negative in $Ti^{2+}_{x}Ti^{3+}_{1-x}ZrF_{7-x}$ (x = 0, 0.5, and 1).[170] $Mg_{1-x}Zr_{1+x}F_{6+2x}$ solid solutions were studied to probe the effect of replacing some Mg^{2+} in $MgZrF_6$ by Zr^{4+}. This substitution was found to introduce edge-sharing polyhedra in place of corner-sharing octahedra and was used to tune the thermal expansion and behavior upon compression.[215] The control of thermal expansion, behavior upon compression, and phase stability of this specific system is discussed further in Chapter 1. In the current chapter, we examine the controlled replacement of Zr^{4+} by Nb^{5+} in the NTE material $CaZrF_6$. Unlike $YbZrF_7$, $Mg_{1-x}Zr_{1+x}F_{6+2x}$, and $Ti^{2+}_{x}Ti^{3+}_{1-x}ZrF_{7-x}$ a high level of cation ordering is maintained, even at high Nb^{5+} substitution levels, as the Nb^{5+} goes exclusively onto the Zr^{4+} site. This leaves little room for the possibility of edge sharing polyhedra, which have been shown to rely on the higher valent cations. Variable temperature and high-pressure synchrotron X-ray diffraction were utilized to study the thermal expansion and compression of $CaZr_{0.75}Nb_{0.25}F_{6.25}$, $CaZr_{0.5}Nb_{0.5}F_{6.5}$, and $CaZr_{0.25}Nb_{0.75}F_{6.75.}$ $CaNbF_7$ was not studied as well crystallized samples of this

composition could not be prepared, although other workers have made this material.[220] The initial syntheses, thermal expansion characterization, and behavior upon compression characterization was performed by Brett Hester and is outlined in detail in his thesis.[86] Later syntheses for local structure characterization, density measurements, and thermal history studies were performed by Samuel Baxter.

1.16 Experimental

1.16.1 Syntheses

CaF_2 (99.5%, Alfa Aesar) and NbF_5 (99.5%, STREM) and ZrF_4 (99.9%, STREM) were used to prepare $Ca[Zr^{(IV)}_{1-x}Nb^{(V)}_x]F_{6+x}$ via solid state reaction using a procedure adapted from Chassaing et al.[220] The appropriate molar ratios were thoroughly ground together under a dry nitrogen atmosphere and placed into a nickel tube, which was then sealed by arc-welding under argon. The nickel tube was then sealed in an evacuated fused silica ampule. The samples were heated to 650 °C at a rate of 5.2 °C/min, held at 650 °C for 3 days, and cooled to 25 °C at a rate of 0.43 °C/min. This process was repeated to improve their crystallinity. The products were light grey powders, which were single phase by powder X-ray diffraction (see Figure C.1 for example). Synthesis of x = 0.75 sample was reperformed using the same method for subsequent neutron PDF and thermal history-dependent analyses.

1.16.2 Variable Temperature X-ray Powder Diffraction Measurements

Powder X-ray diffraction data were collected using the 17-BM beamline at the Advanced Photon Source, Argonne National Laboratory. Samples of $CaZr_{0.75}Nb_{0.25}F_{6.25}$,

$CaZr_{0.5}Nb_{0.5}F_{6.5}$, and $CaZr_{0.25}Nb_{0.75}F_{6.75}$ were packed and sealed in 0.8 mm diameter Kapton tubes. Diffraction data were recorded on a Perkin-Elmer 2D detector using a wavelength of 0.72768 Å. A LaB_6 sample was used to determine the exact sample to detector distance and other parameters needed for accurate integration of the 2D diffraction data. The sample temperature was controlled using an Oxford Cryosystems Cryostream (100 – 500 K). Subsequent thermal expansion analysis of the x = 0.75 sample was performed for the thermal history-dependent analysis using a similar setup with a Si internal standard using a heating protocol of 100 K – 500 K – 100 K – 500 K – 100K.

1.16.3 High Pressure X-ray Diffraction Measurements

Variable pressure diffraction measurements were also performed at the 17-BM beamline, Advanced Photon Source, Argonne National Laboratory using a wavelength of 0.72768 Å. Samples of $CaZr_{0.75}Nb_{0.25}F_{6.25}$, $CaZr_{0.5}Nb_{0.5}F_{6.5}$, and $CaZr_{0.25}Nb_{0.75}F_{6.75}$ were compressed up to ~ 8 GPa in an easyLab Diacell Bragg-(G) diaphragm diamond anvil cell (DAC). Samples were loaded in a dry nitrogen filled glove-bag with NaCl as an internal pressure standard and Alfa silicone oil (molecular weight of 237 $g \cdot mol^{-1}$) as the pressure-transmitting fluid. The known equation of state and the measured unit cell volume for NaCl were used to calculate the pressure.[222]

1.16.4 Total Scattering Measurements

X-ray total scattering data were acquired using beam line 11-ID-B at the Advanced Photon Source, Argonne National Laboratory. Samples were sealed in Kapton capillary tubes under dry nitrogen using an epoxy adhesive. Data were recorded using a Perkin Elmer 2D amorphous silicon detector, with a sample to detector distance of 22 cm and an X-ray

energy of 86.7 keV. The resulting diffraction data had a usable Q_{max} of ~25 $Å^{-1}$. The software PDFgetX2 was used to obtain pair distribution functions from the X-ray scattering data.[223]

1.16.5 Density Measurements

Powder samples were lightly pressed into pellets, weighed and then loaded into a Micromeritics AccuPyc-2 1340 helium pycnometer for volume determination. The weight of each pellet was used along with its volume to determine the sample densities. All sample handling was performed in a glove box filled with dry nitrogen.

1.16.6 Rietveld Analyses

Rietveld refinements were performed using the General Structure Analysis System (GSAS)[173] coupled with EXPGUI[174] in order to determine unit cell constants as a function of temperature and pressure. A cation ordered cubic ($Fm\bar{3}m$) model was used in these analyses (see Appendix C for details), with niobium replacing some of the zirconium. Good fits could be achieved with this cation ordered model regardless of composition. No attempt was made to incorporate excess fluoride into these analyses due to the limited range of the data in Q-space (Q_{max} ~5.8 $Å^{-1}$ for Cryostream and ~4.6 $Å^{-1}$ for DAC). Examples of fit quality to both the variable temperature and high pressure data are shown in Figure 2.1 and in the supplemental information.

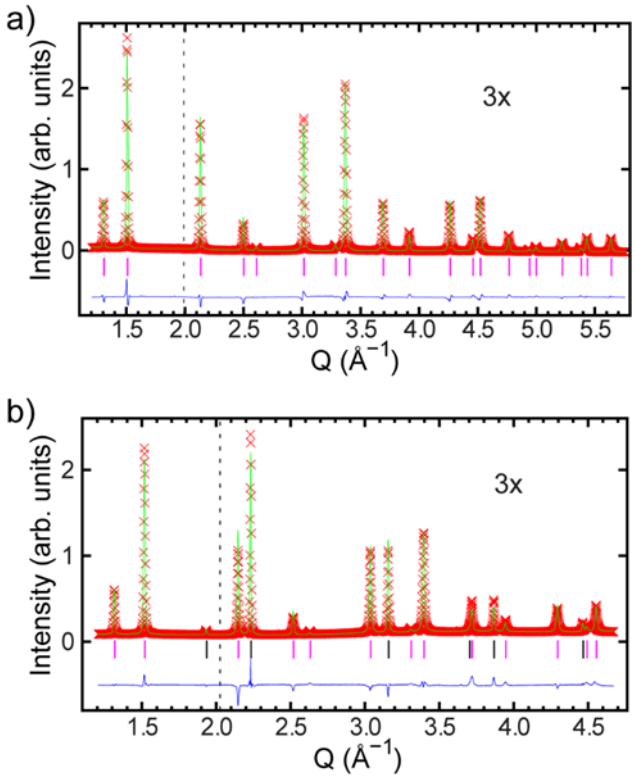

Figure 4.1: Rietveld fits performed on $CaZr_{0.25}Nb_{0.75}F_{6.75}$ samples using a cubic Fm-3m model at a) 300 K on cooling and b) at 0.1 GPa. Magenta tick marks represent the primary fitted Fm-3m phase and black tick marks represent NaCl, used as a pressure standard.

1.17 Results and Discussion

1.17.1 Defect Mechanism and Local Structure

$Ca[Zr^{(IV)}_{1-x}Nb^{(V)}_{x}]F_{6+x}$ solid solutions were analyzed primarily using x-ray diffraction. The local structure was probed initially using x-ray total scattering. The PDFs, figure 4.2, show no obvious differences between the local structures across the entire solid solution range and that of the parent $CaZrF_6$. This contrasts with older and more recent reports on cubic fluoride-excess solid solutions that take on an ReO_3-type phase. Of these related materials, $TiZrF_7$, $YbZrF_7$, and $Mg_{1-x}Zr_{1+x}F_{6+2x}$ show well defined peaks between 3 and 4 Å that are

not predicted using a defect-free structural model.[170,215,216] In $TiZrF_7$, this peak has been attributed to a new M-F distance that results from the formation of edge-sharing polyhedra. Although the other related works also claim that the defect mechanism involves the formation of edge-sharing polyhedra, the identity of these 3-4 Å peaks is not agreed upon. In $YbZrF_7$ and $Mg_{1-x}Zr_{1+x}F_{6+2x}$ solid solutions the peaks are attributed to a shorter M-M distance and this is backed up with geometric calculations as well as comparative neutron and x-ray diffraction data (see chapter 2). If the current niobium substituted materials accommodated the same anion interstitial model then the PDFs should also show a correlation peak in this range. However, as indicated in figure 4.2, there is no such peak representing a shorter M-M distance. This suggests that the excess fluoride is not present as interstitials or that it is incorporated in an entirely different mechanism, such as through cation vacancies.

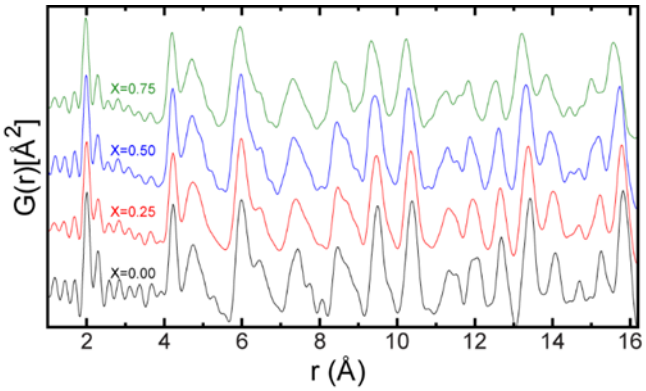

Figure 4.2: Pair distribution functions derived from the x-ray total scattering data for $Ca[Zr^{(IV)}_{1-x}Nb^{(V)}_{x}]F_{6+x}$.

If some other defect mechanism were present in $Ca[Zr(IV)_{1-x}Nb(V)_x]F_{6+x}$ solid solutions to a significant degree, it should be elucidated through density measurements which have been found to directly correlate with specific defect mechanisms in ReO_3-type fluorides

and other crystalline ceramic materials. The density measurements for this set of solid solutions, figure 4.3a, show a clear correlation with the anion interstitial defect model. On the other hand the densities calculated for the cation vacancy model are significantly below the measured densities of the samples. These results indicate that excess fluoride is being incorporated into interstitial sites, but the PDF data shows that it is not through the formation of edge-sharing polyhedra, as seen in previous fluoride-excess materials. One possibility of an alternative anion interstitial mechanism would involve the formation of terminal fluoride ions that results in the formation of higher-coordinate corner-sharing polyhedra from corner-sharing octahedra as niobium is incorporated in place of Zr. Such a change in local structural features is not unreasonable given that the Zr/Nb always has six Ca nearest neighbor cations in $CaM^{IV}F_6$ materials, but the disorder introduced in the previous fluoride excess materials such as $YbZrF_7$ and $Mg_{1-x}Zr_{1+x}F_{6+2x}$ solid solutions allows for Zr-Zr nearest neighbor pairing.

The 2-3 Å range in $Mg_{1-x}Zr_{1+x}F_{6+2x}$ solid solutions has given rise to a peak at around 2.5 Å representative of a new smaller F-F distance as the Zr:Mg ratio is increased, seen using neutron diffraction. This change in local structure is again consistent with the formation of edge-sharing polyhedra, but similar changes in the nearest neighbor F-F region would also be broadly consistent with what is expected as terminal fluoride is introduced.

Room temperature lattice constants for the sample set are shown to decrease with increasing niobium content (figure 4.2b). Lattice constants for $CaZrF_6$ and $CaNbF_7$ were taken from the literature. [213,220] These experimental values are compared to a model representing a reduction in lattice constant solely due to the replacement of six coordinate Zr^{4+} (0.72 Å) with six coordinate Nb^{5+} (0.64 Å)(dotted purple line in figure 4.2b). The

replacement of Zr^{4+} with seven coordinate Nb^{5+} (0.69 Å) is also calculated (cyan line) without any changes in the M-F-M linking geometry. The agreement between experimental data and the replacement of six coordinate Zr^{4+} with six coordinate Nb^{5+} is clear. However, density data indicated the presence of interstitial fluoride. Therefore, the coordination environment for some cations must be greater than six. This suggests that structural bending in the M-F-M linking geometry is likely present to some degree.

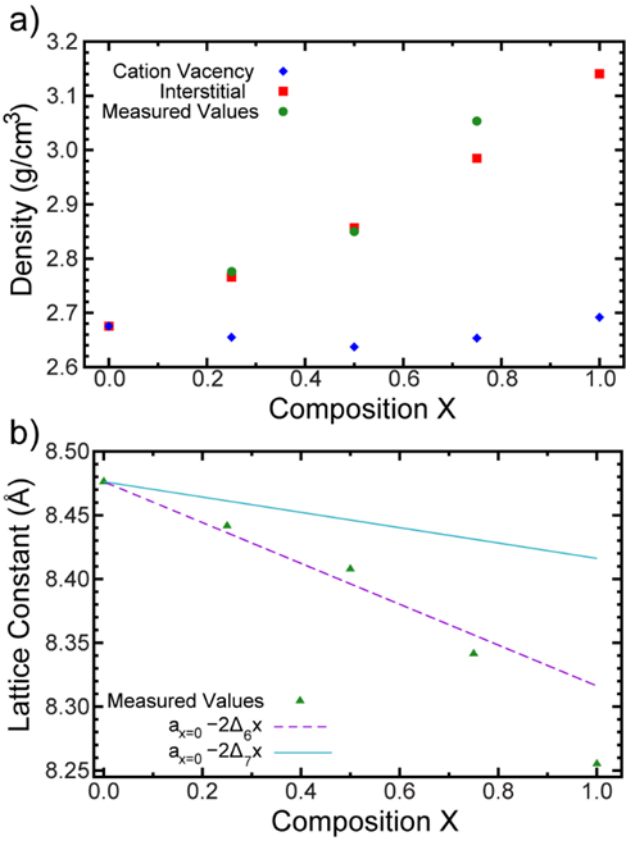

Figure 4.3: a) Densities and b) lattice constants versus composition for $Ca[Zr^{(IV)}_{1-x}Nb^{(V)}_x]F_{6+x}$. The lattice constants for x = 0 and 1 ($CaZrF_6$ and $CaNbF_7$) were obtained from the literature.[213,220] Δ_6 = (radius of 6 coordinate Zr^{4+} - radius of 6 coordinate Nb^{5+}) = 0.08, and Δ_7 = (radius of 6 coordinate Zr^{4+} - radius of 7 coordinate Nb^{5+}) = 0.03.

1.17.2 Thermal Expansion

The Rietveld method was used to analyze the variable temperature x-ray diffraction data. A cubic Fm-3m fit was used to determine lattice constants, cell volumes, and relevant atomic parameters. The resulting CTEs for $CaZr_{0.75}Nb_{0.25}F_{6.25}$ are shown below in figure 4.3a. Initially on heating from 100 K (red), the materials shows a relatively steady decrease in volume up until around 300 K. At ~300 K, the volume begins to level out and then decreases on heating to above 400 K. As the material is cooled, a smoother trend in cell volume vs. temperature is seen as the volume increases down to 100 K. This behavior indicates a strong thermal history dependence on the cell volume of this material. This means defects introduced through Nb^{5+} substitution can apparently rearrange close to ambient temperatures. This same type of thermal history dependence has been seen in $YbZrF_7$. [216,221] The difference in behavior on heating/cooling suggests that the defects might be immobile on the time scale of the experiment, but on heating above 300 K they begin to rearrange into what could be considered a high-temperature metastable phase. Additionally, on cooling, the original 300 K phase configuration is not recovered. This is likely because the cooling process is rapid compared to the structural reorganization rate. The CTE was calculated only for the smoother cooling data and displays a maximum magnitude NTE at α_v = -48 ppm K^{-1}, at 129 K.

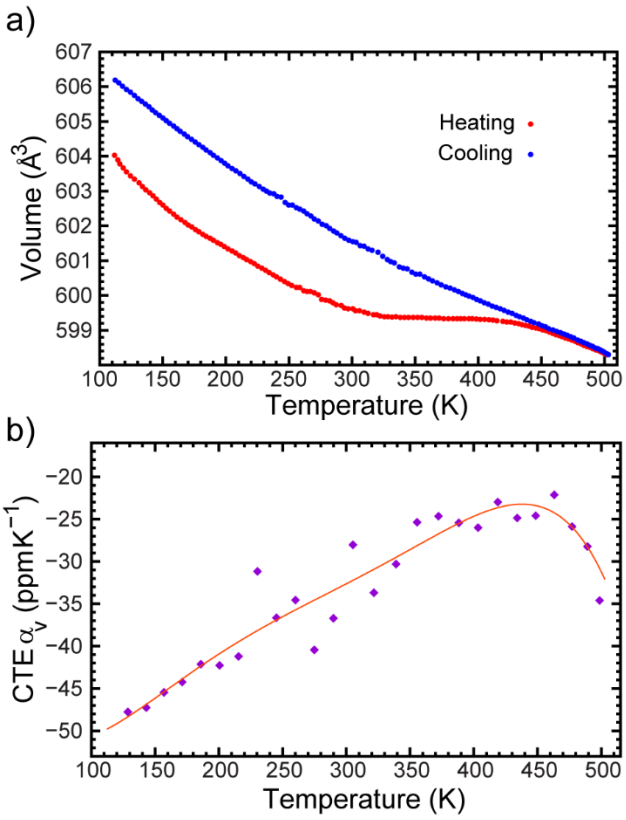

Figure 4.4: a) Unit cell volume on heating (red)/cooling (blue) and b) volumetric coefficient of thermal expansion (CTE) calculated between every fifth point (purple) and from a six term polynomial (orange), which was fit to volume versus temperature for $CaZr_{0.75}Nb_{0.25}F_{6.25}$.

In a manner similar to the x = 0.25 sample, the x = 0.50 sample displayed high thermal history dependence when heating and cooling (figure 4.5), coupled with strong NTE on cooling from 500 K. During initial heating from 100 K, there is an anomaly occurring near 300 K. This behavior is likely linked to defect rearrangement/relaxation as in the x = 0.25 sample. Yet again, the first cooling segment does not reproduce the thermal behavior displayed during heating. The CTE for this smoother cooling segment was found to be α_v = -84 ppm K^{-1} at 499 K , α_v = -31 ppm K^{-1} at 403.3 K, and α_v = -46 ppm K^{-1} at 129 K.

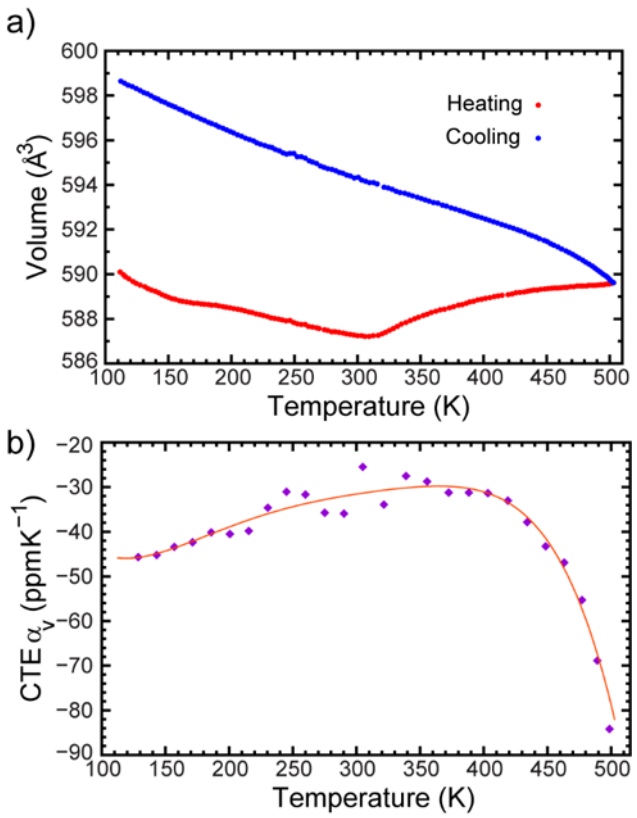

Figure 4.5: a) Unit cell volume on heating (red)/cooling (blue) and b) volumetric coefficient of thermal expansion (CTE) calculated between every fifth point (purple) and from six term polynomial fit to volume curve (orange) versus temperature for $CaZr_{0.5}Nb_{0.5}F_{6.5}$

The greatest thermal history dependence was seen in the x = 0.75 sample, which has the highest amount of Nb^{5+} substituted into it (figure 4.6). This is not surprising, as this sample would have the highest amount of the primary defect (anion interstitials). This sample, like the x = 0.50 sample, also shows an anomaly at around 300 K where the thermal behavior does not appear to follow a direct trend.

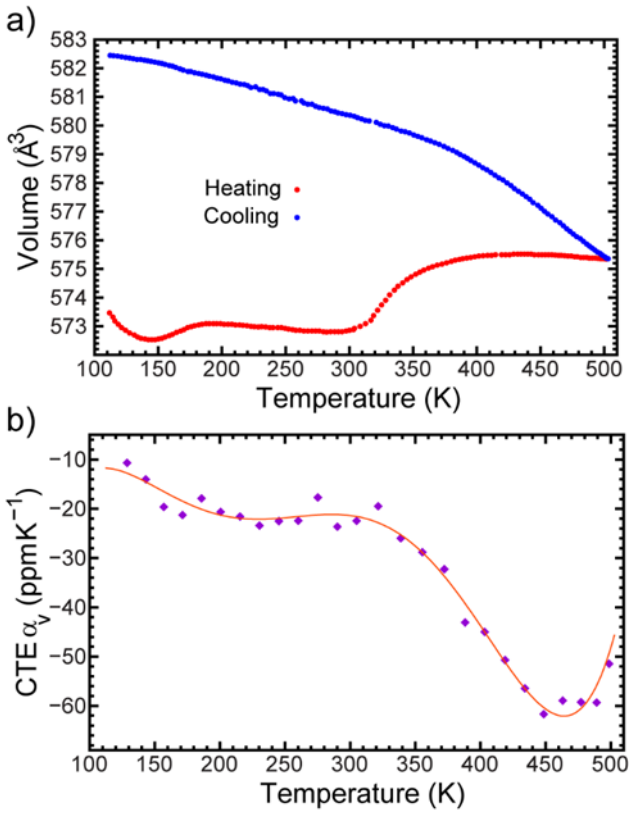

Figure 4.6: a) Unit cell volume on heating (red)/cooling (blue) and b) volumetric coefficient of thermal expansion (CTE) calculated between every fifth point (purple) and from six term polynomial fit to volume curve (orange) versus temperature for $CaZr_{0.25}Nb_{0.75}F_{6.75}$.

Table 4.1 below shows a direct comparison of the CTE values collected at different temperature for the entire sample set, including the parent structures $CaZrF_6$ and $CaNbF_7$. It is apparent that the thermal expansion is effected by the introduction of Nb^{5+}, but this does not appear to be a viable method for controlling the thermal expansion or creating a 'tunable' thermal expansion system because of the varying influence that the defects have on the thermal history dependence of this system.

Table 4.1: Comparison of CTEs at select temperatures for $Ca[Zr(IV)_{1-x}Nb(V)_x]F_{6+x}$ with those for $CaZrF_6$ and $CaNbF_6$.[150,213] The values were obtained from the data recorded while cooling from 500 K

	$\alpha_{v(120K)}$	$\alpha_{v(300K)}$	$\alpha_{v(450K)}$
$CaNbF_6$	-67.3	-36.0	-24.7
$CaZrF_6$	-52.6	-34.6	-25.6
$CaZr_{0.75}Nb_{0.25}F_{6.25}$	-49.0	-32.6	-23.5
$CaZr_{0.5}Nb_{0.5}F_{6.5}$	-45.9	-31.5	-42.1
$CaZr_{0.25}Nb_{0.75}F_{6.75}$	-12.1	-21.4	-60.7

Further investigation of the thermal behavior of these materials was performed involving temperature cycling to try and deduce the magnitude and breadth of the exhibited thermal history dependence. Figure 4.7 shows a contour plot for the x = 0.75 sample, where it is apparent that the thermal history dependence appears to fade away after the first temperature cycle.

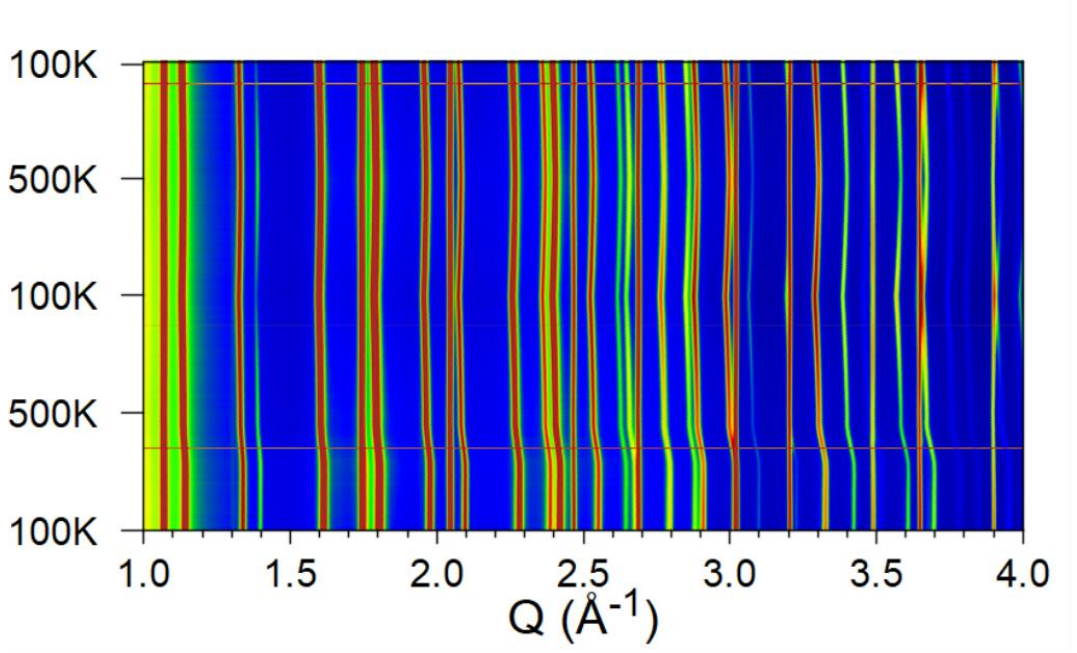

Figure 4.7: X-ray diffraction data collected during thermal cycling of $CaZr_{0.25}Nb_{0.75}F_{6.75}$.

The diffraction patterns were fit to a cubic Fm-3m model and cell volumes were extracted in GSAS-II. Cell volume vs. temperature can be seen in figure 4.8. Here, it is clear that the thermal history dependence initially seen within the first heating and cooling ramps is not reproduced upon subsequent thermal cycling. This indicates that the timescale with which the defects are mobile is much longer than that of the thermal cycling.

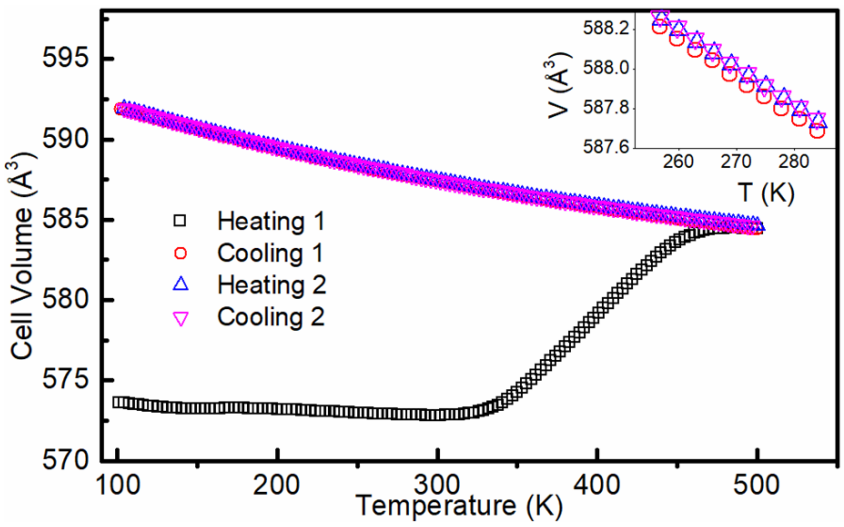

Figure 4.8: Cell volume vs. temperature for $CaZr_{0.25}Nb_{0.75}F_{6.75}$ upon thermal cycling.

1.17.3 Response to Compression

Materials used for the variable temperature data collection were also used in variable pressure studies in DACs. $CaZr_{0.75}Nb_{0.25}F_{6.25}$ is shown to exhibit two phase transitions, both of which are unique in that they are not exhibited in the parent $CaZrF_6$ material. The first transition, at ~0.68 GPa, shows the cubic phase transitioning to a currently unidentified phase that resembles an initial transition exhibited by $CaNbF_6$ in previous studies.[150] This phase maintains until another transition at ~2.5 GPa. At this point the material begins to disorder, possibly in the direction of an amorphous 'phase'. After a max pressure of close to 8 GPa, a decompression down to 3 GPa is performed, showing partial recovery of the second high-pressure phase. EoSFit7 fits similar to those performed in chapter 2 were used to fit a 3rd order Birch Murnaghan equation of state to unit cell volume vs. pressure for this sample. Fitting led to an estimated zero pressure bulk modulus of 40.5(8) GPa and a

pressure derivative (K_0) of -25(1). These values are very close to the parent $CaZrF_6$ material.[213]

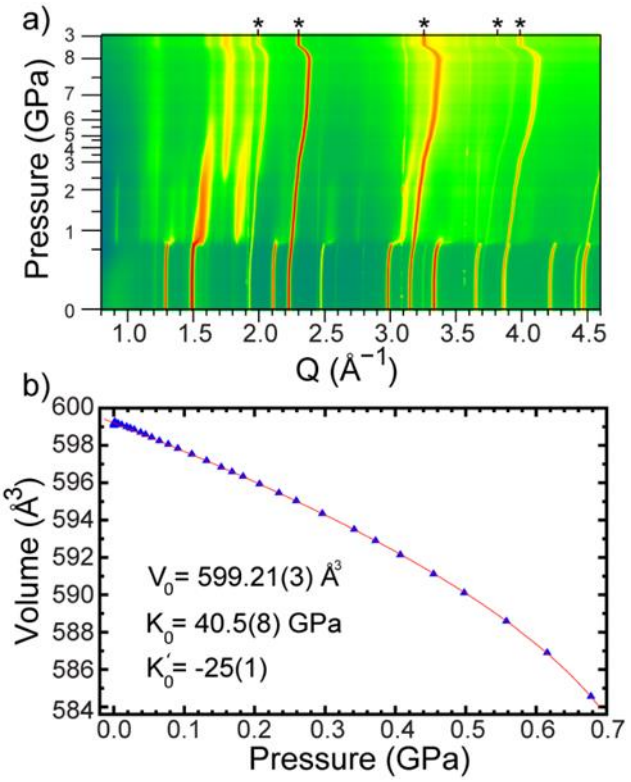

Figure 4.9: a) X-ray powder diffraction data versus pressure and b) unit cell volume versus pressure for cubic $CaZr_{0.75}Nb_{0.25}F_{6.25}$ along with the best fit using a 3rd order Birch-Murnaghan equation of state (red).

The behavior upon compression of the x = 0.50 varies significantly from that of the 0.25 sample. As the sample is compressed it undergoes the more typical ReO_3-type high-pressure phase transition from cubic to rhombohedral ($R\bar{3}$). This symmetry lowering phase transition involves octahedral tilting. A model representing this phase was fit to the diffraction data and lattice constants were determined. Like many ReO_3-type fluorides, it displays high anisotropic elastic behavior and a negative linear compressibility parallel to the c-axis. This phase is also elastically very soft with a bulk modulus between 3 and 7

GPa in the pressure range 0.7 – 1.1 GPa (figure C10). At ~1.1 GPa an abrupt phase transition occurs to another currently unidentified phase. The ordering appears to have suffered in the same way as the second transition in the x = 0.25 sample. However, in contrast to the x = 0.25 sample, the high pressure phase does not recover upon decompression to 3.4 GPa.

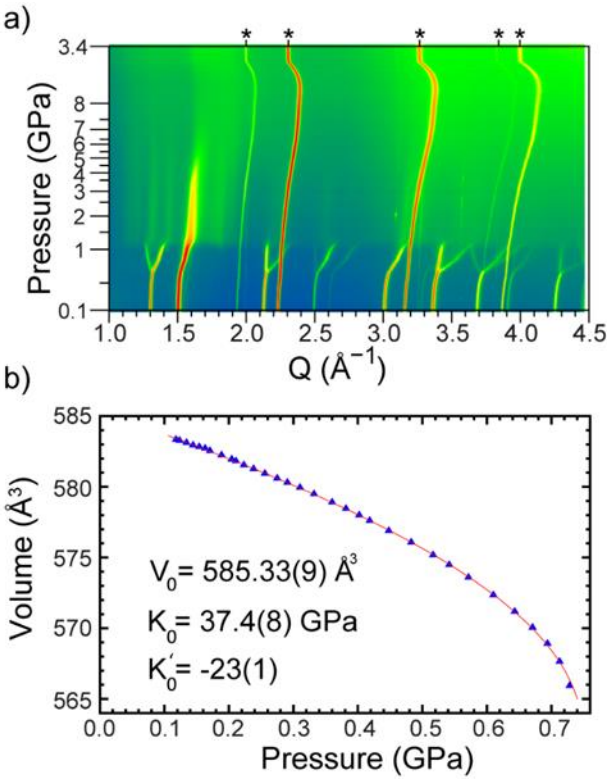

Figure 4.10: a) X-ray powder diffraction data versus pressure, and b) unit cell volume versus pressure for cubic $CaZr_{0.5}Nb_{0.5}F_{6.5}$ along with the best fit using a 3rd order Birch-Murnaghan equation of state (red). The starting pressure for the experiment was ~ 0.1 GPa.

Stark changes in the phase behavior upon compression were seen when raising the Niobium (V) content from x = 0.25 to x = 0.50, but the elastic properties changed very little. Figure 4.8 shows that the same EoS fits performed on the x = 0.50 sample yielded bulk moduli in

the same range (37.4(8) GPa) and a pressure derivative that is nearly identical to the x = 0.25 sample.

The x = 0.75 sample shows very similar phase behavior upon compression as the x = 0.50 sample. There is an initial rhombohedral phase transition occurring at 0.77 GPa and a second transition at ~ 1.3 GPa indicative of a loss of ordering beyond this pressure. Upon decompression to 3.7 GPa there does not appear to be any noticeable recovery of the highest-pressure phase intensities.

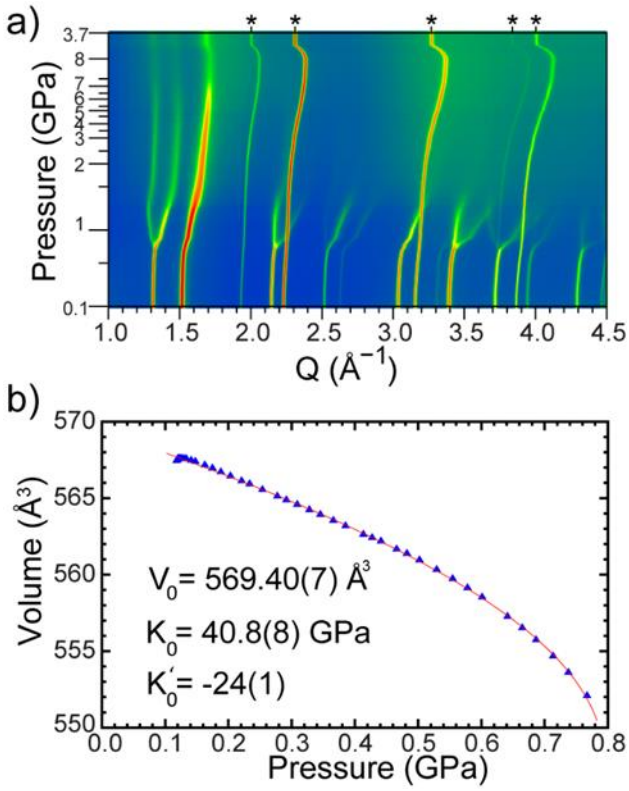

Figure 4.11: a) X-ray powder diffraction data versus pressure, and b) unit cell volume versus pressure for cubic $CaZr_{0.25}Nb_{0.75}F_{6.75}$ along with the best fit using a 3rd order

Birch-Murnaghan equation of state (red). The starting pressure for the experiment was ~ 0.1 GPa.

EoS fits to the volume vs. pressure data for the x = 0.75 sample show a bulk moduli and pressure derivative nearly identical to that of the x = 0.25 sample and very close to that of the x = 0.50 sample, indicating that the specific structure modifications that accompany an increase in Niobium (V) content do not alter the behavior upon compression significantly. This is very different from the changes in behavior seen when introducing edge-sharing polyhedral defects in other related fluoride-excess materials, such as those discussed in chapters 2 and 3 of this thesis. The overall changes in behavior upon compression within the composition range of this sample set are displayed in table 4-2.

Table 4.2: Summary of the observed response to pressure for $Ca[Zr^{(IV)}_{1-x}Nb^{(V)}_{x}]F_{6+x}$. Values for x = 0 are from a prior report,[213] where K_0' was only given for the analysis of unit cell volume versus both pressure and temperature.

	x=0	x=0.25	x=0.5	x=0.75
First crystalline to crystalline phase transition (GPa)	N/A	0.68(1)	0.73(1)	0.77(2)
Disordering pressure (GPa)	0.4	~2.5	~1.1	~1.3
K_o for the cubic phase (GPa)	42.1(8)	40.5(8)	37.4(8)	40.8(8)
K_o'	-26(4)	-25(1)	-23(1)	-24(1)

While all three niobium substituted $Ca[Zr^{(IV)}_{1-x}Nb^{(V)}_{x}]F_{6+x}$ samples showed a phase transition at close to 0.7 GPa, the phase that formed above this pressure does not have the same symmetry in the x=0.25 sample as it does for the x=0.50 and x = 0.75 samples. All three samples eventually amorphized after their second high-pressure phase transition, but their ability to recover the high-pressure phase intensities on decompression was varied,

again drawing a distinction between the x = 0.25 sample and the other two $Ca[Zr^{(IV)}_{1-x}Nb^{(V)}_{x}]F_{6+x}$ compositions. It is notable how little the niobium (V) substitution effects the bulk moduli and pressure derivatives of this sample. This is a major indicator that the formation of uniquely bound polyhedra (such as edge-shared) is unlikely and that some other anion interstitial defect mechanism must be at play.

1.18 Conclusions

The replacement of Zr^{IV} with Nb^{V} in $CaZrF_6$ appears to introduce an anion interstitial defect mechanism, as indicated by density measurements of the sample set. However, x-ray total scattering data on suggests that the defect mechanism does not involve the formation of edge-sharing polyhedra, as it did in other related fluoride-excess ReO_3-type materials. Subsequently performed neutron diffraction data also indicates that there is no significant change in the local structure throughout the solid solution range. Neither PDF indicates that an anion interstitial mechanism is not possible. A proposed alternative defect mechanism involves the formation of terminal fluoride, but future endeavors involving neutron-sourced pair distribution functions (as at least one necessary component) might elucidate further the differences between the excess fluoride incorporation of $Ca[Zr^{(IV)}_{1-x}Nb^{(V)}_{x}]F_{6+x}$ and the other related systems such as $Mg_{1-x}Zr_{1+x}F_{6+2x}$, TiZrF7 and $YbZrF_7$. The thermal expansion behavior is found to change with Nb^{V} substitution. Unfortunately, the immense thermal history dependence exhibited makes the direct comparison within the sample set difficult. This is indicative of mobile defects at close to room temperature. The subsequent measurements of the thermal expansion of the x = 0.75 sample showed the extent of the thermal history dependence upon cycling. These experiments indicate that the

thermal history dependence occurs on a timescale much larger than that used in the cycling, but the structure is likely to relax to the room temperature phase again, eventually.

On compression, all $Ca[Zr^{(IV)}_{1-x}Nb^{(V)}_{x}]F_{6+x}$ samples between x = 0.25 and x = 0.75 undergo a phase transition at close to 0.7 GPa. The nature of this phase transition appears to be similar for the x = 0.50 and x = 0.75 samples, as both transition from the cubic phase exhibited under ambient conditions to a higher-pressure rhombohedral phase involving coordinated tilting of the octahedra present in the structures. This specific transition is not consistent with the formation of edge-sharing polyhedra, as the connectivity would inhibit any correlated tilting that is reliant on corner-shared components. Finally, the elastic properties do not appear to change much with differing levels of Nb^{V} substitution. This again suggests that the incorporation of interstitial fluoride in this specific system does not lead to the formation of edge-sharing polyhedra and thus, control of thermal and pressure behavior through this method of defect introduction does not measure up to that of the related methods in chapters 2 and 3 of this thesis.

NEGATIVE THERMAL EXPANSION DESIGN STRATEGIES IN A DIVERSE SERIES OF METAL–ORGANIC FRAMEWORKS

This chapter is directly adapted from Negative Thermal Expansion Design Strategies in a Diverse Series of Metal–Organic Frameworks. Advanced Functional Materials ***2019****, 29, 1904669 with permissions from Nicholas Burtch and Samuel J. Baxter (thesis author) et al and Advanced Functional Materials.*[224] *An explanation for the various contributions of the thesis author and collaborators is outlined at the end of the introduction.*

1.19 Introduction

Just like in the previously discussed metal fluoride systems, MOFs have also been found to display the anomalous property of NTE. Because of the detriments of PTE, such as stress and even catastrophic device failure in confined environments, MOFs offer another potential path towards ZTE composites and near-ZTE materials. The organic constituents of MOFs enable a larger degree of structural flexibility which has further promoted their potential for achieving high magnitude NTE. This larger degree of flexibility has also contributed to the ability to modify the constituents of a MOF structure while maintaining the same overarching topology. Because of the increasing interest in tailoring thermal expansion through chemical modifications, MOFs have especially been of interest due to their vast chemical diversity and modular build. More information on MOFs and their contributions to this field can be found in section 1.2.3.6. The following chapter will demonstrate the interchangeability of MOF components as well as design strategies for tailoring thermal expansion in this class of materials. By modifying the metal constant,

ligand identity and sterics, topology, and even guest species, it is shown that the thermal expansion characteristics of MOFs can be modified both drastically and systematically. Within the coming sections, syntheses were performed by the thesis author as well as Ashley Bird and Andreas Schneemann. Experimental analysis was performed by the thesis author, Ashley Bird, Andreas Schneemann, Angus Wilkinson, and Nicholas Burtch. Diffraction characterization and analysis was performed primarily by the thesis author. Simulation calculations were all performed by Jurn Heinen and David Dubbeldam. Writing of the original works was a collaboration, but the lead direction and layout were designed by Nicholas Burtch.

1.20 Experimental

Syntheses and other experimental details are given in the supplemental section D. Nitrogen adsorption was measured at 77 K for reach sample to confirm porosity characteristics before storage under an argon atmosphere until later thermal expansion experiments could be performed. Laboratory diffraction experiments were measured in a sealed quartz capillary and subjected to changes in temperature induced by a nitrogen cryostream by the thesis author, Ashley Bird, and Andreas Schneemann. Synchrotron-sourced diffraction and total scattering data were collected at beamlines 17-BM-B and 11-ID-B of the Advanced Photon Source (APS) at Argonne National Laboratory using Kapton capillaries that were sealed in an argon environment before the diffraction experiments by the thesis author, Ashley Bird, Nicholas Burtch, and Angus Wilkinson. Lattice parameters were extracted from the samples using Le Bail and Pawley analysis using the GSAS-II software suite by the thesis author. The Average linear CTEs were calculated from the resulting lattice parameters from 10-100°C and the errors are reported with asymptotic standard errors from

linear regression analysis. The RASPA molecular simulation software for adsorption and diffusion in flexible porous materials was used for classical simulations by Jurn Heinen and David Dubbeldam.

1.21 Results

Various design strategies have been achieved for a variety of different MOF systems. The primary MOF systems investigated in this work involve the previously discussed M-DMOF series where ligand sterics, topology, and metal identity have been explored, the prototypical MOF-5 where guest loading effects on thermal expansion have been explored, and in the previously mentioned UiO-66/67 series where ligand length and defect concentration have been utilized to control thermal expansion. Figure 5.1 below outlines the basic design strategy for this exploration. The M_2L_2(DABCO) MOFs contain the 1,4-diazabi-cyclo[2,2,2]octane (DABCO) pillaring ligand and a paddlewheel shaped metal node bound by 8 oxygen species from the benzene-1,4-dicarboxylate (BDC) ligand forming $Zn_4O(CO_2)_6$ clusters. This series has been of specific interest because of the ability to modify its structure while not changing the overall symmetry of the P4/mmm unit cell, although in one case we have changed the topology and thus the unit cell symmetry, as will be discussed. IRMOF-1 in an archetypal MOF, so any relevant tailoring of its thermal expansion has the potential to translate into a wide variety of different structures that make use of its primary building blocks. In these works, it is experimentally shown that incorporation of a guest species can be used as a strategy to modify the thermal expansion magnitude. Finally, the thermal expansion of the Zr_6O_8-based UiO series is shown to undergo drastic changes associated with the length of it's BDC ligand. The CTEs of each system were analyzed using both in-house and synchrotron-sourced x-ray diffraction

techniques. Heating and cooling were generally done using a nitrogen cryostream for variable temperature diffraction experiments in between 10 and 100 °C. This temperature range represents a relevant range for the application of MOFs from a mechanical and thermal properties standpoint. Near linear thermal expansion behavior led to a relatively straightforward comparison of the average CTEs over this range for the different materials.

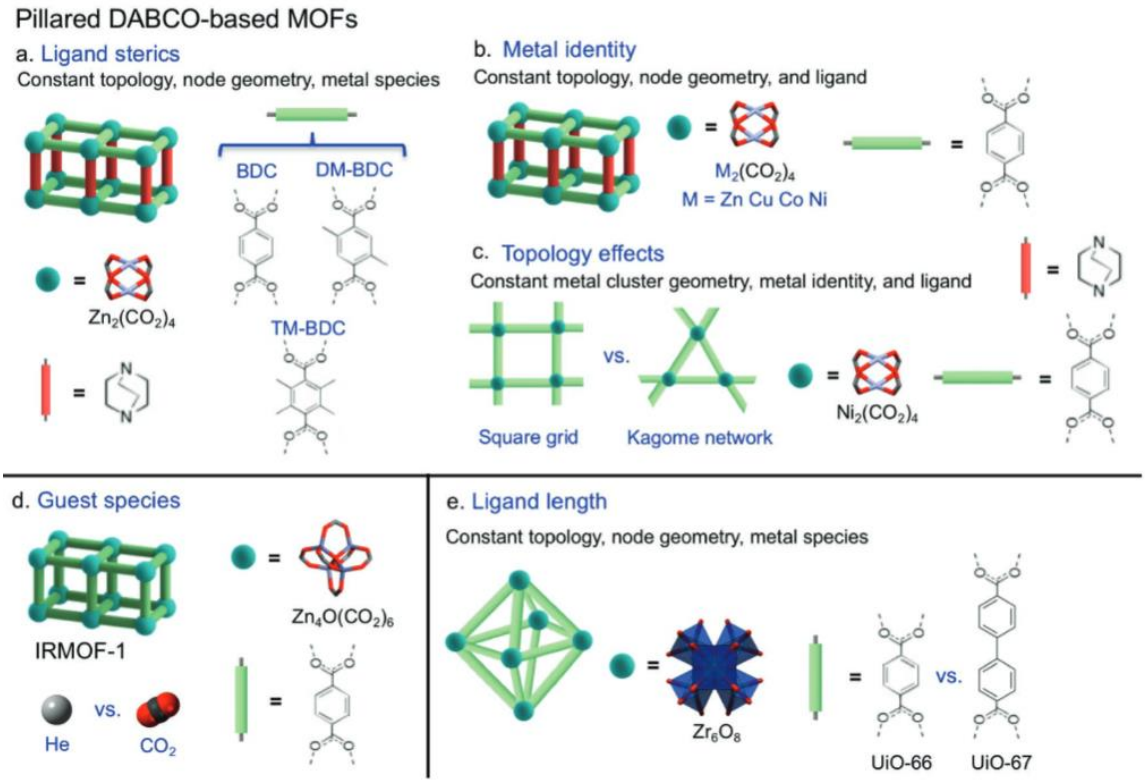

Figure 5.1: Overview of design strategies for thermal expansion contron in MOFs. A)modifying steric bulk of the organic linker, b) modifying the metal identity of the DMOF series, c) changing topology of the DMOF series, d) utilizing guest species for control of thermal expansion, and e) chaning ligand length and defect concentration to change the thermal expansion in the UiO series.

1.21.1 Ligand Steric Effects:

The first set of experiments to be discussed involves the M-DMOF series. Control of thermal expansion of this series through linker modification is done both in chapter 45 and

6. Adsorption, chemical stability, and flexible framework dynamics have all utilized ligand design as an emerging strategy for tuning these properties. When this strategy is applied the Zn-DMOF, the CTE can be changed from an average positive value to a negative one in the a/b-direction along the BDC units. Changing the thermal expansion of this axis does not appear to drastically effect the thermal expansion of the pillaring DABCO direction. This change in CTE is associated with large differences in the steric hindrance between BDC and its dimethylated and tetramethylated analogs DM-BDC (2,5-dimethyl-BDC) and TM-BDC (2,3,5,6-tetramethyl-BDC). Sterics around the bonding points of this linker can drastically effect the phonon density of states of this material as BDC is swapped out for its methyl functionalized variants. The phonons associated with NTE in MOFs involve twisting and bending of the organic linker as well as the metal node, and any inhibition of these vibrational modes is expected to effect the thermal expansion behavior. In this case, the linear CTE from 10-100°C changes from α = -9.6(9) ppm/K in Zn-DMOF-BDC, to α = -5.4(5) in Zn-DMOF-DM-BDC, and to α = 4.2(2) ppm/K in Zn-DMOF-TM-BDC (figure 4.2a). These results obtained from diffraction data are comparable to computed average CTEs obtained from molecular dynamics simulations on models for these three structures (α = -6.7, -6.4, and 4.1 ppm/K, respectively). The main differences in thermal expansion derive from the bulkiness of the benzene ring on each BDC-based ligand. As methyl functionalization increases, a torsion angle between the aromatic ring and the carboxylic acid groups is imposed. The importance of these structural changes on the thermal expansion is later explored using molecular simulation analysis (figure 5.2 b/c).

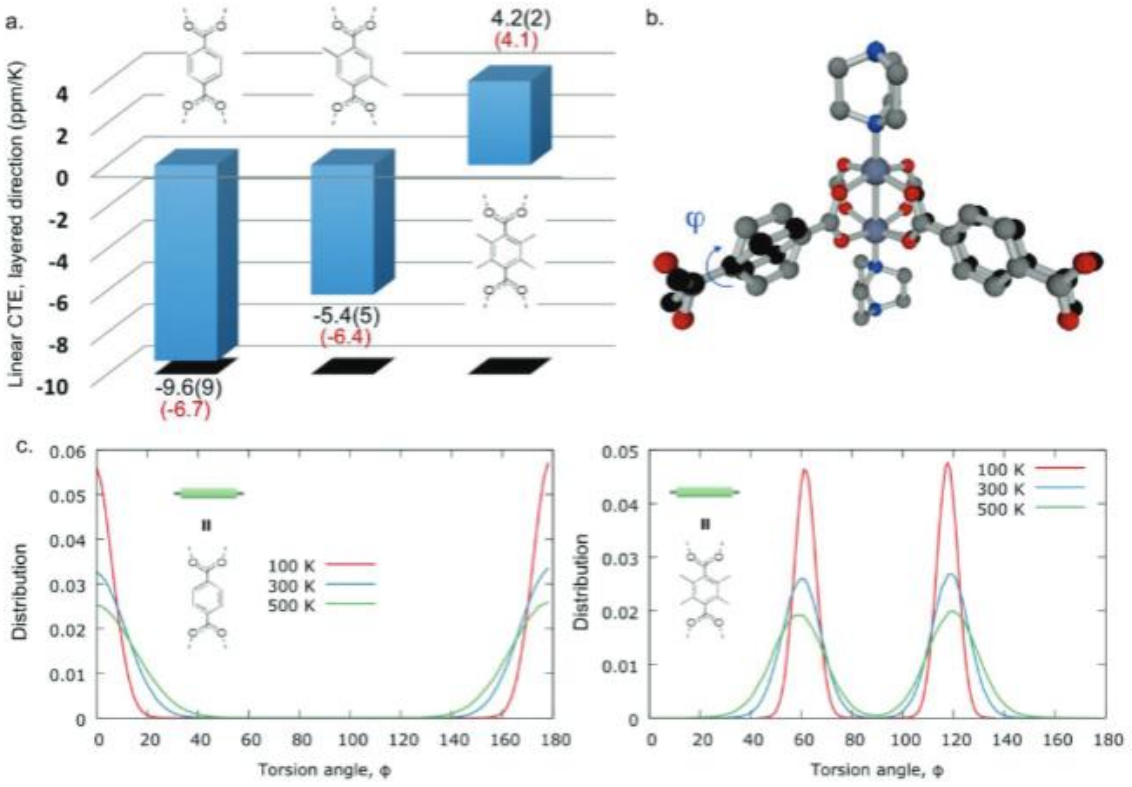

Figure 5.2: Thermal expansion and structural dynamics evolved from modifications in ligand sterics. a) Average linear CTE from 10-100 °C in Zn-DMOF variants. b) depictions of the torsion angles exhibited across the BDC-derivative organic linkers. c) normalized dihedral angle distributions profile for the BDC (left) and TM-BDC (right) structures as a function of temperature.

The distribution of these torsion angles remains Gaussian across the temperature ranges simulated, but the profiles of the bell-shaped curves in Zn-DMOF-BDC are wider than those of Zn-DMOF-TM-BDC. This indicates a decrease in the range of motions for the BDC linker in Zn-DMOF-TM-BDC due to the steric hindrance of its methyl groups. It was also found that imposing the torsion angle on BDC without the presence of methyl functional groups does not significantly change the NTE magnitude (figure D38, supporting information). Further simulations show that as the bulkiness of the methyl groups is slowly reduced, the magnitude of the NTE begins to rise (Figures D39 and D40) which further suggests the importance of the steric repulsion that these groups experience.

The syntheses and variable temperature experiments for this section were performed by Ashley Bird, Nicholas Burtch, and the thesis author. The diffraction and thermal expansion analyses were performed by the thesis author and Nicholas Burtch. The computational work on torsion angles and effects of ligand sterics on CTE were performed by Jurn Heinen and David Dubbeldam.

1.21.2 Topological and Metal Effects

M-DMOFs that posses $Ni_2(CO_2)_4$ cluster as opposed to $Zn_2(CO_2)_4$ clusters are found to exhibit either a square or Kagome layered network motif (see figure 4.1c). In the square (P4/mmm) network there exists one uniform pore size in the layered direction that contains a 90° angle between all ligand directions around the metal cluster. In the Kagome network there are two distinct pore openings and a non-90° angle between ligands around the metal cluster. Previous work[27] shows that the Kagome network phase is kinetically favored over the square phase and syntheses performed by Ashley Bird confirm the dual-presence of these phases under standard synthetic conditions for a M-DMOF. Because of the geometrical constraints of the two phases, it is highly unlikely that they can coexist within the same framework system. Because of this, it is assumed that the thermal expansion of each phase (separated into different unique crystals within the overall bulk sample) do not influence one another and can be measured independently using diffraction of the bulk sample. The diffraction patterns exhibit well-distinguished peaks for the two phases and show NTE in the layered direction for both structural variants (figure D14). The Kagome network was found to exhibit slightly higher magnitudes of NTE, as presented in figure

4.2.

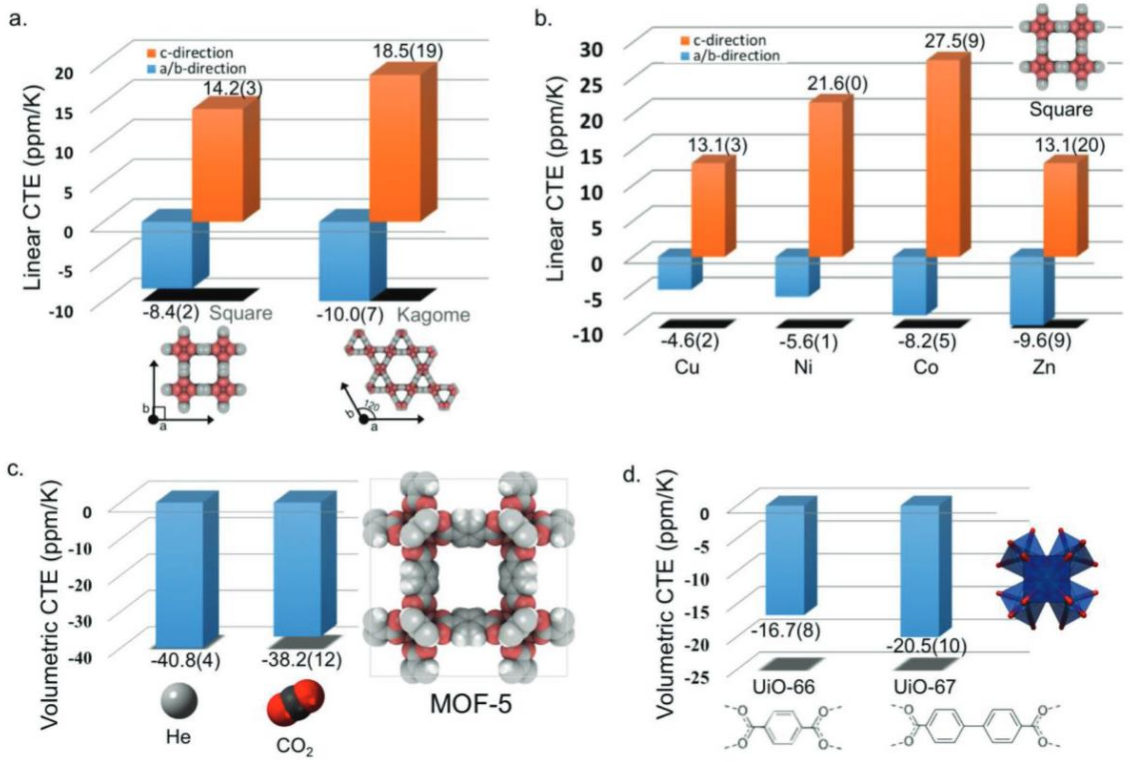

Figure 5.3 Thermal expansion behavior due to a) changing the structural topology in Ni-DMOFs, b) changing the metal identity in M-DMOF (Cu, Ni, Co, Zn), c) infiltration of a guest species in MOF-5, and d) linker length in the UiO-66/67 series.

Molecular simulations of the square vs. Kagome thermal behaviors agree with the experimental changes seen for the CTEs.

It was also found that by changing the metal identity of M-DMOF (Cu, Ni, Co, Zn), that the thermal expansion of the a/b-axis and c-axis can be modified (Figure 5.3b). The square topology is exhibited in all these variants, allowing for an easy comparison of their thermal expansion across the measured temperature region. Similar to the parents Zn-DMOF structure, each of these variants exhibit NTE along the a/b-axis and PTE along the c-axis. Along the a/b-axis, it is seen that as the distance between adjacent paddlewheels increases

(in correlation with lattice constant) the magnitude of NTE along this direction increases. This could be due to decreased steric interactions as well as increased flexibility. In contrast, the c-axis decreases in PTE magnitude going from left to right across the periodic table. Various components of these trends are difficult to deconvolute (with respect to their contribution to CTE), such as the presence of Jahn-Teller effects in the Cu-DMOF species or changes in atomic radii, bond strength, and effective charge of the bonding atoms across this series.

The syntheses for the experiments of this section were performed by Ashley Bird and the thesis author and the variable temperature experiments, diffraction analysis, and thermal expansion analysis were performed by the thesis author and Nicholas Burtch.

1.21.3 Guest effects

The thermal expansion of MOF-5 has been extensively studied over the past 10 years both experimentally and computationally, It has been agreed upon that transverse displacements of various components of the crystal structure (both metal node and linker) contribute highly to NTE, and that inhibition of these transverse vibrational modes can lead to decreases in the overall NTE magnitude exhibited. Because of the porosity of MOF-5, several different gases have been found to penetrate its structure. Incorporation of these guest species in the pore structure through variation of the gas environment of MOF-5 (while maintaining 1 atm total pressure) leads to slight changes in its overall CTE. Changing the gas environment from CO_2 to He leads to a change in the average volumetric CTE from α = -38.2(12) ppm/K to α = -40.8(4) ppm/K. Upon saturation with a target absorbate, temperature swings experienced in selective sensing applications are relevant to

these types of changes associated with CTE and gas environment. In MOF-5, CO_2 has a stronger framework interaction than He and adsorbs to a higher equilibrium loading at a given temperature. This can be related back to their general heats of adsorption in MOF-5. Unfortunately, it is very difficult to differentiate between loading effects and the inherent CTE in a MOF because the loading amounts of the guest species are also temperature dependent. A molecular model parameterized to capture the CO_2 adsorption behavior over the experimental temperature range was used to obtain approximate loadings of 4.5, 1.6, 0.8, and 0.3 mol/Kg at 240, 270, 300, 330, and 360 K, respectively. These loadings and the general predicted behavior agree well with computationally predicted behavior of host-guest interactions on the CTE of MOF-5 for other guest species such as benzene, isopropanol, and propane molecules.

The guest loading experiments were performed by Ashley Bird and Nicholas Burtch, and the thesis author (along with Nicholas Burtch) performed the diffraction and thermal expansion analysis.

1.22 Discussion

As mentioned previously, the ideal candidate for the NTE component of a near-ZTE composite material will have a negative CTE of large magnitude in order to minimize the amount of needed material for the composite application. It is also noted that, generally, single-phase polycrystalline materials such as ceramics are subject to anisotropic stresses associated with thermal expansion. This can lead to microcracking and other issues. Figure 5.4 below shows a ‘selection guide’ developed by Nicholas Burtch and the thesis author that shows a variety of different materials and representative average volumetric CTEs.

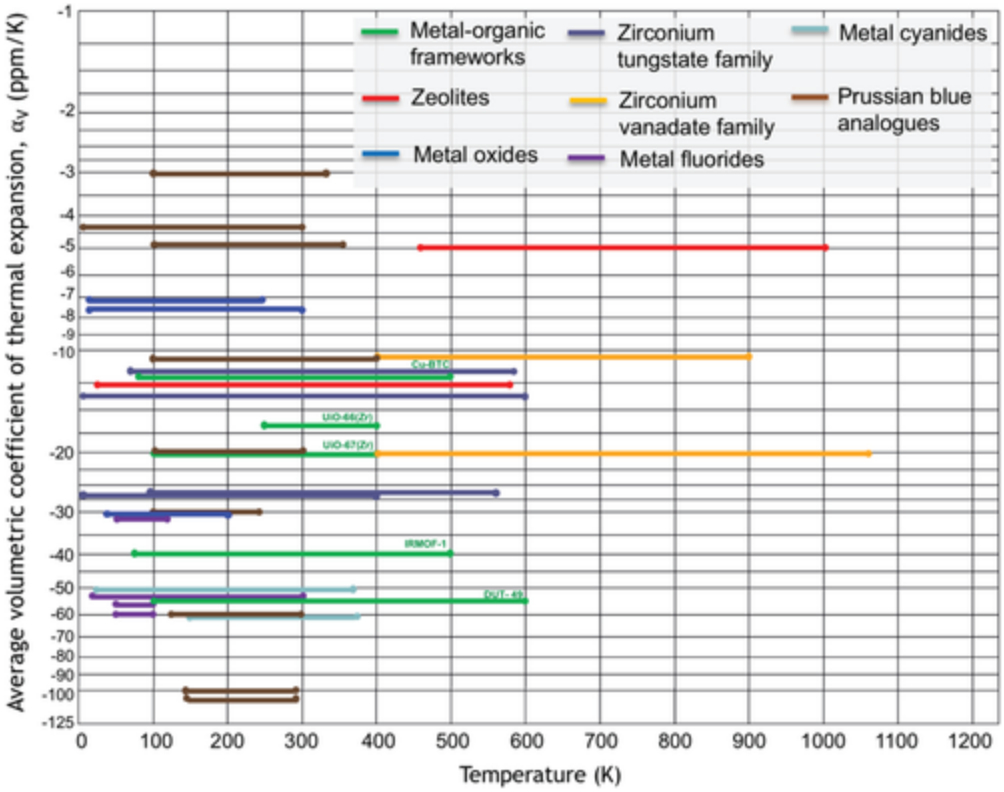

Figure 5.4: 'Selection Guide' for isotropic NTE crystalline materials. Reported values indicate average columetric CTEs across various temperature ranges for comparison. Values are based on literature and progressing research will reveal better candidates for such a figure in the future. For more information please refer to the cited publication.[224]

In comparison to other materials classes, MOFs offer a broader spectrum of structural tunability. The ability to modify the symmetry and identity around metal nodes as well as the flexibility, length, and functionalization of the organic linkers while maintaining the basic framework topology have led to an immense degree of structural modularity. In section 1 it was stated that phonon-mediated high magnitude NTE is reliant on a soft or 'flexible' structure. Of the known crystalline material classes, MOFs might be some of the softest materials to display long range order ever discovered. Earlier work by Cheetham et al found that MOFs of the ZIF family such as ZIF-8 ($Zn(MeIM)_2$, MeIM = 2-methylimidazolate) display bulk moduli within the low tens of GPa, and MOFs with much

longer linkers are suspected to have even softer elastic properties.[225,226] This being said, ZIF-8 actually behaves as a PTE material (α_v = 19.6(9) ppm/K).[224] This example shows that there is no single metric or structural parameter that can be used to predict high magnitude NTE, but instead that perhaps a collective set of parameters can be used as shown in the previous sections. Currently, there also exists a large gap in the application-based research of NTE MOFs. Translating the nanoscale (crystallographic) NTE to macroscopic (bulk) thermal expansion involves changes in not only the unit cell structure, but also the microstructure of the MOF and the PTE matrix within a composite (these changes could be interdependent). Progressing this area of the field is necessary before wide-scale implementation of MOFs in NTE-related applications.

1.23 Conclusion

This work is additive and complements previous work while drawing many of its conclusions from the related experimental and computational literature. A large portion of the theory comes from previous DFT and molecular dynamics calculations performed on both MOFs and similar framework materials. In this work, 5 design strategies are illustrated for tailoring the thermal behavior of MOFs by interchanging structural features and guest environment. Expanding upon this work involves more experimental studies on a wider variety of MOF topologies and will likely receive significant contributions from progressing database prediction techniques such as machine learning. In a general sense, a stronger fundamental understanding of thermal expansion in MOFs is necessary for advancing their utility in all applications that involve significant temperature fluctuation.

TUNING THERMAL EXPANSION IN METAL-ORGANIC FRAMEWORKS USING A MIXED LINKER SOLID SOLUTION APPROACH

This chapter is directly adapted from "Tuning Thermal Expansion in Metal Organic Frameworks Using a Mixed Linker Solid Solution Approach" Journal of the American Chemical Society **2019**, *141*, 12849-12854 *with permissions from Samuel J. Baxter (thesis author) et al and JACS.*[227]

1.24 Introduction

Although most materials display positive thermal expansion (PTE) due to the inherent anharmonicity of bond potentials,[1,13,228] some display the anomalous properties of negative thermal expansion (NTE) or near-zero thermal expansion (ZTE).[6,7,56] In principle, NTE materials can be used to compensate for the PTE of a matrix resulting in a controlled thermal expansion composite.[229,230] NTE in open framework materials[3,231] such as metal oxides,[1,13,56,228,232] metal fluorides/oxyfluorides,[25,29,80] cyanides,[33,36,233-235] and metal-organic frameworks (MOFs),[236-241] typically arises from the presence of low frequency vibrational modes that soften on volume reduction.[3,231] Strategies for controlling NTE in a given framework, such as the formation of solid solutions or the insertion of guest molecules,[13,104,105,242] can be thought of as methods for modifying the vibrational modes and their response to volume change.

MOFs, unlike typical framework solids, offer structure types more amenable to systematic change due to their modular buildup.[89] Construction of countless MOF topologies, using

different metals (or metal clusters) and organic ligands, is possible.[243] The preparation of solid solutions incorporating different ligands or metal clusters in a single-phase material enables fine tuning of material properties.[244,245] Although NTE has been reported in a number of MOFs[237,246], studies leveraging the modular build up and controlled exchangeability of building blocks, or the preparation of solid solutions, to manipulate thermal behavior are scarce.[11,164] To our knowledge there is no experimental evidence of tunable thermal expansion from negative to positive via the formation of MOF solid solutions in the peer-reviewed scientific literature, although there have been reports where the magnitude of thermal expansion has been tuned by incorporating guest molecules, isovalent metals, and structural defects.[11,107,242,247]

Zn-DMOF, $Zn_2(bdc)_2(dabco)$, is the parent framework of an anisotropic pillard-layered MOF family whose members are known to exhibit NTE in some directions and PTE in others.[248,249] **Zn-DMOF** is tetragonal and contains Zn_2 paddlewheels connected in their equatorial plane by 1,4-benzenedicarboxylate (bdc^{2-}) forming $Zn_2(bdc)_2$ layers that exhibit NTE. These layers are connected by 1,4-diazabicyclo[2.2.2]octane (dabco), which forms a pillar connecting the planes to one another (see Figure 6.1). Studies examining the flexibility, water stability, and thermal expansion of **Zn-DMOF,** and related functionalized forms, have been reported in the literature.[250-256] The Zn-DMOF platform is capable of accommodating a range of ligand substitutions, including TM-bdc^{2-} (2,3,5,6-tetramethyl-1,4-benzenedicarboxylate), which forms a compound isostructural to the parent framework, denoted **Zn-DMOF-TM** ($Zn_2(TM\text{-}bdc)_2(dabco)$).[257] A solid solution containing equal parts of TM-bdc^{2-} and bdc^{2-} was recently reported,[250] suggesting that solid solution formation may be a viable approach for tuning the thermal expansion coefficients

between the values of the parent end members **Zn-DMOF** and **Zn-DMOF-TM**. In this contribution, we report the preparation of $Zn_2(bdc)_{2-2x}(TM\text{-}bdc)_{2x}(dabco)$ (x = 0.0, 0.17, 0.45, 0.67, and 1.0), herein termed **Zn-DMOF-TM$_x$** and show that the TM-bdc/bdc ratio in the solid solution has a marked effect on thermal expansion properties of the framework.

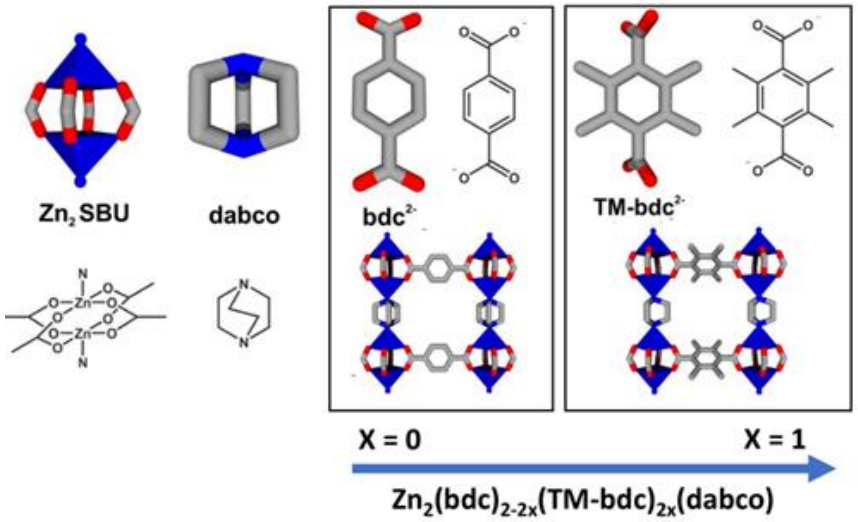

Figure 6.1: Secondary building unit and organic ligands present in the pillared Zn-DMOF-TM$_x$ solid solution. C, N, O are shown in grey, blue, and red respectively. The blue polyhedra represent the coordination environment around the Zn^{2+}. Hydrogen is omitted for the sake of clarity.

1.25 Experimental

1.25.1 Syntheses

$Zn(NO_3)_2 \cdot 6H_2O$ (98%), 1,4-benzenedicarboxylic acid (H_2bdc) (98%), and 1,4-diazabicyclo[2.2.2]octane (dabco) (>99%) were purchased from Sigma Aldrich. 2,3,5,6-tetramethyl-1,4-benzenedicarboxylate ($H_2TM\text{-}bdc$) (98.1%) was purchased from CHEM SERVICE inc. All chemicals were used without further purification.

Similar to the reported literature procedure for Zn-DMOF, Zn-DMOF-TMx solid solutions were formed by dissolving $Zn(NO_3)_2 \cdot 6H_2O$, dabco, H_2bdc, and H_2TM-bdc in dimethylformamide (DMF) in varying molar amounts.[250] As an example, **Zn-DMOF-TM$_{0.45}$** was synthesized using 0.180 g (6.05 mmol) of $Zn(NO_3)_2 \bullet 6H_2O$, 0.050 g (3.01 mmol) H_2bdc, 0.067 g (3.01 mmol) H_2TM-bdc, 0.036 g (3.20 mmol) dabco, and 9 mL of DMF. The initially formed solution was sonicated to help ensure complete dissolution. Upon standing a turbid suspension formed. The white colloid was separated via centrifugation. The remaining clear solution was placed into a glass vial, capped and heated at 120 °C for 48 hours. The resulting large clear crystals were washed by replacing the mother liquor with dry DMF for one hour and then further washed/solvent exchanged with dry chloroform three times over the course of three days. Each solid solution sample was dried under nitrogen flow before drying at 120 °C for 10 hours under vacuum.

1.25.2 X-ray Powder Diffraction.

Data were collected at beamline 11-ID-B of the Advanced Photon Source, Argonne National Laboratory, using a wavelength of $\lambda = 0.2113$ Å. Powder diffraction patterns were recorded at a sample to detector distance of 1000 mm on a Perkin Elmer amorphous silicon 2D detector. The samples were mounted in borosilicate capillaries under helium flow, using a previously described flow cell.[258] The sample temperature was controlled using an Oxford Cryosystems Cryostream.

1.25.3 Porosity and Surface Area Measurements.

Porosity measurements were performed using a Micromeritics ASAP 2020 instrument. 50-100 mg of each sample was activated at 120 °C for 10 hours before the collection of nitrogen isotherms at 77 K.

1.25.4 NMR measurements.

^{1}H-NMR measurements were performed using a Bruker 500'54 Ascend (500 MHz) using solutions containing approximately 5 mg of each sample dissolved in 0.5 mL of DMSO-d_6 and 50 µl of D_2SO_4.

1.25.5 IR measurements.

Spectra where collected using an Agilent Technologies Cary-630, equipped with an ATR accessory. The measurements were performed in an Argon filled glovebox to minimize noise. A background spectrum was collected prior to each measurement.

1.26 Results and Discussion

1.26.1 Sample Purity, Composition, and Porosity

Powder X-ray diffraction patterns collected using synchrotron-radiation (Figure 6.2) indicate that all prepared compositions (Zn-DMOF-TM_x; x = 0.0, 0.17, 0.45, 0.67, and 1.0) crystallize in the tetragonal space group *P*4/*mmm* at room temperature. For **Zn-DMOF** a small impurity peak at $2\theta = 1.48°$ was present. However, the size of this reflection, and the absence of any other significant reflections corresponding to any impurity, indicate that the thermal expansion of the main phase can be studied without interference from the impurity. The sample's room temperature a-axis lattice constant, obtained using Le Bail fits in

GSAS-II,[259] change in an approximately linear fashion over the composition range examined while the c-axis displays linearity from x = 0.17 to x = 1.0 (Figure E.1). Tabulated lattice constants and representative fits to the diffraction data (Figure E.2) are available in the Supporting Information.

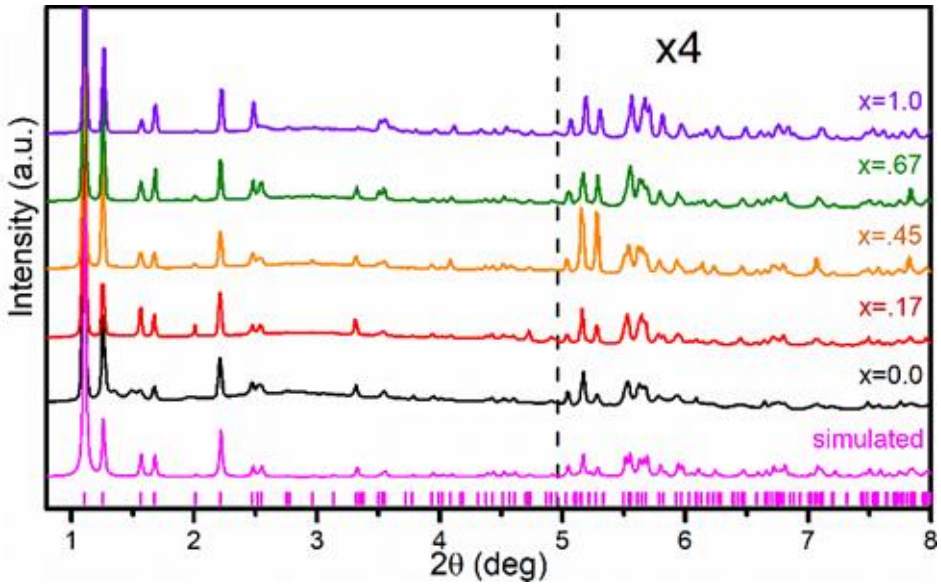

Figure 6.2: Synchrotron XRD patterns collected at room temperature for the Zn-DMOF-TM$_x$ samples. Magenta tick marks at the bottom of the plot indicate the expected peak positions for the *P*4/*mmm* phase simulated for the parent Zn-DMOF structure.

The ^{1}H NMR and IR spectra for each material indicate that the samples contain no significant non-crystalline impurities or remnant solvent from the syntheses (Figures E.3 & E.4). The ratio of the two ligands in the solid solution samples was controlled by changing the relative amounts of H_2bdc and H_2TM-bdc used in the syntheses. Figure 6.3 compares the H_2bdc to H_2TM-bdc ratio used in the syntheses with that incorporated into the MOF, as ascertained by ^{1}H-NMR on dissolved powder and single crystal samples of the MOF solid solution. The x = 0.45 powder and the x = 0.43 single crystal data points in this figure are from the same synthesis batch. The results shown in Figure 6.3 indicate that

the ratio of linker units incorporated into the MOF is close to that used in the syntheses and that the ratio incorporated into a single crystal is close to that of bulk powder made under the same conditions.

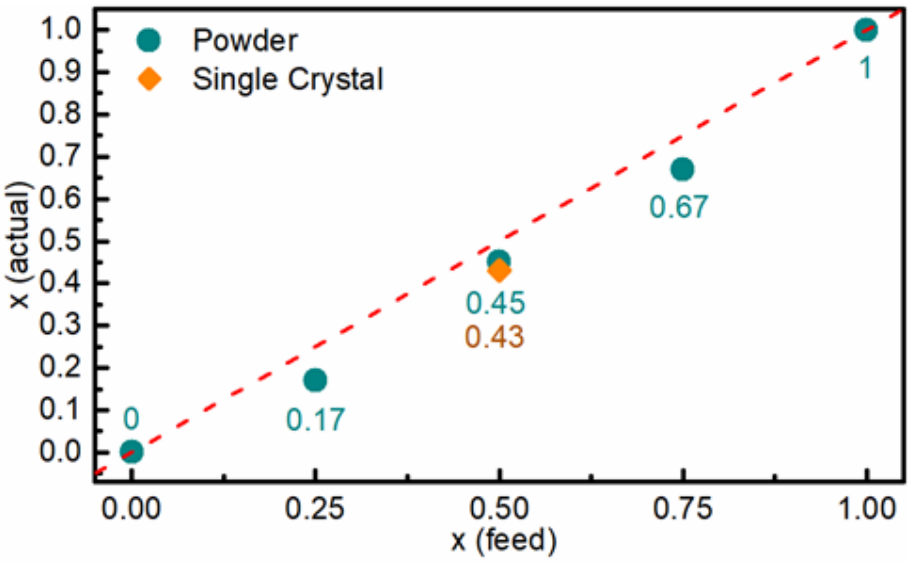

Figure 6.3: A comparison of the TM-bdc$_2$ fraction, X = [TM-bdc^{2-}]/ ([TM-bdc^{2-}] + [bdc^{2-}]), in the syntheses (feed) with that incorporated into the prepared Zn-DMOF-TM$_x$ samples (actual). The teal circles are for powder samples and the orange diamond is for a single crystal. The red dashed line indicates exact equivalence between the fraction used in the syntheses and that incorporated into the samples.

N_2 adsorption isotherms were collected at 77 K to assess the porosity of the samples. The BET surface area for the **Zn-DMOF** sample was 2119 m^2g^{-1} which is consistent with previous reports.[260] A decrease in both pore volume and BET surface area (Figure 6.4) was observed with increasing incorporation of the bulkier TM-bdc^{2-} ligand. For the samples **Zn-DMOF-TM$_{0.17}$**, **Zn-DMOF-TM$_{0.45}$**, **Zn-DMOF-TM$_{0.67}$** and **Zn-DMOF-TM$_{1.0}$** the BET surface areas were 1743, 1444, 1280, and 1067 m^2g^{-1}, respectively, and the nitrogen uptakes were 430, 369, 337 and 305 cm^3g^{-1} at p/p_0 = 1.

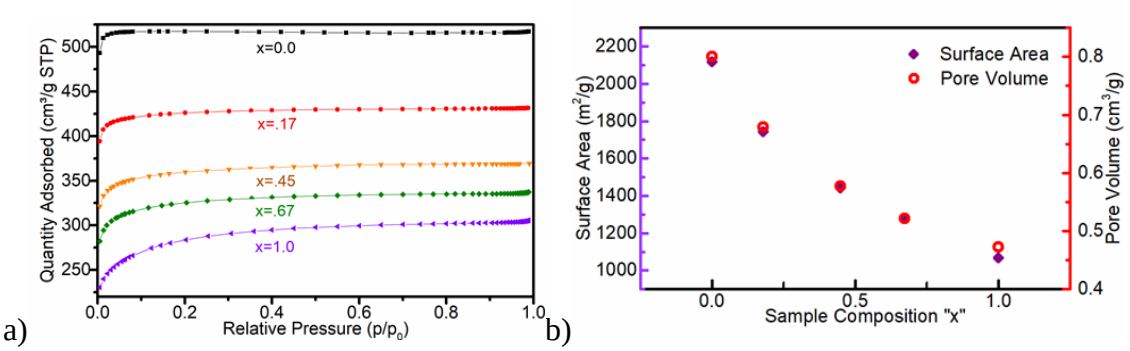

Figure 6.4: a) N_2 adsorption isotherms for Zn-DMOF-TM_x samples. The lines are guides to the eye. b) Comparison of BET surface area (purple, filled circles) and pore volume (red, empty circles).

1.27 Thermal Expansion

Each sample was investigated by variable temperature powder diffraction over the temperature range150 - 375 K. The lattice constants determined by Le Bail fits to these data are available in appendix E (Tables E.1 – E.5). The variation of the normalized lattice constant *a*, with temperature is shown in Figure 6.5. The parent Zn-DMOF shows NTE in the *a*-*b* plane over most of the studied temperature range. However, as the TM-bdc content is increased the magnitude of this negative thermal expansion decreases and the thermal expansion becomes positive for high values of x.

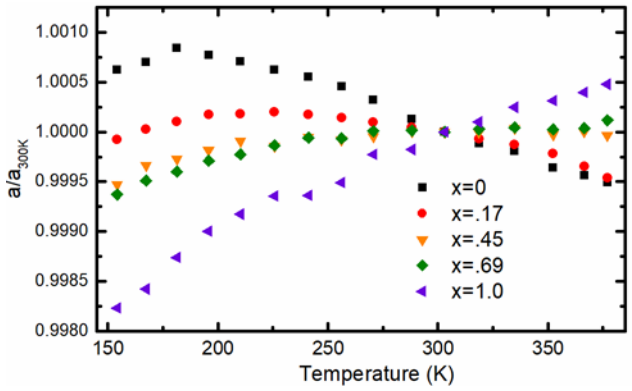

Figure 6.5: Variation of a/a_{300} for the Zn-DMOF-TM$_x$ samples as a function of temperature and composition.

For each sample, linear coefficients of thermal expansion (CTE) in the *a*-*b* plane were estimated by differentiating a 3rd-order polynomial fit to lattice constant vs. temperature. The individual polynomial fits and the derived CTEs can be found in the supplemental information (Figure E.6). For the parent **Zn-DMOF** structure (x = 0.0), the linear CTE in the *a*-*b* plane reaches a minimum of ~-10 ppm/K at ~288 K. The observed minimum linear CTE generally increases as the fraction of TM-bdc in the samples rises, crossing through zero to become positive at close to x = 0.5. In each case, the temperature at which the minimum CTE is observed is 288 K or higher.

In contrast to the behavior in the *a*-*b* plane, the thermal expansion parallel to the crystallographic c-axis is positive for all compositions (Figure E.5). Linear CTEs, estimated from 2nd order polynomials fitted to the lattice constants as a function of temperature (Figure E.7), are strongly positive across the entire sample series at all temperatures, with average values falling in the range 15 - 21 ppm/K. The distinct responses of the thermal expansion in the *a*-*b* plane and parallel to the *c*-axis to changes in composition are not surprising, as the methyl groups on the TM-dbc ligands have been

previously shown via solid-state NMR and molecular simulations to have minimal interaction with the pillaring dabco ligands.[261]

Four of the five compositions studied exhibit ZTE along the a/b-axes in the temperature range studied. The temperature at which zero thermal expansion occurs changes in an approximately linear manner with sample composition, indicating near-direct tunability of the phenomenon (Figure 6.6).

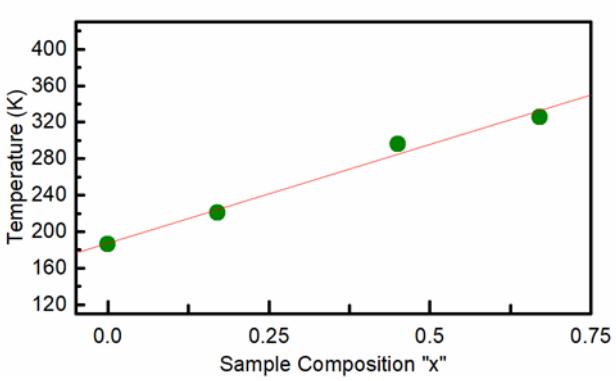

Figure 6.6: The temperature at which zero thermal expansion (ZTE) in the a-b plane occurs as a function of composition for Zn-DMOF-TM$_x$ (0.0 < x < 0.67). The x = 1.0 sample does not display ZTE in the temperature range studied.

1.28 Conclusion

Single phase mixed linker **Zn-DMOF-TM$_x$** solid solutions can be prepared using a simple solvothermal synthetic approach across the entire composition range $0 < x < 1$. ^{1}H NMR spectroscopy showed an almost linear relationship between the ratio of the two linkers, bdc^{2-} and TM-bdc^{2-}, in the reaction mixture and the final solid solution products. The pore volume, BET surface area, and room temperature lattice constants change smoothly with composition. As the composition is changed, the thermal expansion in the a-b plane evolves from predominantly negative for x = 0 to positive for x = 1.0. This high level of tunability

for the **Zn-DMOF-TM$_x$** system suggests that the systematic substitution of functionalized ligands into other MOF frameworks will provide access to many different families of controlled thermal expansion materials. While many other MOFs are known to accept functionalized versions of their organic linkers,[244] at this time there is little experimental or computational evidence regarding how this effects their thermal behavior.

SYNTHESIS OF A NEW HYBRID PEROVSKITE BY INCORPORATION OF HE INTO SCF_3

1.29 Introduction

The perovskite family of materials spans a wide range of compositions[262] and its members display many distinct technologically significant properties. The mineral perovskite ($CaTiO_3$) was discovered in 1839 in the Ural Mountains of Russia by Gustav Rose and named after the acclaimed Russian mineralogist Lev Perovski.[263] The perovskite structure was described initially in 1926 by Victor Goldschmidt who pioneered some of the earliest scientific investigations into the structural diversity of perovskites.[264] In the basic formula, ABX_3, 'A' and 'B' are typically cations with very different atomic radii, and X is an anion that bonds to both cation types creating corner sharing BX_6 octahedra, with the larger A cation nestled in the center cavity space with 12-fold cuboctahedral coordination.

Depending upon chemical composition, a wide variety of distortions away from this prototypical structure occur. Cation ordering,[265,266] vacancies and vacancy ordering,[267] cooperative tilting of the BX_6 octahedra,[196,268-272] and displacement of the B- and/or A-site cations away from their ideal positions[273,274] are common. The B-site has been found to accommodate a large variety of metals and the A-site has been found to tolerate cations of many different sizes including cationic organic species[262] and neutral molecules such as N_2.[275-277] The X-site has been expanded far beyond the initial oxide structures to commonly include nitrides and halides, as well as molecular anions. The formation of cubic, or distorted perovskites, based on the atomic radii of the A-, B-, and X-site species can be

predicted using the Goldschmidt tolerance factor.[278] Perovskite applications include photovoltaics, dielectrics, ferroelectrics, oxide and proton conductors in fuel cells and catalytic membrane reactors, and scintillators.[264,279-281]

The structurally related ReO_3-type materials (BX_3) have also been extensively investigated due to their structural flexibility and modularity.[264] The chemical diversity of this structure type ranges from simple fluorides and oxides, like ScF_3 and ReO_3, to much more complex materials with molecular linkers such as cyanide CN^-, hypophosphite ($M^{III}(H_2POO)_3$, and larger polyatomic linkers such as those found in IRMOF-1. Characteristically, ReO_3-type structures are more open that typical ABX_3 perovskites (see section 1.2.3.3). This becomes obvious when comparing the more expanded structures containing polyatomic linkers such as extended phosphites and MOFs. This openness greatly influences the properties of ReO_3-type materials. It leads to greater mechanical flexibility, which can give rise to the related properties of negative thermal expansion (NTE), softening upon compression (SUC), and the ability to adsorb guest species into the empty A-site, such as Helium.[185]

The cation-ordered cubic ReO_3-type fluoride with the formula $CaZrF_6$ has been found to exhibit strong NTE over a wide temperature range and SUC.[85] This is attributed to low frequency vibrational modes involving transverse motion of the fluoride. Recently, it was reported that helium can be forced into the initially vacant A-sites, to create defect perovskites $(He_{2-x}\square_x)$-$(CaZr)F_6$.[185] Neutron diffraction, along with gas uptake and release measurements, demonstrated that helium could be forced into the structure at 300 K, and trapped inside the material at ambient pressure and low temperatures (~100 K). Rietveld analyses of neutron diffraction data and the gas release measurements showed that at 500 MPa and 300 K a stoichiometry of $He[CaZr]F_6$ could be achieved, which corresponds to

filling ~50% of the available A-sites. It was found that the insertion of helium gas into $CaZrF_6$ elastically stiffens the material and reduces the magnitude of its NTE as the A-site becomes occupied. Upon compression in helium at 300 K, the structural disordering that typically occurs at < 0.5 GPa for $CaZrF_6$, when compressed in other media, moves to much higher pressures.[282] The preparation of $[He_{2-x}\square_x][CaZr]F_6$ is the first example of a controlled synthesis for a perovskite with a neutral species on the A-site, and it suggests that a large family of related materials may be experimentally accessible. In this chapter, ScF_3 is investigated for its ability to take up helium at elevated temperatures and trap it upon decompression to ambient pressure and temperature conditions. ScF_3, like $CaZrF_6$ has an ReO_3-type structure and shows strong negative thermal expansion over a wide temperature range.[153] However, its ambient temperature unit cell constant (~4.01 Å) is much smaller than that for $CaZrF_6$, so the apertures for helium to penetrate into the structure are more restricted. This leads to the potential for this material to trap a neutral species under non-ambient conditions and hold the species species under ambient conditions, a feature not yet seen for this class of storage materials. Prior studies of ScF_3 at room temperature and below in high pressure helium gas (< 0.3 GPa), showed no evidence of helium penetration.[153]

1.30 Experimental section

1.30.1 Materials

ScF3 (99.9%) was purchased from STREM Chemicals.

1.30.2 High-Pressure X-ray Diffraction and Gas Loading

High-pressure X-ray diffraction data were collected at beamline 16-BM-D of the Advanced Photon Source, Argonne National laboratory. A focused X-ray beam (3.5 x 4.7 μm FWHM) of wavelength of 0.41328 Å (~30 keV) was employed, along with a MAR345 image plate detector, for the measurements. A ScF_3 – CaF_2 (~4:1) mixture was loaded, along with Au and ruby balls as additional pressure standards, into two symmetric DACs. The DACs were equipped with 600 μm cullet diamonds and laser drilled (350 μm hole) pre-indented rhenium gaskets. The two cells were loaded with helium and neon respectively using the GSE CARS gas loading facility,[283] to give an initial pressure between 0.1 and 0.5 GPa. The cells were mounted in an evacuated enclosure that allowed them to be externally heated and the pressure in the DAC to be increased using a diaphragm. Sample pressure was principally determined using the unit cell volume for CaF_2 along with its known equation of state.[172]

1.30.3 Rietveld Analysis

Rietveld refinements were used to determine structural parameters and lattice constants of ScF3 and CaF_2. All the fits were done using the General Structure Analysis System-II (GSAS-II). An example fit is shown below in figure 7.1.

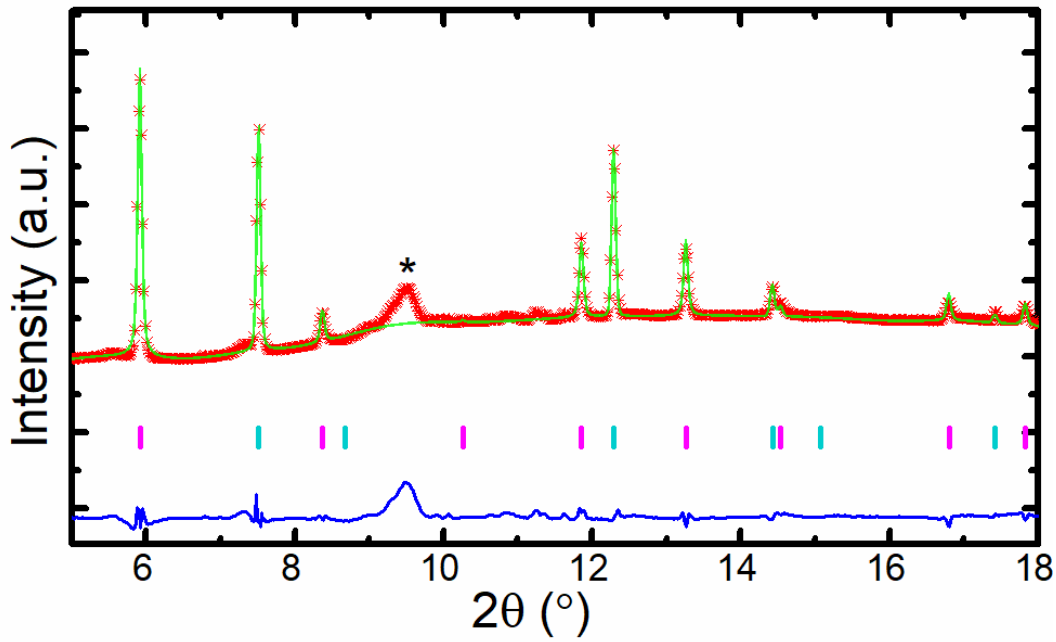

Figure 7.1: Rietveld fit to ScF_3 in a DAC at 0.09 GPa and 300 K collected using a wavelength of 0.41328 Å (~30 keV). The pink and cyan tag marks indicate the peak postions for the ScF_3 and CaF_2 respectively. * indicates scattering from the polymer windows on the heating apparatus.

1.31 Results and Discussion

On initial heating to 300 ºC of the DAC loaded with ScF_3 in helium, the pressure as indicted by the internal pressure standard increased to 0.98 GPa. The diffraction data recorded during the heating (Figure 7.2) show no signs of a phase transition. This is consistent with the previously published pressure temperature phase diagram for ScF_3 at less than 300 K,[153] which indicates that at 300 K[25] a cubic (Pm-3m) to rhombohedral (R-3c) phase transition is expected at ~ 0.7 GPa. Linear extrapolation of the published phase boundary suggests that at 300 ºC, a transition would not be expected below ~1.4 GPa

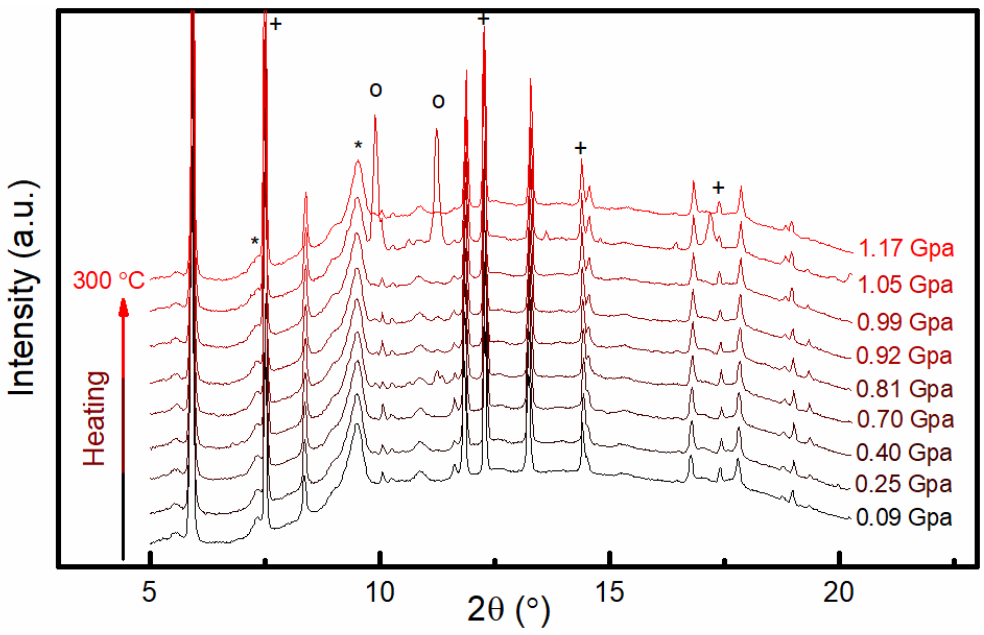

Figure 7.2: Diffracton data for ScF_3 as the DAC is heated in a helium atmosphere. * peaks from a polymer window on the heating apparatus. O - peaks from the rhenium gasket and + peaks from the CaF_2 pressure calibration standard.

After heating to 300 °C, the pressure was increased to 4.95 GPa in stages while recording diffraction data. The diffraction data on compression (Figure 7.3) indicate that the ScF_3 remains cubic, although the appearance of some weak peaks in the range 2Θ 6 – 7º may indicate that small fraction of the sample transforms to a previously reported high pressure orthorhombic phase of ScF_3. This assignment is tentative, as the original environment and thermodynamic conditions are not reproduced in this experiment, but the appearance of two small peaks between the first two cubic peaks at higher pressures is consistent with the reported X-ray diffraction data for orthorhombic ScF_3-II (β-YF3 structure). However, in the original report for ScF_3-II, the phase is reported at 10.8 GPa and 756 K.29 Notably, there is no indication of a rhombohedral phase on compression. This suggests that, similar to $CaZrF_6$ at room temperature, helium penetrates into ScF_3 at 300°C and stabilizes the cubic phase against this initial phase transition on compression.

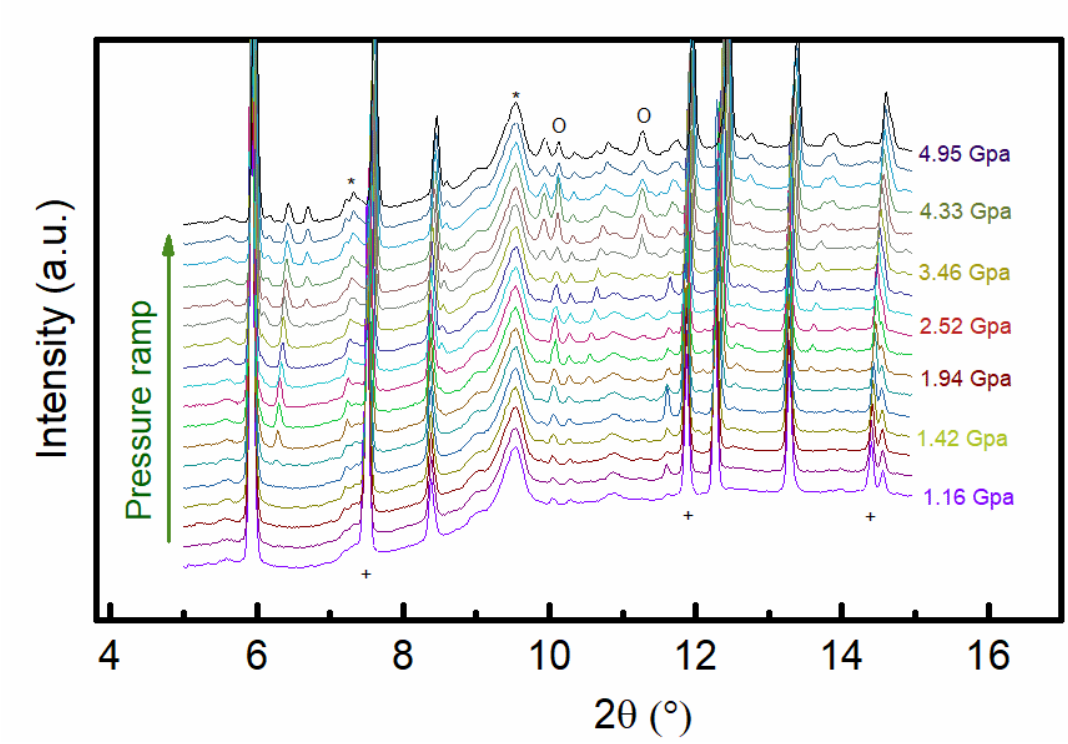

Figure 7.3: Pressure ramp of ScF_3 confined in helium atmosphere within a DAC. * Indicate peaks from the polymer window of heating apparatus. O symbol indicates peaks from the rhenium gasket and + symbol indicates CaF_2 pressure calibration standard.

After leaving the sample at 300°C for 1.5 hours and maximum pressure, the cell was cooled back to room temperature while recording diffraction data (Figure 7.4). On cooling the pressure increased ~6.79 GPa, presumably due to the thermal expansion of the DAC. The cubic form of ScF_3 was retained to ambient temperature, strongly supporting the penetration of helium into the material.

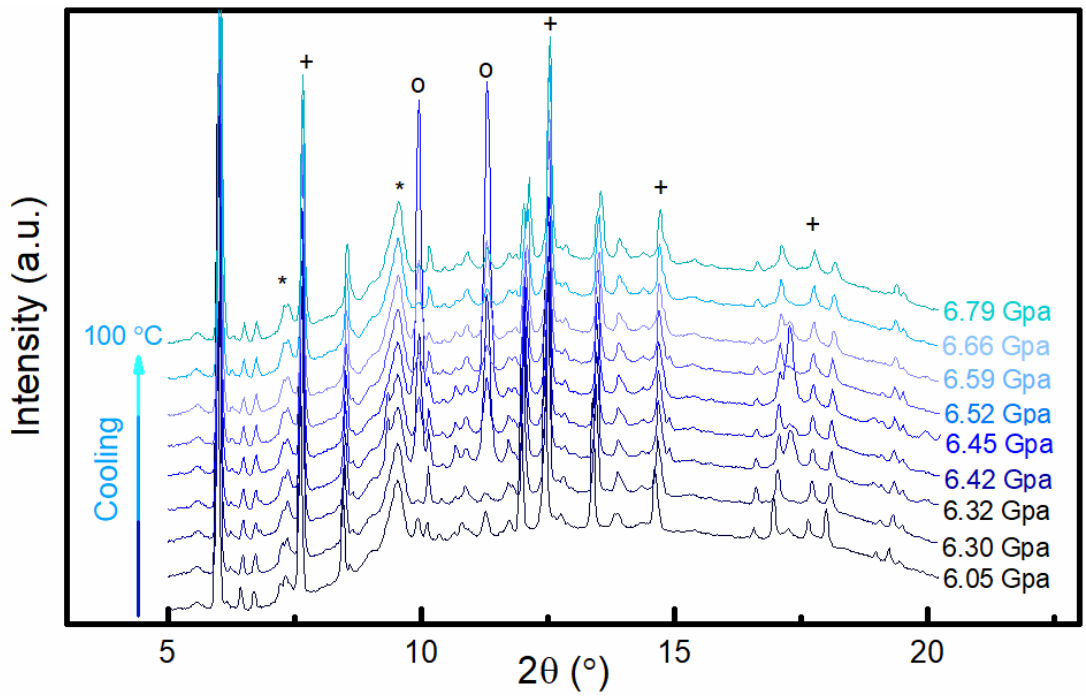

Figure 7.4: Cooling ramp of ScF_3 confined in helium atmosphere within a DAC. * Indicate peaks from the polymer window of heating apparatus. O symbol indicates peaks from the rhenium gasket and + symbol indicates CaF_2 pressure calibration standard.

Finally, data was recorded after the DAC was fully decompressed at room temperature outside of the heating apparatus (Figure 7.5). It can be seen that the peaks from the polymer window of the temperature control apparatus are no longer present, but that two small peaks (~6.4 and ~7.1º 2Θ) from the pressure-induced impurity phase are still present, consistent with the formation of the previously described orthorhombic ScF_3-II phase.

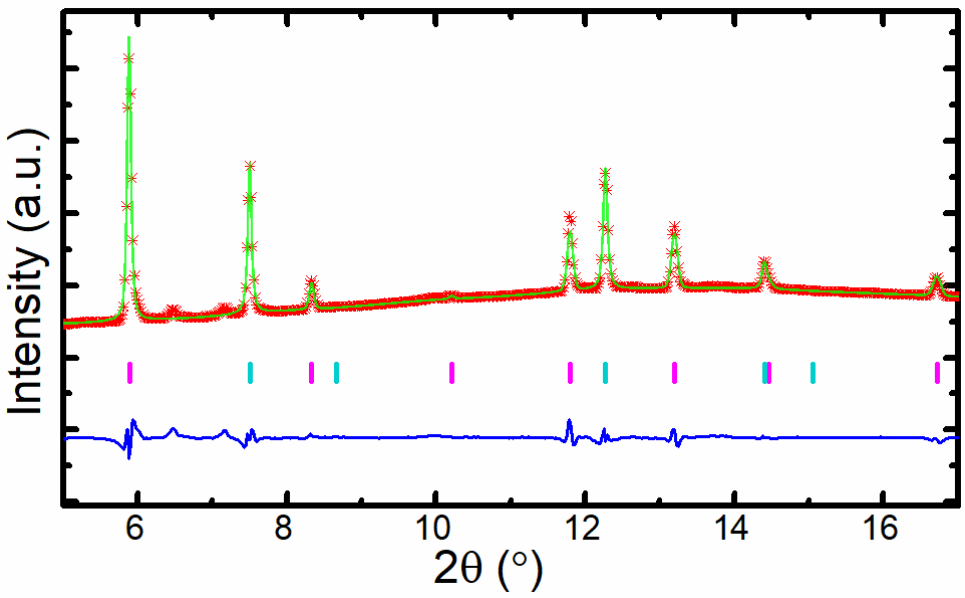

Figure 7.5: Rietveld refinement of decompressed ScF_3 under ambient conditions using a wavelength of 0.41328 Å (~30 keV).

The unit cell volume for ScF_3 as it was compressed, heated and cooled are shown in Figure 7.6a. Similar to what was seen for CaZrF6 at room temperature, the unit volume for ScF_3 at 300 °C initially increases on compression (1.0 – 1.7 GPa), indicating that helium is being forced into the material as the pressure goes up. At around 1.7 GPa, a maximum in the unit cell volume is reached, and the unit cell volume decreases on further compression. The change in volume over the pressure range 1.9 – 4.8 GPa indicates an average bulk modulus of 124.3 GPa, which is significantly higher than expected for unloaded or pristine ScF_3, especially because of its negative pressure derivative. This kind of drastic increase in bulk modulus upon guest loading is likely due to an inhibition of the structure's natural flexibility that relies on the unoccupied void space.

In Figure 7.6b, the observed unit cell volumes are compared with those estimated using a Murnaghan pressure-temperature equation of state for ScF_3 assuming a bulk modulus of

60 GPa, a pressure derivative of 4, and a linear change in the volumetric CTE from -27 to -72 ppm/K. The observed decrease in unit cell volume while initially heating to 300 ºC is significantly less than that predicted by the equation of state, suggesting that some helium is able to penetrate into the ScF_3 at temperatures below 300 ºC. It is notable, that the unit cell volume determined from the cooled and then fully decompressed material is larger than that of pristine ScF_3, suggesting that the recovered sample contains trapped helium.

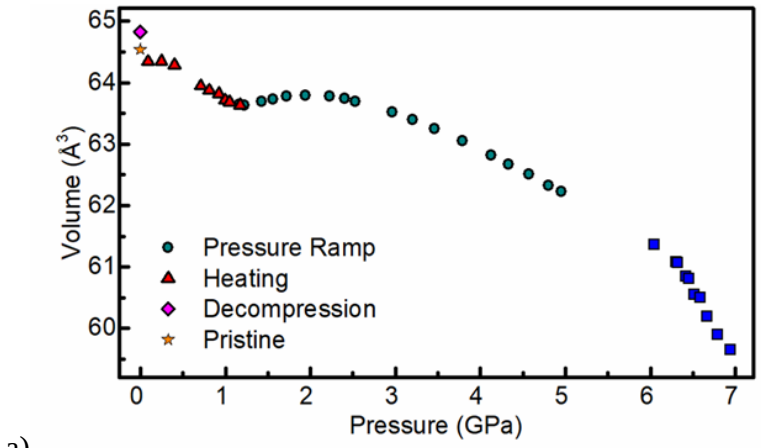

a)

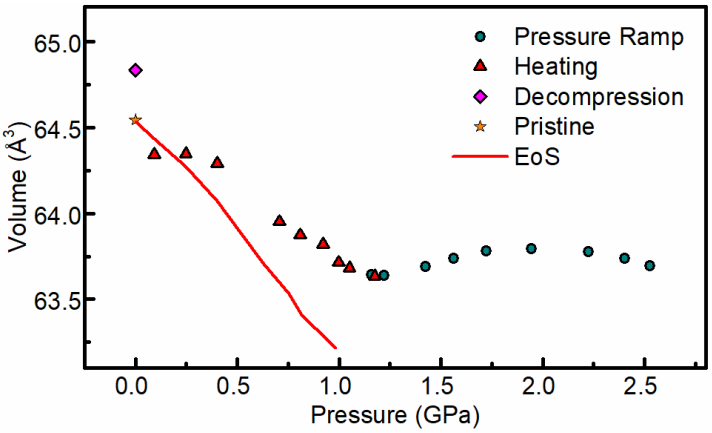

b)

Figure 7.6: a) Unit cell volume vs. pressure for ScF_3 as it is heated (red triangles), compressed at 300 ºC (green circles), and cooled to room temperature (blue squares). The unit cell volumes for the sample after complete decompression at room temperature (magenta diamond) and pristine ScF_3 (yellow star) are shown for comparison. b) An expanded region of the unit cell volume versus pressure plot along with a prediction of the unit cell volume for pure ScF_3 from a Murnaghan equation of state (red line) for the presures/temperatures achieved while initially heating the sample.

1.3.2 Comparison between the behavior of ScF_3 and $CaZrF_6$ on compression in helium

Neutron diffraction and gas uptake / release measurements for $CaZrF_6$ in helium indicate that at room temperature helium penetrates into $CaZrF_6$ < 0.1 GPa and at a pressure of 0.5

GPa approximately half of the vacant A-sites in ReO_3-type $CaZrF_6$ are filled to give a perovskite of approximate composition [He][CaZr]F_6, where □ indicates a vacant A-site.[185] Higher pressure room temperature diffraction measurements for $CaZrF_6$, performed using helium loaded diamond anvil cells by Hester et al.,[200] show that the unit cell volume for this material goes through a maximum at ~0.7 GPa and that the insertion of helium into the structure stabilizes the perovskite phase against amorphization up to ~ 3GPa. The behavior of ScF_3 on compression in helium is qualitatively similar but quantitatively different from that of $CaZrF_6$. Prior work on ScF_3 at < 0. 3 GPa and ~300 K,[153] provides no indication of helium penetration at room temperature, and the observation that ScF_3 recovered from ~ 5 GPa/300 ºC, by cooling followed by decompression to ambient, has a larger lattice constant than pristine ScF_3 suggests that helium can't penetrate into or leave the A-sites in ScF_3 at room temperature. The pressure observed for the maximum in the unit cell versus pressure curve for ScF_3 at 300 ºC (~1.7 GPa) is much greater than that seen for $CaZrF_6$ at 300 K (0.7 GPa), likely indicating a difference in the thermodynamics for helium uptake in these two materials. The different kinetics for helium migration within ScF_3 and $CaZrF_6$ can be qualitatively understood from a consideration of their unit cell constants. The 4.01 Å unit cell constant for ScF_3 indicates that the minimum F – F distance across the apertures separating one A-site from another is 4.01 Å, but in the case of the cation ordered double ReO_3-type material, $CaZrF_6$, it's lattice constant (8.48 Å) implies a minimum F – F distance of 4.24 Å. These different aperture sizes are reflected in estimates, by J. McDaniel using DFT calculations for a 2 x 2 x2 supercell,[284] of the activation barrier for helium migration between different A-sites (Table 7.1).

Table 7.1: A comparision between estimates for the activation barrier for helium migration between A-sites in ReO_3-type fluorides and the F- F distances that define their pore sizes. [284]

	F – F distance (Å)	Activation barrier (kcal/mol)
$CaZrF_6$	4.24	8.5
ScF_3	4.01	13.4

Prior low temperature high pressure neutron diffraction and gas release measurements on $CaZrF_6$ indicate that at ~ 150 K helium is unable to migrate through the material on a time scale of an hour. Given this observation, the estimated difference in barrier heights between ScF_3 and $CaZrF_6$ suggests that helium migration in ScF_3 should not be possible at < 240 K. In the light of this estimate, further work on ScF_3 in helium at 300 K needs to be done to confirm, or refute, the suggestion from our recovered sample that helium in fact immobile in ScF_3 at room temperature.

1.32 Conclusion

The current data suggest that He penetrates the pores of ScF_3 before 300°C and 1 GPa, but the exact conditions necessary for infiltration is currently unknown. As expected, there is no phase transition during the heating ramp to the max temperature, but interestingly, the cubic phase persists to far beyond the predicted pressure phase stability of the uninfiltrated material and there is an impurity phase that develops just beyond 1.5 GPa that resembles a previously reported orthorhombic ScF_3-II (YF_3 structure). Similar to ScF_3-II, this orthorhombic impurity phase remains upon recovery to ambient conditions. Diffraction

data for the quenched sample indicate a cubic lattice constant much greater than that of the pre-experiment pristine sample. This is consistent with the infiltration of a guest species at high temperature that is now trapped under ambient conditions. These results are also broadly consistent with the activation barrier (for diffusion) estimations of ScF_3 vs. $CaZrF_6$. Like $CaZrF_6$, the lattice constant begins to raise over the expected pressure-temperature 'loading' region of the experiment, but this behavior begins at higher temperatures and pressures for ScF_3, correlating with its smaller pore aperture and higher activation barrier to diffusion. Future work for this system will involve gas uptake/release measurements to facilitate a more quantitative description of He loading in this system. Room temperature high-pressure experiments can also be performed to definitely rule out the possibility of He entering at room temperature.

CONCLUSIONS

1.33 Tunable thermal expansion and behavior upon compression of mixed-metal Fluorides

Tunable thermal expansion and behavior upon compression have been explored for three mixed-metal fluoride systems. For each of these systems the metal ratio was varied from that of a stoichiometric parent structure to that of a fluoride-excess solid solution. The long range and local structures of these systems were characterized using a combination of density measurements, low temperature neutron/x-ray-sourced Rietveld refinements, and neutron/x-ray-sourced PDF analysis. These materials were originally chosen because the ReO_3-type structure is simple and fairly straight-forward in structural modification and analysis, but it was found that different modification strategies yielded strong differences in the capability to control behavior within these systems. The strategy applied to the systems in chapters 2&3 involved replacing some amount of the lower valent metal in $M^{2+}M^{4+}F_6$ and $M^{3+}F_3$ systems with the higher valent Zr^{4+} metal creating M^{4+}-rich solid solutions. Density measurements for both $Mg_{1-x}Zr_{1+x}F_{6+2x}$ and $Sc_{1-x}Zr_xF_{3+x}$ solid solutions indicate a strong match with an anion interstitial defect mechanism, leading to the classification of these systems as “fluoride-excess” solid solutions. PDF measurements in these systems also support this classification and correlate strongly with the proposed introduction of edge-sharing polyhedra within the initial ReO_3-type structure exhibited by the parent structures. This drastic change in the local structure of these materials was found to significantly inhibit the flexibility inherent to the parent structures. These changes have been shown to lead to tunable thermal expansion and behavior upon compression through

systematic modification of the local structure. The proposed change was also reflected in the measured lattice constants of both systems which were shown to decrease linearly with x. The $Mg_{1-x}Zr_{1+x}F_{6+2x}$ system showed tunable thermal expansion from strong NTE to modest PTE over the measured temperature range using compositions between x = 0.0 and x = 0.5. These major changes reflect what is seen in the compression experiments which showed increases in the bulk modulus and pressure derivative as the Zr^{4+} content was increased. Interestingly, a cubic to rhombohedral low-temperature phase transition exhibited by the parent $MgZrF_6$ material was eliminated entirely with a modest increase in the Zr^{4+} content. The related low-pressure phase transition of $MgZrF_6$ (from cubic to rhombohedral) was pushed to higher pressures with higher x and eventually eliminated entirely over the measured pressure range in the x = 0.5 sample. Similar changes in thermal behavior had already been known for the $Sc_{1-x}Zr_{1+x}F_{3+x}$ system, and the variable-pressure data in chapter 3 has strongly correlated with what was seen in the Mg-Zr system. Chapter 4 introduced a strategy for control of thermal expansion through the work of Brett Hester which involved replacing Zr^{4+} with varying amounts of Nb^{5+} in $[Zr^{4+}_{1-x}Nb^{5+}_{x}]F_{6+x}$ as a comparative study to the previous method of structure and thermodynamic behavior control. Density measurements once again showed a strong correlation with an anion interstitial defect mechanism, but this time the x-ray-sourced PDF data did not support the introduction of edge-sharing polyhedra and instead showed no significant changes in local structure. This prompted the proposal of a new anion interstitial defect mechanism for these solid solutions potentially involving higher coordinate polyhedra with unbound terminal fluoride. This theory coincided with the insignificant changes in the flexibility of these systems. Unfortunately, these systems were found to exhibit extreme history-dependent

thermal behavior which made the initial comparison of their thermal expansion difficult. It was found that the history-dependence had a relatively short time-span, and that thermal cycling could eliminate this effect for a long enough duration to remeasure the change in cell volume with temperature for the x = 0.75 sample.

The two strategies here can be compared to previous strategies for property control in mixed-metal fluorides that involved swapping the metal identity in $M^{2+}M^{4+}F_6$ with different metals of the same oxidation state.[282] This related strategy afforded very limited control of the thermal expansion and behavior upon compression, but did show significant changes in thermal expansion, behavior upon compression, and phase stability with metal identity. It also introduced the $CaNbF_6$ system as one of the strongest known NTE systems, according to Goodwin et al.[143]

1.34 Tunable thermal expansion of MOFs

The next strategies for control of thermal expansion were performed on a diverse set of MOFs. Within the investigated systems, the effects of modifying metal identity, ligand length, ligand sterics, general topology, and guest inclusion were probed.

Much like the mixed-metal fluorides, the magnitude of thermal expansion in the M_2L_2(DABCO) MOFs (M= Zn, Co, Ni, or Cu, L= bdc) could be varied with metal identity, but this strategy lacked systematic tunability. However, it was found that by modifying the ligand sterics through the inclusion of bulky methyl groups around the benzene ring of the bdc linker along the a-axis, the thermal expansion could be changed from negative to positive. This led to further exploration of this approach involving the systematic introduction of these bulky methyl groups in $Zn_2(bdc)_{2-2x}(TM\text{-}bdc)_{2x}$(dabco) (x = 0.0, 0.17,

0.45, 0.67, and 1.0) solid solutions. This system showed direct linear tunability of the thermal expansion along the a-axis through varying the systematic introduction of a tetramethylated analog of bdc in the synthesis feed. The ratio of TM-bdc to bdc in the products was measured using both powder and single crystal ^{1}H-NMR techniques, and the expected changes in surface area and pore volume were analyzed using BET analysis and basic porosimetry techniques. The thermal expansion of the c-axis was not shown to significantly change with the variation of x, which is expected because this layer is linked together through an unchanged pillar ligand (DABCO). Furthermore, direct changes in the topology of this system from a square-grid network to a Kagome network led to slight changes in the thermal expansion behavior that were in agreement with simulation.

Similar to changes in metal identity, modifying the guest species included within the porous framework known as IRMOF-1 did not show tunable changes in the thermal behavior, but did afford significant changes in the thermal expansion with guest species and opens the door to a new strategy that could potentially lead to thermal behavior control by incorporating a wider variety of guest species at various partial pressures into the strategic design.

1.35 Synthesis of hybrid perovskites

The current data suggest that He penetrates the pores of ScF_3 before 300°C and 1 GPa, but the exact conditions necessary for infiltration is currently unknown. As expected, there is no phase transition during the heating ramp to the max temperature, but interestingly, the cubic phase persists to far beyond the predicted pressure phase stability of the uninfiltrated material and there is an impurity phase that develops just beyond 1.5 GPa that resembles a

previously reported orthorhombic ScF_3-II (YF_3 structure). Similar to ScF_3-II, this orthorhombic impurity phase remains upon quenching to ambient conditions. Diffraction data for the quenched sample indicate a cubic lattice constant much greater than that of the pre-experiment pristine sample. This is consistent with the infiltration of a guest species at high temperature that is now trapped under ambient conditions. These results are also broadly consistent with activation barrier (for diffusion) estimations of ScF_3 vs. $CaZrF_6$. Like $CaZrF_6$, the lattice constant begins to raise over the expected pressure-temperature 'loading' region of the experiment, but this behaviour begins at higher temperatures and pressures for ScF_3, correlating with its smaller pore aperture and higher activation barrier to diffusion.

Appendix A. SUPPLEMENTARY MATERIAL FOR CHAPTER 2

A.1 Figures

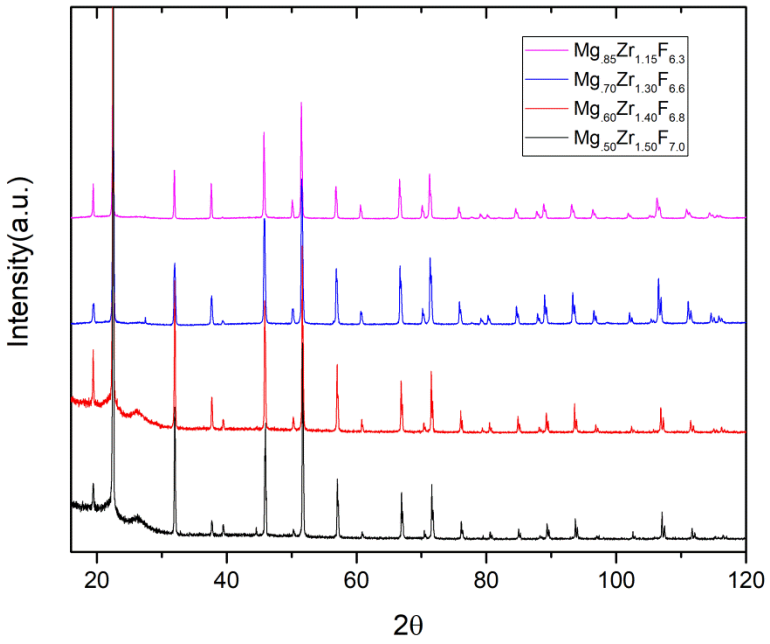

Figure A.1: Laboratory powder X-ray diffraction data for the $Mg_{1-x}Zr_{1+x}F_{6+2x}$ samples collected using Cu-kα radiation. The samples were contained in a flat plate holder covered by a Kapton film. The film gives rise to scattering, including the hump seen at 2θ ~ 28° in the two lower patterns.

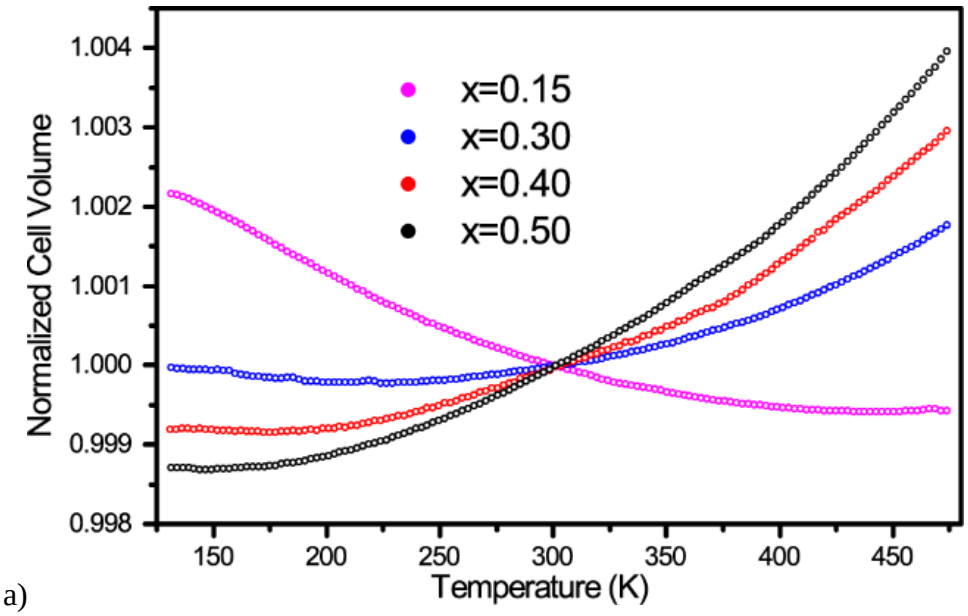

a)

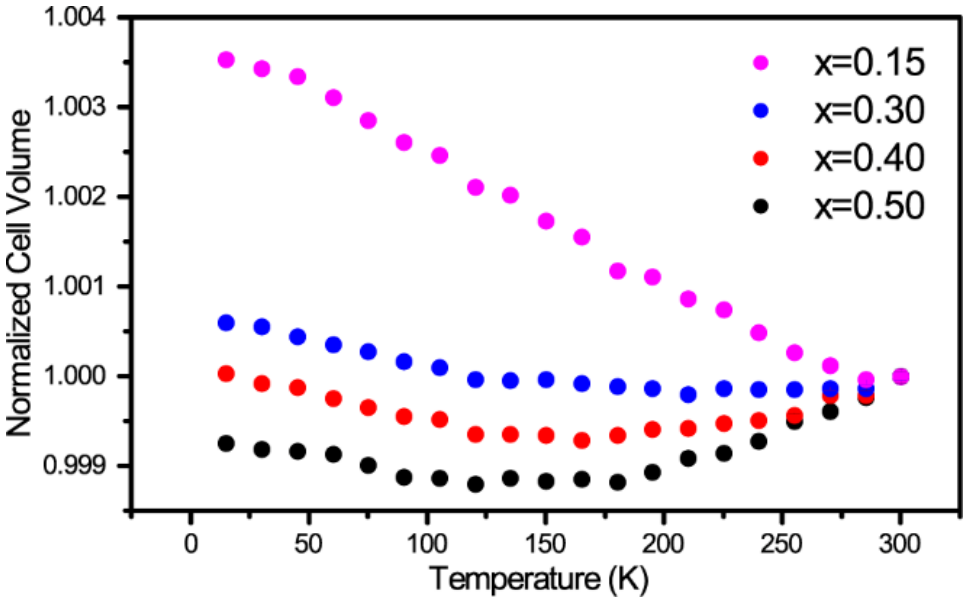

b)

Figure A.2: Normalized unit cell volume versus temperature for the Mg1-xZr1+xF6+2x samples derived from the a) synchrotron X-ray data on heating and b) the neutron diffraction data.

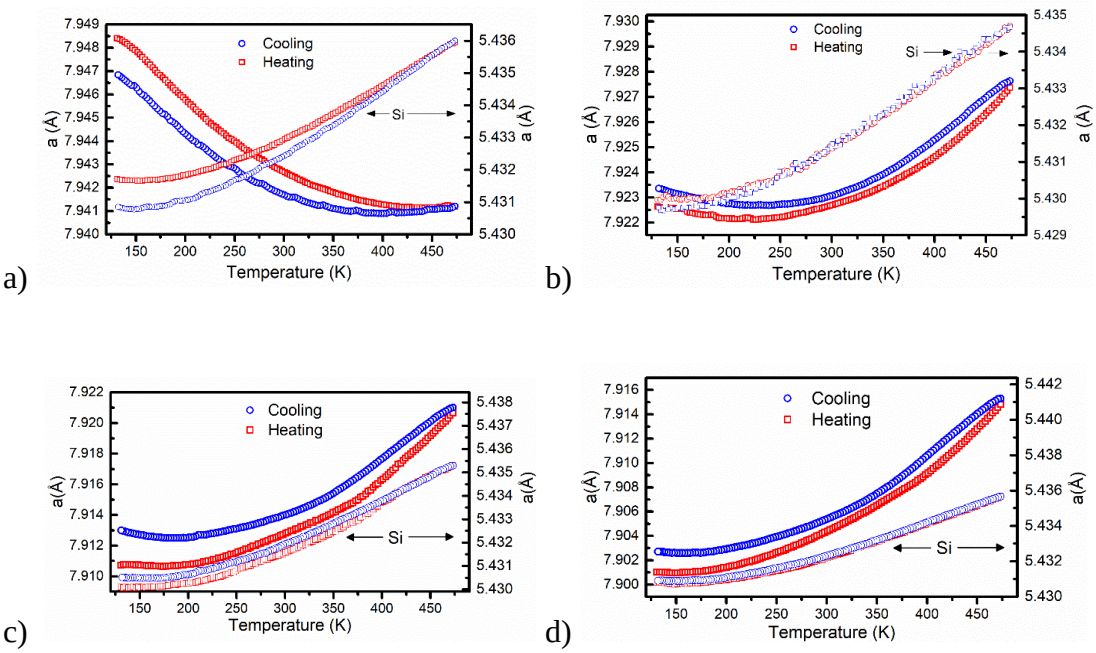

Figure A.3: Lattice constant versus temperature for the $Mg_{1-x}Zr_{1+x}F_{6+2x}$ samples, and a silicon internal standard, as determined in the synchrotron experiments: a) x = 0.15, b) x = 0.30, c) x = 0.40 and d) x = 0.50. In each plot, the left (sample) and right (silicon) hand axes cover the same range (□a/a). For the x = 0.30, 0.40 and 0.50 samples the lattice constant for the sample does not reproduced well on heating and cooling even though the silicon lattice constant reproduces quite well. This is believed to be due to the relaxation of defects in these highly nonstoichiometric materials. Note that in each case the sample lattice constant has increased after heating from ~ 130 to 475 K and then cooling back to 130 K. For the x = 0.15 sample, the lattice constants for the sample and the silicon reproduce poorly on heating followed by cooling and the apparent lattice constants are both smaller after heating followed by cooling. This is attributed to a small drift in wavelength during the measurements for this sample. This sample was the first sample to be measured during the beam time and the beam line optics were apparently not fully thermally equilibrated prior to the start of the measurements.

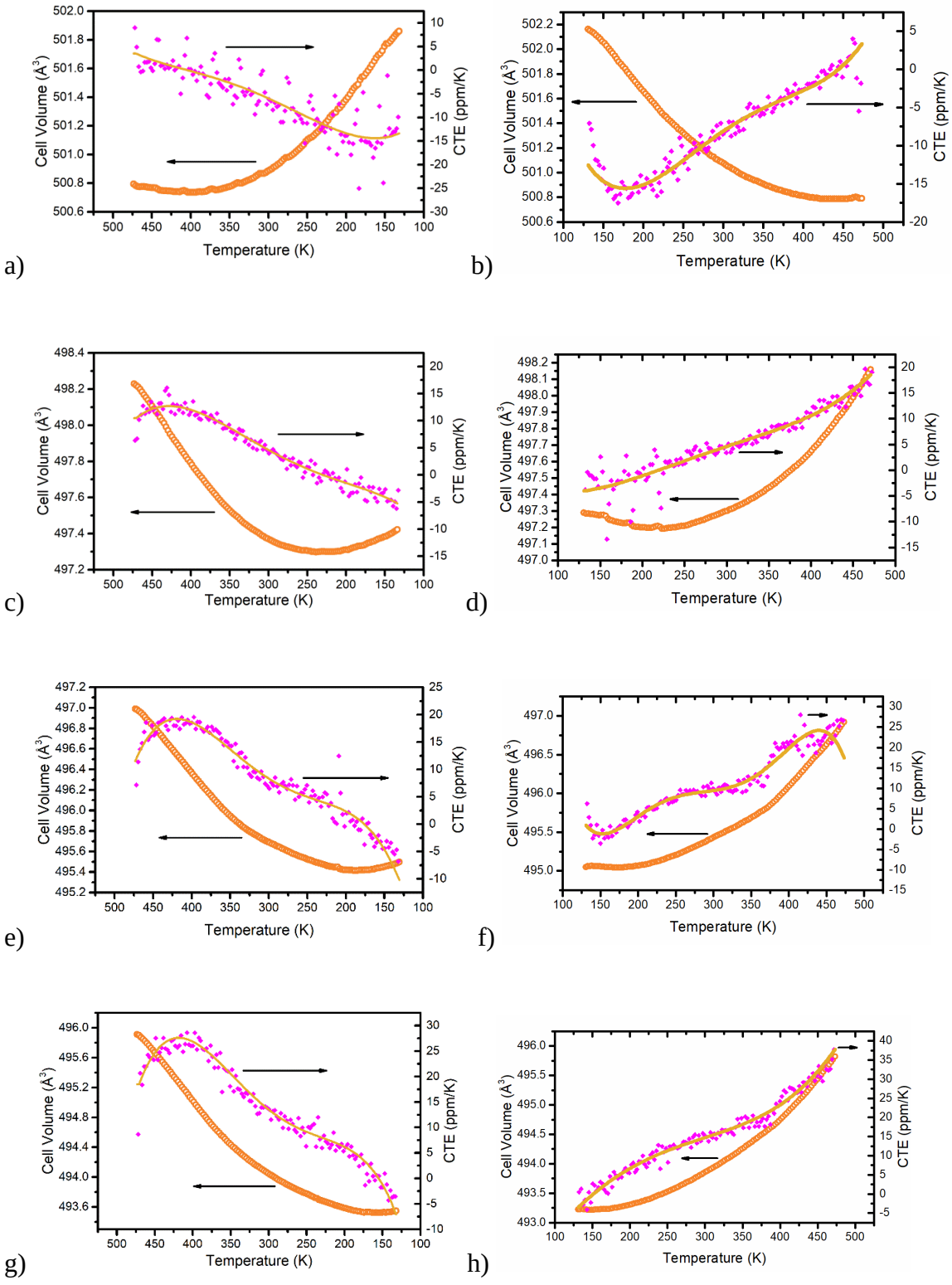

Figure A.4: Unit cell volumes and CTEs for Mg1-xZr1+xF6+2x, a) x = 0.15 on cooling, b) x = 0.15 on heating, c) x = 0.30 on cooling, d) x = 0.30 on heating, e) x =

0.40 on cooling, f) x = 0.40 on heating, g) x =0.50 on cooling and h) x = 0.50 on heating. The CTEs represented by the solid orange line were calculated by differentiating a 5th order polynomial that had been fit to volume versus temperature.

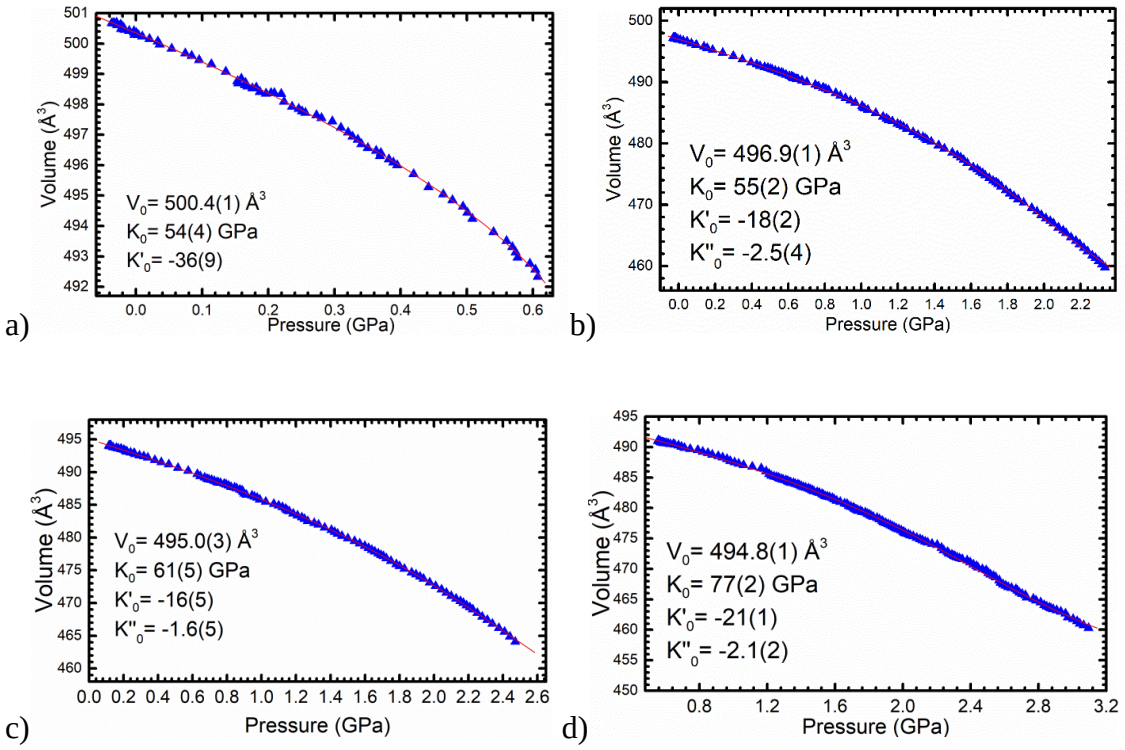

Figure A.5: Birch-Murnaghan equations of state fit to volume vs. pressure for the a) x =0.15, b) x = 0.30, c) x = 0.40 and d) x = 0.50 $Mg_{1-x}Zr_{1+x}F_{6+2x}$ samples. A 3rd order EoS was used for the x = 0.15 sample and 4th order EoSs were used for the other samples. The starting pressure for the measurement on the x = 0.50 sample was 0.56 GPa.

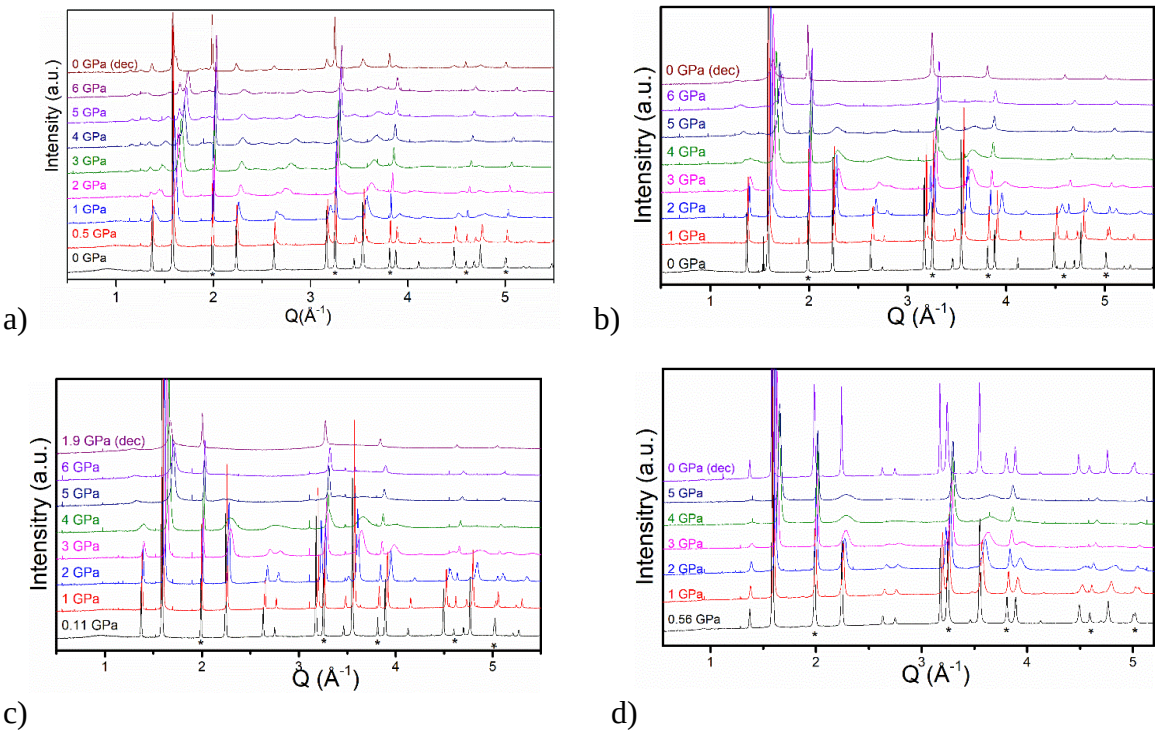

Figure Error! No text of specified style in document.**.6: Selected diffraction patterns at different pressures for the a) x = 0.15, b) x = 0.30 c) x = 0.40 and d) x = 0.50 Mg1-xZr1+xF6+2x samples.**

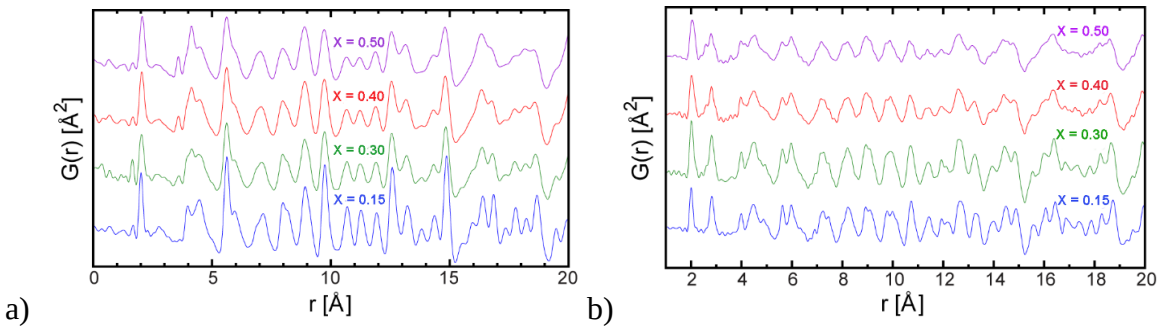

Figure A.7: a) X-ray (Q_{max} ~ 25Å^{-1}) and b) neutron (Q_{max} ~ 35Å^{-1}) derived PDFs for each $Mg_{1-x}Zr_{1+x}F_{6+2x}$ sample out to r = 20 Å.

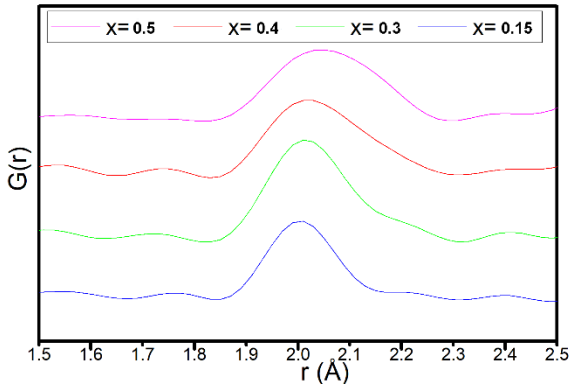

Figure A.8: Neutron derived PDFs at close to r = 2.0 Å for each Mg1-xZr1+xF6+2x sample.

A.2 Tables

Table A.1: Lattice constant and unit cell volume versus temperature for $Mg_{0.85}Zr_{1.15}F_{6.3}$ as determined from the Le Bail analysis of the synchrotron X-ray diffraction data.

Temperature (K)	R_{wp} (%)	a (Å)	Volume (Å^3)
130.89	2.53	7.94842(2)	502.160(4)
133.55	2.56	7.94837(2)	502.150(4)
136.12	2.67	7.94831(2)	502.140(4)
138.70	2.63	7.94825(2)	502.127(4)
141.27	2.66	7.94816(2)	502.112(4)
143.85	2.63	7.94808(2)	502.096(4)
146.42	2.61	7.94800(2)	502.080(4)
148.91	2.76	7.94790(2)	502.062(4)
151.49	2.55	7.94781(2)	502.045(4)
154.06	2.51	7.94771(2)	502.026(4)
156.64	2.59	7.94760(2)	502.006(4)
159.21	2.61	7.94750(2)	501.986(4)
161.79	2.61	7.94739(2)	501.965(4)
164.36	2.59	7.94728(2)	501.944(4)
166.94	2.65	7.94716(2)	501.922(4)
169.51	2.56	7.94704(2)	501.900(4)
172.09	2.55	7.94693(2)	501.878(4)
174.66	2.57	7.94683(2)	501.859(4)
177.24	2.56	7.94673(2)	501.839(4)
179.81	2.57	7.94662(2)	501.819(4)
182.39	2.65	7.94650(2)	501.797(4)
184.96	2.57	7.94639(2)	501.776(4)
187.45	2.58	7.94628(2)	501.756(4)
190.03	2.59	7.94618(2)	501.736(4)
192.69	2.59	7.94608(2)	501.716(4)
195.18	2.63	7.94597(2)	501.696(4)
197.75	2.61	7.94587(2)	501.678(4)
200.33	2.60	7.94577(2)	501.658(4)
202.91	2.66	7.94566(2)	501.638(4)
205.48	2.69	7.94557(2)	501.620(4)
208.06	2.77	7.94546(2)	501.600(4)
210.63	2.65	7.94536(2)	501.581(4)

Table A.1 continued…

Temperature (K)	R_{wp} (%)	a (Å)	Volume (Å^3)
213.21	2.64	7.94525(2)	501.560(4)
215.78	2.64	7.94516(2)	501.543(4)
218.36	2.73	7.94505(2)	501.522(4)
220.93	2.65	7.94495(2)	501.502(4)
223.51	2.80	7.94484(2)	501.482(4)
226.08	2.70	7.94475(2)	501.464(4)
228.66	2.71	7.94467(2)	501.449(4)
231.23	2.69	7.94458(2)	501.433(4)
233.81	2.95	7.94450(3)	501.417(5)
236.38	2.96	7.94442(2)	501.403(5)
238.96	2.88	7.94433(2)	501.385(5)
241.53	2.83	7.94424(2)	501.369(5)
244.11	2.73	7.94414(2)	501.350(4)
246.68	2.84	7.94408(3)	501.339(5)
249.26	3.02	7.94401(2)	501.326(5)
251.83	2.90	7.94393(3)	501.310(5)
254.49	3.04	7.94385(2)	501.295(5)
256.98	2.87	7.94376(3)	501.278(5)
259.56	2.98	7.94369(3)	501.264(5)
262.13	2.94	7.94362(2)	501.251(5)
264.71	2.87	7.94355(3)	501.238(5)
267.29	3.08	7.94348(3)	501.225(5)
269.86	3.21	7.94341(3)	501.211(5)
272.44	3.40	7.94335(3)	501.200(6)
275.01	3.03	7.94328(3)	501.187(5)
277.59	2.97	7.94321(3)	501.174(5)
280.16	3.05	7.94314(3)	501.160(5)
282.74	2.95	7.94307(3)	501.147(5)
285.31	3.04	7.94301(3)	501.135(5)
287.89	3.13	7.94295(3)	501.125(5)
290.46	3.00	7.94289(3)	501.113(5)
293.04	3.07	7.94284(3)	501.103(5)
295.61	3.17	7.94278(3)	501.092(5)
298.19	3.05	7.94273(3)	501.082(5)
300.76	3.22	7.94267(3)	501.071(5)
303.34	3.19	7.94262(3)	501.061(5)
305.91	3.27	7.94256(3)	501.051(5)
308.49	3.03	7.94251(3)	501.042(5)
311.06	3.35	7.94245(3)	501.031(6)
313.64	3.42	7.94241(3)	501.022(6)

Table A.1 continued…

Temperature (K)	R_{wp} (%)	a (Å)	Volume (Å^3)
316.21	3.21	7.94235(3)	501.011(5)
318.79	3.15	7.94230(3)	501.001(5)
321.36	3.65	7.94224(3)	500.991(6)
323.94	3.87	7.94220(4)	500.982(6)
326.51	4.00	7.94214(4)	500.972(7)
329.09	4.30	7.94210(3)	500.964(7)
331.67	3.71	7.94207(3)	500.957(6)
334.24	3.88	7.94204(3)	500.951(6)
336.82	3.41	7.94199(3)	500.944(6)
339.39	3.82	7.94196(3)	500.937(6)
341.97	3.35	7.94192(3)	500.930(6)
344.54	3.40	7.94189(3)	500.923(6)
347.12	3.56	7.94185(3)	500.915(6)
349.69	2.98	7.94181(3)	500.908(5)
352.27	3.28	7.94177(3)	500.901(6)
354.84	3.47	7.94173(3)	500.894(6)
357.42	3.53	7.94171(3)	500.889(6)
359.99	3.48	7.94168(3)	500.883(6)
362.57	3.58	7.94164(4)	500.876(6)
365.14	4.01	7.94160(3)	500.869(7)
367.72	3.71	7.94157(3)	500.863(6)
370.29	3.70	7.94154(3)	500.858(6)
372.87	3.34	7.94152(3)	500.853(6)
375.44	3.42	7.94149(3)	500.847(6)
378.02	3.61	7.94146(3)	500.843(6)
380.59	3.50	7.94144(3)	500.839(6)
383.17	3.89	7.94142(4)	500.835(7)
385.74	4.03	7.94139(3)	500.829(7)
388.32	3.87	7.94137(3)	500.826(7)
390.89	3.56	7.94136(4)	500.823(6)
393.47	4.13	7.94133(3)	500.818(7)
396.05	3.79	7.94131(3)	500.815(6)
398.62	3.77	7.94130(3)	500.811(6)
401.20	3.68	7.94128(4)	500.808(6)
403.77	4.09	7.94126(4)	500.804(7)
406.35	3.90	7.94125(3)	500.802(7)
408.92	3.86	7.94123(4)	500.799(7)
411.50	4.53	7.94122(4)	500.797(7)
414.07	4.41	7.94121(4)	500.795(7)
416.65	4.49	7.94120(4)	500.792(7)

Table A.1 continued…

Temperature (K)	R_{wp} (%)	a (Å)	Volume (Å^3)
419.22	4.27	7.94119(5)	500.791(7)
421.80	5.09	7.94117(5)	500.788(7)
424.37	5.05	7.94117(4)	500.788(7)
426.95	4.85	7.94117(5)	500.787(7)
429.52	4.98	7.94117(4)	500.787(7)
432.10	4.87	7.94116(4)	500.786(7)
434.67	4.90	7.94116(4)	500.786(7)
437.25	4.81	7.94116(4)	500.786(7)
439.82	4.92	7.94116(5)	500.786(7)
442.40	5.52	7.94116(5)	500.785(7)
444.97	5.30	7.94116(4)	500.785(7)
447.55	4.80	7.94116(4)	500.787(7)
450.12	4.90	7.94116(5)	500.785(7)
452.70	5.28	7.94116(5)	500.786(7)
455.27	5.12	7.94117(4)	500.787(7)
457.85	4.86	7.94118(4)	500.789(7)
460.43	4.71	7.94119(3)	500.791(7)
463.00	3.66	7.94122(3)	500.796(6)
465.58	3.25	7.94124(3)	500.800(6)
468.15	3.58	7.94123(5)	500.799(6)
470.73	5.04	7.94119(6)	500.792(7)
473.30	6.41	7.94118(4)	500.790(7)
473.30	4.62	7.94121(6)	500.795(7)
470.73	6.45	7.94115(6)	500.783(7)
468.15	6.74	7.94111(6)	500.777(7)
465.58	7.05	7.94111(6)	500.776(7)
463.00	6.29	7.94111(6)	500.776(7)
460.34	6.37	7.94111(6)	500.776(7)
457.85	6.30	7.94110(5)	500.774(7)
455.27	5.86	7.94109(5)	500.772(7)
452.70	5.47	7.94108(5)	500.770(7)
450.12	5.05	7.94107(4)	500.769(7)
447.55	4.24	7.94107(3)	500.769(7)
444.97	3.73	7.94106(5)	500.768(6)
442.40	5.11	7.94102(7)	500.759(7)
439.82	7.28	7.94098(6)	500.751(7)
437.25	7.02	7.94097(6)	500.750(7)
434.67	7.01	7.94096(6)	500.748(7)
432.10	6.70	7.94096(6)	500.748(7)
429.44	6.09	7.94095(6)	500.746(7)

Table A.1 continued…

Temperature (K)	R_{wp} (%)	a (Å)	Volume (Å^3)
426.95	6.23	7.94095(5)	500.746(7)
424.37	5.82	7.94094(6)	500.745(7)
421.80	6.24	7.94093(6)	500.742(7)
419.22	6.24	7.94093(6)	500.742(7)
416.56	6.33	7.94093(5)	500.741(7)
414.07	5.61	7.94092(4)	500.740(7)
411.50	4.39	7.94095(3)	500.747(7)
408.92	3.66	7.94097(4)	500.749(6)
406.26	4.93	7.94094(6)	500.745(7)
403.77	7.06	7.94090(7)	500.736(7)
401.20	7.58	7.94090(6)	500.736(7)
398.53	6.98	7.94090(6)	500.736(7)
396.05	7.24	7.94090(7)	500.737(7)
393.47	7.58	7.94090(6)	500.737(7)
390.81	7.15	7.94092(6)	500.740(7)
388.32	7.26	7.94092(7)	500.741(7)
385.74	7.40	7.94092(6)	500.740(7)
383.17	7.09	7.94092(6)	500.741(7)
380.59	6.74	7.94093(5)	500.743(7)
378.02	5.43	7.94097(4)	500.749(7)
375.44	4.55	7.94101(4)	500.757(7)
372.87	4.27	7.94103(5)	500.761(7)
370.29	5.78	7.94101(7)	500.758(7)
367.72	8.64	7.94099(7)	500.753(7)
365.06	9.00	7.94099(7)	500.754(7)
362.57	8.04	7.94101(7)	500.757(7)
359.99	7.96	7.94103(7)	500.761(7)
357.42	7.63	7.94106(7)	500.766(7)
354.84	7.63	7.94107(6)	500.768(7)
352.27	7.25	7.94110(7)	500.774(7)
349.69	7.58	7.94111(6)	500.776(7)
347.03	7.42	7.94114(5)	500.781(7)
344.54	6.14	7.94118(4)	500.790(7)
341.97	4.55	7.94122(3)	500.797(7)
339.39	3.99	7.94126(6)	500.804(7)
336.82	7.11	7.94124(7)	500.801(7)
334.24	9.48	7.94124(7)	500.801(7)
331.67	8.78	7.94127(7)	500.807(7)
329.09	8.47	7.94131(7)	500.814(7)
326.51	8.33	7.94134(7)	500.819(7)

Table A.1 continued…

Temperature (K)	R_{wp} (%)	a (Å)	Volume (Å^3)
323.94	8.32	7.94137(6)	500.825(7)
321.36	7.51	7.94140(6)	500.831(7)
318.79	7.52	7.94143(5)	500.837(7)
316.21	6.28	7.94150(5)	500.850(7)
313.64	5.43	7.94155(4)	500.859(7)
311.06	4.65	7.94159(5)	500.867(7)
308.49	6.06	7.94160(7)	500.869(7)
305.91	9.60	7.94160(7)	500.869(7)
303.34	9.95	7.94163(7)	500.875(7)
300.76	8.82	7.94168(7)	500.884(7)
298.19	9.60	7.94172(7)	500.892(7)
295.53	8.76	7.94177(7)	500.901(7)
293.04	8.51	7.94182(7)	500.911(7)
290.46	8.70	7.94187(7)	500.920(7)
287.80	9.12	7.94193(7)	500.930(7)
285.31	8.76	7.94197(6)	500.940(7)
282.74	6.60	7.94205(5)	500.954(7)
280.16	5.30	7.94212(4)	500.968(7)
277.59	5.03	7.94218(7)	500.979(7)
275.01	8.12	7.94219(7)	500.981(7)
272.44	9.85	7.94221(7)	500.985(7)
269.77	10.21	7.94227(7)	500.996(7)
267.20	10.75	7.94232(7)	501.006(7)
264.71	9.38	7.94240(7)	501.019(7)
262.05	8.88	7.94246(7)	501.032(7)
259.47	8.90	7.94252(7)	501.044(7)
256.90	8.53	7.94260(7)	501.057(7)
254.41	8.55	7.94267(5)	501.071(7)
251.83	5.68	7.94277(5)	501.091(7)
249.17	5.51	7.94285(6)	501.106(7)
246.60	7.44	7.94290(7)	501.115(7)
244.02	10.59	7.94294(7)	501.122(7)
241.45	11.31	7.94299(7)	501.132(7)
238.87	10.75	7.94307(7)	501.147(7)
236.30	10.95	7.94314(7)	501.161(7)
233.72	9.60	7.94322(7)	501.175(7)
231.15	10.16	7.94330(7)	501.191(7)
228.57	8.90	7.94338(7)	501.206(7)
226.00	9.25	7.94347(7)	501.223(7)
223.42	8.68	7.94355(5)	501.239(7)

Table A.1 continued…

Temperature (K)	R_{wp} (%)	a (Å)	Volume (Å^3)
220.85	6.53	7.94367(6)	501.260(7)
218.27	6.74	7.94375(6)	501.276(7)
215.70	7.53	7.94382(7)	501.288(7)
213.12	11.17	7.94385(7)	501.295(7)
210.54	12.50	7.94397(7)	501.318(7)
207.97	11.28	7.94402(7)	501.327(7)
205.39	11.35	7.94412(7)	501.345(7)
202.82	10.65	7.94422(7)	501.364(7)
200.24	10.70	7.94431(7)	501.382(7)
197.67	9.84	7.94441(7)	501.400(7)
195.09	9.54	7.94451(6)	501.420(7)
192.43	6.97	7.94464(5)	501.444(7)
189.86	6.48	7.94474(6)	501.464(7)
187.28	7.72	7.94482(7)	501.479(7)
184.71	11.89	7.94488(7)	501.490(7)
182.13	12.77	7.94505(7)	501.522(7)
179.56	12.67	7.94515(7)	501.541(7)
176.90	11.98	7.94518(7)	501.547(7)
174.32	11.05	7.94529(7)	501.567(7)
171.75	10.94	7.94539(7)	501.586(7)
169.08	10.31	7.94550(7)	501.607(7)
166.51	10.38	7.94561(7)	501.627(7)
163.85	8.49	7.94574(5)	501.652(7)
161.27	6.63	7.94585(5)	501.673(7)
158.61	6.18	7.94596(7)	501.694(7)
155.95	10.10	7.94601(7)	501.704(7)
153.38	12.37	7.94612(7)	501.724(7)
150.80	12.97	7.94628(7)	501.755(7)
148.22	13.07	7.94638(7)	501.773(7)
145.65	11.91	7.94638(7)	501.774(7)
143.16	11.47	7.94647(7)	501.790(7)
140.76	11.57	7.94655(7)	501.806(7)
138.35	10.94	7.94664(7)	501.822(7)
136.04	9.02	7.94672(6)	501.837(7)
133.89	7.35	7.94679(6)	501.851(7)
131.92	6.86	7.94684(7)	501.860(7)

Table A.2: Lattice constant and unit cell volume versus temperature for $Mg_{0.7}Zr_{1.3}F_{6.6}$ as determined from the Le Bail analysis of the synchrotron X-ray diffraction data.

Temperature (K)	R_{wp} (%)	a (Å)	Volume (Å^3)
130.89	2.14	7.92262(2)	497.287(3)
133.55	3.19	7.92260(3)	497.282(5)
136.12	3.26	7.92259(3)	497.281(5)
138.70	3.26	7.92259(3)	497.280(5)
141.27	2.74	7.92258(2)	497.279(4)
143.85	2.26	7.92257(2)	497.277(4)
146.42	2.16	7.92256(2)	497.274(3)
149.00	2.05	7.92254(2)	497.271(3)
151.57	3.82	7.92255(3)	497.274(6)
154.06	4.76	7.92255(4)	497.273(7)
156.64	5.26	7.92253(4)	497.269(7)
159.21	2.37	7.92244(2)	497.252(4)
161.79	4.64	7.92239(4)	497.243(7)
164.36	3.83	7.92238(3)	497.241(6)
166.94	2.66	7.92235(2)	497.236(4)
169.51	2.48	7.92233(2)	497.232(4)
172.09	2.31	7.92232(2)	497.230(4)
174.66	2.50	7.92230(2)	497.227(4)
177.24	2.41	7.92229(2)	497.224(4)
179.81	2.24	7.92229(2)	497.224(4)
182.39	4.26	7.92231(4)	497.228(7)
184.96	4.96	7.92230(4)	497.226(7)
187.54	2.27	7.92223(2)	497.214(4)
190.03	3.21	7.92218(3)	497.204(5)
192.60	3.53	7.92217(3)	497.201(6)
195.18	3.46	7.92217(3)	497.201(6)
197.75	2.82	7.92216(2)	497.201(5)
200.33	2.45	7.92215(2)	497.199(4)
202.91	2.08	7.92216(2)	497.199(3)
205.48	2.30	7.92214(2)	497.197(4)
208.06	2.13	7.92213(2)	497.195(3)
210.63	2.04	7.92214(2)	497.196(3)
213.21	2.26	7.92215(2)	497.198(4)
215.78	4.49	7.92218(4)	497.203(7)
218.36	5.53	7.92220(5)	497.206(7)
220.93	2.52	7.92217(2)	497.201(4)
223.51	2.91	7.92212(3)	497.191(5)

Table A.2 continued…

Temperature (K)	R_{wp} (%)	a (Å)	Volume (Å^3)
226.08	3.53	7.92211(3)	497.191(6)
228.66	2.88	7.92212(3)	497.193(5)
231.23	3.17	7.92213(3)	497.195(5)
233.81	2.66	7.92215(2)	497.197(4)
236.38	2.33	7.92215(2)	497.198(4)
238.96	2.33	7.92216(2)	497.199(4)
241.53	2.23	7.92217(2)	497.202(4)
244.11	2.25	7.92218(2)	497.203(4)
246.68	2.06	7.92219(2)	497.206(3)
249.26	2.17	7.92220(2)	497.207(4)
251.83	2.25	7.92221(2)	497.209(4)
254.41	2.01	7.92223(2)	497.214(3)
256.98	2.07	7.92226(2)	497.218(3)
259.56	2.46	7.92228(2)	497.222(4)
262.13	2.10	7.92231(2)	497.227(3)
264.71	2.33	7.92234(2)	497.233(4)
267.29	2.03	7.92235(2)	497.236(3)
269.86	2.05	7.92238(2)	497.241(3)
272.44	2.02	7.92240(2)	497.244(3)
275.01	2.03	7.92242(2)	497.248(3)
277.59	2.05	7.92245(2)	497.254(3)
280.16	2.05	7.92248(2)	497.260(3)
282.74	2.04	7.92251(2)	497.265(3)
285.31	2.09	7.92253(2)	497.269(3)
287.89	2.07	7.92255(2)	497.273(3)
290.46	2.06	7.92258(2)	497.278(3)
293.04	2.03	7.92261(2)	497.284(3)
295.61	2.08	7.92264(2)	497.290(3)
298.19	2.08	7.92267(2)	497.295(3)
300.76	2.06	7.92269(2)	497.300(3)
303.34	2.02	7.92273(2)	497.306(3)
305.91	2.03	7.92275(2)	497.311(3)
308.49	2.05	7.92278(2)	497.316(3)
311.06	2.08	7.92281(2)	497.322(3)
313.64	2.09	7.92285(2)	497.329(3)
316.21	2.08	7.92288(2)	497.335(3)
318.79	2.05	7.92291(2)	497.341(3)
321.36	2.11	7.92295(2)	497.349(3)
323.94	2.05	7.92299(2)	497.355(3)
326.51	2.06	7.92303(2)	497.363(3)

Temperature (K)	R_{wp} (%)	a (Å)	Volume (Å^3)
329.09	2.04	7.92307(2)	497.371(3)
331.67	2.06	7.92311(2)	497.378(3)
334.24	2.06	7.92315(2)	497.386(3)
336.82	2.05	7.92318(2)	497.393(3)
339.39	2.20	7.92324(2)	497.402(4)
341.97	2.08	7.92328(2)	497.411(3)
344.54	2.05	7.92332(2)	497.419(3)
347.12	2.15	7.92338(2)	497.429(4)
349.69	2.37	7.92342(2)	497.437(4)
352.27	2.06	7.92347(2)	497.447(3)
354.84	2.12	7.92353(2)	497.457(3)
357.42	2.32	7.92358(2)	497.467(4)
359.99	2.08	7.92364(2)	497.478(3)
362.57	2.08	7.92369(2)	497.489(3)
365.14	2.14	7.92375(2)	497.500(3)
367.72	2.05	7.92381(2)	497.510(3)
370.29	2.05	7.92387(2)	497.522(3)
372.87	2.15	7.92393(2)	497.533(4)
375.44	2.12	7.92398(2)	497.543(3)
378.02	2.10	7.92404(2)	497.554(3)
380.59	2.10	7.92410(2)	497.565(3)
383.17	2.24	7.92415(2)	497.575(4)
385.74	2.09	7.92422(2)	497.588(3)
388.32	2.08	7.92429(2)	497.600(3)
390.89	2.15	7.92434(2)	497.611(4)
393.47	2.26	7.92441(2)	497.624(4)
396.05	2.31	7.92449(2)	497.638(4)
398.62	2.15	7.92456(2)	497.651(4)
401.20	2.16	7.92463(2)	497.666(4)
403.77	2.24	7.92472(2)	497.681(4)
406.35	2.56	7.92480(2)	497.697(4)
408.92	2.57	7.92487(2)	497.710(4)
411.50	2.34	7.92496(2)	497.728(4)
414.07	2.35	7.92504(2)	497.743(4)
416.65	2.25	7.92514(2)	497.760(4)
419.22	2.33	7.92521(2)	497.775(4)
421.80	2.26	7.92530(2)	497.792(4)
424.37	2.34	7.92539(2)	497.809(4)
426.95	2.16	7.92549(2)	497.827(4)
429.52	2.37	7.92558(2)	497.843(4)

Temperature (K)	R_{wp} (%)	a (Å)	Volume (Å^3)
432.10	2.35	7.92567(2)	497.861(4)
434.67	2.38	7.92576(2)	497.877(4)
437.25	2.30	7.92585(2)	497.894(4)
439.82	2.29	7.92594(2)	497.912(4)
442.40	2.19	7.92603(2)	497.928(4)
444.97	2.35	7.92612(2)	497.947(4)
447.55	2.56	7.92623(2)	497.967(4)
450.12	2.40	7.92634(2)	497.988(4)
452.70	2.24	7.92645(2)	498.007(4)
455.27	2.45	7.92655(2)	498.027(4)
457.85	2.26	7.92666(2)	498.047(4)
460.43	2.53	7.92676(2)	498.066(4)
463.00	2.49	7.92687(2)	498.087(4)
465.58	2.48	7.92701(2)	498.113(4)
468.15	2.48	7.92712(2)	498.135(4)
470.73	2.45	7.92724(2)	498.156(4)
473.30	2.74	7.92737(2)	498.180(5)
473.30	2.31	7.92762(2)	498.228(4)
470.73	2.89	7.92758(3)	498.220(5)
468.15	2.66	7.92753(2)	498.212(4)
465.58	2.50	7.92747(2)	498.199(4)
463.00	2.40	7.92739(2)	498.184(4)
460.43	3.25	7.92730(3)	498.168(5)
457.85	2.55	7.92722(2)	498.154(4)
455.27	3.14	7.92714(3)	498.139(5)
452.70	3.11	7.92706(3)	498.123(5)
450.12	2.87	7.92697(3)	498.106(5)
447.55	2.85	7.92689(2)	498.091(5)
444.89	2.85	7.92680(2)	498.074(5)
442.40	2.93	7.92673(3)	498.061(5)
439.82	2.68	7.92664(2)	498.043(4)
437.25	2.80	7.92655(2)	498.026(5)
434.67	2.69	7.92647(2)	498.011(4)
432.01	4.42	7.92636(4)	497.990(7)
429.52	4.98	7.92625(4)	497.970(7)
426.95	5.73	7.92615(5)	497.951(7)
424.37	5.17	7.92607(5)	497.937(7)
421.71	5.80	7.92598(5)	497.919(7)
419.22	5.32	7.92591(5)	497.906(7)
416.65	6.32	7.92582(5)	497.889(7)

Temperature (K)	R_{wp} (%)	a (Å)	Volume (Å^3)
414.07	5.79	7.92574(5)	497.874(7)
411.50	6.60	7.92565(6)	497.857(7)
408.92	6.38	7.92557(6)	497.843(7)
406.35	6.50	7.92548(6)	497.825(7)
403.77	6.50	7.92540(6)	497.810(7)
401.11	5.83	7.92533(5)	497.796(7)
398.62	5.78	7.92524(5)	497.781(7)
396.05	5.93	7.92515(5)	497.763(7)
393.47	6.26	7.92508(5)	497.749(7)
390.89	6.16	7.92500(5)	497.735(7)
388.32	6.62	7.92493(6)	497.721(7)
385.74	6.89	7.92486(6)	497.708(7)
383.17	5.49	7.92478(5)	497.694(7)
380.59	5.63	7.92471(5)	497.680(7)
378.02	6.02	7.92464(5)	497.666(7)
375.44	6.21	7.92456(5)	497.652(7)
372.87	6.44	7.92449(6)	497.638(7)
370.29	5.91	7.92442(5)	497.625(7)
367.72	5.85	7.92435(5)	497.612(7)
365.14	6.33	7.92428(5)	497.598(7)
362.57	5.71	7.92421(5)	497.585(7)
359.99	5.80	7.92414(5)	497.573(7)
357.42	5.21	7.92408(5)	497.562(7)
354.84	5.56	7.92402(5)	497.551(7)
352.27	5.94	7.92396(5)	497.539(7)
349.69	6.31	7.92390(5)	497.528(7)
347.12	6.72	7.92385(6)	497.517(7)
344.54	6.05	7.92380(5)	497.508(7)
341.97	7.29	7.92375(6)	497.499(7)
339.39	6.60	7.92370(6)	497.490(7)
336.82	7.21	7.92364(6)	497.479(7)
334.24	6.27	7.92358(5)	497.468(7)
331.67	6.55	7.92353(6)	497.458(7)
329.09	7.02	7.92349(6)	497.450(7)
326.51	6.75	7.92344(6)	497.441(7)
323.94	6.74	7.92340(6)	497.434(7)
321.36	6.98	7.92336(6)	497.426(7)
318.79	7.63	7.92333(7)	497.419(7)
316.21	7.25	7.92329(6)	497.412(7)
313.64	6.77	7.92325(6)	497.406(7)

Temperature (K)	R_{wp} (%)	a (Å)	Volume (Å^3)
311.06	6.98	7.92322(6)	497.399(7)
308.49	7.37	7.92317(6)	497.390(7)
305.91	7.24	7.92314(6)	497.384(7)
303.34	7.52	7.92310(6)	497.377(7)
300.76	7.64	7.92307(7)	497.371(7)
298.10	7.23	7.92304(6)	497.366(7)
295.53	7.44	7.92301(6)	497.360(7)
293.04	7.27	7.92298(6)	497.354(7)
290.46	7.98	7.92295(7)	497.349(7)
287.89	7.07	7.92293(6)	497.344(7)
285.31	6.86	7.92291(6)	497.340(7)
282.65	7.91	7.92288(7)	497.336(7)
280.16	7.59	7.92286(6)	497.332(7)
277.59	7.19	7.92284(6)	497.328(7)
274.92	6.62	7.92283(6)	497.326(7)
272.44	7.37	7.92282(6)	497.323(7)
269.86	7.12	7.92280(6)	497.321(7)
267.20	7.30	7.92278(6)	497.316(7)
264.71	7.28	7.92277(6)	497.315(7)
262.13	6.91	7.92276(6)	497.312(7)
259.56	6.56	7.92274(6)	497.310(7)
256.90	7.83	7.92273(7)	497.307(7)
254.41	6.82	7.92273(6)	497.307(7)
251.75	6.98	7.92273(6)	497.306(7)
249.26	7.26	7.92272(6)	497.305(7)
246.60	6.52	7.92271(6)	497.303(7)
244.02	6.77	7.92269(6)	497.300(7)
241.45	6.10	7.92269(5)	497.300(7)
238.87	6.77	7.92268(6)	497.297(7)
236.30	6.58	7.92269(6)	497.299(7)
233.72	7.10	7.92269(6)	497.299(7)
231.15	6.49	7.92270(6)	497.300(7)
228.57	6.38	7.92269(5)	497.300(7)
226.00	6.62	7.92269(6)	497.299(7)
223.42	6.80	7.92269(6)	497.299(7)
220.85	6.96	7.92269(6)	497.299(7)
218.27	6.69	7.92269(6)	497.300(7)
215.70	6.70	7.92269(6)	497.299(7)
213.12	6.93	7.92270(6)	497.300(7)
210.54	6.91	7.92270(6)	497.301(7)

Temperature (K)	R_{wp} (%)	a (Å)	Volume (Å^3)
207.97	7.05	7.92271(6)	497.302(7)
205.39	7.47	7.92272(6)	497.305(7)
202.82	7.25	7.92274(6)	497.309(7)
200.24	7.65	7.92275(7)	497.311(7)
197.67	7.72	7.92274(7)	497.309(7)
195.01	7.04	7.92277(6)	497.315(7)
192.43	7.29	7.92279(6)	497.319(7)
189.86	7.35	7.92282(6)	497.323(7)
187.28	7.53	7.92283(6)	497.326(7)
184.71	7.56	7.92285(6)	497.330(7)
182.13	8.03	7.92286(7)	497.332(7)
179.47	7.72	7.92286(7)	497.332(7)
176.90	8.21	7.92288(7)	497.336(7)
174.32	7.61	7.92291(6)	497.341(7)
171.75	7.27	7.92294(6)	497.347(7)
169.08	8.14	7.92296(7)	497.351(7)
166.51	7.29	7.92298(6)	497.354(7)
163.93	7.79	7.92300(7)	497.358(7)
161.27	7.25	7.92303(6)	497.363(7)
158.61	7.27	7.92306(6)	497.370(7)
155.95	7.30	7.92308(6)	497.373(7)
153.38	7.85	7.92310(7)	497.377(7)
150.80	8.02	7.92313(7)	497.381(7)
148.22	8.61	7.92315(7)	497.385(7)
145.65	7.67	7.92318(6)	497.392(7)
143.16	7.75	7.92321(7)	497.397(7)
140.76	8.53	7.92324(7)	497.402(7)
138.35	8.13	7.92327(7)	497.409(7)
136.04	8.27	7.92330(7)	497.415(7)
133.89	7.72	7.92334(6)	497.422(7)
131.92	7.96	7.92335(7)	497.425(7)

Table A.3: Lattice constant and unit cell volume versus temperature for $Mg_{0.6}Zr_{1.4}F_{6.8}$ as determined from the Le Bail analysis of the synchrotron X-ray diffraction data.

Temperature (K)	R_{wp} (%)	a (Å)	Volume (Å^3)
130.80	2.11	7.91073(2)	495.050(3)
133.37	2.12	7.91077(2)	495.058(3)
135.95	2.14	7.91079(2)	495.061(3)
138.53	2.13	7.91079(2)	495.063(3)
141.10	2.12	7.91078(2)	495.060(3)
143.68	2.13	7.91077(2)	495.058(3)
146.25	2.14	7.91078(2)	495.059(3)
148.83	2.14	7.91077(2)	495.057(4)
151.40	2.13	7.91074(2)	495.053(3)
153.98	2.15	7.91074(2)	495.053(4)
156.55	2.13	7.91072(2)	495.050(3)
159.13	2.12	7.91072(2)	495.048(3)
161.70	2.16	7.91070(2)	495.045(4)
164.28	2.14	7.91071(2)	495.046(4)
166.85	2.15	7.91070(2)	495.044(4)
169.43	2.16	7.91069(2)	495.044(4)
172.00	2.14	7.91069(2)	495.043(4)
174.58	2.14	7.91069(2)	495.043(4)
177.15	2.16	7.91069(2)	495.044(4)
179.73	2.17	7.91070(2)	495.045(4)
182.30	2.12	7.91071(2)	495.048(3)
184.88	2.16	7.91073(2)	495.051(4)
187.45	2.14	7.91073(2)	495.051(4)
190.03	2.15	7.91074(2)	495.053(4)
192.60	2.15	7.91076(2)	495.055(4)
195.18	2.18	7.91077(2)	495.058(4)
197.75	2.16	7.91079(2)	495.063(4)
200.33	2.17	7.91082(2)	495.068(4)
202.91	2.13	7.91083(2)	495.070(4)
205.48	2.16	7.91086(2)	495.075(4)
208.06	2.17	7.91088(2)	495.079(4)
210.63	2.18	7.91090(2)	495.083(4)
213.21	2.18	7.91094(2)	495.090(4)
215.78	2.18	7.91097(2)	495.097(4)
218.36	2.15	7.91101(2)	495.103(4)
220.93	2.15	7.91104(2)	495.109(4)

Temperature (K)	R_{wp} (%)	a (Å)	Volume (Å^3)
223.51	2.10	7.91108(2)	495.116(3)
226.08	2.14	7.91111(2)	495.122(4)
228.66	2.15	7.91115(2)	495.130(4)
231.23	2.14	7.9112(2)	495.139(4)
233.81	2.14	7.91124(2)	495.147(4)
236.38	2.15	7.91129(2)	495.156(4)
238.96	2.13	7.91134(2)	495.166(4)
241.53	2.12	7.91138(2)	495.174(4)
244.11	2.10	7.91143(2)	495.183(3)
246.68	2.10	7.91148(2)	495.191(3)
249.26	2.11	7.91153(2)	495.200(3)
251.83	2.10	7.91157(2)	495.209(3)
254.41	2.12	7.91163(2)	495.220(4)
256.98	2.10	7.91170(2)	495.232(3)
259.56	2.09	7.91175(2)	495.243(3)
262.13	2.12	7.91181(2)	495.254(4)
264.71	2.09	7.91188(2)	495.266(3)
267.29	2.10	7.91193(2)	495.277(3)
269.86	2.11	7.91200(2)	495.289(3)
272.44	2.10	7.91206(2)	495.300(3)
275.01	2.10	7.91212(2)	495.312(3)
277.59	2.11	7.91219(2)	495.324(3)
280.16	2.13	7.91225(2)	495.336(4)
282.74	2.11	7.91231(2)	495.347(3)
285.31	2.12	7.91236(2)	495.357(4)
287.89	2.12	7.91243(2)	495.371(4)
290.46	2.16	7.91249(2)	495.381(4)
293.04	2.11	7.91256(2)	495.395(3)
295.61	2.11	7.91263(2)	495.407(3)
298.19	2.11	7.91270(2)	495.422(3)
300.76	2.11	7.91277(2)	495.434(3)
303.34	2.12	7.91283(2)	495.446(4)
305.91	2.15	7.91289(2)	495.457(4)
308.49	2.11	7.91296(2)	495.470(3)
311.06	2.15	7.91302(2)	495.481(4)
313.64	2.09	7.91309(2)	495.495(3)
316.21	2.13	7.91317(2)	495.509(4)
318.79	2.11	7.91324(2)	495.522(3)
321.36	2.14	7.91331(2)	495.534(4)
323.94	2.10	7.91337(2)	495.546(3)

Temperature (K)	R_{wp} (%)	a (Å)	Volume (Å^3)
326.51	2.14	7.91343(2)	495.558(4)
329.09	2.10	7.91350(2)	495.570(3)
331.67	2.16	7.91356(2)	495.582(4)
334.24	2.11	7.91364(2)	495.598(4)
336.82	2.10	7.91372(2)	495.612(3)
339.39	2.17	7.91378(2)	495.624(4)
341.97	2.10	7.91386(2)	495.639(3)
344.54	2.31	7.91393(2)	495.651(4)
347.12	2.08	7.91401(2)	495.667(3)
349.69	2.13	7.91409(2)	495.681(4)
352.27	2.08	7.91417(2)	495.697(3)
354.84	2.13	7.91426(2)	495.713(4)
357.42	2.07	7.91435(2)	495.730(3)
359.99	2.10	7.91443(2)	495.745(4)
362.57	2.05	7.91451(2)	495.762(3)
365.14	2.09	7.91459(2)	495.775(3)
367.72	2.14	7.91466(2)	495.789(4)
370.29	2.03	7.91476(2)	495.808(3)
372.87	2.33	7.91485(2)	495.824(4)
375.44	1.99	7.91496(2)	495.845(3)
378.02	2.01	7.91508(2)	495.868(3)
380.59	1.98	7.91520(2)	495.891(3)
383.17	2.03	7.91535(2)	495.918(3)
385.74	2.13	7.91548(2)	495.943(4)
388.32	2.01	7.91561(2)	495.968(3)
390.89	2.08	7.91575(2)	495.994(4)
393.47	2.07	7.91589(2)	496.021(4)
396.05	2.09	7.91603(2)	496.046(4)
398.62	1.93	7.91617(2)	496.074(3)
401.20	2.02	7.91631(2)	496.100(3)
403.77	1.96	7.91646(2)	496.127(3)
406.35	1.97	7.91661(2)	496.155(3)
408.92	1.99	7.91676(2)	496.184(3)
411.50	2.00	7.91690(2)	496.210(3)
414.07	2.03	7.91703(2)	496.235(3)
416.65	2.68	7.91722(2)	496.270(3)
419.22	2.02	7.91734(2)	496.294(3)
421.80	1.94	7.91752(2)	496.326(3)
424.37	1.99	7.91767(2)	496.355(3)
426.95	1.93	7.91781(2)	496.382(3)

Temperature (K)	R_{wp} (%)	a (Å)	Volume (Å^3)
429.52	2.00	7.91797(2)	496.411(3)
432.10	1.97	7.91812(2)	496.440(3)
434.67	1.97	7.91826(2)	496.467(3)
437.25	1.97	7.91839(2)	496.491(3)
439.82	2.00	7.91854(2)	496.518(3)
442.40	1.98	7.91868(2)	496.545(3)
444.97	1.88	7.91883(2)	496.572(3)
447.55	2.04	7.91898(2)	496.601(3)
450.12	2.04	7.91914(2)	496.631(3)
452.70	2.03	7.91930(2)	496.662(3)
455.27	1.93	7.91948(2)	496.695(3)
457.85	1.93	7.91962(2)	496.722(3)
460.43	1.86	7.91979(2)	496.754(3)
463.00	1.96	7.91995(2)	496.784(3)
465.58	2.02	7.92013(2)	496.818(3)
468.15	2.02	7.92030(2)	496.850(3)
470.73	1.99	7.92049(2)	496.884(3)
473.30	2.02	7.92067(2)	496.918(3)
473.30	1.98	7.92105(2)	496.991(3)
470.73	2.04	7.92100(2)	496.982(3)
468.15	2.04	7.92093(2)	496.967(3)
465.58	2.03	7.92083(2)	496.950(3)
463.00	2.04	7.92073(2)	496.931(3)
460.43	2.04	7.92062(2)	496.910(3)
457.85	2.02	7.92049(2)	496.886(3)
455.27	2.04	7.92039(2)	496.866(3)
452.70	2.05	7.92028(2)	496.846(3)
450.12	2.04	7.92016(2)	496.823(3)
447.55	2.04	7.92005(2)	496.802(3)
444.97	2.03	7.91993(2)	496.780(3)
442.40	2.04	7.91981(2)	496.757(3)
439.82	2.05	7.91968(2)	496.733(3)
437.25	1.99	7.91955(2)	496.709(3)
434.67	2.04	7.91942(2)	496.684(3)
432.10	1.99	7.91930(2)	496.661(3)
429.52	2.00	7.91918(2)	496.639(3)
426.95	2.00	7.91905(2)	496.615(3)
424.37	2.01	7.91892(2)	496.590(3)
421.80	1.99	7.91880(2)	496.567(3)
419.22	2.00	7.91868(2)	496.544(3)

Temperature (K)	R_{wp} (%)	a (Å)	Volume (Å^3)
416.65	2.00	7.91855(2)	496.520(3)
414.07	2.05	7.91843(2)	496.497(3)
411.50	1.97	7.91830(2)	496.472(3)
408.92	2.05	7.91817(2)	496.449(3)
406.35	2.00	7.91805(2)	496.426(3)
403.77	2.01	7.91792(2)	496.401(3)
401.20	2.05	7.91779(2)	496.378(3)
398.62	2.02	7.91767(2)	496.354(3)
396.05	2.01	7.91753(2)	496.329(3)
393.47	2.02	7.91741(2)	496.307(3)
390.89	2.02	7.91729(2)	496.283(3)
388.32	2.02	7.91716(2)	496.259(3)
385.74	2.12	7.91704(2)	496.237(4)
383.17	2.03	7.91693(2)	496.215(3)
380.59	2.12	7.91681(2)	496.193(4)
378.02	2.11	7.91669(2)	496.170(4)
375.44	2.00	7.91658(2)	496.149(3)
372.87	2.12	7.91645(2)	496.126(4)
370.29	2.02	7.91634(2)	496.104(3)
367.72	2.03	7.91622(2)	496.082(3)
365.14	2.00	7.91611(2)	496.061(3)
362.57	2.14	7.91599(2)	496.039(4)
359.99	2.04	7.91589(2)	496.019(3)
357.42	2.07	7.91579(2)	496.001(3)
354.84	2.01	7.91569(2)	495.982(3)
352.27	2.07	7.91558(2)	495.962(3)
349.69	2.07	7.91549(2)	495.944(3)
347.12	2.04	7.91539(2)	495.926(3)
344.54	2.08	7.91531(2)	495.911(3)
341.97	2.04	7.91521(2)	495.892(3)
339.39	2.06	7.91514(2)	495.879(3)
336.82	2.06	7.91505(2)	495.863(3)
334.24	2.08	7.91496(2)	495.846(3)
331.67	2.07	7.91489(2)	495.832(3)
329.09	2.08	7.91481(2)	495.817(3)
326.51	2.08	7.91474(2)	495.804(3)
323.94	2.09	7.91468(2)	495.792(3)
321.36	2.10	7.91462(2)	495.781(3)
318.79	2.10	7.91455(2)	495.769(3)
316.21	2.08	7.91449(2)	495.757(3)

Temperature (K)	R_{wp} (%)	a (Å)	Volume (Å^3)
313.64	2.10	7.91443(2)	495.746(3)
311.06	2.08	7.91437(2)	495.735(3)
308.49	2.10	7.91431(2)	495.723(3)
305.91	2.10	7.91425(2)	495.712(3)
303.34	2.09	7.9142(2)	495.703(3)
300.76	2.11	7.91415(2)	495.694(3)
298.19	2.10	7.91411(2)	495.685(3)
295.61	2.11	7.91406(2)	495.676(3)
293.04	2.11	7.91401(2)	495.667(3)
290.46	2.13	7.91395(2)	495.656(4)
287.89	2.11	7.91390(2)	495.647(3)
285.31	2.11	7.91386(2)	495.639(3)
282.74	2.10	7.91382(2)	495.630(3)
280.16	2.12	7.91376(2)	495.620(3)
277.59	2.12	7.91372(2)	495.611(3)
275.01	2.11	7.91367(2)	495.603(3)
272.44	2.13	7.91362(2)	495.594(4)
269.86	2.11	7.91357(2)	495.584(3)
267.29	2.13	7.91352(2)	495.575(4)
264.71	2.13	7.91349(2)	495.569(4)
262.13	2.16	7.91344(2)	495.560(4)
259.56	2.14	7.91341(2)	495.553(4)
256.98	2.14	7.91337(2)	495.546(4)
254.41	2.13	7.91333(2)	495.539(4)
251.83	2.15	7.91329(2)	495.531(4)
249.26	2.14	7.91324(2)	495.522(4)
246.68	2.14	7.91321(2)	495.517(4)
244.11	2.14	7.91318(2)	495.510(4)
241.53	2.16	7.91314(2)	495.503(4)
238.96	2.15	7.91310(2)	495.496(4)
236.38	2.16	7.91307(2)	495.490(4)
233.81	2.16	7.91304(2)	495.484(4)
231.23	2.17	7.91302(2)	495.480(4)
228.66	2.18	7.91298(2)	495.474(4)
226.08	2.17	7.91294(2)	495.466(4)
223.51	2.18	7.91291(2)	495.459(4)
220.93	2.17	7.91288(2)	495.455(4)
218.36	2.18	7.91286(2)	495.450(4)
215.78	2.19	7.91285(2)	495.449(4)
213.21	2.18	7.91285(2)	495.448(4)

Temperature (K)	R_{wp} (%)	a (Å)	Volume (Å^3)
210.63	2.17	7.91285(2)	495.448(4)
208.06	2.19	7.91276(2)	495.432(4)
205.48	2.19	7.91272(2)	495.425(4)
202.91	2.19	7.91271(2)	495.423(4)
200.33	2.20	7.91271(2)	495.423(4)
197.75	2.21	7.91270(2)	495.421(4)
195.18	2.19	7.91269(2)	495.418(4)
192.60	2.21	7.91268(2)	495.417(4)
190.03	2.21	7.91268(2)	495.416(4)
187.54	2.21	7.91268(2)	495.417(4)
184.96	2.21	7.91268(2)	495.416(4)
182.39	2.21	7.91268(2)	495.418(4)
179.81	2.22	7.91269(2)	495.419(4)
177.15	2.22	7.91268(2)	495.418(4)
174.66	2.22	7.91271(2)	495.422(4)
172.09	2.22	7.91271(2)	495.422(4)
169.51	2.21	7.91271(2)	495.422(4)
166.85	2.22	7.91272(2)	495.424(4)
164.28	2.24	7.91274(2)	495.428(4)
161.70	2.23	7.91277(2)	495.433(4)
159.13	2.23	7.91279(2)	495.437(4)
156.47	2.23	7.91280(2)	495.440(4)
153.89	2.21	7.91282(2)	495.444(4)
151.23	2.21	7.91286(2)	495.450(4)
148.57	2.21	7.91289(2)	495.456(4)
145.99	2.20	7.91291(2)	495.460(4)
143.33	2.21	7.91294(2)	495.465(4)
140.67	2.21	7.91296(2)	495.470(4)
138.10	2.21	7.91300(2)	495.476(4)
135.61	2.19	7.91303(2)	495.483(4)
133.20	2.19	7.91306(2)	495.489(4)
130.89	2.19	7.91310(2)	495.496(4)

Table A.4: Lattice constant and unit cell volume versus temperature for $Mg_{0.5}Zr_{1.5}F_{7.0}$ as determined from the Le Bail analysis of the synchrotron X-ray diffraction data.

Temperature (K)	Rwp (%)	a (Å)	Volume (Å^3)
130.89	1.74	7.90100(4)	493.226(7)
133.55	1.73	7.90100(4)	493.226(7)
136.12	1.74	7.90101(4)	493.228(7)
138.70	1.72	7.90099(4)	493.224(7)
141.27	1.72	7.90098(4)	493.222(7)
143.85	1.72	7.90095(4)	493.217(7)
146.42	1.71	7.90095(4)	493.218(7)
149.00	1.71	7.90094(4)	493.215(7)
151.49	1.70	7.90096(4)	493.218(7)
154.06	1.71	7.90097(4)	493.221(7)
156.64	1.71	7.90098(4)	493.222(7)
159.21	1.70	7.90099(4)	493.224(7)
161.79	1.71	7.90101(4)	493.228(7)
164.36	1.72	7.90103(4)	493.232(7)
166.94	1.71	7.90104(4)	493.233(7)
169.51	1.71	7.90104(4)	493.234(7)
172.09	1.71	7.90104(4)	493.234(7)
174.66	1.70	7.90107(4)	493.240(7)
177.24	1.70	7.90108(4)	493.242(7)
179.81	1.70	7.90112(4)	493.249(7)
182.30	1.70	7.90115(4)	493.255(7)
184.96	1.70	7.90118(4)	493.261(7)
187.54	1.71	7.90121(4)	493.266(7)
190.03	1.70	7.90124(4)	493.272(7)
192.60	1.69	7.90128(4)	493.279(7)
195.18	1.68	7.90133(4)	493.288(7)
197.75	1.69	7.90137(4)	493.295(7)
200.33	1.70	7.90140(4)	493.302(7)
202.91	1.69	7.90145(4)	493.311(7)
205.48	1.70	7.90151(4)	493.322(7)
208.06	1.70	7.90155(4)	493.329(7)
210.63	1.69	7.90159(4)	493.337(7)
213.21	1.68	7.90165(4)	493.348(7)
215.78	1.68	7.90171(4)	493.358(7)
218.36	1.69	7.90177(4)	493.371(7)
220.93	1.68	7.90183(4)	493.381(7)

Temperature (K)	Rwp (%)	a (Å)	Volume (Å^3)
223.51	1.68	7.90187(4)	493.390(7)
226.08	1.68	7.90193(4)	493.400(7)
228.66	1.67	7.90200(4)	493.413(7)
231.23	1.67	7.90207(4)	493.427(7)
233.81	1.67	7.90213(4)	493.438(7)
236.38	1.66	7.90221(4)	493.453(7)
238.96	1.66	7.90230(4)	493.469(7)
241.53	1.65	7.90234(4)	493.477(7)
244.11	1.66	7.90242(4)	493.493(7)
246.68	1.66	7.90250(4)	493.507(7)
249.26	1.65	7.90258(4)	493.522(7)
251.83	1.65	7.90263(4)	493.532(7)
254.41	1.66	7.90272(4)	493.548(7)
256.98	1.64	7.90280(4)	493.563(7)
259.56	1.64	7.90289(4)	493.580(7)
262.13	1.65	7.90297(4)	493.595(7)
264.71	1.64	7.90305(4)	493.610(7)
267.29	1.64	7.90313(4)	493.626(7)
269.86	1.64	7.90322(4)	493.642(7)
272.44	1.62	7.90331(4)	493.659(7)
275.01	1.63	7.90340(4)	493.677(7)
277.59	1.63	7.90349(4)	493.693(7)
280.16	1.63	7.90359(4)	493.712(7)
282.74	1.62	7.90367(4)	493.727(7)
285.31	1.63	7.90377(4)	493.746(7)
287.89	1.62	7.90388(4)	493.766(7)
290.46	1.61	7.90397(4)	493.783(7)
293.04	1.62	7.90407(4)	493.802(7)
295.61	1.61	7.90417(4)	493.820(7)
298.19	1.61	7.90427(4)	493.840(7)
300.76	1.62	7.90438(4)	493.859(7)
303.34	1.62	7.90448(4)	493.878(7)
305.91	1.61	7.90457(4)	493.895(7)
308.49	1.62	7.90468(4)	493.916(7)
311.06	1.60	7.90478(4)	493.935(7)
313.64	1.60	7.90489(4)	493.955(7)
316.21	1.60	7.90498(4)	493.973(7)
318.79	1.61	7.90509(4)	493.993(7)
321.36	1.60	7.90520(4)	494.013(7)
323.94	1.59	7.90531(4)	494.034(7)

Temperature (K)	Rwp (%)	a (Å)	Volume (Å^3)
326.51	1.60	7.90542(4)	494.055(7)
329.09	1.61	7.90554(4)	494.077(7)
331.67	1.61	7.90565(4)	494.097(7)
334.24	1.62	7.90576(4)	494.118(7)
336.82	1.60	7.90587(4)	494.139(7)
339.39	1.60	7.90597(4)	494.158(7)
341.97	1.60	7.90609(4)	494.181(7)
344.54	1.61	7.90623(4)	494.206(7)
347.12	1.60	7.90635(4)	494.229(7)
349.69	1.60	7.90648(4)	494.254(7)
352.27	1.59	7.90660(4)	494.276(7)
354.84	1.61	7.90674(4)	494.302(7)
357.42	1.60	7.90687(4)	494.327(7)
359.99	1.60	7.90699(4)	494.349(7)
362.57	1.61	7.90712(4)	494.373(7)
365.14	1.62	7.90726(4)	494.399(7)
367.72	1.63	7.90738(4)	494.421(7)
370.29	1.61	7.90750(4)	494.445(7)
372.87	1.61	7.90762(4)	494.468(7)
375.44	1.61	7.90775(4)	494.492(7)
378.02	1.60	7.90789(4)	494.517(7)
380.59	1.59	7.90801(4)	494.539(7)
383.17	1.58	7.90814(4)	494.564(7)
385.74	1.58	7.90828(4)	494.590(7)
388.32	1.57	7.90840(4)	494.613(7)
390.89	1.56	7.90855(4)	494.641(7)
393.47	1.56	7.90869(4)	494.668(7)
396.05	1.56	7.90885(4)	494.698(7)
398.62	1.55	7.90901(4)	494.727(7)
401.20	1.55	7.90917(4)	494.758(7)
403.77	1.55	7.90934(4)	494.790(7)
406.35	1.54	7.90953(4)	494.825(7)
408.92	1.52	7.90971(3)	494.858(7)
411.50	1.53	7.90987(3)	494.890(7)
414.07	1.51	7.91006(3)	494.925(6)
416.65	1.52	7.91025(3)	494.960(6)
419.22	1.50	7.91043(3)	494.995(6)
421.80	1.50	7.91061(3)	495.029(6)
424.37	1.49	7.91079(3)	495.063(6)
426.95	1.50	7.91099(3)	495.099(6)

Temperature (K)	Rwp (%)	a (Å)	Volume (Å^3)
429.52	1.49	7.91117(3)	495.133(6)
432.10	1.48	7.91136(3)	495.170(6)
434.67	1.49	7.91156(3)	495.207(6)
437.25	1.49	7.91175(3)	495.243(6)
439.82	1.49	7.91196(3)	495.281(6)
442.40	1.48	7.91216(3)	495.320(6)
444.97	1.48	7.91238(3)	495.360(6)
447.55	1.48	7.91258(3)	495.398(6)
450.12	1.48	7.91279(3)	495.437(6)
452.70	1.48	7.91301(3)	495.480(6)
455.27	1.48	7.91322(3)	495.519(6)
457.85	1.48	7.91342(3)	495.556(6)
460.43	1.49	7.91365(3)	495.600(6)
463.00	1.50	7.91387(3)	495.641(6)
465.58	1.49	7.91409(3)	495.682(6)
468.15	1.50	7.91431(3)	495.724(6)
470.73	1.51	7.91455(3)	495.769(6)
473.30	1.51	7.91481(3)	495.817(6)
473.30	1.54	7.91531(4)	495.910(7)
470.73	1.56	7.91525(4)	495.899(7)
468.15	1.54	7.91511(4)	495.873(7)
465.49	1.55	7.91498(4)	495.849(7)
463.00	1.56	7.91484(4)	495.822(7)
460.34	1.55	7.91468(4)	495.793(7)
457.85	1.56	7.91452(4)	495.763(7)
455.27	1.56	7.91436(4)	495.733(7)
452.70	1.56	7.91420(4)	495.703(7)
450.12	1.57	7.91404(4)	495.673(7)
447.46	1.57	7.91385(4)	495.636(7)
444.97	1.56	7.91370(4)	495.608(7)
442.31	1.57	7.91352(4)	495.575(7)
439.82	1.56	7.91335(4)	495.543(7)
437.25	1.57	7.91317(4)	495.508(7)
434.67	1.57	7.91299(4)	495.476(7)
432.01	1.57	7.91282(4)	495.443(7)
429.44	1.57	7.91265(4)	495.411(7)
426.95	1.57	7.91247(4)	495.378(7)
424.37	1.58	7.91229(4)	495.343(7)
421.80	1.59	7.91211(4)	495.310(7)
419.22	1.57	7.91194(4)	495.277(7)

Temperature (K)	Rwp (%)	a (Å)	Volume (Å^3)
416.65	1.58	7.91176(4)	495.244(7)
414.07	1.58	7.91157(4)	495.208(7)
411.41	1.59	7.91139(4)	495.175(7)
408.84	1.58	7.91121(4)	495.142(7)
406.35	1.59	7.91103(4)	495.106(7)
403.77	1.60	7.91085(4)	495.073(7)
401.20	1.60	7.91067(4)	495.040(7)
398.62	1.60	7.91050(4)	495.007(7)
396.05	1.60	7.91030(4)	494.970(7)
393.47	1.61	7.91013(4)	494.938(7)
390.81	1.61	7.90994(4)	494.902(7)
388.32	1.61	7.90976(4)	494.868(7)
385.74	1.60	7.90959(4)	494.836(7)
383.17	1.61	7.90941(4)	494.804(7)
380.59	1.61	7.90924(4)	494.771(7)
378.02	1.62	7.90908(4)	494.742(7)
375.44	1.62	7.90891(4)	494.709(7)
372.87	1.62	7.90875(4)	494.678(7)
370.21	1.62	7.90859(4)	494.650(7)
367.72	1.62	7.90843(4)	494.620(7)
365.14	1.63	7.90829(4)	494.592(7)
362.57	1.61	7.90812(4)	494.561(7)
359.99	1.62	7.90800(4)	494.539(7)
357.42	1.62	7.90786(4)	494.512(7)
354.84	1.62	7.90771(4)	494.485(7)
352.27	1.63	7.90757(4)	494.458(7)
349.61	1.63	7.90744(4)	494.434(7)
347.12	1.63	7.90730(4)	494.408(7)
344.54	1.62	7.90719(4)	494.386(7)
341.97	1.62	7.90705(4)	494.360(7)
339.39	1.64	7.90693(4)	494.338(7)
336.82	1.64	7.90681(4)	494.316(7)
334.24	1.64	7.90670(4)	494.295(7)
331.67	1.64	7.90659(4)	494.274(7)
329.09	1.65	7.90648(4)	494.253(7)
326.51	1.65	7.90637(4)	494.232(7)
323.94	1.64	7.90626(4)	494.212(7)
321.36	1.64	7.90616(4)	494.193(7)
318.79	1.65	7.90605(4)	494.172(7)
316.21	1.66	7.90595(4)	494.154(7)

Temperature (K)	Rwp (%)	a (Å)	Volume (Å^3)
313.64	1.67	7.90587(4)	494.138(7)
311.06	1.66	7.90578(4)	494.122(7)
308.49	1.67	7.90568(4)	494.104(7)
305.91	1.68	7.90559(4)	494.086(7)
303.34	1.68	7.90549(4)	494.068(7)
300.76	1.68	7.90540(4)	494.051(7)
298.19	1.69	7.90531(4)	494.033(7)
295.61	1.67	7.90523(4)	494.019(7)
293.04	1.69	7.90514(4)	494.002(7)
290.46	1.69	7.90505(4)	493.985(7)
287.89	1.69	7.90497(4)	493.970(7)
285.31	1.69	7.90489(4)	493.955(7)
282.74	1.69	7.90480(4)	493.939(7)
280.16	1.70	7.90473(4)	493.926(7)
277.59	1.70	7.90465(4)	493.910(7)
275.01	1.70	7.90457(4)	493.896(7)
272.44	1.72	7.90451(4)	493.884(7)
269.86	1.71	7.90443(4)	493.869(7)
267.29	1.71	7.90436(4)	493.855(7)
264.62	1.72	7.90429(4)	493.843(7)
262.05	1.72	7.90423(4)	493.831(7)
259.56	1.73	7.90415(4)	493.817(7)
256.98	1.72	7.90410(4)	493.806(7)
254.32	1.73	7.90403(4)	493.793(7)
251.83	1.73	7.90397(4)	493.782(7)
249.17	1.73	7.90392(4)	493.774(7)
246.60	1.73	7.90385(4)	493.761(7)
244.02	1.73	7.90379(4)	493.748(7)
241.45	1.74	7.90372(4)	493.735(7)
238.87	1.75	7.90364(4)	493.722(7)
236.30	1.75	7.90360(4)	493.714(7)
233.72	1.75	7.90352(4)	493.698(7)
231.15	1.76	7.90347(4)	493.689(7)
228.57	1.75	7.90343(4)	493.681(7)
226.00	1.76	7.90337(4)	493.670(7)
223.42	1.76	7.90332(4)	493.661(7)
220.85	1.76	7.90328(4)	493.653(7)
218.27	1.76	7.90324(4)	493.645(7)
215.70	1.76	7.90319(4)	493.637(7)
213.12	1.76	7.90313(4)	493.625(7)

Temperature (K)	Rwp (%)	a (Å)	Volume (Å^3)
210.54	1.76	7.90309(4)	493.618(7)
207.97	1.77	7.90305(4)	493.610(7)
205.39	1.78	7.90301(4)	493.602(7)
202.82	1.78	7.90296(4)	493.594(7)
200.24	1.77	7.90292(4)	493.587(7)
197.58	1.78	7.90288(4)	493.579(7)
195.01	1.77	7.90284(4)	493.570(7)
192.43	1.78	7.90281(4)	493.565(7)
189.86	1.78	7.90276(4)	493.557(7)
187.28	1.77	7.90273(4)	493.551(7)
184.71	1.78	7.90271(4)	493.546(7)
182.13	1.77	7.90268(4)	493.541(7)
179.47	1.78	7.90266(4)	493.537(7)
176.90	1.77	7.90263(4)	493.531(7)
174.32	1.77	7.90261(4)	493.528(7)
171.66	1.77	7.90262(4)	493.530(7)
169.08	1.77	7.90261(4)	493.528(7)
166.51	1.77	7.90262(4)	493.529(7)
163.85	1.76	7.90260(4)	493.525(7)
161.19	1.77	7.90259(4)	493.525(7)
158.61	1.77	7.90260(4)	493.525(7)
155.95	1.77	7.90259(4)	493.525(7)
153.38	1.79	7.90259(4)	493.524(7)
150.80	1.78	7.90260(4)	493.526(7)
148.22	1.79	7.90261(4)	493.528(7)
145.74	1.78	7.90261(4)	493.527(7)
143.16	1.78	7.90261(4)	493.529(7)
140.76	1.78	7.90264(4)	493.534(7)
138.35	1.79	7.90266(4)	493.537(7)
136.12	1.79	7.90268(4)	493.541(7)
134.06	1.78	7.90270(4)	493.544(7)
132.09	1.78	7.90272(4)	493.548(7)

Table A.5: Lattice constant and unit cell volume versus temperature for $Mg_{0.85}Zr_{1.15}F_{6.3}$ as determined from the Le Bail analysis of the neutron diffraction data.

Temperature (K)	R_{wp} (%)	a (Å)	Volume (Å^3)
10.00	4.16	7.9515(2)	502.75(3)
15.00	5.72	7.9515(2)	502.74(3)
30.00	5.71	7.9512(2)	502.69(3)
45.00	5.59	7.9509(2)	502.64(3)
60.00	5.56	7.9503(4)	502.52(3)
75.00	4.88	7.9497(4)	502.40(3)
90.00	4.71	7.9490(4)	502.26(3)
105.01	4.49	7.9485(4)	502.18(3)
120.01	4.70	7.9475(4)	501.99(3)
135.01	4.70	7.9473(4)	501.96(3)
150.01	4.83	7.9466(4)	501.81(3)
165.01	4.54	7.9461(4)	501.72(3)
180.01	4.80	7.9452(4)	501.54(3)
195.01	4.90	7.9450(4)	501.50(3)
210.02	4.71	7.9444(4)	501.39(3)
225.02	4.85	7.9440(4)	501.32(3)
240.02	4.82	7.9433(4)	501.19(3)
255.02	5.18	7.9427(4)	501.08(3)
270.02	5.17	7.9423(4)	501.01(3)
285.02	5.56	7.9420(4)	500.94(3)
300.01	5.49	7.9420(4)	500.95(3)

Table A.6: Lattice constant and unit cell volume versus temperature for $Mg_{0.7}Zr_{1.3}F_{6.6}$ as determined from the Le Bail analysis of the neutron diffraction data.

Temperature (K)	R_{wp} (%)	a (Å)	Volume (Å^3)
10.00	2.61	7.92664(8)	498.04(2)
15.00	2.82	7.92664(8)	498.04(2)
30.00	2.86	7.92654(8)	498.02(2)
45.00	2.68	7.92623(9)	497.97(2)
60.00	2.76	7.92599(9)	497.92(2)
75.00	2.71	7.92579(9)	497.88(2)
90.00	2.60	7.9255(9)	497.83(2)
105.01	2.59	7.92533(9)	497.80(2)
120.01	2.78	7.92497(9)	497.73(2)
135.01	2.71	7.92494(9)	497.72(2)
150.01	2.60	7.92495(9)	497.73(2)
165.01	2.71	7.92484(9)	497.70(2)
180.01	2.61	7.92476(9)	497.69(2)
195.01	2.58	7.92469(9)	497.68(2)
210.02	2.69	7.92454(9)	497.65(2)
225.01	2.48	7.92469(9)	497.68(2)
240.02	2.47	7.92467(9)	497.67(2)
255.02	2.55	7.92466(9)	497.67(2)
270.02	2.62	7.92472(9)	497.68(2)
285.02	2.70	7.9247(9)	497.68(2)
300.01	2.70	7.92506(9)	497.75(2)

Table A.7: Lattice constant and unit cell volume versus temperature for $Mg_{0.6}Zr_{1.4}F_{6.8}$ as determined from the Le Bail analysis of the neutron diffraction data.

Temperature (K)	R_{wp} (%)	a (Å)	Volume (Å^3)
10.00	3.19	7.9140(1)	495.66(2)
15.00	3.19	7.9140(1)	495.67(2)
30.00	3.10	7.9138(1)	495.62(2)
45.00	3.05	7.9136(1)	495.60(2)
60.00	3.07	7.9133(1)	495.54(2)
75.00	3.05	7.9130(1)	495.48(2)
90.01	3.22	7.9128(1)	495.44(2)
105.01	3.27	7.9127(1)	495.42(2)
120.01	3.13	7.9123(1)	495.34(3)
135.01	3.11	7.9123(1)	495.34(3)
150.01	3.19	7.9122(1)	495.33(2)
165.01	3.01	7.9121(1)	495.31(3)
180.01	3.24	7.9122(1)	495.33(3)
195.01	3.22	7.9124(1)	495.37(3)
210.01	3.21	7.9124(1)	495.37(3)
225.02	3.10	7.9126(1)	495.40(3)
240.02	2.93	7.9127(1)	495.41(3)
255.02	3.24	7.9128(1)	495.44(3)
270.02	3.20	7.9134(1)	495.55(3)
285.01	3.08	7.9134(1)	495.55(3)
300.01	3.08	7.9140(1)	495.66(3)

Table A.8: Lattice constant and unit cell volume versus temperature for $Mg_{0.5}Zr_{1.5}F_{7.0}$ as determined from the Le Bail analysis of the neutron diffraction data.

Temperature (K)	R_{wp} (%)	a (Å)	Volume (Å^3)
10.00	2.03	7.9028(1)	493.57(1)
15.00	4.24	7.9027(2)	493.54(3)
30.00	4.15	7.9026(2)	493.52(3)
45.00	4.50	7.9026(2)	493.53(3)
60.00	4.17	7.9025(2)	493.51(3)
75.01	4.29	7.9020(2)	493.42(3)
90.00	4.33	7.9016(2)	493.34(3)
105.01	4.36	7.9018(2)	493.37(3)
120.01	4.11	7.9014(2)	493.31(3)
135.01	4.51	7.9016(2)	493.35(3)
150.01	4.26	7.9015(2)	493.32(3)
165.01	4.25	7.9016(2)	493.34(4)
180.01	4.26	7.9019(2)	493.39(3)
195.01	4.24	7.9018(2)	493.37(4)
210.01	4.16	7.9023(2)	493.47(4)
225.02	4.13	7.9023(2)	493.47(4)
240.01	4.39	7.9028(2)	493.56(4)
255.02	4.02	7.9032(2)	493.65(4)
270.02	4.31	7.9035(2)	493.69(4)
285.02	4.27	7.9040(2)	493.79(4)
300.02	4.38	7.9046(2)	493.90(4)

Table A.9: Weighted profile R factor, unit cell constant for the $Mg_{0.85}Zr_{1.15}F_{6.3}$ sample, unit cell volumes for both the sample and the CaF_2 pressure marker, and the pressure estimated from the CaF_2 assuming a unit cell volume for CaF_2 at zero pressure of 163.03 Å^3.

R_{wp} (%)	Sample lattice constant, a (Å)	Sample unit cell volume, V (Å^3)	CaF_2 unit cell volume, V (Å^3)	Pressure (GPa)
7.92	7.9346(6)	499.55(7)	163.10(7)	-0.04(8)
7.30	7.9346(2)	499.55(4)	163.10(3)	-0.03(5)
7.22	7.9406(2)	500.69(4)	163.09(3)	-0.03(5)
7.43	7.9406(2)	500.67(4)	163.09(3)	-0.03(5)
7.58	7.9405(2)	500.67(4)	163.10(3)	-0.03(5)
7.67	7.9405(2)	500.66(4)	163.10(3)	-0.03(5)
7.55	7.9405(2)	500.66(4)	163.10(3)	-0.03(5)
7.79	7.9406(2)	500.67(4)	163.10(3)	-0.04(5)
7.69	7.9404(2)	500.64(4)	163.09(3)	-0.03(5)
7.92	7.9403(2)	500.61(4)	163.09(3)	-0.03(5)
8.09	7.9404(2)	500.63(4)	163.08(4)	-0.02(5)
7.84	7.9399(2)	500.55(4)	163.07(3)	-0.02(5)
7.45	7.9397(2)	500.52(4)	163.07(3)	-0.02(5)
7.42	7.9395(2)	500.48(4)	163.07(3)	-0.02(5)
7.59	7.9395(2)	500.47(4)	163.07(3)	-0.02(5)
7.05	7.9394(2)	500.45(4)	163.06(3)	-0.02(5)
7.02	7.9392(2)	500.42(4)	163.05(3)	-0.01(5)
7.20	7.9390(2)	500.37(4)	163.04(3)	0.00(5)
7.14	7.9392(2)	500.41(3)	163.04(3)	0.00(5)
7.76	7.9388(2)	500.34(4)	163.03(3)	0.00(5)
7.85	7.9385(2)	500.29(4)	163.03(4)	0.00(5)
7.55	7.9385(2)	500.28(4)	163.02(3)	0.00(5)
7.65	7.9382(2)	500.23(4)	163.01(3)	0.01(5)
7.10	7.9378(2)	500.15(4)	162.99(3)	0.02(5)
7.29	7.9374(2)	500.07(4)	162.96(3)	0.03(5)
6.87	7.9368(2)	499.97(3)	162.96(3)	0.04(5)
7.08	7.9361(2)	499.83(3)	162.92(3)	0.05(5)
6.87	7.9353(2)	499.68(3)	162.88(3)	0.07(5)
6.88	7.9348(2)	499.59(3)	162.86(3)	0.08(5)
6.97	7.9341(2)	499.46(3)	162.84(3)	0.10(5)
6.85	7.9334(2)	499.32(3)	162.80(3)	0.11(5)
7.02	7.9321(2)	499.07(3)	162.76(3)	0.14(5)
7.06	7.9309(2)	498.85(3)	162.71(3)	0.16(5)
7.02	7.9304(2)	498.76(3)	162.72(3)	0.15(5)
7.07	7.9302(2)	498.71(3)	162.70(3)	0.17(5)

R_{wp} (%)	Sample lattice constant, a (Å)	Sample unit cell volume, V (Å^3)	CaF_2 unit cell volume, V (Å^3)	Pressure (GPa)
7.30	7.9300(2)	498.69(4)	162.72(3)	0.15(5)
6.84	7.9298(2)	498.64(3)	162.70(3)	0.16(5)
7.04	7.9295(2)	498.59(3)	162.69(3)	0.17(5)
7.30	7.9292(2)	498.53(3)	162.68(3)	0.18(5)
6.75	7.9293(7)	498.55(3)	162.67(3)	0.18(5)
6.79	7.9286(2)	498.41(3)	162.66(3)	0.19(5)
6.57	7.9282(7)	498.35(3)	162.64(3)	0.20(5)
6.73	7.9283(7)	498.37(3)	162.62(3)	0.20(5)
6.77	7.9283(7)	498.37(3)	162.61(3)	0.21(5)
6.91	7.9283(7)	498.37(3)	162.61(3)	0.21(5)
6.66	7.9282(7)	498.34(3)	162.59(3)	0.22(5)
6.53	7.9269(7)	498.09(3)	162.58(3)	0.22(5)
6.89	7.9260(2)	497.92(3)	162.56(3)	0.24(5)
7.26	7.9256(2)	497.85(3)	162.54(3)	0.25(5)
7.00	7.9252(2)	497.77(3)	162.53(3)	0.25(5)
7.03	7.9249(2)	497.72(3)	162.52(3)	0.26(5)
6.64	7.9245(2)	497.64(3)	162.49(3)	0.27(5)
6.93	7.9240(2)	497.55(3)	162.47(3)	0.28(5)
6.92	7.9234(2)	497.44(3)	162.44(3)	0.30(5)
6.56	7.9223(2)	497.23(3)	162.41(3)	0.31(5)
6.22	7.9215(2)	497.08(3)	162.39(3)	0.32(5)
5.97	7.9208(7)	496.94(3)	162.38(3)	0.33(5)
5.74	7.9202(7)	496.84(3)	162.36(3)	0.34(5)
5.44	7.9194(7)	496.69(3)	162.35(3)	0.34(5)
5.77	7.9188(7)	496.56(3)	162.33(3)	0.35(5)
6.09	7.9183(2)	496.47(3)	162.31(3)	0.36(6)
6.21	7.9179(2)	496.40(3)	162.30(3)	0.37(6)
6.02	7.9174(2)	496.30(3)	162.30(3)	0.37(6)
7.04	7.9168(2)	496.19(4)	162.27(3)	0.38(6)
6.88	7.9162(2)	496.09(3)	162.26(3)	0.39(6)
6.61	7.9158(2)	496.00(3)	162.25(3)	0.39(6)
7.16	7.9143(2)	495.71(4)	162.20(3)	0.42(6)
7.12	7.9119(2)	495.28(4)	162.16(3)	0.44(6)
7.34	7.9107(2)	495.04(4)	162.11(3)	0.46(6)
7.19	7.9096(2)	494.85(4)	162.08(3)	0.48(6)
7.22	7.9085(2)	494.64(4)	162.05(3)	0.49(6)
6.92	7.9075(2)	494.44(4)	162.04(3)	0.50(6)
7.11	7.9064(2)	494.24(4)	162.03(3)	0.51(6)
6.95	7.9041(2)	493.80(5)	161.96(3)	0.54(6)
7.00	7.9025(2)	493.51(5)	161.93(3)	0.56(6)

R_{wp} (%)	Sample lattice constant, a (Å)	Sample unit cell volume, V (Å^3)	CaF_2 unit cell volume, V (Å^3)	Pressure (GPa)
7.24	7.9014(3)	493.31(5)	161.91(3)	0.57(6)
7.46	7.9005(3)	493.13(5)	161.90(3)	0.57(6)
7.35	7.8996(3)	492.96(5)	161.89(3)	0.58(6)
7.08	7.8985(3)	492.76(5)	161.86(3)	0.60(6)
7.31	7.8975(3)	492.57(5)	161.84(3)	0.60(6)
7.40	7.8962(3)	492.33(6)	161.84(3)	0.61(6)

Table A.10: Weighted profile R factor, unit cell constant for the $Mg_{0.7}Zr_{1.3}F_{6.6}$ sample, unit cell volumes for both the sample and the CaF_2 pressure marker, and the pressure estimated from the CaF_2 assuming a unit cell volume for CaF_2 at zero pressure of 163.03 $Å^3$.

R_{wp} (%)	Sample lattice constant, a (Å)	Sample unit cell volume, V ($Å^3$)	CaF_2 unit cell volume, V ($Å^3$)	Pressure (GPa)
3.28	7.9162(1)	496.08(2)	163.08(7)	-0.02(5)
4.45	7.9218(1)	497.13(1)	163.08(4)	-0.02(5)
4.22	7.9218(1)	497.13(1)	163.08(5)	-0.02(5)
4.82	7.9220(1)	497.16(1)	163.08(4)	-0.03(5)
5.05	7.9219(1)	497.16(2)	163.07(5)	-0.02(5)
4.47	7.9219(1)	497.14(1)	163.08(5)	-0.03(5)
4.76	7.9221(1)	497.19(1)	163.07(4)	-0.02(5)
4.31	7.9219(1)	497.15(1)	163.07(4)	-0.02(5)
4.77	7.9223(1)	497.22(1)	163.08(4)	-0.02(5)
6.33	7.9224(1)	497.24(2)	163.09(4)	-0.03(5)
5.39	7.9220(1)	497.17(2)	163.09(4)	-0.03(5)
4.94	7.9222(1)	497.21(1)	163.08(4)	-0.03(5)
4.92	7.9223(1)	497.23(1)	163.08(4)	-0.03(5)
4.61	7.9222(1)	497.21(1)	163.09(4)	-0.03(5)
4.74	7.9221(1)	497.18(1)	163.09(4)	-0.03(5)
4.43	7.9221(1)	497.18(1)	163.09(4)	-0.03(5)
4.98	7.9221(1)	497.19(1)	163.08(4)	-0.02(5)
5.19	7.9218(1)	497.14(2)	163.06(4)	-0.02(5)
5.93	7.9216(1)	497.09(2)	163.05(4)	-0.01(5)
6.18	7.9211(1)	497.00(2)	163.04(4)	0.00(5)
5.67	7.9205(1)	496.88(2)	163.02(4)	0.01(5)
5.61	7.9198(1)	496.75(2)	162.98(4)	0.02(5)
5.71	7.9191(1)	496.62(2)	162.94(4)	0.05(5)
5.28	7.9175(1)	496.33(2)	162.89(4)	0.07(5)
6.18	7.9163(1)	496.10(2)	162.84(4)	0.10(5)
6.09	7.9146(1)	495.78(2)	162.75(4)	0.14(5)
6.32	7.9135(1)	495.57(2)	162.72(4)	0.16(5)

R_{wp} (%)	Sample lattice constant, a (Å)	Sample unit cell volume, V (Å^3)	CaF_2 unit cell volume, V (Å^3)	Pressure (GPa)
5.19	7.9117(1)	495.23(1)	162.66(4)	0.19(5)
5.12	7.9092(1)	494.76(1)	162.55(4)	0.24(5)
5.31	7.9065(1)	494.25(1)	162.43(4)	0.30(6)
4.56	7.9034(1)	493.68(1)	162.34(4)	0.35(6)
5.28	7.9010(1)	493.22(1)	162.24(4)	0.40(6)
4.60	7.8991(1)	492.88(1)	162.18(5)	0.43(6)
5.37	7.8978(1)	492.62(1)	162.15(4)	0.45(6)
4.65	7.8968(1)	492.44(1)	162.10(4)	0.47(6)
5.46	7.8961(1)	492.31(2)	162.06(4)	0.49(6)
4.95	7.8952(1)	492.15(1)	162.04(4)	0.50(6)
5.93	7.8945(1)	492.01(2)	162.02(4)	0.51(6)
5.46	7.8938(1)	491.87(1)	161.99(5)	0.53(6)
5.94	7.8928(1)	491.69(2)	161.95(5)	0.55(6)
6.24	7.8920(1)	491.54(2)	161.92(5)	0.56(6)
6.39	7.8912(1)	491.40(2)	161.90(5)	0.57(6)
6.27	7.8901(1)	491.19(2)	161.88(4)	0.59(6)
5.80	7.8890(1)	490.97(2)	161.84(4)	0.61(6)
5.62	7.8885(1)	490.88(1)	161.82(4)	0.62(6)
6.73	7.8878(1)	490.76(2)	161.80(4)	0.62(6)
5.31	7.8873(1)	490.67(1)	161.79(4)	0.63(6)
6.48	7.8867(1)	490.56(2)	161.78(4)	0.64(6)
5.44	7.8863(1)	490.49(1)	161.77(4)	0.64(6)
6.27	7.8861(1)	490.45(2)	161.75(4)	0.65(6)
5.53	7.8851(1)	490.26(1)	161.71(4)	0.68(6)
5.86	7.8836(1)	489.98(2)	161.65(4)	0.70(6)
6.20	7.8814(1)	489.56(2)	161.57(4)	0.75(6)
6.22	7.8799(1)	489.28(2)	161.53(4)	0.77(6)
6.43	7.8790(1)	489.11(2)	161.48(4)	0.79(6)
6.08	7.8777(1)	488.88(2)	161.46(4)	0.81(6)
6.34	7.8769(1)	488.72(2)	161.43(4)	0.82(6)
6.13	7.8742(1)	488.22(2)	161.35(4)	0.86(6)
7.84	7.8718(1)	487.77(3)	161.31(4)	0.89(7)
6.58	7.8696(1)	487.36(2)	161.25(4)	0.91(7)
6.95	7.8674(1)	486.97(2)	161.20(4)	0.94(7)
6.94	7.8656(1)	486.63(2)	161.15(4)	0.97(7)
7.12	7.8627(1)	486.08(2)	161.08(4)	1.00(7)
7.47	7.8615(1)	485.87(2)	161.07(4)	1.01(7)
7.72	7.8606(1)	485.70(2)	161.06(4)	1.02(7)
7.76	7.8594(1)	485.48(2)	161.03(4)	1.04(7)
7.60	7.8566(1)	484.95(2)	160.94(4)	1.08(7)

R_{wp} (%)	Sample lattice constant, a (Å)	Sample unit cell volume, V (Å^3)	CaF_2 unit cell volume, V (Å^3)	Pressure (GPa)
8.46	7.8533(1)	484.35(3)	160.87(4)	1.12(7)
8.53	7.8516(1)	484.03(3)	160.83(4)	1.14(7)
9.61	7.8503(2)	483.80(3)	160.81(4)	1.15(7)
8.23	7.8493(1)	483.61(3)	160.77(4)	1.17(7)
9.51	7.8470(2)	483.19(3)	160.72(4)	1.20(7)
8.25	7.8458(2)	482.97(3)	160.70(4)	1.21(7)
7.27	7.8446(1)	482.73(3)	160.67(4)	1.23(7)
7.08	7.8425(1)	482.36(3)	160.63(4)	1.25(8)
7.34	7.8396(1)	481.81(2)	160.57(4)	1.28(8)
6.07	7.8372(1)	481.38(2)	160.52(4)	1.31(8)
5.98	7.8352(1)	481.01(2)	160.47(4)	1.34(8)
5.92	7.8341(1)	480.81(2)	160.45(4)	1.35(8)
5.81	7.8330(1)	480.60(2)	160.43(4)	1.36(8)
5.90	7.8311(1)	480.26(2)	160.38(4)	1.38(8)
6.02	7.8281(1)	479.70(2)	160.31(4)	1.42(8)
6.18	7.8252(1)	479.16(2)	160.25(4)	1.45(8)
6.20	7.8215(1)	478.48(2)	160.18(4)	1.50(8)
5.79	7.8191(1)	478.05(2)	160.13(4)	1.53(8)
5.73	7.8170(1)	477.67(2)	160.09(4)	1.54(8)
5.69	7.8151(1)	477.31(2)	160.07(4)	1.56(8)
5.57	7.8124(1)	476.82(2)	160.03(4)	1.58(8)
5.57	7.8085(1)	476.11(2)	159.97(4)	1.61(9)
5.57	7.8066(1)	475.76(2)	159.93(4)	1.63(9)
5.56	7.8046(1)	475.40(2)	159.91(4)	1.65(9)
5.59	7.8031(1)	475.13(2)	159.88(4)	1.66(9)
5.64	7.8013(1)	474.80(2)	159.85(4)	1.68(9)
5.54	7.7986(1)	474.29(2)	159.81(4)	1.70(9)
5.68	7.7965(1)	473.91(2)	159.78(4)	1.72(9)
5.70	7.7950(1)	473.65(2)	159.75(4)	1.74(9)
5.86	7.7936(1)	473.38(3)	159.73(4)	1.75(9)
5.60	7.7913(1)	472.96(2)	159.70(4)	1.77(9)
6.02	7.7879(2)	472.34(3)	159.65(4)	1.79(9)
6.24	7.7851(2)	471.84(3)	159.61(4)	1.81(9)
6.28	7.7828(2)	471.42(3)	159.58(4)	1.83(9)
6.34	7.7799(2)	470.89(3)	159.53(4)	1.86(9)
6.59	7.7767(2)	470.32(4)	159.48(4)	1.89(9)
6.86	7.7720(2)	469.46(4)	159.40(4)	1.93(10)
6.46	7.7687(2)	468.87(4)	159.35(4)	1.96(10)
6.61	7.7658(2)	468.33(4)	159.31(4)	1.99(10)
6.72	7.7628(2)	467.79(4)	159.27(4)	2.01(10)

R_{wp} (%)	Sample lattice constant, a (Å)	Sample unit cell volume, V (Å^3)	CaF_2 unit cell volume, V (Å^3)	Pressure (GPa)
6.71	7.7602(2)	467.32(4)	159.23(4)	2.03(10)
6.85	7.7580(2)	466.93(4)	159.20(4)	2.05(10)
7.07	7.7543(2)	466.27(4)	159.15(4)	2.08(10)
7.11	7.7517(3)	465.78(5)	159.11(4)	2.10(10)
7.33	7.7494(3)	465.37(5)	159.08(4)	2.12(10)
7.30	7.7455(3)	464.68(5)	159.03(4)	2.15(10)
7.28	7.7422(3)	464.08(5)	158.99(4)	2.17(10)
7.69	7.7392(3)	463.55(5)	158.95(4)	2.19(10)
8.00	7.7359(3)	462.95(6)	158.91(4)	2.22(10)
8.06	7.7327(3)	462.38(6)	158.88(4)	2.24(11)
8.28	7.7290(4)	461.71(7)	158.83(4)	2.26(11)
8.11	7.7267(4)	461.30(7)	158.80(4)	2.28(11)
8.28	7.7240(4)	460.82(7)	158.78(4)	2.30(11)
8.80	7.7209(4)	460.25(7)	158.75(4)	2.31(11)
8.37	7.7182(4)	459.77(7)	158.72(4)	2.33(11)
8.75	7.7144(4)	459.09(7)	158.70(4)	2.34(11)
8.81	7.7096(4)	458.25(7)	158.65(4)	2.37(11)
5.61	7.7096(4)	458.25(7)	158.60(4)	2.40(11)

Table A.11: Weighted profile R factor, unit cell constant for the $Mg_{0.6}Zr_{1.4}F_{6.8}$ sample, unit cell volumes for both the sample and the CaF_2 pressure marker, and the pressure estimated from the CaF_2 assuming a unit cell volume for CaF_2 at zero pressure of 163.03 Å^3.

R_{wp} (%)	Sample lattice constant, a (Å)	Sample unit cell volume, V (Å^3)	CaF_2 unit cell volume, V (Å^3)	Pressure (GPa)
4.47	7.90514(6)	494.00(1)	162.81(1)	0.11(5)
4.59	7.90523(7)	494.02(1)	162.82(1)	0.10(5)
4.75	7.90529(7)	494.03(1)	162.82(1)	0.11(5)
5.06	7.90535(7)	494.04(1)	162.81(1)	0.11(5)
4.70	7.90529(7)	494.03(1)	162.81(1)	0.11(5)
5.05	7.90535(7)	494.04(1)	162.80(1)	0.12(5)
5.31	7.90538(7)	494.05(1)	162.80(1)	0.11(5)
5.26	7.90527(7)	494.03(1)	162.81(1)	0.11(5)
4.56	7.90496(6)	493.97(1)	162.80(1)	0.12(5)
4.84	7.90490(7)	493.96(1)	162.79(1)	0.12(5)
4.99	7.90506(7)	493.99(1)	162.79(1)	0.12(5)
4.95	7.90482(7)	493.94(1)	162.08(1)	0.11(5)
4.68	7.90396(6)	493.78(1)	162.77(1)	0.13(5)
4.60	7.90350(6)	493.69(1)	162.73(1)	0.15(5)
4.63	7.90312(7)	493.62(1)	162.71(1)	0.16(5)
4.67	7.90282(6)	493.57(1)	162.66(1)	0.18(5)
5.00	7.90238(7)	493.48(1)	162.67(1)	0.18(5)
4.65	7.90182(6)	493.38(1)	162.64(1)	0.20(5)
4.78	7.90090(7)	493.21(1)	162.62(1)	0.21(5)
4.77	7.90033(6)	493.10(1)	162.60(1)	0.21(5)
4.69	7.89977(6)	493.00(1)	162.56(1)	0.23(5)
5.04	7.89925(7)	492.90(1)	162.52(1)	0.25(5)
5.31	7.89846(7)	492.75(1)	162.51(1)	0.26(5)
4.35	7.89740(6)	492.55(1)	162.46(1)	0.28(5)
4.61	7.89653(6)	492.39(1)	162.41(1)	0.31(5)
5.66	7.89546(7)	492.19(1)	162.37(1)	0.33(5)

R_{wp} (%)	Sample lattice constant, a (Å)	Sample unit cell volume, V (Å^3)	CaF_2 unit cell volume, V (Å^3)	Pressure (GPa)
4.56	7.89357(6)	491.84(1)	162.29(1)	0.37(5)
4.78	7.89187(6)	491.52(1)	162.22(1)	0.41(5)
5.29	7.88998(7)	491.16(1)	162.13(1)	0.45(5)
5.61	7.88713(8)	490.63(1)	162.03(1)	0.51(6)
5.86	7.88479(8)	490.20(1)	161.91(1)	0.57(6)
6.16	7.88207(8)	489.69(2)	161.81(2)	0.62(6)
6.09	7.88040(8)	489.38(2)	161.78(2)	0.64(6)
6.52	7.87920(7)	489.15(2)	161.73(2)	0.66(6)
6.04	7.87813(8)	488.96(2)	161.71(2)	0.67(6)
6.23	7.87763(8)	488.86(2)	161.69(2)	0.68(6)
6.39	7.87719(8)	488.78(2)	161.65(2)	0.70(6)
7.17	7.87636(7)	488.63(2)	161.62(2)	0.72(6)
7.11	7.87557(7)	488.48(2)	161.60(2)	0.73(6)
6.80	7.87504(7)	488.38(2)	161.58(2)	0.74(6)
7.11	7.87479(7)	488.33(2)	161.55(2)	0.75(6)
8.39	7.87420(1)	488.23(2)	161.51(2)	0.78(6)
8.81	7.87360(1)	488.11(2)	161.49(2)	0.79(6)
8.84	7.87260(1)	487.93(2)	161.47(2)	0.80(6)
8.31	7.8716(1)	487.73(2)	161.44(2)	0.81(6)
8.22	7.8710(1)	487.62(2)	161.40(2)	0.84(6)
7.97	7.8704(1)	487.52(2)	161.38(2)	0.85(6)
8.93	7.8694(1)	487.32(2)	161.34(2)	0.87(6)
8.35	7.8687(1)	487.20(2)	161.32(2)	0.88(6)
9.67	7.8675(1)	486.97(3)	161.30(2)	0.89(6)
9.17	7.8661(1)	486.71(2)	161.29(2)	0.89(6)
8.19	7.8650(1)	486.52(2)	161.26(2)	0.91(6)
8.34	7.8643(1)	486.39(2)	161.22(2)	0.93(7)
9.24	7.8636(1)	486.25(2)	161.20(2)	0.94(7)
10.05	7.8626(1)	486.07(3)	161.16(2)	0.96(7)
9.99	7.8612(1)	485.80(3)	161.13(2)	0.98(7)
10.75	7.8593(2)	485.46(3)	161.07(2)	1.01(7)
11.36	7.8574(2)	485.10(3)	160.98(3)	1.06(7)
11.01	7.8561(2)	484.87(3)	160.93(3)	1.09(7)
15.17	7.8543(2)	484.54(4)	160.89(5)	1.11(7)
14.36	7.8529(2)	484.28(4)	160.84(4)	1.14(7)
15.86	7.8516(2)	484.03(4)	160.82(4)	1.15(7)
15.97	7.8509(2)	483.90(4)	160.79(4)	1.16(7)
18.29	7.8490(3)	483.55(7)	160.75(4)	1.18(8)
20.45	7.8475(3)	483.28(7)	160.70(5)	1.21(8)
9.22	7.8452(3)	482.86(6)	160.65(2)	1.24(8)

R_{wp} (%)	Sample lattice constant, a (Å)	Sample unit cell volume, V (Å^3)	CaF_2 unit cell volume, V (Å^3)	Pressure (GPa)
8.47	7.8446(3)	482.73(7)	160.63(2)	1.25(8)
16.29	7.8419(3)	482.24(7)	160.59(2)	1.27(8)
9.07	7.8418(3)	482.22(6)	160.53(2)	1.31(8)
10.16	7.8402(3)	481.93(6)	160.48(2)	1.33(8)
11.85	7.8377(4)	481.47(7)	160.42(2)	1.36(8)
10.73	7.8358(4)	481.12(7)	160.36(2)	1.40(8)
10.81	7.8344(4)	480.86(7)	160.32(2)	1.42(8)
13.08	7.8328(4)	480.57(7)	160.28(3)	1.44(8)
11.65	7.8312(4)	480.27(7)	160.24(2)	1.46(8)
10.97	7.8292(4)	479.89(7)	160.18(2)	1.50(8)
9.56	7.8268(4)	479.47(7)	160.11(2)	1.54(8)
9.60	7.8246(4)	479.05(7)	160.06(2)	1.57(8)
7.54	7.8226(2)	478.70(4)	160.01(2)	1.59(8)
7.44	7.8211(2)	478.41(3)	159.97(2)	1.61(8)
7.67	7.8193(1)	478.09(3)	159.93(2)	1.63(9)
8.11	7.8180(1)	477.84(2)	159.90(2)	1.65(9)
7.48	7.8166(1)	477.58(2)	159.86(2)	1.67(9)
6.80	7.8152(1)	477.34(2)	159.83(2)	1.69(9)
6.78	7.8141(1)	477.14(2)	159.81(2)	1.70(9)
6.84	7.8125(1)	476.84(2)	159.78(2)	1.72(9)
6.63	7.8103(1)	476.44(2)	159.74(2)	1.74(9)
6.58	7.8076(1)	475.94(2)	159.69(2)	1.77(9)
6.97	7.8060(1)	475.66(2)	159.66(2)	1.79(9)
6.68	7.8037(1)	475.22(2)	159.61(2)	1.81(9)
6.76	7.8007(1)	474.68(2)	159.54(2)	1.86(9)
6.84	7.7989(1)	474.36(3)	159.50(3)	1.88(9)
6.90	7.7971(1)	474.03(3)	159.46(3)	1.90(9)
7.31	7.7953(2)	473.70(3)	159.43(3)	1.92(10)
7.67	7.7921(2)	473.11(3)	159.36(3)	1.96(10)
8.55	7.7891(2)	472.57(4)	159.30(3)	1.99(10)
8.17	7.7863(2)	472.06(3)	159.25(3)	2.02(10)
8.79	7.7836(2)	471.56(4)	159.19(4)	2.06(10)
9.13	7.7809(2)	471.07(4)	159.14(4)	2.08(10)
9.65	7.7787(2)	470.67(4)	159.11(5)	2.10(10)
9.31	7.7767(2)	470.31(4)	159.04(4)	2.14(10)
9.68	7.7750(2)	470.00(4)	159.03(5)	2.15(10)
9.81	7.7731(2)	469.65(4)	158.97(4)	2.18(10)
9.70	7.7712(2)	469.31(4)	158.96(5)	2.19(11)
10.15	7.7695(2)	469.01(4)	158.90(4)	2.22(11)
9.94	7.7664(2)	468.45(4)	158.88(5)	2.24(11)

R_{wp} (%)	Sample lattice constant, a (Å)	Sample unit cell volume, V (Å^3)	CaF_2 unit cell volume, V (Å^3)	Pressure (GPa)
10.56	7.7635(3)	467.92(7)	158.81(5)	2.28(11)
11.14	7.7607(3)	467.42(7)	158.76(5)	2.30(11)
11.57	7.7575(3)	466.84(6)	158.71(6)	2.34(11)
10.37	7.7540(3)	466.20(7)	158.64(5)	2.37(11)
11.34	7.7507(3)	465.60(7)	158.57(5)	2.42(11)

Table A.12: Weighted profile R factor, unit cell constant for the $Mg_{0.5}Zr_{1.5}F_7$ sample, unit cell volumes for both the sample and the CaF_2 pressure marker, and the pressure estimated from the CaF_2 assuming a unit cell volume for CaF_2 at zero pressure of 163.03 Å^3.

R_{wp} (%)	Sample lattice constant, a (Å)	Sample unit cell volume, V (Å^3)	CaF_2 unit cell volume, V (Å^3)	Pressure (GPa)
4.39	7.8897(6)	491.11(7)	161.93(4)	0.56(6)
4.37	7.8897(2)	491.11(4)	161.93(4)	0.56(6)
4.41	7.8890(2)	490.98(4)	161.93(4)	0.56(6)
4.46	7.8890(2)	490.98(4)	161.93(4)	0.56(6)
4.45	7.8890(2)	490.98(4)	161.93(4)	0.56(6)
4.53	7.8890(2)	490.99(5)	161.93(4)	0.56(6)
4.69	7.8890(3)	490.99(5)	161.93(4)	0.56(6)
4.61	7.8890(2)	490.97(4)	161.92(4)	0.56(6)
4.72	7.8888(3)	490.95(5)	161.91(4)	0.57(6)
4.75	7.8885(3)	490.89(5)	161.91(4)	0.57(6)
4.65	7.8881(2)	490.81(5)	161.90(4)	0.57(6)
4.69	7.8878(3)	490.77(5)	161.90(4)	0.58(6)
4.85	7.8878(3)	490.75(5)	161.89(4)	0.58(6)
5.01	7.8876(3)	490.72(5)	161.89(4)	0.58(6)
5.03	7.8874(3)	490.69(5)	161.88(4)	0.58(6)
5.05	7.8872(3)	490.65(5)	161.87(4)	0.59(6)
5.16	7.8871(3)	490.63(5)	161.86(4)	0.60(6)
5.32	7.8870(3)	490.61(6)	161.84(4)	0.60(6)
5.48	7.8868(3)	490.57(6)	161.82(5)	0.61(6)
5.50	7.8864(3)	490.50(6)	161.80(5)	0.63(6)
5.89	7.8862(4)	490.46(7)	161.76(6)	0.65(7)
6.30	7.8858(4)	490.38(7)	161.75(4)	0.65(6)
6.64	7.8850(4)	490.24(8)	161.70(4)	0.68(6)

R_{wp} (%)	Sample lattice constant, a (Å)	Sample unit cell volume, V (Å^3)	CaF_2 unit cell volume, V (Å^3)	Pressure (GPa)
5.04	7.8840(3)	490.05(5)	161.67(4)	0.69(6)
5.03	7.8830(3)	489.86(6)	161.64(4)	0.71(6)
5.16	7.8820(3)	489.68(6)	161.57(4)	0.74(6)
5.14	7.8811(3)	489.52(6)	161.49(7)	0.79(7)
5.03	7.8796(3)	489.23(6)	161.43(7)	0.82(7)
7.01	7.8783(5)	488.99(7)	161.37(8)	0.85(8)
7.05	7.8770(5)	488.74(7)	161.32(8)	0.88(8)
7.47	7.8758(6)	488.52(7)	161.26(7)	0.91(8)
7.36	7.8746(6)	488.29(7)	161.21(8)	0.94(8)
7.73	7.8730(6)	488.00(7)	161.16(7)	0.96(7)
7.28	7.8715(5)	487.71(7)	161.13(6)	0.98(7)
7.00	7.8702(5)	487.48(7)	161.08(5)	1.01(7)
6.54	7.8691(5)	487.27(7)	161.03(5)	1.03(7)
6.32	7.8678(4)	487.03(8)	160.98(5)	1.06(7)
6.05	7.8664(4)	486.77(8)	160.88(5)	1.11(7)
6.77	7.8649(4)	486.50(7)	160.79(5)	1.16(7)
5.93	7.8622(4)	486.00(7)	160.73(5)	1.19(8)
5.87	7.8598(4)	485.55(7)	160.70(5)	1.21(8)
5.77	7.8585(4)	485.31(7)	160.68(5)	1.22(8)
6.03	7.8578(4)	485.18(7)	160.65(5)	1.24(8)
5.79	7.8571(4)	485.05(7)	160.62(5)	1.25(8)
5.78	7.8564(4)	484.93(7)	160.60(5)	1.26(8)
6.06	7.8558(4)	484.81(7)	160.58(5)	1.27(8)
6.01	7.8553(4)	484.71(7)	160.56(5)	1.29(8)
6.00	7.8548(4)	484.62(7)	160.55(5)	1.30(8)
6.00	7.8543(4)	484.54(7)	160.52(5)	1.31(8)
6.00	7.8538(4)	484.44(7)	160.50(6)	1.32(8)
6.14	7.8532(4)	484.33(8)	160.49(5)	1.32(8)
6.24	7.8526(4)	484.22(8)	160.48(5)	1.33(8)
6.04	7.8522(4)	484.13(7)	160.46(5)	1.34(8)
6.12	7.8518(4)	484.07(8)	160.44(6)	1.35(8)
6.08	7.8512(4)	483.96(8)	160.42(6)	1.37(8)
6.31	7.8506(4)	483.84(8)	160.39(6)	1.38(8)
6.32	7.8499(4)	483.72(8)	160.37(6)	1.39(8)
6.41	7.8491(5)	483.57(8)	160.35(6)	1.40(8)
6.34	7.8484(4)	483.43(8)	160.33(6)	1.41(8)
6.35	7.8477(4)	483.31(8)	160.31(6)	1.43(9)
6.49	7.8471(5)	483.20(7)	160.28(7)	1.44(9)
6.49	7.8463(5)	483.05(7)	160.26(7)	1.45(9)
6.77	7.8454(5)	482.89(7)	160.24(7)	1.47(9)

R_{wp} (%)	Sample lattice constant, a (Å)	Sample unit cell volume, V (Å^3)	CaF_2 unit cell volume, V (Å^3)	Pressure (GPa)
6.73	7.8446(5)	482.74(7)	160.22(6)	1.47(9)
6.63	7.8438(5)	482.60(7)	160.18(7)	1.49(9)
7.26	7.8431(5)	482.46(7)	160.16(7)	1.51(9)
6.67	7.8421(5)	482.29(7)	160.13(8)	1.52(9)
6.53	7.8411(5)	482.10(7)	160.12(7)	1.53(9)
6.83	7.8404(5)	481.96(7)	160.10(8)	1.54(9)
6.41	7.8398(5)	481.85(7)	160.08(8)	1.55(9)
6.54	7.8393(5)	481.76(1)	160.05(6)	1.57(9)
6.52	7.8385(5)	481.62(1)	160.02(6)	1.58(9)
6.39	7.8373(5)	481.39(1)	160.00(6)	1.59(9)
6.69	7.8362(5)	481.18(1)	159.98(6)	1.61(9)
6.90	7.8353(6)	481.02(1)	159.94(6)	1.63(9)
8.03	7.8338(6)	480.74(1)	159.89(7)	1.66(7)
5.51	7.8337(4)	480.73(1)	159.89(6)	1.66(9)
7.45	7.8332(7)	480.63(1)	159.87(6)	1.67(9)
8.48	7.8316(6)	480.34(1)	159.85(6)	1.68(9)
10.05	7.8308(6)	480.19(1)	159.83(6)	1.69(9)
8.21	7.8302(6)	480.08(1)	159.80(6)	1.71(9)
8.25	7.8291(6)	479.88(1)	159.79(7)	1.71(10)
7.84	7.8284(6)	479.75(1)	159.78(6)	1.72(9)
7.92	7.8279(6)	479.65(1)	159.76(6)	1.73(9)
7.30	7.8273(6)	479.54(1)	159.75(7)	1.74(10)
6.46	7.8271(5)	479.52(1)	159.73(7)	1.75(10)
7.04	7.8262(5)	479.36(1)	159.71(7)	1.76(10)
6.30	7.8256(5)	479.25(1)	159.68(6)	1.78(10)
6.73	7.8246(5)	479.05(1)	159.65(6)	1.79(10)
6.14	7.8237(4)	478.89(1)	159.63(6)	1.80(10)
5.76	7.8226(4)	478.70(1)	159.62(5)	1.81(10)
5.65	7.8217(4)	478.53(1)	159.59(5)	1.83(10)
6.01	7.8209(4)	478.38(1)	159.56(6)	1.85(10)
6.08	7.8195(4)	478.12(1)	159.53(6)	1.86(10)
6.13	7.8181(4)	477.85(1)	159.50(8)	1.88(10)
6.24	7.8169(4)	477.65(1)	159.49(7)	1.89(10)
6.63	7.8162(4)	477.51(1)	159.47(7)	1.90(10)
6.60	7.8153(4)	477.35(1)	159.44(8)	1.91(10)
6.68	7.8143(4)	477.17(1)	159.42(8)	1.93(10)
6.66	7.8132(4)	476.97(1)	159.40(7)	1.94(10)
6.87	7.8122(5)	476.78(1)	159.37(7)	1.95(10)
6.87	7.8113(4)	476.62(1)	159.36(7)	1.96(10)
6.91	7.8105(4)	476.48(1)	159.33(7)	1.98(10)

R_{wp} (%)	Sample lattice constant, a (Å)	Sample unit cell volume, V (Å^3)	CaF_2 unit cell volume, V (Å^3)	Pressure (GPa)
6.90	7.8096(4)	476.30(1)	159.31(7)	1.99(10)
7.00	7.8085(4)	476.10(1)	159.28(7)	2.00(10)
7.07	7.8076(4)	475.94(1)	159.27(7)	2.01(11)
7.11	7.8069(4)	475.81(1)	159.26(7)	2.02(11)
7.43	7.8062(5)	475.69(1)	159.23(8)	2.03(11)
7.38	7.8052(5)	475.50(1)	159.21(7)	2.04(11)
7.53	7.8044(5)	475.36(1)	159.18(7)	2.06(11)
7.46	7.8030(5)	475.11(1)	159.15(7)	2.08(11)
7.66	7.8018(5)	474.88(1)	159.11(7)	2.10(11)
9.02	7.8007(6)	474.68(1)	159.09(7)	2.12(11)
8.75	7.7995(6)	474.47(1)	159.06(7)	2.13(11)
8.55	7.7988(5)	474.33(1)	159.03(7)	2.15(11)
8.77	7.7976(6)	474.11(1)	158.99(7)	2.17(11)
8.85	7.7965(5)	473.91(1)	158.94(7)	2.20(12)
8.35	7.7939(5)	473.44(1)	158.89(7)	2.23(12)
8.38	7.7917(5)	473.03(1)	158.87(7)	2.24(12)
8.51	7.7902(6)	472.77(1)	158.83(8)	2.26(12)
8.59	7.7889(5)	472.52(1)	158.82(8)	2.27(12)
8.67	7.7879(5)	472.34(1)	158.79(8)	2.29(12)
8.79	7.7869(5)	472.16(1)	158.77(8)	2.30(12)
8.86	7.7860(6)	472.00(1)	158.76(8)	2.31(12)
8.90	7.7853(6)	471.88(1)	158.74(8)	2.32(12)
8.85	7.7846(6)	471.75(1)	158.71(8)	2.33(12)
8.73	7.7838(6)	471.59(1)	158.68(8)	2.35(12)
9.11	7.7825(6)	471.36(1)	158.64(7)	2.38(12)
9.35	7.7809(7)	471.08(1)	158.61(8)	2.40(12)
9.46	7.7790(7)	470.73(1)	158.57(8)	2.42(12)
9.27	7.7774(7)	470.43(1)	158.54(8)	2.43(12)
9.54	7.7761(7)	470.20(1)	158.53(8)	2.44(12)
10.33	7.7748(7)	469.97(1)	158.48(8)	2.47(12)
9.95	7.7737(7)	469.76(1)	158.45(8)	2.49(12)
10.02	7.7713(7)	469.33(1)	158.42(8)	2.50(12)
10.14	7.7698(7)	469.05(1)	158.40(8)	2.52(12)
10.12	7.7687(7)	468.85(1)	158.37(7)	2.53(12)
10.21	7.7673(7)	468.62(1)	158.35(7)	2.55(13)
10.50	7.7645(6)	468.10(1)	158.32(8)	2.57(13)
11.00	7.7623(6)	467.71(1)	158.30(7)	2.58(13)
10.33	7.7608(6)	467.43(1)	158.28(7)	2.59(13)
10.32	7.7596(6)	467.22(1)	158.25(7)	2.61(13)
10.39	7.7585(6)	467.02(1)	158.23(7)	2.62(13)

R_{wp} (%)	Sample lattice constant, a (Å)	Sample unit cell volume, V (Å^3)	CaF_2 unit cell volume, V (Å^3)	Pressure (GPa)
10.31	7.7576(6)	466.86(1)	158.20(7)	2.64(13)
10.47	7.7566(6)	466.68(1)	158.15(7)	2.67(13)
11.10	7.7551(7)	466.40(1)	158.13(7)	2.68(13)
12.32	7.7534(7)	466.10(1)	158.12(7)	2.69(13)
11.88	7.7522(7)	465.89(1)	158.09(7)	2.70(13)
11.96	7.7508(7)	465.64(1)	158.06(7)	2.72(13)
12.23	7.7490(7)	465.31(1)	158.04(7)	2.73(13)
12.57	7.7477(7)	465.06(1)	157.98(8)	2.77(13)
12.77	7.7462(7)	464.80(1)	157.95(7)	2.79(13)
13.28	7.7444(7)	464.48(1)	157.91(7)	2.81(13)
12.69	7.7419(7)	464.03(1)	157.87(7)	2.83(13)
12.71	7.7408(7)	463.82(1)	157.85(8)	2.85(13)
13.01	7.7398(7)	463.64(1)	157.83(8)	2.86(13)
13.14	7.7389(7)	463.49(1)	157.81(8)	2.87(13)
13.40	7.7382(8)	463.36(1)	157.79(8)	2.89(13)
13.42	7.7372(8)	463.18(1)	157.75(8)	2.91(13)
13.80	7.7360(8)	462.97(1)	157.71(7)	2.93(13)
14.53	7.7342(7)	462.65(2)	157.67(8)	2.96(14)
14.53	7.7308(7)	462.04(1)	157.64(8)	2.97(14)
14.63	7.7292(8)	461.75(1)	157.60(8)	3.00(14)
14.64	7.7272(8)	461.39(1)	157.56(8)	3.03(14)
15.11	7.7251(8)	461.02(1)	157.53(8)	3.04(14)
14.82	7.7235(8)	460.73(1)	157.49(8)	3.07(14)
14.67	7.7212(7)	460.31(1)	157.45(8)	3.10(14)
14.78	7.7192(7)	459.96(1)	157.43(7)	3.11(14)
14.72	7.7177(7)	459.69(1)	157.33(7)	3.17(14)
14.99	7.7158(7)	459.34(1)	157.30(7)	3.19(14)
15.71	7.7113(8)	458.55(1)	157.25(7)	3.22(14)
18.29	7.7094(8)	458.20(1)	157.19(7)	3.25(14)
15.55	7.7069(8)	457.75(1)	157.14(7)	3.29(15)
15.80	7.7042(8)	457.29(2)	157.10(7)	3.31(15)
15.89	7.7017(7)	456.83(2)	157.00(7)	3.37(15)
16.08	7.6985(7)	456.27(2)	156.95(7)	3.41(15)
17.60	7.6948(7)	455.61(2)	156.91(7)	3.43(15)
17.30	7.6923(7)	455.16(2)	156.86(7)	3.46(15)
17.12	7.6904(7)	454.82(2)	156.78(6)	3.51(15)
17.25	7.6877(7)	454.34(2)	156.72(6)	3.55(15)
17.18	7.6837(7)	453.63(2)	156.67(6)	3.58(15)
17.01	7.6807(7)	453.11(2)	156.61(6)	3.62(15)
16.40	7.6781(7)	452.64(2)	156.54(6)	3.67(16)

R_{wp} (%)	Sample lattice constant, a (Å)	Sample unit cell volume, V (Å^3)	CaF_2 unit cell volume, V (Å^3)	Pressure (GPa)
16.99	7.6747(7)	452.04(2)	156.47(6)	3.71(16)
16.54	7.6713(7)	451.44(2)	156.40(6)	3.75(16)
16.66	7.6678(7)	450.83(2)	156.33(6)	3.80(16)
16.44	7.6644(7)	450.23(2)	156.25(6)	3.85(16)
16.27	7.6607(7)	449.57(2)	156.14(5)	3.92(16)
17.58	7.6568(7)	448.89(2)	156.05(6)	3.98(17)

Appendix B.**SUPPLEMENTARY MATERIAL FOR CHAPTER 3**

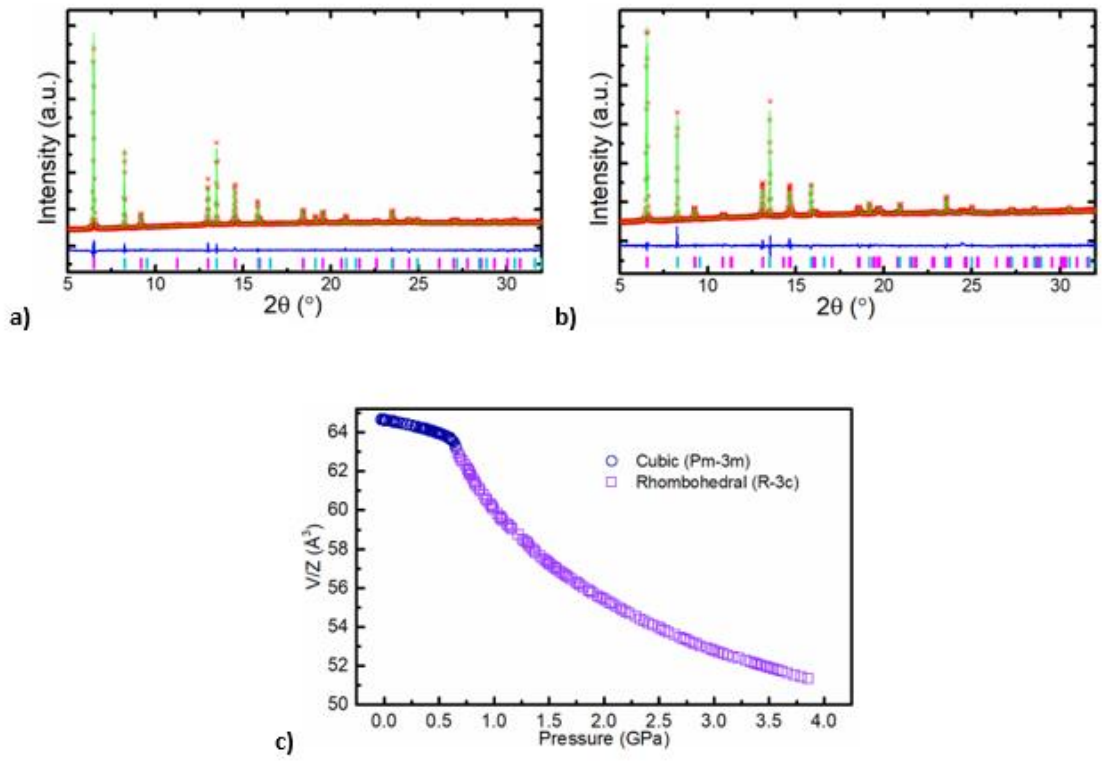

Figure B.1: Example Rietveld/LeBail fits to diffraction patterns for a) cubic (Pm-3m) and b) rhombohedral (R-3c, 0.69 GPa) ScF_3. Pink and cyan tic marks indicate the locations of the peaks for R-3c ScF_3 and CaF_2 phase respectively. c) V/Z for cubic and rhombohedral phases vs. pressure.

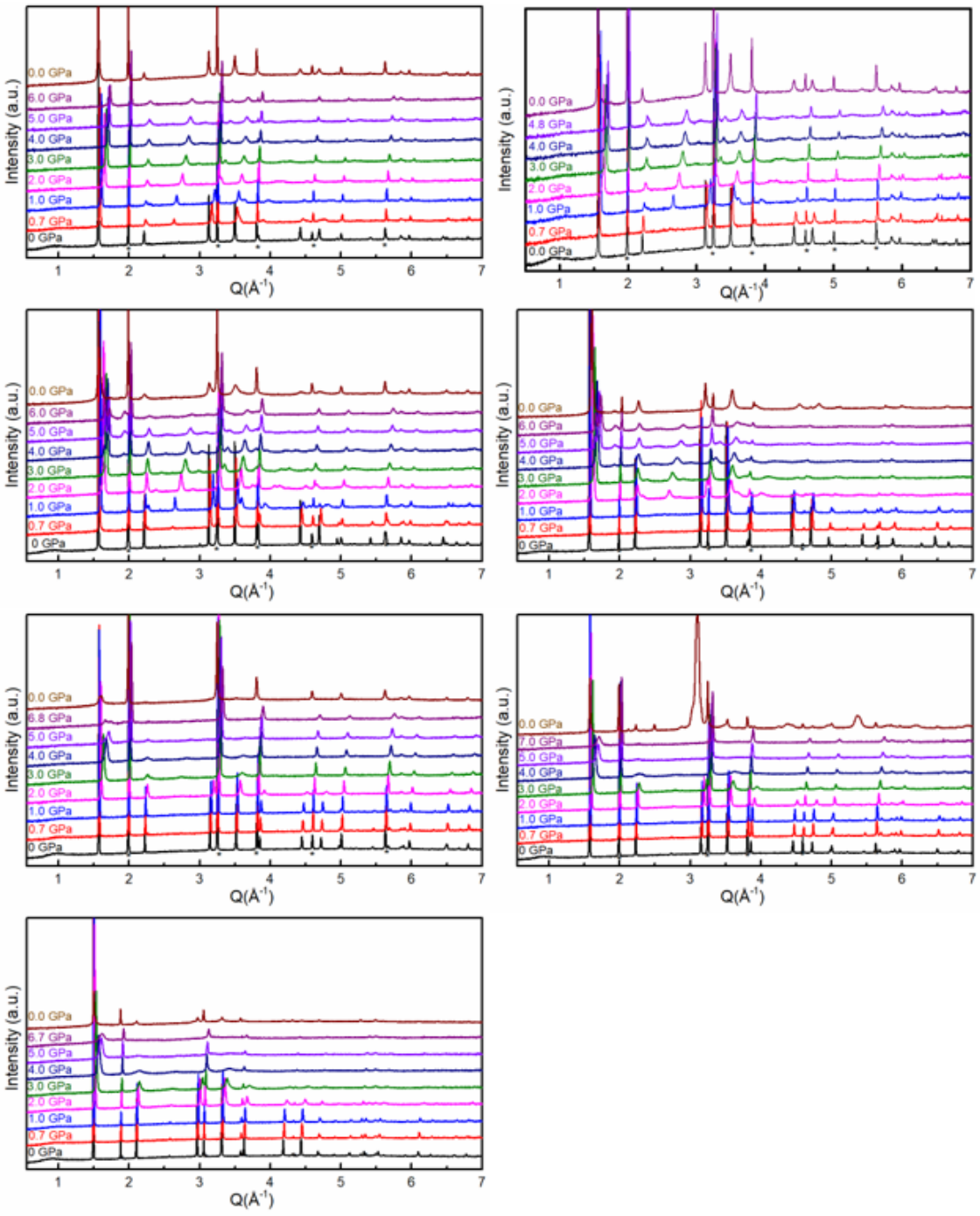

Figure B.2: Diffraction patterns at select pressures for the a) x = 0.0a, b) x = 0.0b, c) x = 0.1, d) x = 0.2, e) x = 0.3, f) x = 0.4 and g) x = 0.5 $Sc_{1-x}Zr_xF_{3+x}$ samples. In each panel, the data shown at the top is after complete decompression. Peaks marked with an astrisk are from the CaF2 pressure calibrant.

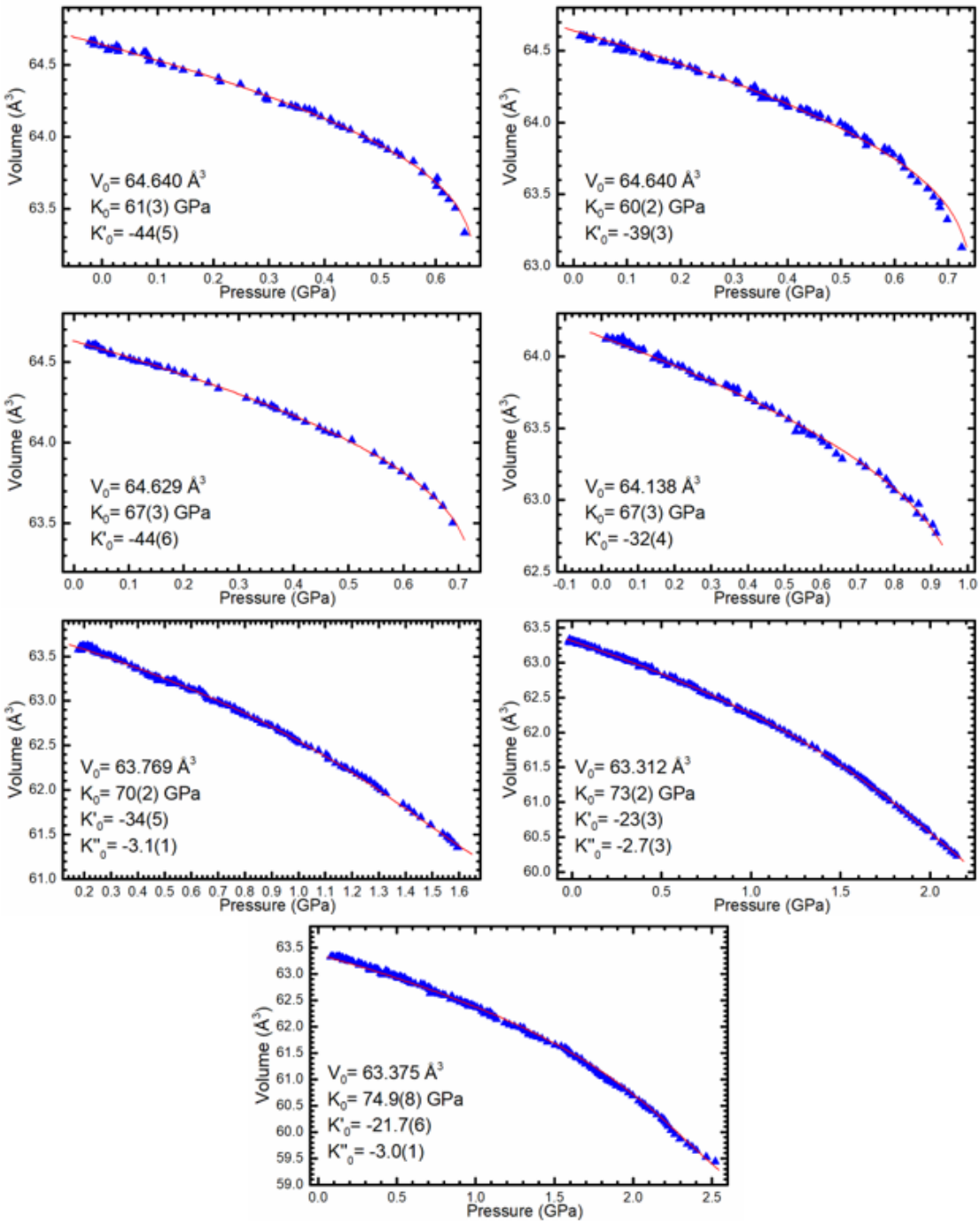

Figure B.3: Birch-Murnaghan equation of state fits to the cell volume for cubic $Sc_{1-x}Zr_xF_{3+x}$ vs. pressure. a) x = 0.0a, b) x = 0.0b, c) x = 0.1, d) x = 0.2, e) x = 0.3, f) x = 0.4 and g) x = 0.5.

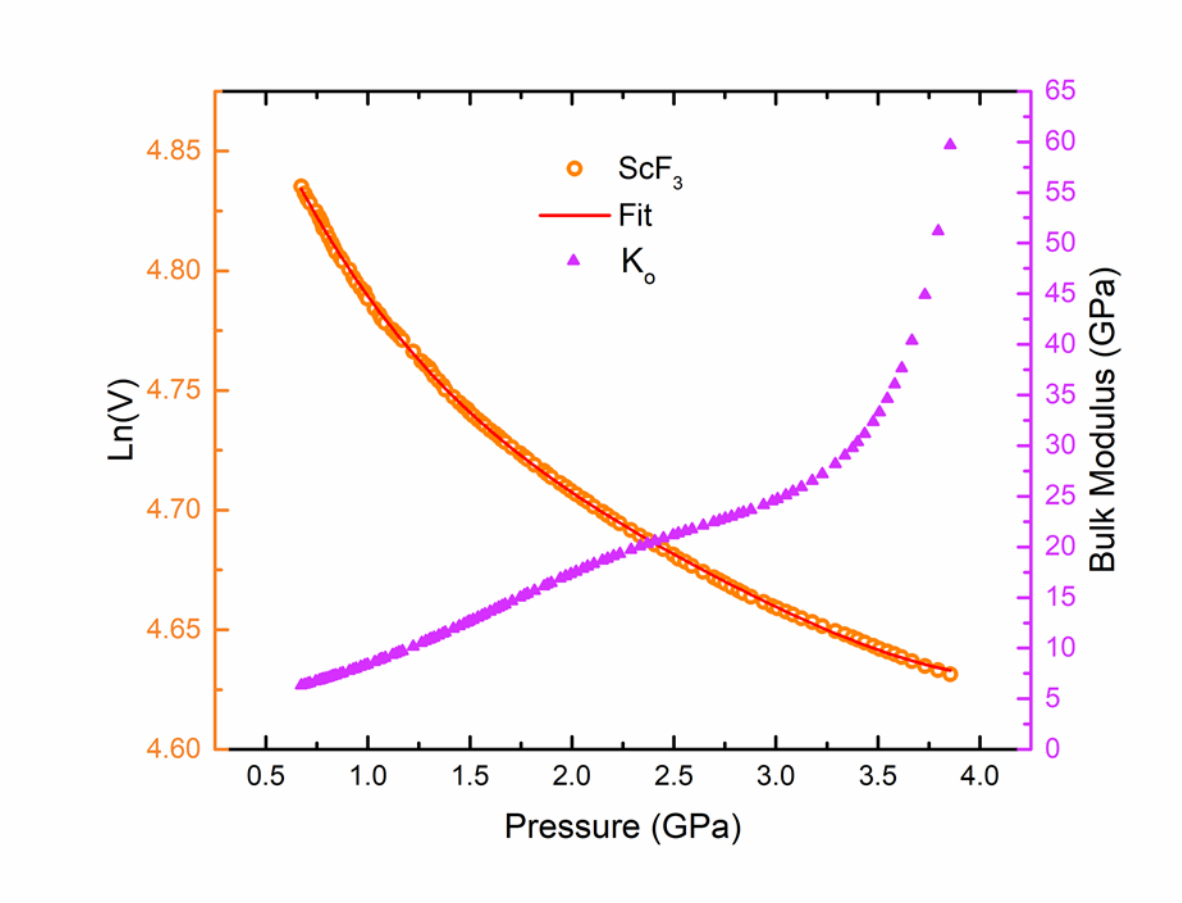

Figure B.4: 4th order polynomial fit to the Ln(V) vs. pressure data for rhombohedral ScF_3 and bulk moduli (violet) calculated from the derivative of this fit.

B.1 Supplementary Tables

Table B.1: Weighted profile R factors for both sample and pressure standard, lattice constant for the x=0.0a sample, unit cell volumes for both the sample and the CaF_2 pressure standard, and the pressure calculated from the CaF_2 using the decompression cell volume as V_0.

sample Rwp(%)	Sample lattice constant, a (Å)	sample unit cell volume, V (Å^3)	Rwp(%)	CaF2 cell volume, V (Å^3)	Pressure (GPa)
10.8	4.0139(2)	64.667(8)	3.35	163.40(3)	-0.01(5)
10.0	4.0139(2)	64.667(7)	3.27	163.40(3)	-0.01(5)
10.0	4.0138(2)	64.666(7)	3.2	163.40(3)	-0.02(5)
11.2	4.0138(2)	64.666(8)	3.32	163.41(3)	-0.02(5)
10.1	4.0138(2)	64.664(8)	3.17	163.41(3)	-0.02(5)
11.1	4.0138(2)	64.664(8)	3.34	163.40(3)	-0.01(5)
10.4	4.0138(2)	64.664(8)	3.18	163.40(3)	-0.02(5)
10.1	4.0134(2)	64.644(8)	3.18	163.40(2)	-0.01(5)
10.0	4.0132(2)	64.636(7)	3.12	163.37(2)	0.00(5)
10.4	4.0132(2)	64.635(7)	3.27	163.32(3)	0.03(5)
10.2	4.0129(2)	64.620(8)	3.37	163.31(2)	0.03(5)
10.3	4.0127(2)	64.614(8)	3.22	163.34(3)	0.01(5)
10.5	4.0127(2)	64.614(8)	3.23	163.33(3)	0.02(5)
9.7	4.0125(1)	64.604(7)	3.18	163.35(2)	0.01(5)
10.5	4.0124(2)	64.597(8)	3.2	163.31(3)	0.03(5)
10.2	4.0123(2)	64.591(8)	3.22	163.26(3)	0.05(5)
10.7	4.0123(2)	64.591(8)	3.24	163.26(2)	0.06(5)
10.8	4.0123(2)	64.591(8)	3.31	163.22(2)	0.08(5)
10.7	4.0123(2)	64.591(8)	3.67	163.21(2)	0.08(5)
10.1	4.0117(2)	64.561(8)	3.37	163.20(2)	0.08(5)
9.5	4.0113(1)	64.545(7)	3.25	163.20(2)	0.09(5)
9.8	4.0110(2)	64.531(7)	3.45	163.20(2)	0.08(5)
9.3	4.0109(1)	64.523(7)	3.35	163.16(3)	0.10(5)
8.7	4.0105(1)	64.506(6)	3.29	163.15(2)	0.11(5)
9.3	4.0102(1)	64.489(7)	3.26	163.11(2)	0.13(5)
9.7	4.0097(2)	64.465(7)	3.54	163.08(2)	0.15(5)
10.1	4.0092(2)	64.441(8)	3.29	163.02(2)	0.17(5)
10.4	4.0085(2)	64.410(8)	3.28	162.95(2)	0.21(5)
9.5	4.0080(1)	64.386(7)	3.41	162.94(2)	0.21(5)
10.3	4.0076(2)	64.367(7)	3.34	162.87(3)	0.25(5)
10.1	4.0065(2)	64.312(8)	3.31	162.81(2)	0.28(5)
10.3	4.0059(2)	64.284(8)	3.27	162.78(3)	0.30(5)
9.7	4.0056(1)	64.270(7)	3.41	162.78(2)	0.29(5)

sample Rwp(%)	Sample lattice constant, a (Å)	sample unit cell volume, V (Å^3)	Rwp(%)	CaF2 cell volume, V (Å^3)	Pressure (GPa)
10.6	4.0054(2)	64.259(9)	3.66	162.78(2)	0.30(5)
9.8	4.0048(1)	64.231(7)	3.52	162.72(2)	0.32(5)
9.8	4.0046(1)	64.219(7)	3.16	162.69(3)	0.34(5)
9.6	4.0044(1)	64.211(7)	3.16	162.68(3)	0.35(5)
9.1	4.0042(1)	64.202(7)	3.24	162.67(2)	0.35(5)
9.4	4.0041(1)	64.197(7)	3.32	162.64(3)	0.36(5)
8.8	4.0039(1)	64.190(6)	3.27	162.63(2)	0.37(5)
8.8	4.0037(1)	64.179(6)	3.3	162.61(2)	0.38(5)
8.3	4.0034(1)	64.162(6)	3.23	162.61(2)	0.38(5)
8.6	4.0029(1)	64.141(6)	3.24	162.59(2)	0.39(5)
8.4	4.0026(1)	64.125(6)	3.23	162.55(2)	0.41(6)
8.0	4.0022(1)	64.105(6)	3.21	162.55(2)	0.41(6)
11.1	4.0017(2)	64.080(9)	3.24	162.52(2)	0.43(6)
10.6	4.0014(2)	64.067(8)	3.38	162.51(2)	0.43(6)
10.7	4.0011(2)	64.051(8)	3.31	162.48(2)	0.45(6)
10.7	4.0002(2)	64.012(8)	3.33	162.44(2)	0.47(6)
10.8	3.9996(2)	63.980(8)	3.48	162.43(2)	0.48(6)
10.5	3.9993(2)	63.965(8)	3.4	162.40(2)	0.49(6)
10.1	3.9991(2)	63.956(8)	3.37	162.39(2)	0.50(6)
9.6	3.9987(1)	63.940(7)	3.32	162.37(2)	0.50(6)
10.9	3.9981(2)	63.910(9)	3.3	162.35(2)	0.51(6)
10.4	3.9978(2)	63.893(8)	3.46	162.32(2)	0.53(6)
11.3	3.9973(2)	63.87(10)	3.52	162.31(2)	0.54(6)
10.4	3.9965(2)	63.832(8)	3.48	162.26(2)	0.56(6)
11.1	3.9949(2)	63.754(9)	3.37	162.23(2)	0.58(6)
10.4	3.9941(2)	63.715(8)	3.32	162.18(2)	0.60(6)
10.5	3.9937(2)	63.696(9)	3.37	162.19(2)	0.60(6)
10.6	3.9928(2)	63.656(9)	3.45	162.18(2)	0.60(6)
10.2	3.9919(2)	63.613(9)	3.5	162.16(2)	0.61(6)
10.5	3.9910(2)	63.567(10)	3.49	162.14(2)	0.62(6)
9.8	3.9897(2)	63.5070(8)	3.49	162.12(2)	0.64(6)
10.0	3.9861(2)	63.334(10)	3.32	162.09(2)	0.65(6)
9.5	3.9827(2)	63.1720(9)	3.06	162.08(2)	0.65(6)

R-3c RWP (%)	a (Å) \ α (°)	sample unit cell volume, V (Å^3)	Rwp(%)	CaF2 cell volume, V (Å^3)	Pressure (GPa)
2.83	5.63(2) \ 59.81(3)	125.861(7)	2.86	162.01(2)	0.69(6)

R-3c RWP (%)	a (Å) \ α (°)	sample unit cell volume, V (Å^3)	Rwp(%)	CaF2 cell volume, V (Å^3)	Pressure (GPa)
3.13	5.63(2) \ 59.71(3)	125.487(8)	2.89	161.99(2)	0.70(6)
3.21	5.63(2) \ 59.64(3)	125.214(8)	2.93	161.96(2)	0.72(6)
3.00	5.63(1) \ 59.57(2)	125.010(8)	2.99	161.91(2)	0.74(6)
2.97	5.63(1) \ 59.48(2)	124.578(8)	3.10	161.88(2)	0.76(6)
3.52	5.63(2) \ 59.43(3)	124.259(5)	2.93	161.87(2)	0.77(6)
3.20	5.63(2) \ 59.40(2)	124.135(9)	2.96	161.85(2)	0.77(6)
3.24	5.62(2) \ 59.37(2)	124.032(9)	3.06	161.85(2)	0.78(6)
3.05	5.62(1) \ 59.32(2)	123.840(9)	3.10	161.84(2)	0.78(6)
2.91	5.62(1) \ 59.25(2)	123.673(8)	3.18	161.81(2)	0.80(6)
2.87	5.62(1) \ 59.24(2)	123.522(8)	3.43	161.79(2)	0.81(6)
2.83	5.62(1) \ 59.18(2)	123.198(8)	3.67	161.76(2)	0.82(6)
2.95	5.62(1) \ 59.13(2)	122.918(9)	3.85	161.74(2)	0.83(6)
2.95	5.62(1) \ 59.07(2)	122.704(9)	4.01	161.72(2)	0.84(6)
2.95	5.62(1) \ 59.02(2)	122.468(9)	4.22	161.68(2)	0.87(6)
2.99	5.61(1) \ 58.96(2)	122.175(9)	4.36	161.66(2)	0.88(6)
2.91	5.61(1) \ 58.91(2)	121.987(8)	4.31	161.60(2)	0.91(6)
3.02	5.61(2) \ 58.83(2)	121.561(9)	4.33	161.56(2)	0.93(7)
3.09	5.61(2) \ 58.74(2)	121.163(9)	4.30	161.54(2)	0.94(7)
3.36	5.61(2) \ 58.68(3)	120.937(10)	4.42	161.49(2)	0.96(7)
2.96	5.61(2) \ 58.60(2)	120.638(9)	4.50	161.46(2)	0.98(7)
3.22	5.61(2) \ 58.56(3)	120.455(10)	4.34	161.45(2)	0.99(7)
3.13	5.61(2) \ 58.52(3)	120.316(10)	4.32	161.43(2)	1.00(7)
3.11	5.60(2) \ 58.47(3)	120.092(10)	4.28	161.36(2)	1.03(7)
3.22	5.60(2) \ 58.29(3)	119.597(10)	4.25	161.32(2)	1.06(7)
3.23	5.60(2) \ 58.22(3)	119.311(10)	4.37	161.31(2)	1.06(7)
3.36	5.60(2) \ 58.19(3)	119.193(11)	4.32	161.30(2)	1.07(7)
3.54	5.60(2) \ 58.13(3)	119.071(11)	4.19	161.27(2)	1.09(7)
3.20	5.60(2) \ 58.10(3)	118.886(10)	4.05	161.20(2)	1.12(7)
3.06	5.60(2) \ 58.00(3)	118.560(10)	3.93	161.17(2)	1.14(7)
3.00	5.60(2) \ 57.95(3)	118.394(10)	3.90	161.14(2)	1.15(7)
2.95	5.60(2) \ 57.90(3)	118.221(10)	3.86	161.11(2)	1.17(7)
2.93	5.60(2) \ 57.86(3)	118.043(10)	3.70	161.01(2)	1.22(7)
2.92	5.60(2) \ 57.72(3)	117.467(10)	3.58	160.94(2)	1.26(7)
2.85	5.60(2) \ 57.59(3)	116.993(10)	3.52	160.90(2)	1.28(7)
2.87	5.59(2) \ 57.54(3)	116.810(10)	3.49	160.87(2)	1.30(8)
2.90	5.59(2) \ 57.50(3)	116.670(10)	3.42	160.85(2)	1.31(8)
3.02	5.59(2) \ 57.45(3)	116.532(11)	3.39	160.83(2)	1.32(8)
3.07	5.59(2) \ 57.38(3)	116.272(11)	3.34	160.78(2)	1.35(8)
3.45	5.59(3) \ 57.32(4)	116.048(13)	3.28	160.75(2)	1.37(8)

R-3c RWP (%)	a (Å) \ α (°)	sample unit cell volume, V (Å^3)	Rwp(%)	CaF2 cell volume, V (Å^3)	Pressure (GPa)
3.32	5.59(3) \ 57.25(4)	115.829(12)	3.26	160.73(2)	1.38(8)
3.39	5.59(3) \ 57.19(4)	115.627(12)	3.03	160.65(2)	1.42(8)
3.49	5.59(3) \ 57.07(4)	115.267(13)	3.02	160.60(2)	1.45(8)
3.54	5.59(3) \ 56.99(4)	115.004(14)	2.99	160.56(2)	1.47(8)
3.82	5.59(4) \ 56.94(5)	114.808(15)	2.96	160.53(2)	1.49(8)
3.31	5.59(3) \ 56.89(4)	114.665(13)	2.87	160.51(2)	1.50(8)
3.56	5.59(2) \ 56.84(3)	114.524(13)	2.81	160.48(2)	1.52(8)
3.57	5.59(2) \ 56.80(3)	114.373(13)	2.73	160.44(2)	1.54(8)
3.47	5.59(2) \ 56.75(3)	114.177(13)	2.68	160.40(2)	1.56(8)
3.42	5.59(2) \ 56.72(3)	114.022(13)	2.70	160.38(2)	1.57(8)
3.52	5.59(2) \ 56.68(3)	113.906(13)	2.70	160.33(2)	1.60(8)
3.43	5.59(2) \ 56.62(3)	113.685(13)	2.75	160.28(2)	1.62(8)
3.44	5.59(2) \ 56.58(3)	113.516(13)	2.74	160.25(2)	1.64(9)
3.36	5.59(2) \ 56.53(3)	113.370(13)	2.68	160.22(2)	1.66(9)
3.36	5.59(2) \ 56.50(3)	113.237(13)	2.71	160.20(2)	1.67(9)
3.27	5.59(2) \ 56.46(3)	113.116(12)	2.76	160.14(2)	1.71(9)
3.21	5.58(2) \ 56.40(3)	112.861(12)	2.79	160.06(2)	1.75(9)
3.20	5.58(2) \ 56.31(3)	112.584(13)	2.81	160.03(2)	1.77(9)
3.21	5.58(2) \ 56.27(3)	112.428(13)	2.85	160.00(2)	1.78(9)
3.18	5.58(2) \ 56.24(3)	112.306(12)	2.91	159.94(2)	1.82(9)
3.15	5.58(2) \ 56.18(3)	112.044(12)	2.94	159.86(2)	1.86(9)
3.12	5.58(2) \ 56.10(3)	111.765(12)	2.96	159.83(2)	1.88(9)
3.07	5.58(2) \ 56.05(3)	111.633(12)	2.98	159.80(2)	1.90(9)
3.12	5.58(2) \ 56.00(3)	111.476(13)	3.02	159.72(2)	1.94(9)
3.07	5.58(2) \ 55.94(3)	111.189(13)	3.08	159.67(2)	1.97(7)
3.10	5.58(2) \ 55.88(3)	111.018(13)	3.09	159.63(2)	1.99(7)
3.05	5.58(2) \ 55.82(3)	110.854(13)	3.11	159.58(2)	2.02(7)
2.96	5.58(2) \ 55.79(3)	110.675(12)	3.10	159.52(2)	2.05(7)
2.91	5.58(2) \ 55.73(3)	110.474(12)	3.10	159.48(2)	2.08(7)
2.86	5.58(2) \ 55.69(3)	110.328(12)	3.11	159.43(2)	2.11(7)
2.85	5.58(2) \ 55.63(3)	110.110(12)	3.13	159.36(2)	2.15(7)
2.79	5.57(2) \ 55.55(3)	109.868(12)	3.14	159.32(2)	2.17(7)
3.00	5.57(2) \ 55.51(3)	109.718(13)	3.16	159.26(2)	2.20(7)
2.90	5.57(2) \ 55.46(3)	109.527(12)	3.22	159.21(2)	2.23(7)
2.94	5.57(2) \ 55.41(3)	109.336(13)	3.26	159.12(2)	2.29(7)
3.01	5.57(3) \ 55.30(3)	109.038(13)	3.35	159.04(2)	2.33(7)
2.89	5.57(2) \ 55.23(3)	108.777(13)	3.37	158.98(2)	2.37(7)
3.24	5.57(3) \ 55.17(4)	108.577(15)	3.46	158.92(2)	2.41(7)

R-3c RWP (%)	a (Å) \ α (°)	sample unit cell volume, V (Å^3)	Rwp(%)	CaF2 cell volume, V (Å^3)	Pressure (GPa)
3.25	5.57(3) \ 55.09(4)	108.377(15)	3.54	158.85(2)	2.45(7)
3.36	5.57(3) \ 55.01(4)	108.165(15)	3.56	158.77(2)	2.50(7)
3.18	5.57(3) \ 54.93(4)	107.914(15)	3.61	158.72(2)	2.52(7)
3.64	5.57(2) \ 54.88(3)	107.741(14)	3.64	158.67(2)	2.56(7)
3.25	5.57(3) \ 54.84(3)	107.596(15)	3.64	158.61(2)	2.59(7)
3.30	5.57(3) \ 54.79(3)	107.422(15)	3.66	158.52(2)	2.64(7)
3.24	5.57(2) \ 54.72(3)	107.155(15)	3.62	158.43(2)	2.70(7)
3.01	5.57(3) \ 54.67(3)	106.905(14)	3.67	158.39(2)	2.72(7)
3.25	5.57(3) \ 54.62(3)	106.767(15)	3.64	158.34(2)	2.75(7)
3.07	5.57(2) \ 54.58(3)	106.631(15)	3.61	158.29(2)	2.78(7)
3.06	5.57(3) \ 54.52(3)	106.473(14)	3.69	158.23(2)	2.82(7)
3.58	5.57(3) \ 54.49(4)	106.314(17)	3.63	158.19(2)	2.84(7)
3.03	5.57(3) \ 54.45(4)	106.209(15)	3.66	158.13(2)	2.88(7)
3.11	5.57(3) \ 54.38(3)	106.029(15)	3.59	158.03(2)	2.94(7)
3.06	5.57(3) \ 54.31(4)	105.798(15)	3.65	157.96(2)	2.98(7)
3.35	5.57(3) \ 54.29(4)	105.629(16)	3.64	157.92(2)	3.01(7)
3.38	5.57(3) \ 54.26(4)	105.532(16)	3.64	157.85(2)	3.05(7)
3.40	5.57(3) \ 54.18(4)	105.379(17)	3.63	157.79(2)	3.08(7)
3.37	5.57(3) \ 54.15(4)	105.240(17)	3.66	157.73(2)	3.13(7)
3.34	5.56(3) \ 54.10(4)	105.081(17)	3.63	157.64(2)	3.18(7)
3.38	5.56(3) \ 54.07(4)	104.914(17)	3.60	157.56(2)	3.23(7)
3.29	5.56(3) \ 54.00(4)	104.741(16)	3.58	157.46(2)	3.29(7)
3.57	5.56(3) \ 53.93(3)	104.523(15)	3.59	157.38(2)	3.34(7)
3.25	5.56(3) \ 53.88(4)	104.386(16)	3.57	157.32(2)	3.38(7)
3.18	5.56(3) \ 53.86(4)	104.249(16)	3.55	157.28(2)	3.40(7)
3.75	5.56(3) \ 53.85(4)	104.150(19)	3.58	157.23(2)	3.44(7)
3.65	5.56(3) \ 53.82(4)	104.021(18)	3.54	157.16(2)	3.48(7)
3.59	5.56(3) \ 53.78(4)	103.875(18)	3.57	157.11(2)	3.51(7)
3.66	5.56(3) \ 53.75(4)	103.755(19)	3.53	157.05(2)	3.55(7)
3.67	5.56(3) \ 53.70(4)	103.633(19)	3.56	157.00(2)	3.58(7)
3.56	5.56(3) \ 53.69(4)	103.519(18)	3.56	156.94(2)	3.62(7)
3.63	5.56(3) \ 53.64(4)	103.396(19)	3.59	156.86(2)	3.67(7)
3.61	5.56(3) \ 53.61(4)	103.216(19)	3.58	156.76(2)	3.73(7)
3.64	5.56(3) \ 53.51(4)	103.015(19)	3.56	156.66(2)	3.79(7)
3.60	5.56(3) \ 53.44(4)	102.833(19)	3.61	156.57(2)	3.85(7)
3.68	5.56(3) \ 53.42(4)	102.660(19)	3.59	156.42(2)	3.95(7)
			3.6	156.26(2)	4.05(7)
			3.6	156.12(2)	4.15(7)
			3.6	156.00(2)	4.23(7)

R-3c RWP (%)	a (Å) \ α (°)	sample unit cell volume, V (Å^3)	Rwp(%)	CaF2 cell volume, V (Å^3)	Pressure (GPa)
			3.61	155.92(2)	4.28(7)
			3.59	155.85(2)	4.32(7)
			3.62	155.79(2)	4.37(7)
			3.62	155.72(2)	4.41(7)
			3.57	155.64(3)	4.46(7)
			3.55	155.56(3)	4.52(7)
			3.55	155.48(3)	4.57(7)
			3.56	155.43(2)	4.61(7)
			3.62	155.35(3)	4.66(7)
			3.58	155.26(2)	4.72(7)
			3.55	155.18(2)	4.78(7)
			3.52	155.07(2)	4.85(7)
			3.47	154.96(2)	4.93(7)
			3.48	154.84(2)	5.01(7)
			3.46	154.69(2)	5.12(7)
			3.48	154.49(2)	5.25(7)
			3.44	154.34(2)	5.36(7)
			3.29	154.16(2)	5.49(7)
			3.19	153.99(2)	5.61(7)
			3.17	153.86(2)	5.70(7)
			3.07	153.72(2)	5.80(7)
			3.09	153.64(2)	5.86(7)
			3.09	153.58(2)	5.91(7)
			3.07	153.51(2)	5.96(7)
			3.01	153.43(2)	6.02(7)
			3.02	153.36(2)	6.07(7)
			3.01	153.29(2)	6.12(7)
			2.99	153.24(2)	6.15(7)
			2.95	153.20(2)	6.19(7)
			2.96	153.16(2)	6.21(7)
			2.96	153.14(2)	6.23(7)
			2.93	153.12(2)	6.24(7)
			2.91	153.11(2)	6.25(7)
			2.94	153.12(2)	6.25(7)
			2.94	153.12(2)	6.24(7)
			2.9	153.14(2)	6.23(7)
			2.94	153.17(2)	6.20(7)
			2.95	153.24(2)	6.16(7)
			2.90	153.32(2)	6.10(7)

R-3c RWP (%)	a (Å) \ α (°)	sample unit cell volume, V (Å^3)	Rwp(%)	CaF2 cell volume, V (Å^3)	Pressure (GPa)
			2.93	153.41(2)	6.03(7)
			2.97	153.52(2)	5.95(7)
			2.92	153.63(2)	5.87(7)
			2.92	153.76(1)	5.78(7)
			2.96	153.89(1)	5.68(7)
			2.96	154.05(1)	5.57(7)
			2.95	154.23(1)	5.44(7)
			2.99	154.44(1)	5.29(7)
			3.06	154.70(1)	5.11(7)
			3.08	155.03(1)	4.88(7)
			3.12	155.42(1)	4.61(7)
			3.23	155.87(1)	4.31(7)
			3.22	156.23(1)	4.08(7)
			3.22	156.29(1)	4.04(7)
			3.19	156.32(1)	4.02(7)
			3.23	156.33(1)	4.01(7)
			3.24	156.35(1)	4.00(7)
			3.20	156.36(1)	3.99(7)
			3.24	156.36(1)	3.99(7)

Table B.2: Weighted profile R factors for both sample and pressure standard, lattice constant for the x=0.0b sample, unit cell volumes for both the sample and the CaF_2 pressure standard, and the pressure calculated from the CaF_2 using the decompression cell volume as V_0.

sample Rwp(%)	Sample lattice constant, a (Å)	sample unit cell volume, V (Å^3)	CaF_2 Rwp(%)	CaF2 cell volume, V (Å^3)	Pressure (GPa)
9.3	4.0125(2)	64.60(1)	9.1	163.26(1)	0.00(7)
9.4	4.0125(2)	64.60(1)	7.8	163.30(2)	0.00(5)
9.4	4.0125(2)	64.60(1)	7.7	163.30(2)	0.00(5)
9.3	4.0125(2)	64.60(1)	7.6	163.30(2)	0.00(5)
9.3	4.0125(2)	64.60(1)	7.6	163.30(2)	0.00(5)
9.0	4.0125(2)	64.60(1)	7.6	163.29(2)	0.00(5)
8.6	4.0125(2)	64.60(1)	7.5	163.29(2)	0.00(5)
8.9	4.0125(2)	64.60(1)	7.4	163.27(2)	0.02(5)
8.2	4.0125(2)	64.60(1)	7.5	163.27(2)	0.01(5)
8.4	4.0125(2)	64.60(1)	7.5	163.25(2)	0.02(5)
8.3	4.0125(2)	64.60(1)	7.5	163.27(2)	0.02(5)
8.0	4.0124(2)	64.60(1)	7.5	163.24(2)	0.03(5)
8.6	4.0123(2)	64.59(1)	7.5	163.24(2)	0.03(5)
8.9	4.0120(2)	64.58(1)	7.5	163.22(2)	0.04(5)
8.5	4.0117(2)	64.56(1)	7.6	163.23(2)	0.03(5)
8.9	4.0116(2)	64.56(1)	7.6	163.18(2)	0.06(5)
9.0	4.0115(2)	64.55(1)	7.6	163.18(2)	0.06(5)
9.1	4.0113(2)	64.54(1)	7.6	163.14(2)	0.08(5)
9.2	4.0111(2)	64.53(1)	7.5	163.12(2)	0.09(5)
8.4	4.0110(2)	64.53(1)	7.6	163.10(2)	0.10(5)
9.6	4.0108(3)	64.52(1)	7.6	163.12(2)	0.09(5)
9.7	4.0107(3)	64.51(1)	7.6	163.10(2)	0.10(5)
10.2	4.0105(3)	64.51(1)	7.6	163.09(1)	0.10(5)
9.2	4.0104(3)	64.50(1)	7.7	163.13(2)	0.08(5)
8.6	4.0102(2)	64.49(1)	7.7	163.10(2)	0.10(5)
9.5	4.0099(3)	64.48(1)	7.6	163.07(2)	0.11(5)
9.9	4.0098(3)	64.47(1)	7.9	163.03(2)	0.13(5)
9.4	4.0096(3)	64.46(1)	7.7	163.03(2)	0.13(5)
9.4	4.0095(3)	64.46(1)	7.6	163.01(2)	0.14(5)
9.4	4.0093(2)	64.45(1)	7.6	163.01(2)	0.14(5)
9.4	4.0091(3)	64.44(1)	7.6	163.00(2)	0.15(5)
10.4	4.0088(3)	64.42(1)	7.6	162.97(2)	0.17(5)
10.2	4.0087(3)	64.42(1)	7.7	162.95(2)	0.17(5)
10.1	4.0085(3)	64.41(1)	7.7	162.92(2)	0.19(5)
10.7	4.0082(3)	64.39(1)	7.7	162.89(2)	0.20(5)

sample Rwp(%)	Sample lattice constant, a (Å)	sample unit cell volume, V (Å^3)	CaF_2 Rwp(%)	CaF2 cell volume, V (Å^3)	Pressure (GPa)
10.8	4.0080(3)	64.39(2)	7.7	162.90(1)	0.20(5)
11.9	4.0078(3)	64.38(2)	7.7	162.86(1)	0.22(5)
10.5	4.0074(3)	64.36(1)	7.9	162.84(1)	0.23(5)
10.4	4.0072(3)	64.35(1)	7.8	162.83(1)	0.24(5)
11.4	4.0068(3)	64.33(2)	7.8	162.82(1)	0.24(5)
10.6	4.0064(3)	64.31(2)	8.0	162.78(2)	0.26(5)
10.5	4.0060(3)	64.29(2)	7.9	162.74(2)	0.28(5)
9.3	4.0056(3)	64.27(1)	7.8	162.69(2)	0.31(5)
10.1	4.0053(3)	64.25(1)	7.8	162.68(2)	0.31(5)
9.8	4.0048(3)	64.23(1)	7.8	162.62(2)	0.34(5)
10.8	4.0046(3)	64.22(2)	7.9	162.63(2)	0.33(5)
10.3	4.0043(3)	64.21(2)	7.9	162.61(2)	0.35(5)
10.9	4.0042(3)	64.20(2)	7.9	162.62(2)	0.34(5)
11.0	4.0042(3)	64.20(2)	7.9	162.59(2)	0.36(5)
12.5	4.0040(3)	64.19(2)	7.9	162.58(2)	0.36(5)
12.0	4.0038(3)	64.18(2)	8.0	162.58(2)	0.36(5)
10.9	4.0037(3)	64.18(2)	8.0	162.58(2)	0.36(5)
11.4	4.0035(3)	64.17(2)	7.9	162.59(2)	0.35(5)
11.7	4.0035(3)	64.17(2)	8.0	162.59(2)	0.35(5)
11.7	4.0035(3)	64.17(2)	8.0	162.57(2)	0.37(5)
11.5	4.0033(3)	64.16(2)	8.0	162.54(2)	0.38(5)
12.0	4.003(3)	64.15(2)	7.9	162.52(2)	0.39(5)
11.7	4.0029(3)	64.14(2)	8.1	162.50(2)	0.40(5)
10.8	4.0028(3)	64.13(2)	8.0	162.52(2)	0.39(5)
10.8	4.0026(3)	64.13(2)	8.1	162.52(2)	0.39(5)
10.1	4.0023(3)	64.11(1)	8.0	162.50(2)	0.40(5)
10.5	4.0020(3)	64.10(1)	7.9	162.50(2)	0.40(5)
10.7	4.0019(3)	64.09(1)	7.9	162.45(1)	0.43(5)
10.7	4.0018(3)	64.09(1)	7.9	162.43(1)	0.44(5)
10.0	4.0017(3)	64.08(1)	7.8	162.45(1)	0.43(5)
10.1	4.0016(2)	64.08(1)	7.8	162.42(1)	0.44(5)
9.5	4.0014(2)	64.07(1)	7.8	162.42(1)	0.44(5)
9.1	4.0012(2)	64.06(1)	7.9	162.42(1)	0.44(5)
9.3	4.0011(2)	64.05(1)	7.9	162.40(2)	0.45(5)
9.2	4.0010(2)	64.05(1)	7.9	162.38(2)	0.46(6)
9.0	4.0006(2)	64.03(1)	8.0	162.40(2)	0.45(5)
9.2	4.0004(2)	64.02(1)	8.1	162.38(2)	0.46(6)
9.2	4.0000(2)	64.00(1)	8.1	162.35(2)	0.48(6)
9.3	3.9996(2)	63.98(1)	8.2	162.31(2)	0.50(6)

sample Rwp(%)	Sample lattice constant, a (Å)	sample unit cell volume, V (Å^3)	CaF_2 Rwp(%)	CaF2 cell volume, V (Å^3)	Pressure (GPa)
9.4	3.9992(2)	63.96(1)	8.0	162.29(1)	0.51(6)
9.2	3.9989(2)	63.95(1)	7.8	162.28(2)	0.52(6)
9.3	3.9986(2)	63.93(1)	8.0	162.27(2)	0.52(6)
9.4	3.9984(2)	63.92(1)	8.1	162.28(2)	0.52(6)
9.4	3.9981(2)	63.91(1)	8.1	162.28(2)	0.52(6)
9.1	3.9978(2)	63.90(1)	8.2	162.25(2)	0.53(6)
9.2	3.9976(2)	63.88(1)	7.9	162.22(2)	0.55(6)
9.3	3.9973(2)	63.87(1)	7.7	162.21(2)	0.55(6)
9.8	3.9970(2)	63.86(1)	7.7	162.21(2)	0.55(6)
9.7	3.9967(2)	63.84(1)	7.7	162.19(1)	0.56(6)
9.4	3.9963(2)	63.82(1)	7.7	162.21(1)	0.55(6)
9.1	3.9961(2)	63.81(1)	7.9	162.15(2)	0.58(6)
9.0	3.9958(2)	63.80(1)	7.7	162.13(2)	0.59(6)
9.2	3.9954(2)	63.78(1)	7.8	162.15(2)	0.58(6)
9.1	3.9948(2)	63.75(1)	7.6	162.11(2)	0.60(6)
9.1	3.9944(2)	63.73(1)	7.6	162.09(2)	0.61(6)
8.9	3.9934(2)	63.69(1)	7.5	162.08(2)	0.62(6)
8.6	3.9923(2)	63.63(1)	7.6	162.07(2)	0.62(6)
8.8	3.9914(2)	63.59(1)	7.5	162.05(2)	0.63(6)
9.4	3.9903(3)	63.54(1)	7.4	162.03(2)	0.65(6)
9.3	3.9892(3)	63.48(1)	7.4	161.99(1)	0.66(6)
9.2	3.9884(3)	63.44(1)	7.4	161.97(1)	0.68(6)
9.3	3.9877(3)	63.41(1)	7.4	161.95(1)	0.69(6)
9.1	3.9859(3)	63.33(1)	7.4	161.95(1)	0.69(6)
9.3	3.9818(3)	63.13(2)	7.1	161.92(1)	0.70(6)
-	-	-	6.9	161.87(1)	0.73(6)
-	-	-	6.7	161.86(1)	0.73(6)
-	-	-	6.5	161.86(1)	0.73(6)
-	-	-	6.3	161.85(1)	0.74(6)
-	-	-	6.1	161.84(1)	0.74(6)
-	-	-	6.1	161.83(1)	0.75(6)
-	-	-	6.1	161.81(1)	0.76(6)
-	-	-	5.9	161.80(1)	0.76(6)
-	-	-	5.9	161.78(1)	0.78(6)
-	-	-	5.8	161.75(1)	0.79(6)
-	-	-	5.7	161.74(1)	0.80(6)
-	-	-	5.7	161.72(1)	0.81(6)
-	-	-	5.8	161.71(1)	0.81(6)
-	-	-	5.6	161.68(1)	0.83(6)

sample Rwp(%)	Sample lattice constant, a (Å)	sample unit cell volume, V (Å^3)	CaF_2 Rwp(%)	CaF2 cell volume, V (Å^3)	Pressure (GPa)
-	-	-	5.5	161.64(1)	0.85(6)
-	-	-	5.4	161.61(1)	0.86(6)
-	-	-	5.4	161.59(1)	0.87(6)
-	-	-	5.5	161.59(1)	0.88(6)
-	-	-	5.5	161.59(1)	0.88(6)
-	-	-	5.7	161.56(1)	0.89(6)
-	-	-	5.6	161.55(1)	0.90(6)
-	-	-	5.7	161.54(1)	0.90(6)
-	-	-	5.9	161.53(1)	0.91(6)
-	-	-	5.9	161.53(1)	0.91(6)
-	-	-	5.8	161.51(1)	0.92(6)
-	-	-	5.5	161.48(1)	0.93(6)
-	-	-	5.4	161.44(1)	0.96(7)
-	-	-	5.6	161.40(1)	0.98(7)
-	-	-	5.5	161.40(1)	0.98(7)
-	-	-	5.3	161.38(1)	0.99(7)
-	-	-	5.2	161.36(1)	1.00(7)
-	-	-	5.2	161.35(1)	1.00(7)
-	-	-	5.1	161.33(1)	1.01(7)
-	-	-	5.0	161.31(1)	1.02(7)
-	-	-	5.0	161.31(1)	1.02(7)
-	-	-	5.0	161.25(1)	1.06(7)
-	-	-	4.9	161.23(1)	1.07(7)
-	-	-	4.8	161.21(1)	1.08(7)
-	-	-	4.9	161.20(1)	1.08(7)
-	-	-	4.9	161.17(1)	1.10(7)
-	-	-	4.8	161.13(1)	1.12(7)
-	-	-	4.8	161.11(1)	1.13(7)
-	-	-	4.7	161.07(1)	1.15(7)
-	-	-	4.8	161.04(1)	1.17(7)
-	-	-	4.7	161.02(1)	1.18(7)
-	-	-	4.7	161.00(1)	1.19(7)
-	-	-	4.7	160.97(1)	1.21(7)
-	-	-	4.7	160.96(1)	1.21(7)
-	-	-	4.8	160.94(1)	1.22(7)
-	-	-	4.8	160.92(1)	1.23(7)
-	-	-	4.7	160.90(1)	1.24(7)
-	-	-	4.5	160.89(1)	1.25(7)
-	-	-	4.5	160.87(1)	1.26(7)

sample Rwp(%)	Sample lattice constant, a (Å)	sample unit cell volume, V (Å^3)	CaF_2 Rwp(%)	CaF2 cell volume, V (Å^3)	Pressure (GPa)
-	-	-	4.5	160.84(1)	1.28(7)
-	-	-	4.5	160.78(1)	1.31(7)
-	-	-	4.5	160.73(1)	1.34(8)
-	-	-	4.6	160.69(1)	1.36(8)
-	-	-	4.6	160.66(1)	1.38(8)
-	-	-	4.5	160.62(1)	1.40(8)
-	-	-	4.5	160.60(1)	1.41(8)
-	-	-	4.5	160.59(1)	1.42(8)
-	-	-	4.4	160.57(1)	1.43(8)
-	-	-	4.6	160.53(1)	1.45(8)
-	-	-	4.7	160.52(1)	1.46(8)
-	-	-	4.7	160.48(1)	1.47(8)
-	-	-	4.4	160.43(1)	1.50(8)
-	-	-	4.4	160.41(1)	1.52(8)
-	-	-	4.5	160.38(1)	1.53(8)
-	-	-	4.5	160.35(1)	1.55(8)
-	-	-	4.5	160.31(1)	1.57(8)
-	-	-	4.6	160.28(1)	1.58(8)
-	-	-	4.6	160.25(1)	1.60(8)
-	-	-	4.6	160.21(1)	1.63(8)
-	-	-	4.6	160.18(1)	1.64(8)
-	-	-	4.6	160.15(1)	1.66(9)
-	-	-	4.6	160.13(1)	1.67(9)
-	-	-	4.6	160.09(1)	1.69(9)
-	-	-	4.6	160.07(1)	1.70(9)
-	-	-	4.5	160.05(1)	1.71(9)
-	-	-	4.3	160.02(1)	1.73(9)
-	-	-	4.3	159.96(1)	1.77(9)
-	-	-	4.3	159.93(1)	1.79(9)
-	-	-	4.4	159.91(1)	1.79(9)
-	-	-	4.4	159.90(1)	1.80(9)
-	-	-	4.4	159.86(1)	1.82(9)
-	-	-	4.4	159.83(1)	1.84(9)
-	-	-	4.5	159.79(1)	1.86(9)
-	-	-	4.5	159.77(1)	1.87(9)
-	-	-	4.5	159.75(1)	1.88(9)
-	-	-	4.5	159.73(1)	1.89(9)
-	-	-	4.4	159.72(1)	1.90(9)
-	-	-	4.4	159.71(1)	1.91(9)

sample Rwp(%)	Sample lattice constant, a (Å)	sample unit cell volume, V (Å^3)	CaF_2 Rwp(%)	CaF2 cell volume, V (Å^3)	Pressure (GPa)
-	-	-	4.5	159.70(1)	1.92(9)
-	-	-	4.5	159.67(1)	1.93(9)
-	-	-	4.4	159.64(1)	1.95(9)
-	-	-	4.4	159.61(1)	1.96(7)
-	-	-	4.4	159.58(1)	1.98(7)
-	-	-	4.4	159.54(1)	2.01(7)
-	-	-	4.5	159.47(1)	2.04(7)
-	-	-	4.5	159.44(1)	2.06(7)
-	-	-	4.5	159.40(1)	2.08(7)
-	-	-	4.5	159.38(1)	2.10(7)
-	-	-	4.5	159.36(1)	2.11(7)
-	-	-	4.6	159.33(1)	2.13(7)
-	-	-	4.6	159.30(1)	2.14(7)
-	-	-	4.6	159.28(1)	2.16(7)
-	-	-	4.6	159.25(1)	2.17(7)
-	-	-	4.7	159.21(1)	2.20(7)
-	-	-	4.8	159.16(1)	2.22(7)
-	-	-	4.7	159.14(1)	2.24(7)
-	-	-	4.7	159.12(1)	2.25(7)
-	-	-	4.7	159.09(1)	2.27(7)
-	-	-	4.7	159.03(1)	2.30(7)
-	-	-	4.7	158.99(1)	2.33(7)
-	-	-	4.7	158.95(1)	2.35(7)
-	-	-	4.7	158.92(1)	2.36(7)
-	-	-	4.5	158.88(1)	2.39(7)
-	-	-	4.6	158.80(1)	2.44(7)
-	-	-	4.6	158.76(1)	2.46(7)
-	-	-	4.6	158.73(1)	2.48(7)
-	-	-	4.6	158.71(1)	2.49(7)
-	-	-	4.7	158.69(1)	2.50(7)
-	-	-	4.6	158.67(1)	2.51(7)
-	-	-	4.5	158.62(1)	2.54(7)
-	-	-	4.5	158.56(1)	2.58(7)
-	-	-	4.5	158.51(1)	2.61(7)
-	-	-	4.6	158.46(1)	2.64(7)
-	-	-	4.4	158.37(1)	2.69(7)
-	-	-	4.5	158.27(1)	2.75(7)
-	-	-	4.4	158.21(1)	2.79(7)
-	-	-	4.5	158.17(1)	2.81(7)

sample Rwp(%)	Sample lattice constant, a (Å)	sample unit cell volume, V (Å^3)	CaF_2 Rwp(%)	CaF2 cell volume, V (Å^3)	Pressure (GPa)
-	-	-	4.4	158.15(1)	2.82(7)
-	-	-	4.5	158.11(1)	2.85(7)
-	-	-	4.5	158.08(1)	2.86(7)
-	-	-	4.5	158.06(1)	2.88(7)
-	-	-	4.6	158.02(1)	2.90(7)
-	-	-	4.4	157.92(1)	2.96(7)
-	-	-	4.4	157.84(1)	3.01(7)
-	-	-	4.4	157.79(1)	3.04(7)
-	-	-	4.4	157.74(1)	3.08(7)
-	-	-	4.4	157.67(1)	3.12(7)
-	-	-	4.4	157.63(1)	3.14(7)
-	-	-	4.5	157.57(1)	3.18(7)
-	-	-	4.5	157.50(1)	3.22(7)
-	-	-	4.5	157.44(1)	3.26(7)
-	-	-	4.5	157.35(1)	3.32(7)
-	-	-	4.5	157.28(1)	3.36(7)
-	-	-	4.5	157.21(1)	3.40(7)
-	-	-	4.5	157.17(1)	3.43(7)
-	-	-	4.5	157.13(1)	3.45(7)
-	-	-	4.4	157.00(1)	3.53(7)
-	-	-	4.5	156.92(1)	3.59(7)
-	-	-	4.5	156.88(1)	3.61(7)
-	-	-	4.5	156.86(1)	3.63(7)
-	-	-	4.6	156.82(1)	3.65(7)
-	-	-	4.5	156.78(1)	3.68(7)
-	-	-	4.6	156.75(1)	3.69(7)
-	-	-	4.6	156.72(1)	3.71(7)
-	-	-	4.6	156.69(1)	3.74(7)
-	-	-	4.6	156.64(1)	3.76(7)
-	-	-	4.5	156.60(1)	3.79(7)
-	-	-	4.5	156.54(1)	3.83(7)
-	-	-	4.5	156.46(1)	3.88(7)
-	-	-	4.6	156.40(1)	3.92(7)
-	-	-	4.5	156.36(1)	3.95(7)
-	-	-	4.5	156.32(1)	3.97(7)
-	-	-	4.5	156.27(1)	4.00(7)
-	-	-	4.6	156.22(1)	4.03(7)
-	-	-	4.6	156.18(1)	4.06(7)
-	-	-	4.6	156.14(1)	4.09(7)

sample Rwp(%)	Sample lattice constant, a (Å)	sample unit cell volume, V (Å^3)	CaF_2 Rwp(%)	CaF2 cell volume, V (Å^3)	Pressure (GPa)
-	-	-	4.6	156.09(1)	4.12(7)
-	-	-	4.5	156.04(1)	4.16(7)
-	-	-	4.5	155.98(1)	4.20(7)
-	-	-	4.5	155.93(1)	4.23(7)
-	-	-	4.5	155.88(1)	4.26(7)
-	-	-	4.5	155.85(1)	4.28(7)
-	-	-	4.4	155.81(1)	4.31(7)
-	-	-	4.4	155.73(1)	4.36(7)
-	-	-	4.4	155.67(1)	4.40(7)
-	-	-	4.4	155.59(1)	4.45(7)
-	-	-	4.4	155.51(1)	4.51(7)
-	-	-	4.4	155.42(1)	4.57(7)
-	-	-	4.4	155.36(1)	4.61(7)
-	-	-	4.3	155.31(1)	4.64(7)
-	-	-	4.3	155.27(1)	4.67(7)
-	-	-	4.3	155.23(1)	4.70(7)
-	-	-	4.4	155.19(1)	4.72(7)
-	-	-	4.4	155.17(1)	4.74(7)
-	-	-	4.3	155.14(1)	4.76(7)
-	-	-	4.3	155.12(1)	4.77(7)
-	-	-	4.3	155.10(1)	4.79(7)
-	-	-	4.3	155.08(1)	4.80(7)
-	-	-	4.3	155.07(1)	4.81(7)
-	-	-	4.3	155.07(1)	4.81(7)
-	-	-	4.3	155.08(1)	4.80(7)
-	-	-	4.3	155.11(1)	4.78(7)
-	-	-	4.4	155.15(1)	4.76(7)
-	-	-	4.5	155.19(1)	4.73(7)
-	-	-	4.6	155.24(1)	4.69(7)
-	-	-	4.6	155.31(1)	4.64(7)
-	-	-	4.6	155.38(1)	4.60(7)
-	-	-	4.6	155.45(1)	4.55(7)
-	-	-	4.6	155.54(1)	4.49(7)
-	-	-	4.6	155.64(1)	4.42(7)
-	-	-	4.5	155.76(1)	4.34(7)
-	-	-	4.5	155.92(1)	4.23(7)
-	-	-	4.6	156.14(1)	4.09(7)
-	-	-	4.4	156.42(1)	3.91(7)
-	-	-	4.4	156.77(1)	3.68(7)

sample Rwp(%)	Sample lattice constant, a (Å)	sample unit cell volume, V (Å^3)	CaF_2 Rwp(%)	CaF2 cell volume, V (Å^3)	Pressure (GPa)
-	-	-	4.5	157.25(1)	3.38(7)
-	-	-	4.7	157.96(1)	2.94(7)
-	-	-	4.6	158.34(1)	2.71(7)
-	-	-	4.6	158.52(1)	2.60(7)
-	-	-	4.7	158.65(1)	2.52(7)
-	-	-	4.8	158.77(1)	2.45(7)
-	-	-	4.7	158.87(1)	2.39(7)
-	-	-	4.7	158.96(1)	2.34(7)
-	-	-	4.7	159.03(1)	2.30(7)
-	-	-	4.7	159.09(1)	2.26(7)
-	-	-	4.6	159.15(1)	2.23(7)
-	-	-	4.7	159.21(1)	2.20(7)
-	-	-	4.7	159.25(1)	2.17(7)
-	-	-	4.7	159.30(1)	2.14(7)
-	-	-	4.6	159.35(1)	2.11(7)
-	-	-	4.6	159.39(1)	2.09(7)
-	-	-	4.6	159.43(1)	2.07(7)
-	-	-	4.5	159.45(1)	2.06(7)
-	-	-	4.5	159.47(1)	2.05(7)
-	-	-	4.5	159.49(1)	2.03(7)
-	-	-	4.5	159.53(1)	2.01(7)
-	-	-	4.4	159.55(1)	2.00(7)
-	-	-	4.5	159.58(1)	1.98(7)
-	-	-	4.4	159.61(1)	1.97(7)
-	-	-	4.5	159.63(1)	1.95(9)
-	-	-	4.5	159.65(1)	1.94(9)
-	-	-	4.5	159.68(1)	1.93(9)
-	-	-	4.5	159.70(1)	1.91(9)
-	-	-	4.5	159.73(1)	1.90(9)
-	-	-	4.5	159.75(1)	1.88(9)
-	-	-	4.5	159.78(1)	1.87(9)
-	-	-	4.4	159.79(1)	1.86(9)
-	-	-	4.5	159.81(1)	1.85(9)
-	-	-	4.5	159.82(1)	1.84(9)
-	-	-	4.5	159.84(1)	1.83(9)
-	-	-	4.5	159.86(1)	1.82(9)
-	-	-	4.4	159.87(1)	1.81(9)
-	-	-	4.2	159.94(1)	1.78(9)
-	-	-	4.2	160.14(1)	1.66(9)

sample Rwp(%)	Sample lattice constant, a (Å)	sample unit cell volume, V (Å^3)	CaF_2 Rwp(%)	CaF2 cell volume, V (Å^3)	Pressure (GPa)
-	-	-	4.4	160.42(1)	1.51(8)
-	-	-	4.4	160.62(1)	1.40(8)
-	-	-	4.4	160.73(1)	1.34(8)
-	-	-	4.4	160.80(1)	1.30(7)
-	-	-	4.5	160.81(1)	1.29(7)
-	-	-	4.6	160.86(1)	1.27(7)
-	-	-	4.8	160.88(1)	1.25(7)
-	-	-	4.7	160.92(1)	1.23(7)
-	-	-	4.7	160.93(1)	1.23(7)
-	-	-	4.7	160.95(1)	1.22(7)
-	-	-	4.9	161.00(1)	1.19(7)
-	-	-	4.8	161.01(1)	1.19(7)
-	-	-	4.8	160.99(1)	1.20(7)
-	-	-	4.9	161.02(1)	1.18(7)
-	-	-	4.8	161.05(1)	1.16(7)
-	-	-	4.8	161.05(1)	1.16(7)
-	-	-	4.9	161.06(1)	1.16(7)
-	-	-	5.0	161.04(1)	1.17(7)
-	-	-	5.0	161.06(1)	1.16(7)
-	-	-	4.9	161.07(1)	1.15(7)
-	-	-	4.9	161.08(1)	1.15(7)
-	-	-	4.9	161.07(1)	1.15(7)
-	-	-	4.9	161.06(1)	1.16(7)
-	-	-	5.1	161.06(1)	1.16(7)
-	-	-	5.1	161.07(1)	1.15(7)
-	-	-	5.1	161.08(1)	1.15(7)
-	-	-	5.1	161.09(1)	1.14(7)
-	-	-	5.1	161.09(1)	1.14(7)
-	-	-	5.2	161.11(1)	1.13(7)
-	-	-	5.1	161.11(1)	1.13(7)
-	-	-	5.1	161.10(1)	1.14(7)
-	-	-	5.1	161.10(1)	1.14(7)
-	-	-	5.0	161.10(1)	1.13(7)
-	-	-	5.1	161.11(1)	1.13(7)
-	-	-	5.1	161.13(1)	1.12(7)
-	-	-	5.0	161.13(1)	1.12(7)
-	-	-	5.0	161.13(1)	1.12(7)
-	-	-	5.0	161.13(1)	1.12(7)
-	-	-	5.0	161.14(1)	1.12(7)

sample Rwp(%)	Sample lattice constant, a (Å)	sample unit cell volume, V (Å^3)	CaF_2 Rwp(%)	CaF2 cell volume, V (Å^3)	Pressure (GPa)
-	-	-	5.0	161.15(1)	1.11(7)
-	-	-	4.5	161.16(1)	1.11(7)

Table B.3: Weighted profile R factors for both sample and pressure standard, lattice constant for the x=0.1 sample, unit cell volumes for both the sample and the CaF_2 pressure standard, and the pressure calculated from the CaF_2 using the decompression cell volume as V_0.

sample Rwp(%)	Sample lattice constant, a (Å)	sample unit cell volume, V (Å^3)	CaF_2 Rwp(%)	CaF2 cell volume, V (Å^3)	Pressure (GPa)
6.9	4.013(1)	64.626(5)	5.7	163.37(4)	0.02(5)
9.7	4.013(1)	64.627(6)	7.1	163.37(4)	0.02(5)
9.8	4.013(1)	64.627(6)	7.2	163.36(4)	0.02(5)
10.3	4.013(1)	64.628(7)	7.6	163.35(4)	0.02(5)
10.4	4.013(2)	64.626(8)	7.8	163.36(4)	0.02(5)
11.0	4.0129(2)	64.621(8)	8.1	163.36(4)	0.02(5)
10.8	4.0129(2)	64.619(8)	8.2	163.36(4)	0.02(5)
10.6	4.0128(1)	64.618(7)	7.8	163.34(4)	0.03(5)
10.0	4.0127(1)	64.610(6)	7.3	163.31(4)	0.04(5)
10.7	4.0129(2)	64.623(8)	7.9	163.36(4)	0.02(5)
10.4	4.0131(1)	64.632(7)	7.8	163.34(4)	0.03(5)
10.0	4.0131(1)	64.633(7)	7.4	163.33(4)	0.03(5)
10.8	4.0130(2)	64.624(8)	7.9	163.34(4)	0.03(5)
10.9	4.0130(2)	64.627(8)	8.1	163.32(4)	0.04(5)
10.6	4.0130(2)	64.625(8)	7.8	163.33(4)	0.03(5)
9.6	4.0130(1)	64.627(6)	7.0	163.34(4)	0.03(5)
10.5	4.0129(2)	64.622(8)	7.8	163.35(4)	0.02(5)
10.2	4.0131(2)	64.631(8)	7.6	163.32(4)	0.04(5)
10.7	4.0129(2)	64.623(8)	8.0	163.33(4)	0.03(5)
10.5	4.0129(2)	64.622(8)	7.8	163.32(4)	0.04(5)
10.5	4.0129(2)	64.619(8)	7.7	163.33(4)	0.03(5)
11.0	4.0132(1)	64.634(7)	8.0	163.31(4)	0.05(5)
10.6	4.0131(2)	64.631(7)	7.8	163.33(4)	0.03(5)
10.2	4.0130(1)	64.626(6)	7.4	163.32(4)	0.04(5)
11.2	4.0130(1)	64.625(6)	8.2	163.36(4)	0.02(5)
10.4	4.0129(1)	64.622(7)	7.7	163.34(4)	0.03(5)
10.5	4.0130(1)	64.626(7)	7.8	163.34(4)	0.03(5)
10.7	4.0129(1)	64.624(7)	7.9	163.36(4)	0.02(5)
10.4	4.0130(1)	64.625(6)	7.8	163.35(4)	0.03(5)
10.9	4.0130(1)	64.628(7)	8.2	163.34(4)	0.03(5)
10.5	4.0130(1)	64.624(7)	7.8	163.34(4)	0.03(5)
10.7	4.0127(1)	64.614(6)	7.6	163.34(4)	0.03(5)
10.5	4.0130(1)	64.626(6)	7.5	163.35(4)	0.03(5)
10.8	4.0131(1)	64.630(6)	7.8	163.30(4)	0.05(5)
10.4	4.0130(1)	64.627(6)	7.5	163.33(4)	0.03(5)

sample Rwp(%)	Sample lattice constant, a (Å)	sample unit cell volume, V (Å^3)	CaF_2 Rwp(%)	CaF2 cell volume, V (Å^3)	Pressure (GPa)
10.5	4.0130(1)	64.625(7)	7.8	163.35(4)	0.02(5)
10.3	4.0131(1)	64.630(6)	7.4	163.34(4)	0.03(5)
10.3	4.0129(1)	64.622(6)	7.3	163.32(4)	0.04(5)
10.7	4.0128(1)	64.616(7)	7.9	163.32(4)	0.04(5)
10.1	4.0130(1)	64.627(6)	7.4	163.33(4)	0.03(5)
10.1	4.0129(1)	64.623(6)	7.3	163.32(4)	0.04(5)
10.0	4.0129(1)	64.622(6)	7.1	163.34(4)	0.03(5)
10.5	4.0127(1)	64.614(6)	7.7	163.34(4)	0.03(5)
10.1	4.0128(1)	64.616(6)	7.2	163.32(4)	0.04(5)
10.7	4.0129(1)	64.620(7)	7.7	163.35(3)	0.02(5)
10.0	4.0129(1)	64.620(6)	7.2	163.35(4)	0.03(5)
11.2	4.0129(1)	64.622(6)	8.1	163.36(4)	0.02(5)
10.1	4.0128(1)	64.619(6)	7.4	163.35(4)	0.02(5)
10.5	4.0128(1)	64.617(7)	7.8	163.33(4)	0.04(5)
9.7	4.0129(1)	64.624(6)	6.9	163.34(4)	0.03(5)
10.4	4.0130(1)	64.627(6)	7.5	163.32(4)	0.04(5)
10.7	4.0130(1)	64.624(6)	7.8	163.34(4)	0.03(5)
10.5	4.0129(1)	64.623(6)	7.5	163.33(4)	0.03(5)
11.0	4.0129(1)	64.619(6)	7.7	163.34(4)	0.03(5)
10.9	4.0128(1)	64.618(6)	7.9	163.33(4)	0.03(5)
11.3	4.0128(2)	64.618(8)	8.3	163.32(4)	0.04(5)
10.9	4.0129(1)	64.620(7)	8.0	163.31(4)	0.05(5)
11.5	4.0128(2)	64.617(7)	8.4	163.31(4)	0.04(5)
10.6	4.0129(1)	64.622(7)	7.8	163.34(4)	0.03(5)
11.3	4.013(1)	64.627(7)	8.3	163.35(4)	0.03(5)
11.2	4.013(1)	64.625(7)	8.2	163.33(4)	0.03(5)
11.9	4.0129(2)	64.622(8)	8.7	163.33(4)	0.03(5)
11.4	4.0129(1)	64.620(7)	8.3	163.35(4)	0.03(5)
11.6	4.0128(2)	64.618(7)	8.5	163.36(4)	0.02(5)
11.7	4.0127(2)	64.614(7)	8.3	163.34(4)	0.03(5)
10.6	4.0126(1)	64.608(6)	6.8	163.33(4)	0.03(5)
10.5	4.0126(1)	64.608(6)	6.8	163.35(4)	0.03(5)
10.1	4.0127(1)	64.612(6)	6.5	163.37(4)	0.02(5)
9.7	4.0128(1)	64.617(6)	6.5	163.36(4)	0.02(5)
8.6	4.0129(1)	64.622(6)	6.1	163.33(4)	0.03(5)
9.6	4.0129(1)	64.621(6)	6.5	163.33(4)	0.03(5)
8.6	4.0130(1)	64.625(5)	6.0	163.33(4)	0.04(5)
10.0	4.0130(1)	64.625(6)	6.6	163.31(4)	0.04(5)
9.0	4.0127(1)	64.614(6)	6.1	163.33(4)	0.03(5)

sample Rwp(%)	Sample lattice constant, a (Å)	sample unit cell volume, V (Å^3)	CaF_2 Rwp(%)	CaF2 cell volume, V (Å^3)	Pressure (GPa)
8.5	4.0126(1)	64.608(5)	5.8	163.35(4)	0.02(5)
9.0	4.0127(1)	64.610(5)	6.0	163.34(4)	0.03(5)
7.5	4.0126(1)	64.606(5)	5.3	163.34(4)	0.03(5)
7.3	4.0128(1)	64.614(5)	5.3	163.34(4)	0.03(5)
8.4	4.0128(1)	64.617(5)	5.7	163.33(4)	0.03(5)
8.0	4.0130(1)	64.624(5)	5.5	163.34(4)	0.03(5)
7.7	4.0128(1)	64.618(5)	5.3	163.34(4)	0.03(5)
7.9	4.0128(1)	64.618(5)	5.5	163.34(4)	0.03(5)
7.9	4.0130(1)	64.625(5)	5.5	163.33(3)	0.04(5)
8.0	4.0129(1)	64.622(5)	5.6	163.34(4)	0.03(5)
8.2	4.0128(1)	64.618(5)	5.7	163.35(4)	0.02(5)
7.7	4.0128(1)	64.616(5)	5.4	163.33(3)	0.03(5)
7.6	4.0128(1)	64.616(5)	5.5	163.33(4)	0.03(5)
7.7	4.0127(1)	64.610(6)	5.7	163.35(3)	0.03(5)
7.6	4.0126(1)	64.606(5)	5.4	163.32(4)	0.04(5)
7.5	4.0127(1)	64.610(5)	5.5	163.30(4)	0.05(5)
7.5	4.0125(1)	64.604(5)	5.4	163.32(4)	0.04(5)
7.4	4.0125(1)	64.604(5)	5.3	163.30(3)	0.05(5)
7.4	4.0125(1)	64.604(5)	5.3	163.32(3)	0.04(5)
7.4	4.0124(1)	64.599(5)	5.3	163.33(3)	0.04(5)
7.6	4.0124(1)	64.599(5)	5.6	163.33(3)	0.03(5)
7.6	4.0124(1)	64.595(5)	5.5	163.33(4)	0.03(5)
7.1	4.0126(1)	64.606(5)	5.3	163.32(4)	0.04(5)
8.0	4.0125(1)	64.603(5)	5.6	163.33(3)	0.04(5)
8.3	4.0124(1)	64.599(5)	5.7	163.34(4)	0.03(5)
7.4	4.0124(1)	64.597(5)	5.4	163.33(4)	0.04(5)
7.4	4.0122(1)	64.590(5)	5.3	163.31(4)	0.04(5)
8.3	4.0119(1)	64.574(5)	5.8	163.30(4)	0.05(5)
7.9	4.0118(1)	64.567(5)	5.8	163.29(4)	0.05(5)
8.3	4.0117(1)	64.561(5)	5.8	163.27(4)	0.07(5)
8.7	4.0115(1)	64.554(6)	6.0	163.26(4)	0.07(5)
8.9	4.0113(1)	64.545(6)	5.9	163.26(3)	0.07(5)
8.4	4.0110(1)	64.531(6)	5.8	163.22(3)	0.09(5)
7.8	4.0108(1)	64.522(6)	5.6	163.20(4)	0.10(5)
8.1	4.0106(1)	64.509(6)	5.7	163.18(4)	0.11(5)
8.2	4.0105(1)	64.503(6)	5.8	163.16(4)	0.12(5)
7.6	4.0104(1)	64.500(5)	5.4	163.13(4)	0.13(5)
7.7	4.0102(1)	64.492(5)	5.4	163.12(4)	0.14(5)
7.6	4.0100(1)	64.480(5)	5.4	163.11(4)	0.15(5)

sample Rwp(%)	Sample lattice constant, a (Å)	sample unit cell volume, V (Å^3)	CaF_2 Rwp(%)	CaF2 cell volume, V (Å^3)	Pressure (GPa)
8.2	4.0098(1)	64.472(5)	5.7	163.09(4)	0.15(5)
7.4	4.0097(1)	64.468(5)	5.2	163.08(4)	0.16(5)
7.6	4.0096(1)	64.462(5)	5.3	163.06(4)	0.17(5)
7.2	4.0092(1)	64.444(5)	5.0	163.03(4)	0.18(5)
7.3	4.0090(1)	64.432(5)	5.0	163.00(4)	0.20(5)
7.1	4.0088(1)	64.424(5)	4.9	162.99(4)	0.20(5)
8.1	4.0083(1)	64.400(6)	5.3	162.96(4)	0.22(5)
7.7	4.0077(1)	64.371(5)	5.0	162.91(4)	0.24(5)
8.2	4.0070(1)	64.337(5)	5.2	162.87(4)	0.26(6)
8.2	4.0057(1)	64.276(6)	5.2	162.77(4)	0.31(6)
8.7	4.0054(1)	64.258(6)	5.5	162.73(4)	0.33(6)
8.2	4.0050(1)	64.241(6)	5.2	162.71(4)	0.35(6)
8.2	4.0048(1)	64.229(6)	5.1	162.69(4)	0.36(6)
8.3	4.0046(1)	64.221(6)	5.2	162.68(4)	0.36(6)
9.1	4.0043(1)	64.208(6)	5.7	162.66(4)	0.37(6)
8.3	4.0039(1)	64.188(6)	5.4	162.63(4)	0.39(6)
9.3	4.0035(1)	64.171(7)	5.9	162.61(4)	0.40(6)
8.7	4.0032(1)	64.153(6)	5.6	162.60(4)	0.40(6)
10.0	4.0027(2)	64.128(7)	6.3	162.56(4)	0.42(6)
9.3	4.0020(1)	64.095(7)	5.8	162.51(4)	0.45(6)
9.7	4.0015(2)	64.073(8)	6.1	162.49(4)	0.46(6)
9.7	4.0012(2)	64.059(8)	6.1	162.47(4)	0.47(6)
9.9	4.0010(2)	64.046(8)	6.2	162.45(3)	0.48(6)
9.6	4.0003(2)	64.016(8)	6.0	162.40(4)	0.51(6)
8.9	3.9986(2)	63.934(8)	5.5	162.32(4)	0.55(6)
9.3	3.9976(2)	63.884(8)	5.7	162.29(4)	0.56(6)
9.1	3.9970(2)	63.857(8)	5.5	162.26(4)	0.58(6)
8.3	3.9963(1)	63.822(7)	5.0	162.22(3)	0.60(6)
7.8	3.9955(1)	63.785(7)	4.7	162.19(3)	0.61(6)
7.8	3.9942(1)	63.723(7)	4.5	162.14(4)	0.64(6)
7.8	3.9931(2)	63.667(7)	4.5	162.11(4)	0.65(6)
7.4	3.9918(2)	63.607(7)	4.0	162.08(3)	0.67(6)
8.5	3.9896(2)	63.504(9)	4.8	162.04(3)	0.69(6)
8.5	3.9849(3)	63.280(9)	4.3	161.98(3)	0.73(6)
-	-	-	4.2	161.94(3)	0.75(6)
-	-	-	4.4	161.92(3)	0.76(6)
-	-	-	4.1	161.89(3)	0.77(6)
-	-	-	4.1	161.86(3)	0.79(6)
-	-	-	4.0	161.81(3)	0.81(6)

sample Rwp(%)	Sample lattice constant, a (Å)	sample unit cell volume, V (Å^3)	CaF_2 Rwp(%)	CaF2 cell volume, V (Å^3)	Pressure (GPa)
-	-	-	4.4	161.75(3)	0.85(6)
-	-	-	4.7	161.65(3)	0.90(9)
-	-		5.1	161.59(3)	0.93(9)
-	-	-	5.2	161.55(3)	0.95(9)
-	-	-	5.5	161.50(3)	0.98(9)
-	-		6.3	161.42(3)	1.02(9)
-	-	-	6.7	161.38(3)	1.04(9)
-	-	-	6.7	161.34(3)	1.06(9)
-	-	-	6.8	161.30(3)	1.08(9)
-	-	-	6.8	161.27(3)	1.10(9)
-	-	-	6.4	161.23(3)	1.12(9)
-	-	-	6.4	161.16(3)	1.16(9)
-	-	-	6.6	161.1(3)	1.19(9)
-	-	-	6.7	161.04(3)	1.23(9)
-	-	-	6.5	160.99(3)	1.25(9)
-	-	-	6.7	160.95(3)	1.27(9)
-	-	-	6.6	160.90(3)	1.30(9)
-	-	-	6.5	160.82(3)	1.35(9)
-	-	-	6.2	160.74(3)	1.39(9)
-	-	-	6.3	160.70(3)	1.41(9)
-	-	-	6.3	160.67(3)	1.43(9)
-	-	-	6.5	160.65(3)	1.44(9)
-	-	-	6.5	160.63(3)	1.45(9)
-	-	-	6.4	160.61(3)	1.46(9)
-	-	-	6.0	160.57(3)	1.48(9)
-	-	-	6.2	160.54(3)	1.50(9)
-	-	-	6.1	160.51(3)	1.51(9)
-	-	-	6.3	160.49(3)	1.52(9)
-	-	-	6.0	160.47(3)	1.54(9)
-	-	-	6.0	160.43(3)	1.56(9)
-	-	-	6.1	160.40(3)	1.58(9)
-	-	-	6.0	160.36(3)	1.60(9)
-	-	-	6.2	160.32(3)	1.62(9)
-	-	-	5.9	160.28(3)	1.64(9)
-	-	-	6.0	160.25(3)	1.66(9)
-	-	-	5.9	160.21(3)	1.68(9)
-	-	-	6.1	160.18(3)	1.70(9)
-	-	-	5.9	160.14(3)	1.72(9)
-	-	-	5.8	160.08(3)	1.76(9)

sample Rwp(%)	Sample lattice constant, a (Å)	sample unit cell volume, V (Å^3)	CaF_2 Rwp(%)	CaF2 cell volume, V (Å^3)	Pressure (GPa)
-	-	-	6.0	160.03(3)	1.78(9)
-	-	-	6.2	160.00(3)	1.80(9)
-	-	-	5.9	159.98(3)	1.81(9)
-	-	-	6.3	159.96(3)	1.82(9)
-	-	-	6.2	159.92(3)	1.84(9)
-	-	-	7.0	159.87(3)	1.87(9)
-	-	-	6.8	159.81(3)	1.91(9)
-	-	-	6.6	159.74(3)	1.95(9)
-	-	-	6.8	159.70(3)	1.97(9)
-	-	-	7.1	159.67(3)	1.99(9)
-	-	-	7.2	159.61(3)	2.02(9)
-	-	-	6.8	159.53(3)	2.07(9)
-	-	-	6.6	159.49(3)	2.09(9)
-	-	-	6.4	159.45(3)	2.12(9)
-	-	-	6.5	159.41(3)	2.14(9)
-	-	-	6.5	159.31(4)	2.20(9)
-	-	-	6.0	159.27(3)	2.22(9)
-	-	-	6.2	159.23(4)	2.24(9)
-	-	-	6.1	159.21(4)	2.25(9)
-	-	-	6.2	159.19(4)	2.27(9)
-	-	-	6.0	159.14(4)	2.29(9)
-	-	-	6.2	159.10(4)	2.31(9)
-	-	-	5.9	159.07(4)	2.34(9)
-	-	-	5.9	159.02(4)	2.37(9)
-	-	-	5.8	158.93(4)	2.42(9)
-	-	-	6.0	158.85(4)	2.47(9)
-	-	-	6.0	158.80(4)	2.49(9)
-	-	-	5.9	158.76(4)	2.52(9)
-	-	-	5.8	158.69(4)	2.56(9)
-	-	-	5.8	158.63(4)	2.60(9)
-	-	-	5.7	158.58(4)	2.63(9)
-	-	-	6.3	158.52(4)	2.66(9)
-	-	-	6.0	158.48(4)	2.69(9)
-	-	-	5.8	158.44(4)	2.71(9)
-	-	-	5.8	158.37(4)	2.75(9)
-	-	-	5.8	158.3(4)	2.79(9)
-	-	-	6.0	158.25(4)	2.82(9)
-	-	-	5.9	158.21(4)	2.85(9)
-	-	-	6.3	158.18(4)	2.86(9)

sample Rwp(%)	Sample lattice constant, a (Å)	sample unit cell volume, V (Å^3)	CaF_2 Rwp(%)	CaF2 cell volume, V (Å^3)	Pressure (GPa)
-	-	-	6.1	158.15(4)	2.89(9)
-	-	-	5.7	158.09(4)	2.92(9)
-	-	-	6.2	158.03(4)	2.96(9)
-	-	-	6.4	157.97(4)	3.00(9)
-	-	-	5.9	157.92(4)	3.02(9)
-	-	-	6.3	157.87(4)	3.06(9)
-	-	-	6.3	157.77(4)	3.11(9)
-	-	-	6.4	157.69(4)	3.16(9)
-	-	-	6.5	157.64(4)	3.19(9)
-	-	-	6.9	157.61(4)	3.21(9)
-	-	-	6.7	157.58(4)	3.23(9)
-	-	-	7.3	157.54(4)	3.26(9)
-	-	-	7.4	157.46(4)	3.31(9)
-	-	-	7.4	157.40(4)	3.35(9)
-	-	-	7.1	157.36(4)	3.37(9)
-	-	-	7.1	157.32(4)	3.39(9)
-	-	-	7.5	157.26(4)	3.44(9)
-	-	-	7.7	157.20(4)	3.47(9)
-	-	-	8.0	157.16(4)	3.50(9)
-	-	-	8.1	157.11(4)	3.53(9)
-	-	-	8.6	157.03(4)	3.58(9)
-	-	-	8.6	156.94(4)	3.64(9)
-	-	-	9.1	156.87(4)	3.68(9)
-	-	-	9.1	156.75(4)	3.76(9)
-	-	-	9.3	156.64(4)	3.83(9)
-	-	-	9.8	156.57(4)	3.88(9)
-	-	-	9.4	156.48(4)	3.93(9)
-	-	-	9.6	156.42(4)	3.97(9)
-	-	-	9.8	156.35(4)	4.02(9)
-	-	-	9.9	156.29(4)	4.06(9)
-	-	-	10.1	156.19(4)	4.12(9)
-	-	-	10.0	156.11(4)	4.17(9)
-	-	-	9.9	156.06(4)	4.21(9)
-	-	-	10.2	155.98(4)	4.26(9)
-	-	-	9.9	155.90(4)	4.31(9)
-	-	-	10.4	155.82(4)	4.37(9)
-	-	-	9.9	155.73(4)	4.42(9)
-	-	-	9.7	155.65(4)	4.48(9)
-	-	-	10.0	155.57(4)	4.54(9)

sample Rwp(%)	Sample lattice constant, a (Å)	sample unit cell volume, V (Å^3)	CaF_2 Rwp(%)	CaF2 cell volume, V (Å^3)	Pressure (GPa)
-	-	-	9.9	155.51(4)	4.58(9)
-	-	-	9.8	155.43(4)	4.63(9)
-	-	-	9.6	155.35(4)	4.68(9)
-	-	-	9.6	155.29(4)	4.73(9)
-	-	-	9.6	155.20(4)	4.78(9)
-	-	-	9.5	155.13(4)	4.83(9)
-	-	-	9.6	155.04(4)	4.89(9)
-	-	-	9.0	154.87(4)	5.01(9)
-	-	-	8.7	154.69(3)	5.13(9)
-	-	-	8.5	154.58(3)	5.21(9)
-	-	-	8.8	154.48(4)	5.28(9)
-	-	-	8.5	154.39(3)	5.35(9)
-	-	-	7.8	154.22(3)	5.46(9)
-	-	-	7.6	154.13(3)	5.53(9)
-	-	-	7.1	154.06(3)	5.58(9)
-	-	-	7.3	154.00(3)	5.62(9)
-	-	-	6.9	153.91(3)	5.69(9)
-	-	-	6.4	153.85(3)	5.73(9)
-	-	-	6.5	153.81(3)	5.76(9)
-	-	-	6.4	153.79(3)	5.78(9)
-	-	-	6.3	153.76(3)	5.80(9)
-	-	-	5.9	153.74(3)	5.81(9)
-	-	-	6.0	153.74(3)	5.81(9)
-	-	-	5.8	153.74(3)	5.81(9)
-	-	-	5.8	153.75(3)	5.80(9)
-	-	-	6.0	153.81(3)	5.76(9)
-	-	-	6.0	153.89(3)	5.70(9)
-	-	-	5.8	153.98(3)	5.64(9)
-	-	-	5.8	154.08(9)	5.57(9)
-	-	-	5.8	154.19(9)	5.49(9)
-	-	-	5.8	154.30(9)	5.41(9)
-	-	-	5.8	154.42(9)	5.32(9)
-	-	-	5.7	154.55(9)	5.23(9)
-	-	-	5.9	154.68(9)	5.14(9)
-	-	-	5.8	154.86(9)	5.02(9)
-	-	-	5.8	155.06(9)	4.88(9)
-	-	-	5.9	155.34(9)	4.69(9)
-	-	-	5.8	155.72(9)	4.43(9)
-	-	-	5.7	156.14(9)	4.15(9)

sample Rwp(%)	Sample lattice constant, a (Å)	sample unit cell volume, V (Å^3)	CaF_2 Rwp(%)	CaF2 cell volume, V (Å^3)	Pressure (GPa)
-	-	-	5.7	156.73(9)	3.77(9)
-	-	-	5.4	157.26(9)	3.43(9)
-	-	-	5.2	157.48(9)	3.29(9)
-	-	-	6.8	157.51(9)	3.28(9)

Table B.4: Weighted profile R factors for both sample and pressure standard, lattice constant for the x=0.2 sample, unit cell volumes for both the sample and the CaF_2 pressure standard, and the pressure calculated from the CaF_2 using the decompression cell volume as V_0.

sample Rwp(%)	Sample lattice constant, a (Å)	sample unit cell volume, V (Å^3)	CaF_2 Rwp(%)	CaF2 cell volume, V (Å^3)	Pressure (GPa)
4.5	4.00276(3)	64.133(1)	5.5	163.31(13)	0.01(9)
4.2	4.00272(3)	64.131(1)	5.1	163.30(13)	0.01(9)
4.2	4.00266(3)	64.128(1)	5.2	163.30(13)	0.01(9)
5.0	4.00264(3)	64.127(2)	5.6	163.31(13)	0.00(9)
4.6	4.00271(3)	64.130(1)	5.3	163.28(13)	0.02(9)
4.6	4.00278(3)	64.133(1)	5.0	163.28(13)	0.02(9)
5.1	4.00265(3)	64.127(2)	5.2	163.27(14)	0.02(9)
5.1	4.00245(3)	64.118(2)	5.2	163.28(14)	0.02(9)
5.3	4.00259(3)	64.125(2)	5.2	163.26(14)	0.03(9)
5.6	4.00272(3)	64.130(2)	5.4	163.26(13)	0.03(9)
6.1	4.00250(4)	64.120(2)	5.7	163.25(14)	0.03(9)
7.1	4.00246(4)	64.118(2)	6.0	163.23(14)	0.05(9)
6.9	4.00262(4)	64.126(2)	5.9	163.26(13)	0.03(9)
7.6	4.00259(5)	64.125(2)	6.2	163.24(14)	0.04(9)
8.0	4.00254(5)	64.122(2)	6.5	163.26(14)	0.03(9)
6.7	4.00267(4)	64.128(2)	5.7	163.25(13)	0.04(9)
7.3	4.00253(5)	64.121(2)	6.3	163.29(13)	0.01(9)
7.6	4.00265(5)	64.127(2)	6.5	163.28(14)	0.02(9)
7.9	4.00261(5)	64.126(2)	6.5	163.26(14)	0.03(9)
7.7	4.00256(5)	64.123(2)	6.6	163.27(13)	0.02(9)
6.0	4.00257(4)	64.123(2)	5.5	163.28(12)	0.02(9)
6.2	4.00273(4)	64.131(2)	5.7	163.28(13)	0.02(9)
5.6	4.00255(3)	64.122(2)	5.4	163.27(13)	0.02(9)
5.5	4.00267(3)	64.128(2)	5.4	163.26(12)	0.03(9)
5.5	4.00266(3)	64.128(2)	5.3	163.27(12)	0.02(9)
5.6	4.00276(3)	64.132(2)	5.2	163.27(12)	0.02(9)
5.5	4.00266(3)	64.128(2)	5.1	163.28(12)	0.02(9)
4.3	4.00285(3)	64.137(1)	5.3	163.28(12)	0.02(9)
4.0	4.00274(3)	64.132(1)	5.0	163.25(12)	0.03(9)
4.0	4.00265(3)	64.127(1)	5.0	163.26(12)	0.03(9)
4.4	4.00285(3)	64.137(1)	4.9	163.27(12)	0.02(9)
4.1	4.00265(3)	64.127(1)	5.1	163.29(12)	0.01(9)
4.5	4.00264(3)	64.127(1)	5.0	163.27(13)	0.03(9)
4.6	4.00272(3)	64.131(1)	5.1	163.24(12)	0.04(9)
4.3	4.00268(3)	64.129(1)	5.2	163.27(12)	0.02(9)

sample Rwp(%)	Sample lattice constant, a (Å)	sample unit cell volume, V (Å^3)	CaF_2 Rwp(%)	CaF2 cell volume, V (Å^3)	Pressure (GPa)
4.4	4.00257(3)	64.124(1)	4.8	163.28(12)	0.02(9)
4.6	4.00271(3)	64.130(1)	5.1	163.27(12)	0.02(9)
4.5	4.00267(3)	64.128(1)	5.1	163.24(11)	0.04(9)
4.2	4.00270(3)	64.130(1)	5.0	163.28(11)	0.02(9)
4.3	4.00268(3)	64.129(1)	5.0	163.25(11)	0.03(9)
4.4	4.00280(3)	64.135(1)	4.8	163.29(11)	0.01(9)
4.5	4.00265(3)	64.127(1)	4.9	163.29(11)	0.01(9)
4.6	4.00281(3)	64.135(1)	5.0	163.29(11)	0.02(9)
4.9	4.00274(3)	64.132(1)	4.9	163.28(11)	0.02(9)
4.3	4.00261(3)	64.125(1)	5.1	163.27(11)	0.02(9)
5.0	4.00269(3)	64.129(2)	5.2	163.27(11)	0.02(9)
4.7	4.00280(3)	64.134(1)	5.0	163.28(11)	0.02(9)
4.4	4.00249(3)	64.119(1)	4.9	163.29(11)	0.01(9)
4.7	4.00282(3)	64.135(1)	5.1	163.28(11)	0.02(9)
4.7	4.00260(3)	64.125(1)	4.9	163.26(12)	0.03(9)
4.2	4.00253(3)	64.121(1)	5.1	163.29(12)	0.01(9)
4.4	4.00235(3)	64.113(1)	5.4	163.27(13)	0.02(9)
4.4	4.00252(3)	64.121(1)	5.0	163.29(12)	0.01(9)
5.0	4.00278(3)	64.133(1)	5.5	163.29(12)	0.01(9)
5.0	4.00278(3)	64.134(2)	5.1	163.20(11)	0.06(9)
4.4	4.00257(3)	64.124(1)	5.0	163.26(11)	0.03(9)
4.7	4.00259(3)	64.124(1)	5.1	163.28(12)	0.02(9)
4.6	4.00251(3)	64.121(1)	5.4	163.25(11)	0.03(9)
4.7	4.00253(3)	64.122(1)	4.9	163.26(11)	0.03(9)
4.6	4.00228(3)	64.110(1)	4.9	163.23(11)	0.04(9)
4.3	4.00246(3)	64.118(1)	4.7	163.23(11)	0.04(9)
4.5	4.00241(3)	64.116(1)	4.8	163.23(11)	0.04(9)
5.1	4.00242(3)	64.116(2)	5.3	163.22(11)	0.05(9)
4.5	4.00233(3)	64.112(1)	5.3	163.23(11)	0.04(9)
4.7	4.00204(3)	64.098(1)	5.3	163.22(11)	0.05(9)
4.3	4.00204(3)	64.098(1)	5.1	163.19(11)	0.06(9)
4.5	4.00196(3)	64.094(1)	5.2	163.18(11)	0.07(9)
5.0	4.00194(3)	64.093(1)	5.0	163.17(11)	0.07(9)
4.9	4.00189(3)	64.091(1)	4.9	163.16(11)	0.08(9)
4.7	4.00173(3)	64.083(1)	5.1	163.17(12)	0.07(9)
4.7	4.00165(3)	64.079(1)	5.0	163.16(11)	0.08(9)
4.9	4.00167(3)	64.080(1)	5.2	163.19(11)	0.06(9)
4.9	4.00140(3)	64.067(1)	4.9	163.14(11)	0.09(9)
5.2	4.00124(3)	64.060(1)	5.0	163.14(11)	0.09(9)

sample Rwp(%)	Sample lattice constant, a (Å)	sample unit cell volume, V (Å^3)	CaF_2 Rwp(%)	CaF2 cell volume, V (Å^3)	Pressure (GPa)
5.1	4.00107(3)	64.051(1)	5.0	163.09(11)	0.11(9)
5.5	4.00102(3)	64.049(2)	5.1	163.11(11)	0.10(9)
5.1	4.00086(3)	64.041(1)	5.1	163.10(12)	0.11(9)
4.8	4.00028(3)	64.014(1)	5.2	163.01(11)	0.16(9)
4.6	3.99996(3)	63.998(1)	5.2	163.02(12)	0.15(9)
4.6	3.99993(3)	63.997(1)	5.3	163.01(11)	0.15(9)
4.5	3.99968(3)	63.985(1)	5.0	163.03(11)	0.14(9)
4.4	3.99968(3)	63.985(1)	4.8	162.99(11)	0.16(9)
4.6	3.99935(3)	63.969(1)	5.1	162.99(11)	0.16(9)
4.8	3.99944(3)	63.973(1)	5.2	162.99(11)	0.16(9)
4.6	3.99935(3)	63.969(1)	5.2	162.97(11)	0.17(9)
4.8	3.99904(3)	63.954(1)	5.4	162.94(11)	0.19(9)
4.9	3.99880(3)	63.942(1)	5.4	162.96(11)	0.18(9)
4.7	3.99870(3)	63.937(1)	5.1	162.90(11)	0.21(9)
5.0	3.99852(3)	63.929(1)	5.1	162.87(11)	0.22(9)
5.4	3.99839(3)	63.923(2)	5.1	162.87(11)	0.22(9)
5.8	3.99786(4)	63.897(2)	5.3	162.84(11)	0.24(9)
4.6	3.99743(3)	63.877(1)	5.3	162.82(11)	0.25(9)
4.8	3.99713(3)	63.862(1)	5.5	162.78(11)	0.27(9)
5.0	3.99696(3)	63.854(1)	5.5	162.79(11)	0.27(9)
4.7	3.99682(3)	63.848(1)	5.0	162.77(11)	0.28(9)
5.0	3.99653(3)	63.834(2)	5.2	162.73(11)	0.29(9)
5.2	3.99616(3)	63.816(2)	5.3	162.71(11)	0.31(9)
5.0	3.99585(3)	63.801(2)	4.9	162.64(11)	0.34(9)
5.2	3.99565(3)	63.792(2)	4.9	162.63(11)	0.35(9)
5.3	3.99547(3)	63.783(2)	5.0	162.60(11)	0.36(9)
5.3	3.99526(3)	63.773(2)	5.0	162.58(11)	0.37(9)
5.3	3.99502(3)	63.761(2)	5.0	162.58(11)	0.37(9)
5.1	3.99466(3)	63.744(2)	5.0	162.58(11)	0.37(9)
4.6	3.99432(3)	63.728(1)	5.0	162.51(11)	0.41(9)
4.3	3.99387(3)	63.706(1)	5.1	162.52(12)	0.40(9)
4.4	3.99342(3)	63.685(1)	5.0	162.48(11)	0.42(9)
4.6	3.99270(3)	63.650(1)	5.1	162.45(11)	0.44(9)
7.9	3.99278(5)	63.654(2)	5.2	162.43(11)	0.45(9)
8.1	3.99248(5)	63.640(3)	5.1	162.40(11)	0.47(9)
8.3	3.99172(5)	63.603(3)	5.0	162.35(11)	0.49(9)
8.2	3.99083(5)	63.561(3)	4.9	162.31(11)	0.51(9)
8.3	3.98996(5)	63.519(3)	4.8	162.25(11)	0.54(9)
8.3	3.98912(5)	63.479(3)	5.1	162.27(11)	0.53(9)

sample Rwp(%)	Sample lattice constant, a (Å)	sample unit cell volume, V (Å^3)	CaF_2 Rwp(%)	CaF2 cell volume, V (Å^3)	Pressure (GPa)
8.2	3.9894(5)	63.493(3)	5.0	162.23(12)	0.55(9)
8.8	3.98912(5)	63.479(3)	4.9	162.23(11)	0.55(9)
8.5	3.98867(5)	63.458(3)	5.0	162.20(11)	0.57(9)
8.6	3.98846(5)	63.448(3)	4.9	162.18(11)	0.58(9)
8.2	3.98805(5)	63.428(3)	4.9	162.13(12)	0.60(9)
8.1	3.98755(5)	63.404(2)	4.9	162.12(12)	0.60(9)
8.1	3.98692(5)	63.374(2)	4.8	162.09(11)	0.62(9)
8.2	3.98582(5)	63.322(2)	4.9	162.05(11)	0.64(9)
8.3	3.98512(5)	63.288(3)	4.8	162.02(11)	0.66(9)
4.8	3.98454(3)	63.261(2)	4.8	161.93(12)	0.71(9)
4.8	3.98387(3)	63.229(2)	4.8	161.90(11)	0.72(9)
4.8	3.98311(3)	63.193(2)	4.8	161.83(11)	0.76(9)
4.7	3.98209(3)	63.144(2)	4.7	161.79(11)	0.78(9)
4.7	3.98127(3)	63.105(2)	4.7	161.77(11)	0.79(9)
4.9	3.98051(3)	63.069(2)	4.5	161.75(11)	0.80(9)
5.6	3.97949(4)	63.020(2)	4.5	161.70(11)	0.83(9)
7.3	3.97917(5)	63.005(2)	4.6	161.67(12)	0.84(9)
7.4	3.97852(5)	62.974(3)	4.5	161.63(12)	0.87(9)
7.4	3.97709(5)	62.907(3)	4.5	161.63(11)	0.86(9)
4.6	3.97636(4)	62.872(2)	4.4	161.60(11)	0.88(9)
4.6	3.97545(4)	62.829(2)	4.4	161.55(11)	0.90(9)
4.5	3.97426(4)	62.772(2)	4.4	161.54(11)	0.91(9)
4.5	3.97234(4)	62.681(2)	4.5	161.48(11)	0.94(9)
-	-	-	4.6	161.40(11)	0.99(9)
-	-	-	4.6	161.36(11)	1.01(9)
-	-	-	5.3	161.32(11)	1.03(9)
-	-	-	5.2	161.29(11)	1.05(9)
-	-	-	5.2	161.23(11)	1.08(9)
-	-	-	5.2	161.23(11)	1.08(9)
-	-	-	5.6	161.20(11)	1.09(9)
-	-	-	5.7	161.17(11)	1.11(9)
-	-	-	5.8	161.16(11)	1.12(9)
-	-	-	6.2	161.15(11)	1.12(9)
-	-	-	6.6	161.10(11)	1.15(9)
-	-	-	6.6	161.04(11)	1.18(9)
-	-	-	5.9	160.99(9)	1.21(9)
-	-	-	5.9	160.99(11)	1.21(9)
-	-	-	5.7	160.95(11)	1.23(9)
-	-	-	5.7	160.86(11)	1.28(9)

sample Rwp(%)	Sample lattice constant, a (Å)	sample unit cell volume, V (Å^3)	CaF_2 Rwp(%)	CaF2 cell volume, V (Å^3)	Pressure (GPa)
-	-	-	5.7	160.79(9)	1.32(9)
-	-	-	6.1	160.72(9)	1.35(9)
-	-	-	6.3	160.68(9)	1.38(9)
-	-	-	7.4	160.66(11)	1.39(9)
-	-	-	8.0	160.59(11)	1.43(9)
-	-	-	7.7	160.54(9)	1.45(9)
-	-	-	8.4	160.51(9)	1.47(9)
-	-	-	8.5	160.44(9)	1.51(9)
-	-	-	8.8	160.39(9)	1.54(9)
-	-	-	8.6	160.35(8)	1.56(9)
-	-	-	8.7	160.33(9)	1.57(9)
-	-	-	8.5	160.30(9)	1.58(9)
-	-	-	9.2	160.28(11)	1.60(9)
-	-	-	9.0	160.24(11)	1.62(9)
-	-	-	9.1	160.24(11)	1.62(9)
-	-	-	8.9	160.19(11)	1.65(9)
-	-	-	9.3	160.17(11)	1.66(9)
-	-	-	9.0	160.11(11)	1.69(9)
-	-	-	8.9	160.05(11)	1.73(9)
-	-	-	8.7	160.01(11)	1.75(9)
-	-	-	9.2	160.01(11)	1.75(9)
-	-	-	8.8	160.00(11)	1.75(9)
-	-	-	9.1	160.03(11)	1.74(9)
-	-	-	9.1	159.98(11)	1.76(9)
-	-	-	9.2	160.20(11)	1.64(9)
-	-	-	9.6	160.58(11)	1.43(9)
-	-	-	8.5	159.87(11)	1.83(9)
-	-	-	9.0	159.85(11)	1.84(9)
-	-	-	9.3	159.84(11)	1.84(9)
-	-	-	8.7	159.82(11)	1.86(9)
-	-	-	9.1	159.78(11)	1.88(9)
-	-	-	9.6	159.75(11)	1.89(9)
-	-	-	8.9	159.73(11)	1.90(9)
-	-	-	9.4	159.67(11)	1.94(9)
-	-	-	9.3	159.63(11)	1.96(9)
-	-	-	9.1	159.61(11)	1.97(9)
-	-	-	9.5	159.59(11)	1.99(9)
-	-	-	9.8	159.57(11)	2.00(9)
-	-	-	10.0	159.55(11)	2.01(9)

sample Rwp(%)	Sample lattice constant, a (Å)	sample unit cell volume, V (Å^3)	CaF_2 Rwp(%)	CaF2 cell volume, V (Å^3)	Pressure (GPa)
-	-	-	10.0	159.51(11)	2.03(9)
-	-	-	10.1	159.49(11)	2.05(9)
-	-	-	10.9	159.47(11)	2.06(9)
-	-	-	11.0	159.43(11)	2.08(9)
-	-	-	10.8	159.39(11)	2.10(9)
-	-	-	5.0	159.34(11)	2.13(9)
-	-	-	4.9	159.26(9)	2.18(9)
-	-	-	4.5	159.17(9)	2.23(9)
-	-	-	4.1	159.12(11)	2.26(9)
-	-	-	4.1	158.99(11)	2.34(9)
-	-	-	3.9	158.85(11)	2.42(9)
-	-	-	4.2	158.77(11)	2.46(9)
-	-	-	3.9	158.70(9)	2.50(9)
-	-	-	4.2	158.65(11)	2.54(9)
-	-	-	3.9	158.58(9)	2.58(9)
-	-	-	3.8	158.49(9)	2.63(9)
-	-	-	3.9	158.43(9)	2.67(9)
-	-	-	4.1	158.39(9)	2.69(9)
-	-	-	3.9	158.26(9)	2.77(9)
-	-	-	4.1	158.12(11)	2.86(9)
-	-	-	4.4	157.97(11)	2.94(9)
-	-	-	4.5	157.86(11)	3.01(9)
-	-	-	4.6	157.79(11)	3.05(9)
-	-	-	4.9	157.73(15)	3.09(9)
-	-	-	5.6	157.59(24)	3.18(9)
-	-	-	5.1	157.58(17)	3.18(9)
-	-	-	5.4	157.52(17)	3.22(9)
-	-	-	5.3	157.48(17)	3.24(9)
-	-	-	5.4	157.47(17)	3.26(9)
-	-	-	4.9	157.42(18)	3.29(9)
-	-	-	5.1	157.38(17)	3.31(9)
-	-	-	4.4	157.33(18)	3.34(9)
-	-	-	4.5	157.26(18)	3.38(9)
-	-	-	4.1	157.18(19)	3.44(9)
-	-	-	4.2	157.12(19)	3.48(9)
-	-	-	4.0	157.08(19)	3.50(9)
-	-	-	3.9	157.02(20)	3.53(9)
-	-	-	3.9	157.01(20)	3.54(9)
-	-	-	3.8	156.97(20)	3.57(9)

sample Rwp(%)	Sample lattice constant, a (Å)	sample unit cell volume, V (Å^3)	CaF_2 Rwp(%)	CaF2 cell volume, V (Å^3)	Pressure (GPa)
-	-	-	3.7	156.93(21)	3.60(9)
-	-	-	3.7	156.86(21)	3.64(9)
-	-	-	3.6	156.79(21)	3.68(9)
-	-	-	3.6	156.76(21)	3.70(9)
-	-	-	3.6	156.70(21)	3.74(9)
-	-	-	3.6	156.67(21)	3.76(9)
-	-	-	3.5	156.62(21)	3.79(9)
-	-	-	3.5	156.57(21)	3.82(9)
-	-	-	3.5	156.57(21)	3.82(9)
-	-	-	3.5	156.50(21)	3.87(9)
-	-	-	3.5	156.43(20)	3.91(9)
-	-	-	3.8	156.37(9)	3.95(9)
-	-	-	3.9	156.30(8)	4.00(9)
-	-	-	3.9	156.23(9)	4.04(9)
-	-	-	3.6	156.18(9)	4.08(9)
-	-	-	3.6	156.13(9)	4.11(9)
-	-	-	3.6	156.06(9)	4.15(9)
-	-	-	3.9	156.02(8)	4.18(9)
-	-	-	3.8	155.98(8)	4.21(9)
-	-	-	3.7	155.95(9)	4.23(9)
-	-	-	3.9	155.89(8)	4.26(9)
-	-	-	4.0	155.83(8)	4.31(9)
-	-	-	4.2	155.77(8)	4.35(9)
-	-	-	4.2	155.65(7)	4.43(9)
-	-	-	3.9	155.56(7)	4.49(9)
-	-	-	4.2	155.47(7)	4.55(9)
-	-	-	3.7	155.37(7)	4.62(9)
-	-	-	4.2	155.30(16)	4.66(9)
-	-	-	4.4	155.25(16)	4.70(9)
-	-	-	4.7	155.18(15)	4.75(9)
-	-	-	4.4	155.09(15)	4.81(9)
-	-	-	4.5	155.06(15)	4.83(9)
-	-	-	4.4	155.00(15)	4.87(9)
-	-	-	4.9	154.95(15)	4.90(9)
-	-	-	4.6	154.90(15)	4.94(9)
-	-	-	4.6	154.85(15)	4.97(9)
-	-	-	5.0	154.77(14)	5.03(9)
-	-	-	4.7	154.66(14)	5.10(9)
-	-	-	4.8	154.59(14)	5.15(9)

sample Rwp(%)	Sample lattice constant, a (Å)	sample unit cell volume, V (Å^3)	CaF_2 Rwp(%)	CaF2 cell volume, V (Å^3)	Pressure (GPa)
-	-	-	4.9	154.52(14)	5.20(9)
-	-	-	4.7	154.46(14)	5.24(9)
-	-	-	5.4	154.38(14)	5.30(9)
-	-	-	5.1	154.31(14)	5.35(9)
-	-	-	4.6	154.24(14)	5.39(9)
-	-	-	4.7	154.15(14)	5.46(9)
-	-	-	5.2	154.11(14)	5.49(9)
-	-	-	5.7	154.05(13)	5.53(9)
-	-	-	5.5	154.00(13)	5.57(9)
-	-	-	6.0	153.91(13)	5.63(9)
-	-	-	6.0	153.84(13)	5.68(9)
-	-	-	5.8	153.73(13)	5.76(9)
-	-	-	5.9	153.63(13)	5.84(9)
-	-	-	6.4	153.56(12)	5.88(9)
-	-	-	6.5	153.47(12)	5.95(9)
-	-	-	6.3	153.38(12)	6.02(9)
-	-	-	6.3	153.31(12)	6.06(9)
-	-	-	6.5	153.23(12)	6.13(9)
-	-	-	6.4	153.16(12)	6.18(9)
-	-	-	6.4	153.11(12)	6.21(9)
-	-	-	6.2	153.08(12)	6.24(9)
-	-	-	6.3	153.04(12)	6.27(9)
-	-	-	6.2	153.02(12)	6.28(9)
-	-	-	6.3	153.00(12)	6.29(9)
-	-	-	6.3	153.01(12)	6.29(9)
-	-	-	6.2	153.04(12)	6.27(9)
-	-	-	6.0	153.10(12)	6.23(9)
-	-	-	5.9	153.17(12)	6.17(9)
-	-	-	5.7	153.27(12)	6.10(9)
-	-	-	5.7	153.38(12)	6.02(9)
-	-	-	5.7	153.48(12)	5.94(9)
-	-	-	5.5	153.61(12)	5.85(9)
-	-	-	5.2	153.77(12)	5.73(9)
-	-	-	5.1	153.93(12)	5.62(9)
-	-	-	5.0	154.11(12)	5.49(9)
-	-	-	4.8	154.35(12)	5.32(9)
-	-	-	5.4	154.67(12)	5.10(9)
-	-	-	5.1	155.07(12)	4.82(9)
-	-	-	4.7	155.50(12)	4.53(9)

sample Rwp(%)	Sample lattice constant, a (Å)	sample unit cell volume, V (Å^3)	CaF_2 Rwp(%)	CaF2 cell volume, V (Å^3)	Pressure (GPa)
-	-	-	4.8	156.02(12)	4.18(9)
-	-	-	4.7	156.59(12)	3.81(9)
-	-	-	4.9	157.11(12)	3.48(9)
-	-	-	5.0	157.27(12)	3.38(9)
-	-	-	4.8	157.30(12)	3.36(9)
-	-	-	4.9	157.32(12)	3.35(9)
-	-	-	4.8	157.34(12)	3.34(9)
-	-	-	5.2	157.35(12)	3.32(9)
-	-	-	5.0	157.36(12)	3.32(9)
-	-	-	4.9	157.35(12)	3.33(9)

Table B.5: Weighted profile R factors for both sample and pressure standard, lattice constant for the x=0.3 sample, unit cell volumes for both the sample and the CaF_2 pressure standard, and the pressure calculated from the CaF_2 using the decompression cell volume as V_0.

sample Rwp(%)	Sample lattice constant, a (Å)	sample unit cell volume, V (Å^3)	CaF_2 Rwp(%)	CaF2 cell volume, V (Å^3)	Pressure (GPa)
5.0	3.99109(7)	63.573(3)	3.7	163.01(2)	0.19(5)
5.2	3.99130(7)	63.584(3)	3.7	163.01(2)	0.19(5)
5.1	3.99123(7)	63.580(3)	3.7	163.03(2)	0.18(5)
5.0	3.99116(7)	63.577(4)	3.7	163.03(2)	0.18(5)
5.3	3.99159(8)	63.597(4)	3.7	163.02(2)	0.18(5)
5.1	3.99182(8)	63.608(4)	3.9	163.02(2)	0.18(5)
4.9	3.99186(8)	63.610(4)	3.7	163.02(1)	0.18(5)
4.7	3.99176(8)	63.605(4)	3.7	163.01(1)	0.19(5)
4.7	3.99184(8)	63.609(4)	3.8	163.00(1)	0.19(5)
4.7	3.99177(8)	63.606(4)	3.6	163.00(1)	0.19(5)
4.6	3.99168(8)	63.601(4)	3.8	163.01(1)	0.19(5)
4.7	3.99167(8)	63.601(4)	3.6	162.99(1)	0.20(5)
4.8	3.99198(9)	63.616(4)	3.6	163.00(1)	0.19(5)
5.0	3.99199(8)	63.616(4)	3.5	162.99(1)	0.20(5)
5.3	3.99169(8)	63.602(4)	3.4	162.98(1)	0.20(5)
4.8	3.99143(8)	63.590(4)	3.4	163.00(1)	0.19(5)
4.7	3.99160(8)	63.598(4)	3.7	162.99(1)	0.20(5)
4.6	3.99163(8)	63.599(4)	4.0	162.98(1)	0.20(5)
5.1	3.99208(8)	63.621(4)	4.0	162.96(1)	0.21(5)
4.8	3.99182(8)	63.608(4)	3.7	162.97(1)	0.21(5)
4.8	3.99165(8)	63.600(4)	3.8	162.95(1)	0.22(5)
5.0	3.99147(8)	63.591(4)	3.8	162.95(1)	0.22(5)
5.3	3.99179(8)	63.607(4)	3.8	162.95(1)	0.22(5)
5.6	3.99191(8)	63.613(4)	3.8	162.93(1)	0.23(5)
4.9	3.99089(8)	63.564(4)	3.8	162.92(1)	0.23(5)
5.1	3.99122(8)	63.580(4)	3.6	162.90(1)	0.24(5)
4.9	3.99087(7)	63.563(3)	3.9	162.91(1)	0.24(5)
4.8	3.99066(7)	63.553(4)	3.6	162.90(1)	0.24(5)
4.7	3.99045(8)	63.543(4)	3.9	162.89(1)	0.25(5)
4.8	3.99034(8)	63.537(4)	4.2	162.87(1)	0.26(5)
4.8	3.99029(8)	63.535(4)	3.8	162.87(1)	0.26(5)
4.8	3.99004(8)	63.523(4)	4.0	162.84(1)	0.27(5)
5.0	3.98969(8)	63.506(4)	4.1	162.83(1)	0.28(5)
4.8	3.98972(8)	63.508(4)	3.8	162.81(1)	0.29(5)
4.9	3.98972(8)	63.508(4)	3.8	162.80(1)	0.29(5)

sample Rwp(%)	Sample lattice constant, a (Å)	sample unit cell volume, V (Å^3)	CaF_2 Rwp(%)	CaF2 cell volume, V (Å^3)	Pressure (GPa)
5.0	3.98959(8)	63.501(4)	4.0	162.79(1)	0.30(5)
5.1	3.98939(8)	63.492(4)	3.8	162.76(1)	0.32(5)
4.9	3.98899(7)	63.473(3)	3.8	162.75(1)	0.32(5)
4.9	3.98861(7)	63.455(4)	4.1	162.73(1)	0.33(5)
5.3	3.98869(8)	63.459(4)	3.9	162.72(1)	0.34(5)
5.1	3.98827(8)	63.439(4)	4.1	162.69(1)	0.35(5)
5.2	3.98747(8)	63.400(4)	4.1	162.64(1)	0.38(5)
5.9	3.98675(5)	63.366(5)	4.0	162.61(1)	0.39(5)
5.9	3.98669(9)	63.363(4)	4.2	162.59(1)	0.40(5)
5.8	3.98593(10)	63.327(5)	4.1	162.55(1)	0.42(5)
6.3	3.98538(10)	63.301(5)	4.3	162.52(1)	0.44(5)
6.7	3.98506(10)	63.286(5)	4.3	162.51(1)	0.44(5)
6.9	3.98479(10)	63.273(5)	4.7	162.49(1)	0.45(5)
6.4	3.98476(10)	63.271(5)	4.6	162.47(1)	0.46(5)
6.0	3.98489(9)	63.277(4)	4.4	162.46(1)	0.47(6)
6.3	3.98454(9)	63.261(5)	4.8	162.45(1)	0.47(6)
6.3	3.98455(9)	63.261(5)	4.3	162.44(1)	0.48(6)
6.7	3.98412(10)	63.241(5)	4.2	162.44(1)	0.48(6)
6.2	3.98404(9)	63.237(4)	4.4	162.44(1)	0.48(6)
6.9	3.98392(10)	63.231(5)	4.4	162.44(1)	0.48(6)
6.6	3.98385(9)	63.228(4)	4.4	162.44(1)	0.48(6)
7.0	3.98385(9)	63.228(4)	4.5	162.44(1)	0.47(6)
6.2	3.98403(9)	63.237(4)	4.4	162.44(1)	0.48(6)
6.6	3.98378(9)	63.225(4)	4.3	162.39(1)	0.50(6)
5.6	3.98403(8)	63.236(4)	4.1	162.37(1)	0.51(6)
6.0	3.98355(9)	63.214(4)	3.9	162.35(1)	0.52(6)
6.7	3.98318(9)	63.196(4)	4.0	162.36(1)	0.52(6)
6.6	3.98339(9)	63.206(4)	4.1	162.35(1)	0.52(6)
6.4	3.98372(9)	63.222(4)	4.0	162.34(1)	0.53(6)
5.2	3.98397(8)	63.233(4)	4.0	162.33(1)	0.54(6)
5.6	3.98373(8)	63.222(4)	4.0	162.31(1)	0.54(6)
5.7	3.98351(8)	63.212(4)	4.3	162.31(1)	0.54(6)
5.1	3.98319(7)	63.197(4)	4.6	162.31(1)	0.55(6)
5.4	3.98300(8)	63.188(4)	4.2	162.28(1)	0.56(6)
5.4	3.98252(8)	63.164(4)	4.2	162.26(1)	0.57(6)
5.2	3.98217(7)	63.148(3)	3.9	162.22(1)	0.59(6)
5.5	3.98190(8)	63.135(4)	4.1	162.22(1)	0.59(6)
5.7	3.98164(8)	63.123(4)	4.1	162.20(1)	0.60(6)
6.0	3.98154(8)	63.118(4)	4.0	162.19(1)	0.61(6)

sample Rwp(%)	Sample lattice constant, a (Å)	sample unit cell volume, V (Å^3)	CaF_2 Rwp(%)	CaF2 cell volume, V (Å^3)	Pressure (GPa)
5.7	3.98155(8)	63.118(4)	4.3	162.18(1)	0.61(6)
6.0	3.98155(8)	63.119(4)	4.8	162.15(1)	0.63(6)
6.6	3.98156(9)	63.119(4)	4.6	162.14(1)	0.63(6)
6.1	3.98098(9)	63.091(4)	4.7	162.12(1)	0.64(6)
5.3	3.98035(8)	63.062(4)	4.7	162.10(1)	0.65(6)
5.3	3.97981(8)	63.036(4)	4.9	162.09(1)	0.66(6)
5.2	3.97942(8)	63.017(4)	4.7	162.08(1)	0.66(6)
5.4	3.97900(8)	62.997(4)	4.9	162.04(1)	0.68(6)
5.4	3.97893(8)	62.994(4)	4.9	162.01(1)	0.70(6)
5.5	3.97885(8)	62.990(4)	5.2	162.00(1)	0.70(6)
5.3	3.97864(8)	62.980(4)	5.0	161.98(1)	0.71(6)
5.6	3.97823(8)	62.961(4)	5.1	161.98(1)	0.72(6)
5.4	3.97813(8)	62.956(4)	4.8	161.95(1)	0.73(6)
5.5	3.97794(8)	62.947(4)	4.7	161.93(1)	0.74(6)
5.3	3.97757(8)	62.929(4)	4.7	161.90(1)	0.76(6)
5.0	3.97709(8)	62.907(4)	4.4	161.89(1)	0.76(6)
4.8	3.97686(7)	62.896(3)	4.2	161.89(1)	0.76(6)
5.0	3.97683(8)	62.894(4)	4.1	161.88(1)	0.77(6)
4.9	3.97652(8)	62.880(4)	4.4	161.86(1)	0.78(6)
4.9	3.97643(8)	62.875(4)	4.3	161.85(1)	0.78(6)
5.0	3.97619(8)	62.864(4)	4.5	161.83(1)	0.79(6)
5.0	3.97603(7)	62.856(4)	4.5	161.83(1)	0.80(6)
5.6	3.97581(8)	62.846(4)	4.6	161.82(1)	0.80(6)
5.1	3.97552(7)	62.832(4)	4.4	161.80(1)	0.81(6)
5.4	3.97504(8)	62.809(4)	4.5	161.76(1)	0.83(6)
5.2	3.97452(7)	62.785(3)	4.6	161.73(1)	0.85(6)
5.7	3.97378(8)	62.750(4)	4.6	161.71(1)	0.86(6)
4.9	3.97365(7)	62.743(3)	4.4	161.67(1)	0.88(6)
5.2	3.97340(8)	62.732(4)	4.6	161.65(1)	0.89(6)
5.1	3.97307(8)	62.716(4)	4.5	161.63(1)	0.90(6)
5.1	3.97260(8)	62.694(4)	4.9	161.59(1)	0.92(6)
5.0	3.97211(7)	62.671(3)	5.0	161.58(1)	0.93(6)
4.8	3.97190(7)	62.661(3)	4.9	161.57(1)	0.93(6)
5.2	3.97150(8)	62.642(4)	4.8	161.55(1)	0.94(9)
4.9	3.97120(7)	62.628(4)	4.2	161.52(1)	0.96(9)
5.0	3.97072(8)	62.605(4)	4.2	161.49(1)	0.97(9)
5.2	3.97035(8)	62.588(4)	4.8	161.48(1)	0.98(9)
5.0	3.96984(8)	62.563(4)	4.4	161.47(1)	0.99(9)
4.8	3.96946(8)	62.545(4)	4.0	161.45(1)	1.00(9)

sample Rwp(%)	Sample lattice constant, a (Å)	sample unit cell volume, V (Å^3)	CaF_2 Rwp(%)	CaF2 cell volume, V (Å^3)	Pressure (GPa)
4.5	3.96915(7)	62.531(3)	3.9	161.43(1)	1.00(9)
4.4	3.96858(7)	62.504(3)	4.0	161.39(1)	1.03(9)
4.5	3.96803(7)	62.478(3)	4.0	161.36(1)	1.05(9)
4.8	3.96736(7)	62.446(4)	3.9	161.30(1)	1.07(9)
4.7	3.96630(7)	62.396(3)	4.1	161.25(1)	1.10(9)
4.9	3.96571(8)	62.368(4)	4.0	161.23(1)	1.11(9)
5.0	3.96533(8)	62.350(4)	4.0	161.23(1)	1.11(9)
4.6	3.96433(8)	62.303(4)	4.0	161.18(1)	1.14(9)
4.7	3.96358(8)	62.268(4)	4.2	161.15(1)	1.16(9)
4.5	3.96322(8)	62.251(4)	4.1	161.12(1)	1.17(9)
4.6	3.96299(8)	62.240(4)	4.1	161.11(1)	1.18(9)
4.6	3.96246(8)	62.215(4)	4.2	161.07(1)	1.20(9)
4.5	3.96177(8)	62.182(4)	4.3	161.04(1)	1.22(9)
4.5	3.96121(8)	62.156(4)	4.2	161.00(1)	1.24(9)
4.5	3.96066(8)	62.130(4)	4.1	160.98(1)	1.25(9)
4.5	3.96009(8)	62.103(4)	4.3	160.94(1)	1.27(9)
4.5	3.95921(8)	62.062(4)	4.2	160.91(1)	1.29(9)
4.2	3.95847(8)	62.027(4)	4.3	160.89(1)	1.30(9)
4.3	3.95796(8)	62.003(4)	4.2	160.87(1)	1.31(9)
4.1	3.95718(8)	61.966(4)	4.2	160.84(1)	1.33(9)
4.0	3.95455(8)	61.843(4)	4.6	160.72(1)	1.39(9)
4.1	3.95353(8)	61.795(4)	4.6	160.68(1)	1.41(9)
4.1	3.95250(8)	61.747(4)	4.3	160.65(1)	1.43(9)
4.2	3.95133(9)	61.692(4)	4.1	160.60(1)	1.46(9)
4.1	3.94948(9)	61.605(4)	4.0	160.53(1)	1.49(9)
4.2	3.94747(9)	61.512(4)	4.1	160.45(1)	1.54(9)
4.2	3.94672(9)	61.476(4)	4.1	160.42(1)	1.56(9)
4.3	3.94630(9)	61.457(4)	4.0	160.41(1)	1.56(9)
4.4	3.94583(10)	61.435(4)	4.0	160.40(1)	1.57(9)
4.2	3.94510(9)	61.401(4)	4.0	160.38(1)	1.58(9)
4.1	3.94418(9)	61.358(4)	4.1	160.35(1)	1.59(9)
4.2	3.94268(9)	61.288(4)	4.2	160.31(1)	1.62(9)
4.3	3.94187(10)	61.250(5)	4.2	160.29(1)	1.63(9)
-	-	-	4.2	160.27(1)	1.64(9)
-	-	-	4.2	160.25(1)	1.65(9)
-	-	-	4.2	160.22(1)	1.67(9)
-	-	-	4.3	160.20(1)	1.68(9)
-	-	-	4.3	160.18(1)	1.69(9)
-	-	-	4.3	160.12(1)	1.72(9)

sample Rwp(%)	Sample lattice constant, a (Å)	sample unit cell volume, V (Å^3)	CaF_2 Rwp(%)	CaF2 cell volume, V (Å^3)	Pressure (GPa)
-	-	-	4.4	160.07(1)	1.75(9)
-	-	-	4.4	160.03(1)	1.78(9)
-	-	-	4.5	159.99(1)	1.80(9)
-	-	-	4.5	159.94(1)	1.82(9)
-	-	-	4.5	159.91(1)	1.84(9)
-	-	-	4.6	159.85(1)	1.88(9)
-	-	-	4.6	159.81(1)	1.90(9)
-	-	-	4.6	159.78(1)	1.92(9)
-	-	-	4.6	159.72(1)	1.95(9)
-	-	-	4.6	159.69(1)	1.97(9)
-	-	-	4.6	159.67(1)	1.98(9)
-	-	-	4.6	159.64(1)	2.00(9)
-	-	-	4.6	159.62(1)	2.01(9)
-	-	-	4.7	159.59(1)	2.02(9)
-	-	-	4.6	159.53(1)	2.06(9)
-	-	-	4.6	159.48(1)	2.09(9)
-	-	-	4.5	159.46(1)	2.10(9)
-	-	-	4.5	159.42(1)	2.12(9)
-	-	-	4.5	159.39(1)	2.14(9)
-	-	-	4.4	159.37(1)	2.15(9)
-	-	-	4.4	159.33(1)	2.17(9)
-	-	-	4.4	159.31(1)	2.19(9)
-	-	-	4.4	159.24(1)	2.23(9)
-	-	-	4.4	159.17(1)	2.27(9)
-	-	-	4.3	159.14(1)	2.29(9)
-	-	-	4.3	159.10(1)	2.31(9)
-	-	-	4.3	159.08(1)	2.32(9)
-	-	-	4.2	159.03(1)	2.35(9)
-	-	-	4.3	158.99(1)	2.37(9)
-	-	-	4.3	158.94(1)	2.40(9)
-	-	-	4.3	158.90(1)	2.43(9)
-	-	-	4.4	158.84(1)	2.46(9)
-	-	-	4.4	158.78(1)	2.50(9)
-	-	-	4.4	158.69(1)	2.55(9)
-	-	-	4.4	158.62(1)	2.59(9)
-	-	-	4.5	158.56(1)	2.63(9)
-	-	-	4.7	158.49(1)	2.67(9)
-	-	-	5.0	158.40(1)	2.72(9)
-	-	-	5.2	158.35(1)	2.75(9)

sample Rwp(%)	Sample lattice constant, a (Å)	sample unit cell volume, V (Å^3)	CaF_2 Rwp(%)	CaF2 cell volume, V (Å^3)	Pressure (GPa)
-	-	-	5.4	158.29(1)	2.79(9)
-	-	-	5.5	158.25(1)	2.82(9)
-	-	-	5.7	158.20(1)	2.84(9)
-	-	-	5.9	158.16(1)	2.87(9)
-	-	-	6.1	158.11(1)	2.90(9)
-	-	-	6.4	158.05(1)	2.94(9)
-	-	-	6.7	157.98(1)	2.98(9)
-	-	-	6.8	157.94(1)	3.00(9)
-	-	-	6.9	157.92(1)	3.02(9)
-	-	-	7.0	157.88(1)	3.04(9)
-	-	-	7.2	157.85(1)	3.06(9)
-	-	-	7.3	157.82(1)	3.08(9)
-	-	-	7.3	157.79(1)	3.09(9)
-	-	-	7.4	157.75(1)	3.12(9)
-	-	-	7.6	157.69(1)	3.16(9)
-	-	-	7.7	157.63(1)	3.19(9)
-	-	-	7.8	157.58(1)	3.23(9)
-	-	-	7.9	157.51(1)	3.27(9)
-	-	-	7.9	157.36(1)	3.36(9)
-	-	-	7.9	157.24(1)	3.44(9)
-	-	-	7.8	157.15(1)	3.50(9)
-	-	-	7.7	157.08(1)	3.54(9)
-	-	-	7.6	157.00(1)	3.59(9)
-	-	-	7.4	156.94(1)	3.63(9)
-	-	-	7.4	156.88(1)	3.67(9)
-	-	-	7.3	156.82(1)	3.70(9)
-	-	-	7.1	156.76(1)	3.74(9)
-	-	-	7.0	156.68(1)	3.79(9)
-	-	-	6.9	156.63(1)	3.83(9)
-	-	-	6.9	156.57(1)	3.87(9)
-	-	-	6.7	156.49(1)	3.92(9)
-	-	-	6.6	156.41(1)	3.97(9)
-	-	-	6.4	156.35(1)	4.01(9)
-	-	-	6.3	156.29(1)	4.05(9)
-	-	-	6.2	156.22(1)	4.09(9)
-	-	-	6.1	156.17(1)	4.13(9)
-	-	-	6.0	156.09(1)	4.18(9)
-	-	-	6.0	155.97(1)	4.26(9)
-	-	-	5.8	155.86(1)	4.33(9)

sample Rwp(%)	Sample lattice constant, a (Å)	sample unit cell volume, V (Å^3)	CaF_2 Rwp(%)	CaF2 cell volume, V (Å^3)	Pressure (GPa)
-	-	-	5.6	155.74(1)	4.41(9)
-	-	-	5.5	155.60(1)	4.50(9)
-	-	-	5.3	155.53(1)	4.55(9)
-	-	-	5.2	155.46(1)	4.60(9)
-	-	-	5.1	155.39(1)	4.65(9)
-	-	-	5.1	155.31(1)	4.70(9)
-	-	-	5.0	155.23(1)	4.75(9)
-	-	-	4.9	155.18(1)	4.79(9)
-	-	-	4.8	155.11(1)	4.83(9)
-	-	-	4.7	155.06(1)	4.87(9)
-	-	-	4.7	154.99(1)	4.92(9)
-	-	-	5.8	154.93(1)	4.96(9)
-	-	-	5.8	154.87(1)	5.00(9)
-	-	-	5.7	154.80(1)	5.05(9)
-	-	-	5.4	154.68(1)	5.13(9)
-	-	-	5.4	154.56(1)	5.22(9)
-	-	-	5.3	154.46(1)	5.29(9)
-	-	-	5.1	154.37(1)	5.35(9)
-	-	-	5.2	154.26(1)	5.43(9)
-	-	-	5.3	154.15(1)	5.51(9)
-	-	-	5.0	154.07(1)	5.56(9)
-	-	-	5.0	154.00(1)	5.62(9)
-	-	-	5.1	153.95(1)	5.65(9)
-	-	-	5.1	153.90(1)	5.69(9)
-	-	-	5.1	153.84(1)	5.73(9)
-	-	-	5.0	153.78(1)	5.77(9)
-	-	-	4.8	153.74(1)	5.80(9)
-	-	-	5.2	153.70(1)	5.83(9)
-	-	-	5.3	153.64(1)	5.87(9)
-	-	-	4.9	153.59(1)	5.91(9)
-	-	-	4.9	153.53(1)	5.96(9)
-	-	-	4.9	153.43(1)	6.03(9)
-	-	-	4.7	153.33(1)	6.10(9)
-	-	-	5.0	153.25(1)	6.16(9)
-	-	-	4.2	153.18(1)	6.21(9)
-	-	-	4.1	153.12(1)	6.25(9)
-	-	-	4.2	153.07(1)	6.29(9)
-	-	-	4.1	153.02(1)	6.33(9)
-	-	-	4.4	152.99(1)	6.35(9)

sample Rwp(%)	Sample lattice constant, a (Å)	sample unit cell volume, V (Å^3)	CaF_2 Rwp(%)	CaF2 cell volume, V (Å^3)	Pressure (GPa)
-	-	-	4.0	152.97(1)	6.37(9)
-	-	-	4.0	152.94(1)	6.39(9)
-	-	-	4.0	152.91(1)	6.41(9)
-	-	-	4.1	152.86(1)	6.45(9)
-	-	-	4.0	152.83(1)	6.47(9)
-	-	-	4.3	152.80(1)	6.49(9)
-	-	-	4.1	152.76(1)	6.52(9)
-	-	-	4.0	152.73(1)	6.54(9)
-	-	-	3.9	152.71(1)	6.57(9)
-	-	-	3.8	152.67(1)	6.59(9)
-	-	-	3.8	152.63(1)	6.62(9)
-	-	-	4.0	152.59(1)	6.65(9)
-	-	-	4.1	152.56(1)	6.68(9)
-	-	-	4.1	152.53(1)	6.70(9)
-	-	-	4.1	152.50(1)	6.72(9)
-	-	-	4.3	152.47(1)	6.75(9)
-	-	-	4.2	152.43(1)	6.78(9)
-	-	-	4.2	152.41(1)	6.79(9)
-	-	-	4.3	152.39(1)	6.81(9)
-	-	-	4.5	152.37(1)	6.82(9)
-	-	-	4.1	152.35(1)	6.83(9)
-	-	-	4.3	152.34(1)	6.84(9)
-	-	-	4.5	152.34(1)	6.84(9)
-	-	-	4.2	152.34(1)	6.84(9)
-	-	-	4.1	152.38(1)	6.81(9)
-	-	-	4.4	152.47(1)	6.74(9)
-	-	-	4.6	152.57(1)	6.67(9)
-	-	-	4.3	152.68(1)	6.58(9)
-	-	-	4.2	152.80(1)	6.50(9)
-	-	-	4.3	152.93(1)	6.40(9)
-	-	-	4.4	153.07(1)	6.29(9)
-	-	-	4.2	153.22(1)	6.18(9)
-	-	-	4.2	153.42(1)	6.03(9)
-	-	-	4.2	153.63(1)	5.88(9)
-	-	-	4.1	153.89(1)	5.69(9)
-	-	-	4.1	154.19(1)	5.48(9)
-	-	-	4.2	154.56(1)	5.22(9)
-	-	-	4.2	155.03(1)	4.89(9)
-	-	-	4.2	155.57(1)	4.53(9)

sample Rwp(%)	Sample lattice constant, a (Å)	sample unit cell volume, V (Å^3)	CaF_2 Rwp(%)	CaF2 cell volume, V (Å^3)	Pressure (GPa)
-	-	-	4.3	156.17(1)	4.13(9)
-	-	-	4.2	156.81(1)	3.71(9)
-	-	-	4.2	157.03(1)	3.57(9)

Table B.6: Weighted profile R factors for both sample and pressure standard, lattice constant for the x=0.4 sample, unit cell volumes for both the sample and the CaF_2 pressure standard, and the pressure calculated from the CaF_2 using the decompression cell volume as V_0.

sample Rwp(%)	Sample lattice constant, a (Å)	sample unit cell volume, V (Å^3)	CaF_2 Rwp(%)	CaF2 cell volume, V (Å^3)	Pressure (GPa)
10.0	3.9859(1)	63.327(6)	5.8	163.36(2)	-0.01(5)
9.5	3.9859(1)	63.328(6)	5.5	163.36(2)	-0.01(5)
9.7	3.9860(1)	63.329(6)	5.6	163.36(2)	-0.01(5)
8.5	3.9859(1)	63.327(5)	5.2	163.36(2)	-0.01(5)
8.3	3.9860(1)	63.328(5)	5.1	163.36(2)	-0.01(5)
4.1	3.9859(1)	63.325(3)	5.2	163.36(2)	-0.01(5)
4.4	3.9858(1)	63.322(3)	5.7	163.36(2)	-0.01(5)
4.2	3.9860(1)	63.331(3)	5.5	163.36(2)	-0.01(5)
4.2	3.9860(1)	63.331(3)	5.9	163.36(2)	-0.01(5)
4.2	3.9858(1)	63.322(3)	5.9	163.36(2)	-0.01(5)
4.2	3.9856(1)	63.313(3)	6.0	163.36(2)	-0.01(5)
5.3	3.9853(1)	63.298(3)	6.6	163.37(2)	-0.02(5)
5.5	3.9851(1)	63.289(3)	6.7	163.36(2)	-0.01(5)
6.7	3.9854(1)	63.302(5)	7.4	163.33(2)	0.00(5)
5.4	3.9854(1)	63.302(4)	6.9	163.33(2)	0.01(5)
5.8	3.9852(1)	63.290(4)	7.0	163.33(2)	0.00(5)
8.8	3.9855(1)	63.305(7)	8.4	163.33(3)	0.00(5)
7.0	3.9855(1)	63.308(5)	7.5	163.33(2)	0.00(5)
6.5	3.9852(1)	63.294(4)	7.2	163.32(2)	0.01(5)
7.3	3.9854(1)	63.303(5)	7.6	163.32(2)	0.01(5)
8.1	3.9854(1)	63.303(6)	8.0	163.32(2)	0.01(5)
9.0	3.9855(1)	63.307(5)	8.3	163.34(2)	0.00(5)
6.3	3.9854(1)	63.301(4)	7.1	163.32(2)	0.01(5)
8.6	3.9854(1)	63.30(5)	8.2	163.31(2)	0.01(5)
6.6	3.9853(1)	63.298(4)	6.9	163.30(3)	0.02(5)
5.9	3.9851(1)	63.286(4)	6.5	163.29(2)	0.02(5)
5.0	3.9852(1)	63.291(3)	6.0	163.29(2)	0.03(5)
4.9	3.9849(1)	63.280(3)	5.9	163.28(2)	0.03(5)
5.5	3.9847(1)	63.270(3)	6.2	163.27(2)	0.03(5)
4.9	3.9851(1)	63.289(3)	5.6	163.27(2)	0.03(5)
4.9	3.9851(1)	63.285(3)	5.5	163.26(2)	0.04(5)
5.2	3.9850(1)	63.285(3)	5.8	163.25(2)	0.04(5)
4.9	3.9846(1)	63.266(3)	5.7	163.22(2)	0.06(5)
4.9	3.9845(1)	63.261(3)	5.7	163.21(2)	0.06(5)
4.7	3.9844(1)	63.256(3)	5.3	163.20(2)	0.07(5)

sample Rwp(%)	Sample lattice constant, a (Å)	sample unit cell volume, V (Å^3)	CaF_2 Rwp(%)	CaF2 cell volume, V (Å^3)	Pressure (GPa)
5.4	3.9845(1)	63.259(4)	5.1	163.19(2)	0.07(5)
9.3	3.9841(1)	63.240(5)	5.3	163.16(2)	0.09(5)
8.8	3.9840(1)	63.235(5)	5.2	163.14(2)	0.10(5)
8.9	3.9835(1)	63.209(5)	5.2	163.13(2)	0.01(5)
8.2	3.9837(1)	63.223(4)	5.0	163.11(2)	0.11(5)
7.8	3.9836(1)	63.215(4)	4.9	163.08(2)	0.13(5)
8.8	3.9832(1)	63.198(5)	5.1	163.03(2)	0.15(5)
8.3	3.9825(1)	63.166(4)	5.0	163.03(2)	0.15(5)
8.1	3.9821(1)	63.144(4)	4.9	162.97(2)	0.18(5)
8.6	3.9820(1)	63.139(5)	5.2	162.94(2)	0.20(5)
7.9	3.9816(1)	63.123(4)	5.0	162.92(2)	0.21(5)
8.2	3.9813(1)	63.108(4)	5.0	162.90(2)	0.22(5)
7.7	3.9814(1)	63.114(4)	4.8	162.89(2)	0.23(5)
8.5	3.9812(1)	63.104(5)	5.2	162.85(2)	0.25(5)
8.2	3.9810(1)	63.092(5)	5.1	162.83(2)	0.25(5)
7.9	3.9809(1)	63.089(4)	5.3	162.83(2)	0.26(5)
8.4	3.9807(1)	63.077(5)	4.9	162.81(2)	0.26(5)
8.6	3.9806(1)	63.071(5)	5.0	162.81(2)	0.26(5)
8.5	3.9806(1)	63.071(5)	5.1	162.80(2)	0.27(5)
9.3	3.9807(1)	63.077(5)	5.3	162.80(2)	0.27(5)
8.4	3.9806(1)	63.072(5)	5.1	162.76(2)	0.29(5)
8.5	3.9804(1)	63.062(5)	5.1	162.77(2)	0.28(5)
8.4	3.9803(1)	63.059(4)	5.0	162.75(2)	0.29(5)
8.0	3.9799(1)	63.042(4)	5.1	162.73(2)	0.30(5)
8.4	3.9798(1)	63.035(4)	5.1	162.73(2)	0.31(5)
8.5	3.9796(1)	63.027(4)	5.4	162.71(2)	0.31(5)
8.5	3.9795(1)	63.023(4)	5.3	162.71(2)	0.32(5)
8.2	3.9795(1)	63.020(4)	5.1	162.69(2)	0.33(5)
7.9	3.9794(1)	63.015(4)	5.0	162.66(2)	0.34(5)
8.5	3.9790(1)	62.998(4)	5.0	162.63(2)	0.35(5)
8.5	3.9790(1)	62.996(5)	5.2	162.61(2)	0.36(5)
7.3	3.9782(1)	62.959(4)	5.0	162.59(2)	0.38(5)
8.2	3.9778(1)	62.940(4)	5.2	162.59(2)	0.38(5)
7.6	3.9780(1)	62.949(4)	4.8	162.57(2)	0.39(5)
7.4	3.9778(1)	62.941(4)	4.8	162.57(2)	0.39(5)
9.1	3.9778(1)	62.942(5)	5.2	162.54(2)	0.40(5)
8.1	3.9779(1)	62.943(4)	4.9	162.53(2)	0.41(5)
7.8	3.9779(1)	62.947(4)	4.9	162.52(2)	0.41(5)
8.6	3.9778(1)	62.941(5)	5.1	162.52(2)	0.41(5)

sample Rwp(%)	Sample lattice constant, a (Å)	sample unit cell volume, V (Å^3)	CaF_2 Rwp(%)	CaF2 cell volume, V (Å^3)	Pressure (GPa)
8.2	3.9775(1)	62.928(5)	5.0	162.49(2)	0.43(6)
7.3	3.9776(1)	62.932(4)	4.8	162.45(2)	0.45(6)
7.5	3.9768(1)	62.895(4)	4.7	162.46(2)	0.44(6)
7.6	3.9766(1)	62.884(4)	4.9	162.44(2)	0.45(6)
8.5	3.9762(1)	62.866(4)	5.1	162.43(2)	0.46(6)
7.4	3.9761(1)	62.858(4)	4.8	162.40(2)	0.47(6)
7.3	3.9761(1)	62.858(4)	4.8	162.39(2)	0.48(6)
7.8	3.9753(1)	62.820(4)	4.9	162.32(2)	0.52(6)
7.4	3.9749(1)	62.802(4)	4.8	162.25(2)	0.55(6)
8.3	3.9745(1)	62.785(4)	4.8	162.25(2)	0.55(6)
8.5	3.9745(1)	62.784(4)	5.0	162.23(2)	0.56(6)
9.1	3.9745(1)	62.784(5)	5.1	162.20(2)	0.58(6)
8.4	3.9743(1)	62.772(4)	4.9	162.20(2)	0.58(6)
8.2	3.9738(1)	62.751(4)	5.0	162.18(2)	0.59(6)
8.4	3.9730(1)	62.714(4)	4.9	162.14(2)	0.61(6)
7.8	3.9729(1)	62.709(4)	4.7	162.11(2)	0.62(6)
9.4	3.9725(1)	62.690(5)	5.2	162.07(2)	0.65(6)
10.7	3.9726(1)	62.694(6)	5.9	162.05(2)	0.65(6)
9.5	3.9725(1)	62.688(5)	5.1	162.04(2)	0.66(6)
8.4	3.9721(1)	62.671(5)	4.8	162.01(2)	0.67(6)
8.3	3.9717(1)	62.653(4)	4.7	161.99(2)	0.69(6)
9.3	3.9712(1)	62.629(5)	5.0	161.96(2)	0.70(6)
8.9	3.9703(1)	62.585(5)	4.9	161.93(2)	0.72(6)
9.1	3.9700(1)	62.573(5)	5.0	161.89(2)	0.74(6)
9.3	3.9700(1)	62.570(5)	5.1	161.89(2)	0.74(6)
9.1	3.9697(1)	62.557(5)	4.9	161.87(2)	0.75(6)
8.8	3.9691(1)	62.530(5)	4.9	161.84(2)	0.77(6)
8.3	3.9688(1)	62.512(5)	4.7	161.80(2)	0.78(6)
8.4	3.9686(1)	62.505(5)	4.7	161.74(2)	0.82(6)
7.6	3.9685(1)	62.500(4)	4.5	161.73(2)	0.82(6)
8.6	3.9682(1)	62.486(5)	4.8	161.72(2)	0.83(6)
8.6	3.9677(1)	62.461(5)	4.7	161.69(2)	0.85(6)
9.2	3.9671(1)	62.436(5)	4.7	161.65(2)	0.87(6)
8.1	3.9666(1)	62.412(4)	4.7	161.62(2)	0.88(6)
8.6	3.9655(1)	62.359(5)	4.9	161.54(2)	0.92(9)
7.6	3.9651(1)	62.338(4)	4.7	161.52(2)	0.93(9)
7.5	3.9648(1)	62.327(4)	4.7	161.52(2)	0.93(9)
7.3	3.9645(1)	62.313(4)	4.6	161.49(2)	0.95(9)
6.9	3.9641(1)	62.292(4)	4.4	161.45(2)	0.97(9)

sample Rwp(%)	Sample lattice constant, a (Å)	sample unit cell volume, V (Å^3)	CaF_2 Rwp(%)	CaF2 cell volume, V (Å^3)	Pressure (GPa)
7.5	3.9636(1)	62.268(4)	4.5	161.40(2)	0.99(9)
7.3	3.9633(1)	62.257(4)	4.4	161.39(2)	1.00(9)
7.1	3.9631(1)	62.247(4)	4.3	161.38(2)	1.01(9)
7.0	3.9629(1)	62.235(4)	4.3	161.35(2)	1.02(9)
7.5	3.9626(1)	62.222(4)	4.4	161.34(2)	1.03(9)
6.9	3.9625(1)	62.216(4)	4.4	161.32(2)	1.04(9)
6.3	3.9620(1)	62.196(4)	4.5	161.29(2)	1.06(9)
6.4	3.9617(1)	62.180(4)	4.4	161.28(2)	1.06(9)
6.7	3.9614(1)	62.164(4)	4.4	161.25(2)	1.08(9)
6.5	3.9609(1)	62.140(4)	4.5	161.21(2)	1.10(9)
6.7	3.9605(1)	62.121(4)	4.9	161.17(2)	1.12(9)
7.1	3.9598(1)	62.091(4)	4.5	161.15(2)	1.13(9)
6.6	3.9591(1)	62.055(4)	4.5	161.10(2)	1.16(9)
6.8	3.9584(1)	62.024(4)	4.4	161.05(2)	1.18(9)
6.5	3.9575(1)	61.980(4)	4.4	161.00(2)	1.21(9)
7.8	3.9570(1)	61.957(4)	4.5	160.98(2)	1.22(9)
7.1	3.9563(1)	61.927(4)	4.3	160.93(2)	1.25(9)
6.7	3.9556(1)	61.893(4)	4.3	160.89(2)	1.27(9)
7.0	3.9547(1)	61.850(4)	4.4	160.84(2)	1.30(9)
7.3	3.9538(1)	61.807(3)	4.2	160.77(2)	1.34(9)
6.8	3.9528(1)	61.763(4)	4.2	160.71(2)	1.37(9)
7.2	3.9514(1)	61.694(4)	4.2	160.63(2)	1.41(9)
6.7	3.9508(1)	61.666(4)	4.2	160.60(2)	1.43(9)
7.2	3.9502(1)	61.641(4)	4.2	160.57(2)	1.45(9)
7.2	3.9497(1)	61.617(4)	4.2	160.54(2)	1.46(9)
6.7	3.9492(1)	61.593(4)	4.3	160.52(2)	1.47(9)
8.0	3.9487(1)	61.570(4)	4.4	160.51(2)	1.48(9)
7.0	3.9482(1)	61.544(4)	4.2	160.48(2)	1.50(9)
7.9	3.9473(1)	61.504(5)	4.4	160.43(2)	1.52(9)
7.7	3.9466(1)	61.473(4)	4.2	160.39(2)	1.55(9)
9.1	3.9460(1)	61.443(5)	4.7	160.36(2)	1.56(9)
8.9	3.9455(1)	61.420(5)	4.7	160.34(2)	1.58(9)
9.6	3.9446(1)	61.379(6)	5.0	160.30(2)	1.60(9)
9.4	3.9440(1)	61.349(6)	5.0	160.27(2)	1.61(9)
9.4	3.9434(1)	61.322(6)	5.0	160.24(2)	1.63(9)
9.5	3.9429(1)	61.297(6)	5.0	160.22(2)	1.64(9)
9.8	3.9423(1)	61.271(6)	5.2	160.20(2)	1.65(9)
9.9	3.9417(1)	61.242(5)	5.2	160.17(2)	1.67(9)
8.7	3.9411(1)	61.215(5)	4.7	160.15(2)	1.68(9)

sample Rwp(%)	Sample lattice constant, a (Å)	sample unit cell volume, V (Å^3)	CaF_2 Rwp(%)	CaF2 cell volume, V (Å^3)	Pressure (GPa)
8.2	3.9406(1)	61.193(5)	4.5	160.13(2)	1.69(9)
8.2	3.9396(1)	61.143(5)	4.5	160.09(2)	1.71(9)
10.1	3.9387(1)	61.101(5)	5.1	160.05(2)	1.74(9)
8.5	3.9383(1)	61.085(6)	4.6	160.03(2)	1.75(9)
9.0	3.9379(1)	61.063(6)	4.7	160.01(2)	1.76(9)
9.5	3.9369(1)	61.018(5)	4.9	159.98(2)	1.78(9)
9.8	3.9354(1)	60.951(5)	5.0	159.92(2)	1.81(9)
8.8	3.9346(1)	60.911(6)	4.8	159.88(2)	1.84(9)
10.2	3.9337(1)	60.871(5)	5.2	159.85(2)	1.85(9)
9.4	3.9326(1)	60.818(5)	5.0	159.80(2)	1.88(9)
9.3	3.9318(1)	60.780(5)	5.1	159.77(2)	1.90(9)
9.6	3.9307(1)	60.733(5)	5.2	159.73(2)	1.92(9)
8.3	3.9299(1)	60.694(6)	4.9	159.69(2)	1.94(9)
9.8	3.9288(1)	60.641(5)	5.4	159.65(2)	1.96(9)
9.0	3.9281(1)	60.612(5)	5.2	159.62(2)	1.98(9)
9.8	3.9276(1)	60.587(5)	5.5	159.60(2)	1.99(9)
10.7	3.9258(1)	60.504(5)	5.7	159.55(2)	2.02(9)
10.6	3.9242(1)	60.431(5)	5.7	159.48(2)	2.06(9)
11.6	3.9235(1)	60.397(5)	6.2	159.45(2)	2.08(9)
11.1	3.9227(1)	60.359(5)	6.0	159.43(2)	2.09(9)
10.6	3.9214(1)	60.300(5)	5.7	159.38(2)	2.12(9)
10.8	3.9206(1)	60.265(5)	5.9	159.35(2)	2.14(9)
12.4	3.9198(1)	60.229(5)	6.7	159.33(2)	2.15(9)
-	-	-	6.4	159.29(2)	2.17(9)
-	-	-	6.4	159.24(2)	2.20(9)
-	-	-	6.4	159.19(2)	2.23(9)
-	-	-	6.3	159.14(2)	2.26(9)
-	-	-	6.3	159.12(2)	2.27(9)
-	-	-	5.9	159.09(2)	2.29(9)
-	-	-	5.7	159.07(2)	2.30(9)
-	-	-	5.5	159.02(2)	2.33(9)
-	-	-	5.6	158.98(2)	2.35(9)
-	-	-	5.4	158.95(2)	2.37(9)
-	-	-	5.2	158.91(2)	2.39(9)
-	-	-	5.5	158.86(2)	2.42(9)
-	-	-	5.4	158.81(2)	2.45(9)
-	-	-	5.2	158.78(2)	2.47(9)
-	-	-	5.1	158.75(2)	2.49(9)
-	-	-	5.1	158.71(2)	2.51(9)

sample Rwp(%)	Sample lattice constant, a (Å)	sample unit cell volume, V (Å^3)	CaF_2 Rwp(%)	CaF2 cell volume, V (Å^3)	Pressure (GPa)
-	-	-	5.1	158.64(2)	2.55(9)
-	-	-	4.9	158.59(2)	2.58(9)
-	-	-	5.0	158.56(2)	2.60(9)
-	-	-	5.0	158.51(2)	2.63(9)
-	-	-	5.1	158.46(2)	2.66(9)
-	-	-	4.8	158.41(2)	2.69(9)
-	-	-	5.1	158.37(2)	2.71(9)
-	-	-	5.2	158.32(2)	2.74(9)
-	-	-	5.1	158.28(2)	2.77(9)
-	-	-	5.2	158.23(2)	2.80(9)
-	-	-	4.7	158.20(2)	2.82(9)
-	-	-	4.9	158.15(2)	2.85(9)
-	-	-	4.7	158.11(2)	2.87(9)
-	-	-	4.7	158.07(2)	2.90(9)
-	-	-	4.9	157.99(2)	2.94(9)
-	-	-	4.5	157.92(2)	2.99(9)
-	-	-	5.1	157.89(2)	3.01(9)
-	-	-	4.6	157.85(2)	3.03(9)
-	-	-	4.7	157.79(2)	3.07(9)
-	-	-	4.4	157.74(2)	3.10(9)
-	-	-	4.8	157.69(2)	3.13(9)
-	-	-	4.5	157.64(2)	3.16(9)
-	-	-	4.4	157.56(2)	3.21(9)
-	-	-	4.2	157.50(2)	3.24(9)
-	-	-	4.6	157.47(2)	3.27(9)
-	-	-	4.3	157.43(2)	3.29(9)
-	-	-	4.4	157.38(2)	3.32(9)
-	-	-	4.7	157.34(3)	3.35(9)
-	-	-	4.7	157.22(3)	3.42(9)
-	-	-	4.0	157.11(2)	3.49(9)
-	-	-	4.3	157.06(2)	3.52(9)
-	-	-	4.4	157.01(2)	3.56(9)
-	-	-	4.6	156.94(2)	3.60(9)
-	-	-	4.2	156.86(2)	3.65(9)
-	-	-	5.0	156.81(2)	3.68(9)
-	-	-	4.0	156.73(2)	3.73(9)
-	-	-	4.0	156.66(2)	3.78(9)
-	-	-	4.0	156.57(2)	3.83(9)
-	-	-	4.1	156.50(2)	3.88(9)

sample Rwp(%)	Sample lattice constant, a (Å)	sample unit cell volume, V (Å^3)	CaF_2 Rwp(%)	CaF2 cell volume, V (Å^3)	Pressure (GPa)
-	-	-	4.3	156.44(2)	3.92(9)
-	-	-	4.0	156.37(2)	3.96(9)
-	-	-	3.6	156.30(2)	4.01(9)
-	-	-	4.3	156.21(2)	4.07(9)
-	-	-	4.6	156.12(2)	4.13(9)
-	-	-	4.8	156.03(2)	4.19(9)
-	-	-	4.8	155.97(2)	4.23(9)
-	-	-	5.1	155.91(2)	4.26(9)
-	-	-	3.5	155.87(2)	4.29(9)
-	-	-	3.6	155.83(2)	4.32(9)
-	-	-	4.0	155.79(2)	4.35(9)
-	-	-	3.5	155.74(2)	4.38(9)
-	-	-	3.6	155.69(2)	4.42(9)
-	-	-	3.3	155.61(2)	4.46(9)
-	-	-	3.6	155.54(2)	4.51(9)
-	-	-	3.3	155.45(2)	4.57(9)
-	-	-	3.9	155.32(2)	4.66(9)
-	-	-	3.8	155.19(2)	4.75(9)
-	-	-	3.8	155.12(2)	4.80(9)
-	-	-	3.6	155.07(2)	4.83(9)
-	-	-	3.7	155.01(2)	4.87(9)
-	-	-	3.8	154.94(2)	4.92(9)
-	-	-	3.7	154.87(2)	4.97(9)
-	-	-	3.9	154.79(2)	5.03(9)
-	-	-	3.4	154.73(2)	5.07(9)
-	-	-	3.5	154.69(2)	5.10(9)
-	-	-	3.5	154.64(2)	5.13(9)
-	-	-	3.7	154.59(2)	5.16(9)
-	-	-	3.5	154.55(2)	5.19(9)
-	-	-	3.5	154.49(2)	5.24(9)
-	-	-	3.4	154.42(1)	5.28(9)
-	-	-	3.3	154.36(1)	5.32(9)
-	-	-	3.9	154.32(2)	5.36(9)
-	-	-	3.8	154.26(2)	5.39(9)
-	-	-	3.4	154.18(1)	5.45(9)
-	-	-	3.7	154.12(1)	5.50(9)
-	-	-	3.4	154.06(1)	5.54(9)
-	-	-	3.8	154.02(1)	5.57(9)
-	-	-	3.9	153.97(1)	5.60(9)

sample Rwp(%)	Sample lattice constant, a (Å)	sample unit cell volume, V (Å^3)	CaF_2 Rwp(%)	CaF2 cell volume, V (Å^3)	Pressure (GPa)
-	-	-	4.1	153.90(1)	5.65(9)
-	-	-	3.8	153.80(1)	5.72(9)
-	-	-	3.6	153.69(1)	5.80(9)
-	-	-	3.7	153.57(1)	5.89(9)
-	-	-	4.4	153.46(2)	5.97(9)
-	-	-	3.7	153.35(1)	6.05(9)
-	-	-	4.0	153.22(1)	6.15(9)
-	-	-	4.1	153.11(1)	6.23(9)
-	-	-	3.6	153.01(1)	6.30(9)
-	-	-	3.8	152.93(1)	6.37(9)
-	-	-	3.7	152.82(1)	6.44(9)
-	-	-	4.3	152.73(2)	6.51(9)
-	-	-	4.0	152.65(1)	6.57(9)
-	-	-	4.1	152.59(1)	6.62(9)
-	-	-	3.9	152.51(1)	6.68(9)
-	-	-	3.4	152.40(1)	6.76(9)
-	-	-	3.9	152.33(1)	6.82(9)
-	-	-	4.1	152.27(2)	6.86(9)
-	-	-	3.8	152.22(1)	6.90(9)
-	-	-	4.1	152.19(2)	6.92(9)
-	-	-	3.9	152.16(2)	6.94(9)
-	-	-	4.2	152.15(2)	6.95(9)
-	-	-	3.8	152.14(2)	6.96(9)
-	-	-	3.5	152.16(1)	6.95(9)
-	-	-	3.8	152.22(1)	6.90(9)
-	-	-	3.6	152.31(1)	6.84(9)
-	-	-	4.4	152.41(2)	6.75(9)
-	-	-	4.1	152.54(2)	6.66(9)
-	-	-	4.0	152.66(1)	6.57(9)
-	-	-	4.0	152.78(1)	6.48(9)
-	-	-	3.7	152.92(1)	6.37(9)
-	-	-	3.8	153.06(1)	6.27(9)
-	-	-	4.2	153.23(1)	6.14(9)
-	-	-	4.0	153.44(1)	5.99(9)
-	-	-	4.1	153.72(1)	5.78(9)
-	-	-	4.8	154.06(1)	5.54(9)
-	-	-	4.9	154.44(1)	5.27(9)
-	-	-	5.1	154.90(1)	4.95(9)
-	-	-	5.0	155.39(1)	4.61(9)

sample Rwp(%)	Sample lattice constant, a (Å)	sample unit cell volume, V (Å^3)	CaF_2 Rwp(%)	CaF2 cell volume, V (Å^3)	Pressure (GPa)
-	-	-	4.8	156.01(1)	4.20(9)
-	-	-	4.9	156.63(1)	3.79(9)
-	-	-	5.3	156.88(1)	3.63(9)

Table B.7: Weighted profile R factors for both sample and pressure standard, lattice constant for the x=0.5 sample, unit cell volumes for both the sample and the CaF_2 pressure standard, and the pressure calculated from the CaF_2 using the decompression cell volume as V_0.

sample Rwp(%)	Sample lattice constant, a (Å)	sample unit cell volume, V (Å^3)	CaF_2 Rwp(%)	CaF2 cell volume, V (Å^3)	Pressure (GPa)
3.7	3.9861(4)	63.335(2)	6.4	163.25(3)	0.12(5)
3.7	3.9862(4)	63.338(2)	4.9	163.23(2)	0.13(5)
3.7	3.9861(4)	63.335(2)	4.9	163.25(3)	0.12(5)
3.8	3.9862(4)	63.338(2)	4.8	163.25(3)	0.12(5)
3.8	3.9861(4)	63.335(2)	4.7	163.24(3)	0.12(5)
3.7	3.9860(4)	63.331(2)	4.7	163.21(2)	0.14(5)
3.7	3.9860(4)	63.330(2)	4.6	163.20(2)	0.14(5)
3.7	3.9860(4)	63.332(2)	4.6	163.21(2)	0.14(5)
3.7	3.9861(4)	63.333(2)	4.6	163.20(2)	0.15(5)
3.7	3.9859(4)	63.328(2)	4.6	163.20(2)	0.14(5)
3.7	3.986-(4)	63.329(2)	4.5	163.20(2)	0.14(5)
3.7	3.9859(4)	63.327(2)	4.5	163.20(2)	0.14(5)
3.7	3.9858(4)	63.322(2)	4.5	163.21(3)	0.14(5)
3.8	3.9859(4)	63.323(2)	4.5	163.19(3)	0.15(5)
3.9	3.9858(4)	63.322(2)	4.5	163.26(3)	0.11(5)
3.8	3.9858(4)	63.321(2)	4.5	163.32(3)	0.08(5)
3.8	3.9858(4)	63.322(2)	4.4	163.33(3)	0.08(5)
3.8	3.9859(4)	63.324(2)	4.4	163.30(3)	0.09(5)
3.7	3.9859(4)	63.324(2)	4.4	163.32(3)	0.08(5)
3.6	3.9858(4)	63.323(2)	4.4	163.29(3)	0.10(5)
3.6	3.9857(4)	63.316(2)	4.4	163.26(3)	0.12(5)
3.7	3.9858(4)	63.320(2)	4.5	163.21(3)	0.14(5)
3.7	3.9857(4)	63.314(2)	4.6	163.24(3)	0.13(5)
3.7	3.9857(4)	63.314(2)	4.4	163.22(3)	0.13(5)
3.8	3.9855(4)	63.306(2)	4.4	163.22(3)	0.13(5)
3.7	3.9854(4)	63.304(2)	4.4	163.22(3)	0.13(5)
3.7	3.9854(4)	63.301(2)	4.5	163.20(3)	0.14(5)
3.8	3.9853(4)	63.296(2)	4.4	163.17(3)	0.16(5)
3.8	3.9853(4)	63.297(2)	4.4	163.18(3)	0.16(5)
3.7	3.9851(4)	63.287(2)	4.4	163.17(3)	0.16(5)
3.7	3.9850(4)	63.283(2)	4.4	163.13(3)	0.18(5)
3.7	3.9848(4)	63.273(2)	4.4	163.13(3)	0.18(5)
3.6	3.9846(4)	63.264(2)	4.5	163.17(3)	0.16(5)
3.7	3.9846(4)	63.266(2)	4.5	163.13(3)	0.18(5)
3.8	3.9845(4)	63.259(2)	4.5	163.11(3)	0.19(5)

sample Rwp(%)	Sample lattice constant, a (Å)	sample unit cell volume, V (Å^3)	CaF_2 Rwp(%)	CaF2 cell volume, V (Å^3)	Pressure (GPa)
3.8	3.9843(4)	63.249(2)	4.5	163.10(3)	0.20(5)
3.7	3.9841(4)	63.241(2)	4.5	163.09(3)	0.20(5)
3.9	3.9840(4)	63.233(2)	4.5	163.07(3)	0.21(5)
4.0	3.9840(4)	63.234(2)	4.4	163.05(3)	0.22(5)
3.9	3.9835(4)	63.210(2)	4.4	162.98(3)	0.26(5)
3.8	3.9832(4)	63.195(2)	4.5	162.96(3)	0.27(5)
3.8	3.9829(4)	63.184(2)	4.5	162.93(3)	0.28(5)
3.8	3.9827(4)	63.175(2)	4.6	162.96(3)	0.26(5)
3.9	3.9824(4)	63.160(2)	4.5	162.89(3)	0.30(5)
3.7	3.9819(4)	63.136(2)	4.5	162.83(3)	0.33(5)
3.8	3.9817(4)	63.127(2)	4.5	162.84(3)	0.33(5)
3.7	3.9813(4)	63.108(2)	4.5	162.83(3)	0.33(5)
3.8	3.9811(4)	63.099(2)	4.5	162.84(3)	0.32(5)
3.8	3.9811(4)	63.095(2)	4.6	162.79(3)	0.35(5)
3.8	3.9810(4)	63.094(2)	4.6	162.78(2)	0.36(5)
3.8	3.9810(4)	63.093(2)	4.6	162.76(3)	0.37(5)
3.9	3.9808(4)	63.084(2)	4.5	162.76(3)	0.36(5)
4.0	3.9808(4)	63.085(2)	4.4	162.73(3)	0.38(5)
3.9	3.9807(4)	63.076(2)	4.6	162.74(3)	0.38(6)
4.0	3.9805(4)	63.070(2)	4.7	162.83(3)	0.33(5)
4.0	3.9804(4)	63.065(2)	4.5	162.75(3)	0.37(5)
3.8	3.9800(4)	63.046(2)	4.4	162.64(3)	0.43(6)
3.9	3.9798(4)	63.036(2)	4.6	162.63(3)	0.43(6)
3.9	3.9797(4)	63.032(2)	4.6	162.64(3)	0.43(6)
3.7	3.9795(4)	63.021(2)	4.6	162.64(3)	0.43(6)
3.7	3.9795(4)	63.021(2)	4.6	162.62(3)	0.44(6)
3.8	3.9795(4)	63.020(2)	4.5	162.60(3)	0.45(6)
3.8	3.9793(4)	63.013(2)	4.5	162.70(3)	0.40(6)
3.7	3.9791(4)	63.003(2)	4.6	162.61(3)	0.44(6)
3.8	3.9790(4)	62.999(2)	4.5	162.65(3)	0.42(6)
3.7	3.9788(4)	62.989(2)	4.6	162.68(3)	0.41(6)
3.8	3.9787(4)	62.982(2)	4.6	162.62(3)	0.44(6)
3.8	3.9786(4)	62.978(2)	4.5	162.55(3)	0.47(6)
3.8	3.9784(4)	62.969(2)	4.4	162.52(3)	0.49(6)
3.9	3.9784(4)	62.967(2)	4.5	162.55(3)	0.47(6)
3.9	3.9780(4)	62.949(2)	4.5	162.46(2)	0.52(6)
3.7	3.9777(4)	62.934(2)	4.5	162.50(3)	0.50(6)
3.8	3.9776(4)	62.931(2)	4.5	162.45(3)	0.52(6)
3.8	3.9775(4)	62.928(2)	4.5	162.47(3)	0.51(6)

sample Rwp(%)	Sample lattice constant, a (Å)	sample unit cell volume, V (Å^3)	CaF_2 Rwp(%)	CaF2 cell volume, V (Å^3)	Pressure (GPa)
3.8	3.9774(4)	62.921(2)	4.5	162.48(3)	0.51(6)
3.8	3.9772(4)	62.912(2)	4.6	162.43(3)	0.53(6)
3.8	3.9774(4)	62.920(2)	4.4	162.40(3)	0.55(6)
3.8	3.9772(4)	62.911(2)	4.4	162.41(3)	0.54(6)
3.7	3.9768(4)	62.893(2)	4.4	162.40(3)	0.55(6)
3.8	3.9766(4)	62.882(2)	4.4	162.40(3)	0.55(6)
3.9	3.9762(4)	62.864(2)	4.4	162.36(3)	0.57(6)
3.9	3.9759(4)	62.850(2)	4.5	162.34(3)	0.58(6)
3.9	3.9757(4)	62.840(2)	4.4	162.32(3)	0.59(6)
3.9	3.9754(4)	62.824(2)	4.5	162.32(3)	0.59(6)
3.9	3.9751(4)	62.810(2)	4.4	162.27(2)	0.62(6)
3.9	3.9748(4)	62.797(2)	4.5	162.20(3)	0.65(6)
3.8	3.9746(4)	62.79(02)	4.5	162.16(3)	0.67(6)
3.9	3.9746(4)	62.787(2)	4.5	162.20(2)	0.65(6)
3.9	3.9744(4)	62.781(2)	4.5	162.20(2)	0.66(6)
3.9	3.9739(4)	62.755(2)	4.5	162.15(3)	0.68(6)
3.7	3.9735(4)	62.736(2)	4.5	162.10(3)	0.70(6)
3.8	3.9733(4)	62.726(2)	4.4	162.11(3)	0.70(6)
3.8	3.9728(4)	62.702(2)	4.5	162.09(3)	0.71(6)
3.7	3.9725(4)	62.688(2)	4.4	162.07(3)	0.72(6)
3.7	3.9722(4)	62.675(2)	4.3	162.07(3)	0.72(6)
3.7	3.9720(4)	62.664(2)	4.3	162.02(2)	0.75(6)
3.7	3.9715(4)	62.643(2)	4.4	162.03(2)	0.74(6)
3.7	3.9713(4)	62.631(2)	4.3	162.09(2)	0.71(6)
3.7	3.9712(4)	62.628(2)	4.3	162.04(2)	0.74(6)
3.8	3.9711(4)	62.623(2)	4.2	162.01(2)	0.75(6)
3.9	3.9711(4)	62.621(2)	4.3	161.99(2)	0.77(6)
3.9	3.9707(4)	62.604(2)	4.3	161.94(2)	0.79(6)
3.9	3.9704(4)	62.588(2)	4.4	161.91(3)	0.81(6)
3.9	3.9700(4)	62.570(2)	4.4	161.83(2)	0.85(6)
3.9	3.9697(4)	62.556(2)	4.4	161.82(2)	0.85(6)
3.7	3.9691(4)	62.529(2)	4.3	161.84(2)	0.84(6)
3.7	3.9687(4)	62.508(2)	4.3	161.76(3)	0.88(6)
3.7	3.9684(4)	62.494(2)	4.3	161.72(3)	0.91(9)
3.8	3.9680(4)	62.475(2)	4.3	161.73(3)	0.90(9)
3.6	3.9675(4)	62.454(2)	4.2	161.67(3)	0.93(9)
3.5	3.9672(4)	62.439(2)	4.2	161.65(3)	0.94(9)
3.5	3.9670(4)	62.428(2)	4.2	161.64(3)	0.95(9)
3.5	3.9668(4)	62.419(2)	4.2	161.64(3)	0.95(9)

sample Rwp(%)	Sample lattice constant, a (Å)	sample unit cell volume, V (Å^3)	CaF_2 Rwp(%)	CaF2 cell volume, V (Å^3)	Pressure (GPa)
3.6	3.9666(4)	62.411(2)	4.2	161.59(3)	0.98(9)
3.5	3.9664(4)	62.399(2)	4.2	161.61(3)	0.97(9)
3.5	3.9663(4)	62.394(2)	4.2	161.63(2)	0.96(9)
3.6	3.9659(4)	62.379(2)	4.2	161.56(3)	0.99(9)
3.5	3.9655(4)	62.358(2)	4.2	161.53(3)	1.01(9)
3.5	3.9651(4)	62.338(2)	4.1	161.48(3)	1.03(9)
3.5	3.9643(4)	62.301(2)	4.2	161.47(2)	1.04(9)
3.5	3.9638(4)	62.279(2)	4.2	161.41(2)	1.07(9)
3.5	3.9637(4)	62.272(2)	4.2	161.37(3)	1.09(9)
3.5	3.9635(4)	62.265(2)	4.1	161.38(3)	1.09(9)
3.6	3.9632(4)	62.250(2)	4.1	161.44(4)	1.06(9)
3.7	3.9628(4)	62.232(2)	4.1	161.35(2)	1.10(9)
3.6	3.9625(4)	62.218(2)	4.1	161.36(2)	1.10(9)
3.6	3.9622(4)	62.203(2)	4.0	161.36(2)	1.10(9)
3.5	3.9617(4)	62.178(2)	4.0	161.31(2)	1.13(9)
3.5	3.9609(4)	62.141(2)	4.0	161.30(2)	1.13(9)
3.5	3.9594(1)	62.069(2)	3.9	161.20(3)	1.19(9)
3.5	3.9585(1)	62.029(2)	3.9	161.14(2)	1.21(9)
3.6	3.9581(1)	62.008(2)	4.0	161.09(2)	1.25(9)
3.8	3.9575(1)	61.980(2)	4.0	161.02(2)	1.28(9)
3.7	3.9572(1)	61.965(2)	3.9	160.98(2)	1.31(9)
3.6	3.9569(1)	61.953(2)	3.8	160.97(3)	1.31(9)
3.6	3.9562(1)	61.922(2)	3.9	160.96(3)	1.31(9)
3.5	3.9552(1)	61.871(2)	3.9	160.92(2)	1.34(9)
3.5	3.9547(1)	61.851(2)	3.8	160.92(2)	1.34(9)
3.5	3.9543(1)	61.833(2)	3.8	160.87(2)	1.37(9)
3.5	3.9540(1)	61.819(2)	3.9	160.85(2)	1.37(9)
3.6	3.9537(1)	61.801(2)	3.9	160.82(2)	1.39(9)
3.6	3.9529(1)	61.767(2)	3.9	160.76(2)	1.42(9)
3.6	3.9517(1)	61.710(2)	3.8	160.70(2)	1.46(9)
3.7	3.9504(1)	61.648(3)	3.7	160.61(2)	1.51(9)
3.8	3.9497(1)	61.616(3)	3.7	160.55(2)	1.54(9)
3.7	3.9490(1)	61.584(3)	3.6	160.50(2)	1.57(9)
3.7	3.9486(1)	61.562(3)	3.6	160.48(2)	1.58(9)
3.7	3.9479(1)	61.531(3)	3.6	160.46(2)	1.59(9)
3.7	3.9471(1)	61.493(3)	3.6	160.44(2)	1.60(9)
3.7	3.9464(1)	61.462(3)	3.5	160.42(2)	1.61(9)
3.7	3.9456(1)	61.426(3)	3.5	160.38(2)	1.64(9)
3.8	3.9451(1)	61.401(3)	3.5	160.36(2)	1.65(9)

sample Rwp(%)	Sample lattice constant, a (Å)	sample unit cell volume, V (Å^3)	CaF_2 Rwp(%)	CaF2 cell volume, V (Å^3)	Pressure (GPa)
3.7	3.9445(1)	61.371(3)	3.5	160.32(2)	1.67(9)
3.7	3.9438(1)	61.340(3)	3.5	160.30(2)	1.68(9)
3.8	3.9428(1)	61.294(3)	3.5	160.27(2)	1.70(9)
3.8	3.9417(7)	61.243(3)	3.5	160.22(2)	1.73(9)
3.8	3.9409(7)	61.204(3)	3.4	160.19(2)	1.74(9)
3.9	3.9400(7)	61.161(3)	3.4	160.15(2)	1.76(9)
3.9	3.9394(7)	61.133(3)	3.4	160.13(2)	1.77(9)
4.0	3.9387(7)	61.102(3)	3.5	160.12(2)	1.78(9)
4.0	3.9380(7)	61.072(3)	3.5	160.10(2)	1.79(9)
4.0	3.9375(7)	61.047(3)	3.4	160.07(3)	1.81(9)
4.1	3.9365(8)	60.999(4)	3.5	160.03(3)	1.83(9)
4.1	3.9359(8)	60.972(4)	3.5	160.01(3)	1.84(9)
4.1	3.9354(8)	60.949(4)	3.5	159.98(3)	1.86(9)
4.1	3.9347(8)	60.915(4)	3.5	159.95(3)	1.88(9)
4.1	3.9338(8)	60.875(4)	3.6	159.92(3)	1.90(9)
4.2	3.9329(9)	60.834(4)	3.6	159.87(3)	1.92(10)
4.2	3.9322(9)	60.802(4)	3.7	159.84(3)	1.94(10)
4.2	3.9308(9)	60.735(4)	3.7	159.78(3)	1.97(10)
4.2	3.9296(9)	60.681(4)	3.8	159.74(3)	2.00(10)
4.2	3.9276(1)	60.586(4)	3.9	159.67(3)	2.04(10)
4.3	3.9265(1)	60.537(5)	4.0	159.63(3)	2.06(10)
4.3	3.9258(1)	60.503(5)	4.0	159.61(3)	2.07(10)
4.3	3.9251(1)	60.473(5)	4.1	159.60(3)	2.08(10)
4.3	3.9243(1)	60.434(5)	4.2	159.55(3)	2.10(10)
4.3	3.9234(1)	60.394(5)	4.2	159.52(3)	2.12(10)
4.3	3.9219(1)	60.323(5)	4.3	159.47(3)	2.15(10)
4.4	3.9206(1)	60.263(5)	4.5	159.42(3)	2.18(10)
4.4	3.9200(1)	60.236(5)	4.5	159.41(3)	2.19(10)
4.3	3.9196(1)	60.217(5)	4.5	159.40(3)	2.20(10)
4.4	3.9190(1)	60.189(5)	4.6	159.38(3)	2.20(10)
4.4	3.9182(1)	60.155(5)	4.6	159.37(3)	2.21(10)
4.4	3.9172(1)	60.106(5)	4.7	159.35(3)	2.22(11)
4.5	3.9156(1)	60.033(6)	4.9	159.32(3)	2.24(11)
4.5	3.9139(1)	59.955(6)	5.0	159.28(4)	2.26(11)
4.5	3.9120(1)	59.867(6)	5.1	159.22(3)	2.30(11)
4.5	3.9099(1)	59.773(6)	5.1	159.14(3)	2.35(11)
4.6	3.9087(1)	59.718(6)	5.1	159.09(3)	2.37(11)
4.6	3.9070(1)	59.641(5)	5.1	159.04(3)	2.40(11)
4.8	3.9047(1)	59.534(5)	5.1	158.94(3)	2.46(11)

sample Rwp(%)	Sample lattice constant, a (Å)	sample unit cell volume, V (Å^3)	CaF_2 Rwp(%)	CaF2 cell volume, V (Å^3)	Pressure (GPa)
4.6	3.9024(1)	59.430(5)	5.1	158.84(3)	2.52(12)
4.8	3.9016(1)	59.390(5)	4.9	158.79(3)	2.55(12)
-	-	-	5.0	158.73(3)	2.59(12)
-	-	-	4.9	158.65(3)	2.64(12)
-	-	-	4.8	158.59(4)	2.67(12)
-	-	-	4.8	158.54(4)	2.70(12)
-	-	-	4.8	158.51(3)	2.72(12)
-	-	-	4.8	158.46(3)	2.75(12)
-	-	-	4.6	158.40(4)	2.78(12)
-	-	-	4.6	158.31(4)	2.84(13)
-	-	-	4.5	158.23(4)	2.89(13)
-	-	-	4.4	158.16(4)	2.93(13)
-	-	-	4.3	158.10(4)	2.96(13)
-	-	-	4.3	158.05(4)	2.99(13)
-	-	-	4.3	158.01(4)	3.02(13)
-	-	-	4.2	158.13(1)	2.95(13)
-	-	-	4.1	157.91(4)	3.08(13)
-	-	-	4.0	157.86(4)	3.12(14)
-	-	-	4.0	157.83(4)	3.13(14)
-	-	-	4.0	157.79(4)	3.16(14)
-	-	-	3.9	157.75(4)	3.18(14)
-	-	-	3.9	157.73(4)	3.19(14)
-	-	-	3.8	157.7(4)	3.21(14)
-	-	-	3.7	157.65(4)	3.24(14)
-	-	-	3.6	157.58(4)	3.29(14)
-	-	-	3.6	157.52(4)	3.32(14)
-	-	-	3.4	157.59(5)	3.28(14)
-	-	-	3.3	157.50(5)	3.34(14)
-	-	-	3.2	157.42(5)	3.39(14)
-	-	-	3.1	157.29(5)	3.47(14)
-	-	-	3.0	157.43(4)	3.38(14)
-	-	-	2.9	157.40(4)	3.40(14)
-	-	-	2.8	157.37(4)	3.42(15)
-	-	-	2.8	157.35(4)	3.43(15)
-	-	-	2.7	157.31(4)	3.46(15)
-	-	-	2.6	157.26(4)	3.49(15)
-	-	-	2.6	156.99(3)	3.66(15)
-	-	-	2.5	156.95(4)	3.68(15)
-	-	-	2.4	156.91(4)	3.71(15)

sample Rwp(%)	Sample lattice constant, a (Å)	sample unit cell volume, V (Å^3)	CaF_2 Rwp(%)	CaF2 cell volume, V (Å^3)	Pressure (GPa)
-	-	-	2.4	156.87(3)	3.74(16)
-	-	-	2.3	156.76(3)	3.81(16)
-	-	-	2.2	156.70(3)	3.85(16)
-	-	-	2.2	156.68(3)	3.86(16)
-	-	-	2.1	156.65(3)	3.88(16)
-	-	-	2.1	156.62(3)	3.90(16)
-	-	-	2.0	156.58(3)	3.92(16)
-	-	-	2.0	156.30(3)	4.10(17)
-	-	-	1.9	156.27(3)	4.13(17)
-	-	-	1.9	156.25(3)	4.14(17)
-	-	-	1.9	156.22(3)	4.16(17)
-	-	-	1.9	156.19(3)	4.18(17)
-	-	-	1.8	156.15(3)	4.20(17)
-	-	-	1.8	155.88(3)	4.38(18)
-	-	-	1.8	155.85(3)	4.41(18)
-	-	-	1.8	155.79(3)	4.44(18)
-	-	-	1.8	155.72(3)	4.49(18)
-	-	-	1.8	155.62(3)	4.56(18)
-	-	-	1.8	155.57(3)	4.59(18)
-	-	-	1.8	155.55(3)	4.61(18)
-	-	-	1.8	155.51(3)	4.63(18)
-	-	-	1.8	155.48(3)	4.65(19)
-	-	-	1.8	155.17(2)	4.86(19)
-	-	-	1.8	155.13(2)	4.89(19)
-	-	-	1.8	155.11(2)	4.90(19)
-	-	-	1.8	154.87(2)	5.07(20)
-	-	-	1.8	154.83(2)	5.09(20)
-	-	-	1.8	154.80(2)	5.12(20)
-	-	-	1.8	154.78(2)	5.13(20)
-	-	-	1.8	154.76(2)	5.14(20)
-	-	-	1.8	154.72(2)	5.18(20)
-	-	-	1.8	154.49(2)	5.33(21)
-	-	-	1.8	154.48(2)	5.34(21)
-	-	-	1.8	154.47(2)	5.35(21)
-	-	-	1.8	154.45(2)	5.36(21)
-	-	-	1.8	154.42(2)	5.38(21)
-	-	-	1.9	154.38(2)	5.41(21)
-	-	-	1.9	154.04(2)	5.65(22)
-	-	-	1.9	153.99(2)	5.69(22)

sample Rwp(%)	Sample lattice constant, a (Å)	sample unit cell volume, V (Å^3)	CaF_2 Rwp(%)	CaF2 cell volume, V (Å^3)	Pressure (GPa)
-	-	-	1.9	153.89(2)	5.76(22)
-	-	-	1.9	153.71(2)	5.89(22)
-	-	-	1.9	153.64(2)	5.94(23)
-	-	-	1.9	153.60(2)	5.98(23)
-	-	-	1.9	153.35(2)	6.15(23)
-	-	-	1.9	153.32(2)	6.18(23)
-	-	-	1.9	153.30(2)	6.19(23)
-	-	-	1.9	153.26(2)	6.22(23)
-	-	-	1.9	153.23(2)	6.25(24)
-	-	-	1.9	153.19(2)	6.27(24)
-	-	-	1.9	152.99(2)	6.43(24)
-	-	-	1.9	152.97(2)	6.44(24)
-	-	-	1.9	152.94(2)	6.46(24)
-	-	-	1.9	152.89(2)	6.50(24)
-	-	-	1.9	152.87(2)	6.51(24)
-	-	-	1.9	152.85(2)	6.53(24)
-	-	-	1.9	152.63(2)	6.69(25)
-	-	-	1.9	152.62(2)	6.70(25)
-	-	-	1.9	152.60(2)	6.72(25)
-	-	-	1.9	152.60(2)	6.72(25)
-	-	-	1.9	152.58(2)	6.73(25)
-	-	-	1.9	152.57(2)	6.74(25)
-	-	-	1.9	152.57(2)	6.74(25)
-	-	-	1.9	152.56(2)	6.75(25)
-	-	-	1.9	152.57(2)	6.74(25)
-	-	-	1.9	152.57(2)	6.74(25)
-	-	-	1.9	152.58(2)	6.73(25)
-	-	-	1.9	152.60(2)	6.72(25)
-	-	-	1.9	152.63(2)	6.69(25)
-	-	-	1.9	152.64(2)	6.69(25)
-	-	-	1.9	152.67(2)	6.67(25)
-	-	-	1.9	152.71(2)	6.64(25)
-	-	-	1.9	152.73(2)	6.62(25)
-	-	-	1.9	153.03(2)	6.40(25)
-	-	-	1.9	153.33(2)	6.17(25)
-	-	-	1.9	153.43(2)	6.10(25)
-	-	-	1.9	153.95(2)	5.72(25)
-	-	-	1.9	154.49(2)	5.34(25)
-	-	-	1.9	154.89(2)	5.05(25)

sample Rwp(%)	Sample lattice constant, a (Å)	sample unit cell volume, V (Å^3)	CaF_2 Rwp(%)	CaF2 cell volume, V (Å^3)	Pressure (GPa)
-	-	-	1.9	155.60(2)	4.57(25)
-	-	-	1.9	156.03(2)	4.28(25)
-	-	-	1.9	156.38(2)	4.06(25)

Appendix C. **SUPPLEMENTARY MATERIAL FOR CHAPTER 4**

C.1 Supplemental figures

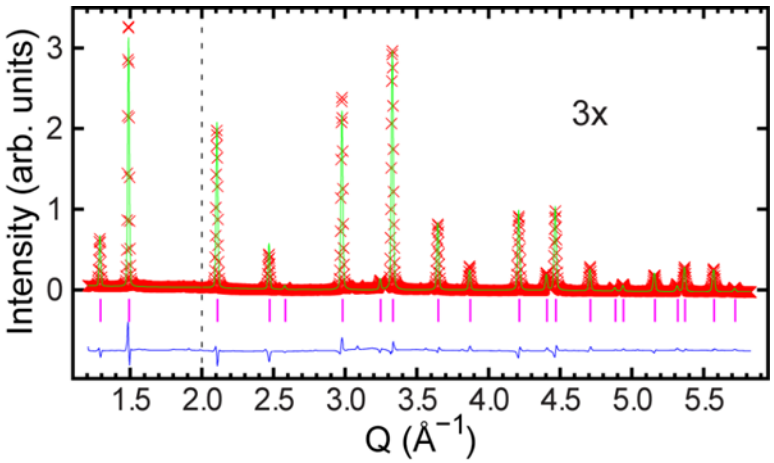

Figure C.1: Rietveld plot showing a fit of a $CaZr_{0.75}Nb_{0.25}F_{6.25}$ cubic $Fm\bar{3}m$ model to the 300 K cooling synchrotron diffraction data. The section of Q has been scaled to show detail but shifted downwards so that the backgrounds for the sections of the plot appear to be the same.

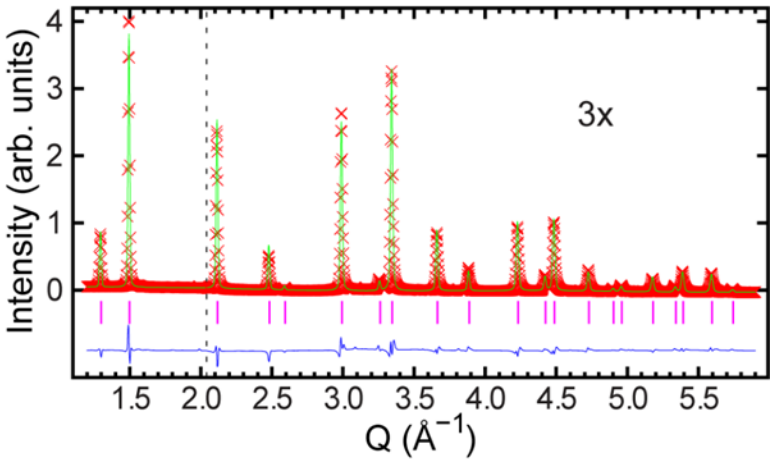

Figure C.2: Rietveld plot showing a fit of a $CaZr_{0.5}Nb_{0.5}F_{6.5}$ cubic $Fm\bar{3}m$ model to the 300 K cooling synchrotron diffraction data. The section of Q has been scaled to show detail but shifted downwards so that the backgrounds for the sections of the plot appear to be the same.

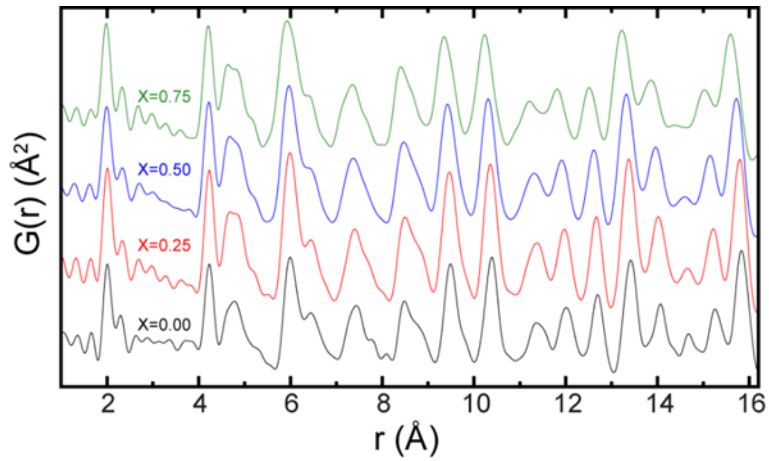

Figure C.3: Pair distribution functions derived from the x-ray total scattering data for Ca[Zr(IV)1-xNb(V)x]F6+x with a Qmax of 20 Å-1.

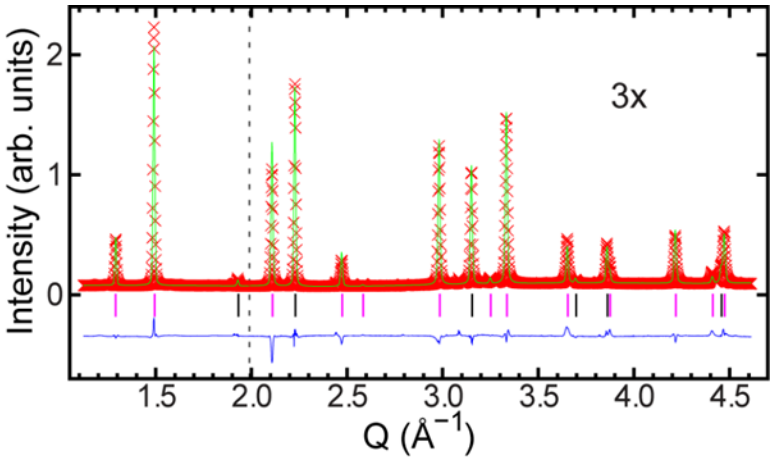

Figure C.4: Rietveld plot showing a fit of a CaZr0.75Nb0.25F6.25 cubic Fm$\bar{3}$m model to the 0 GPa powder x-ray diffraction data obtained in a diamond anvil cell. The section of Q has been scaled to show detail but shifted downwards so that the backgrounds for the sections of the plot appear to be the same.

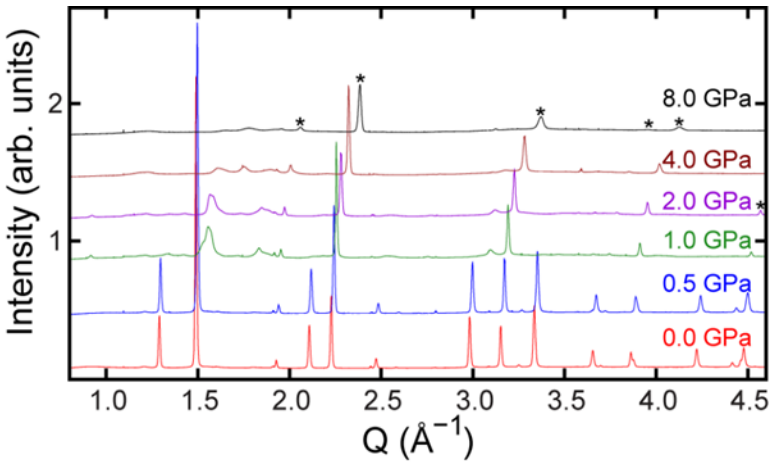

Figure C.5: Select high pressure diffraction patterns of CaZr0.75Nb0.25F6.25 showing phase transition and amorphization, with peaks from NaCl internal pressure standard marked with *.

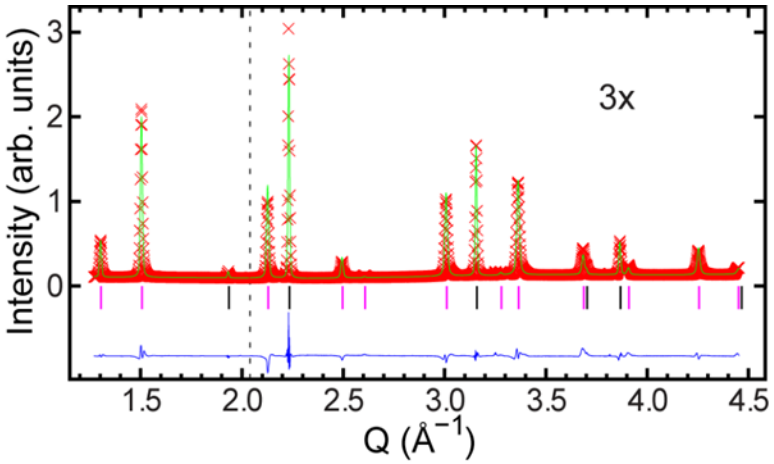

Figure C.6: Rietveld plot showing a fit of a CaZr0.5Nb0.5F6.5 cubic Fm$\bar{3}$m model to the 0.1 GPa powder x-ray diffraction data obtained in a diamond anvil cell. The section of Q has been scaled to show detail but shifted downwards so that the backgrounds for the sections of the plot appear to be the same.

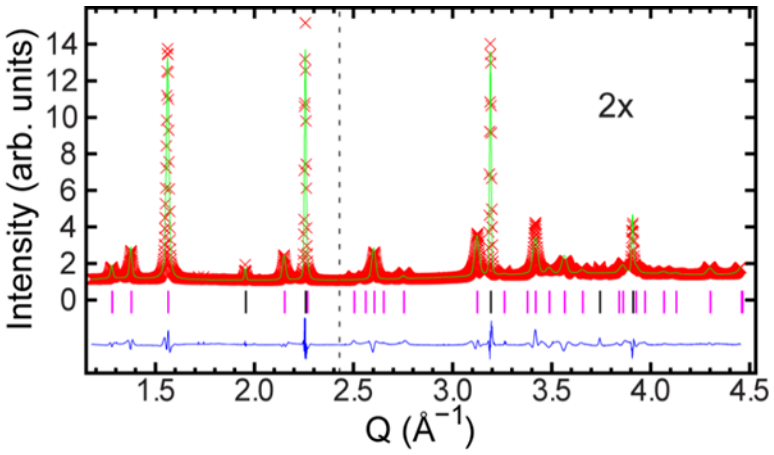

Figure C.7: Rietveld plot showing a fit of a $CaZr_{0.5}Nb_{0.5}F_{6.5}$ cubic $R\bar{3}$ model to the 1.0 GPa powder x-ray diffraction data obtained in a diamond anvil cell. The section of Q has been scaled to show detail but shifted downwards so that the backgrounds for the sections of the plot appear to be the same.

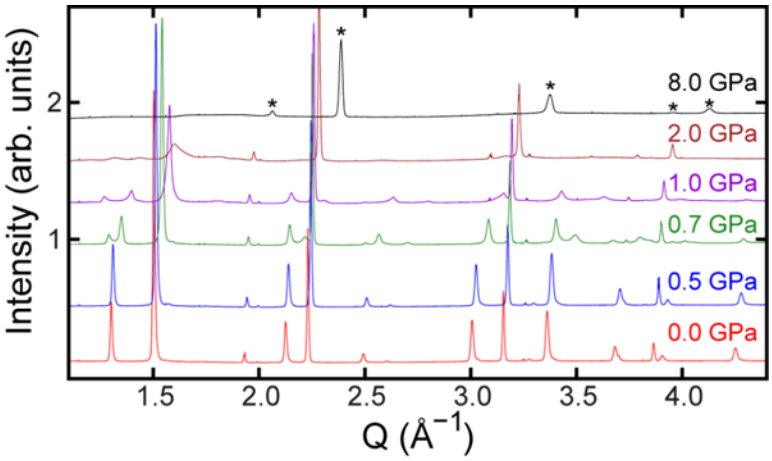

Figure C.8: Select high pressure diffraction patterns of $CaZr_{0.5}Nb_{0.5}F_{6.5}$ showing phase transition and amorphization, with peaks from NaCl internal pressure standard marked with *.

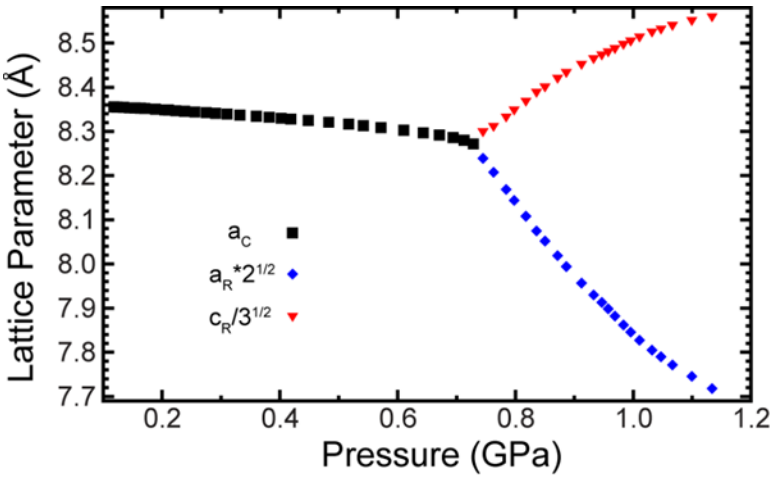

Figure C.9: Pressure dependence of the lattice constants for both the cubic and rhombohedral phase of $CaZr_{0.5}Nb_{0.5}F_{6.5}$. The lattice constants of the rhombohedral phase have been scaled so that they can be compared to the that of the cubic phase.

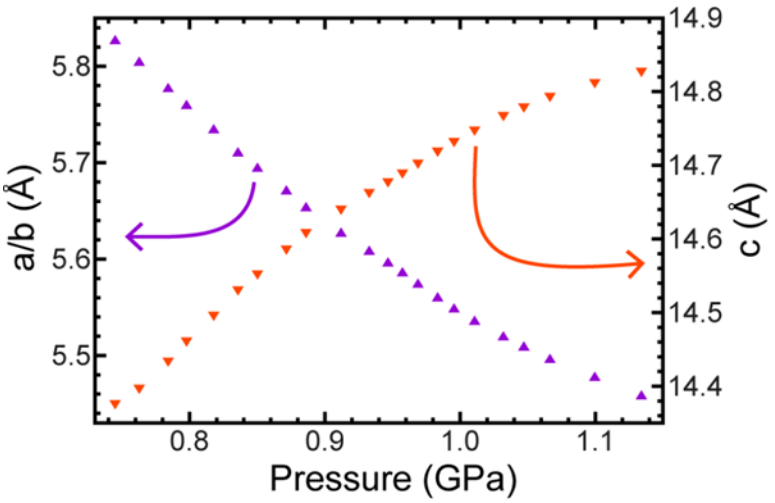

Figure C.10: Lattice constants for high pressure rhombohedral phase of $CaZr_{0.5}Nb_{0.5}F_{6.5}$ showing anisotropic compressibility between a/b and c-axes and

negative linear compressibility parallel to c-axis. Note slight differences in scaling of the two y-axes.

Figure 8.10

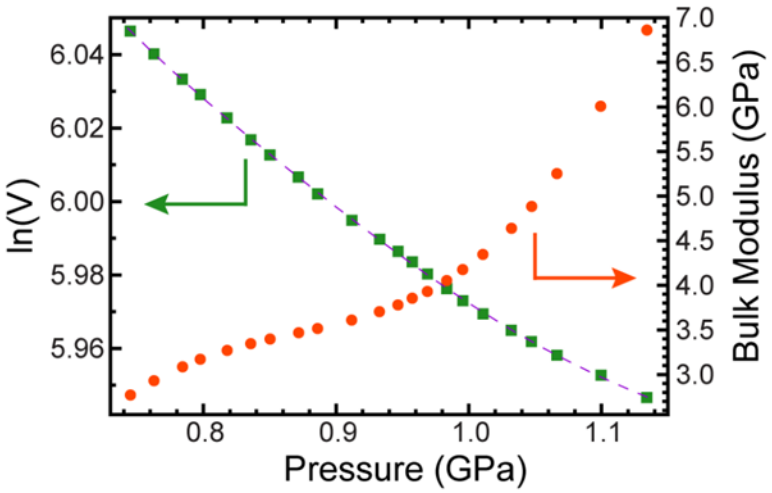

Figure 8.11: Pressure dependence of ln(V) and the bulk modulus for rhombohedral $CaZr_{0.5}Nb_{0.5}F_{6.5}$. A five-term polynomial (purple dotted line) was fit to the ln(V) data and used to calculate bulk moduli.

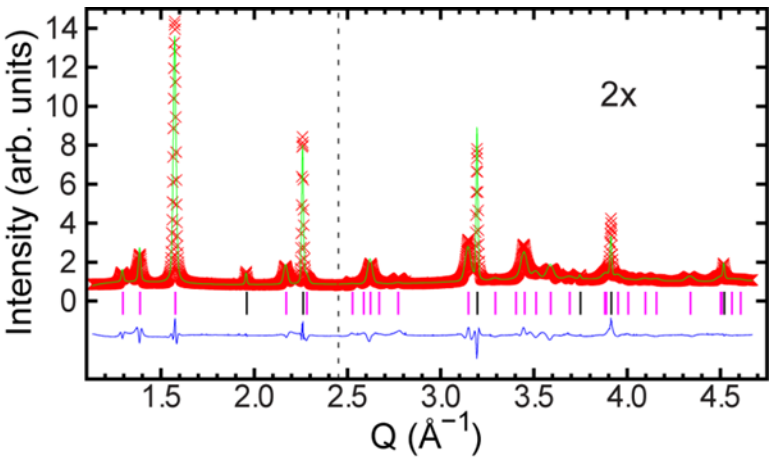

Figure 8.12: Rietveld plot showing a fit of a $CaZr_{0.25}Nb_{0.75}F_{6.75}$ cubic $R\bar{3}$ model to the 1.1 GPa powder x-ray diffraction data obtained in a diamond anvil cell. The section of Q has been scaled to show detail but shifted downwards so that the backgrounds for the sections of the plot appear to be the same.

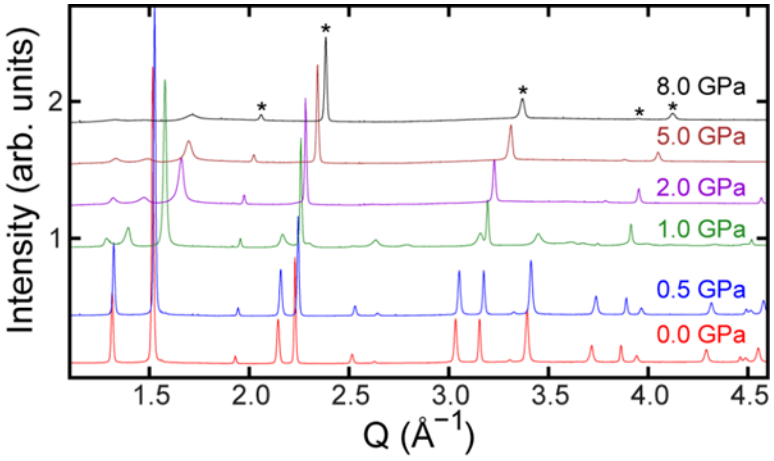

Figure C.11: Select high pressure diffraction patterns of $CaZr_{0.25}Nb_{0.75}F_{6.75}$ showing phase transition, with peaks from NaCl internal pressure standard marked with *.

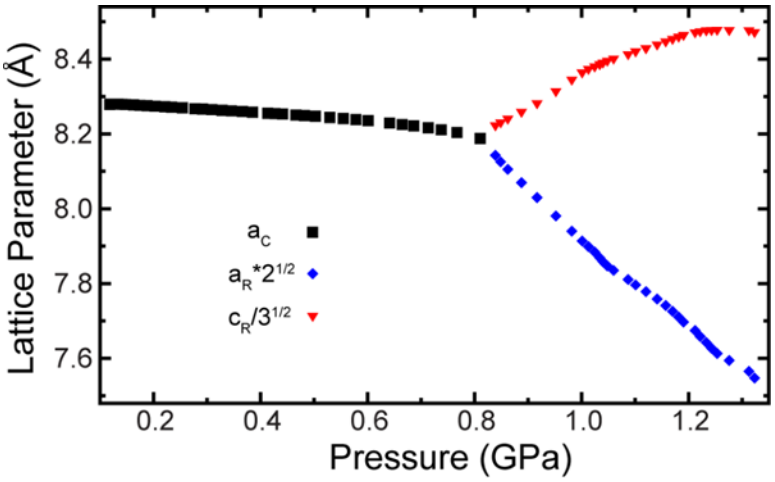

Figure C.12: Pressure dependence of the lattice constants for both the cubic and rhombohedral phase of $CaZr_{0.25}Nb_{0.75}F_{6.75}$. The lattice constants of the rhombohedral phase have been scaled so that they can be compared to the that of the cubic phase.

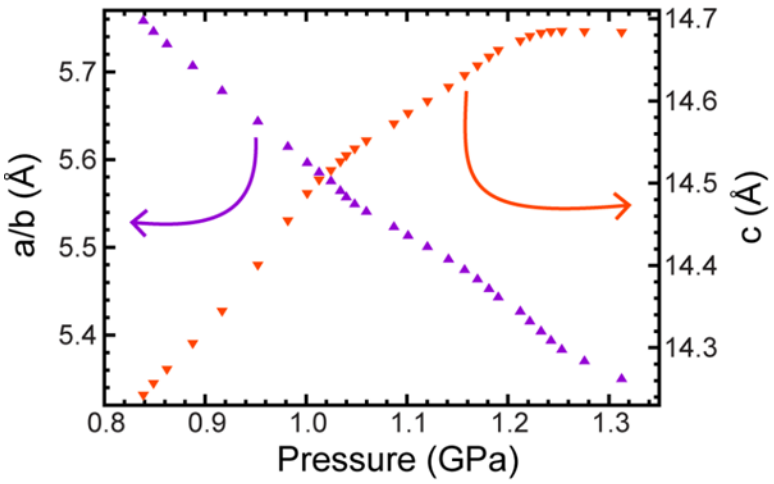

Figure C.13: Lattice constants for high pressure rhombohedral phase of $CaZr_{0.25}Nb_{0.75}F_{6.75}$ showing anisotropic compressibility between a/b and c-axes and

negative linear compressibility parallel to c-axis. Note slight differences in scaling of the two y-axes.

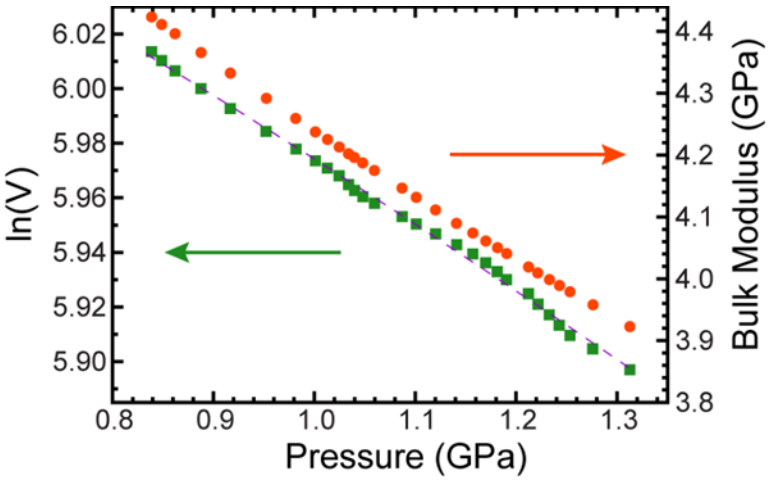

Figure C.14: Pressure dependence of ln(V) and the bulk modulus for rhombohedral $CaZr_{0.25}Nb_{0.75}F_{6.75}$. A two-term polynomial (purple dotted line) was fit to the ln(V) data and used to calculate bulk moduli.

C.2 Supplementary Tables

Table C.1: Lattice constant and unit cell volume for cubic $CaZr_{0.75}Nb_{0.25}F_{6.25}$ as determined from Rietveld analyses of the variable temperature x-ray diffraction data.

Temperature (K)	Rwp	a (Å)	Volume (Å^3)
111.46	0.1086	8.45316(8)	604.03(2)
114.12	0.1086	8.45257(8)	603.90(2)
116.07	0.1086	8.45203(8)	603.79(2)
118.65	0.1086	8.45150(8)	603.67(2)
121.37	0.1086	8.45097(8)	603.56(2)
124.19	0.1086	8.45044(8)	603.45(2)

Temperature (K)	Rwp	a (Å)	Volume (Å^3)
127.46	0.1087	8.44995(8)	603.34(2)
131.11	0.1087	8.44947(8)	603.24(2)
133.81	0.1087	8.44901(8)	603.14(2)
136.62	0.1087	8.44856(8)	603.04(2)
139.47	0.1088	8.44813(8)	602.95(2)
142.26	0.1087	8.44770(8)	602.86(2)
144.97	0.1087	8.44728(8)	602.77(2)
147.61	0.1086	8.44686(8)	602.68(2)
150.20	0.1086	8.44645(8)	602.59(2)
152.81	0.1086	8.44604(8)	602.50(2)
155.51	0.1086	8.44565(8)	602.42(2)
158.33	0.1085	8.44527(8)	602.34(2)
161.25	0.1085	8.44490(8)	602.26(2)
164.16	0.1086	8.44455(8)	602.19(2)
167.27	0.1087	8.44419(8)	602.11(2)
170.10	0.1087	8.44384(8)	602.03(2)
172.94	0.1087	8.44350(8)	601.96(2)
175.79	0.1087	8.44318(8)	601.89(2)
178.66	0.1087	8.44288(8)	601.83(2)
181.54	0.1087	8.44258(8)	601.76(2)
184.42	0.1088	8.44228(8)	601.70(2)
187.29	0.1088	8.44199(8)	601.64(2)
190.16	0.1089	8.44172(8)	601.58(2)
193.02	0.1088	8.44144(8)	601.52(2)
195.89	0.1088	8.44117(8)	601.46(2)
198.78	0.1088	8.44090(8)	601.40(2)
201.71	0.1089	8.44062(8)	601.34(2)
204.68	0.1089	8.44032(8)	601.28(2)
207.68	0.1089	8.44002(8)	601.22(2)
210.69	0.1089	8.43973(8)	601.15(2)
213.63	0.1089	8.43944(8)	601.09(2)
216.41	0.1089	8.43917(8)	601.03(2)
219.55	0.1089	8.43888(8)	600.97(2)
222.45	0.1089	8.43859(8)	600.91(2)
225.35	0.1089	8.43830(8)	600.85(2)
228.45	0.1088	8.43800(8)	600.78(2)
231.45	0.1088	8.43770(8)	600.72(2)
234.35	0.1088	8.43741(8)	600.66(2)
237.25	0.1088	8.43712(8)	600.6(2)
240.25	0.1088	8.43680(8)	600.53(2)

Temperature (K)	Rwp	a (Å)	Volume (Å^3)
243.35	0.1088	8.43652(8)	600.47(2)
246.35	0.1087	8.43624(8)	600.41(2)
249.25	0.1087	8.43596(8)	600.35(2)
252.25	0.1087	8.43569(8)	600.29(2)
256.05	0.1087	8.43544(8)	600.24(2)
258.45	0.1087	8.43539(8)	600.23(2)
261.65	0.1087	8.43496(8)	600.14(2)
264.35	0.1087	8.43486(8)	600.11(2)
266.95	0.1087	8.43485(8)	600.11(2)
270.05	0.1087	8.43467(8)	600.07(2)
273.35	0.1087	8.43441(8)	600.02(2)
275.87	0.1086	8.43379(8)	599.89(2)
278.87	0.1086	8.43369(8)	599.87(2)
282.35	0.1087	8.43364(8)	599.85(2)
284.86	0.1087	8.43337(8)	599.80(2)
287.63	0.1087	8.43312(8)	599.74(2)
291.35	0.1087	8.43301(8)	599.72(2)
293.93	0.1086	8.43268(8)	599.65(2)
296.73	0.1085	8.43253(8)	599.62(2)
300.45	0.1086	8.43257(8)	599.63(2)
302.86	0.1085	8.43228(8)	599.56(2)
306.04	0.1085	8.43225(8)	599.56(2)
309.67	0.1085	8.43211(8)	599.53(2)
312.65	0.1085	8.43194(8)	599.49(2)
316.76	0.1085	8.43171(8)	599.44(2)
319.25	0.1086	8.43177(8)	599.45(2)
322.07	0.1086	8.43157(8)	599.41(2)
325.59	0.1087	8.43144(8)	599.39(2)
328.41	0.1087	8.43150(8)	599.40(2)
331.44	0.1088	8.43143(8)	599.38(2)
334.87	0.1092	8.43149(8)	599.39(2)
338.13	0.1093	8.43137(8)	599.37(2)
341.74	0.1095	8.43136(8)	599.37(2)
344.89	0.1095	8.43138(8)	599.37(2)
348.59	0.1096	8.43136(8)	599.37(2)
351.82	0.1097	8.43140(8)	599.38(2)
355.17	0.1097	8.43138(8)	599.37(2)
358.88	0.1098	8.43133(8)	599.36(2)
362.08	0.1099	8.43132(8)	599.36(2)
365.71	0.1100	8.43128(8)	599.35(2)

Temperature (K)	Rwp	a (Å)	Volume (Å^3)
369.18	0.1101	8.43127(8)	599.35(2)
372.72	0.1101	8.43124(8)	599.34(2)
376.52	0.1102	8.43121(8)	599.33(2)
380.09	0.1102	8.43119(8)	599.33(2)
383.25	0.1102	8.43120(8)	599.33(2)
386.01	0.1104	8.43121(8)	599.34(2)
389.13	0.1104	8.43123(8)	599.34(2)
392.39	0.1103	8.43119(8)	599.33(2)
395.10	0.1103	8.43121(8)	599.34(2)
398.24	0.1103	8.43117(8)	599.33(2)
401.56	0.1103	8.43112(8)	599.32(2)
404.97	0.1103	8.43110(8)	599.31(2)
408.32	0.1104	8.43106(8)	599.30(2)
411.63	0.1104	8.43100(8)	599.29(2)
414.72	0.1104	8.43093(8)	599.28(2)
419.40	0.1104	8.43087(8)	599.26(2)
422.55	0.1104	8.43079(8)	599.25(2)
425.65	0.1104	8.43073(8)	599.23(2)
429.05	0.1105	8.43062(8)	599.21(2)
431.85	0.1104	8.43053(8)	599.19(2)
434.85	0.1104	8.43044(8)	599.17(2)
437.26	0.1105	8.43033(8)	599.15(2)
439.99	0.1105	8.43020(8)	599.12(2)
442.66	0.1105	8.43007(8)	599.09(2)
445.52	0.1105	8.42994(8)	599.07(2)
448.27	0.1106	8.42984(8)	599.04(2)
450.98	0.1106	8.42970(8)	599.01(2)
453.65	0.1106	8.42957(8)	598.99(2)
456.29	0.1106	8.42939(9)	598.95(2)
458.80	0.1107	8.42926(9)	598.92(2)
461.37	0.1107	8.42908(9)	598.88(2)
464.01	0.1107	8.42893(9)	598.85(2)
466.46	0.1107	8.42876(9)	598.81(2)
469.06	0.1107	8.42861(9)	598.78(2)
471.49	0.1108	8.42847(9)	598.75(2)
473.99	0.1109	8.42830(9)	598.71(2)
476.55	0.1108	8.42812(9)	598.68(2)
479.09	0.1108	8.42796(9)	598.64(2)
481.44	0.1109	8.42778(9)	598.61(2)
483.75	0.1108	8.42763(9)	598.57(2)

Temperature (K)	Rwp	a (Å)	Volume (Å^3)
486.10	0.1167	8.42744(9)	598.53(2)
488.48	0.1110	8.42732(9)	598.51(2)
490.72	0.1110	8.42714(9)	598.47(2)
492.85	0.1110	8.42699(9)	598.44(2)
495.09	0.1109	8.42688(9)	598.41(2)
497.18	0.1109	8.42675(9)	598.38(2)
499.37	0.1109	8.42657(9)	598.35(2)
501.73	0.1109	8.42637(9)	598.30(2)
502.87	0.1109	8.42634(9)	598.30(2)
501.76	0.1110	8.42649(9)	598.33(2)
500.16	0.1110	8.42668(9)	598.37(2)
498.56	0.1110	8.42682(9)	598.40(2)
496.65	0.1110	8.42698(9)	598.43(2)
494.66	0.1110	8.42714(9)	598.47(2)
492.72	0.1111	8.42730(9)	598.50(2)
490.64	0.1110	8.42749(9)	598.54(2)
488.47	0.1109	8.42763(9)	598.57(2)
486.18	0.1109	8.42781(9)	598.61(2)
483.77	0.1109	8.42801(9)	598.65(2)
481.25	0.1109	8.42818(9)	598.69(2)
478.63	0.1108	8.42837(9)	598.73(2)
475.96	0.1108	8.42856(9)	598.77(2)
473.25	0.1108	8.42875(9)	598.81(2)
470.54	0.1109	8.42897(9)	598.86(2)
467.92	0.1109	8.42914(9)	598.89(2)
465.20	0.1108	8.42932(9)	598.93(2)
461.85	0.1108	8.42951(9)	598.97(2)
459.11	0.1109	8.42971(9)	599.02(2)
455.75	0.1108	8.42989(8)	599.05(2)
452.93	0.1108	8.43009(8)	599.10(2)
450.25	0.1108	8.43027(8)	599.14(2)
447.73	0.1108	8.43048(8)	599.18(2)
444.38	0.1107	8.43068(8)	599.22(2)
441.44	0.1107	8.43088(8)	599.26(2)
438.59	0.1107	8.43107(8)	599.31(2)
435.78	0.1107	8.43127(8)	599.35(2)
432.70	0.1107	8.43146(8)	599.39(2)
429.76	0.1107	8.43168(8)	599.44(2)
426.67	0.1107	8.43191(8)	599.48(2)
423.56	0.1108	8.43210(8)	599.53(2)

Temperature (K)	Rwp	a (Å)	Volume (Å^3)
420.45	0.1108	8.43232(8)	599.57(2)
417.25	0.1108	8.43252(8)	599.61(2)
414.26	0.1107	8.43273(8)	599.66(2)
411.07	0.1107	8.43291(8)	599.70(2)
408.07	0.1107	8.43314(8)	599.75(2)
404.94	0.1108	8.43337(8)	599.80(2)
401.56	0.1107	8.43358(8)	599.84(2)
398.60	0.1108	8.43382(8)	599.89(2)
395.56	0.1110	8.43405(8)	599.94(2)
392.60	0.1108	8.43423(8)	599.98(2)
389.99	0.1106	8.43438(8)	600.01(2)
387.10	0.1105	8.43457(8)	600.05(2)
384.21	0.1106	8.43482(8)	600.11(2)
381.08	0.1106	8.43509(8)	600.16(2)
377.56	0.1106	8.43536(8)	600.22(2)
374.29	0.1106	8.43551(8)	600.25(2)
370.67	0.1107	8.43577(8)	600.31(2)
367.21	0.1107	8.43604(8)	600.37(2)
363.58	0.1107	8.43630(8)	600.42(2)
360.67	0.1106	8.43658(8)	600.48(2)
357.24	0.1106	8.43683(8)	600.53(2)
353.59	0.1106	8.43721(8)	600.62(2)
350.61	0.1106	8.43721(8)	600.62(2)
347.50	0.1106	8.43745(8)	600.67(2)
343.59	0.1106	8.43794(8)	600.77(2)
340.57	0.1107	8.43798(8)	600.78(2)
337.34	0.1107	8.43820(8)	600.83(2)
333.49	0.1107	8.43874(8)	600.94(2)
330.47	0.1107	8.43890(8)	600.98(2)
327.70	0.1108	8.43916(8)	601.03(2)
324.24	0.1109	8.43964(8)	601.13(2)
320.74	0.1110	8.44012(8)	601.24(2)
315.72	0.1110	8.44038(8)	601.29(2)
312.79	0.1111	8.44057(8)	601.33(2)
309.35	0.1111	8.44098(8)	601.42(2)
306.34	0.1111	8.44108(8)	601.44(2)
303.28	0.1110	8.44151(8)	601.53(2)
300.40	0.1109	8.44156(8)	601.55(2)
297.49	0.1107	8.44178(8)	601.59(2)
294.47	0.1105	8.44201(8)	601.64(2)

Temperature (K)	Rwp	a (Å)	Volume (Å^3)
291.16	0.1108	8.44236(8)	601.72(2)
287.94	0.1108	8.44270(8)	601.79(2)
285.15	0.1109	8.44302(8)	601.86(2)
282.15	0.1111	8.44337(8)	601.93(2)
279.35	0.1111	8.44376(8)	602.01(2)
276.35	0.1111	8.44386(8)	602.04(2)
273.05	0.1112	8.44433(8)	602.14(2)
270.15	0.1114	8.44458(8)	602.19(2)
267.61	0.1114	8.44502(8)	602.29(2)
264.09	0.1115	8.44533(8)	602.35(2)
261.39	0.1119	8.44566(8)	602.42(2)
258.59	0.1120	8.44595(8)	602.48(2)
255.70	0.1121	8.44608(8)	602.51(2)
252.67	0.1119	8.44647(8)	602.60(2)
249.83	0.1119	8.44647(8)	602.60(2)
246.75	0.1119	8.44686(8)	602.68(2)
243.77	0.1119	8.44755(8)	602.83(2)
240.47	0.1119	8.44765(8)	602.85(2)
237.73	0.1120	8.44801(8)	602.93(2)
234.92	0.1121	8.44808(8)	602.94(2)
232.17	0.1120	8.44832(8)	602.99(2)
229.27	0.1121	8.44864(8)	603.06(2)
226.35	0.1121	8.44898(8)	603.13(2)
222.94	0.1121	8.44931(8)	603.20(2)
220.04	0.1122	8.44963(8)	603.27(2)
217.25	0.1122	8.44995(8)	603.34(2)
214.25	0.1123	8.45032(8)	603.42(2)
211.25	0.1125	8.45071(8)	603.50(2)
207.86	0.1124	8.45106(8)	603.58(2)
204.81	0.1123	8.45140(8)	603.65(2)
201.86	0.1122	8.45172(8)	603.72(2)
198.96	0.1122	8.45206(8)	603.79(2)
196.09	0.1123	8.45245(8)	603.88(2)
193.21	0.1125	8.45281(8)	603.95(2)
190.31	0.1125	8.45317(8)	604.03(2)
187.40	0.1125	8.45352(8)	604.10(2)
184.46	0.1125	8.45387(8)	604.18(2)
181.51	0.1124	8.45421(8)	604.25(2)
178.55	0.1124	8.45455(8)	604.33(2)
175.59	0.1125	8.45493(8)	604.41(2)

Temperature (K)	Rwp	a (Å)	Volume (Å^3)
172.64	0.1125	8.45529(8)	604.48(2)
169.71	0.1124	8.45564(8)	604.56(2)
166.80	0.1124	8.45601(8)	604.64(2)
163.93	0.1125	8.45637(8)	604.72(2)
161.09	0.1125	8.45675(8)	604.80(2)
158.28	0.1124	8.45710(8)	604.87(2)
155.50	0.1124	8.45746(8)	604.95(2)
152.74	0.1123	8.45782(8)	605.03(2)
150.00	0.1122	8.45816(8)	605.10(2)
147.27	0.1122	8.45853(8)	605.18(2)
144.53	0.1122	8.45889(8)	605.26(2)
141.78	0.1122	8.45925(8)	605.33(2)
138.99	0.1122	8.45963(8)	605.42(2)
136.16	0.1122	8.46000(8)	605.50(2)
133.28	0.1122	8.46039(8)	605.58(2)
130.35	0.1122	8.46075(8)	605.66(2)
127.35	0.1121	8.46116(8)	605.75(2)
124.31	0.1121	8.46159(8)	605.84(2)
121.23	0.1121	8.46201(8)	605.93(2)
118.15	0.1121	8.46242(8)	606.02(2)
115.10	0.1120	8.46284(8)	606.11(2)
112.14	0.1121	8.46324(8)	606.19(2)

Table C.2: Lattice constant and unit cell volume for cubic $CaZr_{0.5}Nb_{0.5}F_{6.5}$ as determined from Rietveld analyses of the variable temperature x-ray diffraction data.

Temperature (K)	Rwp	a (Å)	Volume (Å^3)
111.53	0.1087	8.3876(1)	590.08(2)
114.12	0.1086	8.3871(1)	589.98(2)
116.07	0.1087	8.3867(1)	589.89(2)
118.65	0.1086	8.3862(1)	589.79(2)
121.51	0.1085	8.3857(1)	589.69(2)
124.19	0.1085	8.3853(1)	589.60(2)
127.46	0.1085	8.3849(1)	589.51(2)
131.11	0.1085	8.3845(1)	589.44(2)
133.81	0.1085	8.3842(1)	589.36(2)
136.62	0.1085	8.3838(1)	589.29(2)
139.47	0.1086	8.3835(1)	589.22(2)

Temperature (K)	Rwp	a (Å)	Volume (Å^3)
142.26	0.1085	8.3832(1)	589.16(2)
144.97	0.1085	8.3829(1)	589.09(2)
147.61	0.1084	8.3826(1)	589.02(2)
150.20	0.1084	8.3823(1)	588.97(2)
152.81	0.1084	8.3820(1)	588.91(2)
155.51	0.1083	8.3818(1)	588.87(2)
158.33	0.1083	8.3816(1)	588.83(2)
161.25	0.1083	8.3815(1)	588.79(2)
164.16	0.1084	8.3813(1)	588.76(2)
167.27	0.1084	8.3812(1)	588.73(2)
170.06	0.1084	8.3811(1)	588.70(2)
172.94	0.1085	8.3810(1)	588.69(2)
175.79	0.1085	8.3809(1)	588.68(2)
178.66	0.1085	8.3808(1)	588.65(2)
181.54	0.1085	8.3807(1)	588.63(2)
184.42	0.1086	8.3806(1)	588.61(2)
187.29	0.1087	8.3806(1)	588.60(2)
190.16	0.1087	8.3805(1)	588.58(2)
193.02	0.1087	8.3804(1)	588.56(2)
195.89	0.1087	8.3802(1)	588.53(2)
198.78	0.1086	8.3801(1)	588.49(2)
201.71	0.1086	8.3799(1)	588.46(2)
204.68	0.1085	8.3797(1)	588.42(2)
207.68	0.1085	8.3796(1)	588.39(2)
210.64	0.1085	8.3794(1)	588.35(2)
213.63	0.1086	8.3792(1)	588.32(2)
216.40	0.1086	8.3791(1)	588.28(2)
219.50	0.1085	8.3788(1)	588.23(2)
222.45	0.1085	8.3786(1)	588.19(2)
225.31	0.1084	8.3784(1)	588.15(2)
228.45	0.1083	8.3782(1)	588.10(2)
231.40	0.1082	8.3780(1)	588.05(2)
234.45	0.1083	8.3778(1)	588.01(2)
237.45	0.1083	8.3776(1)	587.98(2)
240.00	0.1082	8.3775(1)	587.95(2)
243.20	0.1081	8.3773(1)	587.91(2)
246.35	0.1081	8.3773(1)	587.92(2)
249.30	0.1081	8.3769(1)	587.82(2)
252.20	0.1081	8.3767(1)	587.79(2)
255.25	0.1080	8.3765(1)	587.74(2)

Temperature (K)	Rwp	a (Å)	Volume (Å^3)
258.40	0.1080	8.3765(1)	587.74(2)
261.35	0.1079	8.3761(1)	587.66(2)
264.20	0.1078	8.3759(1)	587.62(2)
267.35	0.1078	8.3758(1)	587.60(2)
269.55	0.1077	8.3757(1)	587.58(2)
273.55	0.1077	8.3755(1)	587.52(2)
276.55	0.1076	8.3752(1)	587.48(2)
279.45	0.1075	8.3750(1)	587.43(2)
282.30	0.1075	8.3750(1)	587.43(2)
285.30	0.1074	8.3748(1)	587.39(2)
288.30	0.1074	8.3747(1)	587.37(2)
291.30	0.1073	8.3746(1)	587.33(2)
294.40	0.1072	8.3744(1)	587.30(2)
297.20	0.1072	8.3743(1)	587.27(2)
300.25	0.1071	8.3741(1)	587.23(2)
303.11	0.1071	8.3741(1)	587.25(2)
305.69	0.1070	8.3740(1)	587.23(2)
309.23	0.1069	8.3740(1)	587.22(2)
312.45	0.1069	8.3741(1)	587.23(2)
316.23	0.1067	8.3742(1)	587.25(2)
319.25	0.1066	8.3746(1)	587.34(2)
322.21	0.1066	8.3748(1)	587.39(2)
325.33	0.1066	8.3753(1)	587.48(2)
328.36	0.1064	8.3756(1)	587.56(2)
331.82	0.1063	8.3761(1)	587.65(2)
334.98	0.1063	8.3766(1)	587.77(2)
338.29	0.1062	8.3769(1)	587.83(2)
341.85	0.1060	8.3774(1)	587.92(2)
345.00	0.1060	8.3777(1)	588.00(2)
348.48	0.1059	8.3781(1)	588.08(2)
352.10	0.1058	8.3784(1)	588.15(2)
355.23	0.1057	8.3787(1)	588.21(2)
358.54	0.1060	8.3791(1)	588.29(2)
361.97	0.1063	8.3793(1)	588.33(2)
365.53	0.1063	8.3796(1)	588.40(2)
369.06	0.1062	8.3798(1)	588.44(2)
372.91	0.1061	8.3801(1)	588.49(2)
376.34	0.1060	8.3803(1)	588.55(2)
379.97	0.1059	8.3806(1)	588.60(2)
383.35	0.1062	8.3808(1)	588.65(2)

Temperature (K)	Rwp	a (Å)	Volume (Å^3)
386.11	0.1061	8.3811(1)	588.70(2)
389.13	0.1060	8.3813(1)	588.75(2)
392.19	0.1060	8.3815(1)	588.80(2)
395.15	0.1060	8.3817(1)	588.84(2)
398.35	0.1059	8.3819(1)	588.88(2)
401.61	0.1059	8.3821(1)	588.92(2)
405.02	0.1058	8.3822(1)	588.95(2)
408.37	0.1057	8.3824(1)	588.99(2)
411.52	0.1056	8.3826(1)	589.03(2)
414.77	0.1056	8.3827(1)	589.06(2)
419.29	0.1054	8.3829(1)	589.09(2)
422.60	0.1054	8.3831(1)	589.12(2)
425.70	0.1053	8.3832(1)	589.16(2)
429.05	0.1053	8.3833(1)	589.18(2)
431.90	0.1052	8.3835(1)	589.21(2)
434.85	0.1051	8.3836(1)	589.23(2)
437.21	0.1051	8.3837(1)	589.26(2)
439.94	0.1050	8.3838(1)	589.28(2)
442.71	0.1050	8.3839(1)	589.30(2)
445.43	0.1049	8.3840(1)	589.32(2)
448.32	0.1048	8.3841(1)	589.33(2)
450.94	0.1047	8.3841(1)	589.35(2)
453.56	0.1046	8.3842(1)	589.37(2)
456.29	0.1045	8.3843(1)	589.38(2)
458.84	0.1044	8.3843(1)	589.39(2)
461.50	0.1043	8.3844(1)	589.40(2)
463.97	0.1042	8.3844(1)	589.41(2)
466.54	0.1042	8.3845(1)	589.42(2)
469.02	0.1041	8.3845(1)	589.44(2)
471.57	0.1040	8.3846(1)	589.44(2)
474.07	0.1040	8.3846(1)	589.46(2)
476.59	0.1039	8.3846(1)	589.46(2)
479.05	0.1038	8.3847(1)	589.47(2)
481.44	0.1038	8.3847(1)	589.47(2)
483.83	0.1037	8.3848(1)	589.49(2)
486.18	0.1036	8.3848(1)	589.49(2)
488.44	0.1035	8.3849(1)	589.51(2)
490.69	0.1034	8.3849(1)	589.51(2)
492.92	0.1033	8.3850(1)	589.52(2)
495.06	0.1032	8.3850(1)	589.54(2)

Temperature (K)	Rwp	a (Å)	Volume (Å^3)
497.18	0.1031	8.3851(1)	589.56(2)
499.41	0.1030	8.3852(1)	589.57(2)
501.65	0.1029	8.3852(1)	589.58(2)
502.87	0.1029	8.3853(1)	589.61(2)
501.69	0.1029	8.3857(1)	589.69(2)
500.19	0.1029	8.3861(1)	589.76(2)
498.50	0.1030	8.3865(1)	589.85(2)
496.65	0.1029	8.3869(1)	589.93(2)
494.69	0.1030	8.3873(1)	590.01(2)
492.66	0.1031	8.3877(1)	590.10(2)
490.64	0.1031	8.3881(1)	590.19(2)
488.47	0.1032	8.3885(1)	590.28(2)
486.18	0.1033	8.3889(1)	590.37(2)
483.77	0.1035	8.3894(1)	590.46(2)
481.20	0.1036	8.3898(1)	590.55(2)
478.68	0.1037	8.3902(1)	590.63(2)
475.96	0.1038	8.3906(1)	590.72(2)
473.29	0.1038	8.3910(1)	590.81(2)
470.54	0.1040	8.3914(1)	590.89(2)
467.88	0.1041	8.3918(1)	590.97(2)
465.16	0.1044	8.3922(1)	591.05(2)
461.75	0.1043	8.3926(1)	591.14(2)
459.05	0.1045	8.3930(1)	591.22(2)
455.75	0.1046	8.3934(1)	591.30(2)
452.93	0.1047	8.3937(1)	591.37(2)
450.25	0.1049	8.3941(1)	591.45(2)
447.73	0.1050	8.3944(1)	591.52(2)
444.28	0.1051	8.3948(1)	591.59(2)
441.48	0.1052	8.3951(1)	591.66(2)
438.59	0.1053	8.3954(1)	591.73(2)
435.73	0.1054	8.3957(1)	591.80(2)
432.75	0.1055	8.3960(1)	591.87(2)
429.71	0.1056	8.3964(1)	591.93(2)
426.62	0.1057	8.3967(1)	592.00(2)
423.51	0.1057	8.3970(1)	592.06(2)
420.35	0.1059	8.3973(1)	592.12(2)
417.25	0.1059	8.3975(1)	592.18(2)
414.21	0.1061	8.3978(1)	592.24(2)
411.07	0.1061	8.3981(1)	592.30(2)
407.96	0.1062	8.3984(1)	592.36(2)

Temperature (K)	Rwp	a (Å)	Volume (Å^3)
404.88	0.1062	8.3986(1)	592.42(2)
401.72	0.1064	8.3989(1)	592.48(2)
398.49	0.1064	8.3992(1)	592.54(2)
395.51	0.1065	8.3995(1)	592.59(2)
392.46	0.1064	8.3997(1)	592.63(2)
389.81	0.1065	8.3999(1)	592.69(2)
387.10	0.1067	8.4002(1)	592.74(2)
384.21	0.1067	8.4004(1)	592.80(2)
381.08	0.1067	8.4007(1)	592.86(2)
377.62	0.1068	8.4010(1)	592.92(2)
374.11	0.1068	8.4013(1)	592.98(2)
370.49	0.1069	8.4016(1)	593.05(2)
367.26	0.1069	8.4018(1)	593.09(2)
363.75	0.1070	8.4022(1)	593.18(2)
360.34	0.1070	8.4024(1)	593.21(2)
357.02	0.1070	8.4027(1)	593.27(2)
353.70	0.1071	8.4030(1)	593.33(2)
350.61	0.1071	8.4032(1)	593.39(2)
347.22	0.1071	8.4036(1)	593.46(2)
343.87	0.1071	8.4037(1)	593.50(2)
340.40	0.1072	8.4040(1)	593.56(2)
337.12	0.1072	8.4043(1)	593.62(2)
333.71	0.1072	8.4046(1)	593.67(2)
330.63	0.1073	8.4048(1)	593.73(2)
327.33	0.1073	8.4052(1)	593.80(2)
324.13	0.1073	8.4055(1)	593.87(2)
320.90	0.1073	8.4057(1)	593.90(2)
315.53	0.1074	8.4063(1)	594.04(2)
312.46	0.1074	8.4066(1)	594.10(2)
309.35	0.1074	8.4066(1)	594.10(2)
306.19	0.1075	8.4069(1)	594.16(2)
303.43	0.1076	8.4072(1)	594.22(2)
300.55	0.1076	8.4077(1)	594.33(2)
297.54	0.1076	8.4076(1)	594.32(2)
294.37	0.1077	8.4080(1)	594.41(2)
291.36	0.1077	8.4082(1)	594.45(2)
288.36	0.1077	8.4086(1)	594.52(2)
285.57	0.1077	8.4088(1)	594.56(2)
282.75	0.1078	8.4091(1)	594.64(2)
279.75	0.1077	8.4094(1)	594.69(2)

Temperature (K)	Rwp	a (Å)	Volume (Å^3)
276.44	0.1077	8.4096(1)	594.73(2)
273.50	0.1078	8.4098(1)	594.78(2)
270.50	0.1078	8.4101(1)	594.84(2)
267.56	0.1079	8.4107(1)	594.96(2)
264.02	0.1080	8.4109(1)	595.01(2)
261.44	0.1080	8.4112(1)	595.08(2)
258.54	0.1081	8.4118(1)	595.19(2)
255.45	0.1081	8.4120(1)	595.26(2)
252.33	0.1081	8.4120(1)	595.25(2)
249.44	0.1082	8.4127(1)	595.40(2)
246.51	0.1082	8.4127(1)	595.40(2)
243.77	0.1081	8.4126(1)	595.38(2)
240.81	0.1082	8.4129(1)	595.44(2)
237.88	0.1084	8.4133(1)	595.51(2)
234.92	0.1084	8.4135(1)	595.57(2)
232.12	0.1085	8.4140(1)	595.67(2)
229.27	0.1086	8.4142(1)	595.71(2)
226.40	0.1086	8.4144(1)	595.76(2)
222.94	0.1087	8.4147(1)	595.82(2)
220.04	0.1088	8.4150(1)	595.89(2)
217.25	0.1089	8.4154(1)	595.96(2)
214.30	0.1089	8.4157(1)	596.04(2)
211.30	0.1090	8.4160(1)	596.11(2)
207.86	0.1091	8.4164(1)	596.18(2)
204.81	0.1092	8.4167(1)	596.25(2)
201.86	0.1093	8.4171(1)	596.32(2)
198.96	0.1094	8.4174(1)	596.39(2)
196.09	0.1095	8.4177(1)	596.46(2)
193.21	0.1095	8.4181(1)	596.53(2)
190.36	0.1096	8.4184(1)	596.61(2)
187.40	0.1098	8.4187(1)	596.68(2)
184.46	0.1099	8.4191(1)	596.75(2)
181.51	0.1100	8.4194(1)	596.82(2)
178.55	0.1101	8.4197(1)	596.89(2)
175.59	0.1102	8.4201(1)	596.96(2)
172.64	0.1104	8.4204(1)	597.03(2)
169.71	0.1105	8.4207(1)	597.10(2)
166.80	0.1106	8.4211(1)	597.18(2)
163.93	0.1107	8.4214(1)	597.26(2)
161.09	0.1108	8.4218(1)	597.33(2)

Temperature (K)	Rwp	a (Å)	Volume (Å^3)
158.28	0.1110	8.4221(1)	597.40(2)
155.50	0.1111	8.4225(1)	597.47(2)
152.70	0.1112	8.4228(1)	597.55(2)
150.00	0.1113	8.4231(1)	597.62(2)
147.22	0.1114	8.4235(1)	597.69(2)
144.53	0.1116	8.4239(1)	597.77(2)
141.78	0.1116	8.4242(1)	597.84(2)
138.99	0.1117	8.4245(1)	597.91(2)
136.16	0.1119	8.4249(1)	597.99(2)
133.28	0.1120	8.4253(1)	598.07(2)
130.35	0.1122	8.4256(1)	598.14(2)
127.35	0.1123	8.4260(1)	598.23(2)
124.31	0.1124	8.4264(1)	598.31(2)
121.23	0.1126	8.4268(1)	598.40(2)
118.15	0.1128	8.4272(1)	598.48(2)
115.10	0.1128	8.4276(1)	598.56(2)
112.05	0.1129	8.4280(1)	598.64(2)

Table C.3: Lattice constant and unit cell volume for cubic $CaZr_{0.25}Nb_{0.75}F_{6.75}$ as determined from Rietveld analyses of the variable temperature x-ray diffraction data.

Temperature (K)	Rwp	a (Å)	Volume (Å^3)
111.53	0.0833	8.30812(8)	573.47(2)
114.12	0.0832	8.30742(8)	573.32(2)
116.07	0.0831	8.30678(8)	573.19(2)
118.65	0.0830	8.30619(8)	573.07(2)
121.37	0.0829	8.30566(8)	572.96(2)
124.19	0.0829	8.30517(8)	572.86(2)
127.46	0.0829	8.30474(8)	572.77(2)
131.11	0.0829	8.30437(8)	572.69(2)
133.81	0.0829	8.30407(8)	572.63(2)
136.62	0.0830	8.30382(8)	572.58(2)
139.47	0.0830	8.30368(8)	572.55(2)

Temperature (K)	Rwp	a (Å)	Volume (Å^3)
142.26	0.0831	8.30358(8)	572.53(2)
144.97	0.0831	8.30356(8)	572.52(2)
147.61	0.0832	8.30362(8)	572.54(2)
150.11	0.0832	8.30371(8)	572.55(2)
152.81	0.0831	8.30384(8)	572.58(2)
155.51	0.0832	8.30403(8)	572.62(2)
158.33	0.0833	8.30427(8)	572.67(2)
161.25	0.0835	8.30457(8)	572.73(2)
164.16	0.0836	8.30482(8)	572.78(2)
167.25	0.0836	8.30508(8)	572.84(2)
170.10	0.0837	8.30533(8)	572.89(2)
172.94	0.0838	8.30559(8)	572.94(2)
175.75	0.0837	8.30579(8)	572.99(2)
178.66	0.0838	8.30596(8)	573.02(2)
181.54	0.0839	8.30612(8)	573.05(2)
184.42	0.0840	8.30624(8)	573.08(2)
187.29	0.0840	8.30631(8)	573.09(2)
190.16	0.0840	8.30632(8)	573.10(2)
193.02	0.0840	8.30632(8)	573.10(2)
195.89	0.0840	8.30631(8)	573.09(2)
198.78	0.0839	8.30629(8)	573.09(2)
201.71	0.0839	8.30623(8)	573.08(2)
204.68	0.0838	8.30618(8)	573.06(2)
207.68	0.0839	8.30615(8)	573.06(2)
210.69	0.0839	8.30611(8)	573.05(2)
213.63	0.0839	8.30607(8)	573.04(2)
216.35	0.0839	8.30602(8)	573.03(2)
219.36	0.0839	8.30598(8)	573.02(2)
222.89	0.0838	8.30587(8)	573.00(2)
225.35	0.0837	8.30581(8)	572.99(2)
228.50	0.0837	8.30577(8)	572.98(2)
231.25	0.0840	8.3058(8)	572.99(2)
234.40	0.0840	8.30576(8)	572.98(2)
237.40	0.0839	8.30567(8)	572.96(2)
240.20	0.0841	8.30564(8)	572.95(2)
243.60	0.0843	8.30564(8)	572.95(2)
246.65	0.0844	8.30562(8)	572.95(2)
249.40	0.0843	8.30557(8)	572.94(2)
252.25	0.0840	8.30540(8)	572.90(2)
255.15	0.0838	8.30532(8)	572.89(2)

Temperature (K)	Rwp	a (Å)	Volume (Å^3)
258.10	0.0835	8.30517(8)	572.86(2)
261.35	0.0837	8.30516(8)	572.85(2)
264.15	0.0838	8.30512(8)	572.85(2)
267.35	0.0839	8.30507(8)	572.84(2)
270.40	0.0839	8.30512(8)	572.85(2)
273.50	0.0840	8.30506(8)	572.83(2)
276.60	0.0842	8.30505(8)	572.83(2)
279.45	0.0842	8.30500(8)	572.82(2)
282.20	0.0841	8.30491(8)	572.80(2)
285.25	0.0840	8.30495(8)	572.81(2)
288.25	0.0839	8.30494(8)	572.81(2)
291.35	0.0838	8.30493(8)	572.81(2)
294.45	0.0837	8.30494(8)	572.81(2)
297.30	0.0837	8.30501(8)	572.82(2)
300.20	0.0836	8.30514(8)	572.85(2)
303.20	0.0835	8.30530(8)	572.88(2)
303.99	0.0834	8.30552(8)	572.93(2)
308.63	0.0834	8.30586(8)	573.00(2)
312.55	0.0833	8.30632(8)	573.09(2)
316.86	0.0832	8.30690(8)	573.21(2)
318.87	0.0833	8.30764(8)	573.37(2)
321.92	0.0833	8.30852(8)	573.55(2)
325.12	0.0834	8.30945(8)	573.74(2)
328.57	0.0833	8.31029(8)	573.92(2)
331.66	0.0833	8.31117(8)	574.10(2)
335.20	0.0833	8.31190(8)	574.25(2)
338.18	0.0833	8.31261(8)	574.40(2)
341.85	0.0833	8.31315(8)	574.51(2)
345.12	0.0833	8.31370(8)	574.62(2)
348.37	0.0833	8.31415(8)	574.72(2)
352.05	0.0833	8.3146(8)	574.81(2)
355.11	0.0832	8.31496(8)	574.88(2)
358.60	0.0832	8.31531(8)	574.96(2)
361.97	0.0832	8.31564(8)	575.03(2)
365.47	0.0831	8.31589(8)	575.08(2)
369.12	0.0830	8.31616(8)	575.13(2)
372.66	0.0829	8.31636(8)	575.18(2)
376.40	0.0829	8.31659(8)	575.22(2)
379.97	0.0830	8.31680(8)	575.27(2)
383.25	0.0831	8.31697(8)	575.30(2)

Temperature (K)	Rwp	a (Å)	Volume (Å^3)
386.21	0.0830	8.31713(8)	575.33(2)
389.13	0.0831	8.31728(8)	575.37(2)
392.14	0.0830	8.31740(8)	575.39(2)
395.10	0.0831	8.31750(8)	575.41(2)
398.29	0.0831	8.31759(8)	575.43(2)
401.61	0.0830	8.31767(8)	575.45(2)
404.97	0.0830	8.31773(8)	575.46(2)
408.37	0.0830	8.31778(8)	575.47(2)
411.63	0.0829	8.31783(8)	575.48(2)
414.77	0.0830	8.31787(8)	575.49(2)
419.40	0.0831	8.31792(8)	575.50(2)
422.60	0.0830	8.31794(8)	575.50(2)
425.75	0.0831	8.31796(8)	575.51(2)
429.05	0.0832	8.31799(8)	575.51(2)
431.90	0.0832	8.31801(8)	575.52(2)
434.90	0.0836	8.31801(8)	575.52(2)
437.26	0.0835	8.31799(8)	575.51(2)
439.99	0.0835	8.31797(8)	575.51(2)
442.76	0.0834	8.31797(8)	575.51(2)
445.48	0.0834	8.31795(8)	575.51(2)
448.22	0.0834	8.31795(8)	575.50(2)
450.94	0.0834	8.31793(8)	575.50(2)
453.61	0.0834	8.31793(8)	575.50(2)
456.24	0.0834	8.31793(8)	575.50(2)
458.89	0.0834	8.31790(8)	575.50(2)
461.46	0.0833	8.31785(8)	575.48(2)
463.97	0.0832	8.31784(8)	575.48(2)
466.46	0.0832	8.31778(8)	575.47(2)
469.06	0.0831	8.31775(8)	575.46(2)
471.57	0.0830	8.31771(8)	575.46(2)
474.07	0.0829	8.31766(8)	575.45(2)
476.55	0.0828	8.3176(8)	575.43(2)
479.01	0.0826	8.31757(8)	575.43(2)
481.44	0.0825	8.31751(7)	575.41(2)
483.87	0.0824	8.31747(7)	575.41(2)
486.22	0.0823	8.31742(7)	575.39(2)
488.48	0.0821	8.31738(7)	575.39(2)
490.72	0.0820	8.31734(7)	575.38(2)
492.92	0.0819	8.31732(7)	575.38(2)
495.09	0.0818	8.31729(7)	575.37(2)

Temperature (K)	Rwp	a (Å)	Volume (Å^3)
497.25	0.0814	8.31723(7)	575.36(2)
499.45	0.0811	8.31719(7)	575.35(2)
501.69	0.0809	8.31718(7)	575.35(2)
502.89	0.0807	8.31720(7)	575.35(2)
501.71	0.0805	8.31738(7)	575.39(2)
500.22	0.0805	8.31759(7)	575.43(2)
498.50	0.0805	8.31785(7)	575.48(2)
496.62	0.0805	8.31812(7)	575.54(2)
494.69	0.0804	8.31837(7)	575.59(2)
492.69	0.0803	8.31868(7)	575.66(2)
490.64	0.0802	8.31900(7)	575.72(2)
488.47	0.0802	8.31936(7)	575.8(2)
486.14	0.0802	8.31976(7)	575.88(2)
483.77	0.0802	8.32017(7)	575.97(2)
481.25	0.0801	8.32056(7)	576.05(2)
478.59	0.0800	8.32097(7)	576.13(2)
475.96	0.0799	8.32142(7)	576.23(2)
473.25	0.0800	8.32188(7)	576.32(2)
470.58	0.0800	8.32233(7)	576.42(2)
467.83	0.0799	8.32281(7)	576.51(2)
465.11	0.0799	8.32330(7)	576.62(2)
461.75	0.0800	8.32379(7)	576.72(2)
458.93	0.0799	8.32428(7)	576.82(2)
455.75	0.0798	8.32476(7)	576.92(2)
452.93	0.0798	8.32523(7)	577.02(2)
450.25	0.0797	8.32572(7)	577.12(2)
447.69	0.0798	8.32622(7)	577.22(2)
444.28	0.0797	8.32670(7)	577.32(2)
441.48	0.0797	8.32720(7)	577.43(2)
438.64	0.0797	8.32766(7)	577.52(2)
435.68	0.0797	8.32814(7)	577.62(2)
432.70	0.0797	8.32860(7)	577.72(1)
429.66	0.0797	8.32907(7)	577.82(1)
426.67	0.0797	8.32952(7)	577.91(1)
423.51	0.0796	8.32997(7)	578.00(1)
420.35	0.0797	8.33043(7)	578.10(1)
417.30	0.0797	8.33086(7)	578.19(1)
414.21	0.0797	8.33129(7)	578.28(1)
411.12	0.0797	8.33171(7)	578.37(1)
408.02	0.0797	8.33213(7)	578.45(1)

Temperature (K)	Rwp	a (Å)	Volume (Å^3)
404.88	0.0797	8.33254(7)	578.54(1)
401.72	0.0798	8.33293(7)	578.62(1)
398.54	0.0798	8.33333(7)	578.70(1)
395.40	0.0799	8.33368(7)	578.78(1)
392.51	0.0799	8.33404(7)	578.85(1)
389.77	0.0798	8.33436(7)	578.92(1)
387.06	0.0799	8.33472(7)	578.99(1)
384.16	0.0800	8.33506(7)	579.06(1)
380.97	0.0800	8.33540(7)	579.14(1)
377.50	0.0800	8.33571(7)	579.20(1)
374.06	0.0800	8.33605(7)	579.27(1)
370.67	0.0800	8.33638(7)	579.34(1)
367.09	0.0801	8.33668(7)	579.40(1)
363.63	0.0801	8.33696(7)	579.46(1)
360.45	0.0801	8.33723(7)	579.52(1)
356.96	0.0801	8.33751(7)	579.57(1)
353.87	0.0801	8.33778(7)	579.63(1)
350.61	0.0801	8.33801(7)	579.68(1)
347.16	0.0801	8.33828(7)	579.73(1)
343.81	0.0801	8.33852(7)	579.79(1)
340.35	0.0801	8.33870(7)	579.82(1)
336.96	0.0802	8.33899(7)	579.88(1)
333.99	0.0802	8.33921(7)	579.93(1)
330.58	0.0801	8.33947(7)	579.98(1)
327.28	0.0802	8.33955(7)	580.00(1)
324.34	0.0802	8.33978(7)	580.05(1)
321.07	0.0802	8.34007(7)	580.11(1)
315.53	0.0803	8.34033(7)	580.16(1)
312.35	0.0803	8.34046(7)	580.19(1)
309.30	0.0803	8.34068(7)	580.24(1)
306.39	0.0803	8.34085(7)	580.27(1)
303.47	0.0803	8.34106(7)	580.32(1)
300.64	0.0804	8.34129(7)	580.36(1)
297.54	0.0803	8.34138(7)	580.38(1)
294.37	0.0803	8.34159(7)	580.43(1)
291.26	0.0803	8.34171(7)	580.45(1)
288.36	0.0803	8.34192(7)	580.50(1)
285.57	0.0802	8.34205(7)	580.52(1)
282.75	0.0802	8.34236(7)	580.59(1)
279.75	0.0803	8.34247(7)	580.61(1)

Temperature (K)	Rwp	a (Å)	Volume (Å^3)
276.35	0.0803	8.34260(7)	580.64(1)
273.50	0.0803	8.34274(7)	580.67(1)
270.50	0.0803	8.34315(7)	580.75(1)
267.47	0.0803	8.34311(7)	580.74(1)
264.22	0.0802	8.34336(7)	580.80(1)
262.37	0.0803	8.34368(7)	580.86(1)
257.76	0.0802	8.34371(7)	580.87(1)
256.01	0.0802	8.34408(7)	580.95(1)
252.72	0.0802	8.34403(7)	580.94(1)
249.25	0.0802	8.34422(7)	580.97(1)
246.42	0.0802	8.34464(7)	581.06(1)
244.06	0.0801	8.34482(7)	581.10(1)
240.37	0.0801	8.34486(7)	581.11(1)
237.73	0.0802	8.34497(7)	581.13(1)
234.88	0.0801	8.34532(7)	581.21(1)
232.17	0.0801	8.34562(7)	581.27(1)
229.41	0.0801	8.34559(7)	581.26(1)
226.35	0.0800	8.34607(7)	581.36(1)
222.90	0.0801	8.34594(7)	581.33(1)
220.13	0.0800	8.34628(7)	581.41(1)
217.40	0.0800	8.34643(7)	581.44(1)
214.35	0.0800	8.34650(7)	581.45(1)
211.25	0.0800	8.34669(7)	581.49(1)
207.91	0.0800	8.34684(7)	581.52(1)
204.81	0.0800	8.34700(7)	581.56(1)
202.05	0.0799	8.34720(7)	581.60(1)
199.01	0.0799	8.34736(7)	581.63(1)
196.14	0.0798	8.34752(7)	581.66(1)
193.26	0.0797	8.34767(7)	581.70(1)
190.31	0.0798	8.34783(7)	581.73(1)
187.40	0.0797	8.34798(7)	581.76(1)
184.46	0.0797	8.34812(7)	581.79(1)
181.51	0.0796	8.34827(7)	581.82(1)
178.55	0.0796	8.34841(7)	581.85(1)
175.54	0.0796	8.34856(7)	581.88(1)
173.28	0.0796	8.34864(7)	581.90(1)
169.61	0.0794	8.34880(7)	581.93(1)
166.80	0.0794	8.34904(7)	581.98(1)
163.93	0.0793	8.34927(7)	582.03(1)
161.09	0.0792	8.34950(7)	582.08(1)

Temperature (K)	Rwp	a (Å)	Volume (Å^3)
158.28	0.0792	8.34964(7)	582.11(1)
155.50	0.0790	8.34977(7)	582.14(1)
152.74	0.0789	8.34989(7)	582.16(1)
150.00	0.0788	8.35003(7)	582.19(1)
147.27	0.0788	8.35016(7)	582.22(1)
144.53	0.0787	8.35026(7)	582.24(1)
141.78	0.0786	8.35035(7)	582.26(1)
138.99	0.0785	8.35046(7)	582.28(1)
136.16	0.0784	8.35057(7)	582.30(1)
133.28	0.0783	8.35063(7)	582.31(1)
130.35	0.0782	8.35071(7)	582.33(1)
127.35	0.0781	8.35079(7)	582.35(1)
124.31	0.0780	8.35091(7)	582.37(1)
121.23	0.0779	8.35102(7)	582.40(1)
118.15	0.0777	8.35111(7)	582.42(1)
115.05	0.0777	8.35120(7)	582.43(1)
112.09	0.0776	8.35128(7)	582.45(1)

Table C.4: Unit cell volumes for cubic $CaZr_{0.75}Nb_{0.25}F_{6.25}$ and NaCl as determined from the Rietveld analysis of the high pressure diffraction data. Pressures estimated from the unit cell volume of the NaCl using an equation of state are also given.

a (Å)	$CaZr_{0.75}Nb_{0.25}F_{6.25}$ Volume (Å^3)	NaCl Volume (Å^3)	Pressure (GPa)
8.42993(6)	599.06(1)	179.506(6)	0.000(11)
8.43003(6)	599.08(1)	179.506(6)	0.000(11)
8.43011(6)	599.10(1)	179.506(7)	0.000(12)
8.43018(6)	599.12(1)	179.505(7)	0.001(12)
8.43024(6)	599.13(1)	179.505(6)	0.001(11)
8.43031(6)	599.14(1)	179.507(6)	0.000(11)
8.43037(6)	599.16(1)	179.506(6)	0.000(11)
8.43042(6)	599.17(1)	179.507(6)	0.000(11)
8.43047(6)	599.18(1)	179.509(6)	0.000(11)
8.43052(8)	599.19(2)	179.505(8)	0.001(13)

a (Å)	$CaZr_{0.75}Nb_{0.25}F_{6.25}$ Volume (Å^3)	NaCl Volume (Å^3)	Pressure (GPa)
8.43060(8)	599.20(2)	179.504(8)	0.001(13)
8.43066(6)	599.22(1)	179.505(6)	0.001(11)
8.43072(6)	599.23(1)	179.503(6)	0.001(11)
8.43070(6)	599.23(1)	179.498(6)	0.001(11)
8.43068(6)	599.22(1)	179.498(6)	0.001(11)
8.43075(6)	599.24(1)	179.498(7)	0.001(12)
8.43070(6)	599.23(1)	179.492(6)	0.002(11)
8.43042(6)	599.17(1)	179.462(6)	0.006(11)
8.43008(6)	599.10(1)	179.425(7)	0.011(12)
8.42961(7)	598.99(2)	179.372(8)	0.018(13)
8.42928(6)	598.92(1)	179.333(7)	0.023(12)
8.42887(6)	598.84(1)	179.291(7)	0.029(12)
8.42820(6)	598.69(1)	179.223(7)	0.038(12)
8.42765(6)	598.58(1)	179.172(6)	0.045(11)
8.42698(6)	598.43(1)	179.107(6)	0.054(11)
8.42610(6)	598.25(1)	179.025(6)	0.065(11)
8.42516(6)	598.05(1)	178.933(6)	0.077(11)
8.42415(7)	597.83(2)	178.832(7)	0.091(13)
8.42274(6)	597.53(1)	178.688(6)	0.111(12)
8.42109(6)	597.18(1)	178.535(6)	0.132(12)
8.41944(6)	596.83(1)	178.384(6)	0.153(12)
8.41826(6)	596.58(1)	178.272(5)	0.168(11)
8.41707(6)	596.33(1)	178.160(5)	0.184(11)
8.41520(6)	595.93(1)	177.992(5)	0.207(11)
8.41296(6)	595.45(1)	177.797(5)	0.235(11)
8.41097(6)	595.03(1)	177.623(5)	0.259(11)
8.40777(6)	594.35(1)	177.364(5)	0.296(11)
8.40372(6)	593.49(1)	177.050(5)	0.341(11)
8.40087(6)	592.89(1)	176.840(5)	0.372(11)
8.39736(6)	592.15(1)	176.599(5)	0.407(11)
8.39248(6)	591.11(1)	176.281(6)	0.454(12)
8.38771(6)	590.11(1)	175.990(5)	0.498(12)
8.38046(6)	588.58(1)	175.593(6)	0.558(13)
8.37244(7)	586.89(1)	175.215(6)	0.616(13)
8.36136(8)	584.56(2)	174.814(6)	0.678(13)

Table C.5: Unit cell volumes for cubic $CaZr_{0.5}Nb_{0.5}F_{6.5}$ and NaCl as determined from the Rietveld analysis of the high pressure diffraction data. Pressures estimated from the unit cell volume of the NaCl using an equation of state are also given.

a (Å)	c (Å)	$CaZr_{0.5}Nb_{0.5}F_{6.5}$ Volume (Å^3)	NaCl Volume (Å^3)	Pressure (GPa)
8.35553(8)	-	583.341(17)	178.552(5)	0.118(10)
8.35518(8)	-	583.268(17)	178.512(5)	0.123(10)
8.35448(8)	-	583.120(17)	178.433(5)	0.134(10)
8.35362(8)	-	582.941(17)	178.360(5)	0.144(10)
8.35310(8)	-	582.831(17)	178.291(5)	0.154(10)
8.35253(8)	-	582.712(17)	178.224(5)	0.163(10)
8.35170(8)	-	582.538(17)	178.171(5)	0.171(10)
8.35025(8)	-	582.235(17)	178.042(5)	0.189(10)
8.34887(8)	-	581.946(17)	177.929(5)	0.204(10)
8.34824(8)	-	581.815(17)	177.882(5)	0.211(10)
8.34695(8)	-	581.545(17)	177.795(5)	0.223(10)
8.34562(9)	-	581.268(18)	177.688(5)	0.238(10)
8.34404(8)	-	580.938(17)	177.565(5)	0.256(10)
8.34245(8)	-	580.605(17)	177.430(5)	0.275(10)

a (Å)	c (Å)	$CaZr_{0.5}Nb_{0.5}F_{6.5}$ Volume (Å^3)	NaCl Volume (Å^3)	Pressure (GPa)
8.34100(8)	-	580.302(17)	177.319(5)	0.291(10)
8.33924(8)	-	579.935(17)	177.183(5)	0.310(10)
8.33709(8)	-	579.486(18)	177.032(5)	0.332(10)
8.33428(9)	-	578.900(18)	176.839(5)	0.360(10)
8.33211(9)	-	578.448(18)	176.691(5)	0.382(10)
8.32989(9)	-	577.987(18)	176.552(5)	0.402(10)
8.32804(9)	-	577.601(18)	176.441(5)	0.418(10)
8.32463(9)	-	576.893(18)	176.240(5)	0.448(10)
8.32067(9)	-	576.069(19)	176.007(5)	0.483(11)
8.31633(9)	-	575.168(19)	175.782(5)	0.517(11)
8.31302(9)	-	574.482(19)	175.617(5)	0.542(11)
8.30871(9)	-	573.589(19)	175.420(5)	0.572(11)
8.30267(9)	-	572.339(19)	175.168(5)	0.610(11)
8.29703(9)	-	571.173(19)	174.954(5)	0.643(11)
8.29154(10)	-	570.041(20)	174.777(5)	0.671(11)
8.28603(10)	-	568.905(20)	174.629(5)	0.694(11)
8.27989(10)	-	567.640(20)	174.510(5)	0.713(11)
8.27153(11)	-	565.923(23)	174.411(6)	0.728(12)
5.8258(2)	14.3771(9)	422.584(15)	174.306(5)	0.745(11)
5.8035(2)	14.3982(11)	419.968(18)	174.194(5)	0.763(11)
5.7761(3)	14.4351(12)	417.078(19)	174.060(6)	0.784(12)
5.7587(3)	14.4622(13)	415.346(20)	173.975(6)	0.798(12)
5.7334(3)	14.4974(14)	412.704(21)	173.850(6)	0.818(13)
5.7096(3)	14.5319(14)	410.258(19)	173.739(5)	0.836(11)
5.6936(3)	14.5534(14)	408.569(19)	173.650(5)	0.850(11)
5.6700(3)	14.5871(14)	406.130(19)	173.518(5)	0.872(11)
5.6526(3)	14.6096(13)	404.271(20)	173.429(5)	0.886(11)
5.6262(3)	14.6414(13)	401.362(20)	173.271(5)	0.912(12)
5.6074(3)	14.6640(13)	399.307(19)	173.145(5)	0.933(12)
5.5954(3)	14.6785(13)	397.994(19)	173.061(5)	0.947(12)
5.5851(3)	14.6906(13)	396.852(19)	172.996(4)	0.957(10)
5.5734(3)	14.7039(13)	395.549(19)	172.927(4)	0.969(10)
5.5592(3)	14.7201(15)	393.977(21)	172.840(5)	0.983(12)
5.5477(3)	14.7332(15)	392.695(22)	172.767(4)	0.996(11)
5.5348(3)	14.7489(16)	391.291(23)	172.676(4)	1.011(11)
5.5187(3)	14.7685(18)	389.532(25)	172.550(4)	1.032(11)
5.5082(4)	14.7801(20)	388.351(27)	172.460(4)	1.047(11)
5.4953(4)	14.7945(21)	386.910(29)	172.346(4)	1.066(11)
5.4768(4)	14.8133(25)	384.804(32)	172.151(4)	1.100(11)
5.4575(6)	14.8285(34)	382.483(41)	171.950(4)	1.134(11)

Table C.6: Unit cell volumes for cubic $CaZr_{0.25}Nb_{0.75}F_{6.75}$ and NaCl as determined from the Rietveld analysis of the high pressure diffraction data. Pressures estimated from the unit cell volume of the NaCl using an equation of state are also given

a (Å)	c (Å)	$CaZr_{0.25}Nb_{0.75}F_{6.75}$ Volume (Å^3)	NaCl Volume (Å^3)	Pressure (GPa)
8.27884(7)	-	567.425(14)	178.551(6)	0.118(12)
8.27911(7)	-	567.480(14)	178.547(6)	0.119(12)
8.27936(7)	-	567.532(14)	178.542(6)	0.119(12)
8.27957(7)	-	567.575(14)	178.537(6)	0.120(12)
8.27968(7)	-	567.598(14)	178.524(6)	0.122(12)
8.27968(7)	-	567.598(14)	178.505(6)	0.124(12)
8.27966(7)	-	567.594(14)	178.485(6)	0.127(12)
8.27955(7)	-	567.572(14)	178.461(6)	0.130(12)
8.27948(7)	-	567.556(14)	178.438(6)	0.134(12)
8.27900(7)	-	567.457(14)	178.384(6)	0.141(12)
8.27860(7)	-	567.376(14)	178.335(6)	0.148(12)
8.27749(7)	-	567.148(14)	178.227(6)	0.163(12)
8.27651(7)	-	566.945(14)	178.142(6)	0.175(12)
8.27531(7)	-	566.700(14)	178.046(6)	0.188(12)
8.27404(7)	-	566.438(14)	177.938(6)	0.203(12)
8.27251(7)	-	566.125(14)	177.811(6)	0.221(12)
8.27151(7)	-	565.918(14)	177.721(6)	0.234(12)
8.26972(7)	-	565.552(14)	177.578(6)	0.254(12)
8.26760(7)	-	565.116(14)	177.413(6)	0.277(12)
8.26639(7)	-	564.870(14)	177.313(6)	0.292(12)

a (Å)	c (Å)	$CaZr_{0.25}Nb_{0.75}F_{6.75}$ Volume (Å^3)	NaCl Volume (Å^3)	Pressure (GPa)
8.26492(7)	-	564.568(14)	177.193(6)	0.309(12)
8.26325(7)	-	564.226(14)	177.059(6)	0.328(12)
8.26175(7)	-	563.919(14)	176.940(6)	0.345(12)
8.25987(7)	-	563.533(14)	176.798(6)	0.366(12)
8.25813(7)	-	563.176(14)	176.667(6)	0.385(12)
8.25541(7)	-	562.621(14)	176.474(6)	0.413(12)
8.25439(7)	-	562.413(14)	176.381(6)	0.427(13)
8.25326(7)	-	562.182(14)	176.287(6)	0.441(13)
8.25069(7)	-	561.656(14)	176.119(6)	0.466(13)
8.24928(7)	-	561.370(14)	176.011(6)	0.482(13)
8.24724(7)	-	560.951(14)	175.878(6)	0.502(13)
8.24413(7)	-	560.318(14)	175.698(6)	0.529(13)
8.24120(7)	-	559.720(14)	175.532(6)	0.554(13)
8.23832(7)	-	559.134(14)	175.378(6)	0.578(13)
8.23532(7)	-	558.524(14)	175.227(6)	0.601(13)
8.22908(7)	-	557.255(14)	174.967(6)	0.641(13)
8.22539(7)	-	556.506(15)	174.816(7)	0.665(14)
8.22158(8)	-	555.733(15)	174.677(7)	0.686(14)
8.21632(8)	-	554.667(16)	174.506(7)	0.713(14)
8.21103(8)	-	553.595(17)	174.353(7)	0.737(15)
8.20353(9)	-	552.080(19)	174.167(8)	0.767(16)
8.18764(12)	-	548.878(25)	173.895(9)	0.811(17)
5.7578(2)	14.2429(9)	408.930(16)	173.720(7)	0.839(15)
5.7456(2)	14.2573(10)	407.603(18)	173.659(8)	0.849(16)
5.7312(2)	14.2743(11)	406.043(20)	173.577(8)	0.862(16)
5.7063(3)	14.3059(14)	403.422(22)	173.420(9)	0.888(18)
5.6779(3)	14.3452(17)	400.508(25)	173.242(9)	0.917(18)
5.6431(4)	14.4012(20)	397.160(36)	173.028(9)	0.952(18)
5.6143(4)	14.4551(21)	394.580(36)	172.849(9)	0.982(18)
5.5959(4)	14.4881(20)	392.905(25)	172.734(8)	1.001(17)
5.5851(4)	14.5046(19)	391.833(24)	172.664(8)	1.013(17)
5.5751(3)	14.5161(18)	390.735(24)	172.594(8)	1.025(17)
5.5641(3)	14.5267(18)	389.477(24)	172.538(8)	1.034(17)
5.5568(3)	14.5341(18)	388.651(24)	172.503(8)	1.040(17)
5.5489(3)	14.5424(19)	387.776(24)	172.454(8)	1.048(17)
5.5402(4)	14.5521(19)	386.821(25)	172.385(8)	1.060(17)
5.5228(4)	14.5729(21)	384.947(27)	172.225(8)	1.087(17)
5.5128(4)	14.5858(21)	383.893(27)	172.142(7)	1.101(16)
5.5002(4)	14.6004(22)	382.515(28)	172.030(7)	1.120(16)
5.4861(4)	14.6175(22)	381.008(29)	171.908(7)	1.141(16)

a (Å)	c (Å)	$CaZr_{0.25}Nb_{0.75}F_{6.75}$ Volume (Å^3)	NaCl Volume (Å^3)	Pressure (GPa)
5.4740(4)	14.6318(23)	379.696(29)	171.816(7)	1.157(16)
5.4632(4)	14.6433(23)	378.500(29)	171.742(7)	1.170(16)
5.4522(4)	14.6540(23)	377.256(29)	171.676(7)	1.181(16)
5.4427(4)	14.6622(23)	376.144(30)	171.623(7)	1.190(16)
5.4266(4)	14.6737(23)	374.224(30)	171.498(6)	1.212(15)
5.4152(4)	14.6792(23)	372.790(30)	171.444(6)	1.222(15)
5.4040(4)	14.6831(24)	371.345(31)	171.380(6)	1.233(15)
5.3933(4)	14.6848(25)	369.918(32)	171.324(6)	1.243(15)
5.3831(4)	14.6854(26)	368.540(33)	171.263(6)	1.253(15)
5.3699(5)	14.6849(27)	366.716(35)	171.136(5)	1.276(14)
5.3496(5)	14.6842(28)	363.929(36)	170.928(5)	1.313(14)

Table C.7: Crystallographic parameters for $CaZr_{0.75}Nb_{0.25}F_{6.25}$ at 300 K on cooling derived from the Rietveld analysis of the x-ray diffraction data acquired while using a Cryostream, see Figure S1.

Chemical Formula	$CaZr_{0.75}Nb_{0.25}F_{6.25}$
Space group	$Fm\bar{3}m$
a (Å)	8.44156(8)
λ (Å)	0.72768
μ (cm^{-1})	24
Temperature (K)	300
R_{wp}	0.1109
R_F^2	0.1156

	x	y	z	U_{iso}/U_{eq} (Å^2)	U_{11} (Å^2)	U_{22}/U_{33} (Å^2)
Ca	0	0	0	0.0107(9)	-	-
Zr	$\frac{1}{2}$	$\frac{1}{2}$	$\frac{1}{2}$	0.0274(6)	-	-
Nb	$\frac{1}{2}$	$\frac{1}{2}$	$\frac{1}{2}$	0.0274(6)		
F	0.2617(4)	0	0	0.0362	0.013(2)	0.048(2)

Table C.8: Crystallographic parameters for CaZr0.5Nb0.5F6.5 at 300 K derived on cooling from the Rietveld analysis of the x-ray diffraction data acquired while using a Cryostream, see Figure S2.

Chemical Formula	$CaZr_{0.5}Nb_{0.5}F_{6.5}$
Space group	$Fm\bar{3}m$
a (Å)	8.40767(9)
λ (Å)	0.72768
μ (cm^{-1})	24
Temperature (K)	300
R_{wp}	0.1076
R_F^2	0.1493

	x	y	z	U_{iso}/U_{eq} ($Å^2$)	U_{11} ($Å^2$)	U_{22}/U_{33} ($Å^2$)
Ca	0	0	0	0.0139(9)	-	-
Zr	$\frac{1}{2}$	$\frac{1}{2}$	$\frac{1}{2}$	0.0305(6)	-	-
Nb	$\frac{1}{2}$	$\frac{1}{2}$	$\frac{1}{2}$	0.0305(6)		
F	0.2637(4)	0	0	0.0393	0.018(2)	0.050(2)

Table C.9: Crystallographic parameters for $CaZr_{0.25}Nb_{0.75}F_{6.75}$ at 300 K on cooling derived from the Rietveld analysis of the x-ray diffraction data acquired while using a Cryostream, see Figure 2.1a

Chemical Formula	$CaZr_{0.25}Nb_{0.75}F_{6.75}$

Space group	$Fm\bar{3}m$
a (Å)	8.34129(7)
λ (Å)	0.72768
μ (cm^{-1})	24
Temperature (K)	300
R_{wp}	0.0804
R_F^2	0.0943

	x	y	z	U_{iso}/U_{eq} ($Å^2$)	U_{11} ($Å^2$)	U_{22}/U_{33} ($Å^2$)
Ca	0	0	0	0.0150(8)	-	-
Zr	$\frac{1}{2}$	$\frac{1}{2}$	$\frac{1}{2}$	0.0345(5)	-	-
Nb	$\frac{1}{2}$	$\frac{1}{2}$	$\frac{1}{2}$	0.0345(5)		
F	0.2666(3)	0	0	0.0454	0.012(2)	0.062(2)

Table C.10: Crystallographic parameters for $CaZr_{0.75}Nb_{0.25}F_{6.25}$ at room temperature and ~ 0.0 GPa derived from the Rietveld analysis of the high pressure synchrotron diffraction data collected using a DAC, see Figure S4.

Chemical Formula	$CaZr_{0.75}Nb_{0.25}F_{6.25}$
Space group	$Fm\bar{3}m$
a (Å)	8.43047(6)
λ (Å)	0.72768
Pressure (GPa)	0.0
R_{wp}	0.0410
R_F^2	0.0760

	x	y	z	U_{iso} ($Å^2$)
Ca	0	0	0	0.029(1)
Zr	$\frac{1}{2}$	$\frac{1}{2}$	$\frac{1}{2}$	0.0576(9)
Nb	$\frac{1}{2}$	$\frac{1}{2}$	$\frac{1}{2}$	0.0576(9)
F	0.2619(3)	0	0	0.041(1)

Table C.11: Crystallographic parameters for $CaZr_{0.5}Nb_{0.5}F_{6.5}$ at room temperature and ~ 0.1 GPa derived from the Rietveld analysis of the high pressure synchrotron diffraction data collected using a DAC, see Figure S6.

Chemical Formula	$CaZr_{0.5}Nb_{0.5}F_{6.5}$
Space group	$Fm\bar{3}m$
a (Å)	8.35554(8)
λ (Å)	0.72768
Pressure (GPa)	0.12
R_{wp}	0.0407
R_F^2	0.0823

	x	y	z	U_{iso} ($Å^2$)
Ca	0	0	0	0.037(2)
Zr	$\frac{1}{2}$	$\frac{1}{2}$	$\frac{1}{2}$	0.065(1)
Nb	$\frac{1}{2}$	$\frac{1}{2}$	$\frac{1}{2}$	0.065(1)
F	0.2656(4)	0	0	0.049(2)

Table C.12: Crystallographic parameters for $CaZr_{0.5}Nb_{0.5}F_{6.5}$ at room temperature and ~ 1.0 GPa derived from the Rietveld analysis of the high pressure synchrotron diffraction data collected using a DAC, see Figure S7.

Chemical Formula	$CaZr_{0.5}Nb_{0.5}F_{6.5}$
Space group	$R\bar{3}$
a (Å)	5.5477(3)
ac(Å)	14.733(2)
λ (Å)	0.72768
Pressure (GPa)	1.0
R_{wp}	0.0402
R_F^2	0.0769

	x	y	z	U_{iso} (Å^2)
Ca	0	0	0	-0.013(4)
Zr	0	0	$\frac{1}{2}$	0.197(6)
Nb	0	0	$\frac{1}{2}$	0.197(6)
F	0.093(1)	0.358(1)	0.0882(4)	0.057(3)

Table 8.20: Crystallographic parameters for $CaZr_{0.25}Nb_{0.75}F_{6.75}$ at room temperature and ~ 0.1 GPa derived from the Rietveld analysis of the high pressure synchrotron diffraction data collected using a DAC, see Figure 2.1b

Chemical Formula	$CaZr_{0.25}Nb_{0.75}F_{6.75}$
Space group	$Fm\bar{3}m$
a (Å)	8.27884(7)
λ (Å)	0.72768
Pressure (GPa)	0.12
R_{wp}	0.0388
R_F^2	0.0766

	x	y	z	U_{iso} ($Å^2$)
Ca	0	0	0	0.040(1)
Zr	$\frac{1}{2}$	$\frac{1}{2}$	$\frac{1}{2}$	0.062(9)
Nb	$\frac{1}{2}$	$\frac{1}{2}$	$\frac{1}{2}$	0.062(9)
F	0.2686(3)	0	0	0.054(1)

Table 8.21: Crystallographic parameters for $CaZr_{0.25}Nb_{0.75}F_{6.75}$ at room temperature and ~ 1.1 GPa derived from the Rietveld analysis of the high pressure synchrotron diffraction data collected using a DAC, see Figure S12.

Chemical Formula	$CaZr_{0.25}Nb_{0.75}F_{6.75}$
Space group	$R\bar{3}$
a (Å)	5.5128(4)
ac(Å)	14.586(2)
λ (Å)	0.72768
Pressure (GPa)	1.1
R_{wp}	0.0525
R_F^2	0.1054

	x	y	z	U_{iso} (Å^2)
Ca	0	0	0	-0.019(6)
Zr	0	0	$\frac{1}{2}$	0.259(7)
Nb	0	0	$\frac{1}{2}$	0.259(7)
F	0.103(1)	0.361(1)	0.0869(5)	0.064(4)

Appendix D. SUPPLEMENTARY MATERIAL FOR CHAPTER 5

(reprinted from "Negative Thermal Expansion Design Strategies in a Diverse Series of Metal–Organic Frameworks" Supporting Information as published by Advanced Functional Materials with permissions from Nicholas Burtch and Wiley)

D.1 Synthesis and sample preparation

Synthesis and sample preparation procedures were performed based on previous literature, as summarized below. For solvent wash or exchange steps, samples were centrifuged and then dispersed in fresh solvent for an interval of between 30 minutes to an hour, or overnight for IRMOF-1, before starting the next wash or exchange step. All samples were washed 3 times in the initial reaction solvent, 3 times with chloroform, unless noted otherwise, as an exchange solvent, and then moved to fresh exchange solvent and stored until the evacuation procedures under dynamic vacuum were performed prior to nitrogen isotherm porosity characterization measurements. After porosity characterization, materials were stored in a nitrogen or argon glove box until subsequent powder diffraction or total scattering experiments. Prior to powder diffraction measurements, samples with larger crystal sizes were lightly ground using a mortar and pestle, as needed. M2(BDC)2(DABCO), where M = Co, Ni, Cu, or Zn, BDC = benzene-1,4-dicarboxylate, and DABCO = 1,4-diazabicyclo[2,2,2]octane (M-DMOF) square network samples were synthesized according to the procedure of ref. [1] and evacuated at 120 °C under dynamic vacuum. The Ni-DMOF square vs. Kagome network topology comparison involved the synthesis of a two-phase sample by following the procedures of ref. [2] , except with a

reduced (2 hour) stirring period after mixing of the reagents, and was evacuated at 110 °C. The Zn2(TM-BDC)2(DABCO), where TM-BDC = 2,3,5,6-tetramethyl-BDC, ZnDMOF-TM square network sample was synthesized using the procedure of ref. [3] and evacuated at 110 °C. The Zn2(DM-BDC)2(DABCO), where DM-BDC = 2,5-dimethylBDC, Zn-DMOF-DM square network sample was synthesized following the approach of ref. [4] and evacuated at 110 °C. Zn4O(BDC)3 (IRMOF-1) or MOF-5 was synthesized using the procedure of in ref. [5] whereby a 3:1 mixture of Zn(NO3)2•6H2O and H2BDC is dissolved in DEF and heated at 80 °C. The reaction mixture was removed from heat after 10 h and the mixture transferred to a nitrogen atmosphere before evacuation. UiO-66 and UiO-67 consist of Zr6-based clusters that are 12-connected by either BDC or 4, 4'-biphenyldicarboxylate ligands in their defect-free forms. To compare the effects of ligand length and flexibility while minimizing impacts due to structural defects, which was shown by Goodwin et al. to have a significant effect on the thermal expansion behavior of UiO-66(Hf),[6] synthesis procedures that produce minimal defects in our structures was chosen. For UiO-66, the "UiO-66-Ideal" procedure reported by Shearer et al.[7] was employed using a scaled down total volume of 24mL DMF in a 45mL Teflon lined reactor was used before evacuation at 100 °C. UiO-67 was synthesized according to the procedure of ref. [8] and evacuated at 100 °C. Micron-sized Zn(2-MeIM)2 (MeIM = 2-methylimidazolate) ZIF-8 samples were synthesized according to the procedure of ref. [9] and evacuated at 170 °C. Synthesis and initial purity characterization was performed primarily by Ashley Bird and Nicholas Burtch with help from the thesis author and Andreas Schneemann.

D.2 Porosity characterization

The porosity of all structures was characterized using N2 sorption experiments at 77 K. Experiments were performed using a Micrometrics ASAP 2020 surface area and porosity analyzer. The Brunauer-Emmett-Teller (BET) area of each material was quantified over a pressure range that satisfies the BET consistency criteria. Porosity measurements were collected by Ashley Bird and Nicholas Burtch.

Metal effects: Zn-DMOF, Co-DMOF, Cu-DMOF, Ni-DMOF

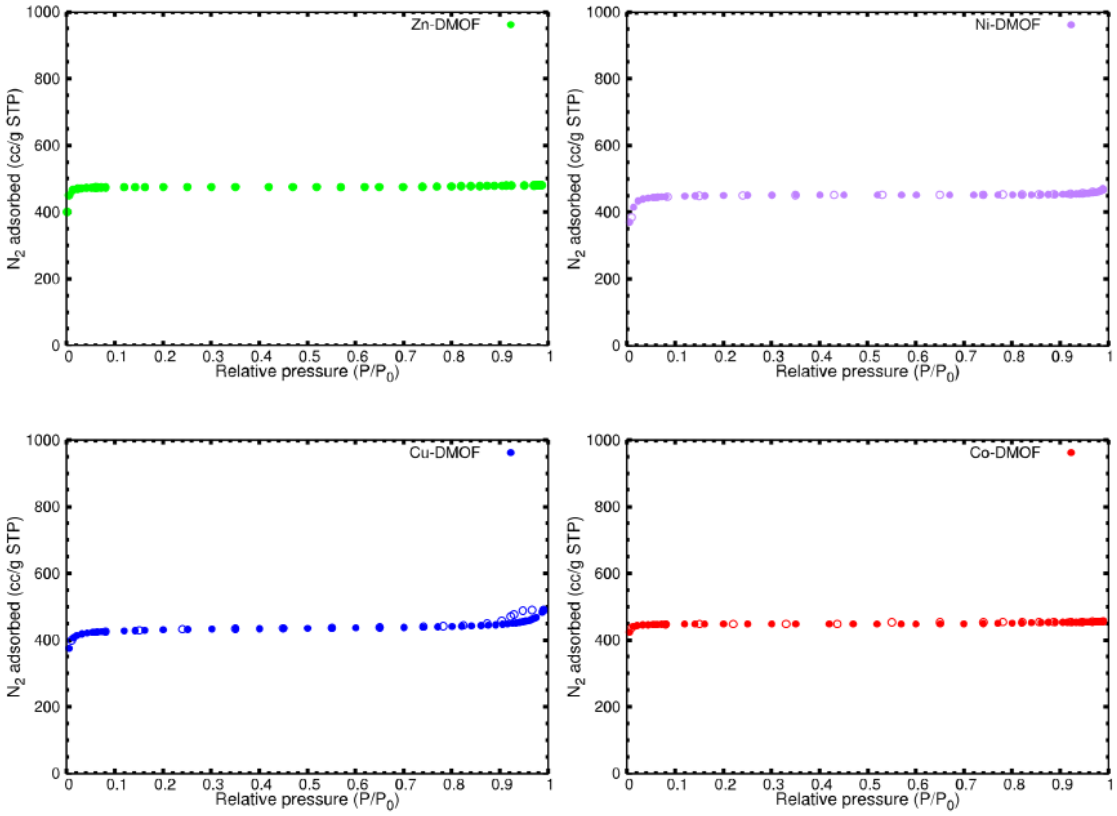

Figure D.1: M-DMOF (M=Zn, Co, Cu or Ni) N2 adsorption (closed symbols) and desorption (open symbols) at 77 K. BET surface area 1940 m^2 /g for Zn-DMOF, 1830 m^2 /g for Ni-DMOF, 1830 m^2 /g for Cu-DMOF and 1930 m^2 /g for Co-DMOF.

Ligand steric effects: Zn-DMOF, Zn-DMOF-DM, and Zn-DMOF-TM

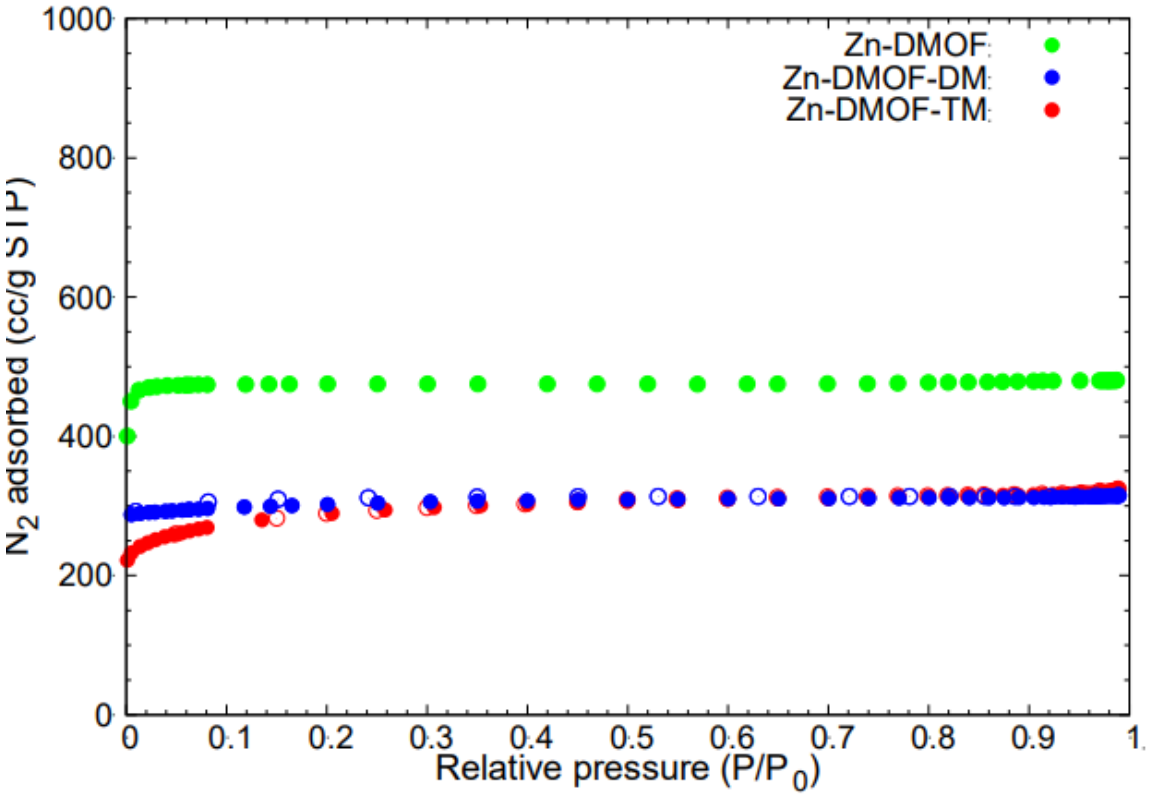

Figure D.2: Zn-DMOF variations with different ligand substituents N_2 adsorption (closed symbols) and desorption (open symbols) at 77 K. BET surface area 1940 m^2 /g for ZnDMOF, 1210 m^2 /g for Zn-DMOF-DM, and 1005 m^2 /g for Zn-DMOF-TM.

Ni-DMOF two-phase (square and Kagome networks)

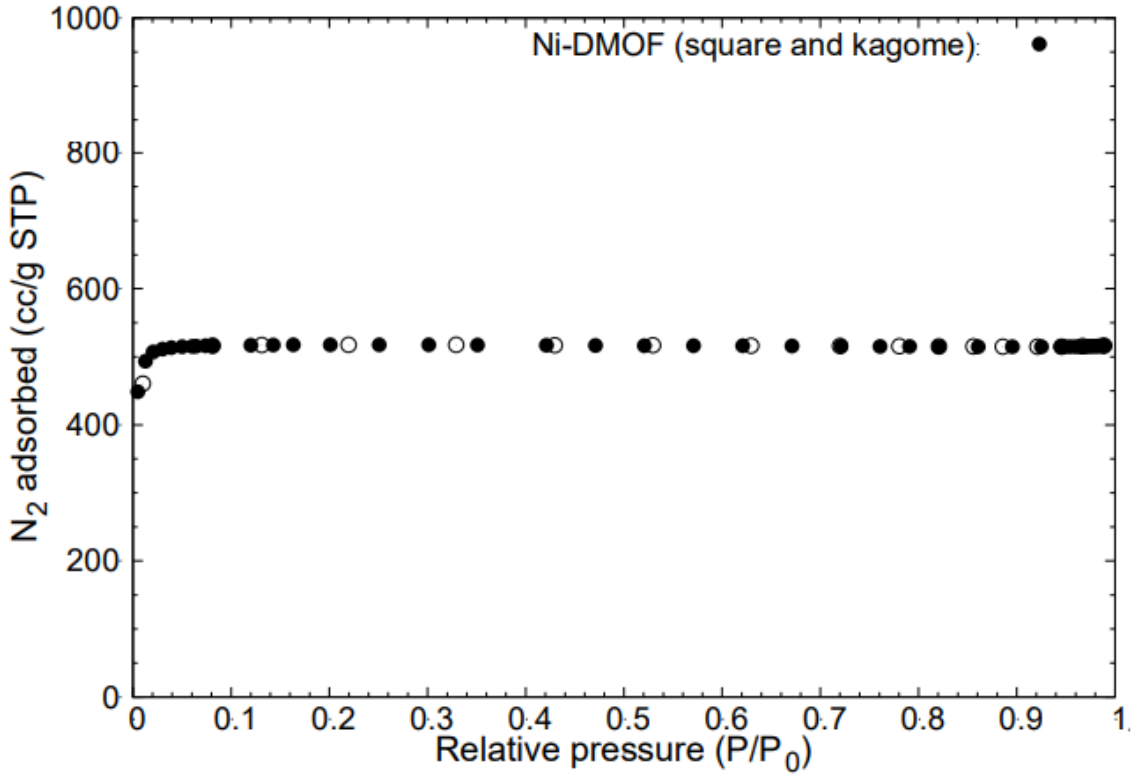

Figure D.3: Ni-DMOF two-phase (square and Kagome network) N_2 adsorption (closed symbols) and desorption (open symbols) at 77 K. BET surface area is 2030 m^2 /g. This BET surface area is between the reported BET surface area of the pure Kagome phase (2130 m^2 /g)[2] and what we obtain for the Ni-DMOF square network (1830 m2 /g, Figure S1) material. A composition of 0.25:0.75 Kagome:square phase was obtained from Rietveld analysis of the sample's powder X-ray diffraction data.

IRMOF-1

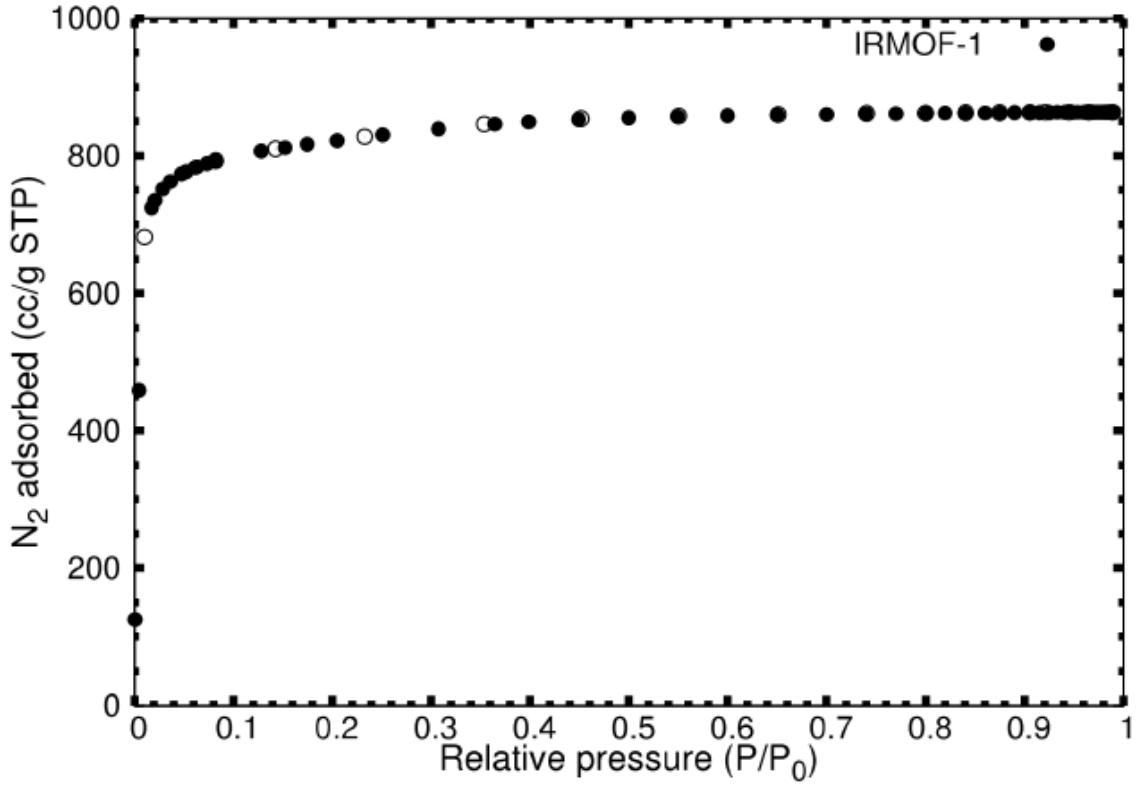

Figure D.4: IRMOF-1 N_2 adsorption (closed symbols) and desorption (open symbols) at 77 K. BET surface area 3460 m^2 /g.

UiO-66 and UiO-67

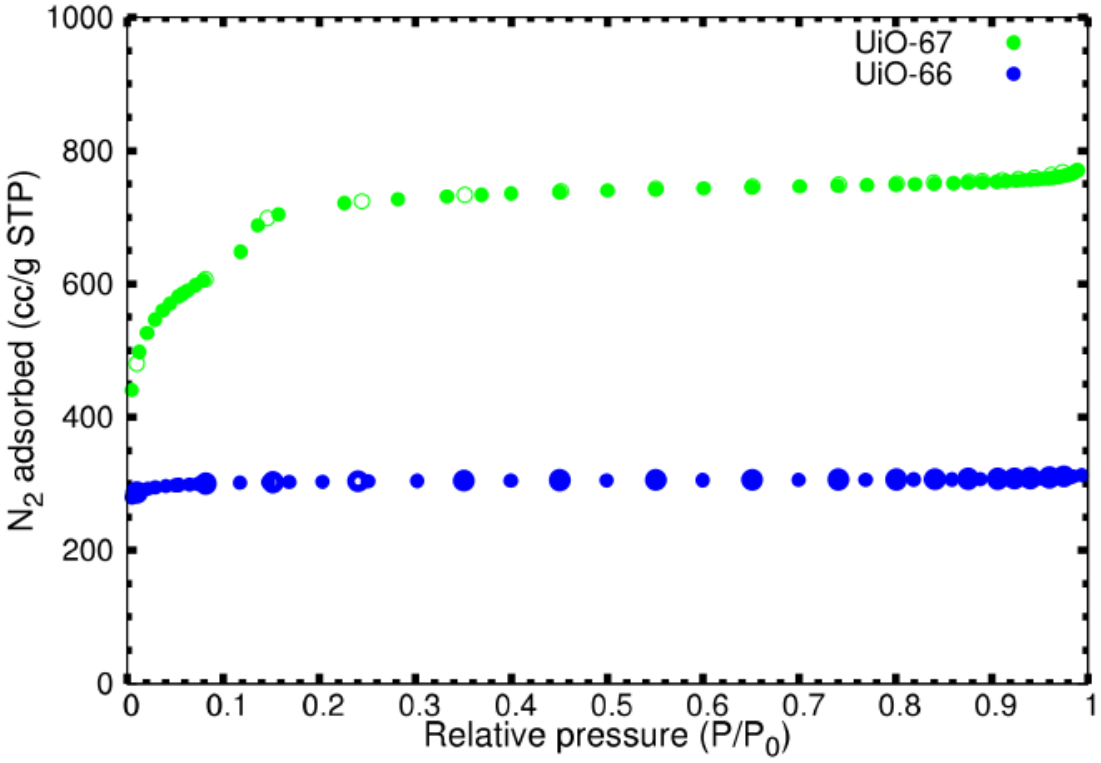

Figure D.5: UiO-66 and UiO-67 N_2 adsorption (closed symbols) and desorption (open symbols) at 77 K. BET surface area 1230 m^2 /g for UiO-66 and 2450 m^2 /g for UiO-67.

ZIF-8

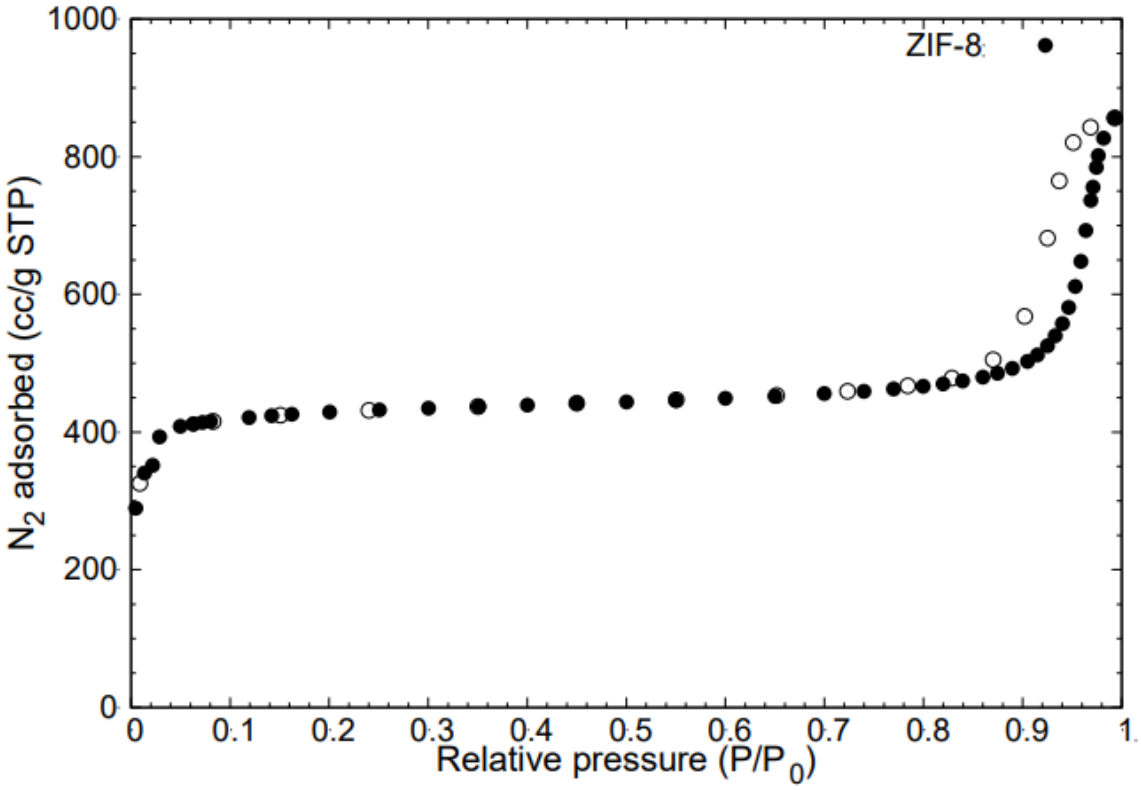

Figure D.6: ZIF-8 N_2 adsorption (closed symbols) and desorption (open symbols) at 77 K. BET surface area 1750 m^2 /g.

D.3 X-ray Characterization

Synchrotron-radiation Powder X-ray diffraction and total scattering data were collected at beamline 17-BM-B (λ = 0.24119 Å) or 11-ID-B (λ = 0.2114 Å) of the Advanced Photon Source (APS) at Argonne National Laboratory. The Cu-DMOF, Ni-DMOF, UiO-66@95°C, IRMOF-1, Zn-DMOF-TM, and ZIF-8 samples were measured at beamline 17-BM-B whereas ZnDMOF, UiO-67@95°C, and UiO-66@220°C where measured at beamline 11-ID-B. The Zn-DMOF-DM, Co-DMOF, and Ni-DMOF two-phase (square and Kagome network) samples were characterized using a laboratory diffractometer. Samples were loaded in a Kapton capillary using a previously described sample cell environment[15] to allow the flow of gas through the capillary and temperature control. The gas environment during these measurements was helium, with the exception of the IRMOF-1 sample measured in the presence of CO2. A temperature calibration run was performed using a thermocouple in the sample position in order to convert the Cryostream setpoint temperatures into approximate sample temperatures. LaB6 was used to calibrate the sample-to-detector distance during the diffraction experiments at ~95 cm (11-ID-B) or ~80 cm (17-BM-B). A distance of ~20 cm was used for total scattering measurements at both beamlines. After mounting at the beamline, samples were heated to ~100 °C for 1-2 hours under flow of helium, unless noted otherwise, such as for UiO-66@220°C. Due to its moisture instability,[16] IRMOF-1 was loaded into a capillary while immersed in chloroform and activated in-situ under flowing helium. Samples were cooled to a Cryostream setpoint temperature of 100 K before heating at a constant rate of ~2 K/min. A correlation between the diffraction and total scattering data during sample heating scans was enabled through dynamically shifting the detector inward to a distance of 20 cm to

collect total scattering data in between diffraction measurements. Pair distribution functions (PDFs) were obtained from the total scattering data, after background subtraction, using a Qmax of 19.76 Å -1 (17-BM-B) or 22.48 (11-ID-B) Å -1 and the xPDFsuite software. In-house diffractometer The Zn-DMOF-DM, Co-DMOF, and Ni-DMOF two-phase (square and Kagome network) were loaded into a 0.7mm ID quartz capillary inside an argon glove box and sealed with wax or epoxy glue before mounting on an Oxford diffractometer (model XX) with Cu-Kα radiation (λ = 1.5418 Å). Temperature was controlled using a nitrogen cryostream with the temperature held at the setpoint temperature for at least 15 minutes of equilibration before data was collected.

D.3.1 Thermal Expansion Analysis:

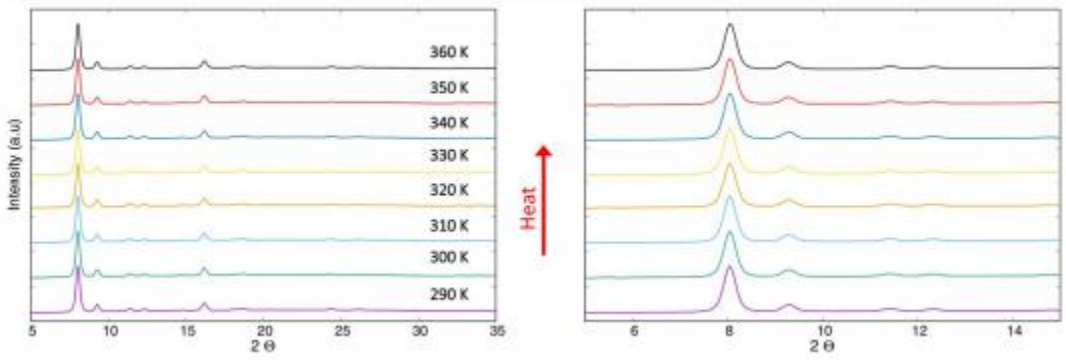

Figure D.7: Diffraction patterns for the Co-DMOF (λ = 1.5418 Å) sample upon heating. For clarity, lower 2θ angles are enlarged on the graph to the right.

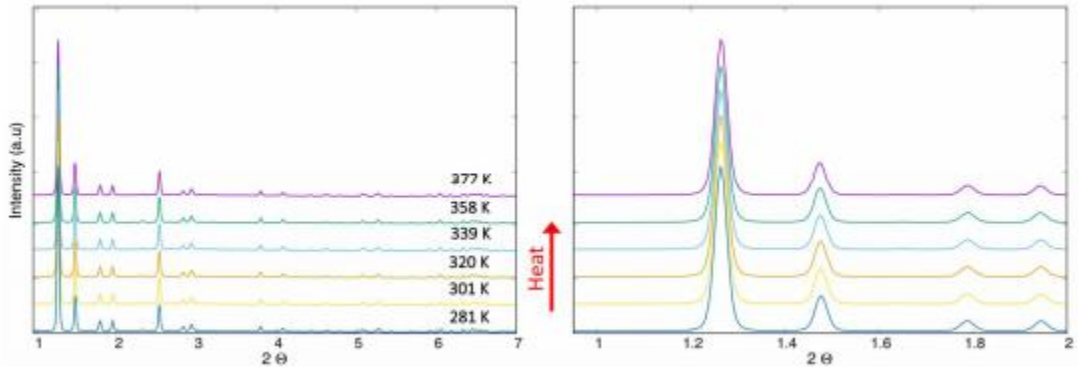

Figure D.8: Diffraction patterns for the Ni-DMOF (λ = 0.24119 Å) sample upon heating. For clarity, lower 2θ angles are enlarged on the graph to the right.

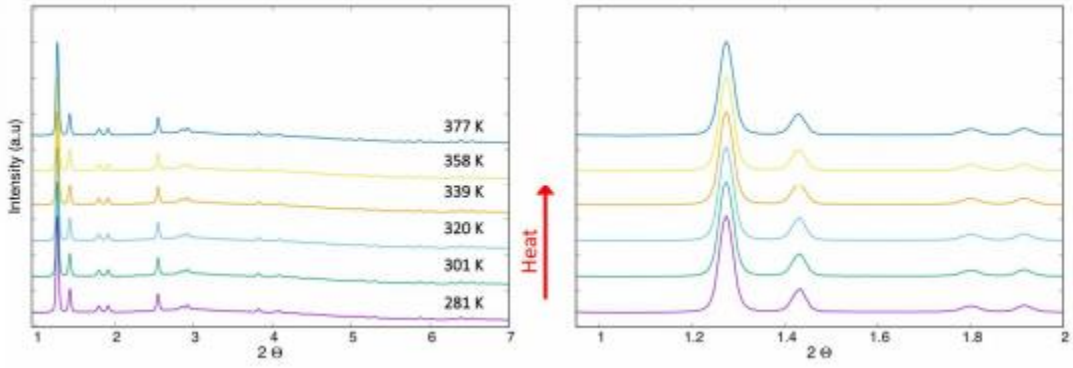

Figure D.9: Diffraction patterns for the Cu-DMOF (λ = 0.24119 Å) sample upon heating. For clarity, lower 2θ angles are enlarged on the graph to the right.

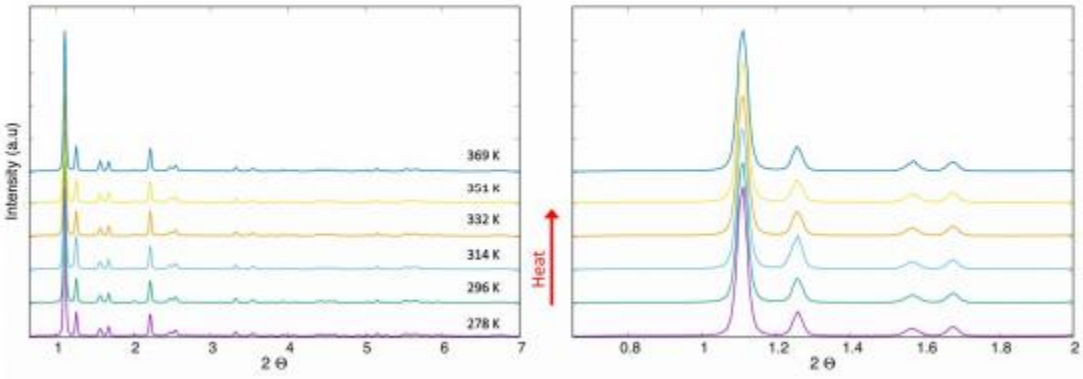

Figure D.10: Diffraction patterns for the Zn-DMOF (λ = 0.2114 Å) sample upon heating. For clarity, lower 2θ angles are enlarged on the graph to the right.

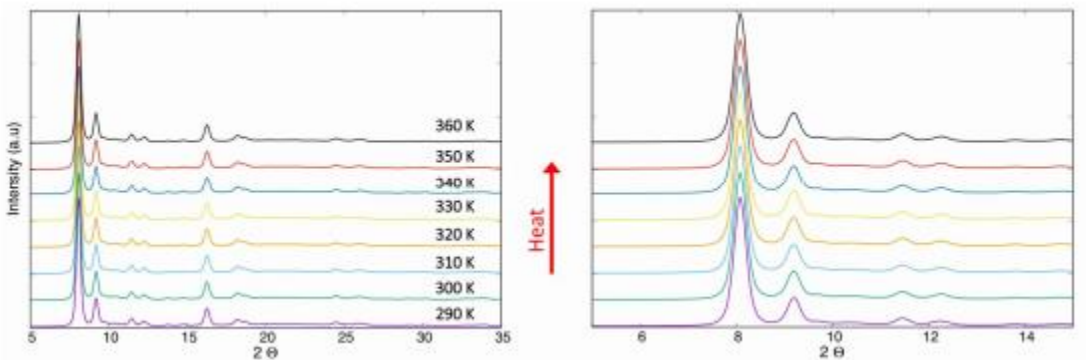

Figure D.11: Diffraction patterns for the Zn-DMOF-DM (λ = 1.5418 Å) sample upon heating. For clarity, lower 2θ angles are enlarged on the graph to the right.

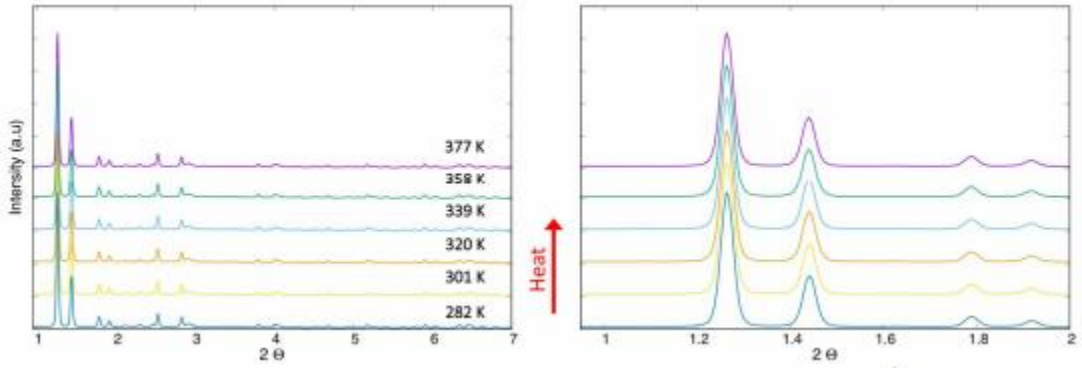

Figure D.12: Diffraction patterns for the Zn-DMOF-TM (λ = 0.24119 Å) sample upon heating. For clarity, lower 2θ angles are enlarged on the graph to the right.

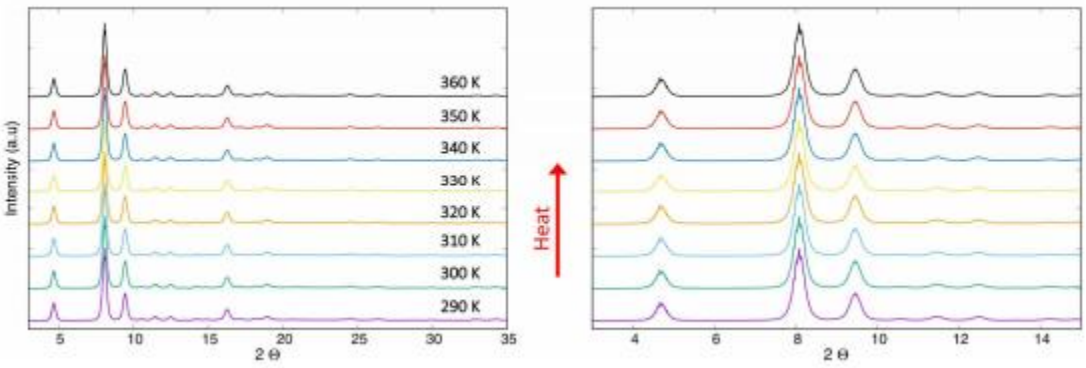

Figure D.13: Diffraction patterns for the Ni-DMOF two-phase square and Kagome network (λ = 1.5418 Å) sample upon heating. For clarity, lower 2θ angles are enlarged on the graph to the right.

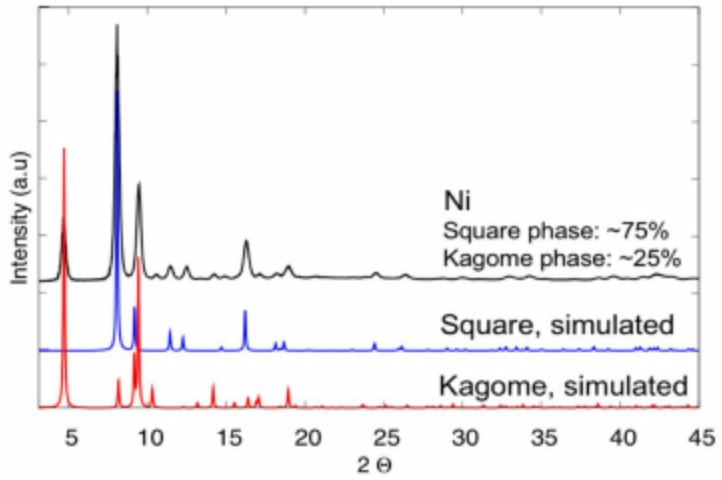

Figure D.14: Diffraction pattern for the Ni-DMOF two-phase square and Kagome network sample and simulated patterns for the square and Kagome phase (λ = 1.5418 Å).

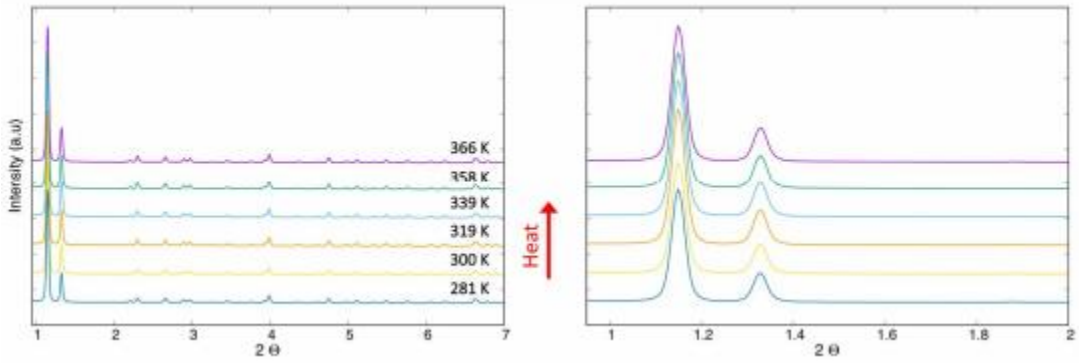

Figure D.15: Diffraction patterns for the UiO-66@95°C (λ = 0.24119 Å) sample upon heating. For clarity, lower 2θ angles are enlarged on the graph to the right.

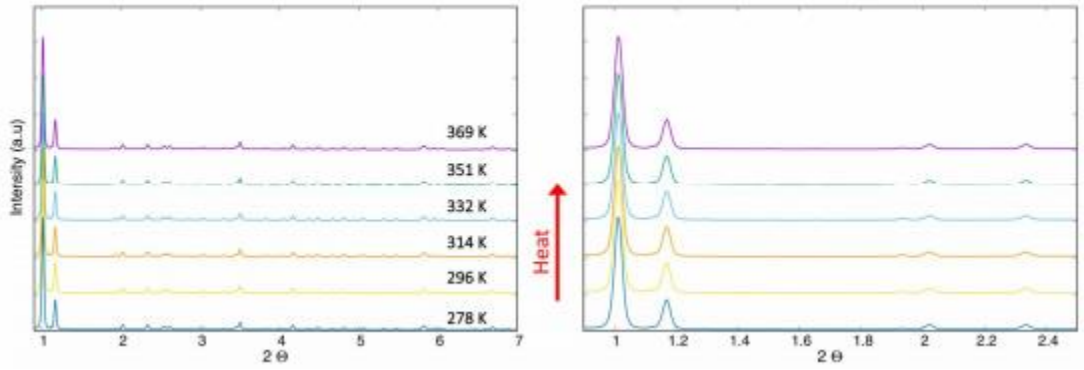

Figure D.16: Diffraction patterns for the UiO-66@220°C (λ = 0.2114 Å) sample upon heating. For clarity, lower 2θ angles are enlarged on the graph to the right.

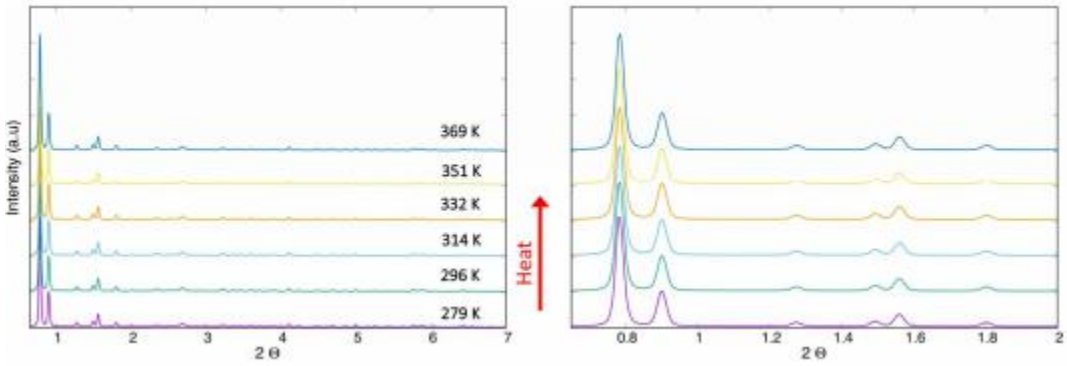

Figure D.17: Diffraction patterns for the UiO-67@95°C (λ = 0.2114 Å) sample upon heating. For clarity, lower 2θ angles are enlarged on the graph to the right.

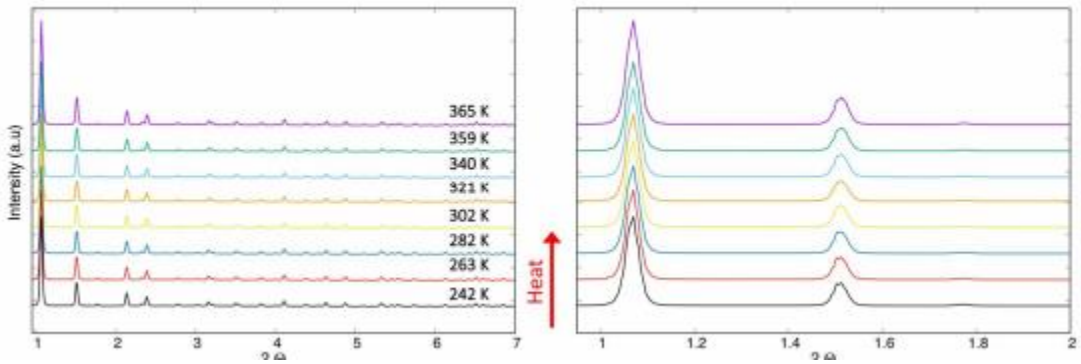

Figure D.18: Diffraction patterns for the IRMOF-1 He (λ = 0.24119 Å) sample upon heating. For clarity, lower 2θ angles are enlarged on the graph to the right.

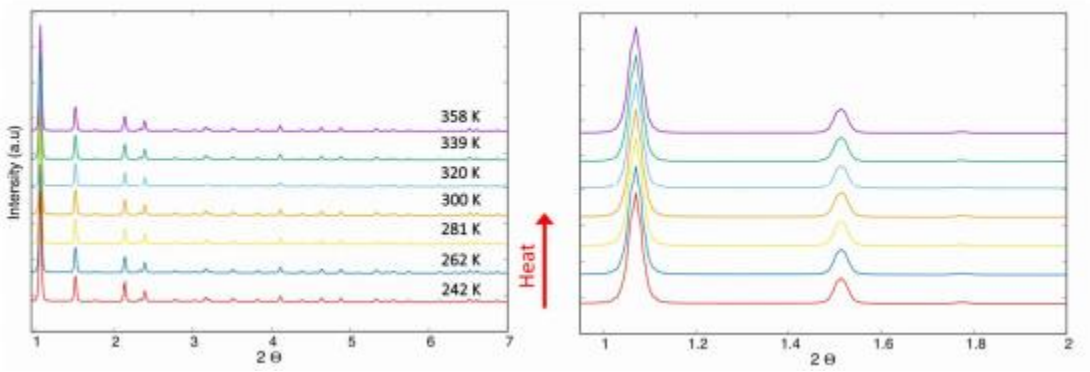

Figure D.19: Diffraction patterns for the IRMOF-1 CO2 (λ = 0.24119 Å) sample upon heating. For clarity, lower 2θ angles are enlarged on the graph to the right.

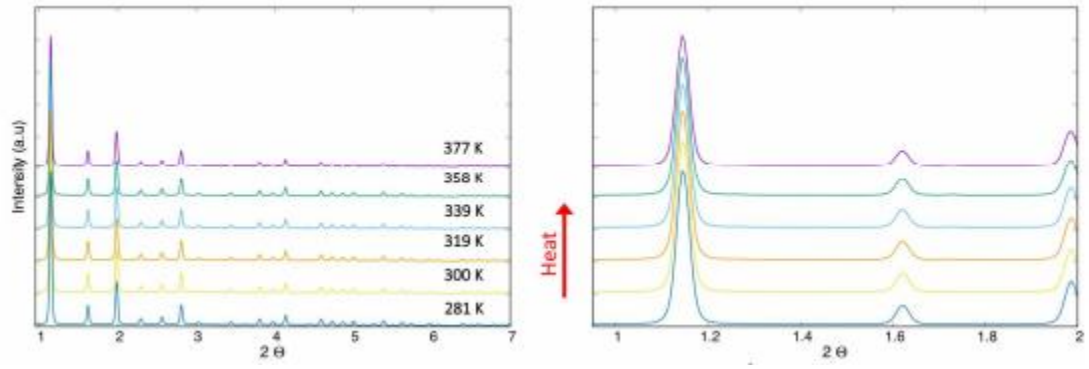

Figure D.20: Diffraction patterns for the ZIF-8 (λ = 0.24119 Å) sample upon heating. For clarity, lower 2θ angles are enlarged on the graph to the right

D.3.2 Average coefficients of thermal expansion

Average coefficients of thermal expansion (CTE) values were obtained by linear regression of the lattice parameters obtained from Pawley analysis[17] using the GSAS-II software[18] upon heating. To enable comparison of CTE values across samples, average CTE values were analyzed over a ~10 to 100 °C temperature range where the lattice parameter vs. temperature behavior was mostly linear for all of the samples. The refined lattice parameters, percent changes in crystallographic dimensions upon heating, and derived CTE values from linear regression analysis of the data are shown in the graphs below. This temperature range was also chosen because it is relevant to NTE applications where MOFs would be most suitable from a mechanical and thermal properties standpoint, such as fillers in organic matrices (e.g. polymers, epoxies, and resins). For IRMOF-1, structural data could be analyzed in the presence of helium or carbon dioxide from a starting temperature of ~ -30 °C. CTE errors estimates are reported as the asymptotic standard error from the regression analysis. These estimated errors do not take into account errors in the cell parameters because, as noted elsewhere, the scatter in the data is often the main contributor to the experimental error in the CTE.

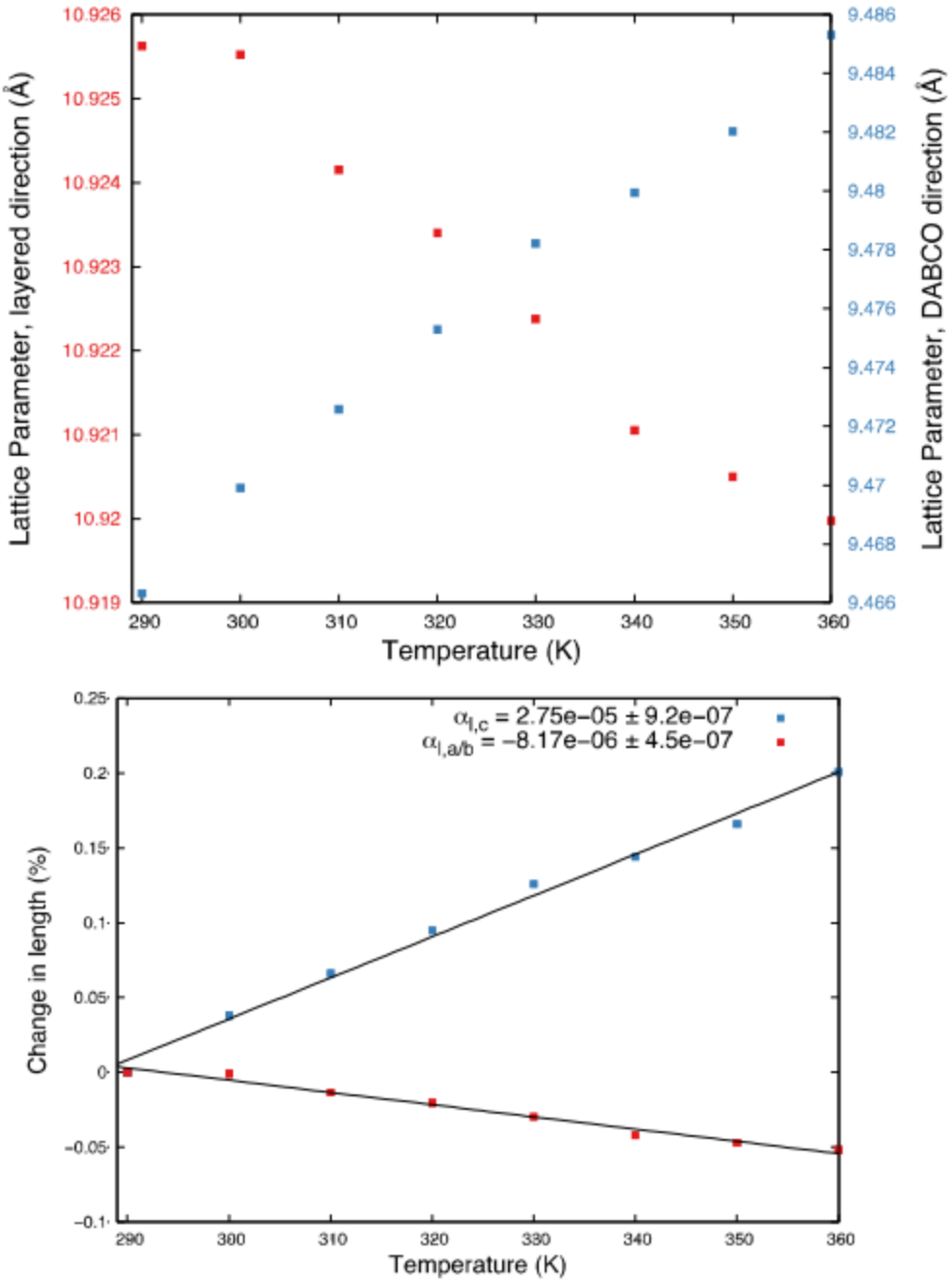

Figure D.21: Evolution of lattice parameters (top) and percent change in lattice parameters (bottom) with temperature upon heating in Co-DMOF. Pawley analysis performed using the P4/mmm space group.

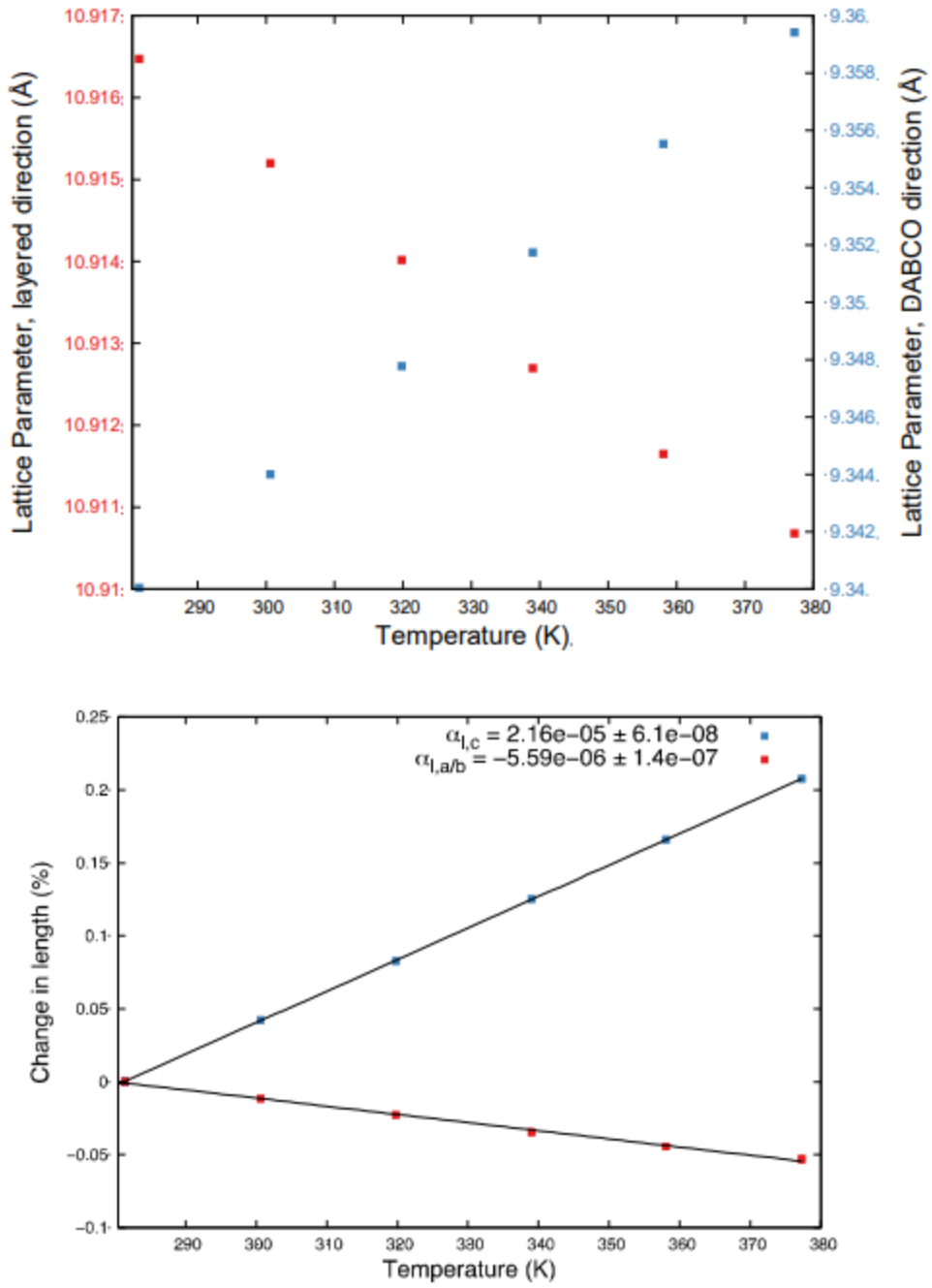

Figure D.22: Evolution of lattice parameters (top) and percent change in lattice parameters (bottom) with temperature upon heating in Ni-DMOF (square network). Pawley analysis performed using the P4/mmm space group.

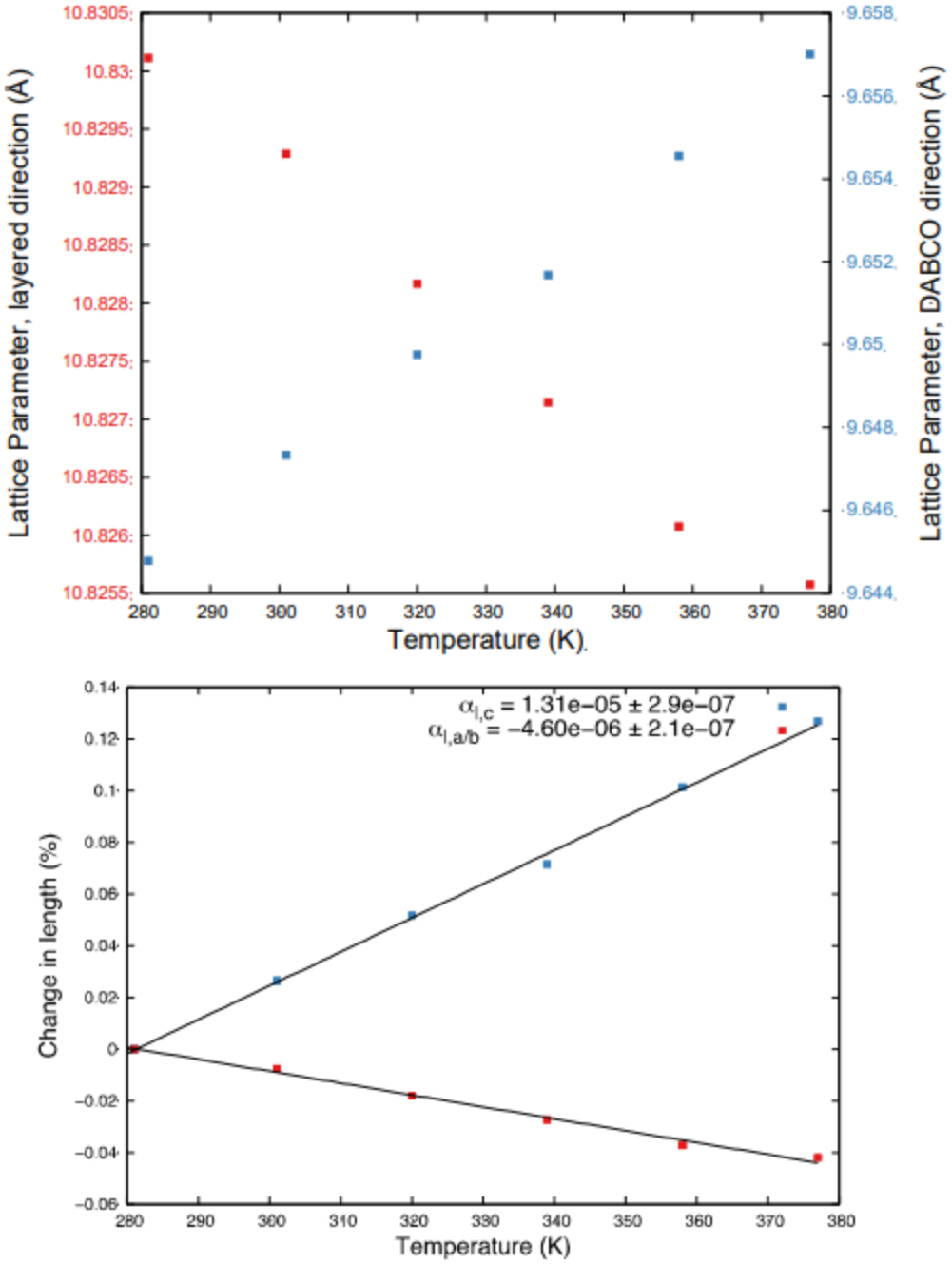

Figure D.23: Evolution of lattice parameters (top) and percent change in lattice parameters (bottom) with temperature upon heating in Cu-DMOF. Pawley analysis performed using the P4/mmm space group.

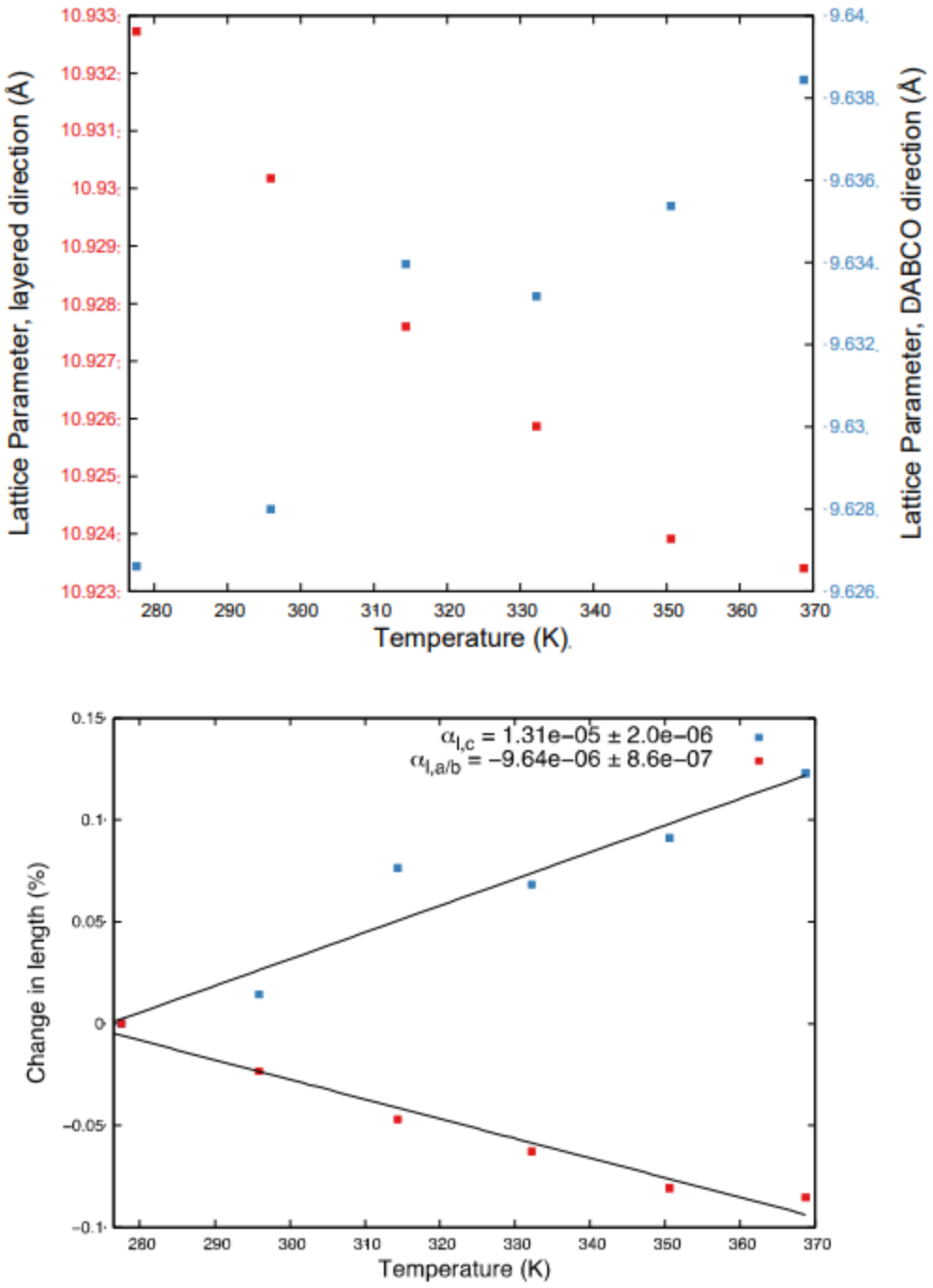

Figure D.24: Evolution of lattice parameters (top) and percent change in lattice parameters (bottom) with temperature upon heating in Zn-DMOF. Pawley analysis performed using the P4/mmm space group.

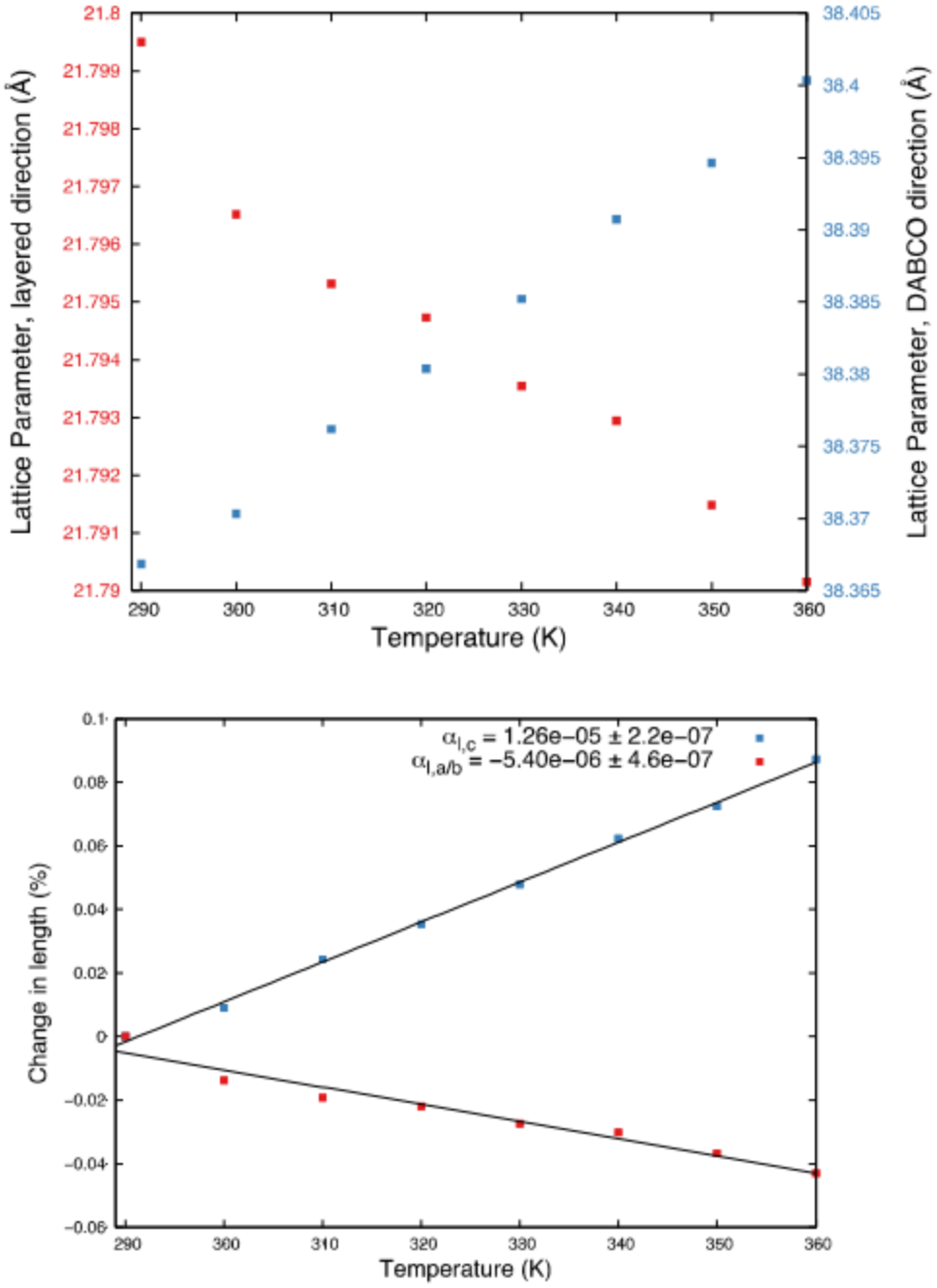

Figure D.25: Evolution of lattice parameters (top) and percent change in lattice parameters (bottom) with temperature upon heating in Zn-DMOF-DM. Pawley analysis performed using the I41/acd space group.

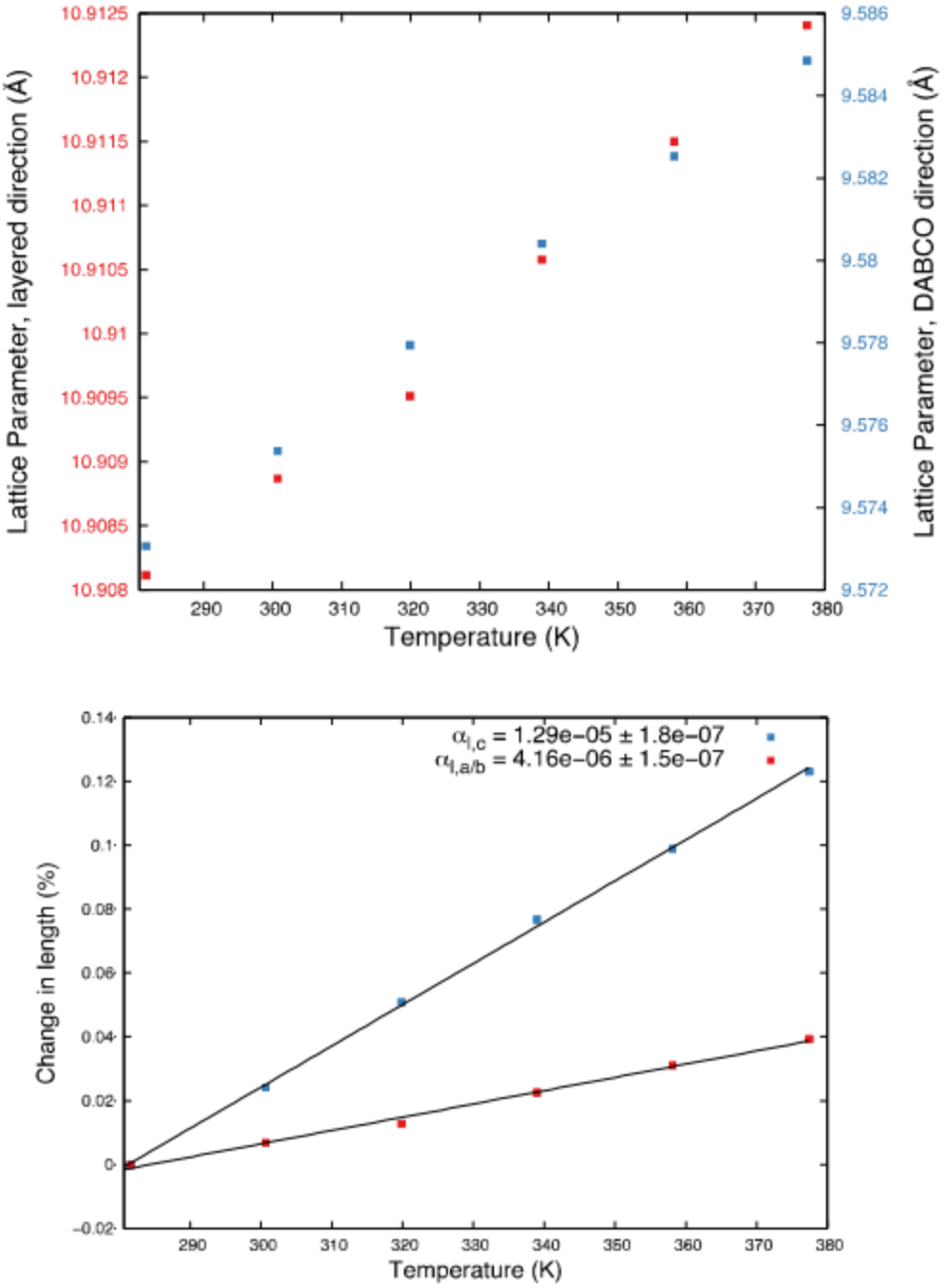

Figure D.26: Evolution of lattice parameters (top) and percent change in lattice parameters (bottom) with temperature upon heating in Zn-DMOF-TM. Pawley analysis performed using the P4/mmm space group.

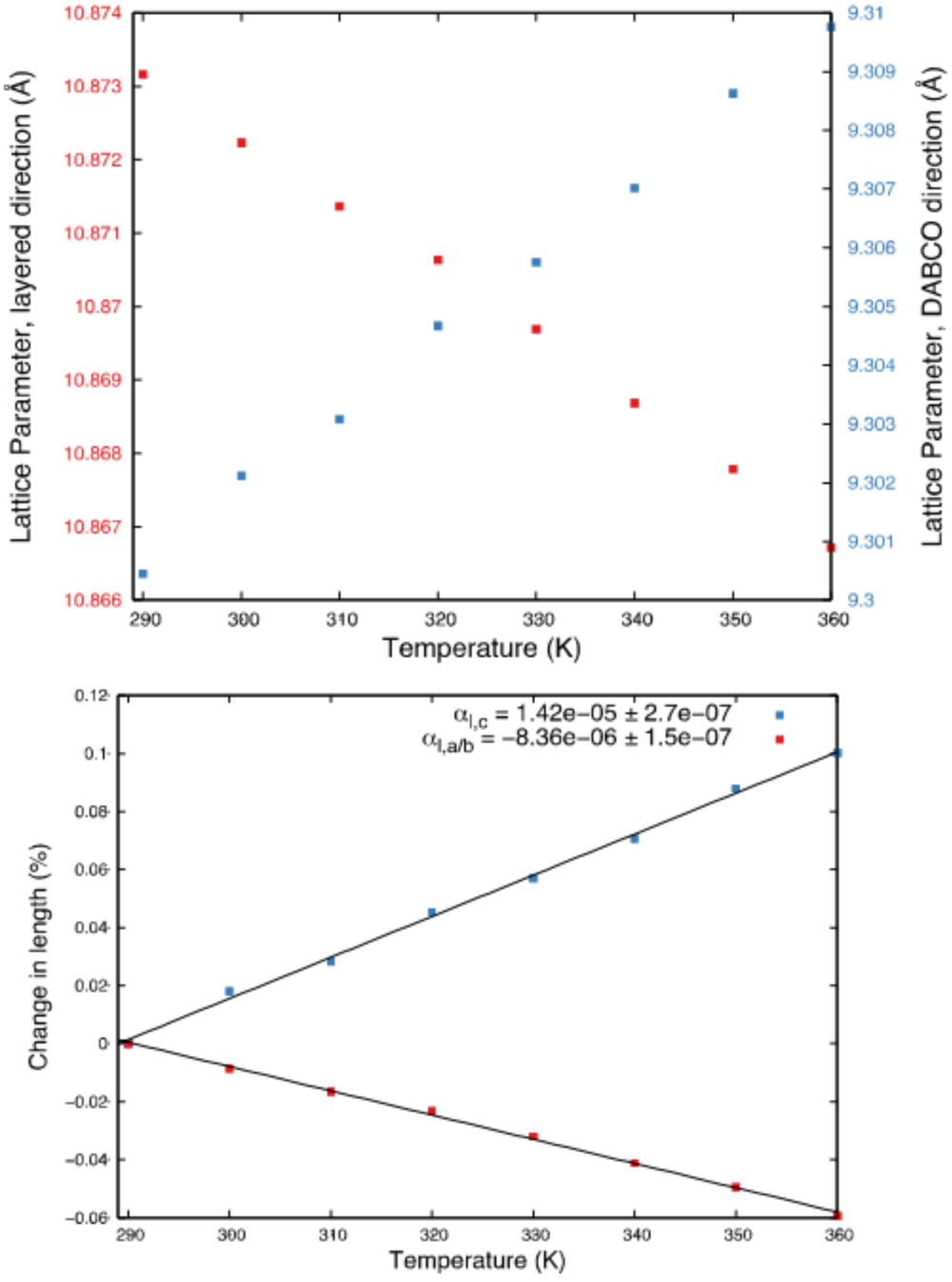

Figure D.27: Evolution of lattice parameters (top) and percent change in lattice parameters (bottom) with temperature upon heating in Ni-DMOF two phase (square network). Pawley analysis performed using the P4/mmm space group.

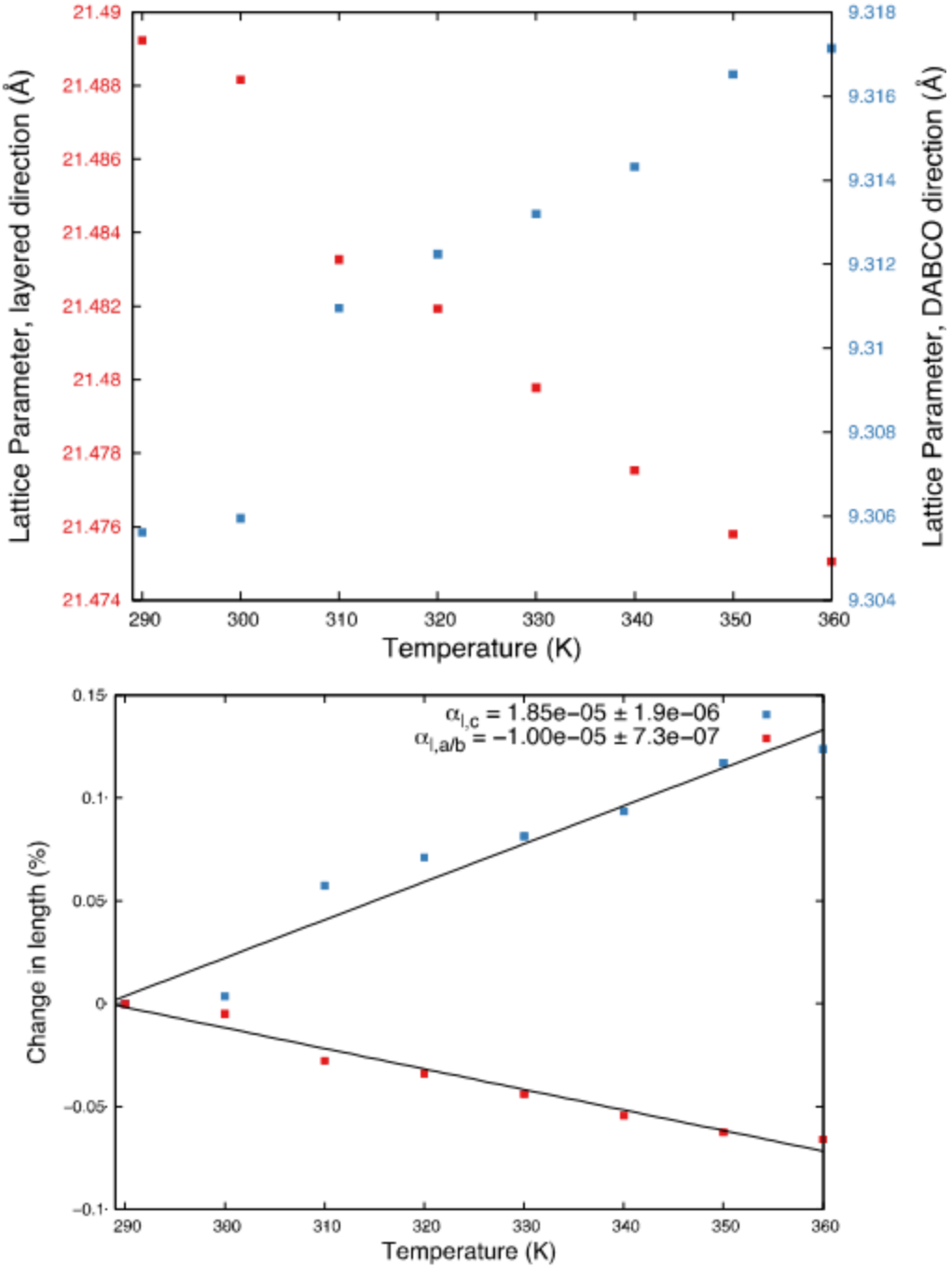

Figure D.28: Evolution of lattice parameters (top) and percent change in lattice parameters (bottom) with temperature upon heating in Ni-DMOF two phase (Kagome network). Pawley analysis performed using the P-3m1 space group.

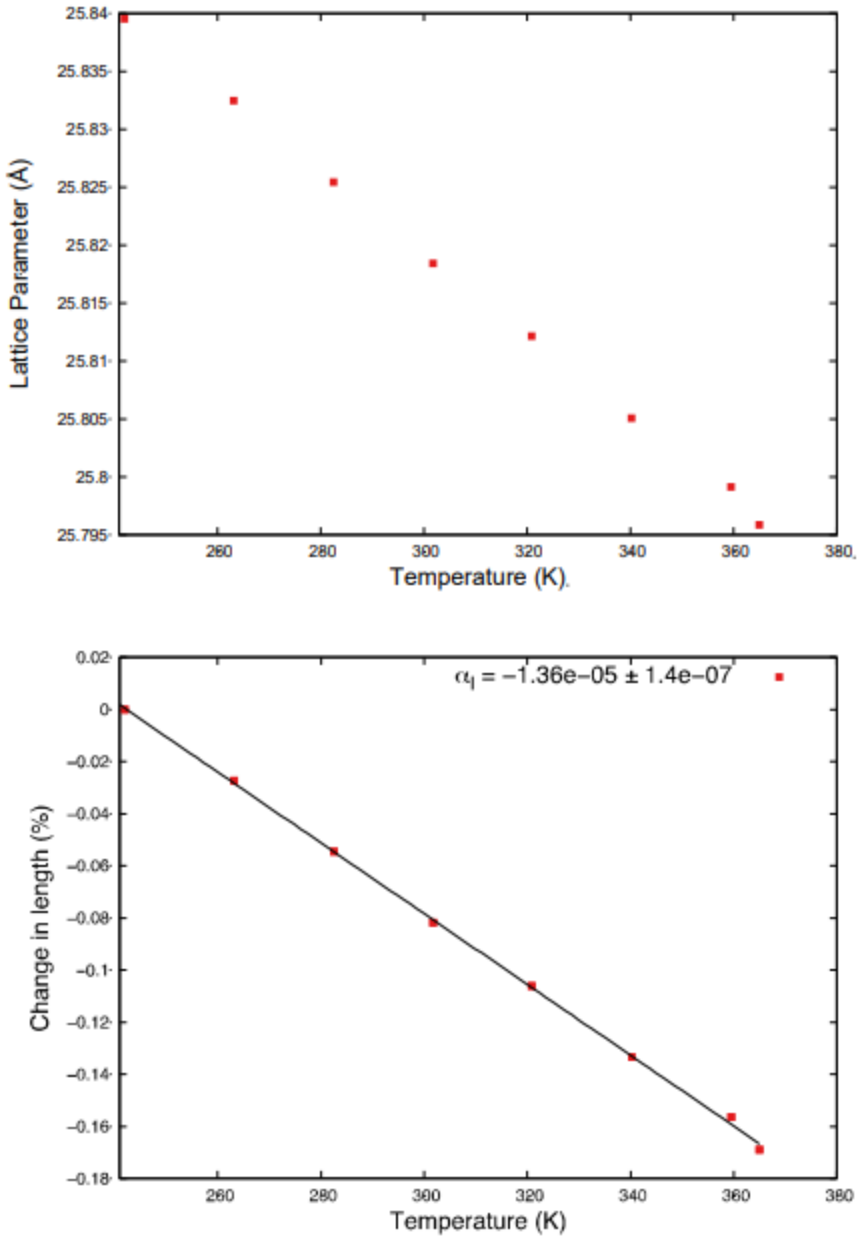

Figure D.29: Evolution of lattice parameters (top) and percent change in lattice parameters (bottom) with temperature upon heating in IRMOF-1 (He). Pawley analysis performed using the Fm-3m space group.

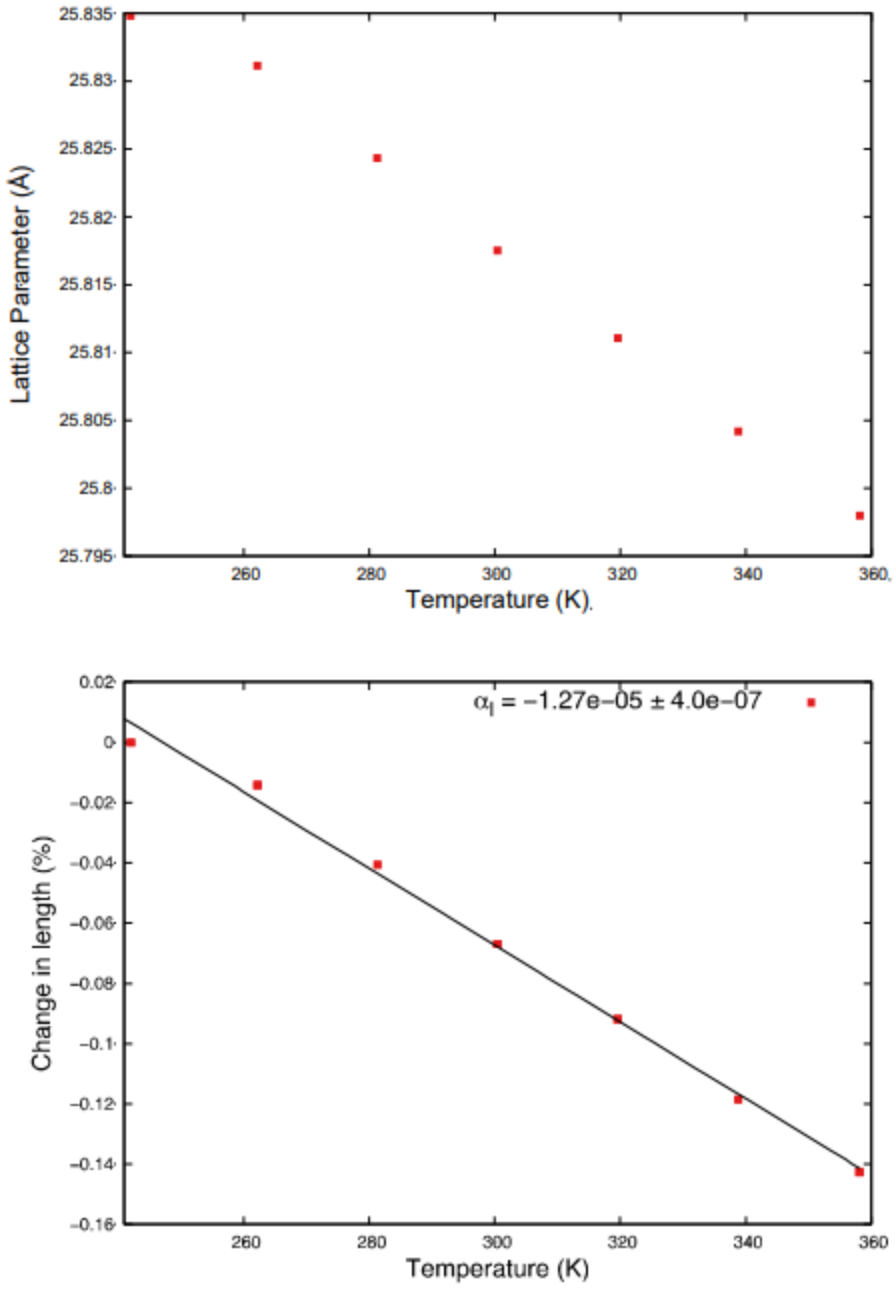

Figure D.30: Evolution of lattice parameters (top) and percent change in lattice parameters (bottom) with temperature upon heating in IRMOF-1 (CO2). Pawley analysis performed using the Fm-3m space group.

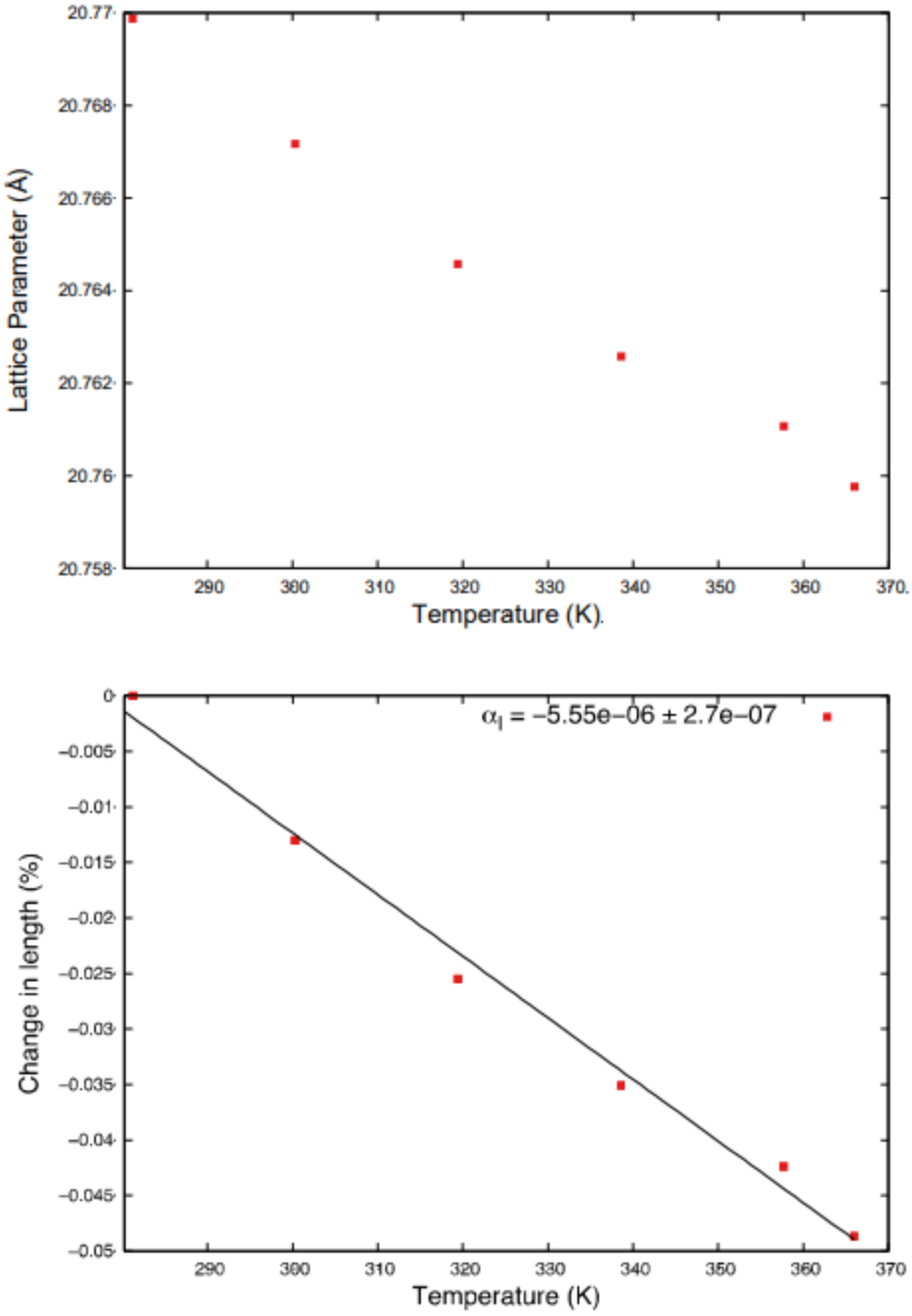

Figure D.31: Evolution of lattice parameters (top) and percent change in lattice parameters (bottom) with temperature upon heating in UiO-66@95°C. Pawley analysis performed using the Fm-3m space group.

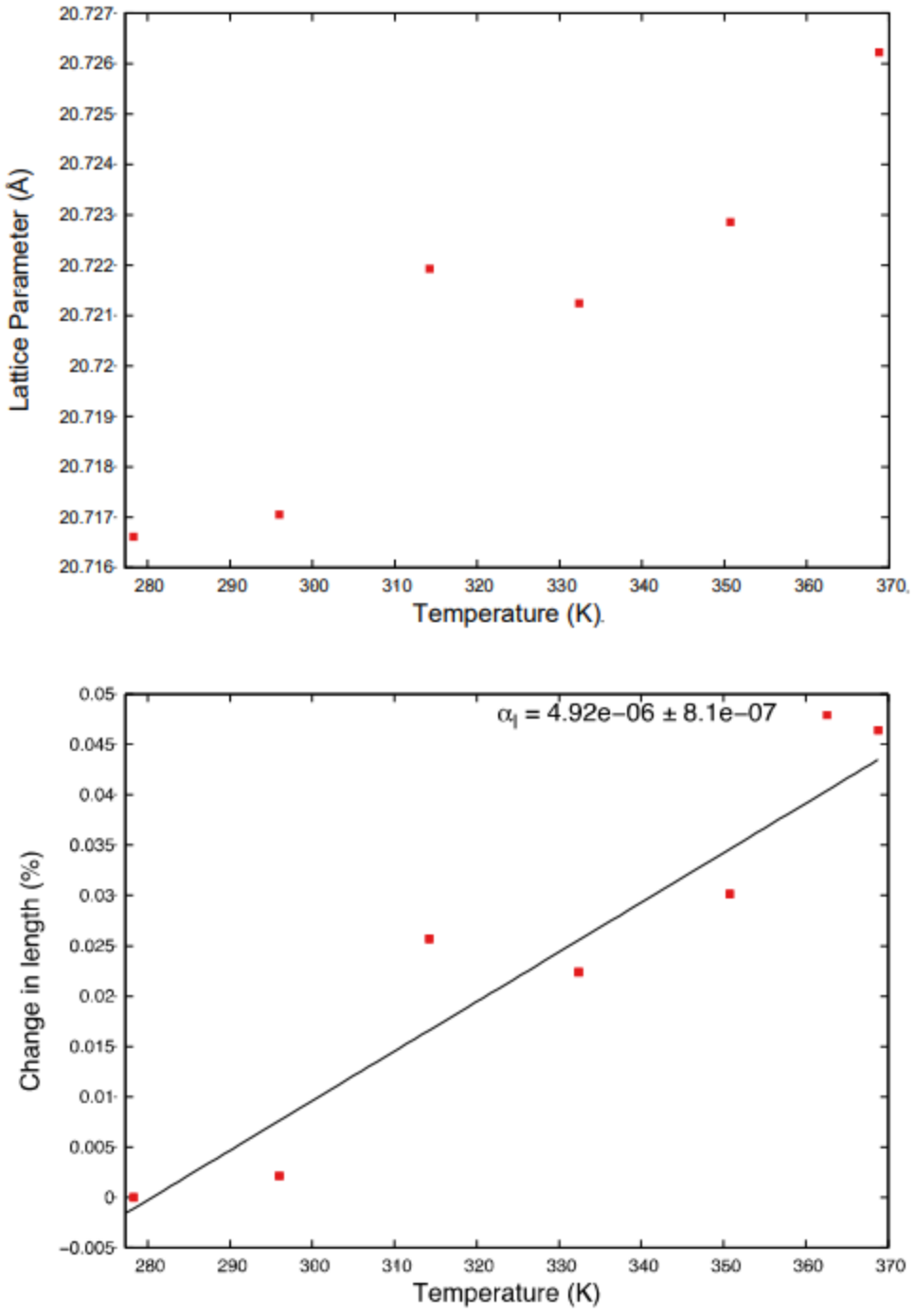

Figure D.32: Evolution of lattice parameters (top) and percent change in lattice parameters (bottom) with temperature upon heating in UiO-66@220°C. Pawley analysis performed using the Fm-3m space group.

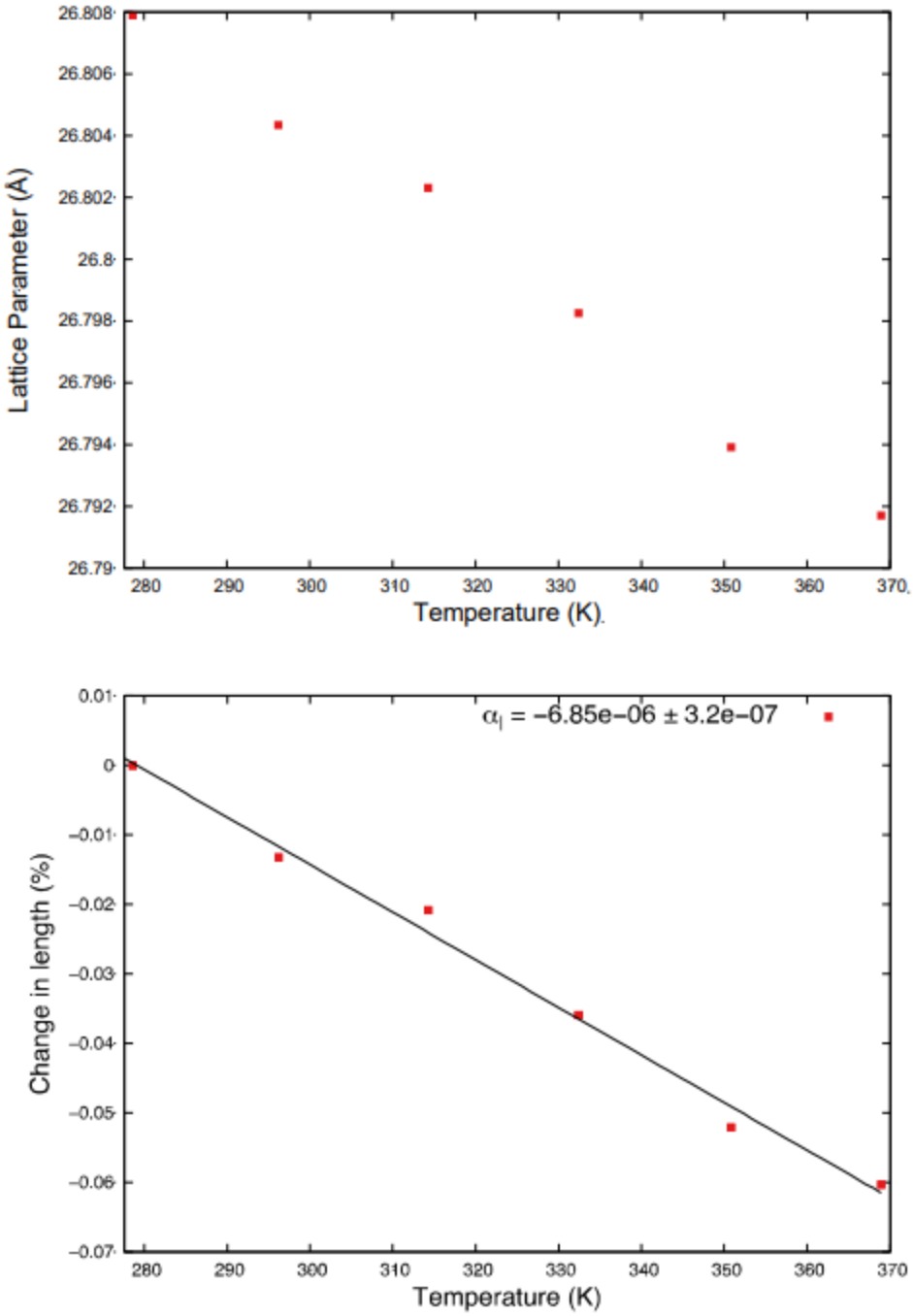

Figure D.33: Evolution of lattice parameters (top) and percent change in lattice parameters (bottom) with temperature upon heating in UiO-67@95°C. Pawley analysis performed using the Fm-3m space group.

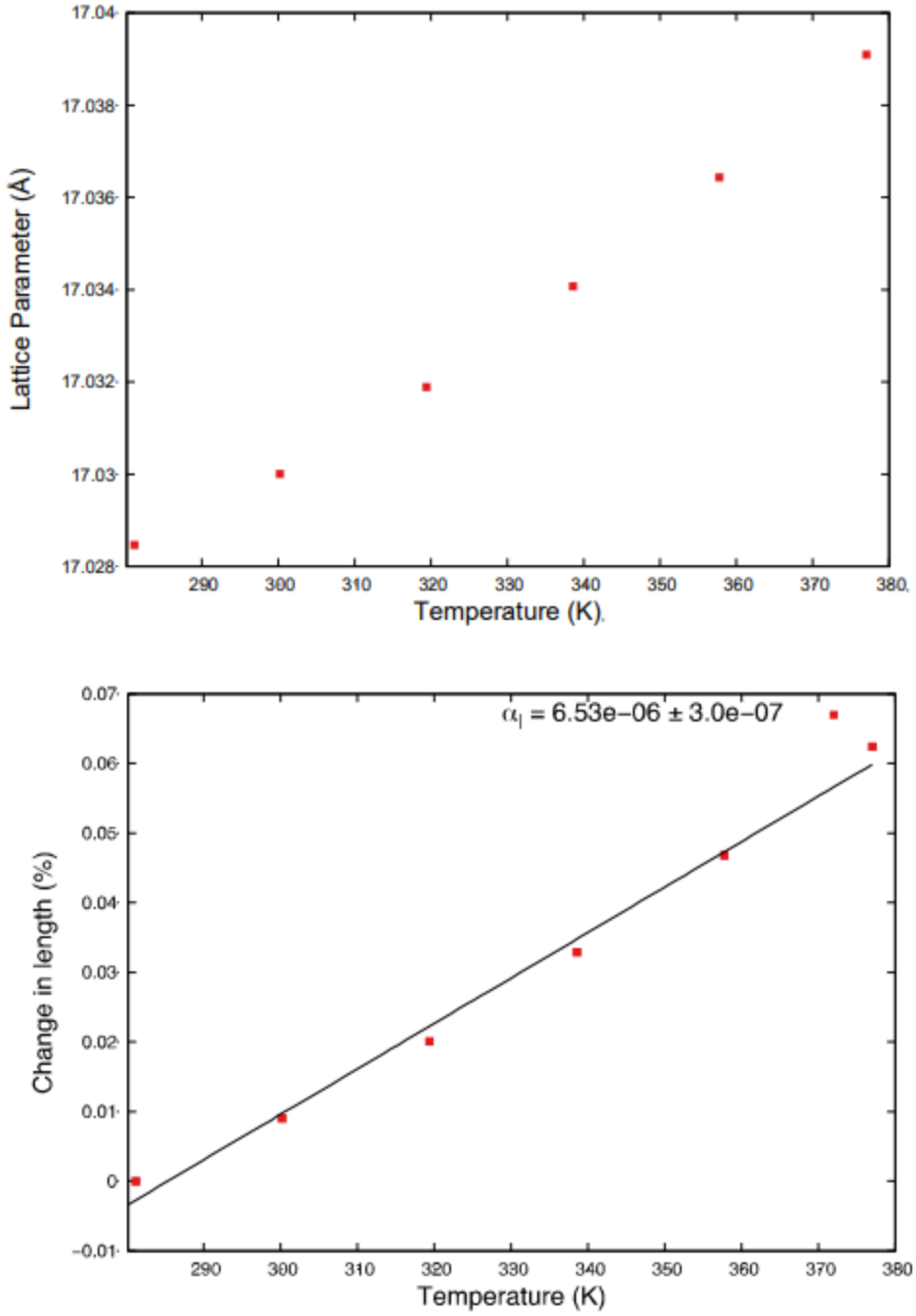

Figure D.34: Evolution of lattice parameters (top) and percent change in lattice parameters (bottom) with temperature upon heating in ZIF-8. Pawley analysis performed using the I-43m space group.

D.4 Molecular Simulation

Molecular Simulation details can be found in the online supplementary for the provided publication. Because the thesis author was not involved in these simulations they will not be discussed further in this supplementary section.

Appendix E. SUPPLEMENTARY MATERIAL FOR CHAPTER 6

E.1 Figures

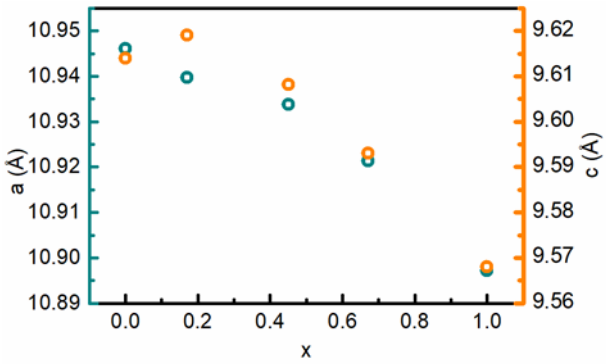

Figure E.1: Variation of the lattice constants, a and c, at 303 K with composition for the solvent-free Zn-DMOF-TM$_x$ samples. "*x*" is the fraction of TM-bdc^{2-} linker in each sample; x = [TM-bdc^{2-}]/ ([TM-bdc^{2-}] + [bdc^{2-}]).

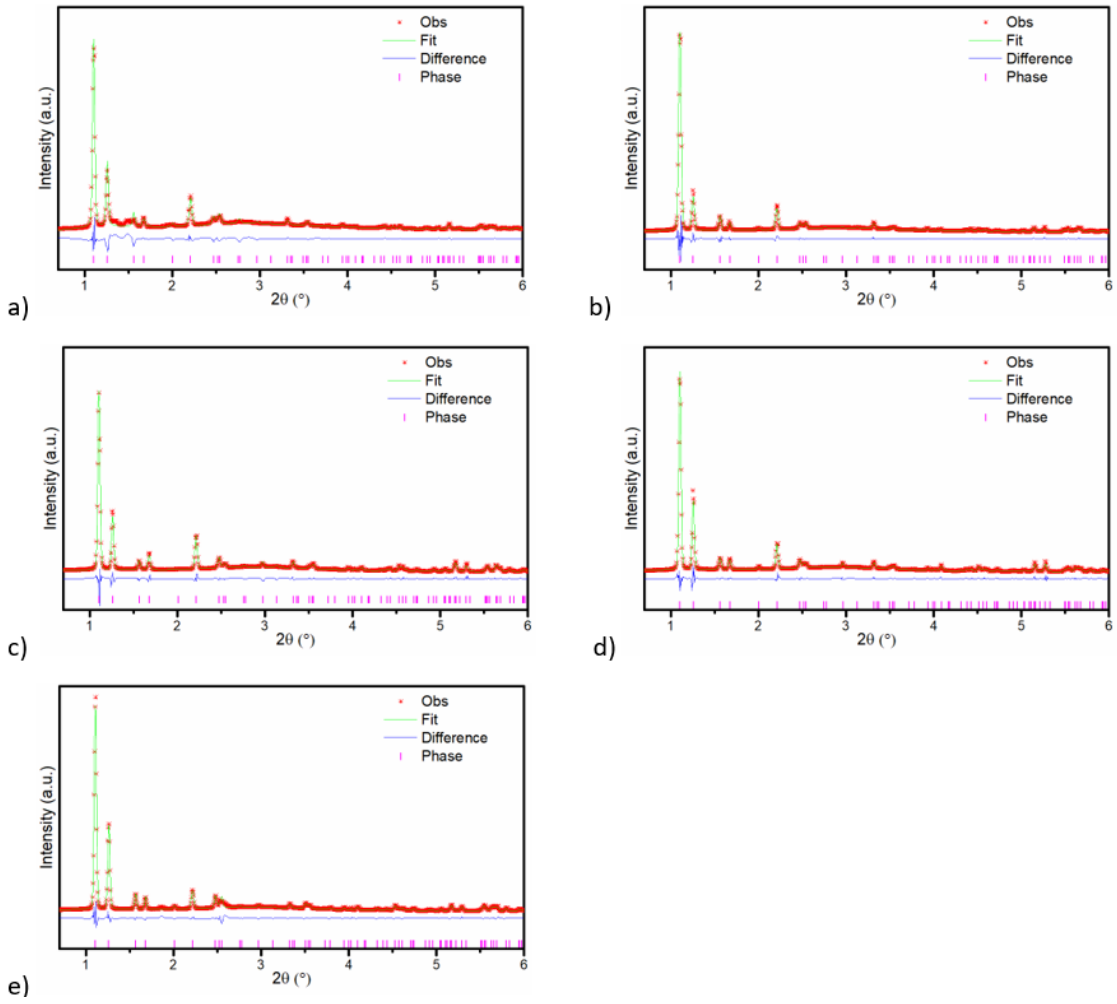

Figure E.2: Example Le Bail fits for the Zn-DMOF-TM$_x$ samples. These fits were performed using GSAS-II and are for data collected at 303 K with λ = 0.2113 Å: a) x = 0.0, b) x = 0.17, c) x = 0.45, d) x = 0.67 and e) x = 1.0. x = [TM-bdc^{2-}]/ ([TM-bdc^{2-}] + [bdc^{2-}]).

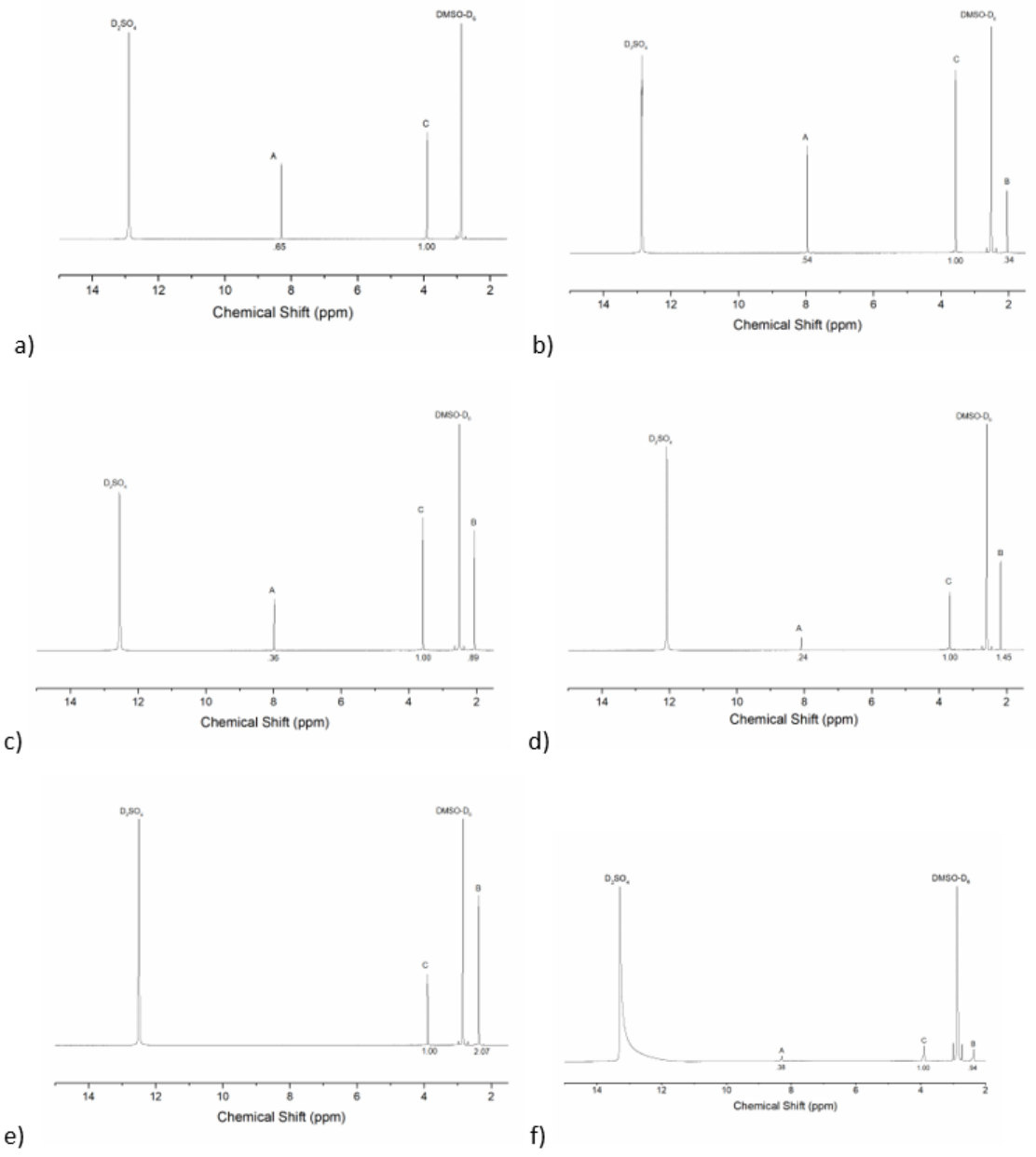

Figure E.3: ^{1}H NMR spectra for Zn-DMOF-TM$_x$ dissolved in D_2SO_4/DMSO-d_6: a) x = 0.0, b) x = 0.17, c) x = 0.45, d) x = 0.67, e) x = 1.0 powder samples and f) x = 0.45 single crystal sample. The peaks labelled A, B, and C are from the bdc^{2-}, DABCO, and TM-bdc^{2-}, respectively.

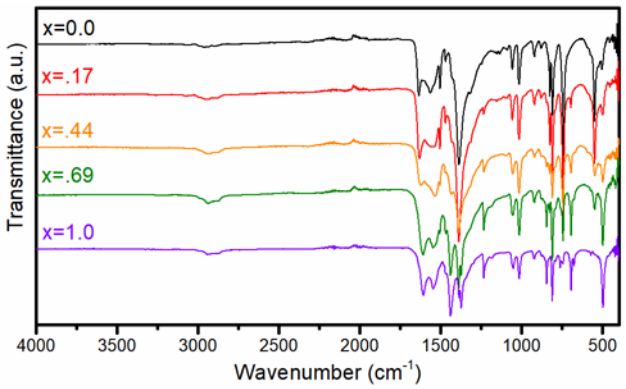

Figure E.4: FTIR data for the Zn-DMOF-TM$_x$ samples.

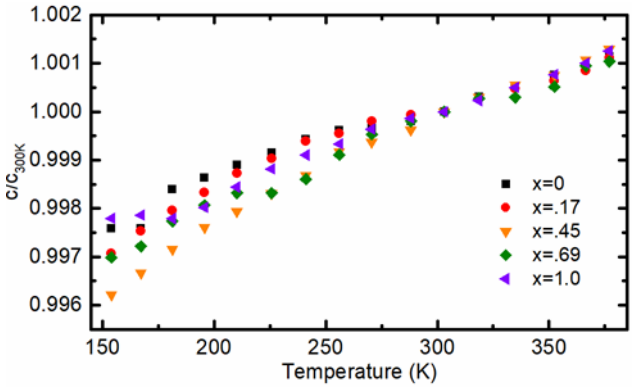

Figure E.5: Normalized lattice constant (c/c$_{300K}$) as a function of temperature for the Zn-DMOF-TM$_x$ samples.

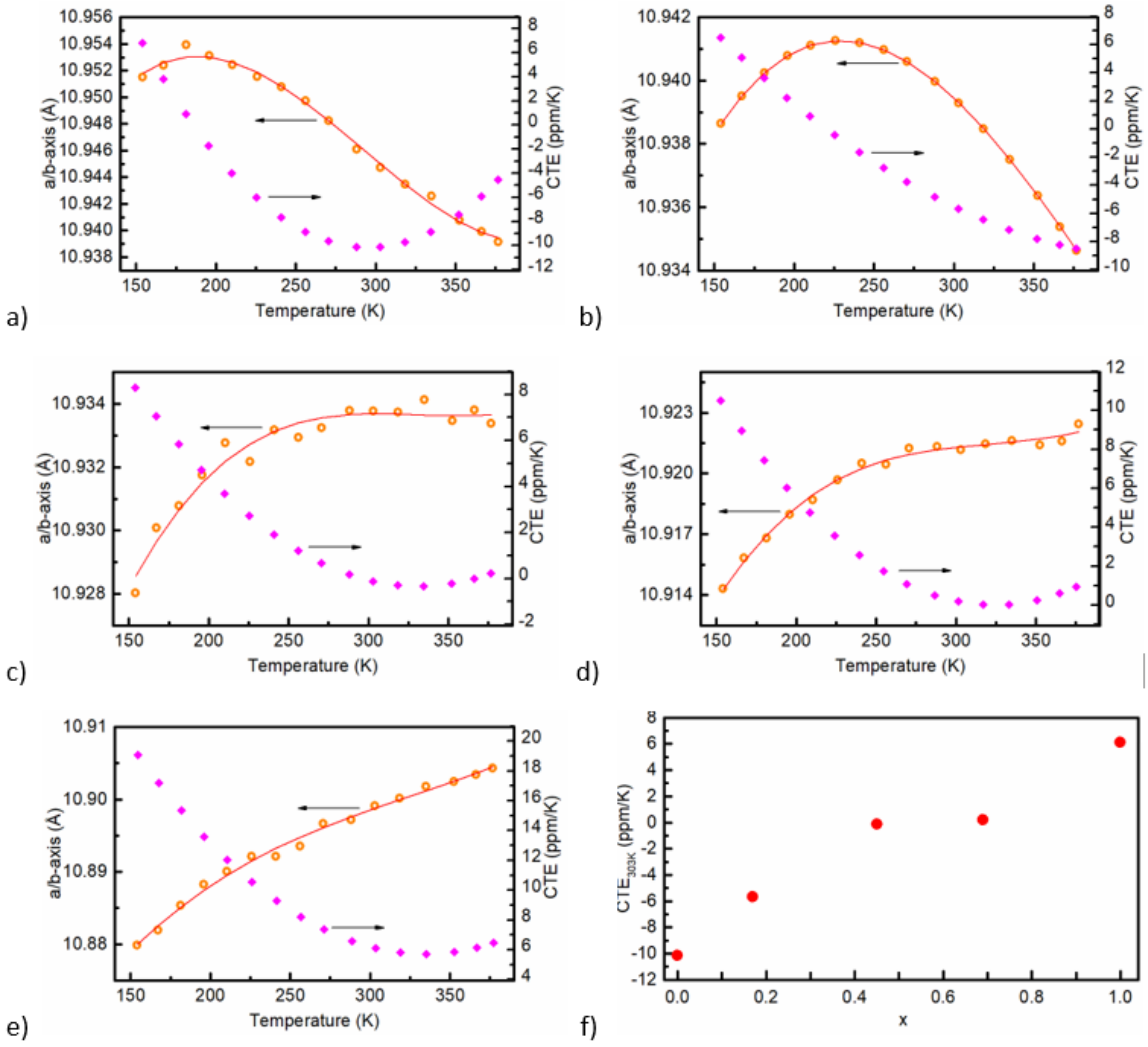

Figure E.6: Lattice constant, *a*, (left y-axis) and the linear CTE (right y-axis) derived from it as a function of temperature for samples with a) x = 0.0, b) x = 0.17, c) x = 0.45, d) x = 0.67 and e) x = 1.0. The CTEs were calculated by differentiating polynomial fits to the lattice constants. f) Linear CTE at ~300 K as a function of composition for the Zn-DMOF-TM$_x$ samples.

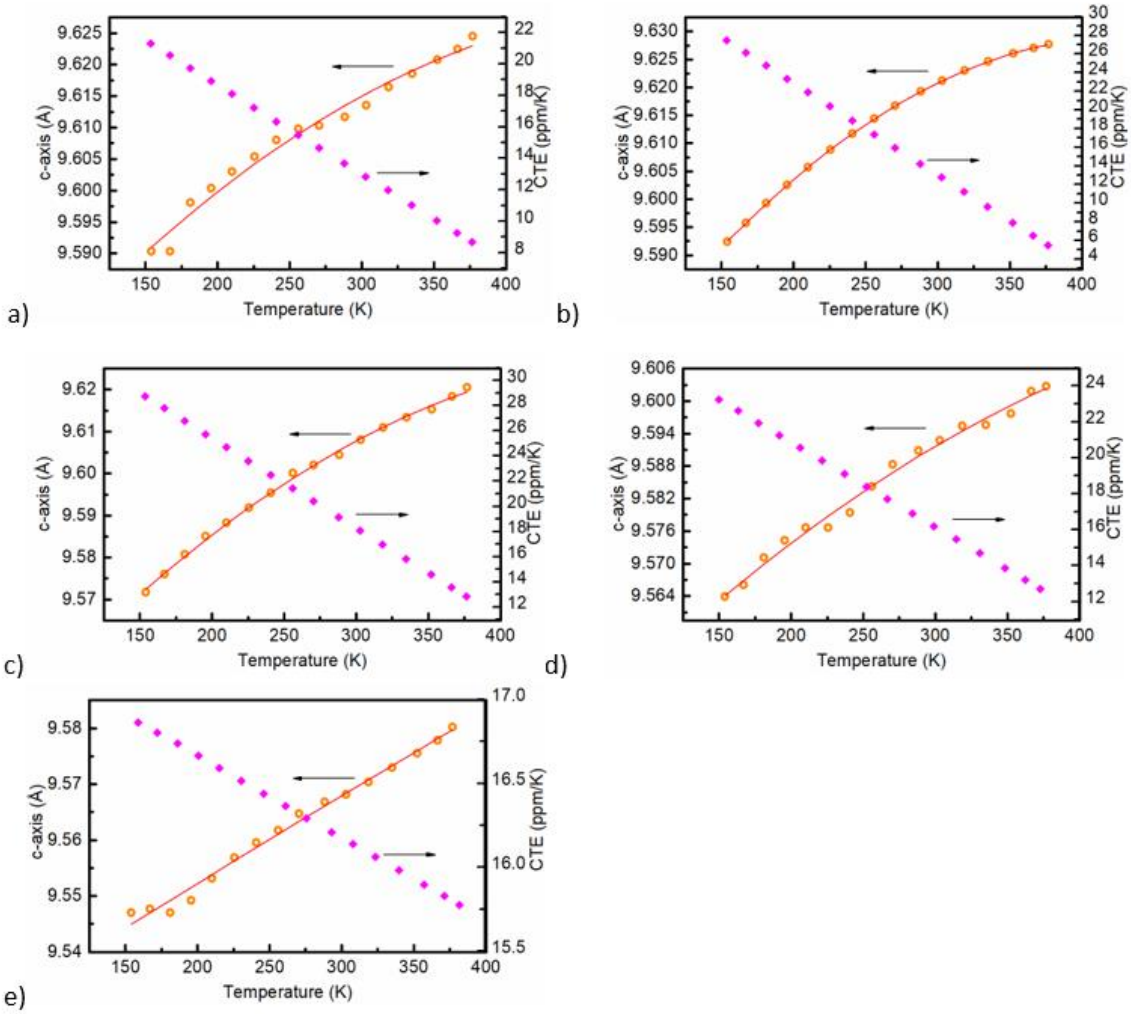

Figure E.7: Lattice constant, c, (left y-axis) and the linear CTE (right y-axis) derived from it as a function of temperature for samples with a) x = 0.0, b) x = 0.17, c) x = 0.45, d) x = 0.67 and e) x = 1.0. The CTEs were calculated by differentiating polynomial fits to the lattice constants.

E.2 Tables

Table E.1: Lattice constants and unit cell volume for Zn-DMOF as a function of temperature as determined by the Le Bail analysis of the synchrotron x-ray diffraction data.

Temperature (K)	R_{wp} (%)	*a/b* (Å)	*c* (Å)	Volume (Å^3)
376	9.31	10.939(1)	9.625(2)	1151.8(3)
366	9.40	10.940(1)	9.623(2)	1151.7(3)
352	9.44	10.941(1)	9.621(2)	1151.7(3)
334	9.42	10.943(1)	9.619(2)	1151.8(3)
318	9.36	10.943(1)	9.617(2)	1151.7(3)
303	9.47	10.945(1)	9.614(2)	1151.6(3)
288	9.51	10.946(1)	9.612(2)	1151.7(3)
270	9.55	10.948(1)	9.611(2)	1152.0(3)
256	9.56	10.950(1)	9.610(2)	1152.2(3)
241	9.45	10.951(1)	9.608(2)	1152.2(3)
225	9.51	10.952(1)	9.606(2)	1152.1(3)
210	9.56	10.952(1)	9.603(2)	1152.0(3)
195	9.53	10.953(1)	9.601(2)	1151.8(3)
181	9.41	10.954(1)	9.599(2)	1151.7(3)
167	9.24	10.952(1)	9.591(2)	1150.4(3)
154	9.56	10.952(1)	9.594(2)	1150.6(4)

Table E.2: Lattice constants and unit cell volume for Zn-DMOF-TM$_{0.17}$ as a function of temperature as determined by the Le Bail analysis of the synchrotron x-ray diffraction data.

Temperature (K)	R_{wp} (%)	a/b (Å)	c (Å)	Volume (Å^3)
376	7.32	10.9342(6)	9.630(1)	1151.3(2)
366	6.89	10.9354(6)	9.627(1)	1151.3(2)
352	6.95	10.9369(6)	9.625(1)	1151.3(2)
334	6.98	10.9378(6)	9.624(1)	1151.3(2)
318	6.92	10.9385(6)	9.622(1)	1151.3(2)
303	6.90	10.9392(6)	9.619(1)	1151.1(2)
288	6.98	10.9397(6)	9.619(1)	1151.1(2)
270	7.04	10.9403(6)	9.617(1)	1151.1(2)
256	7.03	10.9408(6)	9.615(1)	1150.9(2)
241	7.10	10.9412(6)	9.613(1)	1150.8(2)
225	7.16	10.9414(6)	9.610(1)	1150.4(2)
210	7.31	10.9412(6)	9.607(1)	1150.0(2)
195	7.19	10.9411(6)	9.603(1)	1149.6(2)
181	6.78	10.9403(6)	9.599(1)	1149.0(2)
167	6.32	10.9395(5)	9.595(1)	1148.3(2)
154	6.79	10.9384(6)	9.591(1)	1147.6(2)

Table E.3: Lattice constants and unit cell volume for Zn-DMOF-TM$_{0.45}$ as a function of temperature as determined by the Le Bail analysis of the synchrotron x-ray diffraction data.

Temperature (K)	R_{wp} (%)	a/b (Å)	c (Å)	Volume (Å^3)
376	7.32	10.9334(5)	9.6204(6)	1150.0(1)
366	6.89	10.9338(5)	9.6183(6)	1149.8(1)
352	6.95	10.9335(5)	9.6153(6)	1149.4(1)
334	6.98	10.9341(6)	9.6134(6)	1149.3(1)
318	6.92	10.9337(6)	9.6110(6)	1149.0(1)
303	6.90	10.9338(6)	9.6081(6)	1148.6(1)
288	6.98	10.9338(6)	9.6044(6)	1148.2(1)
270	7.04	10.9332(5)	9.6020(6)	1147.8(1)
256	7.03	10.9329(5)	9.6001(6)	1147.5(1)
241	7.10	10.9332(6)	9.5953(7)	1147.0(1)
225	7.16	10.9322(5)	9.5919(5)	1146.3(1)
210	7.31	10.9328(5)	9.5883(5)	1146.0(1)
195	7.19	10.9318(5)	9.5850(5)	1145.4(1)
181	6.78	10.9308(5)	9.5807(6)	1144.7(1)
167	6.32	10.9301(6)	9.5760(6)	1144.0(1)
154	6.79	10.9280(6)	9.5717(6)	1143.1(1)

Table E.4: Lattice constants and unit cell volume for Zn-DMOF-TM$_{0.67}$ as a function of temperature as determined by the Le Bail analysis of the synchrotron x-ray diffraction data.

Temperature (K)	R_{wp} (%)	a/b (Å)	c (Å)	Volume (Å^3)
376	6.49	10.9224(5)	9.603(1)	1145.6(1)
366	6.62	10.9216(5)	9.602(1)	1145.3(1)
352	6.62	10.9214(5)	9.598(1)	1144.8(1)
334	6.75	10.9216(5)	9.596(1)	1144.6(1)
318	6.84	10.9215(5)	9.595(1)	1144.5(1)
303	7.11	10.9212(6)	9.593(1)	1144.1(1)
288	6.97	10.9213(6)	9.591(1)	11440(1)
270	6.98	10.9213(6)	9.588(1)	1143.6(1)
256	6.75	10.9205(5)	9.584(1)	1143.0(1)
241*	42.62*	10.9205(6)	9.579(6)	1142.2(9)
225	6.66	10.9197(5)	9.577(1)	1141.9(1)
210	6.76	10.9187(5)	9.577(1)	1141.7(1)
195	6.86	10.9180(5)	9.574(1)	1141.3(1)
181	7.07	10.9168(6)	9.571(1)	1140.6(1)
167	7.50	10.9158(6)	9.566(1)	1139.8(2)
154	7.96	10.9100(6)	9.564(1)	1139.3(2)

Table E.5: Lattice constants and unit cell volume for Zn-DMOF-TM1.0 as a function of temperature as determined by the Le Bail analysis of the synchrotron x-ray diffraction data.

Temperature (K)	R_{wp} (%)	*a/b* (Å)	*c* (Å)	Volume (Å^3)
376	6.61	10.9043(5)	9.580(1)	1139.1(1)
366	6.53	10.9034(5)	9.578(1)	1138.6(1)
352	6.56	10.9025(5)	9.575(1)	1138.2(1)
334	6.60	10.9018(5)	9.573(1)	1137.7(1)
318	6.81	10.9002(5)	9.570(1)	1137.1(1)
303	6.79	10.8991(5)	9.568(1)	1136.6(1)
288	6.77	10.8972(5)	9.567(1)	1136.0(1)
270	6.92	10.8966(5)	9.565(1)	1135.7(1)
256	7.09	10.8935(5)	9.562(1)	1134.7(1)
241	7.14	10.8922(5)	9.560(1)	1134.1(1)
225	7.07	10.8921(5)	9.557(1)	1133.8(1)
210	7.15	10.8901(5)	9.553(1)	1132.9(1)
195	7.21	10.8882(5)	9.549(1)	1132.1(1)
181	7.32	10.8854(6)	9.547(1)	1131.2(1)
167	7.29	10.8819(6)	9.548(1)	1130.6(1)
154	7.92	10.8799(6)	9.547(1)	1130.1(1)

Appendix F. SUPPLEMENTARY MATERIALS ROR CHAPTER 7

F.1 Tables

Table F.1: Temperatures, pressures, lattice constants, and cell volumes for ScF_3 (sample) and a CaF_2 pressure standard as determined by Rietveld analysis of the synchrotron x-ray diffraction data.

Temperature (K)	Pressure (GPa)	Rwp (%)	Sample Lattice Constant, a (Å)	Sample Volume, (Å^3)	CaF2 Volume, (Å^3)
298	0.09	2.7	4.0071(3)	64.34(2)	162.87(4)
298	0.25	3.1	4.0072(4)	64.35(2)	162.55(5)
323	0.40	3.2	4.0060(4)	64.29(2)	162.48(5)
373	0.71	2.7	3.9990(3)	63.95(1)	162.35(3)
425	0.81	2.7	3.9974(3)	63.87(1)	162.64(3)
472	0.92	2.6	3.9963(2)	63.82(1)	162.91(4)
540	1.00	2.6	3.9940(3)	63.71(1)	163.48(3)
555	1.05	5.1	3.9934(3)	63.68(2)	163.53(6)
573	1.17	2.7	3.9924(3)	63.63(1)	163.45(3)
573	1.16	2.8	3.9925(3)	63.64(1)	163.48(3)
573	1.22	2.6	3.9924(2)	63.64(1)	163.35(3)
573	1.43	2.6	3.9935(2)	63.69(1)	162.93(3)
573	1.56	2.7	3.9945(2)	63.74(1)	162.65(3)
573	1.72	2.7	3.9954(2)	63.78(1)	162.33(3)
573	1.94	2.5	3.9957(2)	63.80(1)	161.89(3)
573	2.22	2.8	3.9953(2)	63.77(1)	161.34(3)
573	2.40	2.8	3.9946(2)	63.74(1)	161.00(3)
573	2.53	2.7	3.9937(2)	63.70(1)	160.76(3)
573	2.96	2.8	3.9900(2)	63.52(1)	159.96(3)
573	3.20	2.7	3.9874(2)	63.40(1)	159.52(3)
573	3.46	2.9	3.9842(2)	63.25(1)	159.06(3)
573	3.78	2.8	3.9803(2)	63.06(1)	158.50(3)
573	4.13	3.3	3.9753(3)	62.82(1)	157.91(3)
573	4.33	3.2	3.9720(3)	62.67(1)	157.57(3)
573	4.57	3.0	3.9687(3)	62.51(1)	157.18(3)
573	4.80	2.9	3.9649(3)	62.33(1)	156.81(3)
572	4.95	3.0	3.9626(3)	62.22(1)	156.56(3)

Temperature (K)	Pressure (GPa)	Rwp (%)	Sample Lattice Constant, a (Å)	Sample Volume, (Å^3)	CaF2 Volume, (Å^3)
545	6.05	3.2	3.9441(3)	61.36(1)	154.69(3)
523	6.30	6.0	3.9381(3)	61.07(3)	154.15(7)
523	6.32	3.8	3.9379(4)	61.06(2)	154.13(4)
498	6.42	9.2	3.9331(3)	60.84(5)	153.82(3)
499	6.45	3.5	3.9323(4)	60.81(2)	153.77(4)
473	6.52	4.5	3.9267(7)	60.55(3)	153.52(5)
473	6.59	3.4	3.9256(3)	60.50(2)	153.42(4)
438	6.67	3.6	3.9188(7)	60.18(3)	153.08(4)
403	6.79	3.8	3.9126(9)	59.89(4)	152.70(4)
373	6.94	3.9	3.9071(9)	59.64(5)	152.32(4)

REFERENCES

(1) Sleight, A. W. Isotropic Negative Thermal Expansion. *Annu. Rev. Mater. Sci.* **1998**, *28*, 29-43.

(2) Barrera, G. D.; Bruno, J. A. O.; Barron, T. H. K.; Allan, N. L. Negative Thermal Expansion. *J. Phys. Condens. Matter* **2005**, *17*, R217-R252.

(3) Dove, M. T.; Fang, H. Negative Thermal Expansion and Associated Anomalous Physical Properties: Review of the Lattice Dynamics Theoretical Foundation. *Rep. Prog. Phys* **2016**, *79*, 066503.

(4) Chu, C. N.; Saka, N.; Suh, N. P. Negative Thermal Expansion Ceramics: A Review. *Materials Science and Engineering* **1987**, *95*, 303-308.

(5) Miller, W.; Smith, C. W.; Mackenzie, D. S.; Evans, K. E. Negative thermal expansion: a review. *Journal of Materials Science* **2009**, *44*, 5441-5451.

(6) Roy, R.; Agrawal, D. K.; McKinstry, H. A. Very Low Thermal Expansion Coefficient Materials. *Annu. Rev. Mater. Sci.* **1989**, *19*, 59-81.

(7) Lind, C. Two Decades of Negative Thermal Expansion Research: Where Do We Stand? *Materials* **2012**, *5*, 1125-1154.

(8) Grüneisen, E. Z. d. f. K. des festen Korpers. *Handb. Phys. 1926, 10, 1-59* **1926**.

(9) Sleight, A. W.; Thundathil, M. A.; Evans, J. S. O. Negative Thermal Expansion Materials. USA Patent 5,514,360.

(10) Evans, J. S. O. Negative Thermal Expansion Materials. *J. Chem. Soc. Dalton Trans.* **1999**, 3317-3326.

(11) Cliffe, M. J.; Hill, J. A.; Murray, C. A.; Coudert, F.-X.; Goodwin, A. L. Defect-Dependent Colossal Negative Thermal Expansion in Uio-66(Hf) Metal–Organic Framework. *Phys. Chem. Chem. Phys.* **2015**, *17*, 11586-11592.

(12) White, G. K.; Choy, C. L. Thermal expansion and Grüneisen parameters of isotropic and oriented polyethylene. *Journal of Polymer Science: Polymer Physics Edition* **1984**, *22*, 835-846.

(13) Takenaka, K. Negative Thermal Expansion Materials: Technological Key for Control of Thermal Expansion. *Sci. Technol. Adv. Mater.* **2012**, *13*, 013001.

(14) Chandra, A.; Meyer, W. H.; Best, A.; Hanewald, A.; Wegner, G. Modifying thermal expansion of polymer composites by blending with a negative thermal expansion material. *Macromol. Mater. Eng.* **2007**, *292*, 295-301.

(15) Yilmaz, S. Phase transformations in thermally cycled Cu/ZrW_2O_8 composites investogated by synchrotron x-ray diffraction. *J. Phys. Condens. Matter*. **2002**, *14*, 365-375.

(16) Wu, Y.; Wang, M. L.; Chen, Z.; Ma, N. H.; Wang, H. W. The effect of phase transformation on the thermal expansion property in Al/ZrW2O8 composites. *Journal of Materials Science* **2013**, *48*, 2928-2933.

(17) Miller, W.; Smith, C. W.; Dooling, P.; Burgess, A. N.; Evans, K. E. Reduced thermal stress in composites via negative thermal expansion particulate fillers. *Compos. Sci. Technol.* **2010**, *70*, 318-327.

(18) Yilmaz, S. Thermal mismatch stress development in Cu-ZrW_2O_8 composite investigated by synchrotron X-ray diffraction. *Compos. Sci. Technol.* **2002**, *62*, 1835-1839.

(19) Attfield, J. P. Mechanisms and Materials for NTE. *Frontiers in Chemistry* **2018**, *6*.

(20) Song, Y.; Chen, J.; Liu, X.; Wang, C.; Gao, Q.; Li, Q.; Hu, L.; Zhang, J.; Zhang, S.; Xing, X. Structure, Magnetism, and Tunable Negative Thermal Expansion in (Hf,Nb)Fe2 Alloys. *Chemistry of Materials* **2017**, *29*, 7078-7082.

(21) Zhao, Y.-Y.; Hu, F.-X.; Bao, L.-F.; Wang, J.; Wu, H.; Huang, Q.-Z.; Wu, R.-R.; Liu, Y.; Shen, F.-R.; Kuang, H.; Zhang, M.; Zuo, W.-L.; Zheng, X.-Q.; Sun, J.-R.; Shen, B.-G. Giant Negative Thermal Expansion in Bonded MnCoGe-Based Compounds with Ni2In-Type Hexagonal Structure. *Journal of the American Chemical Society* **2015**, *137*, 1746-1749.

(22) Huang, R.; Liu, Y.; Fan, W.; Tan, J.; Xiao, F.; Qian, L.; Li, L. Giant Negative Thermal Expansion in $NaZn_{13}$-Type La(Fe, Si, Co)$_{13}$ Compounds. *Journal of the American Chemical Society* **2013**, *135*, 11469-11472.

(23) Takenaka, K.; Takagi, H. Giant negative thermal expansion in Ge-doped anti-perovskite manganese nitrides. *Applied Physics Letters* **2005**, *87*, 261902:(261903).

(24) Liu, Y. M.; Wang, Z. H.; Wu, M. Y.; Sun, Q.; Chao, M. J.; Jia, Y. Negative thermal expansion in isostructural cubic ReO3 and ScF3: A comparative study. *Computational Materials Science* **2015**, *107*, 157-162.

(25) Greve, B. K.; Martin, K. L.; Lee, P. L.; Chupas, P. J.; Chapman, K. W.; Wilkinson, A. P. Pronounced Negative Thermal Expansion from a Simple Structure: Cubic ScF_3. *J. Am. Chem. Soc.* **2010**, *132*, 15496-15498.

(26) Pryde, A. K. A.; Hammonds, K. D.; Dove, M. T.; Heine, V.; Gale, J. D.; Warren, M. C. Origin of the Negative Thermal Expansion in ZrW_2O_8 and ZrV_2O_7. *J. Phys. Condens. Matter* **1996**, *8*, 10973-10982.

(27) Rodriguez, E. E.; Llobet, A.; Proffen, T.; Melot, B. C.; Seshadri, R.; Littlewood, P. B.; Cheetham, A. K. The role of static disorder in negative thermal expansion in ReO_3. *Journal of Applied Physics* **2009**, *105*, 114901:(114906).

(28) Stewart, D. J. Chemical control of negative thermal expansion in ReO3-type fluorides through compositional variation. 2014.

(29) Baxter, S. J.; Hester, B. R.; Wright, B. R.; Wilkinson, A. P. Controlling the Negative Thermal Expansion and Response to Pressure in ReO_3-type Fluorides by the Deliberate Introduction of Excess Fluoride: $Mg_{1-x}Zr_{1+x}F_{6+2x}$, x = 0.15, 0.30, 0.40, and 0.50. *Chem. Mater.* **2019**, *31*, 3440-3448.

(30) Qin, F.; Chen, J.; Aydemir, U.; Sanson, A.; Wang, L.; Pan, Z.; Xu, J.; Sun, C.; Ren, Y.; Deng, J.; Yu, R.; Hu, L.; Snyder, G. J.; Xing, X. Isotropic Zero Thermal Expansion and Local Vibrational Dynamics in (Sc,Fe)F3. *Inorganic Chemistry* **2017**, *56*, 10840-10843.

(31) Wang, L.; Wang, C.; Sun, Y.; Shi, K.; Deng, S.; Lu, H.; Hu, P.; Zhang, X. Metal fluorides, a new family of negative thermal expansion materials. *Journal of Materiomics*.

(32) Morelock, C. R.; Hancock, J. C.; Wilkinson, A. P. Thermal expansion and phase transitions of α-AlF_3. *Journal of Solid State Chemistry* **2014**, *219*, 143-147.

(33) Chapman, K. W.; Chupas, P. J.; Kepert, C. J. Direct Observation of a Transverse Vibrational Mechanism for Negative Thermal Expansion in $Zn(CN)_2$: An Atomic Pair Distribution Function Analysis. *J. Am. Chem. Soc.* **2005**, *127*, 15630-15636.

(34) Keen, D. A.; Dove, M. T.; Evans, J. S. O.; Goodwin, A. L.; Peters, L.; Tucker, M. G. The hydrogen-bonding transition and isotope-dependent negative thermal expansion in H3Co(CN)(6). *Journal of Physics-Condensed Matter* **2010**, *22*, 7.

(35) Phillips, A. E.; Goodwin, A. L.; Halder, G. J.; Southon, P. D.; Kepert, C. J. Nanoporosity and exceptional negative thermal expansion in single-network cadmium cyanide. *Angewandte Chemie-International Edition* **2008**, *47*, 1396-1399.

(36) Goodwin, A. L.; Kepert, C. J. Negative Thermal Expansion and Low-Frequency Modes in Cyanide-Bridged Framework Materials. *Phys. Rev. B* **2005**, *71*, 140301.

(37) Goodwin, A. L.; Keen, D. A.; Tucker, M. G.; Dove, M. T.; Peters, L.; Evans, J. S. O. Argentophilicity-dependent colossal thermal expansion in extended Prussian blue analogues. *Journal of the American Chemical Society* **2008**, *130*, 9660-+.

(38) Amri, M.; Walton, R. I. Negative Thermal Expansion in the Aluminum and Gallium Phosphate Zeotypes with CHA and AEI Structure types. *Chemistry of Materials* **2009**, *21*, 3380-3390.

(39) Fisher, D. J.: *Negative Thermal Expansion Materials*; Materials Research Forum: Millersville, PA 17551, USA, 2018; Vol. 22.

(40) Dubbeldam, D.; Walton, K. S.; Ellis, D. E.; Snurr, R. Q. Exceptional Negative Thermal Expansion in Isoreticular Metal-Organic Frameworks. *Angew. Chem. Int. Ed.* **2007**, *46*, 4496-4499.

(41) Xing, X. R.; Deng, J. X.; Chen, J.; Liu, G. R. Novel thermal expansion of lead titanate. *Rare Metals* **2003**, *22*, 294-297.

(42) Jiang, Y.; Guo, R.; Bhalla, A. S. Single crystal growth and ferroelectric properties of α(Ba1−xSrx)Nb2O6:β(Na1−yKy)NbO3 solid solutions. *Journal of Applied Physics* **1998**, *84*, 5140-5146.

(43) Long, Y. W.; Hayashi, N.; Saito, T.; Azuma, M.; Muranaka, S.; Shimakawa, Y. Temperature-induced A-B intersite charge transfer in an A-site-ordered $LaCu_3Fe_4O_{12}$ perovskite. *Nature* **2009**, *458*, 60-63.

(44) Yamada, I.; Tsuchida, K.; Ohgushi, K.; Hayashi, N.; Kim, J.; Tsuji, N.; Takahashi, R.; Matsushita, M.; Nishiyama, N.; Inoue, T.; Irifune, T.; Kato, K.; Takata, M.; Takano, M. Giant Negative Thermal Expansion in the Iron Perovskite $SrCu_3Fe_4O_{12}$. *Angewandte Chemie-International Edition* **2011**, *50*, 6579-6582.

(45) Yan, X.; Miao, J.; Liu, J.; Wu, X.; Zou, H.; Sha, D.; Cheng, X. Negative thermal expansion, electrical and mechanical properties of antiperovskite Mn3Zn0.5A0.5N (A = Sn, Ag, Ni). *Advances in Applied Ceramics* **2016**, *115*, 422-426.

(46) Hummel, F. A. Thermal Expansion Properties of Some Synthetic Lithia Minerals. *J. Am. Ceram. Soc.* **1951**, *34*, 235-239.

(47) Vepa, S. S. V. S. S.; Umarji, A. M. Effect of substitution on thermal expansion of cordierite ($Mg_2Al_4Si_5O_{18}$). *J. Am. Ceram. Soc.* **1993**, *76*, 1873-1876.

(48) Predecki, P.; Haas, J.; Faber, J.; Hitterman, R. L. Structural Aspects of the Lattice Thermal Expansion of Hexagonal Cordierite. *J. Am. Ceram. Soc.* **1987**, *70*, 175-182.

(49) Ikawa, H.; Otagiri, T.; Imai, O.; Urabe, K.; Udagawa, S. Thermal expansion of high-temperature cordierite and its solid solutions. *Yogyo Kyokaishi* **1986**, *94*, 344-350.

(50) Woodcock, D. A.; Lightfoot, P.; Villaescusa, L. A.; Díaz-Cabañas, M.-J.; Camblor, M. A.; Engberg, D. Negative Thermal Expansion in the Siliceous Zeolites Chabazite and ITQ-4: A Neutron Powder Diffraction Study. *Chem. Mater.* **1999**, *11*, 2508-2514.

(51) Attfield, M. P.; Feygenson, M.; Neuefeind, J. C.; Proffen, T. E.; Lucas, T. C. A.; Hriljac, J. A. Reprobing the mechanism of negative thermal expansion in siliceous faujasite. *Rsc Advances* **2016**, *6*, 19903-19909.

(52) Alabarse, F. G.; Silly, G.; Brubach, J. B.; Roy, P.; Haidoux, A.; Levelut, C.; Bantignies, J. L.; Kohara, S.; Le Floch, S.; Cambon, O.; Haines, J. Anomalous Compressibility and Amorphization in AlPO4-17, the Oxide with the Highest Negative Thermal Expansion. *Journal of Physical Chemistry C* **2017**, *121*, 6852-6863.

(53) Vepa, S. S. V. S. S.; Umarji, A. M. Effect of Substitution of Ca on Thermal Expansion of Cordierite (Mg2Al4Si5O18). *Journal of the American Ceramic Society* **1993**, *76*, 1873-1876.

(54) Graham, J.; Wadsley, A. D.; Weymouth, J. H.; Williams, L. S. A New Ternary Oxide, ZrW_2O_8. *J. Am. Ceram. Soc.* **1959**, *42*, 570.

(55) Auray, M.; Quarton, M. Zirconium Tungstate. *Acta Crystallogr., Section C* **1995**, *51*, 2210-2213.

(56) Mary, T. A.; Evans, J. S. O.; Vogt, T.; Sleight, A. W. Negative Thermal Expansion from 0.3 to 1050 Kelvin in ZrW_2O_8. *Science* **1996**, *272*, 90-92.

(57) Allen, S.; Evans, J. S. O. Negative thermal expansion and oxygen disorder in cubic ZrMo2O8. *Physical Review B* **2003**, *68*, -.

(58) Allen, S.; Ward, R. J.; Hampson, M. R.; Gover, R. K. B.; Evans, J. S. O. Structures and phase transitions of trigonal $ZrMo_2O_8$ and $HfMo_2O_8$. *Acta Crystallogr., Sect. B* **2004**, *60*, 32-40.

(59) Chatterji, T.; Hansen, T. C.; Brunelli, M.; Henry, P. F. Negative thermal expansion of ReO_3 in the extended temperature range. *Applied Physics Letters* **2009**, *94*, 241902:(241903).

(60) Greve, B. K. Exploring the thermal expansion of fluorides and oxyfluorides with ReO_3-type structures: from negative to positive thermal expansion. PhD Thesis, Georgia Institute of Technology, 2011.

(61) Williams, D. J.; Partin, D. E.; Lincoln, F. J.; Kouvetakis, J.; O'Keefe, M. The Disordered Crystal Structures of $Zn(CN)_2$ and $Ga(CN)_3$. *Journal of Solid State Chemistry* **1997**, *134*, 164-169.

(62) Ravindran, T. R.; Arora, A. K.; Chandra, S.; Valsakumar, M. C.; Shekar, N. V. C. Soft modes and negative thermal expansion in Zn(CN)(2) from Raman spectroscopy and first-principles calculations. *Physical Review B* **2007**, *76*.

(63) Chapman, K. W.; Chupas, P. J.; Kepert, C. J. Compositional dependence of negative thermal expansion in the Prussian blue analogues $(MPt^{IV})Pt^{II}(CN)_6$ (M = Mn, Fe, Co, Ni, Cu, Zn, Cd). *Journal of the American Chemical Society* **2006**, *128*, 7009-7014.

(64) Goodwin, A. L.; Kennedy, B. J.; Kepert, C. J. Thermal Expansion Matching via Framework Flexibility in Zinc Dicyanometallates. *Journal of the American Chemical Society* **2009**, *131*, 6334-+.

(65) Adak, S.; Daemen, L. L.; Hartl, M.; Williams, D.; Summerhill, J.; Nakotte, H. Thermal expansion in 3d-metal Prussian Blue Analogs—A survey study. *Journal of Solid State Chemistry* **2011**, *184*, 2854-2861.

(66) Sanson, A.; Giarola, M.; Mariotto, G.; Hu, L.; Chen, J.; Xing, X. R. Lattice dynamics and anharmonicity of CaZrF6 from Raman spectroscopy and ab initio calculations. *Materials Chemistry and Physics* **2016**, *180*, 213-218.

(67) Bocharov, D.; Žguns, P.; Piskunov, S.; Kuzmin, A.; Purans, J. Electronic structure of cubic ScF3 from first-principles calculations. *Low Temperature Physics* **2016**, *42*, 556-560.

(68) Hu, L.; Chen, J.; Sanson, A.; Wu, H.; Rodriguez, C. G.; Olivi, L.; Ren, Y.; Fan, L. L.; Deng, J. X.; Xing, X. R. New Insights into the Negative Thermal Expansion: Direct Experimental Evidence for the "Guitar-String" Effect in Cubic ScF3. *Journal of the American Chemical Society* **2016**, *138*, 8320-8323.

(69) Corrales-Salazar, A.; Brierley, R. T.; Littlewood, P. B.; Guzman-Verri, G. G. Landau theory and giant room-temperature barocaloric effect in MF3 metal trifluorides. *Physical Review Materials* **2017**, *1*, 10.

(70) Ranieri, I. M.; Baldochia, S. L.; Klimm, D. The phase diagram GdF(3)-LuF(3). *Journal of Solid State Chemistry* **2008**, *181*, 1070-1074.

(71) Daniel, P.; Bulou, A.; Rousseau, M.; Nouet, J. STRUCTURAL PHASE-TRANSITIONS AND LATTICE-DYNAMICS IN THE TRIFLUORIDES MF3 (M = AL, CR, GA, V, FE, IN...). *Phase Transitions* **1991**, *33*, 91-97.

(72) Hepworth, M. A.; Jack, K. H.; Peacock, R. D.; Westland, G. J. The Crystal Structures of the Trifluorides of Iron, Cobalt, Ruthenium, Rhodium, Palladium and Iridium. *Acta Crystallographica* **1957**, *10*, 63-69.

(73) Hepworth, M. A.; Jack, K. H. The crystal structure of manganese trifluoride, MnF3. *Acta Crystallographica* **1957**, *10*, 345-351.

(74) Gutmann, V.; Jack, K. H. THE CRYSTAL STRUCTURES OF MOLYBDENUM TRIFLUORIDE, MOF3, AND TANTALUM TRIFLUORIDE, TAF3. *Acta Crystallographica* **1951**, *4*, 244-246.

(75) Sowa, H.; Ahsbahs, H. Pressure-induced octahedron strain in VF3-type compounds. *Acta Crystallographica Section B-Structural Science* **1998**, *54*, 578-584.

(76) Mogusmilankovic, A.; Ravez, J.; Chaminade, J. P.; Hagenmuller, P. Ferroelastic Properties of TiF_3, VF_3, CrF_3, FeF_3, GaF_3, Compounds. *Materials Research Bulletin* **1985**, *20*, 9-17.

(77) Morelock, C. R. Thermal Expansion, Compressibility, and Local Structure of Fluorides and Oxyfluorides with the Rhenium Trioxide Structure. PhD Thesis, Georgia Institute of Technology, 2014.

(78) Hester, B. R.; Wilkinson, A. P. Effects of Composition on Crystal Structure, Thermal Expansion, and Response to Pressure in ReO_3-type $MNbF_6$ (M= Mn and Zn). *J. Solid State Chem.* **2019**, *269*, 428-433.

(79) Hester, B. R.; Wilkinson, A. P. Negative Thermal Expansion, Response to Pressure and Phase Transitions in $CaTiF_6$. *Inorg. Chem.* **2018**, *57*, 11275-11281.

(80) Hester, B. R.; Hancock, J. C.; Lapidus, S. H.; Wilkinson, A. P. Composition, Response to Pressure, and Negative Thermal Expansion in $M^{II}B^{IV}F_6$ (M = Ca, Mg; B = Zr, Nb). *Chem. Mater.* **2017**, *29*, 823-831.

(81) Goubard, F.; Llorente, S.; Bizot, D.; Chassaing, J.; Quarton, M. Antiferrodistortive order in the new solid solution $CrZr_{0.75}Nb_{0.25}F_6$. *Journal of Solid State Chemistry* **1997**, *131*, 231-235.

(82) Goubard, F.; Llorente, S.; Gaubicher, J.; Bizot, D.; Chassaing, J. Powder diffraction data for fluorocomplexes of niobium IV: $MNbF_6$ (M=Ca, Mg, Cd, Zn). *Powder Diffraction* **1998**, *13*, 163-165.

(83) Poulain, M.; Lucas, J. The system MF_2-ZrF_4 (M=Mg,Mn,Fe,Co,Ni,Zn). The fluorozirconates of the cubic rare earths. *Revue de Chimie Minerale* **1975**, *12*, 9-16.

(84) Reinen, D.; Steffens, F. Structure and Bonding in Transition-Metal Fluorides $M^{II}Me^{IV}F_6$ .A. Phase-Transitions. *Zeitschrift fur anorganische und allgemeine Chemie* **1978**, *441*, 63-82.

(85) Hancock, J. C.; Chapman, K. W.; Halder, G. J.; Morelock, C. R.; Kaplan, B. S.; Gallington, L. C.; Bongiorno, A.; Han, C.; Zhou, S.; Wilkinson, A. P. Large negative thermal expansion and anomalous behavior on compression in cubic ReO_3-type $A^{II}B^{IV}F_6$: $CaZrF_6$ and $CaHfF_6$ *Chemistry of Materials* **2015**, *27*, 3912-3918.

(86) Hester, B. Negative Thermal Expansion, Behavior on Compression, and Other Anomalous Behaviors in ReO3-Type Mixed Metal Fluorides (Thesis). *Georgia Institute of Technology* **2019**.

(87) Poulain, M.; Tofield, B. C. The structure of cubic $YbZrF_7$. *Journal of Solid State Chemistry* **1981**, *39*, 314-328.

(88) Ticknor, J. O.; Hester, B. R.; Adkins, J. W.; Xu, W.; Yakovenko, A. A.; Wilkinson, A. P. Zero Thermal Expansion and Abrupt Amorphization on Compression in Anion Excess ReO3-Type Cubic YbZrF7. *Chemistry of Materials* **2018**, *30*, 3071-3077.

(89) James, S. L. Metal-Organic Frameworks. *Chem. Soc. Rev.* **2003**, *32*, 276-288.

(90) Yaghi, O. M.; O'Keeffe, M.; Ockwig, N. W.; Chae, H. K.; Eddaoudi, M.; Kim, J. Reticular synthesis and the design of new materials. *Nature* **2003**, *423*, 705-714.

(91) Lightfoot, P.; Woodcock, D. A.; Maple, M. J.; Villaescusa, L. A.; Wright, P. A. The widespread occurrence of negative thermal expansion in zeolites. *Journal of Materials Chemistry* **2001**, *11*, 212-216.

(92) Dubbeldam, D.; Walton, K. S.; Ellis, D. E.; Snurr, R. Q. Exceptional Negative Thermal Expansion in Isoreticular Metal–Organic Frameworks. *Angewandte Chemie International Edition* **2007**, *46*, 4496-4499.

(93) Cliffe, M. J.; Hill, J. A.; Murray, C. A.; Coudert, F.-X.; Goodwin, A. L. Defect-dependent colossal negative thermal expansion in UiO-66(Hf) metal–organic framework. *Physical Chemistry Chemical Physics* **2015**, *17*, 11586-11592.

(94) Wu, Y.; Kobayashi, A.; Halder, G. J.; Peterson, V. K.; Chapman, K. W.; Lock, N.; Southon, P. D.; Kepert, C. J. Negative Thermal Expansion in the Metal–Organic Framework Material Cu3(1,3,5-benzenetricarboxylate)2. *Angewandte Chemie* **2008**, *120*, 9061-9064.

(95) Henke, S.; Schneemann, A.; Fischer, R. A. Massive Anisotropic Thermal Expansion and Thermo-Responsive Breathing in Metal–Organic Frameworks Modulated by Linker Functionalization. *Advanced Functional Materials* **2013**, *23*, 5990-5996.

(96) Korthuis, V.; Khosrovani, N.; Sleight, A. W.; Roberts, N.; Dupree, R.; Warren, W. W. Negative Thermal Expansion and Phase Transitions in the $ZrV_{2-x}P_xO_7$ Series. *Chem. Mater.* **1995**, *7*, 412-417.

(97) Evans, J. S. O.; Hanson, P. A.; Ibberson, R. M.; Duan, N.; Kameswari, U.; Sleight, A. W. Low-temperature oxygen migration and negative thermal expansion in $ZrW_{2-x}Mo_xO_8$. *Journal of the American Chemical Society* **2000**, *122*, 8694-8699.

(98) Peng, X.; Rong, Y.; Fan, L.; Lin, K.; Zhu, H.; Deng, J.; Chen, J.; Xing, X. Cation deficiency effect on negative thermal expansion of ferroelectric PbTiO3. *Inorganic Chemistry Frontiers* **2015**, *2*, 1091-1094.

(99) Tallentire, S. E.; Child, F.; Fall, I.; Vella-Zarb, L.; Evans, I. R.; Tucker, M. G.; Keen, D. A.; Wilson, C.; Evans, J. S. O. Systematic and Controllable Negative, Zero, and Positive Thermal Expansion in Cubic Zr1-xSnxMo2O8. *Journal of the American Chemical Society* **2013**, *135*, 12849-12856.

(100) Yang, T.; Lin, K.; Wang, N.; Liu, Z.; Wang, Y.; Deng, J.; Chen, J.; Kato, K.; Xing, X. Tunable thermal expansion and high hardness of (0.9−x)PbTiO3–xCaTiO3–0.1Bi(Zn2/3Ta1/3)O3 ceramics. *Inorganic Chemistry Frontiers* **2019**, *6*, 1068-1072.

(101) Xing, X.; Chen, J.; Deng, J.; Liu, G. Solid solution Pb1−xSrxTiO3 and its thermal expansion. *Journal of Alloys and Compounds* **2003**, *360*, 286-289.

(102) Gao, Q.; Chen, J.; Sun, Q.; Chang, D.; Huang, Q.; Wu, H.; Sanson, A.; Milazzo, R.; Zhu, H.; Li, Q.; Liu, Z.; Deng, J.; Xing, X. Switching Between Giant Positive and Negative Thermal Expansions of a YFe(CN)6-based Prussian Blue Analogue Induced by Guest Species. *Angewandte Chemie* **2017**, *129*, 9151-9156.

(103) Morelock, C. R.; Gallington, L. C.; Wilkinson, A. P. Evolution of Negative Thermal Expansion and Phase Transitions in $Sc_{1-x}Ti_xF_3$. *Chem. Mater.* **2014**, *26*, 1936-1940.

(104) Wang, T.; Xu, J.; Hu, L.; Wang, W.; Huang, R.; Han, F.; Pan, Z.; Deng, J.; Ren, Y.; Li, L.; Chen, J.; Xing, X. Tunable Thermal Expansion and Magnetism in Zr-doped ScF_3. *Appl. Phys. Lett* **2016**, *109*, 181901.

(105) Yang, C.; Zhang, Y.; Bai, J.; Qu, B.; Tong, P.; Wang, M.; Lin, J.; Zhang, R.; Tong, H.; Wu, Y.; Song, W.; Sun, Y. Crossover of Thermal Expansion from Positive to Negative by Removing the Excess Fluorines in Cubic ReO_3-type $TiZrF_{7-x}$. *J. Mater. Chem. C.* **2018**, *6*, 5148-5152.

(106) Grobler, I.; Smith, V. J.; Bhatt, P. M.; Herbert, S. A.; Barbour, L. J. Tunable Anisotropic Thermal Expansion of a Porous Zinc(II) Metal–Organic Framework. *Journal of the American Chemical Society* **2013**, *135*, 6411-6414.

(107) Balestra, S. R. G.; Bueno-Perez, R.; Hamad, S.; Dubbeldam, D.; Ruiz-Salvador, A. R.; Calero, S. Controlling Thermal Expansion: A Metal–Organic Frameworks Route. *Chem. Mater.* **2016**, *28*, 8296-8304.

(108) Bueken, B.; Van Velthoven, N.; Krajnc, A.; Smolders, S.; Taulelle, F.; Mellot-Draznieks, C.; Mali, G.; Bennett, T. D.; De Vos, D. Tackling the Defect Conundrum in UiO-66: A Mixed-Linker Approach to Engineering Missing Linker Defects. *Chemistry of Materials* **2017**.

(109) Park, J.; Wang, Z. U.; Sun, L.-B.; Chen, Y.-P.; Zhou, H.-C. Introduction of Functionalized Mesopores to Metal–Organic Frameworks via Metal–Ligand–Fragment Coassembly. *Journal of the American Chemical Society* **2012**, *134*, 20110-20116.

(110) Vermoortele, F.; Bueken, B.; Le Bars, G.; Van de Voorde, B.; Vandichel, M.; Houthoofd, K.; Vimont, A.; Daturi, M.; Waroquier, M.; Van Speybroeck, V.; Kirschhock, C.; De Vos, D. E. Synthesis Modulation as a Tool To Increase the Catalytic Activity of Metal–Organic Frameworks: The Unique Case of UiO-66(Zr). *Journal of the American Chemical Society* **2013**, *135*, 11465-11468.

(111) Barin, G.; Krungleviciute, V.; Gutov, O.; Hupp, J. T.; Yildirim, T.; Farha, O. K. Defect Creation by Linker Fragmentation in Metal–Organic Frameworks and Its Effects on Gas Uptake Properties. *Inorganic Chemistry* **2014**, *53*, 6914-6919.

(112) Balch, D. K.; Dunand, D. C. Copper-Zirconium Tungstate Composites Exhibiting Low and Negative Thermal Expansion Influenced by Reinforcement Phase Transformations. *Metall. Mater. Trans. A* **2004**, *35A*, 1159-1165.

(113) Morelock, C. R.; Suchomel, M. R.; Wilkinson, A. P. A cautionary tale on the use of GE-7031 varnish: Low temperature thermal expansion studies of ScF_3. *Journal of Applied Crystallography* **2013**, *46*, 823-825.

(114) Lecaplain, C.; Javerzac-Galy, C.; Gorodetsky, M. L.; Kippenberg, T. J. Mid-infrared ultra-high-Q resonators based on fluoride crystalline materials. *Nature communications* **2016**, *7*, 13383.

(115) Wang, S. F.; Zhang, J.; Luo, D. W.; Gu, F.; Tang, D. Y.; Dong, Z. L.; Tan, G. E. B.; Que, W. X.; Zhang, T. S.; Li, S.; Kong, L. B. Transparent ceramics: Processing, materials and applications. *Progress in Solid State Chemistry* **2013**, *41*, 20-54.

(116) Fang, H.; Dove, M. T. Pressure-induced softening as a common feature of framework structures with negative thermal expansion. *Physical Review B* **2013**, *87*, 214109.

(117) Cetinkol, M.; Greve, B. K.; Wilkinson, A. P.; Morelock, C. R. Pressure Depence of Thermal Expansion in TaO_2F and ScF_3. **manuscript in preparation**.

(118) Fang, H.; Dove, M. T. A phenomenological expression to describe the temperature dependence of pressure-induced softening in negative thermal expansion materials. *Journal of Physics-Condensed Matter* **2014**, *26*, 115402.

(119) Sanson, A. On the switching between negative and positive thermal expansion in framework materials. *Materials Research Letters* **2019**, *7*, 412-417.

(120) Chapman, K. W.; Chupas, P. J. Pressure Enhancement of Negative Thermal Expansion Behavior and Induced Framework Softening in Zinc Cyanide. *Journal of the American Chemical Society* **2007**, *129*, 10090-10091.

(121) Richet, P.; Gillet, P. Pressure-induced amorphization of minerals: a review. *Eur. J. Mineral.* **1997**, *9*, 907-933.

(122) Bahr, D. F.; Reid, J. A.; Mook, W. M.; Bauer, C. A.; Stumpf, R.; Skulan, A. J.; Moody, N. R.; Simmons, B. A.; Shindel, M. M.; Allendorf, M. D. Mechanical properties of cubic zinc carboxylate IRMOF-1 metal-organic framework crystals. *Physical Review B* **2007**, *76*, 184106.

(123) Biswas, M. M.; Cagin, T. High pressure structural transformation of selected metal organic frameworks – A theoretical investigation. *Materials Chemistry and Physics* **2011**, *131*, 44-51.

(124) Li, H.; Wang, K.; Sun, Y.; Lollar, C. T.; Li, J.; Zhou, H.-C. Recent advances in gas storage and separation using metal–organic frameworks. *Materials Today* **2018**, *21*, 108-121.

(125) Maurin, G.; Serre, C.; Cooper, A.; Férey, G. The new age of MOFs and of their porous-related solids. *Chemical Society Reviews* **2017**, *46*, 3104-3107.

(126) Martinez, C.; Corma, A. Inorganic molecular sieves: Preparation, modification and industrial application in catalytic processes. *Coordination Chemistry Reviews* **2011**, *255*, 1558-1580.

(127) Cheetham, A. K.; Ferey, G.; Loiseau, T. Open-framework inorganic materials. *Angewandte Chemie-International Edition* **1999**, *38*, 3268-3292.

(128) Flanigan, E. M.: Molecular Sieve Zeolites Technology: The First Twenty-Five Years. In *Zeolites: Science and Technology*; Springer, 1984; Vol. 80.

(129) Breck, D. W.: *Zeolite Molecular Sieves*; John Wiley and Sons: New York, 1974.

(130) Marwaha, A.; Dhir, A.; Mahla, S. K.; Mohapatra, S. K. An overview of solid base heterogeneous catalysts for biodiesel production. *Catalysis Reviews* **2018**, *60*, 594-628.

(131) Burtch, N. C.; Heinen, J.; Bennett, T. D.; Dubbeldam, D.; Allendorf, M. D. Mechanical Properties in Metal–Organic Frameworks: Emerging Opportunities and Challenges for Device Functionality and Technological Applications. *Advanced Materials*, *0*, 1704124.

(132) Flanigen, E. M.; Bennett, J. M.; Grose, R. W.; Cohen, J. P.; Patton, R. L.; Kirchner, R. M.; Smith, J. V. Silicalite, a new hydrophobic crystalline silica molecular sieve. *Nature* **1978**, *271*, 512-516.

(133) Yang, R. T.: *Gas Separation by Adsorption Processes*.

(134) Breck, D. W.; Eversole, W. G.; Milton, R. M.; Reed, T. B.; Thomas, T. L. Crystalline Zeolites. I. The Properties of a New Synthetic Zeolite, Type A. *Journal of the American Chemical Society* **1956**, *78*, 5963-5972.

(135) Weitkamp, J.; Fritz, M.; Ernst, S.: ZEOLITES AS MEDIA FOR HYDROGEN STORAGE. In *Proceedings from the Ninth International Zeolite Conference*; von Ballmoos, R., Higgins, J. B., Treacy, M. M. J., Eds.; Butterworth-Heinemann, 1993; pp 11-19.

(136) Simonyan, V. V.; Diep, P.; Johnson, J. K. Molecular simulation of hydrogen adsorption in charged single-walled carbon nanotubes. *The Journal of Chemical Physics* **1999**, *111*, 9778-9783.

(137) Armor, J. N. Emerging importance of shale gas to both the energy & chemicals landscape. *Journal of Energy Chemistry* **2013**, *22*, 21-26.

(138) Wu, H.; Zhou, W.; Yildirim, T. High-Capacity Methane Storage in Metal−Organic Frameworks M2(dhtp): The Important Role of Open Metal Sites. *Journal of the American Chemical Society* **2009**, *131*, 4995-5000.

(139) Chen, J.; Hu, L.; Deng, J.; Xing, X. Negative Thermal Expansion in Functional Materials: Controllable Thermal Expansion by Chemical Modifications. *Chem. Soc. Rev.* **2015**, *44*, 3522-3567.

(140) Attfield, J. P. Mechanisms and Materials for NTE. *Front. Chem. (Lausanne, Switz.)* **2018**, *6*, 6.

(141) Romao, C. P.; Miller, K. J.; Whitman, C. A.; White, M. A.; Marinkovic, B. A.: Negative Thermal Expansion (Thermomiotic) Materials. In *Comprehensive Inorganic Chemistry II*; Reedijk, J., Poeppelmeier, K. R., Eds.; Elsevier: Oxford, 2013; Vol. 4; pp 128-151.

(142) Takenaka, K. Progress of Research in Negative Thermal Expansion Materials: Paradigm Shift in the Control of Thermal Expansion. *Frontiers in Chemistry* **2018**, *6*.

(143) Coates, C. S.; Goodwin, A. L. How to Quantify Isotropic Negative Thermal Expansion: Magnitude, Range, or Both? *Materials Horizons* **2018**.

(144) Chen, J.; Nittala, K.; Forrester, J. S.; Jones, J. L.; Deng, J. X.; Yu, R. B.; Xing, X. R. The Role of Spontaneous Polarization in the Negative Thermal Expansion of Tetragonal $PbTiO_3$-Based Compounds. *Journal of the American Chemical Society* **2011**, *133*, 11114-11117.

(145) Azuma, M.; Chen, W. T.; Seki, H.; Czapski, M.; Olga, S.; Oka, K.; Mizumaki, M.; Watanuki, T.; Ishimatsu, N.; Kawamura, N.; Ishiwata, S.; Tucker, M. G.; Shimakawa, Y.; Attfield, J. P. Colossal negative thermal expansion in $BiNiO_3$ induced by intermetallic charge transfer. *Nature communications* **2011**, *2*, 347.

(146) Ikuya, Y.; Kazuki, T.; Kenya, O.; Naoaki, H.; Jungeun, K.; Naruki, T.; Ryoji, T.; Masafumi, M.; Norimasa, N.; Toru, I.; Tetsuo, I.; Kenichi, K.; Masaki, T.; Mikio, T. Giant Negative Thermal Expansion in the Iron Perovskite $SrCu_3Fe_4O_{12}$. *Angew. Chem. Int. Ed.* **2011**, *50*, 6579-6582.

(147) Mittal, R.; Gupta, M. K.; Chaplot, S. L. Phonons and Anomalous Thermal Expansion Behaviour in Crystalline Solids. *Prog. Mater. Sci.* **2018**, *92*, 360-445.

(148) Dove, M. T.; Fang, H. Negative thermal expansion and associated anomalous physical properties: review of the lattice dynamics theoretical foundation. *Reports on Progress in Physics* **2016**, *79*, 066503.

(149) Varga, T.; Wilkinson, A. P.; Jupe, A. C.; Lind, C.; Bassett, W. A.; Zha, C.-S. Pressure-induced amorphization of cubic ZrW_2O_8 studied in-situ and ex-situ by synchrotron x-ray absorption spectroscopy and diffraction. *Phys. Rev. B* **2005**, *72*, 024117.

(150) Hester, B. R.; Hancock, J. C.; Lapidus, S. H.; Wilkinson, A. P. Composition, Response to Pressure, and Negative Thermal Expansion in $M^{II}B^{IV}F_6$ (M = Ca, Mg; B = Zr, Nb). *Chem. Mater.* **2017**, *29*, 823-831.

(151) Morelock, C. R.; Gallington, L. C.; Wilkinson, A. P. Solid solubility, phase transitions, thermal expansion, and compressibility in $Sc_{1-x}Al_xF_3$. *Journal of Solid State Chemistry* **2015**, *222*, 96-102.

(152) Morelock, C. R.; Greve, B. K.; Gallington, L. C.; Chapman, K. W.; Wilkinson, A. P. Negative Thermal Expansion and Compressibility of $Sc_{1-x}Y_xF_3$ ($x < 0.25$). *Journal of Applied Physics* **2013**, *114*, 213501.

(153) Greve, B. K.; Martin, K. L.; Lee, P. L.; Chupas, P. J.; Chapman, K. W.; Wilkinson, A. P. Pronounced Negative Thermal Expansion from a Simple Structure: Cubic ScF_3. *J. Am. Chem. Soc.* **2010**, *132*, 15496-15498.

(154) Xu, J. L.; Hu, L.; Wang, L.; Deng, J. X.; Chen, J.; Xing, X. R. Controllable Thermal Expansion and Crystal Structure of (Fe1-xNix)ZrF6 Solid Solutions. *Acta Phys.-Chim. Sin.* **2018**, *34*, 339-343.

(155) Han, F.; Hu, L.; Liu, Z.; Li, Q.; Wang, T.; Ren, Y.; Deng, J.; Chen, J.; Xing, X. Local structure and controllable thermal expansion in the solid solution (Mn1-xNix)ZrF6. *Inorganic Chemistry Frontiers* **2017**.

(156) Hu, L.; Chen, J.; Xu, J.; Wang, N.; Han, F.; Ren, Y.; Pan, Z.; Rong, Y.; Huang, R.; Deng, J.; Li, L.; Xing, X. Atomic Linkage Flexibility Tuned Isotropic Negative, Zero, and Positive Thermal Expansion in $MZrF_6$ (M = Ca, Mn, Fe, Co, Ni, and Zn). *Journal of the American Chemical Society* **2016**, *138*, 14530-14533.

(157) Hu, L.; Chen, J.; Fan, L.; Ren, Y.; Huang, Q.; Sanson, A.; Jiang, Z.; Zhou, M.; Rong, Y.; Wang, Y.; Deng, J.; Xing, X. High-Curie-Temperature Ferromagnetism in $(Sc,Fe)F_3$ Fluorides and its Dependence on Chemical Valence. *Advanced Materials* **2015**, *27*, 4592-4596.

(158) Romao, C. P.; Morelock, C. R.; Johnson, M. B.; Zwanziger, J. W.; Wilkinson, A. P.; White, M. A. The heat capacities of thermomiotic ScF_3 and ScF_3–YF_3 solid solutions. *Journal of Materials Science* **2015**, *50*, 3409-3415.

(159) Occhialini, C. A.; Guzman-Verri, G. G.; Handunkanda, S. U.; Hancock, J. N. Negative Thermal Expansion Near the Precipice of Structural Stability in Open Perovskites. *Front. Chem. (Lausanne, Switz.)* **2018**, *6*, 14.

(160) Occhialini, C. A.; Handunkanda, S. U.; Said, A.; Trivedi, S.; Guzman-Verri, G. G.; Hancock, J. N. Negative thermal expansion near two structural quantum phase transitions. *Physical Review Materials* **2017**, *1*, 6.

(161) Handunkanda, S. U.; Curry, E. B.; Voronov, V.; Said, A. H.; Guzmán-Verri, G. G.; Brierley, R. T.; Littlewood, P. B.; Hancock, J. N. Large isotropic negative thermal expansion above a structural quantum phase transition. *Physical Review B* **2015**, *92*, 134101.

(162) Hu, L.; Qin, F.; Sanson, A.; Huang, L.-F.; Pan, Z.; Li, Q.; Sun, Q.; Wang, L.; Guo, F.; Aydemir, U.; Ren, Y.; Sun, C.; Deng, J.; Aquilanti, G.; Rondinelli, J. M.; Chen, J.; Xing, X. Localized Symmetry Breaking for Tuning Thermal Expansion in ScF3 Nanoscale Frameworks. *Journal of the American Chemical Society* **2018**.

(163) Yang, C.; Tong, P.; Lin, J. C.; Guo, X. G.; Zhang, K.; Wang, M.; Wu, Y.; Lin, S.; Huang, P. C.; Xu, W.; Song, W. H.; Sun, Y. P. Size effects on negative thermal expansion in cubic ScF3. *Applied Physics Letters* **2016**, *109*, 023110.

(164) Chen, J.; Gao, Q.; Sanson, A.; Jiang, X.; Huang, Q.; Carnera, A.; Rodriguez, C. G.; Olivi, L.; Wang, L.; Hu, L.; Lin, K.; Ren, Y.; Lin, Z.; Wang, C.; Gu, L.; Deng, J.; Attfield, J. P.; Xing, X. Tunable Thermal Expansion in Framework Materials through Redox Intercalation. *Nat. Commun.* **2017**, *8*, 14441.

(165) Poulain, M.; Lucas, J. The System MF_2 - ZrF_4 (M=Mg ,Mn, Fe, Co, Ni, Zn). The Fluorozirconates of the Cubic Rare Earths. *Rev. Chem. Miner.* **1975**, *12*, 9-16.

(166) Champarnaudmesjard, J. C.; Laval, J. P.; Gaudreau, B. Indium and Titanium Fluorozirconates. *Revue De Chimie Minerale* **1974**, *11*, 735-741.

(167) L'Helgoualch, H.; Poulain, M.; Rannou, J. P.; Lucas, J. Nonstoichiometric MY_{2+X} and MY_{3+X} Cubic Phases in the System ZrF_4/CaF_2. *C.R. Hebd. Seances Acad. Sci. Paris Serie C* **1971**, *272*, 1321-1324.

(168) Wang, T.; Xu, J.; Hu, L.; Wang, W.; Huang, R.; Han, F.; Pan, Z.; Deng, J.; Ren, Y.; Li, L.; Chen, J.; Xing, X. Tunable Thermal Expansion and Magnetism in Zr-Doped ScF_3. *Appl. Phys. Lett.* **2016**, *109*, 181901.

(169) Ticknor, J. O. Using Defects in Anion Excess Rhenium Trioxide Type Fluorides to Control Thermal Expansion; Ytterbium Zirconium Fluoride as a Case Study. B.Sc. research option thesis, Georgia Institute of Technology, 2017.

(170) Yang, C.; Zhang, Y.; Bai, J.; Qu, B.; Tong, P.; Wang, M.; Lin, J.; Zhang, R.; Tong, H.; Wu, Y.; Song, W.; Sun, Y. Crossover of thermal expansion from positive to

negative by removing the excess fluorines in cubic ReO_3-type $TiZrF_{7-x}$. *J. Mater. Chem. C* **2018**, *6*, 5148-5152.

(171) Yang, C.; Zhang, Y.; Bai, J.; Tong, P.; Lin, J.; Tong, H.; Zhang, L.; Wen, W.; Zhang, X.; Sun, Y. Isotropic Low Thermal Expansion over a Wide Temperature Range in $Ti_{1-x}Zr_xF_{3+x}$ ($0.1 \leq x \leq 0.5$) Solid Solutions. *Inorg. Chem.* **2018**.

(172) Angel, R. J. The High-Pressure, High-Tempertaure Equation of State of Calcium Fluoride, CaF_2. *J. Phys. Condens. Matter* **1993**, *5*, L141-L144.

(173) Larson, A. C.; Von Dreele, R. B.: *GSAS - General Structure Analysis System*; Report LA-UR-86-748: Los Alamos Laboratory, 1987.

(174) Toby, B. H. EXPGUI, a graphical user interface for GSAS. *J. Appl. Crystallogr.* **2001**, *34*, 210-213.

(175) Laval, J. P.; Frit, B.; Lucas, J. Crystal-Structure of the $\beta BaZr_2F_{10}$ Compound. Relations with the ReO_3-type and the Fluorozirconate Glasses. *J. Solid State Chem.* **1988**, *72*, 181-192.

(176) Laval, J. P.; Mayet, R. High-Temperature Monoclinic α-$SrHfF_6$, and Isostructural α-$SrZrF_6$: Associating Hf_2F_{12} Bipolyhedra and SrF_8 Snub Disphenoids. *Acta Crystallogr. Sect. C-Struct. Chem.* **2018**, *74*, 229-+.

(177) Laval, J. P. Crystal Chemistry of Anion-Excess ReO_3-Related Phases. III. γ-ZrF_4, a High-Pressure Form of Zirconium Tetrafluoride, and a Comparison of MX_4 Structure Types. *Acta Crystallogr. Sect. C-Struct. Chem.* **2014**, *70*, 742-U744.

(178) Papiernik, R.; Mercurio, D.; Frit, B. The Structure of Zirconium Tetrafluoride, α-ZrF_4. *Acta Crystallographica Section B-Structural Science* **1982**, *38*, 2347-2353.

(179) Angel, R. J.; Gonzalez-Platas, J.; Alvaro, M. EosFit7c and a Fortran module (library) for equation of state calculations. *Zeitschrift Fur Kristallographie* **2014**, *229*, 405-419.

(180) Fang, H.; Dove, M. T.; Phillips, A. E. Common origin of negative thermal expansion and other exotic properties in ceramic and hybrid materials. *Physical Review B* **2014**, *89*, 214103.

(181) Baxter, S. J.; Loske, K. V.; Lloyd Ii, A. J.; Wilkinson, A. P. Controlling the Phase Behavior of Low and Negative Thermal Expansion ReO3-Type Fluorides using Interstitial Anions: Sc1–xZrxF3+x. *Inorganic Chemistry* **2020**.

(182) Hu, L.; Chen, J.; Fan, L.; Ren, Y.; Rong, Y.; Pan, Z.; Deng, J.; Yu, R.; Xing, X. Zero Thermal Expansion and Ferromagnetism in Cubic $Sc_{1-x}M_xF_3$ (M = Ga, Fe) over a Wide Temperature Range. *Journal of the American Chemical Society* **2014**, *136*, 13566-13569.

(183) Han, F.; Chen, J.; Hu, L.; Ren, Y.; Rong, Y. C.; Pan, Z.; Deng, J. X.; Xing, X. R. The Distortion-Adjusted Change of Thermal Expansion Behavior of Cubic Magnetic Semiconductor $(Sc_{1-x}M_x)F_3$ (M = Al, Fe). *J. Am. Ceram. Soc.* **2016**, *99*, 2886-2888.

(184) Han, F.; Hu, L.; Liu, Z.; Li, Q.; Wang, T.; Ren, Y.; Deng, J.; Chen, J.; Xing, X. Local Structure and Controllable Thermal Expansion in the Solid Solution $(Mn_{1-x}Ni_x)ZrF_6$. *Inorg. Chem. Front.* **2017**, *4*, 343-347.

(185) Hester, B. R.; dos Santos, A. M.; Molaison, J. J.; Hancock, J. C.; Wilkinson, A. P. Synthesis of Defect Perovskites $(He_{2-x}\square_x)(CaZr)F_6$ by Inserting Helium into the Negative Thermal Expansion Material $CaZrF_6$. *Journal of the American Chemical Society* **2017**, *139*, 13284-13287.

(186) Yang, C.; Zhang, Y.; Bai, J.; Tong, P.; Lin, J.; Tong, H.; Zhang, L.; Wen, W.; Zhang, X.; Sun, Y. Isotropic Low Thermal Expansion over a Wide Temperature Range in $Ti_{1-x}Zr_xF_{3+x}$ ($0.1 \leq x \leq 0.5$) Solid Solutions. *Inorg. Chem.* **2018**, *57*, 14396-14400.

(187) Baxter, S. J.; Hester, B. R.; Wright, B. R.; Wilkinson, A. P. Controlling the Negative Thermal Expansion and Response to Pressure in ReO_3-type Fluorides by the Deliberate Introduction of Excess Fluoride: $Mg_{1-x}Zr_{1+x}F_{6+2x}$, x = 0.15, 0.30, 0.40, and 0.50. *Chem. Mater.* **2019**, *31*, 3440-3448.

(188) Toby, B. H.; Von Dreele, R. B. GSAS-II: The Genesis of a Modern Open-Source All Purpose Crystallography Software Package. *J. Appl. Crystallogr.* **2013**, *46*, 544-549.

(189) Gonzalez-Platas, J.; Alvaro, M.; Nestola, F.; Angel, R. EosFit7-GUI: a new graphical user interface for equation of state calculations, analyses and teaching. *Journal of Applied Crystallography* **2016**, *49*, 1377-1382.

(190) Shannon, R. D. Revised Effective Ionic Radii and Systematic Studies of Interatomic Distances in Halides and Chalcogenides. *Acta Cryst. A* **1976**, *32*, 751-767.

(191) Aleksandrov, K. S.; Voronov, V. N.; Vtyurin, A. N.; Goryainov, S. V.; Zamkova, N. G.; Zinenko, V. I.; Krylov, A. S. Lattice dynamics and hydrostatic-pressure-induced phase transitions in ScF3. *J. Exp. Theor. Phys.* **2002**, *94*, 977-984.

(192) Aleksandrov, K. S.; Voronov, V. N.; Vtyurin, A. N.; Goryainov, S. A.; Zamkova, N. G.; Zinenko, V. I.; Krylov, A. S. Pressure-induced phase transitions in ScF3 crystal-Raman spectra and lattice dynamics. *Ferroelectrics* **2003**, *284*, 205-219.

(193) Aleksandrov, K. S.; Voronov, V. N.; Vtyurin, A. N.; Krylov, A. S.; Molokeev, M. S.; Pavlovskii, M. S.; Goryainov, S. V.; Likhacheva, A. Y.; Ancharov, A. I. Pressure-induced phase transition in the cubic ScF3 crystal. *Phys. Solid State* **2009**, *51*, 810-816.

(194) Aleksandrov, K. S.; Voronov, N. V.; Vtyurin, A. N.; Krylov, A. S.; Molokeev, M. S.; Oreshonkov, A. S.; Goryainov, S. V.; Likhacheva, A. Y.; Ancharov, A.

I. Structure and lattice dynamics of the high-pressure phase in the ScF3 crystal. *Phys. Solid State* **2011**, *53*, 564-569.

(195) Kennedy, B. J.; Vogt, T. Powder X-ray diffraction study of the rhombohedral to cubic phase transition in TiF_3. *Materials Research Bulletin* **2002**, *37*, 77-83.

(196) Glazer, A. M. Classification of Tilted Octahedra in Perovskites. *Acta Crystallogr.* **1972**, *B28*, 3384-3392.

(197) Bendeliani, N. A.; Atabaeva, E. Y.; Agoshkov, V. M. Polymorphism of ScF_3 and Solid-Solutions based on it at High-Pressures. *Inorganic Materials* **1983**, *19*, 736-739.

(198) Aleksandrova, M. M.; Bendeliani, N. A.; Blank, V. D.; Dyuzheva, T. I. Phase-Transitions in ScF_3 Under Pressure at 300 K. *Inorganic Materials* **1990**, *26*, 1654-1657.

(199) Wilkinson, A. P.; Morelock, C. R.; Greve, B. K.; Jupe, A. C.; Chapman, K. W.; Chupas, P. J.; Kurtz, C. Reducing the background from pressure vessels using a BRIM. *Journal of Applied Crystallography* **2011**, *44*, 1047-1053.

(200) Hester, B. R. Negative Thermal Expansion, Behavior on Compression, and other Anomalous Behaviors in Rhenium Trioxide Structured Mixed Metal Fluorides. PhD thesis, Georgia Institute of Technology, 2019.

(201) Takenaka, K. Negative thermal expansion materials: technological key for control of thermal expansion. *Sci. Technol. Adv. Mater.* **2012**, *13*.

(202) Badrinarayanan, P.; Kessler, M. R. Zirconium tungstate/cyanate ester nanocomposites with tailored thermal expansivity. *Compos. Sci. Technol.* **2011**, *71*, 1385-1391.

(203) Balch, D. K.; Dunand, D. C. Copper-Zirconium Tungstate Composites Exhibiting Low and Negative Thermal Expansion Influenced by Reinforcement Phase Transformations. *Metall. Mater. Trans. A* **2004**, *35A*, 1159-1165.

(204) Della Gaspera, E.; Tucker, R.; Star, K.; Lan, E. H.; Ju, Y. S.; Dunn, B. Copper-Based Conductive Composites with Tailored Thermal Expansion. *ACS Appl. Mater. Interfaces* **2013**, *5*, 10966-10974.

(205) Holzer, H.; Dunand, D. C. Phase transformation and thermal expansion of Cu/ZrW_2O_8 metal matrix composites. *J. Mater. Res.* **1999**, *14*, 780-789.

(206) Jin, S.; Mavoori, H. Low-thermal-expansion copper composites via negative CTE metallic elements. *JOM* **1998**, *50*, 70-72.

(207) Lind, C.; Coleman, M. R.; Kozy, L. C.; Sharma, G. R. Zirconium tungstate/polymer nanocomposites: Challenges and opportunities. *Phys. Status Solidi B* **2011**, *248*, 123-129.

(208) Sigmund, O.; Torquato, S. Composites with extremal thermal expansion coefficients. *Appl. Phys. Lett.* **1996**, *69*, 3203-3205.

(209) Morelock, C. R.; Suchomel, M. R.; Wilkinson, A. P. A cautionary tale on the use of GE-7031 varnish: low-temperature thermal expansion studies of ScF_3. *J. Appl. Crystallogr.* **2013**, *46*.

(210) Yilmaz, S.; Dunand, D. C. Finite-element analysis of thermal expansion and thermal mismatch stresses in a Cu 60vol% ZrW_2O_8 composite. *Compos. Sci. Technol.* **2004**, *64*, 1895-1898.

(211) Tao, J. Z.; Sleight, A. W. The role of rigid unit modes in negative thermal expansion. *J. Solid State Chem.* **2003**, *173*, 442-448.

(212) Hu, L.; Chen, J.; Sanson, A.; Wu, H.; Guglieri Rodriguez, C.; Olivi, L.; Ren, Y.; Fan, L.; Deng, J.; Xing, X. New Insights into the Negative Thermal Expansion: Direct Experimental Evidence for the "Guitar-String" Effect in Cubic ScF_3. *J. Am. Chem. Soc.* **2016**, *138*, 8320-8323.

(213) Hancock, J. C.; Chapman, K. W.; Halder, G. J.; Morelock, C. R.; Kaplan, B. S.; Gallington, L. C.; Bongiorno, A.; Han, C.; Zhou, S.; Wilkinson, A. P. Large negative thermal expansion and anomalous behavior on compression in cubic ReO_3-type $A^{II}B^{IV}F_6$: $CaZrF_6$ and $CaHfF_6$. *Chem. Mater.* **2015**.

(214) Hester, B. R.; Wilkinson, A. P. Effects of Composition on Crystal Structure, Thermal Expansion, and Response to Pressure in ReO3-type MNbF6(M= Mn and Zn). *J. Solid State Chem.* **2018**.

(215) Baxter, S. J. H., B. R.; Wright, B. R.; and Wilkinson, A. P. Controlling the Negative Thermal Expansion and Response to Pressure in ReO_3-type Fluorides by the Deliberate Introduction of Excess Fluoride: $Mg_{2-x}Zr_xF_{4+2x}$. *In Publication Process* **2019**.

(216) Ticknor, J. O.; Hester, B. R.; Adkins, J. W.; Xu, W.; Yakovenko, A. A.; Wilkinson, A. P. Zero Thermal Expansion and Abrupt Amorphization on Compression in Anion Excess ReO_3-Type Cubic $YbZrF_7$. *Chem. Mater.* **2018**.

(217) Morelock, C. R.; Greve, B. K.; Gallington, L. C.; Chapman, K. W.; Wilkinson, A. P. Negative thermal expansion and compressibility of Sc1−xYxF3 ($x \leq 0.25$). *J. Appl. Phys.* **2013**, *114*, 213501.

(218) Poulian, M. P., Mi.; Lucas, J. . Les systemes MF2-ZrF4 (M = Mg, Mn, Fe, Co, Ni, Zn). Les fluorozirconates de terres rares cubiques. *Rev. Chim. Miner.* **1975**, *12*, 9.

(219) Poulain, M.; Poulain, M.; Lucas, J. Structure cristalline de SmZrF7. Relations structurales avec le type ReO3. *J. Solid State Chem.* **1973**, *8*, 132-141.

(220) Monteil, C.; Chassaing, J. Ternary Fluorides of Pentavalent Niobium and Alkaline Earth Elements. I. Fluorides $MNbF_7$ (M = Magnesium, Calcium). *Chemischer Informationsdienst* **1979**, *10*.

(221) Ticknor, J. O. Using Defects in Anion Excess Rhenium Trioxide Type Fluorides to Control Thermal Expansion; Ytterbium Zirconium Fluoride as a Case Study. Georgia Institute of Technology, 2017.

(222) Birch, F. Equation of state and thermodynamic parameters of sodium chloride to 300 kbar in the high-temperature domain. *J. Geophys. Res. B* **1986**, *91*, 4949-4954.

(223) Qiu, X.; Thompson, J. W.; Billinge, S. J. L. PDFgetX2: a GUI-driven program to obtain the pair distribution function from X-ray powder diffraction data. *J. Appl. Crystallogr.* **2004**, *37*, 678.

(224) Burtch, N. C.; Baxter, S. J.; Heinen, J.; Bird, A.; Schneemann, A.; Dubbeldam, D.; Wilkinson, A. P. Negative Thermal Expansion Design Strategies in a Diverse Series of Metal–Organic Frameworks. *Advanced Functional Materials* **2019**, *29*, 1904669.

(225) Bennett, T. D. B. T. D.; Keen, D. A.; Tan, J. C.; Barney, E. R.; Goodwin, A. L.; Cheetham, A. K. Thermal Amorphization of Zeolitic Imidazolate Frameworks. *Angewandte Chemie-International Edition* **2011**, *50*, 3067-3071.

(226) Bennett, T. D.; Simoncic, P.; Moggach, S. A.; Gozzo, F.; Macchi, P.; Keen, D. A.; Tan, J.-C.; Cheetham, A. K. Reversible pressure-induced amorphization of a zeolitic imidazolate framework (ZIF-4). *Chemical Communications* **2011**, *47*, 7983-7985.

(227) Baxter, S. J.; Schneemann, A.; Ready, A. D.; Wijeratne, P.; Wilkinson, A. P.; Burtch, N. C. Tuning Thermal Expansion in Metal–Organic Frameworks Using a Mixed Linker Solid Solution Approach. *Journal of the American Chemical Society* **2019**, *141*, 12849-12854.

(228) Evans, J. S. O.; Mary, T. A.; Sleight, A. W. NegativeThermal Expansion Materials. *Physica B* **1997**, *241-243*, 311-316.

(229) Porous Composite with Negative Thermal Expansion obtained by Photopolymer Additive Manufacturing. *APL Materials* **2015**, *3*, 076103.

(230) Hua, Y.; Ni, Q.-Q.; Yamanaka, A.; Teramoto, Y.; Natsuki, T. The Development of Composites with Negative Thermal Expansion Properties Using High Performance Fibers. *Adv. Compos. Mater.* **2011**, *20*, 463-475.

(231) Mittal, R.; Gupta, M. K.; Chaplot, S. L. Phonons and Anomalous Thermal Expansion Behaviour in Crystalline Solids. *Prog. Mater. Sci.* **2018**, *92*, 360-445.

(232) Chen, J.; Xing, X. R.; Sun, C.; Hu, P. G.; Yu, R. B.; Wang, X. W.; Li, L. H. Zero Thermal Expansion In $Pbtio_3$-Based Perovskites. *J. Am. Chem. Soc.* **2008**, *130*, 1144-+.

(233) Duyker, S. G.; Peterson, V. K.; Kearley, G. J.; Ramirez-Cuesta, A. J.; Kepert, C. J. Negative Thermal Expansion in $LnCo(CN)_6$ (Ln=La, Pr, Sm, Ho, Lu, Y): Mechanisms and Compositional Trends. *Angew. Chem. Int. Ed. Engl.* **2013**, *52*, 5266-5270.

(234) Korčok, J. L.; Leznoff, D. B. Thermal Expansion of Mercury(II) Cyanide and $HgCN(NO_3)$. *Polyhedron* **2013**, *52*, 72-77.

(235) Goodwin, A. L.; Chapman, K. W.; Kepert, C. J. Guest-Dependent Negative Thermal Expansion in Nanoporous Prussian Blue Analogues $(MPt^{IV})Pt^{II}(CN)_6.x\{H_2O\}$ (0 <= x <= 2; M = Zn, Cd). *J. Am. Chem. Soc.* **2005**, *127*, 17980-17981.

(236) Dubbeldam, D.; Walton, K. S.; Ellis, D. E.; Snurr, R. Q. Exceptional Negative Thermal Expansion in Isoreticular Metal-Organic Frameworks. *Angew. Chem. Int. Ed. Engl.* **2007**, *46*, 4496-4499.

(237) Zhou, W.; Wu, H.; Yildirim, T.; Simpson, J. R.; Walker, A. R. H. Origin of the Exceptional Negative Thermal Expansion in Metal-Organic Framework-5 Zn_4O(1,4-benzenedicarboxylate)$_3$. *Phys. Rev. B* **2008**, *78*, 054114.

(238) Lock, N.; Wu, Y.; Christensen, M.; Cameron, L. J.; Peterson, V. K.; Bridgeman, A. J.; Kepert, C. J.; Iversen, B. B. Elucidating Negative Thermal Expansion in MOF-5. *J. Phys. Chem. C* **2010**, *114*, 16181-16186.

(239) Wu, Y.; Peterson, V. K.; Luks, E.; Darwish, T. A.; Kepert, C. J. Interpenetration as a Mechanism for Negative Thermal Expansion in the Metal-Organic Framework $Cu_3(btb)_2$ (MOF-14). *Angew. Chem. Int. Ed. Engl.* **2014**, *53*, 5175-5178.

(240) Wu, Y.; Kobayashi, A.; Halder, Gregory J.; Peterson, Vanessa K.; Chapman, Karena W.; Lock, N.; Southon, Peter D.; Kepert, Cameron J. Negative Thermal Expansion in the Metal-Organic Framework Material Cu_3(1,3,5-benzenetricarboxylate)$_2$. *Angew. Chem. Int. Ed. Engl.* **2008**, *47*, 8929-8932.

(241) Liu, Z.; Gao, Q.; Chen, J.; Deng, J.; Lin, K.; Xing, X. Negative Thermal Expansion in Molecular Materials. *Chem. Commun.* **2018**, *54*, 5164-5176.

(242) Sapnik, A. F.; Geddes, H. S.; Reynolds, E. M.; Yeung, H. H. M.; Goodwin, A. L. Compositional Inhomogeneity and Tuneable Thermal Expansion in Mixed-Metal ZIF-8 Analogues. *Chem Commun.* **2018**, *54*, 9651-9654.

(243) O'Keeffe, M.; Yaghi, O. M. Deconstructing the Crystal Structures of Metal–Organic Frameworks and Related Materials into Their Underlying Nets. *Chem. Rev.* **2012**, *112*, 675-702.

(244) Burrows, A. D. Mixed-Component Metal–Organic Frameworks (Mc-MOFs): Enhancing Functionality Through Solid Solution Formation and Surface Modifications. *Crystengcomm* **2011**, *13*, 3623-3642.

(245) Schrimpf, W.; Jiang, J.; Ji, Z.; Hirschle, P.; Lamb, D. C.; Yaghi, O. M.; Wuttke, S. Chemical Diversity in a Metal–Organic Framework Revealed by Fluorescence Lifetime Imaging. *Nat. Commun.* **2018**, *9*, 1647.

(246) Han, S. S.; Goddard, W. A. Metal-Organic Frameworks Provide Large Negative Thermal Expansion Behavior. *J. Phys. Chem. C* **2007**, *111*, 15185-15191.

(247) Grobler, I.; Smith, V. J.; Bhatt, P. M.; Herbert, S. A.; Barbour, L. J. Tunable Anisotropic Thermal Expansion of a Porous Zinc(II) Metal–Organic Framework. *J. Am. Chem. Soc.* **2013**, *135*, 6411-6414.

(248) Dybtsev, D. N.; Chun, H.; Kim, K. Rigid and Flexible: A Highly Porous Metal–Organic Framework with Unusual Guest-Dependent Dynamic Behavior. *Angew. Chem. Int. Ed. Engl.* **2004**, *43*, 5033-5036.

(249) Burtch, N. C.; Dubbeldam, D.; Walton, K. S. Investigating water and framework dynamics in pillared MOFs. *Mol. Simulat.* **2015**, *41*, 1379-1387.

(250) Jasuja, H.; Burtch, N. C.; Huang, Y.-g.; Cai, Y.; Walton, K. S. Kinetic Water Stability of an Isostructural Family of Zinc-Based Pillared Metal–Organic Frameworks. *Langmuir* **2013**, *29*, 633-642.

(251) Schneemann, A.; Vervoorts, P.; Hante, I.; Tu, M.; Wannapaiboon, S.; Sternemann, C.; Paulus, M.; Wieland, D. C. F.; Henke, S.; Fischer, R. A. Different Breathing Mechanisms in Flexible Pillared-Layered Metal–Organic Frameworks: Impact of the Metal Center. *Chem. Mater.* **2018**, *30*, 1667-1676.

(252) Henke, S.; Schneemann, A.; Fischer, R. A. Massive Anisotropic Thermal Expansion and Thermo-Responsive Breathing in Metal–Organic Frameworks Modulated by Linker Functionalization. *Adv. Funct. Mater.* **2013**, *23*, 5990-5996.

(253) Burtch, N. C.; Walton, K. S. Modulating Adsorption and Stability Properties in Pillared Metal–Organic Frameworks: A Model System for Understanding Ligand Effects. *Acc. Chem. Res.* **2015**, *48*, 2850-2857.

(254) Wannapaiboon, S.; Schneemann, A.; Hante, I.; Tu, M.; Epp, K.; Semrau, A. L.; Sternemann, C.; Paulus, M.; Baxter, S. J.; Kieslich, G.; Fischer, R. A. Control of Structural Flexibility of Layered-Pillared Metal-Organic Frameworks Anchored at Surfaces. *Nat. Commun.* **2019**, *10*, 346.

(255) Schneemann, A.; Rudolf, R.; Baxter, S. J.; Vervoorts, P.; Hante, I.; Khaletskaya, K.; Henke, S.; Kieslich, G.; Fischer, R. A. Flexibility Control in Alkyl Ether-Functionalized Pillared-Layered Mofs by a Cu/Zn Mixed Metal Approach. *Dalton Trans.* **2019**, *48*, 6564-6570.

(256) Wu, Y. Understanding and Controlling Anomalous Thermal Expansion Behaviour in Coordination Framework Materials. Ph.D. Dissertation, University of Sydney, Sydney, Australia 2013. **2013**.

(257) Chun, H.; Dybtsev, D. N.; Kim, H.; Kim, K. Synthesis, X-ray Crystal Structures, and Gas Sorption Properties of Pillared Square Grid Nets Based on Paddle-Wheel Motifs: Implications for Hydrogen Storage in Porous Materials. *Chem.: Eur. J.* **2005**, *11*, 3521-3529.

(258) Chupas, P. J.; Chapman, K. W.; Kurtz, C.; Hanson, J. C.; Lee, P. L.; Grey, C. P. A Versatile Sample-Environment Cell for Non-Ambient X-Ray Scattering Experiments. *J Appl. Cryst.* **2008**, *41*, 822-824.

(259) Toby, B. H.; Von Dreele, R. B. GSAS-II: The Genesis of a Modern Open-Source All Purpose Crystallography Software Package. *J Appl. Cryst.* **2013**, *46*, 544-549.

(260) Jasuja, H.; Jiao, Y.; Burtch, N. C.; Huang, Y.-g.; Walton, K. S. Synthesis of Cobalt-, Nickel-, Copper-, and Zinc-Based, Water-Stable, Pillared Metal–Organic Frameworks. *Langmuir* **2014**, *30*, 14300-14307.

(261) Burtch, N. C.; Torres-Knoop, A.; Foo, G. S.; Leisen, J.; Sievers, C.; Ensing, B.; Dubbeldam, D.; Walton, K. S. Understanding DABCO Nanorotor Dynamics in Isostructural Metal–Organic Frameworks. *j. Phys. Chem. Lett.* **2015**, *6*, 812-816.

(262) Mitchell, R. H.: *Perovskites: Modern and Ancient*; Almaz Press Inc.: Thunder Bay, Ontario, Canada, 2002.

(263) Perovskite Structure Compounds. In *Handbook of Solid State Chemistry*; pp 221-250.

(264) Evans, H. A.; Wu, Y.; Seshadri, R.; Cheetham, A. K. Perovskite-related ReO3-type structures. *Nature Reviews Materials* **2020**.

(265) Vasala, S.; Karppinen, M. $A_2B'B''O_6$ perovskites: A review. *Prog. Solid State Chem.* **2015**, *43*, 1-36.

(266) Howard, C. J.; Kennedy, B. J.; Woodward, P. M. Ordered double perovskites - a group-theoretical analysis. *Acta Crystallographica Section B-Structural Science* **2003**, *59*, 463-471.

(267) Maughan, A. E.; Ganose, A. M.; Scanlon, D. O.; Neilson, J. R. Perspectives and Design Principles of Vacancy-Ordered Double Perovskite Halide Semiconductors. *Chem. Mater.* **2019**, *31*, 1184-1195.

(268) Glazer, A. M. A brief history of tilts. *Phase Transitions* **2011**, *84*, 405-420.

(269) Angel, R. J.; Zhao, J.; Ross, N. L. General rules for predicting phase transitions in perovskites due to octahedral tilting. *Physical Review Letters* **2005**, *95*, 4.

(270) Woodward, P. M. Octahedral tilting in perovskites .2. Structure stabilizing forces. *Acta Crystallographica Section B-Structural Science* **1997**, *53*, 44-66.

(271) Woodward, P. M. Octahedral tilting in perovskites .1. Geometrical considerations. *Acta Crystallographica Section B-Structural Science* **1997**, *53*, 32-43.

(272) Glazer, A. M. Simple Ways Of Determining Perovskite Structures. *Acta Crystallogr.* **1975**, *A31*, 756-762.

(273) Howard, C. J.; Stokes, H. T. Structures and phase transitions in perovskites - a group-theoretical approach. *Acta Crysatollgr.* **2005**, *A61*, 93-111.

(274) Cohen, R. E. Origin of ferroelectricity in perovskite oxides. *Nature* **1992**, *358*, 136-138.

(275) Tessier, F.; Le Gendre, L.; Chevire, F.; Marchand, R.; Navrotsky, A. Thermochemistry of a new class of materials containing dinitrogen pairs in an oxide matrix. *Chemistry of Materials* **2005**, *17*, 3570-3574.

(276) Le Gendre, L.; Marchand, R.; Piriou, B. Raman scattering investigations of dinitrogen entities in oxidized $LaTiO_2N$ perovskite. *European Journal of Solid State and Inorganic Chemistry* **1997**, *34*, 973-982.

(277) Mi, Q. X.; Ping, Y.; Li, Y.; Cao, B. F.; Brunschwig, B. S.; Khalifah, P. G.; Galli, G. A.; Gray, H. B.; Lewis, N. S. Thermally Stable N_2-Intercalated WO_3 Photoanodes for Water Oxidation. *Journal of the American Chemical Society* **2012**, *134*, 18318-18324.

(278) Goldschmidt, V. M. Die Gesetze der Krystallochemie. *Naturwissenschaften* **1926**, *14*, 477-485.

(279) Schaak, R. E.; Mallouk, T. E. Perovskites by Design: A Toolbox of Solid-State Reactions. *Chem. Mater.* **2002**, *14*, 1455-1471.

(280) Schwartz, R. W. Chemical solution Deposition of Perovskite Thin Films. *Chem. Mater.* **1997**, *9*, 2325-2340.

(281) Li, W.; Wang, Z.; Deschler, F.; Gao, S.; Friend, R. H.; Cheetham, A. K. Chemically diverse and multifunctional hybrid organic–inorganic perovskites. *Nature Reviews Materials* **2017**, *2*, 16099.

(282) Hester, B. Negative Thermal Expansion, Behavior on Compression, and Other Anomalous Behaviors in ReO3-Type Mixed Metal Fluorides. *Georgia Institute of Technology Theses* **2019**.

(283) Rivers, M.; Prakapenka, V. B.; Kubo, A.; Pullins, C.; Holl, C. M.; Jacobsen, S. D. The COMPRES/GSECARS gas-loading system for diamond anvil cells at the Advanced Photon Source. *High Pressure Res.* **2008**, *28*, 273-292.

(284) McDaniel, J. G., 2019.